

Society of Automotive Engineers
of China (SAE-China)

Editor

Proceedings of SAE-China Congress 2016: Selected Papers



Lecture Notes in Electrical Engineering

Volume 418

Board of Series editors

Leopoldo Angrisani, Napoli, Italy
Marco Arteaga, Coyoacán, México
Samarjit Chakraborty, München, Germany
Jiming Chen, Hangzhou, P.R. China
Tan Kay Chen, Singapore, Singapore
Rüdiger Dillmann, Karlsruhe, Germany
Haibin Duan, Beijing, China
Gianluigi Ferrari, Parma, Italy
Manuel Ferre, Madrid, Spain
Sandra Hirche, München, Germany
Faryar Jabbari, Irvine, USA
Janusz Kacprzyk, Warsaw, Poland
Alaa Khamis, New Cairo City, Egypt
Torsten Kroeger, Stanford, USA
Tan Cher Ming, Singapore, Singapore
Wolfgang Minker, Ulm, Germany
Pradeep Misra, Dayton, USA
Sebastian Möller, Berlin, Germany
Subhas Mukhopadhyay, Palmerston, New Zealand
Cun-Zheng Ning, Tempe, USA
Toyoaki Nishida, Sakyo-ku, Japan
Bijaya Ketan Panigrahi, New Delhi, India
Federica Pascucci, Roma, Italy
Tariq Samad, Minneapolis, USA
Gan Woon Seng, Nanyang Avenue, Singapore
Germano Veiga, Porto, Portugal
Haitao Wu, Beijing, China
Junjie James Zhang, Charlotte, USA

About this Series

“Lecture Notes in Electrical Engineering (LNEE)” is a book series which reports the latest research and developments in Electrical Engineering, namely:

- Communication, Networks, and Information Theory
- Computer Engineering
- Signal, Image, Speech and Information Processing
- Circuits and Systems
- Bioengineering

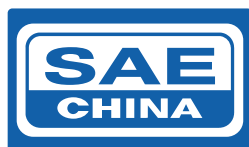
LNEE publishes authored monographs and contributed volumes which present cutting edge research information as well as new perspectives on classical fields, while maintaining Springer’s high standards of academic excellence. Also considered for publication are lecture materials, proceedings, and other related materials of exceptionally high quality and interest. The subject matter should be original and timely, reporting the latest research and developments in all areas of electrical engineering.

The audience for the books in LNEE consists of advanced level students, researchers, and industry professionals working at the forefront of their fields. Much like Springer’s other Lecture Notes series, LNEE will be distributed through Springer’s print and electronic publishing channels.

More information about this series at <http://www.springer.com/series/7818>

Society of Automotive Engineers
of China (SAE-China)
Editor

Proceedings of SAE-China Congress 2016: Selected Papers



 Springer

The Springer logo, which consists of a stylized white chess knight (horse) facing left, positioned above the word 'Springer' in a black serif font.

Editor
Society of Automotive Engineers of China
(SAE-China)
Beijing
China

ISSN 1876-1100 ISSN 1876-1119 (electronic)
Lecture Notes in Electrical Engineering
ISBN 978-981-10-3526-5 ISBN 978-981-10-3527-2 (eBook)
DOI 10.1007/978-981-10-3527-2

Library of Congress Control Number: 2016963192

© Springer Nature Singapore Pte Ltd. 2017

This work is subject to copyright. All rights are reserved by the Publisher, whether the whole or part of the material is concerned, specifically the rights of translation, reprinting, reuse of illustrations, recitation, broadcasting, reproduction on microfilms or in any other physical way, and transmission or information storage and retrieval, electronic adaptation, computer software, or by similar or dissimilar methodology now known or hereafter developed.

The use of general descriptive names, registered names, trademarks, service marks, etc. in this publication does not imply, even in the absence of a specific statement, that such names are exempt from the relevant protective laws and regulations and therefore free for general use.

The publisher, the authors and the editors are safe to assume that the advice and information in this book are believed to be true and accurate at the date of publication. Neither the publisher nor the authors or the editors give a warranty, express or implied, with respect to the material contained herein or for any errors or omissions that may have been made. The publisher remains neutral with regard to jurisdictional claims in published maps and institutional affiliations.

Printed on acid-free paper

This Springer imprint is published by Springer Nature
The registered company is Springer Nature Singapore Pte Ltd.
The registered company address is: 152 Beach Road, #21-01/04 Gateway East, Singapore 189721, Singapore

Contents

1	Effect of Compression Ratio on the Combustion Characteristics of Premixed Charge Induced Ignition for Diesel Engine	1
	Yujie Guo, Jianjun Zhu, Zhiwei Su, Wei Han and Zilong Wu	
2	Study of the Effect of Combustion Chamber Shapes on the Mixture Formation and Combustion Characteristic on CNG-DI Engine	9
	Tao Jiang, Xuedong Lin and Miao Yang	
3	Damage Risk Evaluation and Optimization for BIWS Spots-Weld	23
	Daolin Deng, Yu Zhang and Zhonghao Xu	
4	Fatigue Durability Analysis of a Frame Based on Multi Body Dynamics	31
	Qin Zhang, Fengchong Lan, Jiqing Chen and Qinsheng Huang	
5	Study on Calibration of Secondary Air Injection System in a V12 Engine	45
	Hongzhi Zhao, Wei Wang and Xiaofan Zhong	
6	Research on Soot Filtration and Pressure Drop Characteristics of DPF	55
	Ying Gao, Hongqi Liu, Wei Chen, Tieqiang Fu, Maodong Fang and Jun Li	
7	Research on the Present Situation and Factors of Volatile Organic Compounds in Car Cabin	67
	Jiabao Ren, Shujie Xu, Xuefeng Liu, Wei Liu and Enyou Cui	
8	Optimization Method of Low Exhaust Temperature Emissions of City Buses Meet China V	75
	Tengteng Li, Changyuan Wang, Kongjian Qin and Xiaojun Jing	

9	Analysis and Test Research for Three-Phase Short-Circuit of Permanent Magnet Synchronous Motor for an Electric Vehicle	83
	Sibo Wang, Chao Lu, Xiaoxu Wang and Huichao Zhao	
10	Based on an Improved Sliding Mode Observer for Position Estimation of PMSM	99
	Su Zhou, Daxiang Zhu and Zhe Hu	
11	Simulation Analysis and Research of C70GB Fuel Cell Vehicle	111
	Ping Chen, Chen Liang, Jiangqiu Li and Hongliang Jiang	
12	Electrochemical-Thermal Coupled Model of Lithium-Ion Batteries for Low Temperature Charging	123
	Peng Wu, Jan Romberg, Hao Ge, Yakun Zhang and Jianbo Zhang	
13	Research on Low Frequency Torque Ripple of In-wheel Motor of Four Wheel Independent Drive	133
	Zhe Li, Zheng Ling, Yue Ren, Yinong Li, Ke Wang and Zhenfei Zhan	
14	Relaxed Static Stability for All-Wheel-Drive Electric Vehicle Based on Yaw Moment Control	151
	Jun Ni and Jibin Hu	
15	Test Study on Characteristics of Multi-Hole Injector for Gasoline Direct Injection Engine	161
	Jujiang Liu, Hong Chen, Sicong Lin, Yuhuai Li, Lin Ye and Shuang Zhang	
16	Integrated Exhaust Manifold Type Cylinder Head Structure Design for Gravity Casting Process	171
	Ming Chen, Wenlei Yang, Tianyu Zhang, Donghang Liu and Hanqing Song	
17	Experimental Research on Macroscopic and Microscopic Characteristics of Ethanol-Fatty Acid Methyl Ester Blends Sprays	187
	Junge Li, Xiaocao Yu, Bin Liu, Tiegang Hu and Xibin Wang	
18	An Ultra-High Power Ignition System for EGR-Diluted GDI Engine	197
	Haifeng Lu, Liguang Li, Yintong Liu, Han Gao and Jiyu Shen	
19	Experimental and Simulated Study on the Cylinder Deactivation of Vehicle Gasoline Engine	207
	Shuhai Yu, Xingxing Ma, Zhigang Ma, Rui Liu and Dongxian Song	

20 Study on Effects of Multiple Injection at Intake Stroke on Combustion and Emissions of GDI Engine Under Warm Up Conditions 217
 Wei Dong, Chaojie Pu, Yao Sun, Litao Qiu and Bin Ma

21 Study of Start-Stop Technology on a GDI Engine 229
 Jin Li, Weifei Yu, Peng Zhou, Jianrui Zhang, Tao Chen, Pengyuan Sun and Hua Li

22 The Study of Friction and Wear Capability of Piston Ring Coatings 241
 Wenping Li and Yun Lu

23 Direct Injection Start-Stop Piston Final Stop Position Modelling and Analysis. 249
 Peng Zhou, Jin Li, Jianrui Zhang, Weifei Yu, Qingtao Si and Tuozhou Yu

24 Study on the Impact of Communication Imperfections on Forward Collision Warning and Avoidance Based on V2V Communications. 259
 Minghan Zhu, Hongmao Qin, Jianqiang Wang, Manjiang Hu, Keqiang Li and Zhouwei Kong

25 Wavelet-Based Demodulation Design for Vehicular Communication Network 271
 Yao Ge, Zhan Shu and David Daut

26 Research on Static Viscoelastic and Tribological Properties of PP-EPDM, PP-GF30 and ABS in Automobile 293
 Xiaojia Zhang, Lei Den, Changyong Lin and Bo Liu

27 Study of the Design and Torsion Performance for Carbon Fiber Composite Material Automobile Drive Shaft. 303
 Jiancai Liu, Yingguo Xian, Du Cao, Jianbo Su, Wei Liao, Mingde Ding and Zhong Su

28 Effect of Solution Treatment on Structure and Mechanical Properties of Fe–Mn–Al–Si Light Steel After Cold Rolling 313
 Liang Yao and Wen Shi

29 Damping Analysis and Test Research of a Composite Leaf Spring in a Light Bus. 327
 Wenku Shi, Chen Qian, Qianqian Song, Bo Gao and Jun Ke

30 Analysis on China’s Fuel Consumption Standards and Its Influences on Curb Weight 343
 Xiao Li, Fuquan Zhao, Han Hao and Zongwei Liu

31 Prediction and Study on the Influence of Propeller Shaft to Vehicle Noise Based on BP Neural Network	357
Yongjun Liu, Chaonan Xu, Weilong Niu, Xiuming Zhang and Jun Wei	
32 Optimization and Simulation of SUV Sunroof Buffeting Noise.	365
Xu Gong, Jun Wang, Chaoyi Deng, Penghui Wei, Bo Liu and Lin Li	
33 Semi-active Intake Structure Design and Vehicle Validation	375
Jie Li, Changjun Tan, Donglian Zhang, Shuo Zhang and Liang Yang	
34 Calculation and Application of Sound Insulation of the Vehicle Dash Panel	397
Cheng Peng, Feng Xu, Wei Pan, Min Sun and Yanghui Xu	
35 The Analysis for Casting Axle Cover Leakage	409
Jun Chang, Buliang Zhang, Zhiying Liu and Chuanlong Huang	
36 The Layout Design of Rearview Mirror Based on Vehicle Ergonomics	417
Yingying Xu, Hongfang Ling, Fang Qian, Yuyong Wang and Jianzi Huang	
37 Research on Curve Safety Speed Warning for Vehicle with Risk Prediction	431
Xian Qu, Feng Yu and Shu-en Zhao	
38 Multi Objective Optimization of Vehicle Crashworthiness Based on Combined Surrogate Models	447
Ling Zheng, Yinan Gao, Yinong Li and Zhenfei Zhan	
39 The Influences of Pre-impact Braking Scenarios on Occupant Restraint System During the Full Frontal Impact.	461
Hongyun Li, Chengyue Jiang, Dong Cui, Shugang Xie and Shuang Lu	
40 Rear Seat Belt Usage Models Using FARS and Field Data	469
Yang He, Zhan Shu, Yao Ge and Janice Daniel	
41 Study on Dynamic Torque PID Control for Automobile Diaphragm Spring Clutch Based on Kalman Filter	487
Chen Shao, Xue Bin Wu, Xin Zhang and Hong Wei Chen	

42 Research on Parameters Optimization of Transmission System of Military Off-Road Vehicle 499
 Bo Li, Xueyuan Li, Wei Wu, Junjie Zhou and Chaoheng Qin

43 Study on the Program Load Spectrum of the Suspension Fatigue Bench Test and Correlation 511
 Bing Rong, Zhengwen Tan, Pan Xiao, Yuanyuan Ma, Jianwen Zhou and Chaojie Liu

44 Fatigue Analysis of Car Body Structure Based on Transient Response 523
 Pengbo Wang

45 The Study on Fatigue Test of Cab With Suspension Based on 4-Channel Road Simulation Rig. 533
 Yunkai Gao, Genhai Wang and Jingpeng Han

46 Research on the Fluxless Brazing of Aluminum Air Cooled Oil Cooler 545
 Changxing Mei, Hao Liu, Xiaobo Mai, Yongjin Gao and Renzong Chen

47 Analysis of Manufacturing Technology for the Spherical Head Supporting Part. 557
 Sanhu Zhao, Laitao Zhai, Baoyang Song, Kai Cui, Yang Li and Bo Yu

48 Optimization of Design Parameters of Circular Burring 573
 Wenshan Fu, Yinzhi He and Chunyang Lu

49 Experimental Study on the Application of Hydrogen Detector in Engine Leak Detection. 581
 Qi Wang, Wei Zhu, Lei Chen and Sanyan Cao

50 Investigation on Induction Hardening Treatment of Cylindrical Drive Gear Shaft 589
 Bo Chen, Da-peng Wang, Hang-yu Li, Kai Cui and Bo Jiang

51 Research on Automatic Automobile Air-Conditioning Controller. 605
 Bo Yang, Mingming Wang, Ted S. Huang, Fei Peng and Cong Xin

52 Research on the Control Algorithm of EPS for Vehicle Handling Stability 613
 ChenXi Fang and Shang Liu

53 Research on Flux Weakening Speed Control Strategy for PMSM 629
Lei Qian, Haizhen Liu, Rui He and Weiwen Deng

54 A Study of Three-Way Catalyst Deterioration Monitoring 637
Song Yan, Tonghao Song and Tingwei Liu

55 Functional Safety System Design on EPS 647
Zhihong Wu, Xiezu Su, Yuan Zhu and Luke

Chapter 1

Effect of Compression Ratio on the Combustion Characteristics of Premixed Charge Induced Ignition for Diesel Engine

Yujie Guo, Jianjun Zhu, Zhiwei Su, Wei Han and Zilong Wu

Abstract In order to explore the combustion performance of premixed charge induced ignition for dual fuel engine, an experiment was undertaken on CY25TQ diesel engine to investigate the combustion and emission characteristics by changing the compression ratio. Experimental results show that under the condition of 1200 r/min, when the compression ratio is reduced from 16.9 to 15.4, and the premixed charge induced ignition leading to the start of combustion reaches the maximum delay to 1.5°CA ATDC, the biggest drops of maximum pressure, maximum pressure rise rate and peak of instantaneous heat release rate reach 52, 47 and 29% respectively. But the effective thermal efficiency declines 24%.

Keywords Premixed charge induced ignition · Methanol · F-T diesel · Compression ratio · Combustion

1.1 Introduction

China a country which is rich in coal resources, Coal-based methanol and F-T diesel as the high-level products of coal conversion, which are considered as the alternative fuel of engine that has value of application because the good combustion and emissions properties. When using the premixed charge induced ignition mode, coal-based methanol can be successfully applied to the compression ignition engine. It not only solves the problem that the low efficiency of the traditional gasoline engine, bur also solves the problem that the conventional diesel engine soot and NO_x cannot be reduced at the same time [1].

Y. Guo · J. Zhu (✉) · Z. Su · W. Han · Z. Wu
Department of Vehicle Engineering,
Taiyuan University of Technology, Taiyuan 030024, China
e-mail: nrjsys@163.com

© Springer Nature Singapore Pte Ltd. 2017
Society of Automotive Engineers of China (SAE-China), *Proceedings of SAE-China Congress 2016: Selected Papers*, Lecture Notes in Electrical Engineering 418,
DOI 10.1007/978-981-10-3527-2_1

The basic idea of premixed charge induced ignition mode is using high octane value and light volatile fuel as premixed mixture, and adding the high-cetane fuel in order to ignite the premixed mixture multi-point. Compared with the traditional spark ignition combustion mode, compression ignition combustion with direct injection mode can make the widespread ignition at the multi-point that will accelerate burn rate, get a higher isopycnal and improve the thermal efficiency of engine, thus can realize the domain objection of internal combustion engine energy conservation and environmental protection radically.

The research of Wang [2] about homogeneous charge induced ignition (HCCI) combustion mode showed that: HCCI combustion mode, even better than diesel engine at some operating conditions, can get a higher thermal efficiency. The experimental results of Yao [3] showed that: under the compound combustion mode, using methanol can significantly improve the combustion and engine thermal efficiency because of contain oxygen. Although both at home and abroad a lot of researches about premixed charge induced ignition mode have be conducted, but the problem that maximum pressure rise rate and combustion heat release rate are too high under such mode in heavy load cannot be solved. It restricts the application of premixed charge induced ignition mode in heavy load conditions. In order to improve the engine roughness which under premixed charge induced ignition mode, we use F-T diesel that high-cetane value and light volatile as well the high-cetane fuel coal-based methanol [4, 5] try to extend the range of upper and lower load of premixed charge induced ignition mode, combining with the change of the compression ratio to explore engine combustion characteristic.

1.2 Experimental Fuels, Apparatus and Procedures

Table 1.1 show the comparison of 0# diesel and F-T diesel, ignition delay of F-T diesel is shorter than 0# diesel, so well as the combustion noise. This is mainly related to the physical and chemical properties of itself. F-T diesel has high cetane number which contributed to decrease the ignition delay. Heat release of premixed combustion declined, but diffusion combustion improved [6]. The operating condition used in experiment is $n = 2000$ r/min, BMEP = 0.6 MPa (Table 1.2).

Table 1.1 The combustion parameters of the original diesel engine

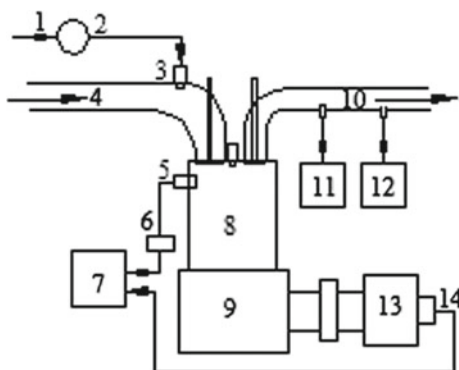
Fuel	0#	F-T
Maximum pressure (MPa)	8.2	5.7
Maximum pressure rise rate (MPa/°CA)	0.8	0.6
Peak of heat release (J/°CA)	163.4	103.8
Start of combustion (°CA)	-10.6	-13.2
Combustion duration (°CA)	51.2	56.6
Maximum combustion temperatures (°C)	1497	1407

Table 1.2 Major parameters of the test engine

Item	Parameter
Combustor type	ω
Bore \times stroke	115 \times 115 mm
Displacement	1.25 L
Compression ratio	17:1
Rated power	12.5 kW/(2200 r/min)
Maximum torque	63.8 N m/(1600 r/min)
Fuel supply advance angle	20 $^{\circ}$ CA BTDC

We applied premixed charge induced ignition mode on a single cylinder direct injection diesel engine, it controlled by measurement and control system. The combustion pressure in cylinder was obtained by cylinder pressure sensor and charge amplifier, and then we used the combustion analyzer to collect and analyze data (Fig. 1.1).

In this experiment, fuel supply advance angle was set in 20 $^{\circ}$ CA BTDC constantly, set the timing of methanol inject is 10 $^{\circ}$ CA BTDC, brake mean effective pressure is 0.6 MPa and the injection starting pressure of F-T diesel is 20 MPa. We tried to find the biggest methanol energy proportion that engine get the limit of misfire by adjusting the proportion of F-T diesel and methanol, then turning down the proportion of methanol and recording the methanol energy proportion multiple times in same operating condition. Finally, changing the compression ratio and repeat the steps above. The methanol energy proportion of different compression ratio is uncertain. We define the methanol energy proportion as the ratio of



1.Methanol 2. Controller 3.Injector 4.Intake 5. Cylinder Pressure Sensor
 6. Charge amplifier 7. Combustion analyzer 8. Cylinder 9. Engine 10. Exhaust
 11. Gas analyzer 12.FTIR 13. Dynamometer 14. Angle instrument

Fig. 1.1 Schematic diagram of experimental setup

methanol energy to total energy cost by operating cycle of engine. By changing the thickness of the cylinder gasket, thus the compression clearance would be changed in order to change the compression ratio in our experiment.

1.3 Results and Discussion

Figure 1.2 shows the effect of compression ratio on the maximum cylinder pressure and the peak value of initial heat release. With the decreasing of compression ratio, the maximum cylinder pressure drops dramatically, and the largest decline is more than 50% in low speed operating conditions. Decreasing when the peak value of initial heat release at low speed, it is greatly increasing at the high speed, and the biggest increase is more than 55%. The maximum cylinder pressure and maximum cylinder pressure with the increase of methanol energy proportion will go to a downward trend.

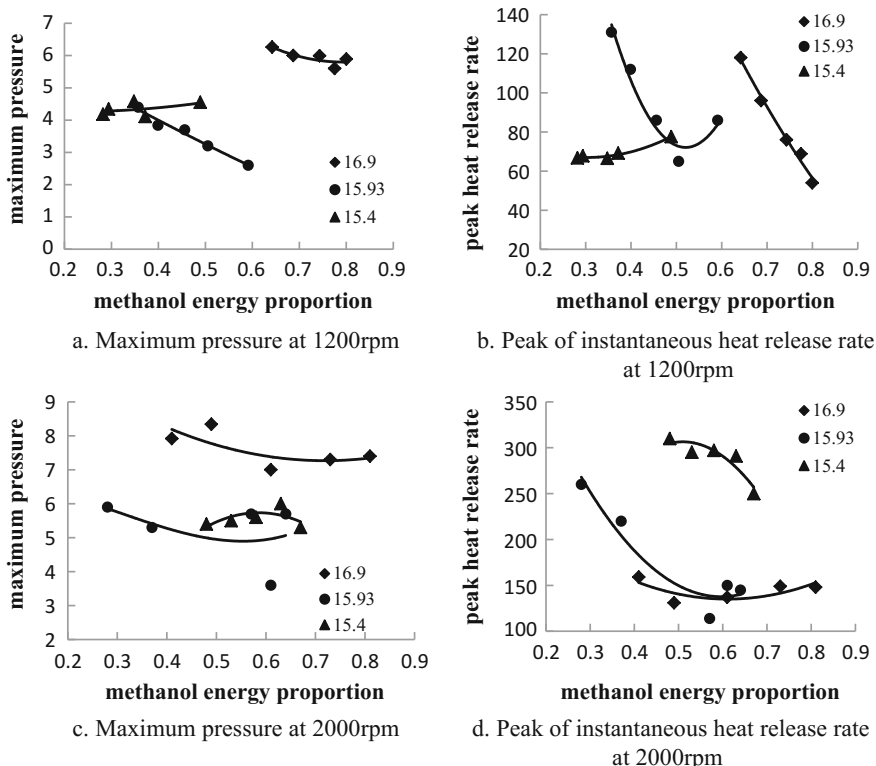


Fig. 1.2 Effects of compression ratio on maximum pressure and peak rate of instantaneous heat release

In the premixed charge induced ignition combustion mode, the maximum cylinder pressure is decided by two factors: the temperature in cylinder and the concentration of premixed mixture [7]. With the decrease of compress ratio and the increase of methanol energy proportion, which will cause the loss of the temperature in cylinder, delay the start timing of combustion. But with the increase of methanol energy proportion, and raising the ratio of premixed charge induced ignition in cylinder, it is helpful to accelerate combustion rate. The change of the maximum cylinder pressure is due to the two factors which affect the speed and timing of combustion. The main factors affecting the peak heat release rate are burning rate, combustion phase and the temperature in cylinder. At the faster of the burning rate, the start timing of combustion is more near the top dead center which leads to the increase of peak heat release rate. As the temperature of engine is low in low speed, the concentration of methanol premixed mixture is lower. And with the decrease of compression ratio aggravates the decline of temperature. They both result in the peak heat release rate decline. But in high speed operating mode, the temperature of engine is high, the time of combustion reaction in cylinder is shorter, and the center of heat release rate curve more closes to the top dead center. So the impact that reduces of compression ratio is less than the positive impact that combustion phase at peak heat release rate.

Figure 1.3 shows the effect of compression ratio on maximum pressure rise rate and the start timing of combustion. With the decrease of compression ratio and the increase of methanol energy proportion, the start timing of combustion is delayed, and the largest delay is 7°CA; In low speed operating conditions, the maximum pressure rise rate is at the downtrend in the process of the compression ratio of 16.9–15.4, and the combustion noise is decreasing. But the performance of high speed operating conditions is entirely different, the increase of methanol energy proportion is negative to improve of maximum pressure rise rate.

That is due to the start timing of combustion which depends on the fuel quality and the thermal condition state of compression process in cylinder. With the decreasing compression ratio, the lower pressure in cylinder leads to the temperature of ignition limit raise. Although the F-T diesel has high cetane number, fuel evaporation is better than diesel. But with the methanol injected into the cylinder, it absorbs a lot of heat in the process of evaporation, resulting in the lower temperature of cylinder which decreases the peak heat release rate and prolongs the ignition delay [4, 8, 9], and finally delays the start timing of combustion. Due to reduce the compression ratio by increasing the clearance volume in our experiment, with the compression ratio reduced, and the start timing of combustion near the top dead center, cycle thermal efficiency of engine is higher. But the physical reaction time in cylinder is long at low speed, the rate of heat removal determines the change of the maximum pressure rise rate. In high speed operating condition, the positive impact of start timing of combustion delay is bigger than the negative impact of temperature decreased on maximum pressure rise rate. When the methanol energy proportion is low, the latent heat of vaporization of methanol has little influence on temperature in cylinder. Therefore when the temperature of cylinder at a high level, it is helpful to accelerate combustion heat release.

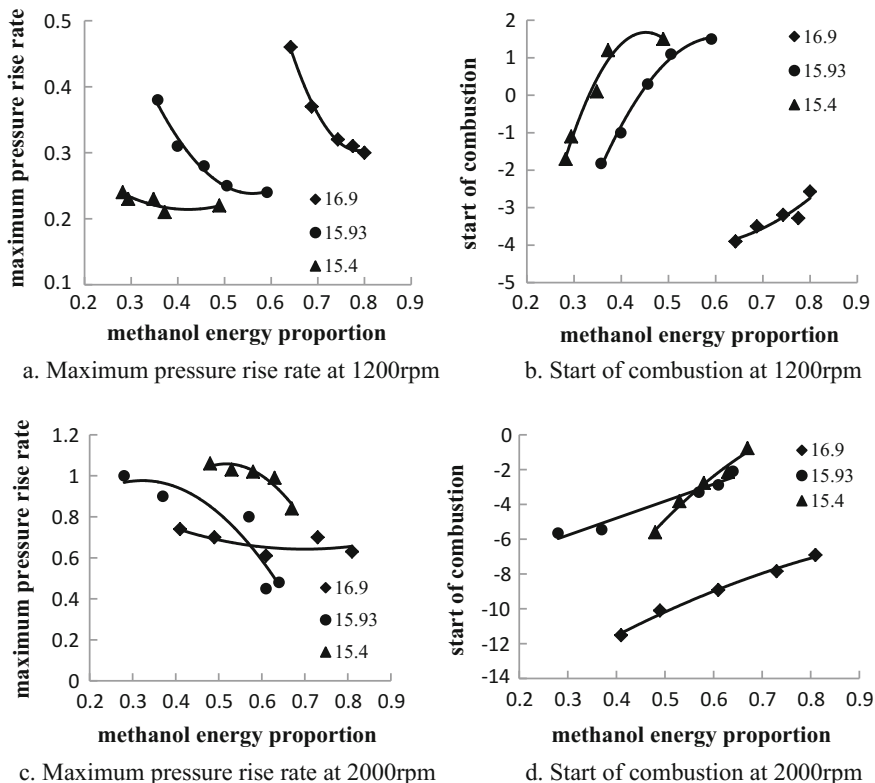


Fig. 1.3 Effects of compression ratio on maximum pressure rise rate and start of combustion

Figure 1.4 reflects the effective thermal efficiency varies with the change of the compression ratio. At low speed, the effective thermal efficiency decreases with the reduction of the compression ratio; At high speed, compression ratio decreases from 16.9 to 15.9, while the effective thermal efficiency is decreased slightly about 5%; But when the compression ratio continues to reduce to 15.4, the effective thermal efficiency will greatly decreased, and the largest drop of 42%, thus the engine fuel economy will be decreased. What is more, compared with the ratio of 15.4, with the increase of methanol energy proportion, the change of effective thermal efficiency is quite different from that of the middle and high compression ratio, and it is in a downward trend.

Because the effective thermal efficiency is not only affected by the compression ratio, but also the isopycnal of the combustion in cylinder. With the decrease of compression ratio, both the temperature in cylinder and brake thermal efficiency are reduced. Figure 1.3d shows that: when compression ratio reduces to 15.4 again in high speed, and the latest start timing of combustion reaches to 1°CA BTDC, it is

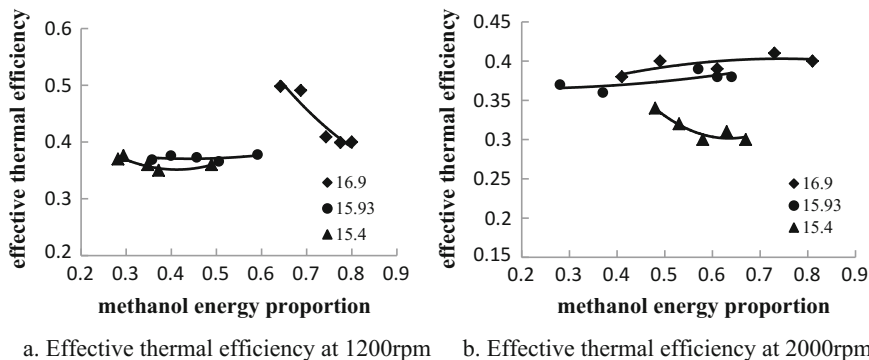


Fig. 1.4 Effects of compression ratio on effective thermal efficiency

very close to the top dead center. Besides, with the increase of methanol energy proportion, the center of combustion heat release is moved back, the combustion efficiency declined and the brake thermal efficiency decreased significantly.

1.4 Summary

- (1) The engine uses premixed charge induced ignition combustion mode, when in the process of compression ratio reduced from 16.9 to 15.4, brake thermal efficiency has a downward trend, and the biggest drop reached 24%, leading to the decrease of the engine economical efficiency.
- (2) With the decrease of compression ratio, the start timing of combustion is delayed, and the largest delay is 7°C_A, which almost near the top dead center; The peak heat release rate is increased in high speed, and the largest increase is 55%; It also leads to the temperature in cylinder and the maximum pressure rise rate raise, which are easy to cause running harshly of engine; Combustion duration shows a rises first and fall later trend.

References

1. Zou H, Wang L, Liu S et al (2007) Effect of pilot diesel quantity on the performance and emissions of dual fuel engine operating with methanol and diesel. *Trans CSICE* 25(5):422–427
2. Jiang H, Wang J, Shuai S et al (2005) Visualization and performance analysis of gasoline homogeneous charge induced ignition by diesel. In: SAE paper, society of automotive engineers, Warrendale Pennsylvania, USA, 2005-01-0136
3. Yao C, Dai Q, Xu H et al (2012) Ignition and combustion characteristics of diesel spray in premixed methanol/air mixture with high temperature. *J Combust Sci Technol* 18(3):193–198

4. Huang Y, Zhou L, Jiang D et al (2005) Study and development of Fischer-Tropsch(F-T)diesel fuel as a clean alternative fuel for diesel engines. *Chin Intern Combust Engine Eng* 26(5):18–23
5. Liu L, Song C, Zhu G et al (2011) Effects of F-T diesel fuel on the performance and emission characteristics of diesel engine with a high-pressure common rail system. *J Fuel Chem Technol* 39(1):75–80
6. Huang Y, Li Y, Ren J et al (2005) Combustion and emission characteristics of a direct injection diesel engine operating on Fischer-Tropsch diesel fuel. *J Fuel Chem Technol* 33(4):492–496
7. Wang J, Shuai S (2011) *Automotive engine fundamentals*. Tsinghua University Press, Beijing, pp 182–186, 343–344
8. Wang L, Liu S, Zou H et al (2007) Combustion and emission characteristics of a DI engine operating on high proportion of methanol-diesel dual fuel. *J Xi'an Jiaotong Univ* 41(1):14–17
9. Sridhar G, Dasappa S, Sridhar H et al (2005) Gaseous emissions using producer gas as fuel in reciprocating engines. In: SAE paper, society of automotive engineers, Warrendale Pennsylvania, USA, 2005-01-1732

Chapter 2

Study of the Effect of Combustion Chamber Shapes on the Mixture Formation and Combustion Characteristic on CNG-DI Engine

Tao Jiang, Xuedong Lin and Miao Yang

Abstract A combustion system model of CNG-DI engine which was modified from a 2.0 L diesel engine was built with software FIRE, the turbulence combustion model of CNG-DI engine was verified with the experimental result of CNG-DI optical engine, on the condition of unchanged 4 valves structure of original engine and the jet location, the spark plug was arranged between the two exhaust valves, the effect of different combustion chamber shapes on the microscopic physical fields such as turbulence characteristic in cylinder was simulated and studied, based on which the effect of combustion chamber shapes on the formation and combustion of mixture and the formation rule of NO was researched. The result shows that the combustion shape has a tremendous influence on the turbulence characteristic of cylinder and distribution characteristics of concentration fields especially besides the spark plug, which plays a decisive role on the whole process of combustion; Not only the production of NO can be inhibited and the combustion propagation speed which is in favour of lean burn can be controlled effectively when the straight mouth combustion chamber was used at the bottom of which has a proper embossment. The amount of NO is closely related to the size of the reaction area and the duration of reaction besides the reaction rate of NO when the CNG fuel is injected into cylinder directly and burned thin, which can be controlled by the rational design of the structure of combustion chamber.

Keywords CNG-DI engine · Lean burn · Injection mode · Mixture formation mechanism · Flame propagation characteristic · NO_x formation rule

The technological development planned project of Jilin province (2015101032JC).

T. Jiang · X. Lin (✉) · M. Yang
State Key Laboratory of Automotive Simulation and Control,
Jilin University, Changchun 130022, China
e-mail: xdlin@jlu.edu.cn

© Springer Nature Singapore Pte Ltd. 2017
Society of Automotive Engineers of China (SAE-China), *Proceedings of SAE-China Congress 2016: Selected Papers*, Lecture Notes in Electrical Engineering 418,
DOI 10.1007/978-981-10-3527-2_2

The diversification of energy sources and lean combustion technology in cylinder has been the trend of vehicle engine with the development of automobile low-carbon. The natural gas has been one of the widely used automotive alternative fuels comparative maturity technically due to its high H/C ratio, clean combustion, low HC, CO and CO₂ and abundant reserves [1]. The development of low-carbon has been effected directly by the loss of volumetric efficiency when the natural gas is injected in intake port, the output power loss of the low heat value of mixture [2]. CNG-DI lean combustion technology is the effectively way to the question [3, 4]. How to improve the combustion stability and reduce the NO production at the same time is the core problem of the CNG-DI lean combustion. The mixture formation mechanism, flame propagation characteristic of lean combustion and NO formation law is the key to deal with the core problem of the lean combustion of CNG-DI engine when the lean combustion of CNG fuel in cylinder is organized.

In the recent years, the combustion characteristic of CNG engine and the effect of flow characteristic on the combustion process of natural gas is thorough researched domestic and overseas [5–7]. But the report of the study the mixture formation mechanism and its influence factor is rare.

In this paper, the effect of different combustion chamber shape on the micro physical field of two gas flow in cylinder and its dynamic distribution characteristic was researched when the 2.0 L DI engine with 4 valves and 4 cylinders was instead with CNG-DI engine with software FIRE base on the optical research of flame propagation characteristic of lean combustion carried out in CNG-DI experimental prototype, based on which the mixture formation law, lean combustion characteristic and NO_x formation law of CNG-DI engine was studied.

2.1 Research Condition and Method

2.1.1 Research Condition of Optical Engine

The main technically parameter of single-cylinder optical prototype used for model validation is shown as Table 2.1. The arrangement diagram of optical test system for the observation of flame propagation characteristic in optical prototype is shown as Fig. 2.1. The arrangement diagram of spark plug and injector is shown as Fig. 2.2, two injector and two spark plug was arranged in the cylinder head; The air intake and exhaust system was arranged in the side of cylinder head for the

Table 2.1 Technical parameters of experimental prototype

Type	Four
Cylinder diameter/mm	135
Stroke/mm	280
Displacement/L	4.0
Compression ratio	6.13

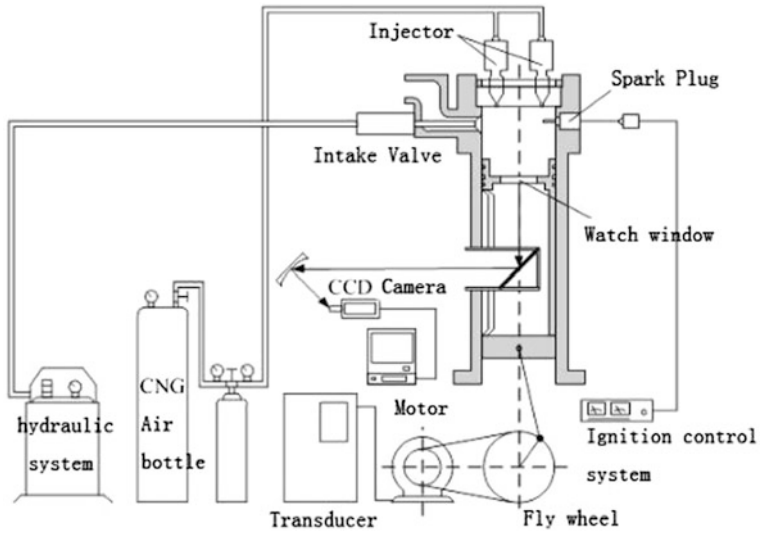


Fig. 2.1 The diagram of experiment facilities

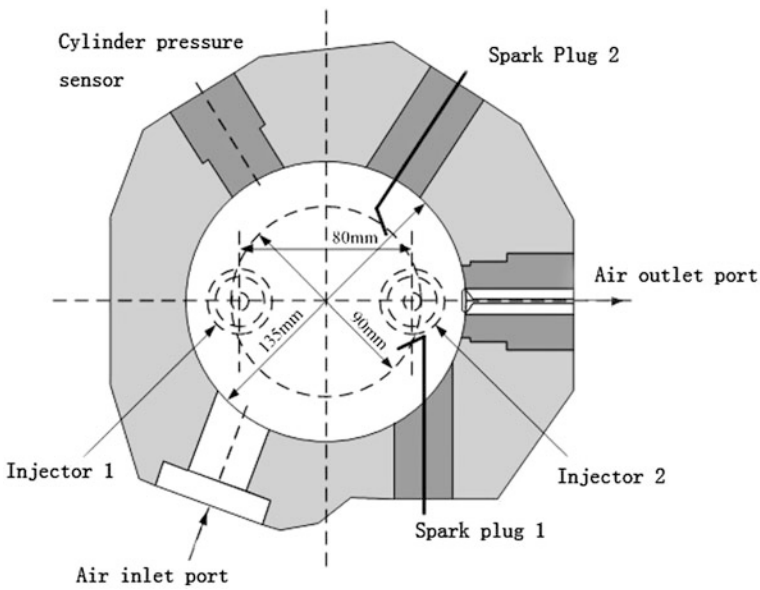


Fig. 2.2 The diagram of the location of spark plug and injector

Table 2.2 The main composition of natural gas fuel

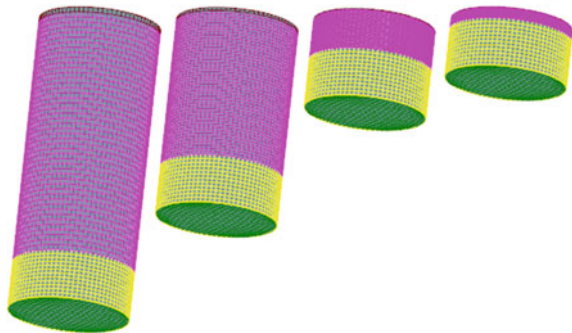
	CH ₄	C ₂ H ₆	C ₃ H ₈	C ₄ H ₁₀	N ₂
vol%	85.45	4.51	3.39	3.71	2.94

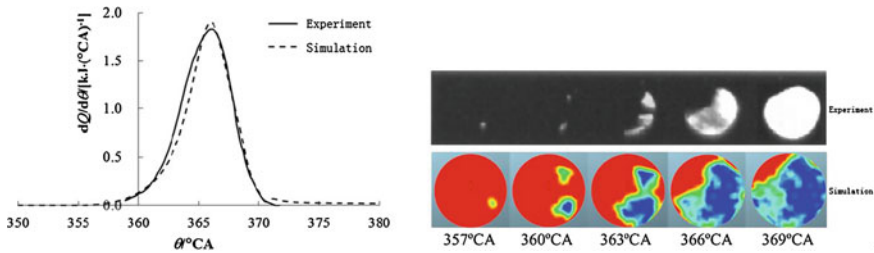
convenience of adjustment of intake eddy, which caused the large of clearance volume, so the combustion ratio was 6.13; The engine rotate speed was 200 r/min which was limited by the characteristic of prototype structural features, but the fundamental research of flame propagation mechanism would not be influenced. The main composition of natural gas was shown as Table 2.2.

The intake vortex intensity was adjusted by the offset of intake axis relative to the center line of cylinder. The initial air flow intensity was improved as high as possible by the adjustment of intake swirl ratio to $sw = 6.0$ according to the low engine rotate speed. The swirl injector was adopted in the experiment, the injection pressure was 5 MPa. The flame propagation process was continuous recorded in 563 picture/s with CCD high-speed camera. The made up indicated diagram was the average result of cylinder pressure measured 10 times in every working condition.

2.1.2 The Simulation Condition and Validation

The flame propagation characteristic and indicator diagram was measured with CNG optical engine to validate the cylinder turbulence and combustion model of CNG-DI engine, then a cylindrical combustion system model was generated directly without the change of compression ratio with software FIRE based on the structure characteristic of optical engine to bring combustion chamber shape into correspondence with prototype. The duration from intake stroke BDC to power stroke BDC was divided into four layers mesh based on the variation law of cylinder volume during the working process of engine was shown as Fig. 2.3.

Fig. 2.3 Simulation mesh



a)The comparison of heat release rate b)The comparison of flame propagation

Fig. 2.4 The comparison of experiment and simulation result

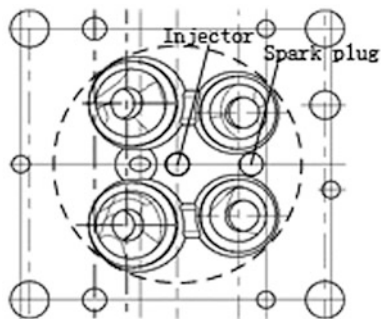
The 0.5°CA was adopted during the injection and combustion period and 1°CA was adopted during the expansion period for simulation time step; The $k-\zeta-f$ model was adopted as turbulence model, the ECFM model was adopted as combustion model and O'Rourke model was adopted as turbulence diffusion model based on the characteristic of CNG gas fuel.

The air flow state of the entrance of the cylinder was supposed uniform and the measured value was adopted as the simulation boundary condition, the average intake pressure was 0.9 bar, the temperature was 350 K; The top of piston was supposed to be the moving boundary and the temperature of which was 593 K, the cylinder wall and the bottom if cylinder head was supposed to be the fixed boundary, the temperature of cylinder wall was 403 K and the temperature of the bottom of cylinder head was 593 K. The comparison of the measured value of heat release rate and flame propagation speed with the simulation result was when the equivalence ratio was $\phi = 0.93$, two point ignition and ignition timing was $(\theta_{i1}, \theta_{i2}) = (-4, -3)^{\circ}\text{CA}$, two injector and injection timing was $\theta_{inj} = -120^{\circ}\text{CA}$ was shown as Fig. 2.4. The result shows that the simulation result and experimental result was in good agreement, which indicates that the built simulation model and algorithm is in accord with actual mixture formation and flame propagation of CNG fuel.

2.1.3 The Technically Condition and Research Program of Prototype

The basic structure of prototype remains unchanged when the 2.0 L DI diesel engine was instead with CNG-Di engine, only the compression ratio was changed from 17.2 to 12 and the improved design was proceed in combustion chamber shape. The arrangement of injector and spark plug was shown as Fig. 2.5 based on the characteristic of 4 air valve structure of original engine. The 6 different kinds of combustion chamber shape was designed aimed at the scheme of injector in center and spark plug in exhaust valve. Among them, the structure of I type combustion

Fig. 2.5 The diagram of injector and spark plug



chamber keep the same as the original diesel engine type; The throat ratio of II type combustion chamber was changed to 1 compared to I type combustion chamber; The throat combustion chamber was changed to dispark one in III type combustion chamber. The effect of throat shape on the mixture formation mechanism was studied on these three combustion chamber; The shape of the bottom of combustion chamber was changed on the fundamental of Straight Port combustion chamber in IV–V combustion chamber: The shallow convex shape in bottom for IV type combustion chamber, flat bottom in V type combustion chamber and flat in piston top for VI type combustion chamber, based which the effect of combustion chamber shape in bottom on mixture formation mechanism was studied.

The establishment of mesh structure model, simulation method and simulation model of simulation prototype was in accordance with the optical prototype, while the simulation boundary condition was confirmed by the measured result during the experimental study of 2.0 L diesel engine. The main technical parameter and simulation condition of simulation prototype was shown in Table 2.3. The maximum torque engine speed working condition was selected as simulation working condition, the cycle injection quantity was supposed to be 34.77 mg, the injection timing was supposed to be 158°CA BTDC and the ignition timing was 6°CA BTDC (Fig. 2.6).

2.2 Simulation Result and Analysis

2.2.1 *The Effect of Combustion Chamber on Turbulence Characteristic in Cylinder*

The effect of different combustion chamber on turbulence characteristic in cylinder when the injection timing was 158°CA BTDC and injection ending timing was 10°CA BTDC of CNG fuel was shown as Fig. 2.7; The TKE in cylinder increased quickly at the start period of injection increased quickly due to the input jet kinetic energy of the certain amount of injected fuel gas during the early stage of

Table 2.3 The technical parameter and simulation condition

<i>The technical parameter</i>	
Type	2.0L 4 cylinder CNG-DI engine
Cylinder bore × stroke	83 × 92/mm
Compression ratio	17.2
Rated power	100 kW/(3800 r/min)
The maximum torque	310 Nm/(2200 r/min)
<i>The simulation working condition</i>	
Rotate speed	2200 r/min
Jet mass	34.8 mg
Injection timing	158°CA BTDC
Injection duration	148°CA
Ignition timing	6°CA BTDC
<i>The simulation condition</i>	
Pressure in the entrance	1.08 bar
Induction swirl ratio	2
The initial TKE	33.443 m ² /s ²
Temperature in piston top	553 K
Cylinder wall	403 K
Cylinder head	403 K

compression stroke, which decreased quickly with the development of compression stroke after peak value. The variation law of TKE would be different due to the different combustion chamber shape with the same jet kinetic energy. The increasing rate of TKE in I type combustion chamber was the fast during the early stage of injection and the peak value of which was the highest; The increasing rate and peak value of TKE in II type combustion chamber decreased obviously. The degree of attenuation of average TKE was different due to the different air flow state in different combustion chamber during the middle stage of compression stroke (270–320°CA). The distribution of cylinder air flow state in different combustion chamber at 300°CA was shown in Fig. 2.8. The turbulence intensity decreased slowly due to the entirely tumble of air flow in the top of piston and air flow in the III and VI type combustion chamber, while the air flow motion state was reverse in other type of combustion chamber(MIVV), so the turbulence intensity decreased quickly. The cylinder clearance volume could be ignored near the end of compression stroke(320–360°CA), the air flow was focused on the combustion chamber; The top of piston of VI type combustion chamber was flat, the turbulence intensity was higher due to the directly compression of tumble in cylinder at the end of the compression stroke; The peak value of turbulence I type combustion chamber with lug boss at the bottom of throat at the early stage of compression stroke was the highest but was weakest at end of the compression process, while the turbulence intensity of I type combustion remained the same level with V type combustion chamber with Straight mouth flat at the end of compression process; The degree of attenuation of turbulence intensity could be improved at the end of compression

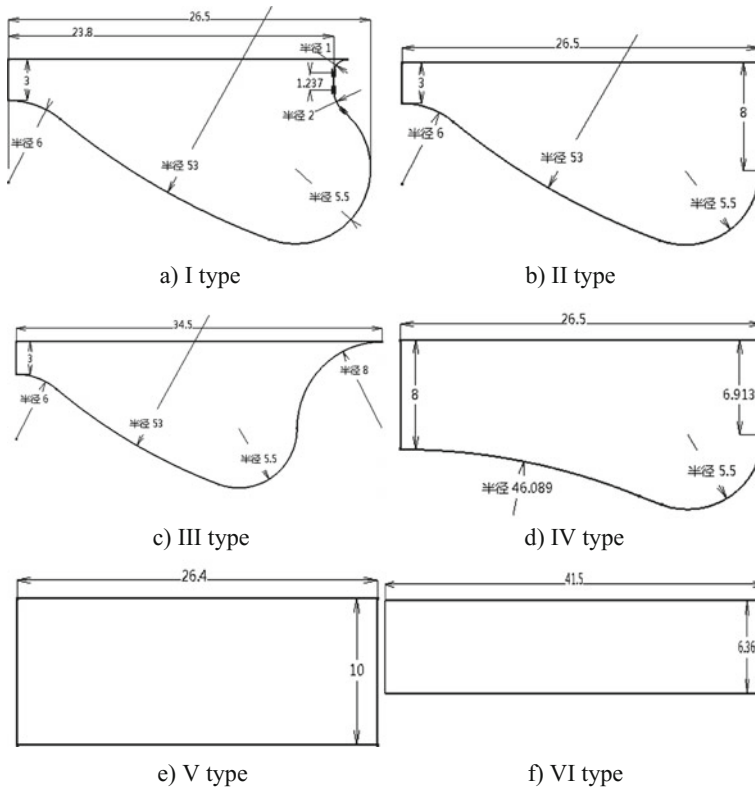
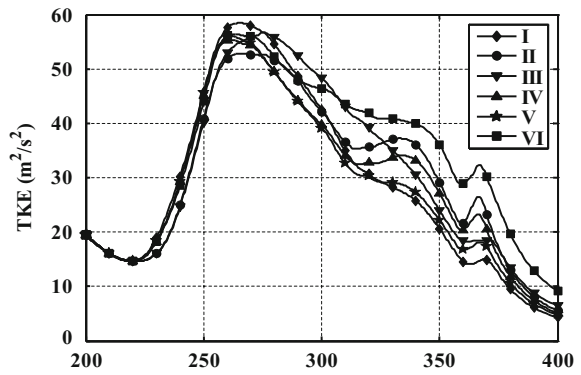


Fig. 2.6 The different combustion chamber shape

Fig. 2.7 The effect of combustion chamber on TKE



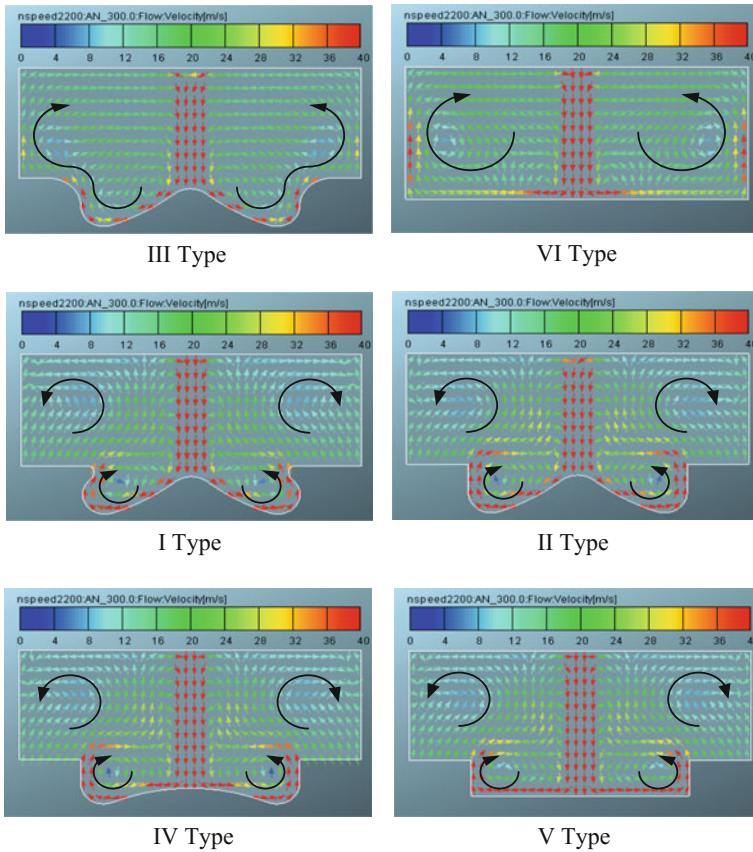


Fig. 2.8 The air flow distribution characteristic at 300°C

stroke when the straight mouth combustion chamber changed from a little heave one in bottom to an open one. The turbulence TKE in cylinder reach the second peak due to the flame propagation after ignition point at 6°CA BTDC.

2.2.2 The Effect of Combustion Chamber Shape on Concentration Field and Combustion Characteristic

The combustion process include ignition process and flame propagation process according to the ignition mode of CNG-DI engine, which is close related to the turbulence characteristic in cylinder and distribution characteristic of concentration field. The effect of concentration field and turbulence intensity near the spark plug is

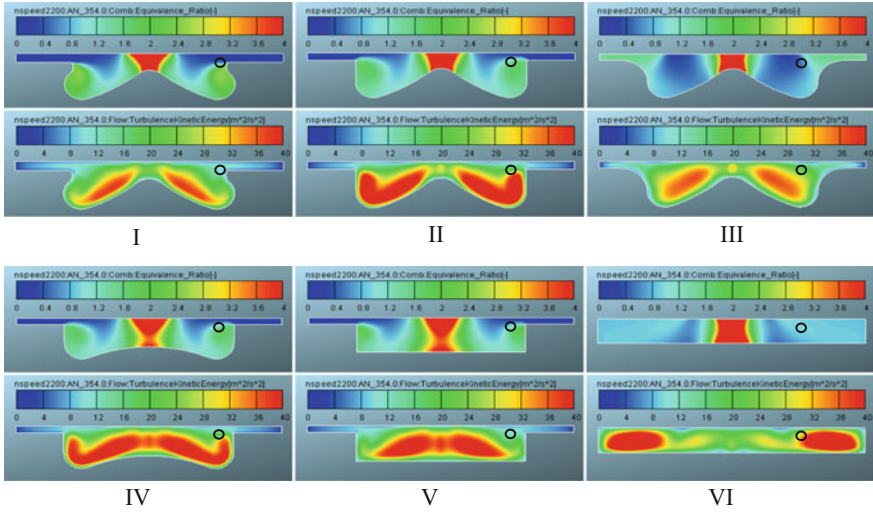


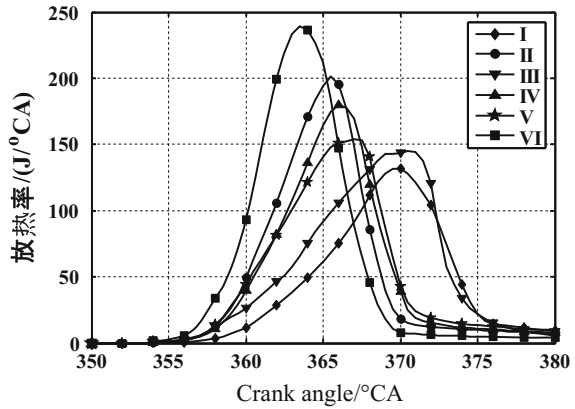
Fig. 2.9 The distribution characteristic of concentration field (up) and TKED (down) at 354°C

of special importance to lean combustion process. The effect of different combustion chamber on mixture concentration field and distribution characteristic of turbulence when the injection timing was 6°CA BTDC was shown as Fig. 2.9, the black circle showed the installation site of spark plug. From which we can know that the combustion chamber has an obvious influence on mixture concentration field and distribution characteristic of TKE, especially near the spark plug. The mixture concentration and turbulence intensity near the spark plug at ignition timing was shown as Table 2.4. From which we can know the mixture concentration near the I type and III type combustion chamber near the spark plug was thinner which was not easy to be ignited. The mixture concentration in V and VI type was most easy to be ignited, the turbulence intensity in V type combustion chamber was lower while the VI type combustion chamber was the highest. So the flame propagation speed was the fastest after the formation of flame nucleus in VI combustion chamber, whose heat release rate was the fastest and peak value was the highest as shown in Fig. 2.10; The turbulence intensity was lower relatively although the mixture concentration in V type combustion chamber was fit for ignition and the fast formation of flame nucleus, so the flame propagation speed is slowly and the peak value and heat release rate was decreased; The formation of flame nucleus was slow, flame propagation speed was low and heat release rate was

Table 2.4 The equivalence ratio and TKE at spark plug at 354°C

Type	I	II	III	IV	V	VI
Equivalence ratio	0.443	1.369	0.651	1.373	1.012	0.926
TKE (m ² /s ²)	10.12	21.33	21.4	20.98	11.73	35.76

Fig. 2.10 The effect of combustion chamber shape on heat release rate

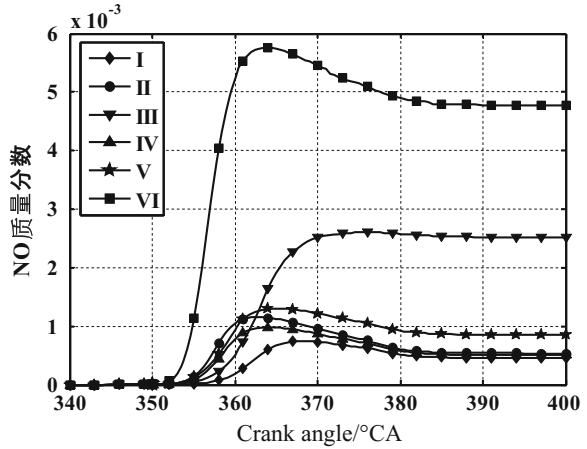


tardiness because the mixture concentration was as lean as the one in I type combustion chamber and not fit for the ignition although the TKE around the spark plug was more powerful in III type combustion chamber. The equivalence ratio and TKE near the spark plug around the ignition timing in II type and IV type combustion chamber was 1.37 and $21 \text{ m}^2/\text{s}^2$ approximately, whose combustion rate could be controlled effectively in spite of its slow combustion rate relative to VI type combustion chamber. The research result shows that not only the mixture concentration and turbulence intensity near the spark plug could be controlled effectively which is convenient for the improving of ignition characteristic but the one in cylinder could be improved which is convenient for the later flame propagation characteristic by the rational designation of throat of combustion chamber and shape of lug boss in bottom.

2.2.3 The Effect of Combustion Chamber Shape on NO Formation Law

The combustion rate of VI type combustion chamber was fastest and its heat release rate was the highest based on the high temperature and oxygen enrichment NO formation law of Zeldovich, so the mass fraction of NO formation increased quickly due to the high temperature and oxygen enrichment zone formed in cylinder, which decreased slowly after the reaching the peak at 364°CA , the NO mass fraction keep the level of 4.8×10^{-3} at the end of the combustion; The heat release rate in III type combustion at the later period of the combustion was higher while at the early stage of the combustion was flat, and the NO production was higher due the lesser mixture concentration distribution gradient in cylinder, but the appearance moment of the peak value of NO production was late relatively, whose NO emission level was about the half of the VI type combustion chamber; The dynamic variation characteristic of NO mass fraction had little difference in spite of the different heat

Fig. 2.11 The effect of combustion chamber shape on NO fraction



release rate curves of other combustion chambers, and the total variation trend keep lower level. The variation characteristic of mixture concentration field, temperature field and NO formation rate during the combustion process in the representative combustion chamber such as VI, III and IV type combustion chamber was shown as Fig. 2.12 to investigate the effect of different combustion chamber on the NO formation mechanism. From which we can know that NO production was related to not only the NO production rate but the size of NO fast production zone and duration of reaction in cylinder. The NO production rate depends on the local temperature and mixture concentration. The NO production was rich due to not only fast heat release rate and high NO formation rate but the wide high temperature and oxygen enrichment zone in VI type combustion chamber during the combustion process; The distribution characteristic of mixture concentration field in combustion chamber could be effectively improved by the designation of combustion chamber throat and bottom shape in III type and IV type combustion chamber, which can effectively control the NO production by reducing the size of zone and duration of NO formation in different degrees. The combustion rate in IV type combustion chamber was fast especially which caused the high temperature and larger mixture concentration gradient in high temperature zone, so the size of the formed NO reaction zone was smaller in spite of the high NO formation rate in local area, which made the final NO emission level lower; The high temperature and oxygen enrichment zone formed in cylinder was wide in spite of low heat release rate and local combustion temperature in III type combustion chamber at the early stage, caused the higher final NO production due to the larger formed reaction zone area in spite of low NO formation rate (Fig. 2.11).

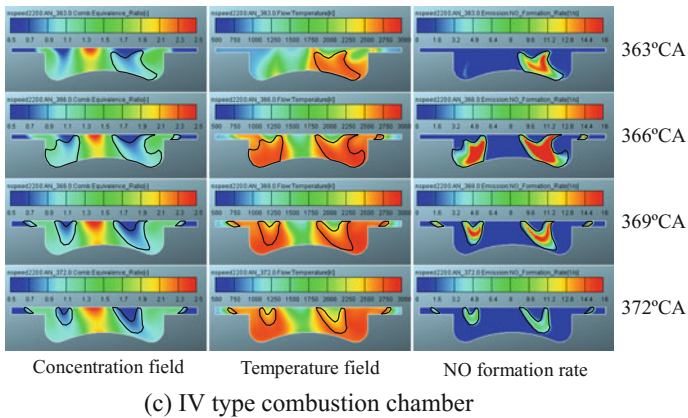
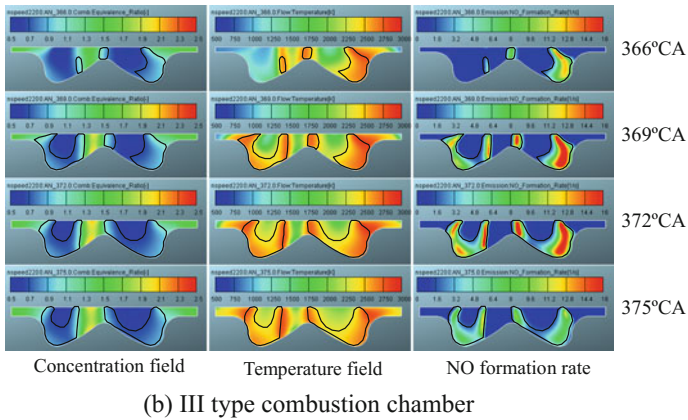
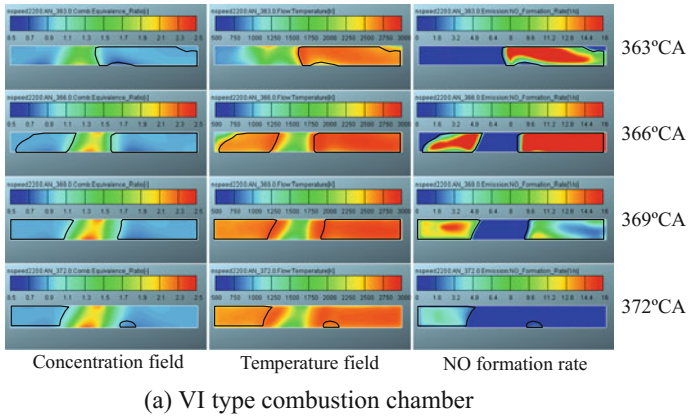


Fig. 2.12 The effect of combustion chamber on formation condition

2.3 Conclusion

- (1) The distribution characteristic of air flow characteristic and concentration field was effected by the combustion chamber of CNG-DI engine, especially near the spark which plays a decisive role on the ignition and flame propagation process in the later period.
- (2) The throat and open mouth combustion chamber is not fit for CNG-DI engine; The NO production is the highest when the flat piston is adopted; Not only the NO production can be reduced effectively but the flame propagation speed can be effectively controlled when the straight port and raised combustion chamber was adopted, which is fit for the organization of lean combustion.
- (3) The NO formation rate depends on the dual condition of temperature and oxygen concentration when the CNG-DI engine is adopted, while the NO final production depends on the NO formation rate, size of reaction zone of NO formation and reaction duration, which can be improved by the rational designation of combustion chamber structure.

References

1. Putrasari Y, Praptijantoa A, Nur A et al (2015) Evaluation of performance and emission of SI engine fuelled with CNG at low and high load condition. *Sci Direct Energy Procedia* 68:147–156
2. Tahira MM, Alia MS, Salim MA et al (2015) Performance analysis of a spark ignition engine using compressed natural gas (CNG) as fuel. *Energy Procedia* 68:355–362
3. Baratta M, Rapetto N, Spessa E (2012) Numerical and experimental analysis of mixture formation and performance in a direct injection CNG engine. *SAE Paper* 2012-01-0401
4. 木戸口善行. 噴射制御による直接噴射式天然ガス内燃機関の希薄燃焼に関する研究. *自動車技術会論文集*, 2010, 41(4):859–864
5. Imran S, Emberson DR, Diez A et al (2014) Natural gas fueled compression ignition engine performance and emissions maps with diesel and RME pilot fuels. *Appl Energy* 124:354–365
6. 焦远景, 司鹏鹏, 杨志勇等. 气道形状对天然气发动机缸内气体流动与燃烧过程影响的研究. *内燃机工程*, 2013, 34(3):26–31
7. Wu C, Deng K, Wang Z (2015) The effect of combustion chamber shape on cylinder flow and lean combustion process in a large bore spark-ignition CNG engine. *J Energy Inst* 89(2):1–8

Chapter 3

Damage Risk Evaluation and Optimization for BIWS Spots-Weld

Daolin Deng, Yu Zhang and Zhonghao Xu

Abstract A spots damage risk evaluation method was proposed based on the spots axial and shears force. The spots damage risk index for a SUV BIW was calculated and evaluated, and the BIWs spots were optimized. The evaluation results show that most of the positions with high risk spots are the same with the damaged spots of the road or bench test. The spots damage problem was solved by optimizing the spots based on risk index. This method can achieve the spots damage risk evaluation and optimization efficiently.

Keywords Axial force · Shear force · Risk index · Evaluation · Optimization

3.1 Introduction

In the modern automobile industry, spot welding as an efficient connection method is widely used in the vehicle and parts manufacturing process [1]. Usually, the number of spot welding of a vehicle is about 3000–5000. Clamping the welding electrode, giving enough electricity and then generated a lot of resistance heat at the contact position for the welding parts. The metal at the center of the hottest areas quickly heated to high plasticity or melting state, a molten pool formed. Keep pressure, off electricity, While the metal cools, a spots welding joint was formed. This leads to a serious stress concentration, so the crack is easy to form and expand around the spots. According to the statistics, more than 80% of the body crack problem are due to the spots damage [2]. Therefore, in the early stage of product design, effectively evaluated and predicted the welding spot of the vehicle by CAE, can reduce the production cost, shorten the development cycle and improve the product quality [3].

D. Deng (✉) · Y. Zhang · Z. Xu
China FAW Co., R&D Center, Changchun 130011, Jilin, China
e-mail: dengdaolin@rdc.faw.com.cn

Currently, there are some researches on the failure prediction of the spots, most are based on the plate stress of the spots, and then combined with the material S-N curve to calculate the spots fatigue life. But the way to get the plate stress is different. There are two kinds: One is through the finite element simulation of the spots to get the force, then using mathematical formula to calculate the plate stress of spots indirectly, Refs. [1–4] are all these way, but the estimate accuracy is low. Another is using a refined finite element model of spots, with the LMS-Virtual-lab-durability to calculate the plate stress, then according to the stress and the material S-N curve to calculate the spots fatigue life directly. Due to use refined spots FE model for the whole vehicle, greatly increased the model difficulty and the number of grid, the modeling and computing efficiency is low [5].

This paper shows a method for evaluating the spots damage risk based on Miner linear rule and engineering test data. Make use of the finite element simulation, obtained the axial force and tangential force of spots, then calculated and the damage risk coefficient of the whole vehicle combined with the engineering test data. Taking a SUV as an example, evaluated the spots damage risk of the whole vehicle, and improved and optimized the high risk spots.

3.2 Method for Spots Damage Risk Evaluation

3.2.1 Linear Damage Theory

According to Miner linear rule, under certain amplitude stress load σ , while the load times is N , parts will lead to damage or failure. Then parts under the amplitude stress σ load times n , a number less than N , will produce damage, and the amplitude stress σ damage rate is n/N . Thus for a part contains different amplitude stress σ_i will produce damage rate, when the sum reaches 1, you can predict failure. Also is to say when:

$$D = \frac{n_1}{N_1} + \frac{n_2}{N_2} + \dots + \frac{n_i}{N_i} = 1 \quad (1)$$

parts will lead to damage or failure, while D is the Miner damage index.

3.2.2 Spots Damage Risk Index

Currently, the fatigue life prediction accuracy based on linear damage not enough, and the fatigue life analysis process is complex and time-consuming. So, want to quickly obtain reasonable results is very difficulty in engineering problem. For the

spots, the loads are the axial force F_n and tangential force F_t from the connected plate. According to the Miner linear rule, the spots damage risk index D_i based on the axial force and tangential force introduced. Calculated as follows:

$$D_i = \frac{F_n}{F_{nc}} + \frac{F_t}{F_{tc}} \tag{2}$$

while the F_n is the axial force, the F_t is the tangential force, the F_{nc} is the axial force limit, and the F_{tc} is the tangential force limit. After a lot of experiments verification, and combined with the engineering experience, When the damage index $D_i < 0.6$ we think is safe, no damage risk; when $0.6 < D_i < 0.8$, thinks is in warning level, needs attention; when $0.8 < D_i < 1.0$, thinks is in danger level, recommendations for improvement; when $1.0 < D_i$ that is serious danger level, must be improved.

The axial force limit and the tangential force limit of spots can be obtained according to the spots strength test. We know almost all the spots failure problem appeared in the connected plate, the spots itself rarely damage. The factors affecting failure are material, plate thickness, as well as the quality of welding process and so on. The influence of welding process on spots strength of the heat affected zone did not considered in this paper. For material, due to the presence of the welding heat affected zone, greatly reduced the spots strength around, the material differences were less affected. And if we consider the factors of the material, the time and cost of the spots strength test will be greatly increased. Therefore, in the spots strength test obtaining force limit, the main consideration is the thickness of the connected plate. Through a series of test to obtain the force limit list, as shown in Fig. 3.1.

In the practical engineering problem, the failure parts in the spots damage are all the parts with thinner thickness. So the minimum thickness of spots connected plate determined the force limit.

Thickness(mm)	Axial force limit (N)	Tangential force limit (N)
0.57	a	aa
0.62	b	bb
0.67	c	cc
0.72	d	dd
0.77	e	ee
...
2.5	g	gg

Fig. 3.1 Spots force limit list diagram

3.3 Application Examples

3.3.1 Finite Element Model

Take a SUV vehicle as an example, evaluated the BIWs spots damage risk, as shown in Fig. 3.2. There are many ways to simulate the spots, the common node method, 3D element, beam element, ACM element, cweld element and so on. In this paper, the BIWs spots connection is all used the cweld element to simulate.

As the spots force limit list are based on the minimum thickness of the connected plate, it is necessary to layer the spots of the vehicle according to the minimum thickness of the connected plate, and establish the spots sets, as shown in Fig. 3.3.

Fig. 3.2 The BIWs spots damage risk evaluation model



Fig. 3.3 The BIWs spots classification

CWELD_ALL	65
CE_Locations_70	8401153
CE_Locations_75	8401154
CE_Locations_80	8401155
CE_Locations_90	8401156
CE_Locations_100	8401157
CE_Locations_120	8401158
CE_Locations_140	8401159
CE_Locations_150	8401160
CE_Locations_160	8401161
CE_Locations_180	8401162
CE_Locations_200	8401163



Fig. 3.4 Acceleration acquisition from road test

<i>Suspension Front</i>	FE	Fx [N]	Fy [N]	Fz [N]	Mx[Nmm]	My[Nmm]	Mz[Nmm]
L_spring_upper_body	102	2077.47	5251.55	15431.56	-1975.80	16597.00	-1941.17
R_spring_upper_body	202	2017.43	-5248.61	15479.76	1995.19	14757.00	1698.00
L_subframe_front_body	103	-1051.66	8.79	1446.00	-3.41	1486.43	-15.55
R_subframe_front_body	203	-1004.99	8.79	1435.76	-3.41	1486.43	-15.55
L_subframe_rear_body	104	-1035.84	-7.68	-186.71	-0.10	44.59	-0.31
R_subframe_rear_body	204	-1011.10	-7.68	-190.06	-0.10	44.59	-0.31

Fig. 3.5 Analysis load list diagram

3.3.2 Determined the Analysis Load

The analysis load obtained by using semi physical method. First, the acceleration signal of the four wheel center in the accelerated failure road test measured, as shown in Fig. 3.4. Used the measured acceleration as input, driven the multi-body dynamics model of the vehicle, and then calculated the force and moment of the connection between the body and the chassis, as shown in Fig. 3.5.

3.3.3 Evaluation Results and Optimization

The BIWs strength analyzed using the obtained load of each connecting point. The spots axial force and tangential force were extracted as previous layered. Then the damage risk index of each spot calculated according to the force limit list by the spots strength test. Figure 3.6 showed the evaluation results diagram.

Evaluation results show, there are 14 spots risk index $0.8 < Di$, 43 spots $0.6 < Di < 0.8$. In the road test and bench test, there were 9 spots damage, and 5

Num	Axial-force	Tangential-force1	Tangential-force2	Tangential-force	Risk-index
873950	120.40	1948.00	-322.90	1974.58	0.89
873983	284.40	-953.60	26.01	953.95	0.88
873968	228.90	-960.80	-68.20	963.22	0.77
874045	-7.86	1737.00	1185.00	2102.71	0.69
873985	270.10	-369.80	261.20	452.74	0.68
873958	30.21	-1839.00	-181.60	1847.94	0.68
873975	219.10	546.50	-473.70	723.22	0.67
874020	-8.73	1524.00	-1095.00	1876.59	0.61
873463	-6.43	-1214.00	1409.00	1859.86	0.61
873990	203.30	431.10	429.10	608.25	0.60
873421	39.61	-750.10	-1360.00	1553.14	0.60
873973	252.60	48.60	270.30	274.63	0.59
873442	-8.99	-1121.00	-1410.00	1801.32	0.58
873970	216.80	-361.60	-231.70	429.46	0.57
873394	35.93	-610.30	1324.00	1457.89	0.56
873948	104.80	691.10	-718.70	997.07	0.54

Fig. 3.6 Evaluation results diagram

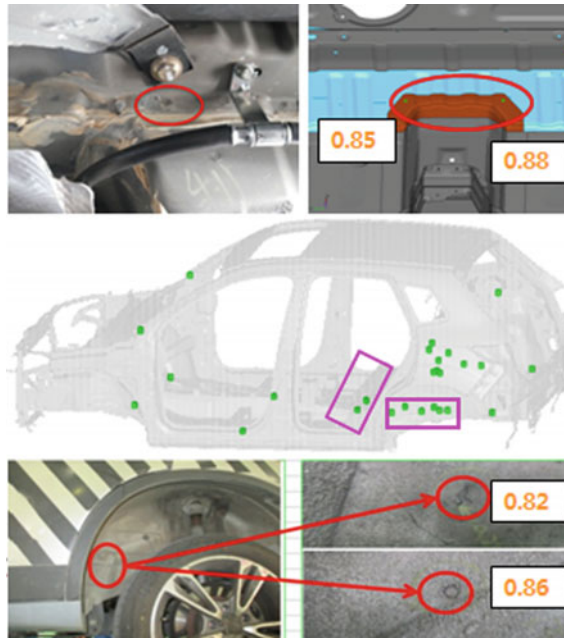


Fig. 3.7 Comparison results of the evaluation and the road test

spots risk index $0.6 < D_i$ among them. Figure 3.7. are the results comparison for the two spots failure location, the road test was in agreement with the evaluation results.

Aiming at the failure problem, the structure of damage position improved and optimized. Figure 3.8. showed the spots damage risk index at the rear wheel cover

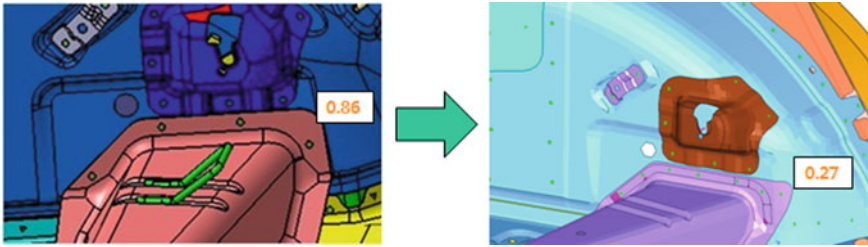


Fig. 3.8 Spots damage risk index before and after the structure optimization

position before and after the structure optimization. Before, the D_i value is 0.86, after D_i value is 0.27. Results showed during the follow-up road test and bench test did not appear spots damage problem.

The results show, the evaluation results are more conservative compared with the test results. Considering a lot of factors affecting the spots damage, and the evaluation method is simple, and efficient. So, the accuracy of the evaluation results can also be accepted, and the application in the product development process is feasible.

3.4 Conclusions

Aiming at spots failure problem, the paper shows a new spots damage risk evaluation and optimization method based on the spots axial force and tangential force. Taking a SUV as an example, evaluated spots damage risk of the whole vehicle, and screened out the high risk spots effectively. The location of high risk spots are in accord with the failure location of the physical test. Using the method, the structure of the spots was improved and optimized, and the spots failure problem was solved. The results show, the evaluation results on the conservative side compared with test results, but the method is simple, efficient, and the accuracy can be accept in the range of engineering. It can provide a reference for the products design and optimization, shorten the product development cycle, save costs, has a very positive meaning.

References

1. Zhu T, Gao F, Liu G (2006) Pre-estimation of fatigue lifetime of welding spots of BIWs. *Automobile Technol* 36(2):37–40 (In Chinese)
2. Peter J, Mikael F (1998) The engineering prediction of spot-weld fatigue life. *China Mech Eng* 9(11):35–37

3. Du Y (2006) Method for fatigue life prediction of automotive spot-welds. *Automotive Eng* 15 (B09):189–192 (In Chinese)
4. Du Z, Zhu P, He J (2006) Fatigue life analysis of car body structure and spot weld based on FEM. *Automotive Eng* 28(10):944–947 (In Chinese)
5. Song K, Qian T, Chen T (2015) A fatigue life prediction method for resistance spot welds based on average stress intensity factor. *J Mech Eng* 51(16):113–119 (In Chinese)

Chapter 4

Fatigue Durability Analysis of a Frame Based on Multi Body Dynamics

Qin Zhang, Fengchong Lan, Jiqing Chen and Qinsheng Huang

Abstract A fatigue analysis procedure for a frame based on virtual prototype and multi-body dynamics is established. The first 5 modes frequencies of the finite element model are calculated and verified by experimental test. The frame model is turned into a flexible body. A rigid flexible coupling model is established with suspensions, tires and the flexible frame body. The dynamic response of the model is analyzed in class D road at a uniform motion, the load-time histories of the connected locations are extracted; The S-N curve of material is fitted through the tensile strength limit; combined with the stress distribution of unique load, the dangerous positions and theirs fatigue life are predicted. The result shows that the frame damage hotspots are mainly distributed in the bracket connected with the body, frequency domain energy of connected location load is within 18Hz, the minimum fatigue life mileage is km. The result has a guiding significance for the research of the fatigue durability of vehicle frame.

Keywords Fatigue durability · Rigid flexible coupling · Multi body dynamics · Frame · Model analysis

4.1 Introduction

The pavement conditions Sport Utility Vehicle (SUV) suffered are more complex than passenger car's, subject to bending, torsion, impact and combinations of them etc. variety of loads, which had a abrupt change and large amplitude during the sport driving. The frame of the body-on-frame absorbs directly impacts came from the road surface, dynamic and alternating loads which are lower than the yield

Q. Zhang (✉) · F. Lan · J. Chen · Q. Huang
School of Mechanical and Automotive Engineering, South China University of Technology,
Guangzhou 510640, China
e-mail: zhangqin0762@163.com

© Springer Nature Singapore Pte Ltd. 2017
Society of Automotive Engineers of China (SAE-China), *Proceedings of SAE-China Congress 2016: Selected Papers*, Lecture Notes in Electrical Engineering 418,
DOI 10.1007/978-981-10-3527-2_4

strength of the material. Fatigue damage would be also caused by experienced certain loads which are lower than yield strength of material. The frame under such load conditions requires not only rigidity and strength to guarantee driving safety, comfort, usage of parts installed in, but also fatigue life to ensure that fatigue failure does not occur when it is subjected to dynamic loads below the yield strength in the life time. The fatigue durability test has a long cycle, a high cost, and need to be carried out after the assembly of prototype. The cost of rectification is high when bugs expose at the prototype. It is necessary to analyze the fatigue life of products for the specific pavement spectrum it works at the beginning of design.

Computer aided design has been widely used in structural strength and stiffness analysis, modal analysis and collision analysis, and the results are in good agreement with experiment. Fan [1] conducted a topology optimization of multi stiffness for a bus frame owned three section; Yang [2] improved the elastic modal frequencies at low order and mode shapes of a box beam frame in the heavy mining truck with finite element method; Liu [3] used compromise programming method to establish a topology optimization model for multi-objective to optimize the stiffness and vibration frequency of a frame; Li [4] conducted a 100% positive impact simulation with the frame filled of aluminum foam materials, and improved the collision performance of the frame; Xin [5] conducted a 40% offset impact simulation of a frame and optimized its collision safety. Many scholars also introduced the actual traffic conditions as the boundary into computer design. Chen [6] measured the strain time history of corn harvester at the chassis frame on the working conditions; Huang [7] predicted the fatigue life of all terrain SUV frame in rigid flexible coupling with the cobbles as the boundary conditions. The fatigue prediction of a special vehicle frame under impact load was studied by Wang et al. [8]. However, the obtain of the actual road conditions and the working circumstance are more difficult, all conditions in the life time can not be encountered even in the professional test field. Therefore, it is necessary to apply the virtual technology of fatigue durability analysis to the frame.

The substructure mode synthesis method is used to established the frame of rigid flexible coupling model, the stress spectrum of connected location is obtained though the excitation of the surface roughness spectrum at the multi body dynamics model; combined with the stress distribution of unit load and fitting S-N curve, fatigue life of the frame is predicted.

4.2 Establishment and Validation of Finite Element Model of Frame

4.2.1 The Establishment of the Finite Element Model of Frame

Frame adopts edge beam edge structure, the section of side rails is square welded by two slot shaped opening, in the anterior segment of the side rails is design with reinforcing plate in order to increase the strength and stiffness. Frame adopts SAPH440 steel plate, connected by welded and bolt. The elastic modulus E of the material is 2.1×10^5 MPa, Poisson's ratio μ is 0.3, the density is 7.85×10^{-6} kg/mm³, yield strength σ_s is 305 Mpa, tensile strength σ_b is 440 MPa. Frame was meshed by the quadrilateral shell element, with the size 10 mm. The welding and bolt connection are simulated by Rbe2 element. The total number of element is 126 239, the total number of nodes is 128 891 and the finite element model of the frame is shown in Fig. 4.1.

4.2.2 Modal Analysis and Verification of Vehicle Frame

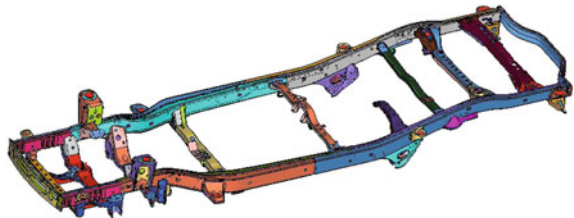
Modal analysis is the process of distinguishing the characteristics of the structure, that is to identify the inherent characteristics, frequency, damping and mode. Those can be obtained by calculating modal analysis and experimental modal analysis.

Calculating modal analysis is done by solving the motion equations of a multi degree system

$$[M]\{\ddot{x}\} + [C]\{\dot{x}\} + [K]\{x\} = \{F\} \quad (4.1)$$

where $\{\ddot{x}\}$ is the acceleration, $\{\dot{x}\}$ is the velocity, $\{x\}$ is the displacement; $[M]$ is the mass matrix, $[C]$ is the damping matrix, $[K]$ is the stiffness matrix, $\{F\}$ for external load vector.

Fig. 4.1 Finite element model of frame



When the system damping is very small, it can be ignored; thus, it is equivalent to the solution of the characteristic equation:

$$([K] - \omega^2[M])\{\varphi\} = 0 \quad (4.2)$$

The Block Lanczos method combines the transform method and the tracing method, with a set of vectors to achieve the recursive calculation, is very efficiency for solving the generalized eigenvalue of large sparse matrix. The Block Lanczos is used to calculate the first 5 order modal frequencies for non rigid.

The modal test uses the free mode, frame are connected by four rubber ropes in the nodes, hung in the customized cradle. The frame is in free state and maintained level, as shown in Fig. 4.2. The natural frequency of the rubber rope suspension system is within 2 Hz. The measuring point is selected to avoid the node of the frame, which is symmetrical and evenly distributed. The modal test uses the free modal test method combined from excitation from single point and picking vibration up from multi-points. That is, An excitation position is selected to apply excitation at frame by a test hammer. At the same time, sensors are used to measure the frequency response information at one excitation. During the measurement, observed the coherence function and frequency response function synchronous, remeasure the points when the coherence function disordered.

As shown in Table 4.1 and Fig. 4.3, the natural frequency of the frame modal test mode and finite element calculated mode are in good agreement, the first 5 order natural frequency error value is less than 5%, the two modes are basically the same, there is no obvious difference in the amplitude, visible in the finite element model has a high precision, can be used as a follow-up study.

Fig. 4.2 Hung of frame



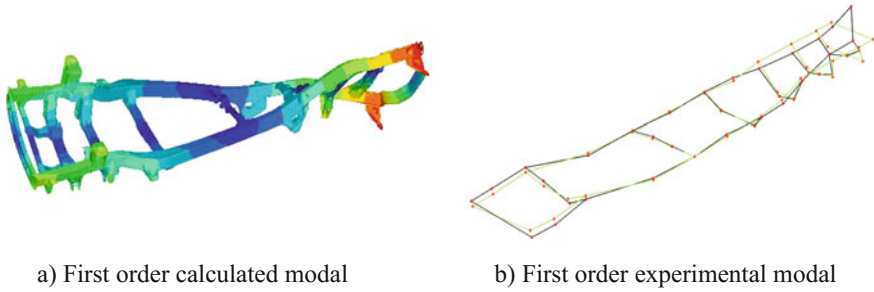


Fig. 4.3 Comparison of frame first order calculated modal and experimental modal

Table 4.1 Comparison of calculated and experimental results

Modal order	Modal description	Calculated (Hz)	Experimental (Hz)	Deviation (%)
1	First order torsion	23.39	24.37	4.02
2	First order bend	29.02	30.19	3.88
3	First order cross bend	34.67	35.06	1.11
4	Second order torsion	48.99	50.75	3.47
5	Local deformation	52.73	55.31	4.67

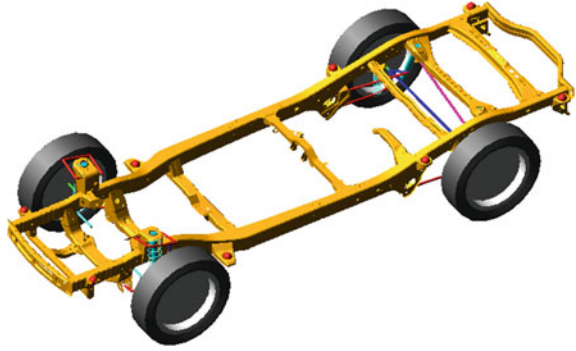
4.3 Vehicle Dynamics Analysis

4.3.1 *The Frame of the Rigid Flexible Coupling Multi-Body Dynamics Model*

The frame suffer most of loads came from the engine, gearbox, clutch, suspensions and bridge which installed on it as a non bearing body, complexity of force amplitude in space and frequency domain decided it is need to be studied as a flexible body.

Considering the effect of elastic and using the Component Model Synthesis, the frame is tuned into a Flexible body. Then establishes the multi-body rigid flexible coupling model of frame-mass-suspension. It considers the connection points between frame and suspensions and body as out nodes, determined the modal degrees of freedom after reduced, according to the Component Mode Synthesis method, used the modal neutral file which contained the frame modal information to generated the frame into a flexible body. Front suspension is double wishbone suspension, rear suspension is five link non independent suspension, the coefficient of suspension mass distribution $\varepsilon = 1$, the body mass is simplified to the 8 connection positions between frame and the body. The vehicle model fitted with a tire model is shown in Fig. 4.4.

Fig. 4.4 Vehicle dynamics model



4.3.2 Establishment of Road Spectrum

The evenness of the road surface generates incentives to the driving vehicle, creates dynamic loads along the tire and suspension system to the frame. The reason for the excitation is the deviation between the ideal reference plane and the road surface in the direction of travel, which is usually called the road roughness function, and can be described by the power spectral density $G_q(n)$ of the vertical displacement.

$$G_q(n) = G_q(n_0) \left(\frac{n}{n_0} \right)^{-w} \tag{4.3}$$

where, n is the spatial frequency, $n = 1/\lambda$, n_0 is the relative spatial frequency, $n_0 = 0.1 \text{ m}^{-1}$; $G_q(n_0)$ is the coefficient of road roughness; W is frequency index.

Pavement roughness can be divided into 8 stages according to the vertical displacement power spectral density when $G_q(n)$ frequency index $W = 2$, as shown in Table 4.2. In order to make the research more general, this paper establishes the virtual pavement spectrum according to the D level road surface standard.

Table 4.2 Standard for classification of road roughness

Pavement class	$G_q(n_0)/(10^{-6} \text{ m}^3)$	$\sigma_q/(10^{-3}\text{m}^3)(0.011\text{m}^{-1} < n < 2.83\text{m}^{-1})$
	Geometric mean	Geometric mean
A	16	3.81
B	64	7.61
C	256	15.23
D	1024	30.45
E	4096	60.90
F	16,384	121.80
G	65,536	243.61
H	262,144	487.22

4.3.3 Vehicle Dynamic Response

Static equilibrium of rigid flexible coupling dynamic model is analyzed firstly, by setting in gravity only to reach a stationary equilibrium. Analyzed the dynamic response in the road roughness of 0, that is the ideal flat surface. The speed of vehicle is 36 km/h. The vehicle can not be immediately changed from static to uniform motion state, there is a transition process during the acceleration, that is, uniform acceleration movement of the stage. The change of vehicle speed in 0–30 s is shown in Fig. 4.5. The speed of vehicle had achieved stability within 2.5 s. According to the left spring force of front suspension showed in Fig. 4.6, the dynamic force of the components achieved stability when the time is 7 s. The accelerated process will affect the dynamic response between 0 and 7 s. Therefore, the analysis of the dynamic load of the frame under this condition should be carried out after 7 s when the response got stable. In this paper, the dynamic loads of some interesting locations is analyzed in 10–30 s.

The force between the parts and the frame are three force components: F_x , F_y and F_z as well as three torque components: T_x , T_y and T_z , that is, the force and

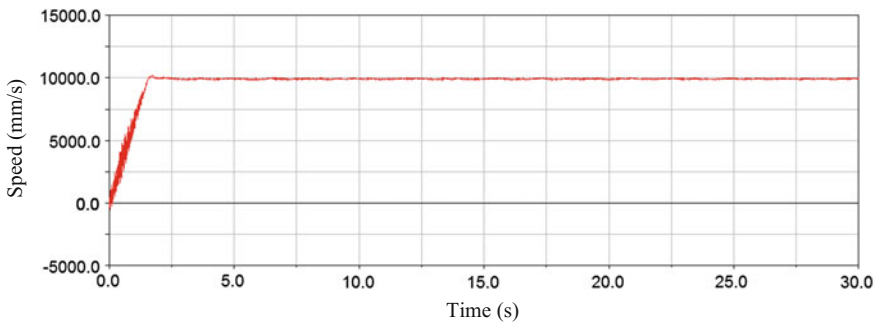


Fig. 4.5 Vehicle speed

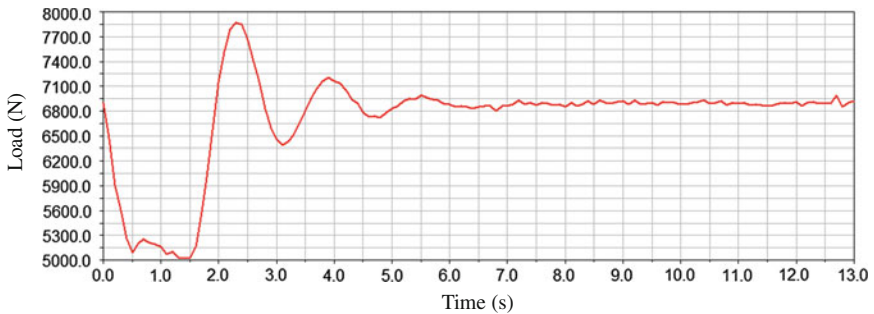
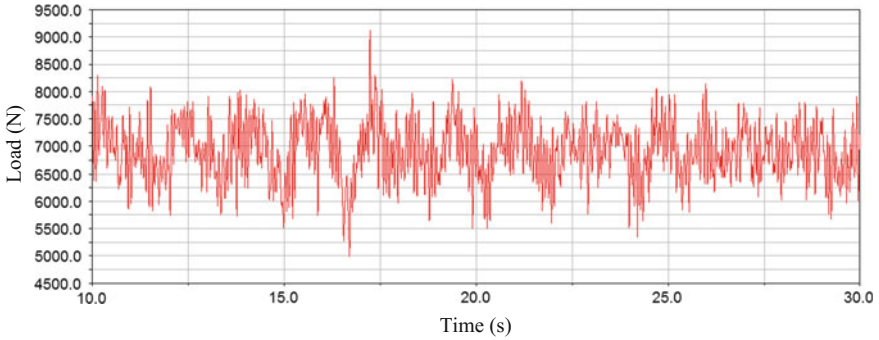


Fig. 4.6 Z direction force at the top of left spring of front suspension on ideal road

Table 4.3 Input load components for fatigue analysis

Connected location	Number	Load component	Total load
To BIW	8	F_z	8
To spring damper of front suspension	2	F_z	2
To rear suspension spring	2	F_z	2
To rear suspension damper	2	F_y, F_z	4

**Fig. 4.7** The Z direction load at the *top* of left spring damper in the front suspension

torque in the direction of the three coordinate axes. Because the torque component are smaller compared with the force component, which are bigger obviously and whose influence on the durability were greater. In order to improve the computational efficiency without sacrificing the accuracy of the simulation, the effect of the torque component which had smaller amplitude on the frame fatigue can be neglected. 16 load components are selected as the load used for calculating the fatigue durability of the frame, as shown in Table 4.3, which suffered more severe condition.

The Z direction load at the top of left spring damper in the front suspension in 10–30 s is shown in Fig. 4.7.

4.4 Fatigue Life Analysis

4.4.1 Fatigue Analysis Method

According to the difference between structure natural frequency and the excitation frequency, fatigue life analysis methods can be divided into three kinds, respectively is static or quasi-static fatigue analysis method, dynamic fatigue analysis method and vibration fatigue analysis method. When the first order natural

frequency of the structure is more than 3 times of the excitation frequency, the static (or quasi-static) fatigue analysis method can get a reasonable result.

According to analyzing the power spectral density of the connection point of the frame, the range of energy distribution of the loads can be obtained. Take the Z direction load at the top of spring shock absorber in the front and left suspension for example, as shown in Fig. 4.8. The frequency is mainly distributed within 0–18 Hz, and the most are the low frequencies of 1 Hz, and first-order natural frequency of the frame is 23.39 Hz. Therefore the (quasi) static fatigue analysis method must be choose to predict the fatigue life of the frame.

The fatigue characteristic curve of material is the basis of the research on fatigue life, and it is generally classified into E-N and S-N curve. The S-N curve is needed to be used to predict the fatigue life for Static (quasi) fatigue analysis methods.

The frame materials is SAPH440, and its physical character is as follow: tensile strength of $\sigma_u = 440$ MPa, stress ratio $r = -1$, the logarithmic standard deviation is 0.1. The S-N curve of SAPH440 is fitted as shown in Fig. 4.9.

4.4.2 Fatigue Life Analysis

Under normal circumstances, the S-N curve is measured under symmetrical cyclic stress(whose $r = -1$, $\sigma_m = 0$), but in fact most force of the parts in structure does not meet the condition, the amplitude of the load are random values owned statistical features usually. Experiments show that the average and amplitude of the stress are related to the cycle times N, and this relationship is first proposed by Haigh. Under the same stress amplitude, the fatigue life of components or materials decreases when the average stress is tensile, and increases when the average stress is compression. The stress cyclic block of a non-zero mean value can be obtained

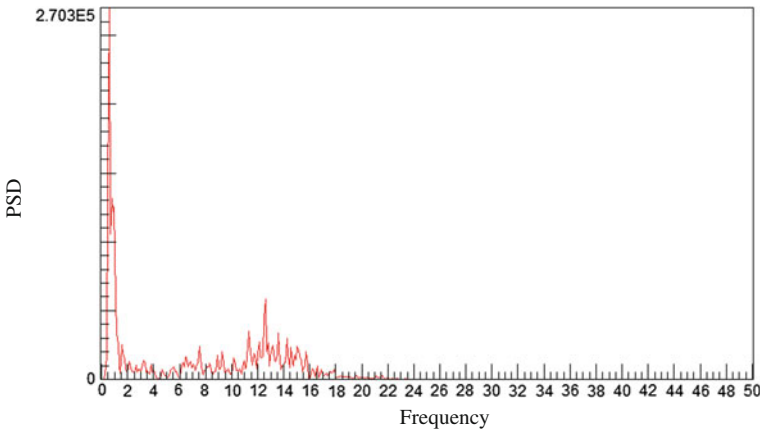


Fig. 4.8 Front suspension *left* spring damper Z to load power spectrum density

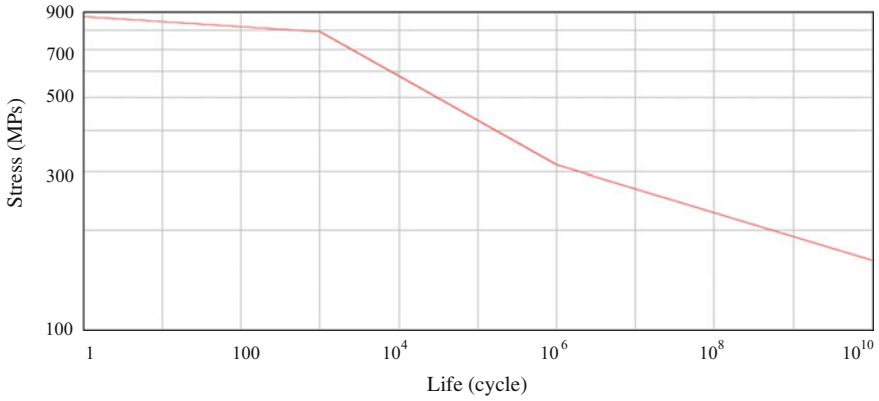


Fig. 4.9 The S-N curve of SAPH440

by counting the load spectrum. But the S-N curve is obtained in the experiment of zero stress average. So the blocks must be converted to the stress cycle which the average is zero and the stress ratio is minus 1 to calculate the fatigue life with the S-N curve. In this paper, Good-man curve is selected to modify the mean of stress.

Miner linear cumulative damage theory is used to accumulate the damage caused by the stress cycle at all levels, and the fatigue life of each grids is obtained with the failure criterion. According to the Miner fatigue cumulative damage theory, under the action of a constant amplitude stress level S , the number of cycle until failure is N , the damage caused by N cycles is calculated by the follow:

$$D = n/N \tag{4.4}$$

Under the action of different stress level S_i , the damage of n_i cycle is

$$D_i = n_i/N_i \tag{4.5}$$

When the cumulative damage is reached to 1, that is, the

$$D = \sum_{i=1}^l \frac{n_i}{N_i} = 1 \tag{4.6}$$

Structure is considered to be destroyed by fatigue. Where n_i is the number of cycles under S_i , which is determined by the load spectrum; N_i is the cycle to the destruction of the life cycle under the action of S_i .

The vehicle structure reliability is related to the safety of passengers, so the survival rate is set to 99%. After simulation, the fatigue life cycle of the frame is obtained, and the locations of the dangerous positions owned the least fatigue life are predicted, as shown in Fig. 4.10.

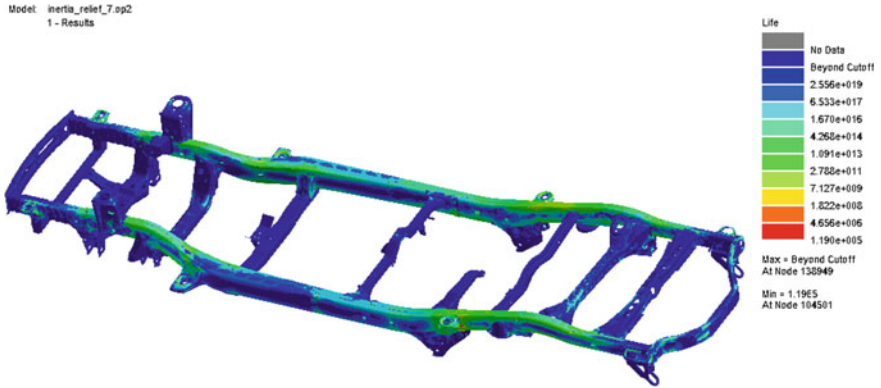


Fig. 4.10 Logarithmic fatigue life of vehicle frame

Fatigue damage is calculated as the number of cycles to calculate the fatigue

$$D_i = v \times t \times n_i \tag{4.7}$$

where, D_i is the fatigue mileage of node, v is the speed, t is time; n_i is the number of cycles.

Table 4.4 Fatigue endurance performance analysis of frame structure

Serial	Node	Location	Damage 10^6	Cycle times/times 10^5	Fatigue mileages/ 10^4 km
1	104501	Nub. 3 rear junction of right side rail and body	8.40	1.19	2.38
2	104500	Nub. 3 front junction of right side rail and body	5.64	1.77	3.55
3	103734	Nub. 3 rear junction of left side rail and body	2.28	4.39	8.79
4	47300	The right of rear cross member	1.50	6.68	13.35
5	31074	Shackle at the junction of left side rail and body	1.50	6.68	13.37
6	47303	The right of rear cross member	1.42	7.04	14.09
7	103730	Nub. 3 front junction of left side rail and body	0.352	0.284	56.88
8	83902	The front at junction of right side rail and first cross member	0.073	0.0137	273.80
9	83977	The rear at junction of right side rail and first cross member	0.0444	0.0225	450.80
10	84279	Nub. 2 front junction of right side rail and body	0.0321	0.0312	623.20

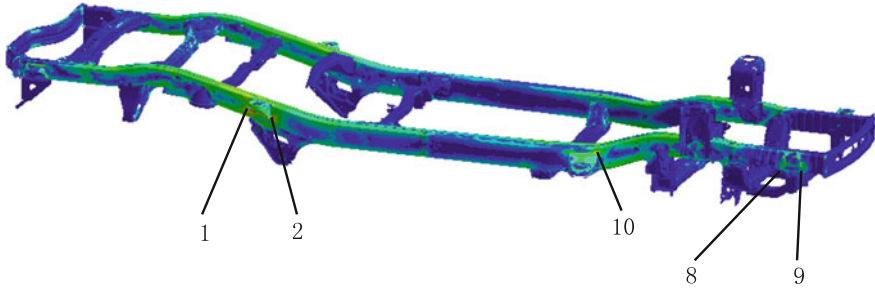


Fig. 4.11 Distribution of partial dangerous location

The load spectrums are recorded at the location above at the constant 10 m/s speed during 20 s the vehicle drove in the computer analysis, fatigue damage cycle times of node 104501 at the largest region is 1.19×10^5 , the fatigue mileage of dangerous zones is calculated for 2.38×10^4 km according to formula (4.7). The fatigue mileages of the largest 10 hot spots in fatigue damage can be seen at Table 4.4, some location of those 10 spots are shown at Fig. 4.11. According to the life-cycle analysis results can be found, the less dangerous location in fatigue life are basically lay out at the junctions of trails and the body. The shape changes abruptly and greatly at the junctions of two components, and the stress concentration is prone to appeared there; the junctions of trails and the body bear the loading came from body directly. The stress and fatigue life results of the danger locations can be considered as a guidance for structure and lightweight design in the future.

4.5 Conclusion

- (1) The finite element model of a SUV frame is established, the first 5 order natural modal frequencies are calculated and compared with the modal test, the vibrations mode are the same, and the deviation of frequencies is acceptable. The accuracy of the finite element model is verified.
- (2) According to the dynamics of a rigid flexible coupling system, the frame is translated into a flexible body, multi-body dynamics system coupling with rigid and flexible is established with the combination of the simplified body quality, suspension model and the tire model. Load history of the connected locations are acquired under the excitation of road surface spectrum. This technical method has certain norms and versatility, can be applied further to study the fatigue durability of the frame under different spectrums of road surface.
- (3) The corresponding fatigue mileage at the most area of two side rails can arrive at 5 million km according to the fatigue durability analysis. Weight can be

reduced by adjusting the frame structure and reducing the material thickness of the frame in a prescribed mileage. The method above has a certain guiding significance for lightweight frame.

References

1. Fan W, Fan Z, Gui L, Dong L (2008) Multi-stiffness topology optimization of bus frame with multiple loading conditions. *Automot Eng* 30(6):31–533
2. Yang Z, Zhao X, Yuqi Wang (2009) Finite element analysis on the frame of heavy mining truck. *J Mech Transm* 33(3):97–99 (in Chinese with English abstract)
3. Liu L, Xin Y, Wang W (2011) Multi-objective topology optimization for an off-road vehicle frame based on compromise programming. *Mech Sci Technol Aerosp Eng* 30(3):382–385
4. Xiao-huo LI, Bai S, Hu Y, Chi Q (2012) Frontal crash simulation of SUV frame with foamed aluminum-filled longitudinal beam. *J Guangxi Univ Nat Sci Ed* 37(5):903–906
5. Xin Y, Dong X (2011) Simulation and safety design of a vehicle's frame in crash performance. *Mech Sci Technol Aerosp Eng* 30(3):359–362
6. Chen Z, Zhou L, Zhao B, Liang X (2015) Study on fatigue life of frame for corn combine chassis machine. *Trans Chin Soc Agric Eng* 31(20):19–25
7. Huang Z, Lu X, Xu W, Chen W (2012) Fatigue life prediction for all-terrain vehicle frame based on modal stress recovery. *J Chongqing Univ Technol (Natural Science)* 26(3): 18–22
8. Wang X, Shi L (2009) A study on the transient response analysis and fatigue life evaluation of a special vehicle frame under impact load. *Automot Eng* 31(8):769–773

Chapter 5

Study on Calibration of Secondary Air Injection System in a V12 Engine

Hongzhi Zhao, Wei Wang and Xiaofan Zhong

Abstract The emission regulation of CHINA 6 is going to be issued, the limits of the emissions will be greatly strict. The utilization of secondary air injection system is proved to be one of the effective methods to reduce the CO and THC emissions in the phase of cold engine. The application of secondary air system in the process of the V12 engine developing, the control strategy, the result of calibration and the diagnostic calibration are introduced, according to the development experience. It's a reference to the engineers who face the similar issue.

Keywords Secondary air injection · Calibration · Emission

5.1 Introduction

Automobile will face the increasingly strict emission regulations as one of the main contributors to air pollution. At the moment, the preparation and implementation of CHINA 6 emission regulation is in intensive process.

As is well-known, the emissions in cold phase of traditional gasoline engine take a remarkable proportion in the emission test cycle, so it's quite important to satisfy CHINA 6 emission regulation that how to reduce the emissions effectively in cold phase. The utilization of secondary air injection (SAI) system is proved to be one of the effective methods. Internationally, the SAI is generally adopted by more and more type of vehicles especially VW series. But it's infrequent in domestic. For a better implementation of the social responsibility of energy conservation and environment protection, China FAW Co., Ltd R&D Center has utilized SAI system in a V12 gasoline engine in 2013 for the first time. The emission results satisfied GB14762-2008 regulation as well the GB18352-2013 (CHINA 5) regulation, the latter is stricter.

H. Zhao · W. Wang (✉) · X. Zhong
China FAW Co., Ltd., R&D Center, Changchun, China
e-mail: wangwei6@rdc.faw.com.cn

According to years of research experience, this paper has overall analyzed and explained how to optimize the control parameters of SAI system. We hope this article could be helpful to the colleagues who are contributing to the similar development work.

5.2 SAI System Scheme

5.2.1 Development Object

The object of emission optimization is one passenger car of red flag brand. The main technical parameters are shown in Table 5.1.

5.2.2 SAI System Structure

There are two banks in this engine, each bank with 6 cylinders, two ECUs are utilized to control each bank separately. Therefore two secondary air pumps are used to inject fresh air to the exhaust system respectively, as shown in Fig. 5.1. The injection position of secondary air is significant to THC emission, the closer to the exhaust valve the better. Literature shows [1] that THC could be reduced by nearly 50% if the injection position is appropriate. Consequently, the position of SAI in V12 engine is designed in the middle of the exhaust tube where is closed to the exhaust valve, as shown in Fig. 5.2.

The mass flow of the pump is an extremely key factor for the application of SAI system. It will lower the exhaust temperature if the mass flow is oversize. On the contrary, the oxygen concentration in the exhaust won't be enough for a better thermal oxidation reaction if the mass flow is undersize. Thus the choice of mass flow should be cautious when adopted the secondary air pump with a constant mass flow. According to experience, the choice of mass flow of secondary air pump should be generally upon matching 5–6 kg/h air mass flow for each 0.5 L displacement. Taking V12 engine whose displacement is 6 L for instance, it needs

Table 5.1 Main technical parameters

Maximum mass/kg	3625
Curb mass/kg	3150
Engine type	V12
Engine displacement/mL	5985
Compression ratio	10.3
Rated power(kW/r/min)	300/5600
Maximum torque (Nm/r/min)	550/4000
Transmission type	6 speed AT

Fig. 5.1 SAI system in V12 engine

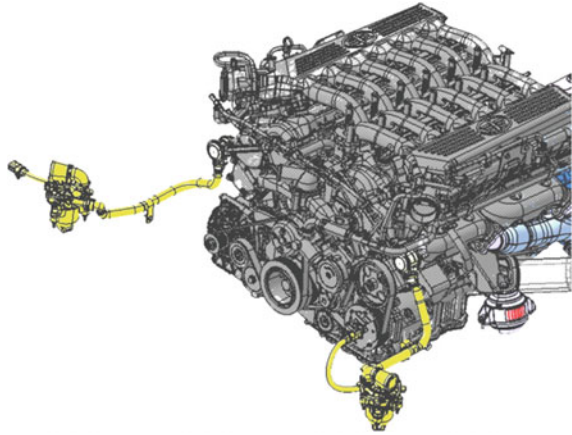


Fig. 5.2 Position of SAI

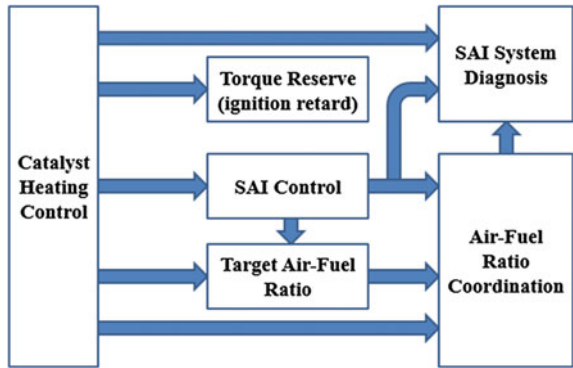


60–72 kg/h air mass flow. It should adopt 2 pumps to satisfy the requirement if choosing 800T2 type secondary air pump whose mass flow is 33.7 kg/h.

5.2.3 SAI Control Strategy

The most effective way is to introduce SAI in the phase of catalyst heating in accordance with the working theory of SAI. Therefore, the control of SAI is based on the catalyst heating strategy, combined with the following measures: increasing target idle speed, retarding ignition angle, enrich mixture. It could improve the thermal oxidation reaction of the exhaust if the secondary air is introduced rationally. Sequentially, the purpose of reducing the exhaust emissions is obtained. The control strategy of SAI is shown in Fig. 5.3.

Fig. 5.3 Control strategy of SAI



5.2.4 Emission Analysis of V12 Engine

Before the application of SAI, we optimized idle speed, air-fuel ratio, ignition angle, fuel injection angle and variable valve timing in the phase of catalyst heating. The emission result (ECE cycle) without SAI shows that THC and NMHC emissions are as high as the GB18352-2013 (CHINA 5) regulation limits, as shown in Table 5.2.

The modal emission performance of type I and type VI test are shown in Figs. 5.4 and 5.5. It is confirmed that the CO and THC emissions are mainly generated in the initial 60 s from the cold start through the analysis of the emission data. The main reason is that to ensure the reliability of cold start and warm-up idle, the mixture is rich what causes the raw emission is badly high. Besides, the exhaust system in this phase is cold, so the catalytic efficiency is extremely low. Therefore, SAI is needed in this phase to reduce emissions.

5.3 Calibration

5.3.1 Emission Analysis of a Foreign Vehicle

For a better research of the effect and calibration strategy of SAI system, a foreign V6 engine was chosen to analyze. The emission results with and without SAI from ECE cycle are compared, as shown in Table 5.3.

Table 5.2 Emission results without SAI

	CO g/km	THC g/km	NMHC g/km	NOx g/km
Type I test (regulation limits)	2.27	0.16	0.108	0.082
Type I test (V12 engine)	0.924	0.114	0.107	0.04
Type VI test (regulation limits)	30	3.2	–	–
Type VI test (V12 engine)	4.411	3.876	–	–

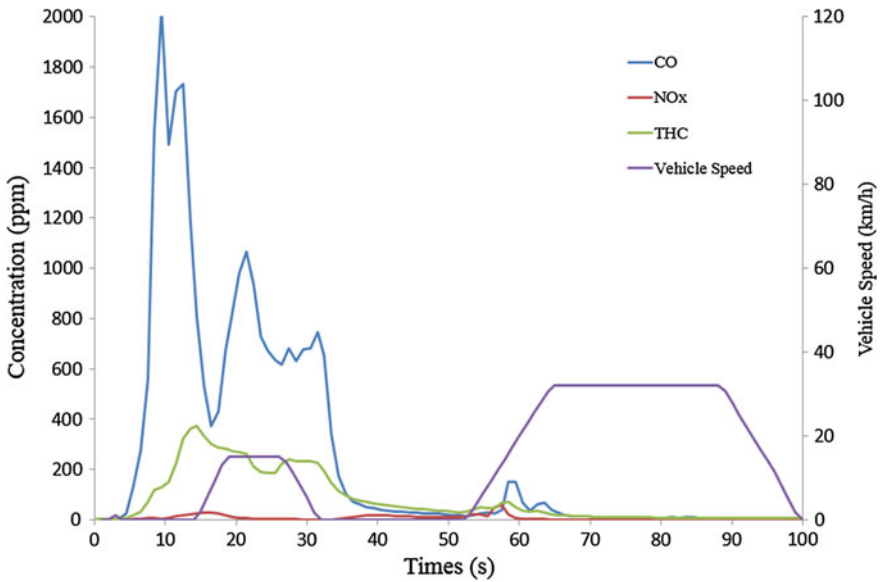


Fig. 5.4 Modal emission performance of type I test

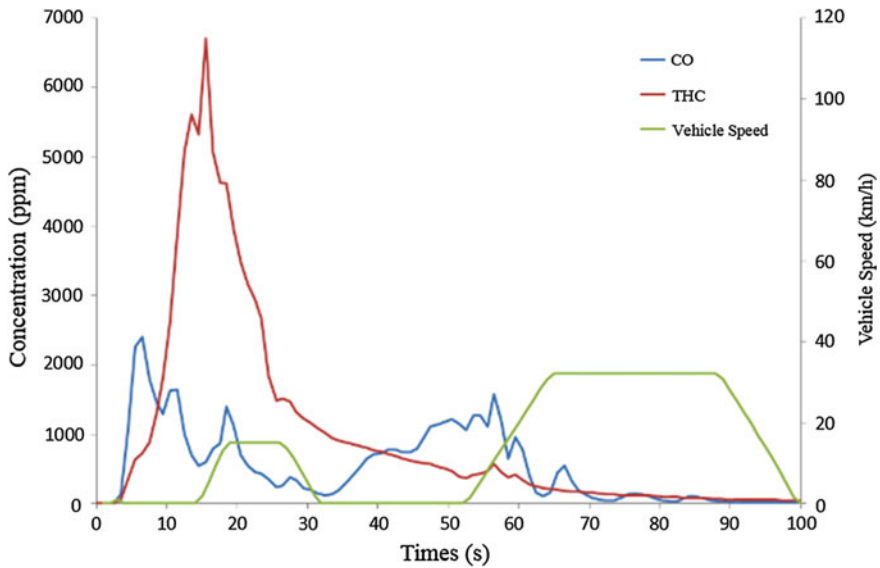


Fig. 5.5 Modal emission performance of type VI test

The process of air-fuel ratio and catalyst temperature in 60 s from engine start are shown in Figs. 5.6, 5.7 and Table 5.4.

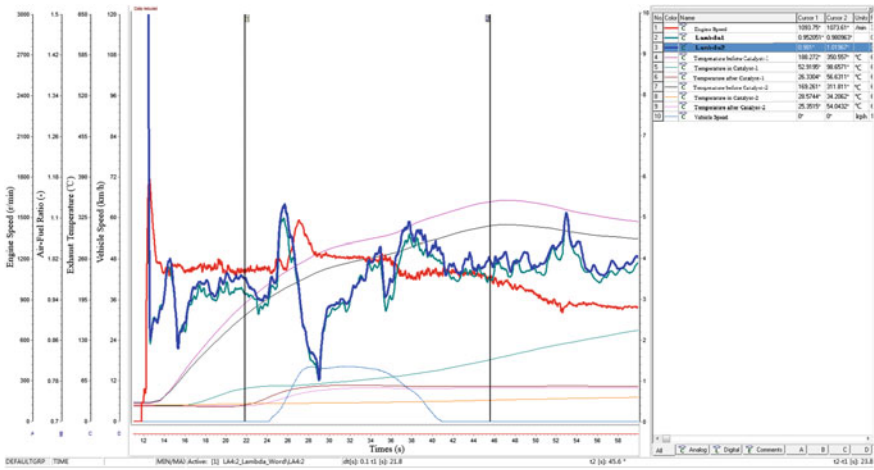


Fig. 5.7 Process without SAI

Table 5.4 Comparison of performance with and without SAI

	Time to catalyst light-off temperature (s)	Time to closed-loop control (s)
SAI on	32.4	43.9
SAI off	75.0	29.5

requirement conditions, it needs to optimize through tests that how long the SAI pump works. The final optimization working time of SAI pump in this vehicle is: 49.5 s in type I test and 70.5 s in type VI test.

5.3.3 Control of Air-Fuel Ratio

In order to benefit the thermal oxidation reaction, the mixture needs to be enriched. The rich mixture would cause unstable combustion, thereby resulting in misfire and THC increasing. While the lean mixture would significantly decrease the effect of SAI due to reduced reactants [1, 2]. According to experience, for a better utilization of SAI, the exhaust lambda should be lower than 1.5–1.6, while higher than 1.05–1.1. There is also opinion that THC emission reaches the minimum when exhaust lambda is around 1.25 [1]. Therefore, the optimized air-fuel ratio should be determined comprehensively according to exhaust temperature, as well the CO and THC emissions. As shown in Figs. 5.8 and 5.9, the emission results are excellent when exhaust lambda is between 1.2 and 1.4 during SAI.

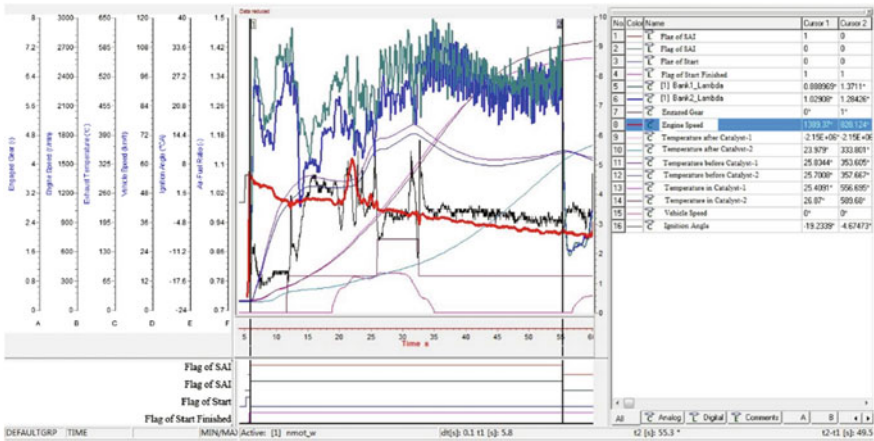


Fig. 5.8 SAI control in type I test

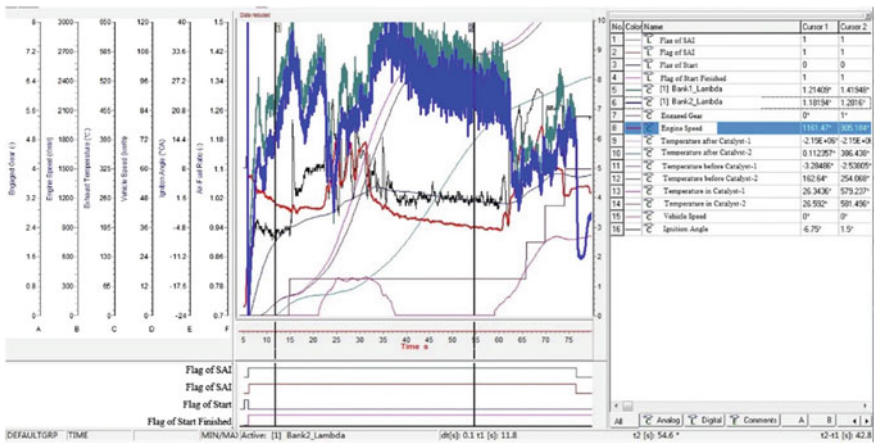


Fig. 5.9 SAI control in type VI test

5.3.4 Control of Ignition Angle

It benefits the reduction of emissions obviously that the optimization of ignition angle in the initial phase of ECE cycle. The proper delayed ignition angle is helpful to improve the exhaust temperature as quickly as possible. Nevertheless, it will cause unstable combustion, even misfire if the ignition angle is too late. This will deteriorate the emissions extremely [3]. However, for SAI system, it needs to furthest improve the exhaust temperature, even increase afterburning which requires greatly enriched mixture. And this is beneficial for the significantly delayed ignition angle meanwhile avoiding misfire.

Before the first engagement of the transmission, that is the initial 6 s in ECE cycle, the ignition angle could be retarded to 20°CA after TDC in type I test to facilitate the thermal oxidation reaction. And it could be maximally retarded to 5°CA after TDC in type VI test caused by poor combustion stability in low temperature. As shown in Figs. 5.8 and 5.9.

5.3.5 Diagnosis of SAI System

It is strict that the diagnostic requirement of the SAI system by the OBD regulation. It should detect the failure of the related electrical components and actuators, as well as the secondary air mass flow. It should be immediately reported and light on the MIL once there is a failure. The diagnosis of SAI system mainly includes 5 phases. Phase 1: the secondary air pump and valve are activated simultaneously to diagnose the second air mass flow. Phase 2: the secondary air pump is activated but not the secondary air valve to diagnose the leakage of the valve. Phase 3: the secondary air pump and valve are deactivated simultaneously to diagnose the offset of the second air mass flow. Phase 4 and 5: the secondary air pump and valve are activated and deactivated simultaneously to diagnose the adaption of the SAI system.

In order to satisfy the diagnosis of the SAI system without pressure sensor, it needs at least 10 s that the upstream oxygen sensor and the SAI pump work meanwhile, so that the EMS could detect the secondary air mass flow by the air-fuel ratio. Please note that this needs a wide-band oxygen sensor. Otherwise, a pressure sensor is needed for the detection of the secondary air mass flow. In addition, to satisfy the IUPR requirement, the SAI system also needs to be activated for 80–100 s in some other conditions.

5.4 Conclusions

The final optimization results show that the CO and THC were reduced by 45 and 42% in type I test while 40 and 56% in type VI test as expected, with the SAI system in the V12 engine. The results are shown in Tables 5.5, 5.6 and 5.7.

Table 5.5 Optimized results of SAI

Parameters	Optimized value		Unit
	Type I test	Type VI test	
working time of SAI	49.5	70.5	s
Exhaust lambda	1.2–1.4	1.2–1.4	–
Minimum ignition angle	≈ -20	≈ -5	°CA
Idle speed	1100–900	1200–1000	r/min

Table 5.6 Emission results of type I test

	CO	THC	NMHC	NO _x
Type I test (regulation limits)	2.27	0.16	0.108	0.082
Type I test (V12 engine)	0.505	0.066	0.06	0.04

Table 5.7 Emission results of type VI test

	CO	THC
Type VI test (regulation limits)	30	3.2
Type VI test (V12 engine)	2.63	1.71

From the point of view of practical application, this paper fully explained how to economize the SAI system to reduce CO and THC emissions. There is also work shows that it could improve the exhaust temperature and then benefit the thermal oxidation reaction [1] if the exhaust VCT is advanced during SAI operation. This is worthy to try if the emission regulation is more stringent. In conclusion, it is a significant method which adopts SAI system combing with GPF, HC adsorption and optimized catalytic converter to satisfy the emission regulation of CHINA 6.

References

1. (Frank) Zhao F (2007) Technologies for near-zero-emission gasoline-powered vehicles. SAE International, New York
2. Hernandez JL et al (2002) A study of the thermo chemical condition in the exhaust manifold using secondary air in a 2.0 L engine. SAE Paper, 2002-01-1676
3. Zhao H et al (2012) Investigation of large displacement gasoline engine to meet Euro V. Intern Combust Engin Parts 11(177):2–3

Chapter 6

Research on Soot Filtration and Pressure Drop Characteristics of DPF

Ying Gao, Hongqi Liu, Wei Chen, Tieqiang Fu, Maodong Fang
and Jun Li

Abstract An integrated DPF filtration model is proposed to study the properties of soot filtration and pressure drop, which includes deep bed filtration model, cake filtration model and pressure drop model. Research results show that the evolution of filtration can be divided into two stages named as deep bed filtration and cake filtration respectively. During deep bed filtration, soot is trapped in the filter wall, which results a rapid pressure drop gradient of 7.6 Pa/s. However, the soot quality only accounts for 1.6% of the total in whole filtration process. Compact soot layer is developed during soot filtration. And a linear increase of pressure drop with the gradient of 1.4 Pa/s during the stage. Besides, the pressure drop caused by the soot layer and cake layer are 54 and 38% respectively in the whole simulation duration.

Keywords DPF · Deep bed filtration · Cake filtration · Pressure drop

6.1 Introduction

As a valid method, DPF is widely used in the diesel vehicle to decrease soot emission. With soot loading increasing, the pressure drop increases at the same time, which will reduce the engine performance. To decrease pressure drop, soot regeneration is needed. By studying the substrate filtrating characteristics, the theoretical foundation is set up to predict the suitable time for regeneration. A visual experimental research has been made to research the characteristics of soot filtration in wall surface and inside the wall by Shigeki [1]. Filtration characteristics in different loading conditions were studied by Xiong Chen [2].

Y. Gao (✉) · H. Liu · W. Chen · J. Li
State Key Laboratory of Automotive Simulation and Control,
Jilin University, Changchun, China
e-mail: gaoying@jlu.edu.cn

T. Fu · M. Fang
China Automotive Technology and Research Center, Tianjin, China

Deep bed filtration and cake filtration models have been used to analysis the characteristics of pressure drop, filtration process and soot mass in this paper. Further, soot distribution and the impact of soot mass to pressure has been studied with pressure drop model.

6.2 Modeling of Soot Filtration

The filtration process of porous wall DPF includes deep bed filtration and cake filtration [3], which is showed in Fig. 6.1. Because of the large numbers and similar of channels, the specific characteristics of DPF are studied based on a single inlet and outlet like schematic Fig. 6.2.

Three substrate mechanisms are assumed when modeling DPF filtration models. First, particles are collected through Brownian diffusion and interception while interception is ignored. Second, to treat the soot in substrate distributed average. Last, to hold the velocity of the exhaust in filter wall is a constant and the physics parameters are the same in clean substrate.

6.2.1 Deep Bed Filtration Model

To study the deep bed filtration process, the filter wall is divided into a few slabs, while model of spherical cell is used in each slab [4]. Defining the spherical unit collector of diameter is b and the diameter of collector is d_c . The deep bed slabs and the collector are showed in Figs. 6.3 and 6.4, respectively.

Fig. 6.1 DPF filtration process

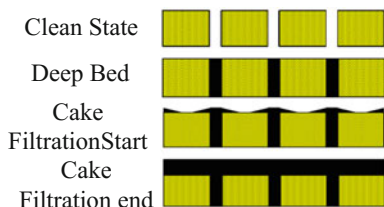


Fig. 6.2 DPF single inlet and outlet

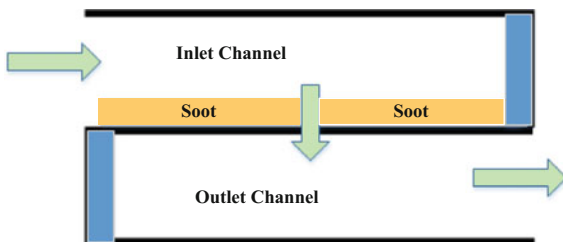


Fig. 6.3 Schematic of deep bed divided into slabs for computational purposes

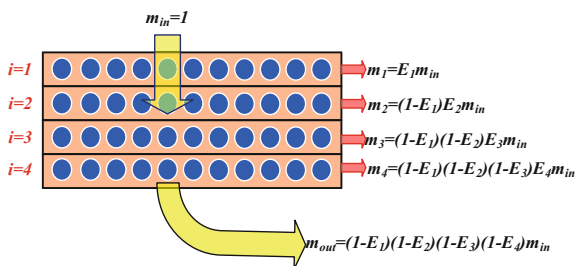
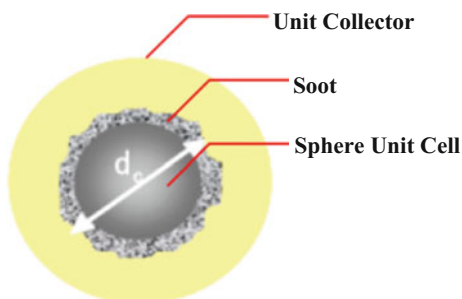


Fig. 6.4 Schematic diagram of spherical collective unit



Soot mass in the deep bed is calculated by Eq. (6.1):

$$m_{wall}(t) = \sum_{i=1}^N [m(i-, t)E(i-, t1)] \quad (6.1)$$

where

N number of divided slabs for deep bed

i serial number of slabs

$E(i)$ collection efficiency for different slabs

Wall collection efficiency is critical to study the retained soot mass. For clean porous wall DPF, the initial collector size d_{c0} and the spherical unit collector of diameter b are defined by Eqs. (6.2) and (6.3):

$$d_{c0} = \frac{3(1 - \varepsilon_0)}{2\varepsilon_0} d_{pore} \quad (6.2)$$

$$b = \left(\frac{d_{c0}^3}{1 - \varepsilon_0} \right)^{\frac{1}{3}} \quad (6.3)$$

where

d_{pore} diameter of the pore in filter wall

ε_0 initial porosity, which is set 0.59 in this paper

Particles are trapped by only one mechanism of Brownian diffusion or interception in the same time [5]. Then, overall collection efficiency for a single collector can be given by Eq. (6.4):

$$\eta_{DR} = \eta_D + \eta_R - \eta_D \eta_R \quad (6.4)$$

where

η_D Brownian diffusion collective efficiency, $\eta_D = 3.5 \cdot g(\varepsilon) \cdot Pe^{-\frac{2}{3}}$

η_R direct interception collective efficiency, $\eta_R = 1.5N_R^2 \frac{(g(\varepsilon))^3}{(1+N_R)^{\frac{3-2\varepsilon}{3\varepsilon}}}$

N_R Dimensionless interception parameter

Pe Peclet Number, which is a dimensionless number that measures the relation between convective and diffusive motion of particles flowing to the surface of a collector [6]

$g(\varepsilon)$ Kuwabara's hydrodynamic factor, which is calculated by Eq. (6.5):

$$g(\varepsilon) = \left[\frac{\varepsilon}{2 - \varepsilon - \frac{9}{5}(1 - \varepsilon)^{\frac{1}{3}} - \frac{1}{5}(1 - \varepsilon)^2} \right]^{\frac{1}{3}} \quad (6.5)$$

The initial value of clean filter wall collective efficiency is expressed in Eq. (6.6):

$$E = 1 - \exp \left[- \frac{3\eta_{DR} \cdot (1 - \varepsilon_0) \cdot w_s}{2\varepsilon_0 d_{c0}} \right] \quad (6.6)$$

With the filtration of deep bed, soot will deposit in the spherical collector unit and form a large unit until the unit diameter reach b . Because of the difference of particles mass retained in different slabs of the filter wall, which is resulted of different flow direction of permeated gas, the diameter of collector, porosity of the substrate and collective efficiency are varied with time. And the collective efficiency in different slabs are calculated by Eq. (6.7):

$$E(i, t) = 1 - \exp \left[- \frac{3\eta_{DR}(i, t) \cdot (1 - \varepsilon(i, t)) \cdot (x_{i+1} - x_i)}{2\varepsilon(i, t) d_c(i, t)} \right] \quad (6.7)$$

The mode of soot filtration will finally turn to cake filtration after deep bed filtration. So the end time of substrate trap is a key parameter. It can help analyzing the retained soot mass in filter and the increase rate of pressure drop during deep bed filtration. By analyzing the physics system of the filter wall, the cake layer comes into being when the first discrete slab reach the maximum trapping mass. The maximum mass of the first discrete slab is calculated by Eq. (6.8):

$$m_{1\max} = \frac{\rho_{\text{soot,wall}} \pi N_{\text{collector}} [(\psi b)^3 - d_{c0}^3]}{6} \quad (6.8)$$

where

- $\rho_{\text{soot,wall}}$ density of the soot in the filter wall
 $N_{\text{collector}}$ number of collector
 ψ a dimensionless ‘percolation’ control constant ($0 < \psi < 1$) [7].

6.2.2 Cake Filtration Model

After entering the cake layer filtration, the particles begin to form a dense cake layer on the wall surface. And because of the gradual formation of the soot accumulation and filter cake layer, the trapping effect in cake layer is higher than the deep bed filtration rate. Based on the mass balance mechanism of soot filtration process, the soot mass should be satisfied Eq. (6.9):

$$\frac{dm_{sc}(z)}{dt} = + \dot{R}_{sc} + v_w(z) \cdot \dot{m}_{\text{soot,inl}} \cdot S_{sc} \quad (6.9)$$

where

- $m_{sc}(z)$ total soot mass in DPF
 \dot{R}_{sc} reaction caused by source term
 $v_w(z)$ dimensionless flow rate
 S_{sc} two sources conversion term expressing the start of cake layer collection

Further, the thickness of cake layer is calculated by Eq. (6.10):

$$w_s = \frac{\alpha - \sqrt{\alpha^2 - \frac{m_c}{N_{\text{cell}} L \rho_{\text{soot,c}}}}}{2} \quad (6.10)$$

where

- α width of DPF, which is set 1.5 mm
 m_c overall retained soot mass
 N_{cell} number of inlet cell
 L filter length, which is set 203.2 mm
 $\rho_{\text{soot,c}}$ density of the cake layer soot.

6.2.3 Pressure Drop Model

In view of the characteristics of DPF structure, the pressure drop is mainly caused by six parts. That includes pressure drop when the exhaust gas flow through cake layer and wall, the pressure drop caused by the resistance in the inlet and outlet channels, the pressure drop caused by the mutation of the DPF import and export circulation section [6]. Then, the total pressure drop of a loaded filter is obtained by summing up above mentioned and shown in Eq. (6.11):

$$\begin{aligned}
 \Delta P &= \Delta P_{wall} + \Delta P_{soot} + \Delta P_{inlet} + \Delta P_{outlet} + \Delta P_{cont \& \exp} \\
 &= \frac{\mu}{k_{wall}} \frac{U\alpha}{4L} w + \frac{\mu}{k_{soot}} \int_0^w u(x) dx + \frac{\mu FUL}{3} \left[\frac{1}{(\alpha - 2w_s)^2} + \frac{1}{\alpha^2} \right] + \zeta \frac{\rho U^2}{2} \\
 &= \frac{\mu Q}{2V_{trap}} (\alpha + w)^2 \left[\frac{w_s}{k_w \alpha} + \frac{1}{2k_{soot}} \ln \left(\frac{\alpha}{\alpha - 2w_s} \right) + \frac{4FL^3}{3} \left(\frac{1}{(\alpha - 2w_s)^4} + \frac{1}{\alpha^4} \right) \right] \\
 &\quad + \frac{\rho Q^2 (\alpha + w_s)^4}{V_{trap}^2 \alpha^2} 2\zeta \left(\frac{L}{\alpha} \right)^2
 \end{aligned} \tag{6.11}$$

where

- Q exhaust flow volume
- W wall thickness equal to 0.3048 mm
- w_s thickness of the soot layer
- k_{wall} wall permeability
- k_{soot} cake layer permeability
- μ exhaust dynamic viscosity
- ρ exhaust gas density
- ζ resistance coefficient.

6.3 Parameter Calibration and Verification of Models

To calibrate the key parameters in model based on experiment data, which are wall surface permeability in clean DPF, wall surface permeability after soot loaded, density of soot, wall surface permeability in cake layer, respectively. And the results of calibration are $k_0 = 2.06 \times 10^{-13}(\text{m}^2)$, $k_{wall} = 5.02 \times 10^{-14}(\text{m}^2)$, $\rho_{soot,c} = 218(\text{kg}/\text{m}^3)$, $k_{soot} = 3.92 \times 10^{-15}(\text{m}^2)$. The pressure drop, which is calculated by the model applied with the parameters after calibration, is compared with the experiment data, and the difference value is showed in Figs. 6.5 and 6.7, while the relative error is showed in Figs. 6.6 and 6.8.

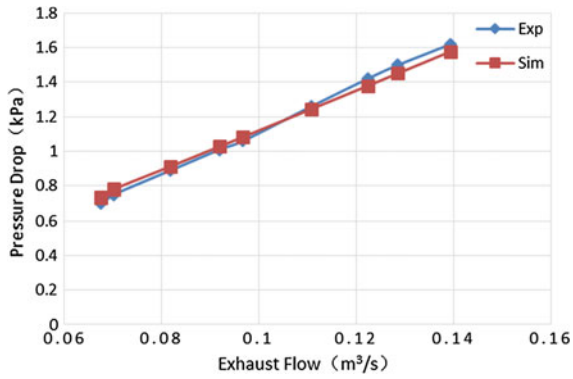


Fig. 6.5 Relation between pressure drop and exhaust mass flow in clean DPF

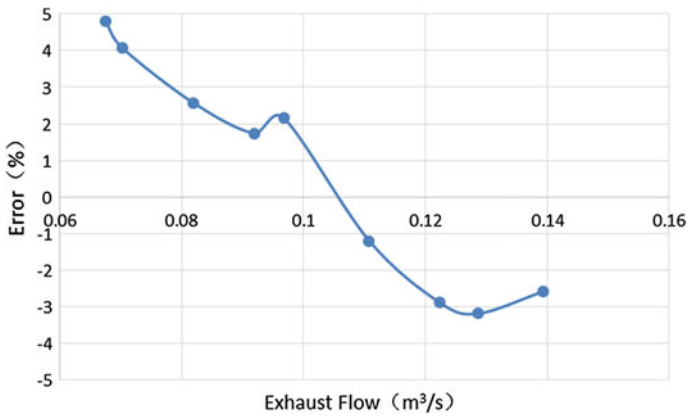


Fig. 6.6 Relative error

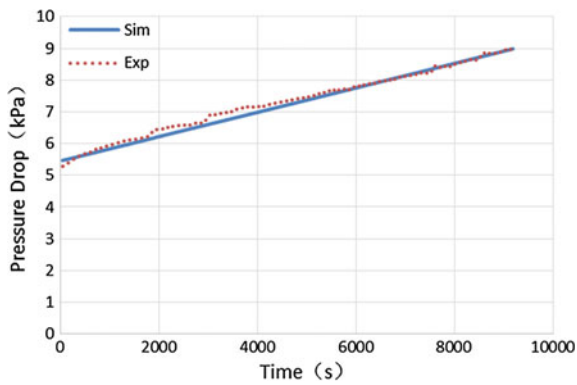


Fig. 6.7 Variation of pressure drop in filtration process

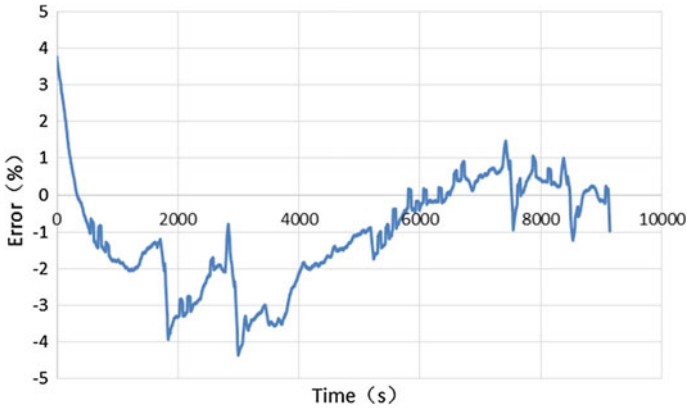


Fig. 6.8 Relative error

The relative error between simulation results and experiment data is within $\pm 5\%$. Results show that the simulation models can be used to study the characteristics of the filter in follow-on work.

6.4 Characteristics Analysis of Soot Filtration

6.4.1 Characteristics Variation of Pressure Drop

It can be seen from Fig. 6.9 that the duration of deep bed filtration phase is 185 s and change gradient of pressure drop is 7.6 Pa/s. And the duration of cake layer filtration phase is 1657 s and change gradient of pressure drop is 1.4 Pa/s in the whole filtration process of DPF. Thus, the degree of pressure drop is greater in deep bed filtration stage than in cake filtration stage with a shorter duration oppositely. As shown in Fig. 6.10, deep-bed filtration occurs inside the wall of DPF, which lead to the decrease of wall surface permeability. The permeability ratio of first discrete layer is minimum of $7.34 \times 10^{-14} \text{ (m}^2\text{)}$ after deep-bed filtration phase, which finally causes that the quantities of pressure drop in wall surface accounts for 78% of whole pressure drop. With the beginning of cake layer filtration, the ratio of pressure drop is increased linearly. And the proportion of pressure drop in soot layer is increased gradually while the one in wall surface and inlet/outlet channels is decreased gradually. By the end of soot filtration, the proportions of pressure drop in soot layer, wall surface and inlet/outlet channels are 54, 38 and 8% of the whole pressure drop respectively.

Fig. 6.9 Variation of pressure drop in process of soot filtration

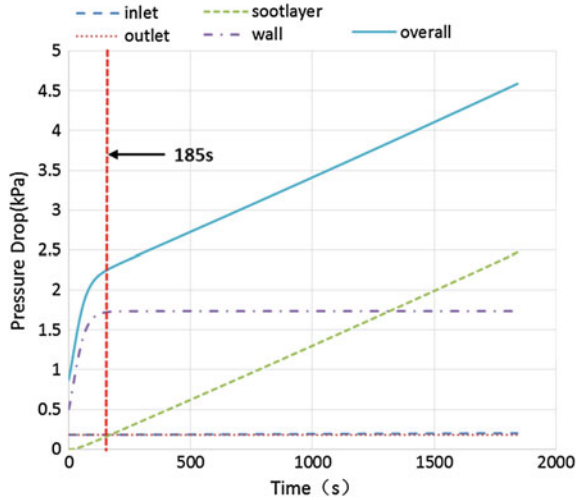
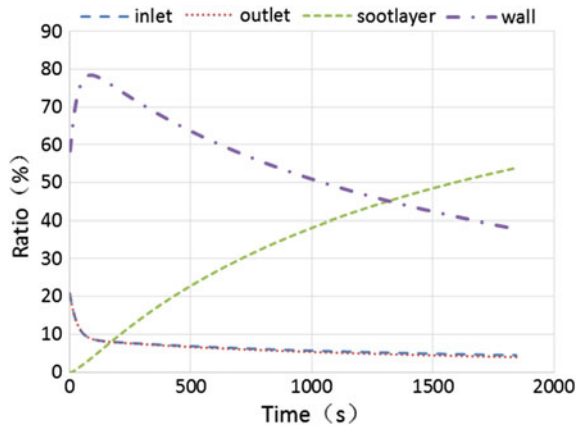


Fig. 6.10 Distribution ratio of pressure drop



6.4.2 Soot Mass Distribution Characteristics

As shown in Fig. 6.11, the retained soot mass is 25 g in filter, while the filtered soot mass retained in wall surface is 0.42 g. And the proportion of soot mass is 1.68% in deep bed filtration stage. It can be seen from Fig. 6.12, the soot mass is decreased along the direction of gas flow, while the soot mass in the first layer of wall surface have a maximum value of 66% of retained soot mass in deep bed. The soot mass is increased linearly in cake layer filtration and the final soot mass is 24.6 g. That accounts 98.4% of soot mass in the filter.

Fig. 6.11 Variation of soot mass

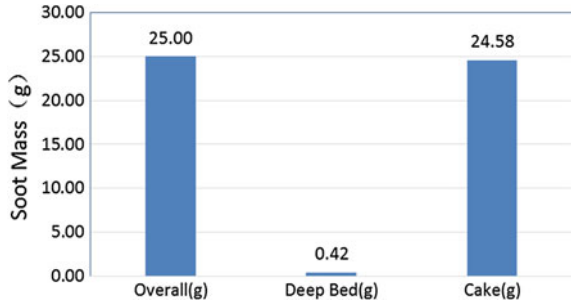
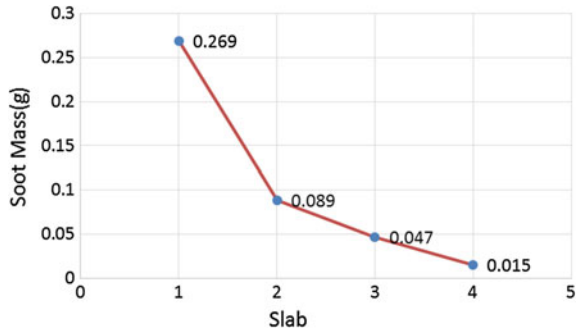


Fig. 6.12 Distribution of soot in different layer of wall surface



6.5 Conclusions

- (1) The integrated model have been built and verified with experiment data. The relative error is within $\pm 5\%$ between simulation results and experiment data.
- (2) The pressure drop in deep bed filtration holds a dominant amount of pressure drop in DPF. The change rate is 7.6 Pa/s during this stage, and the soot mass filtered in deep bed is 1.68%. The pressure drop is linear increase with soot mass in cake layer filtration. And it's proportion is 54% of whole pressure drop with a longer duration than that in deep bed filtration time. The soot mass in the first layer of wall surface have a maximum value of 66% of retained soot mass in deep bed. The soot mass is increased linearly in cake layer filtration, and it accounts 98.4% of soot mass in the filter.

Acknowledgements This research is supported by The National Key Research and Development Programs of China (grant no. 2016YFD0700800). The authors would like to thank Ma Bin, Yan Mingxing and Yang Fan as well as numerous students for excellent research assistance.

References

1. Daido S, Nobuyuki T (2009) Visualization of the PM deposition and oxidation behavior inside the DPF wall [C]. SAE Paper, 2009-01-1473
2. Chen X, Li M, Hou X et al (2013) A study on the filtration characteristics of DPF for diesel vehicle particulates in different driving conditions [J]. *Automot Eng* 35(12):1074–1077
3. Choi S, Kyeong L (2013) Detailed investigation of soot deposition and oxidation characteristics in a diesel particulate filter using optical visualization [C]. SAE Paper, 2013-01-0528
4. Kiran C. Premchand, John H. Johnson, Song-Lin Yang (2009) Development of a 1-D CPF model to simulate active regeneration of a diesel particulate filter, SAE 2009-01-1283
5. Ohara E, Mizuno Y, Miyairi Y, et al (2007) Filtration behavior of diesel particulate filters (1) [C]. SAE Paper, 2007-01-0921
6. Konstandopoulos AG, Kostoglou M, Skaperdas E, et al (2000) Fundamental studies of diesel particulate filters: transient loading, regeneration and aging [C]. SAE Paper 2000-01-1016
7. Konstandopoulos AG (1999) Deposit growth dynamics: particle sticking and scattering phenomena. *J Power Tech* 109(1):262–277

Chapter 7

Research on the Present Situation and Factors of Volatile Organic Compounds in Car Cabin

Jiabao Ren, Shujie Xu, Xuefeng Liu, Wei Liu and Enyou Cui

Abstract This article analyzed cabin indoor VOCs emission of more than 400 vehicles in attainment rate, average concentration and distribution situation. Result showed that in the past two years, the average concentrations of VOCs in vehicle decreased, but the overall compliance rate was still not high, acetaldehyde becoming limiting factor of overall compliance level. Meanwhile, this paper studies the relationship between sampling time, temperature, seasonal factors and VOCs detection results. The results provide a basis for the revision of the vehicle VOCs testing standards and manufacturing enterprise can use it to predict VOCs detection results.

Keywords Vehicle · Vehicle indoor air quality · Volatile organic compounds · VOCs · VIAQ

7.1 Preface

In recent years, with the improvement of people's living standards, people are more strict with cabin interior environment, vehicle indoor air quality has become one of the bottlenecks in the development of China's automotive industry. The Ministry of Environmental Protection of the People's Republic of China has promulgated national standard the HJ/T 400 "Determination of Volatile Organic Compounds and Carbonyl Compounds in Cabin of Vehicles" and GB/T 27630 "Guideline for air quality assessment of passenger car", setting vehicle VOCs detection method as well as VOCs concentration limit in vehicle, guiding the direction for domestic automobile enterprises (Table 7.1).

J. Ren (✉) · S. Xu · X. Liu · W. Liu
China Automotive Technology & Research Center, Tianjin, China
e-mail: renjiabao@catarc.ac.cn

E. Cui
Ningbo Automotive Component Testing CO., Ltd., Ningbo, China

Domestic experts focusing on vehicle indoor air quality also carried out in-depth study, Professor Ge Yunshan conducted a thorough research on the method of air quality inspection, and compare the volatile substances in the car with that in bus [1, 2]. Liu Xuefeng studied the present situation of VIAQ pollution in China's automobile products, and put forward some constructive suggestions for government [3]. However, domestic research has the problems with small sample size, lacking of effective data mining techniques and so on. In this paper, the VOCs of a large number of domestic and foreign cars was analyzed, and the influence of sampling time, temperature and seasonal factors on the VOCs detection results were analyzed. The results provide a basis for the revision of the vehicle VOCs testing standards and manufacturing enterprise can use it to predict VOCs detection results.

7.2 Data

7.2.1 Data Sources

China has the largest automotive production and market in the world, and the manufacturers have accumulates certain experience about air quality control in cabin. China Automotive Technology and Research Center has done a lot of research work on VOCs, and collected hundreds of VOCs test data. Suspicious data were deleted to guarantee the reliability (Table 7.2).

Table 7.1 Limit value of VOCs concentration in the air of cabin in GB/T 27630—2011 (unit: mg/m³)

Category	Name	Limit value
Benzene chemicals	Benzene	≤ 0.11
	Toluene	≤ 1.10
	Ethylbenzene	≤ 1.50
	Xylene	≤ 1.50
	Styrene	≤ 0.26
Aldehydes and ketones	Formaldehyde	≤ 0.10
	Acetaldehyde	≤ 0.05
	Propylene aldehyde	≤ 0.05

Table 7.2 Basic data information

Contents	Details
Test condition	Test date and place
Vehicle information	Vehicle type, production date, interior configuration
VOCs emission situation	The concentration of benzene, toluene, ethylbenzene xylene, styrene, formaldehyde, acetaldehyde, acrolein

7.3 Analysis on VOCs Emission of Vehicle in China

Based on the data collected in recent 2 years, this paper made a comprehensive analysis of the air quality in the domestic car from attainment rate, the mean value of eight hazardous substances and overall data distribution. Because attainment rate of propylene aldehyde is 100%, this article does not do the correlation analysis on it.

7.3.1 Attainment Rate

Figure 7.1 showed the attainment rate of vehicle and seven kinds of VOCs, it described that, compared to 2014, the air quality in China’s automotive products had been greatly improved in 2015. Attainment rate of benzene and propylene was 100%, and attainment rate of other substances increased by 2%, acetaldehyde has become the limiting factor to improve the attainment rate. Vehicle attainment rate has improved 3% in 2015, reaching 48%.

7.3.2 The Mean Value

The average value of VOCs concentration reflects the automobile enterprise VOC management and control level. In order to compare various harmful substances directly, we design the dimensionless mean value coefficient k .

$$k = \frac{\text{Average value of the concentration of certain volatile substance}}{\text{The material limits prescribed in national standard}}$$

Figure 7.2 showed the k value of 2014 and 2015, the figure described that enterprise had a different control capabilities of different hazardous substances.

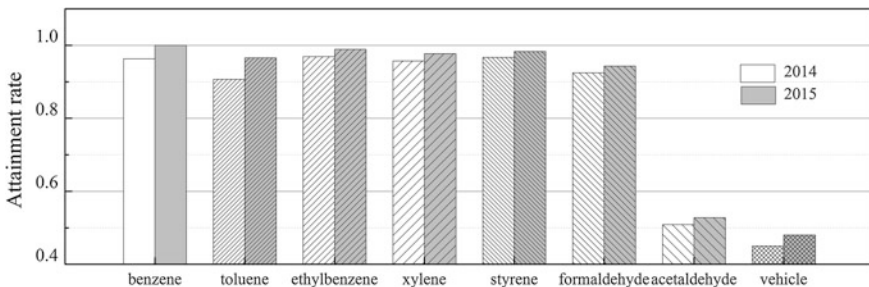


Fig. 7.1 Attainment rate of VOCs and vehicles

In 2014, acetaldehyde, benzene, toluene were more likely to exceed the standard, however, the concentration of benzene had reduced by 70% in 2015, and the order of the substances changed, meanwhile, xylene and toluene reduced a lot.

7.3.3 Data Distribution in 2015

In order to study the overall situation of VOCs emitting in China, we define the ratio coefficient h .

$$h = \frac{\text{Concentration of volatile harmful substances}}{\text{The material limits prescribed in national standard}}$$

Figure 7.3 showed part of the collected VOCs data with box chart. In the picture, the vertical coordinate represent h and the horizontal coordinates represent

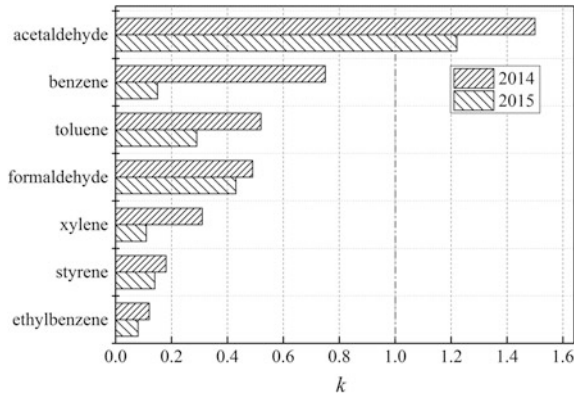


Fig. 7.2 k of 2014 and 2015

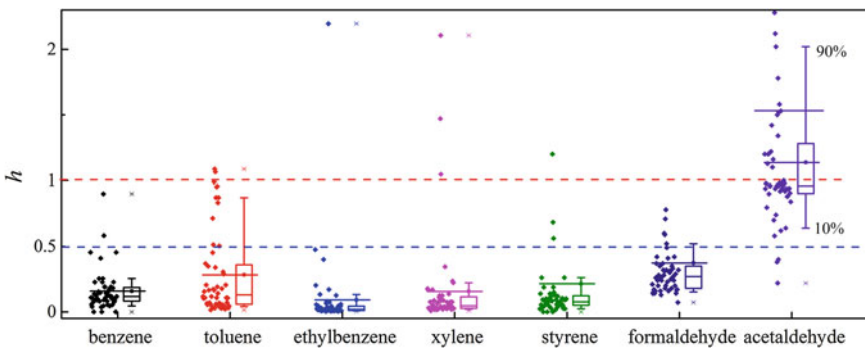


Fig. 7.3 VOCs distribution in 2015

Table 7.3 Statistical analysis of VOC data in 2015

Substance	National standard limit (mg/m ³)	Mean value (mg/m ³)	Median (mg/m ³)	<i>k</i>	Coefficient of variation
Benzene	0.11	0.02	0.013	0.15	0.78
Toluene	1.1	0.32	0.14	0.29	1.19
Ethylbenzene	1.5	0.12	0.026	0.08	3.75
Xylene	1.5	0.16	0.06	0.11	2.59
Styrene	0.26	0.04	0.014	0.14	3.08
Formaldehyde	0.1	0.05	0.04	0.42	1
Acetaldehyde	0.05	0.06	0.05	1.22	0.62

concentration of seven kinds of harmful substances. It was shown that, the VOCs concentration in different vehicle varied dramatically, data of formaldehyde and acetaldehyde was more dispersed than others. Besides, the data in 2015 were statistically analyzed, the results were as follows (Table 7.3).

According to statistical analysis above, mean value shows that acetaldehyde was more difficult to control, coefficient of variation showed that discrete degree of ethylbenzene, styrene and xylene was larger than others, reflecting enterprises had different management and control capabilities about the three substances.

7.4 Study on Influencing of Sample Time, Testing Temperature and Seasonal Factors

Air quality in car is affected by many factors. In this paper, based on the investigating data, combined with data from test, the influence of sample time, test temperature and season were studied. In the process, formaldehyde was used to represent aldehydes, and toluene was used to represent benzene.

7.4.1 Effect of Sample Time on VOCs Test

Vehicle would gradually release VOCs in daily use. Part of the VOCs were left in the producing process, such as volatile solvents in adhesives, others were decomposed from interior parts, such as decomposing from instrument panel under sun light. In this paper, the VOCs concentration changes of a normal used car was recorded.

Figure 7.4 showed the change of formaldehyde and toluene in the cabin in 0–300 days leaving assembly line, assuming that the initial emission concentration is 1, the following conclusions are drawn:

As can be seen in Fig. 7.4, the concentration of formaldehyde and toluene reduced gradually in cabin. 50 day is a key point in the picture, after 50 days

leaving assembly line, the concentrations of each reach just half of that on the assembly line.

The decay rate of formaldehyde is less than toluene. The figure showed that after the concentration of the formaldehyde reduced to half of that in factory, change with time is no longer obvious, but toluene concentration still decreased with the time.

It was concluded that after the product leaving assembly line, formaldehyde concentration was more easier be influences by the surrounding environmental than toluene. So, formaldehyde was more difficult to control than toluene for enterprises.

7.4.2 Effect of Temperature on VOCs Test

The VOCs in vehicle cabin is small molecules, and the effect of temperature on the movement of small molecules is obvious. Figure 7.5 shows the distribution of the

Fig. 7.4 The concentration of formaldehyde and toluene changed with time

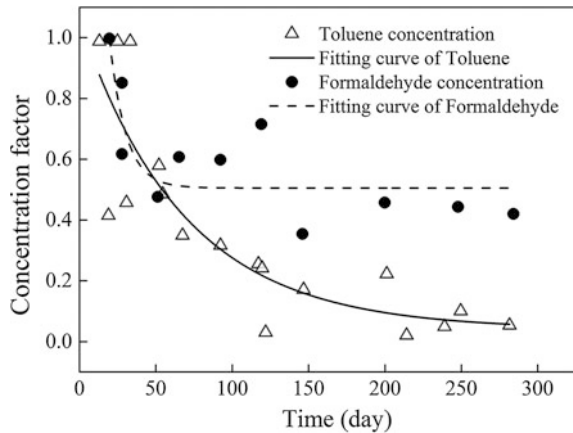
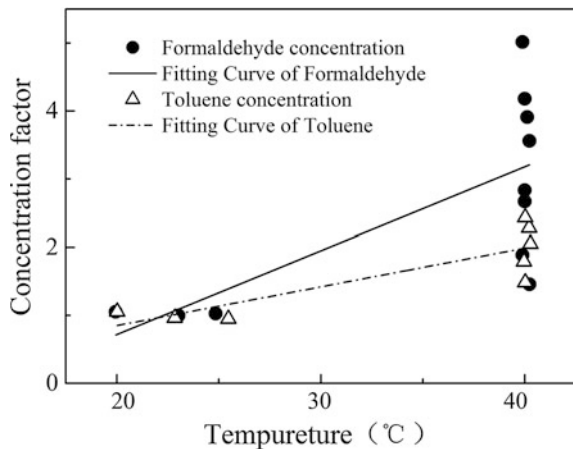


Fig. 7.5 The concentration of formaldehyde and toluene changed with temperature



concentration of formaldehyde and toluene with the detection of temperature changes.

The concentration of formaldehyde and toluene increased with temperature rise. Formaldehyde concentration increased at a faster rate than toluene. As can be seen from the figure, when the temperature rose from 20 to 40 °C, the formaldehyde concentration increased by about 2 times and the concentration of toluene increased by about 1 times.

7.4.3 VOCs Test in Different Seasons

Many experts pointed out that the VOCs concentration detected in different season different a lot. So, the relationship between VOCs emission and the test season was studied.

In the figure above, the coordinates represent the four seasons in one year, and the vertical coordinate represents the average value of certain VOCs concentration detected in this season.

Fig. 7.6 TVOC concentration detected in different seasons

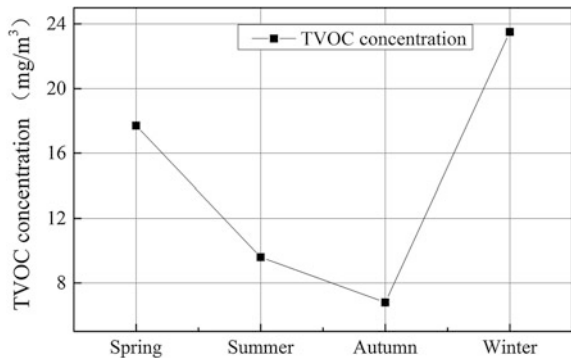


Fig. 7.7 Toluene concentration detected in different seasons

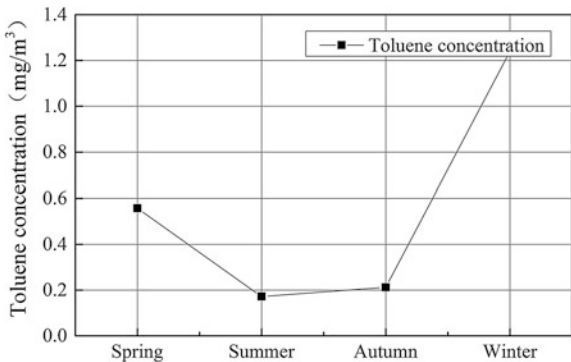


Figure 7.6 showed that TVOC data was sensitive to seasonal factors, of which the average of winter (23.5 mg/m^3) was 3.45 times of that of autumn (6.8 mg/m^3). Figure 7.7 showed the data of toluene, the average of winter (1.2 mg/m^3) was 6 times of that of summer (0.19 mg/m^3).

Due to different vehicle models were used for statistics, the number of data in different seasons was also different, so it was not scientific to derive a mathematical formula with the data. However, these data proved that season had certain influence on VOCs test. The relationship between the VOCs emission and the season remains to be further studied.

7.5 Conclusions

This article analyzed air quality of nearly 400 vehicles through attainment rate, mean value of VOCs concentration and data distribution in 2015. Through the work, it was more convenient for enterprises to quickly locate their level and made reasonable planning of the car VOCs control work.

By analyzing the influence of sampling time, temperature and seasonal factors on VOCs testing, it made a reference to revise existing VOCs testing standards.

At the same time, it also provided a basis for the vehicle enterprises to predict vehicle VOCs concentration after leaving the factory.

References

1. Ge Y (2006) In-car air pollution and its testing technology. *Automot Eng* 28(5):495–503
2. Ge Y (2009) Measurement of in-vehicle concentration of volatile organic compounds. *Automot Eng* 31(3):271–277
3. Liu X (2015) Situation and management policy about China's car VOC. *Environ Sustain Dev* 5:26–29

Chapter 8

Optimization Method of Low Exhaust Temperature Emissions of City Buses Meet China V

Tengteng Li, Changyuan Wang, Kongjian Qin and Xiaojun Jing

Abstract Emission problem of city bus running under low speed and low load is gradually becoming a research hotspot. The city buses were taken as research object in this paper. Emissions of two city bus were tested on heavy duty chassis dynamometer under CCBC. Test results showed that under low speed and low load conditions, because of low transformation efficiency of SCR, NO_x emission of engine was serious, but the NO_x emission of test vehicle can be significantly reduced by using the method of fixing heat insulating material on the exhaust pipe and ECU calibration according to low speed and load conditions of city buses. Test results also showed that after rehabilitation, emission reduction effect of NO_x was above 40%, other emissions do not deteriorate significantly.

Keywords City-bus · Low temperature SCR · Emission · Roller

8.1 Introduction

The technical route of SCR was taken as the standard route to meet China IV and higher emission standard in domestic for most of heavy duty vehicles. This route uses the following method to reduce emissions: inside the engine, the method of combustion optimization was used to reduce the emission of PM, outside the engine, the way of fixing SCR after treatment system on exhaust pipe to reduce emissions of NO_x [1, 2]. The typical characteristics of SCR system are as follows: conversion efficiency of NO_x is obviously influenced by the temperature of the catalyst [3]. The city buses always work at low speed and low load region, low exhaust temperature may cause low conversion efficiency of SCR catalytic, which leads to no effect on reduction of NO_x and high NO_x emission of City buses met IV or higher emission standard under real road driving model [4]. In order to solve the

T. Li (✉) · C. Wang · K. Qin · X. Jing
China Automotive Technology and Research Center, Tianjin 300162, China
e-mail: litengteng@catarc.ac.cn

above problems, enhance the efficiency of low temperature SCR conversion were very important.

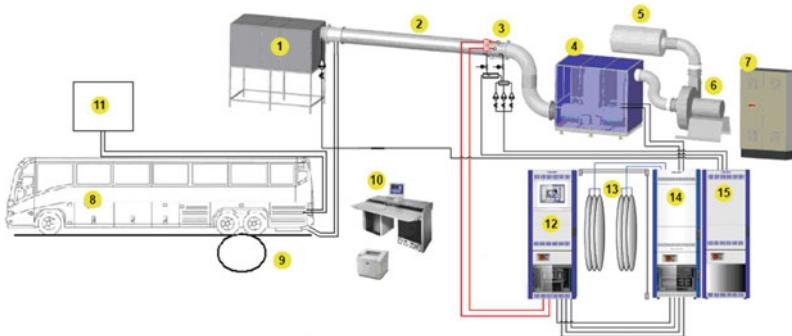
Many studies in this area were carried at home and abroad, such as wrapped with insulation materials to minimize the exhaust pipe cooling, adjusting the nozzle position of the urea, installing mixer, using molecular sieve catalyst and other means [5]. Using the method of insulation materials to minimize the exhaust pipe cooling and ECU calibration under low speed and load conditions can be significantly reduced the NO_x emissions, at the same time have the advance of low-cost and simple operation.

The city buses met China V emission standard were taken as research object in this paper. Emissions and fuel consumption of two city bus were tested on the heavy duty chassis dynamometer under CCBC and C-WTVC. In this paper, test vehicles were reformed, and the application effect of the modification scheme were evaluated.

8.2 Test Program

8.2.1 Test System

As showed in Fig. 8.1, the test system was made up of roller, constant volume system (CVS), particulate sampler system (PSS), gas analyzer and fuel consumption meter.



1—Air Filter; 2—Dilution Tunnel; 3—Sampling Device of PM; 4—Heat Exchanger; 5—Muffler; 6—Fan; 7—Power Distribution Cabinet of CVS; 8—Test Vehicle; 9—Heavy Duty Roller; 10—Master Computer; 11—735S & 753C; 12—Gas Analyzer(AMA I60); 13—Sampling Bags; 14—Control Cabinet of CVS; 15—Control Cabinet of PSS

Fig. 8.1 Test system

8.2.2 Test Vehicle

In this paper, two city buses (meet China V emission standard) were tested, Table 8.1 is the main parameters of two test vehicles.

8.2.3 Test Program

According to GB 27840-2011 [6], the Chinese city bus cycle (CCBC) and Adapted World Transient Vehicle Cycle (C-WTVC) were used to evaluate test vehicles. Test weight of two vehicles are curb weight plus 65% of full load. During the tests, the actual road running resistance of test vehicles was obtained by sliding tests on road. After each test, we calculated fuel consumption and emission of each vehicle. Emission test results of every vehicle were calculated based on GB 17691-2005 [7]. Specific tests were showed in Table 8.2.

Table 8.1 Main parameters of test vehicle

Items	Test vehicle A	Test vehicle B
L × W × H/mm	11,980 × 2550 × 3150	11,980 × 2550 × 3330
Curb weight/kg	11,200	11,800
Gross mass/kg	17,400	18,000
Engine model	6 cylinder + diesel	6 cylinder + diesel
Engine displacement/L	6.7	8.4
Net engine power/kW/r/min	215.4/2500	218/2200
Maximum torque/speed (N m/(r/min))	1100/(1200–1800)	1150/1200–1700
Idle speed/r/min	600–800	650 ± 25
Aftertreatment model	SCR	SCR
Emission level	China V	China V
Maximum speed km/h	100	100

Table 8.2 Test items

Number	Cycle	Load	Items	Remarks
Vehicle A	CCBC	65% load + curb weight	Cold test: 1 time (CCBC: 1) Hot test: 2 time (CCBC: 2)	Cold soaks before cold test: 12 h; Hot state tests were carried out continuously; Rehabilitation schemes: fixing heat insulating material on exhaust pipe, optimization of ECU data
Vehicle B	C-WTVC	65% load + curb weight	Hot test: 2 time (C-WTVC: 2)	
Vehicle B	CCBC	65% load + curb weight	Cold test: 1 time (CCBC: 1) Hot test: 2 time (CCBC: 2)	

Fig. 8.2 Chinese city bus cycle (CCBC)

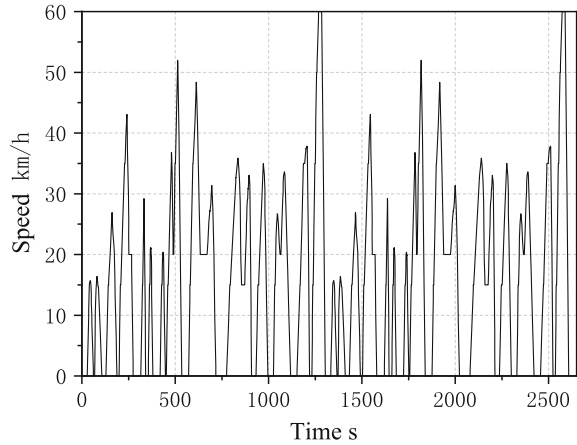
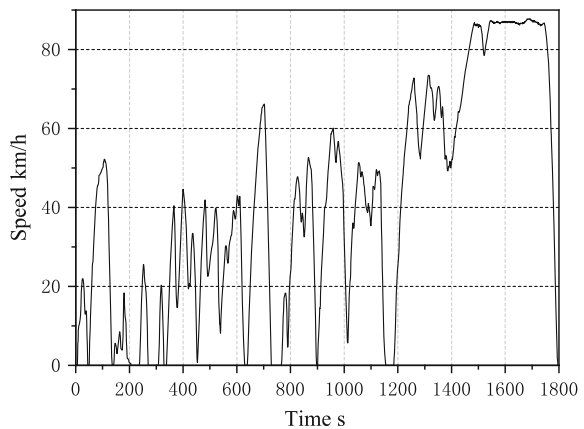


Fig. 8.3 Adapted world transient vehicle cycle (C-WTVC)



Test cycle is so called CCBC (China typical City Bus Cycle) [8], which was developed on the base of driving data collected from several megacities and took as standard cycle by GB19754 (Fig. 8.2).

C-WTVC was derived from the WTVC cycle. In order to meet the dynamic characteristics of domestic vehicles, the acceleration and deceleration condition were modified (Fig. 8.3).

8.3 Result and Discussion

8.3.1 Test Result of Fuel Economy

As showed in Table 8.3, based on CCBC, after rehabilitation of city bus, by the way of fixing heat insulating material on exhaust pipe and the optimization of ECU

Table 8.3 Test result of fuel economy

Test vehicle	Vehicle A		Vehicle B		
Test cycle	CCBC		CCBC		C-WTVC
Vehicle condition	Cold	Hot	Cold	Hot	Hot
Before rehabilitation L/100 km	35.02	30.72	33.10	31.66	25.18
After rehabilitation L/100 km	34.80	29.56	32.86	29.47	24.97
Difference (%)	-0.63	-3.92	-0.73	-6.92	-0.83

data, change of fuel consumption under cold state were not obvious, but the change of fuel consumption under hot state were obvious. Vehicle A were improved by 3.92%, and vehicle B were improved by 6.92%. Based on C-WTVC, the change of fuel consumption under hot state were not obvious. That is because, CCBC was typical city bus test cycle, the rehabilitation method could improve the fuel economy of city bus under the condition of frequently start and stop, low cycle speed. Compared with CCBC, C-WTVC is difference. In the view of fuel economy, the test results confirmed that the reconstruction scheme is low cost, high benefit for user, strong feasibility cost, and focus on special operation conditions of city bus.

8.3.2 Emission Test Results

As showed in Table 8.4, after rehabilitation, the NO_x reduction effect was very obvious: under city bus condition, emission reduction effect of NO_x was 44–50% under cold state, and up to 60% under hot state. Table 8.5 showed comparison of average exhaust temperature before and after rehabilitation under CCBC condition.

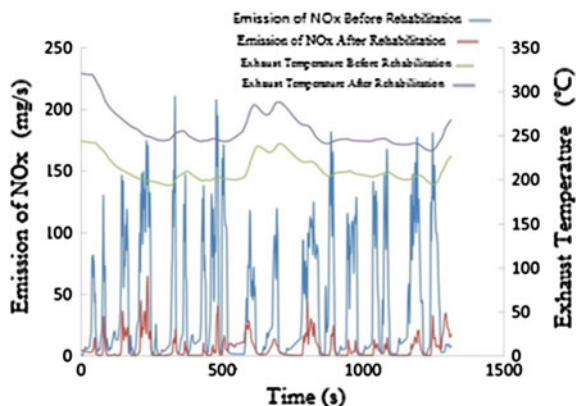
Table 8.4 Comparison of emission results of NO_x

Test vehicle	Vehicle A		Vehicle B		
Test cycle	CCBC		CCBC		C-WTVC
Vehicle condition	Cold	Hot	Cold	Hot	Hot
Before rehabilitation L/100 km	12.58	8.89	16.91	14.37	3.87
After rehabilitation L/100 km	6.29	1.33	9.45	4.01	1.45
Difference (%)	-50.0	-85.0	-44.1	-72.1	-62.6

Table 8.5 Comparison of average exhaust temperature under CCBC

Test vehicle	Vehicle A		Vehicle B	
Vehicle condition	Cold	Hot	Cold	Hot
Before rehabilitation °C	163.6	211.8	152.3	180.5
After rehabilitation °C	182.6	257.6	168.1	221.1
Heating °C	19.0	45.8	15.8	40.6

Fig. 8.4 Comparison results of exhaust temperature and NOx emission of vehicle A under hot condition



As showed in Table 8.5, after rehabilitation, the average exhaust temperature under cold state was increased by 16–19 °C, and increased by 40 °C under hot state, which improved the conversion efficiency of SCR catalyst obviously.

In order to further reduce NOx emission, the engine manufacturer also optimized ECU data, and reduced the urea spray temperature from 210–230 to 190 °C. So comparing with before rehabilitation, the time of urea started to spray was in advance. The above experimental results showed that the improvement of exhaust temperature, and the change of injection strategy could significantly reduce the emissions of NOx.

To further illustrate the change between exhaust temperature and NOx emissions before and after vehicle rehabilitation, the comparison results of exhaust temperature and NOx emission of vehicle A under hot condition were analyzed, as shown in Fig. 8.4. From Fig. 8.4, before rehabilitation, as the preheating of vehicle before test start, the exhaust temperature of test vehicle was 230 °C at the begin of test, but later due to reduction of engine load, exhaust temperature dropped sharply and changed at the temperature of urea spray, which caused the reduction of efficiency of SCR catalyst and the rise of transient NOx emission. After rehabilitation, the exhaust temperature of test vehicle was 321 °C at the begin of test, later due to reduction of engine load, exhaust temperature also dropped, but the exhaust temperature was higher than temperature of the urea spray, which brought the rise of efficiency of SCR catalyst and the reduction of transient NOx emission. From the point of whole cycle, before rehabilitation, the average temperature was 211 °C, and after rehabilitation the average temperature was 257 °C, the catalyst conversion efficiency was increased by more than 80%. So the whole test cycle, NOx emissions after rehabilitation was lower than that before rehabilitation by 85%.

In order to investigate the influence of vehicle rehabilitation on CO, THC and PM, the improvement of various pollutants in addition to NOx before and after rehabilitation was analyzed with the vehicle A. As showed in Table 8.6, after rehabilitation, the emission of THC was worse than before, the emission of CO was improved by 13–36%, the emission of PM was worse than before by 10%. THC

Table 8.6 Comparison of test results of other emissions of vehicle A

Vehicle condition	Cold condition			Hot condition		
	CO	THC	PM	CO	THC	PM
Before rehabilitation L/100 km	1.028	0.065	0.048	0.624	0.029	0.029
After rehabilitation L/100 km	0.888	0.071	0.052	0.400	0.038	0.031
Difference (%)	-13.60	9.20	8.30	-35.90	31.03	6.90

emissions of diesel engine were very low, the deterioration trend would not have a great impact on the emission test results. The PM emissions were worse than before, but PM deterioration was controllable.

8.4 Conclusion

The way of optimization of ECU data and wrapping insulation material around exhaust pipe could improve fuel economy, and achieve a substantial decline of NOx emission. Test results showed a decrease of more than 40%. At the same time, it could ensure that other emissions do not deteriorate significantly, emission reduction effect is remarkable. So from practicality, cost and operational point of view, the reconstruction scheme is feasible.

References

1. Ailing Q (2010) Analysis of technical routes for vehicle diesel engine to meet the national V emission stage. *Shanghai Mot* 2:59–62
2. Jian Huang (2008) Analysis of technical routes for diesel engine to meet high standard emission regulations. *J Fujian Univ Technol* 10:149–152
3. Zhongbiao W, Boqiong J, Yue L, et al (2007) Experimental study on a low-temperature SCR catalyst based on MnOx/TiO2 prepared by sol–gel method. *J Hazard Mater* 145(3):488–494
4. Lin M, Qin K, Yan F, et al (2013) Study on the driving cycle and NOx emission characteristics of city bus. *Adv Mater Res* 718:2457–2462
5. Chen Z, Hu J (2010) Experimental study on improving NOx conversion efficiency of urea-SCR system for diesel engine. *Veh Eng* 191(6):79–82
6. GB/T 27840–2011 (2011) Fuel consumption test methods for heavy-duty commercial vehicles. Published in 2011
7. GB/T 17691-2005 (2005) Limits and measurement methods for exhaust pollutants from compression ignition and gas fuelled positive ignition engines of vehicles (III, IV, IV). Published in 2005
8. National Technical Committee of AUTO Standardization (2013) GB/T 19754-2013 test methods for energy consumption of heavy-duty hybrid electric vehicle. Beijing, Published in 2013

Chapter 9

Analysis and Test Research for Three-Phase Short-Circuit of Permanent Magnet Synchronous Motor for an Electric Vehicle

Sibo Wang, Chao Lu, Xiaoxu Wang and Huichao Zhao

Abstract Permanent magnet synchronous motor (PMSM) is widely used in the electric vehicle as a drive motor. For specific application requirements of the electric vehicle motor system, there are new faults and application characteristics in motor system's three-phase short-circuit. Based on the dq axis coordinate system mathematical model of PMSM, this paper derives the dq axis current transient equations of three-phase transient short-circuit with load or without load in initial state. Combined electric vehicle PMSM operating characteristics, based on the typical working conditions, this paper analyzes the influences of motor demagnetization risk in different conditions by comparing the transient current changing process simulation results of different initial transient dq axis currents. Then according to the characteristics of the three-phase transient short-circuit, designs and builds a test platform, and verifies the correctness of the analysis and mathematical simulation models by testing. It provides an important theoretical analysis and test verification methods for analyzing the electric vehicle PMSM three-phase short-current function and determining the risk of demagnetization.

Keywords Electric vehicle · PMSM · Three-phase transient short-circuit · Transient short-circuit test

9.1 Introduction

Electric vehicles is an important developing trend to cut off emission, nowadays, mainstream OEMs have invested heavily for this kind of future vehicles. Permanent magnet synchronous motor (PMSM) which has been widely used in the electric

S. Wang (✉) · C. Lu · X. Wang · H. Zhao
E-motor system development Sec., Electric Vehicle Dept.,
FAW R&D Center, Changchun, China
e-mail: wang_sibo@rdc.faw.com.cn

vehicle covers many advantages such as high torque and power density, wide range of flux-weakening control and easily maintenance. However, the PMSM system of the vehicle will also bring some new security features such as three-phase short-circuit. Research on three-phase short-circuit of traditional motor system has been done for years in China and abroad, but there are no literatures in-depth study of PMSM three-phase short-circuit for electric vehicles.

There are new fault handling and application characteristics on three-phase short-circuit in the field of electric vehicles. On the one hand, the three-phase short-circuit as a kind of fault may cause the demagnetization of permanent magnets or partial demagnetization [1]. The rising winding temperature and vibration noise caused by short-circuit may lead to the damage of other parts of the vehicle. On the other hand, if critical fault such as the inverter IGBT breakdown or insulation failure on high voltage system happens suddenly during the vehicle moving, the inverter can execute a three-phase active short-circuit to decouple the motor and transmission system in order to avoid the risk of the motor over-speed. This function can guarantee that the inverter thin-film capacitor and power devices are not be broken down by over voltage and also can braking the vehicle and shut down the engine safely by the anti-drag torque [2]. The three-phase short-circuit may be either one kind of fault or one kind of active safety function. The vehicle configurations, motor electromagnetic and heat dissipation solutions, and the safety requirements for electronic control system are all needed to be considered as a safety function. Above all, the three-phase short-circuit condition analysis is crucial for electric vehicles' safety.

Before designing a three-phase active short-circuit function or analyzing the failure modes of the system after three-phase short-circuit, it should be confirmed that there is no risk of reversible demagnetization at the condition of three-phase transient short-circuit. Considering the maximum negative -axis current when the motor working, the demagnetization current limit and safety factor should be set during the design, but there is no security check for motor transient short-circuit conditions [3]. Thus, it is necessary for electric vehicle motor design to analyze the negative-axis current at the three-phase transient short-circuit condition and confirm the current within the maximum range of the demagnetization current by testing. Electric vehicle drive system increases the new motor system, which has different degrees of coupling relationship with engine, transmission and so on as a new source of power. Since the working condition is extremely complex, the motor is usually designed as high output and wide speed range in order to match the power train system. When we are analyzing the three-phase transient short-circuit, the vehicle condition such as low speed start, driving generating etc. shall be considered to evaluate the effect caused by the transient short-circuit demagnetization current. The three-phase transient short-circuit test platform and research method is aimed at steady state or low power permanent magnet synchronous motor [4]. There is a problem of transient test bench speed fluctuation caused by the transient impact [5]. Then to simulate electric vehicle short-circuit condition on the bench, it is worth to study how to solve the speed fluctuation problem caused by three-phase transient short-circuit and ensure the safety of the system and dynamic synchronous sampling.

Based on the dq -axis model of vector control, this paper derives the dq -axis current equations of the electric vehicle motor system at the time of three-phase transient short-circuit. And based on different initial working conditions, this paper analyzes the condition where the maximum demagnetization current occurs during the three-phase transient short-circuit. This paper also gives out the simple simulation algorithm to verify the maximum demagnetization current, and verifies the correctness of the transient short-circuit current equations through the test.

9.2 Three-Phase Transient Short-Circuit Model

Usually, the short-circuit current's curve change over time can be calculated by CAE simulation software in engineering design. In this paper, the process of PMSM transient short-circuit can be analyzed by vector control of the dq -axis model, which can be used to analyze the steady-state and transient process. The algorithm also has a salient feature that is fast operation and evaluation.

Before establishing the mathematical model, the follow assumptions shall be done.

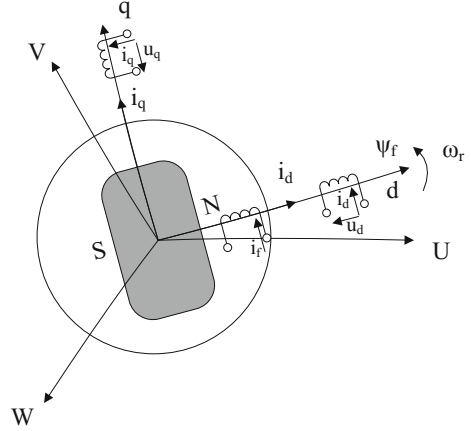
- (1) Ignore the rotor core reluctance, excluding the eddy current and hysteresis loss.
- (2) The conductivity of permanent magnet material is zero, and the magnetic permeability inside the permanent magnet is consistent with the air.
- (3) Permanent magnet excitation magnetic field generates a sine wave induced electromotive force in the phase windings.
- (4) Permanent magnet magnetic field and three-phase armature reaction magnetic field is sinusoidal in the air gap.
- (5) Ignore the effect of the magnetic saturation and the temperature to the motor parameters, the motor parameters are constant.

In this paper, interior permanent magnet synchronous motor (IPMSM) is used to establish a transient short-circuit model of permanent magnet synchronous motors. The model also applies to surface mounted permanent magnet synchronous motor (SPMSM). Interior permanent magnet synchronous motor's L_d and L_q is not equal. Currently, most vehicles with permanent magnet synchronous motor are interior, mainly because in the case of the same current, the output torque can be increased by the reluctance torque.

Figure 9.1 shows a synchronous rotating dq -axis, the U, V, W phase current is transformed into a stationary dq -axis current by the coordinate transformation. Voltage equation is given by

$$\begin{cases} U_d = R_S i_d + L_d \frac{di_d}{dt} - \omega_e L_q i_q \\ U_q = R_S i_q + L_q \frac{di_q}{dt} - \omega_e (L_d i_d + \psi_f) \end{cases} \quad (9.1)$$

Fig. 9.1 Synchronous rotating dq axis



- U_d, U_q Stator voltage dq -axis component,
 i_d, i_q Stator current dq -axis component,
 R_s Stator phase resistance,
 ψ_f Flux linkage generated by permanent magnet,
 $L_d L_q$ Stator winding dq -axis inductance,
 $\omega_e = p_n \times \omega_r, p_n$; Stator current electrical frequency,
 p_n Motor pole pairs,
 ω_r Rotor angular velocity.

Firstly, let's analyze the situation when dq -axis current is zero at the time of the three-phase short-circuit. The dq -axis transient short-circuit current and voltage is given by

$$\begin{cases} i_d(0_-) = 0, & i_q(0_-) = 0 \\ U_d(0_+) = 0, & U_q(0_+) = 0 \end{cases} \quad (9.2)$$

By Laplace transform the differential equations formula (9.1) can be transformed into complex frequency domain equation as (9.3).

$$\begin{cases} R_s i_d(s) + L_d s i_d(s) - \omega_e L_q i_q(s) = 0 \\ R_s i_q(s) + L_d s i_q(s) - \omega_e L_d i_d(s) + \psi_f = 0 \end{cases} \quad (9.3)$$

The formula (9.4) can be calculated by solving Eq. (9.3).

$$\begin{cases} i_q(s) = \frac{-\frac{r}{L_d L_q} \omega \psi_f - \frac{r}{L_q} \omega \psi_f s}{s \left(s^2 + s \left(\frac{r}{L_d} + \frac{r}{L_q} \right) + \frac{r^2}{L_d L_q} + \omega^2 \right)} \\ i_d(s) = \frac{-\frac{1}{L_d} \omega^2 \psi_f}{s \left(s^2 + s \left(\frac{r}{L_d} + \frac{r}{L_q} \right) + \frac{r^2}{L_d L_q} + \omega^2 \right)} \end{cases} \quad (9.4)$$

The denominator can be decomposed into:

$$s \left(s^2 + s \left(\frac{r}{L_d} + \frac{r}{L_q} \right) + \frac{r^2}{L_d L_q} + \omega^2 \right) = s(s - s_1)(s - s_2)$$

where

$$s_1, s_2 = -a \pm j\sqrt{b^2 - a^2} = -\frac{r}{2} \left(\frac{1}{L_d} + \frac{1}{L_q} \right) \pm j\sqrt{\frac{r^2}{L_d L_q} + \omega^2 - \frac{r^2}{4} \left(\frac{1}{L_d} + \frac{1}{L_q} \right)^2}$$

$$a = \frac{r}{2} \left(\frac{1}{L_d} + \frac{1}{L_q} \right), \quad b = \sqrt{\frac{r^2}{L_d L_q} + \omega^2}, \quad c = -\frac{1}{L_d} \omega^2 \psi_f$$

Solve the original function of the formula (9.5).

$$\begin{cases} i_d(s) = -\frac{1}{L_d} \omega^2 \psi_f \frac{1}{s(s-s_1)(s-s_2)} \\ i_d(s) = \frac{c}{b^2} \left(\frac{1}{s} - \frac{s+a}{(s+a)^2 + b^2 - a^2} - \frac{a}{(s+a)^2 + b^2 - a^2} \right) \end{cases} \quad (9.5)$$

The original function is:

$$\begin{aligned} i_d(t) &= \frac{c}{b^2} \left[1 - e^{-at} \left(\cos \sqrt{b^2 - a^2} \cdot t + \frac{a}{\sqrt{b^2 - a^2}} \sin(\sqrt{b^2 - a^2} \cdot t) \right) \right] \\ &= \frac{c}{b^2} \left[1 - \frac{b}{\sqrt{b^2 - a^2}} e^{-at} \sin \left(\sqrt{b^2 - a^2} \cdot t + \arctan \left(\frac{\sqrt{b^2 - a^2}}{a} \right) \right) \right] \end{aligned} \quad (9.6)$$

Similarly

$$\begin{aligned} i_q(s) &= \frac{-\frac{r}{L_d L_q} \omega \psi_f - \frac{r}{L_q} \omega \psi_f s}{s(s - s_1)(s - s_2)} = -\frac{d}{b^2} i_d(s) - \frac{\omega}{L_q} \cdot \psi_f \cdot \frac{1}{(s - s_1)(s - s_2)} \\ &= -\frac{d}{b^2} i_d(s) - \frac{e}{b^2} \cdot \frac{b^2}{(s - s_1)(s - s_2)} \\ &= -\frac{d}{b^2} i_d(t) - \frac{e}{b^2} \cdot \frac{1}{\sqrt{b^2 - a^2}} \cdot e^{-at} \sin(\sqrt{b^2 - a^2} \cdot t) \end{aligned} \quad (9.7)$$

where

$$d = -\frac{r}{L_d L_q} \omega \psi_f, \quad e = \frac{\omega}{L_d} \psi_f$$

The formula (9.7) is a transcendental function. The maximum $-i_d$ current cannot be calculated from this formula. But the response curve can be obtained by computer in engineering generally, so to obtain the maximum $-i_d$ current. This work will be described in detail in the next chapter.

$$\frac{c}{b^2} = -\frac{\omega^2 \psi_f L_q}{r^2 + \omega^2 L_d L_q}, \quad \frac{d}{b^2} = -\frac{r \omega \psi_f}{r^2 + \omega^2 L_d L_q} \quad (9.8)$$

Formula (9.8) are the steady-state final values of dq -axis current respectively, and are also the analytical expressions of the dq -axis steady-state short-circuit.

When the initial values of i_d, i_q is not zero, that is, the motor system has output torque at the time of transient short-circuit. The differential Eq. (9.1) has the following initial conditions.

$$\begin{cases} i_d(0_-) \neq 0, & i_q(0_-) \neq 0 \\ U_d(0_+) = 0, & U_q(0_+) = 0 \end{cases} \quad (9.9)$$

Solve the Laplace transform equations containing the initial value. The solution are:

$$\begin{cases} i_d(s) = \frac{i_d(0_-) \cdot s^2}{s(s-s_1)(s-s_2)} + \frac{\left[\frac{\omega_e L_q}{L_d} \cdot i_q(0_-) + \left(\frac{r}{L_q} - \frac{r}{L_d} \right) \cdot i_d(0_-) \right] \cdot s}{s(s-s_1)(s-s_2)} - \frac{\left[\frac{\omega_e r}{L_d} \cdot i_q(0_-) + \frac{\omega_e^2}{L_d} \psi_f + \frac{r^2}{L_d L_q} \cdot i_d(0_-) \right]}{s(s-s_1)(s-s_2)} \\ i_q(s) = \frac{i_q(0_-) \cdot s^2}{s(s-s_1)(s-s_2)} + \frac{\left[-\frac{r}{L_q} \cdot i_q(0_-) - \frac{\omega_e \psi_f}{L_q} + \frac{i_q(0_-)}{L_d r} - \frac{\omega_e L_d}{L_q} \right] \cdot s}{s(s-s_1)(s-s_2)} - \frac{\frac{\omega \psi_f r}{L_d L_q} + \frac{\omega r}{L_q} \cdot i_d(0_-)}{s(s-s_1)(s-s_2)} \end{cases} \quad (9.10)$$

The above formula can be written is given by

$$\begin{cases} i_d(s) = \frac{A \cdot s^2 + B \cdot s + C}{s(s-s_1)(s-s_2)} \\ i_q(s) = \frac{A' \cdot s^2 + B' \cdot s + C'}{s(s-s_1)(s-s_2)} \end{cases} \quad (9.11)$$

where

$$\begin{cases} A = i_d(0_-) \cdot s^2 \\ B = \left[\frac{\omega_e L_q}{L_d} \cdot i_q(0_-) + \left(\frac{r}{L_q} - \frac{r}{L_d} \right) \cdot i_d(0_-) \right] \\ C = \left[\frac{\omega_e r}{L_d} \cdot i_q(0_-) + \frac{\omega_e^2}{L_d} \psi_f + \frac{r^2}{L_d L_q} \cdot i_d(0_-) \right] \end{cases} \quad (9.12)$$

$$\begin{cases} A' = i_q(0_-) \\ B' = \left[-\frac{r}{L_q} \cdot i_q(0_-) - \frac{\omega_e \psi_f}{L_q} + \frac{i_q(0_-)}{L_d r} - \frac{\omega_e L_d}{L_q} \right] \\ C' = -\frac{\omega \psi_f r}{L_d L_q} + \frac{\omega r}{L_q} \cdot i_d(0_-) \end{cases} \quad (9.13)$$

i_d and i_q can be obtained as

$$\begin{cases} i_d(s) = A \cdot \frac{s}{(s-s_1)(s-s_2)} + B \cdot \frac{1}{(s-s_1)(s-s_2)} + C \cdot \frac{1}{s(s-s_1)(s-s_2)} \\ i_q(s) = A' \cdot \frac{s}{(s-s_1)(s-s_2)} + B' \cdot \frac{1}{(s-s_1)(s-s_2)} + C' \cdot \frac{1}{s(s-s_1)(s-s_2)} \end{cases} \quad (9.14)$$

$$\begin{cases} i_d(t) = \frac{A}{\sqrt{b^2 - a^2}} \cdot \left[\begin{array}{l} -ae^{-at} \sin(\sqrt{b^2 - a^2} \cdot t) \\ + e^{-at} (\sqrt{b^2 - a^2}) \cdot \cos(\sqrt{b^2 - a^2} \cdot t) \end{array} \right] + \frac{B}{\sqrt{b^2 - a^2}} \cdot \left[e^{-at} \sin(\sqrt{b^2 - a^2} \cdot t) \right] \\ + C \cdot \left[1 - \frac{1}{\sqrt{b^2 - a^2}} \cdot e^{-at} \sin \left(\begin{array}{l} \sqrt{b^2 - a^2} \cdot t \\ + \arctan \left(\frac{\sqrt{b^2 - a^2}}{a} \right) \end{array} \right) \right] \\ i_q(t) = \frac{A'}{\sqrt{b^2 - a^2}} \cdot \left[\begin{array}{l} -ae^{-at} \sin(\sqrt{b^2 - a^2} \cdot t) \\ + e^{-at} (\sqrt{b^2 - a^2}) \cdot \cos(\sqrt{b^2 - a^2} \cdot t) \end{array} \right] + \frac{B'}{\sqrt{b^2 - a^2}} \cdot \left[e^{-at} \sin(\sqrt{b^2 - a^2} \cdot t) \right] \\ + C' \cdot \left[1 - \frac{1}{\sqrt{b^2 - a^2}} \cdot e^{-at} \sin \left(\begin{array}{l} \sqrt{b^2 - a^2} \cdot t \\ + \arctan \left(\frac{\sqrt{b^2 - a^2}}{a} \right) \end{array} \right) \right] \end{cases} \quad (9.15)$$

The condition dq -Axis current initial value is not zero and the condition that dq -axis current initial value is zero have the same final steady-state values.

By the above expression we can also see, the three-phase transient short-circuit process is related to the inductance, the resistance and the flux linkage and other parameters of the motor, and also, related to the i_d, i_q initial state, of which the process is more complex, there are more influenced dynamic parameters. In the actual engineering design, the complete system response curve can be drawing by computer solving. So not only the dynamic process of the known parameters' motor can be calculated fast and the risk of demagnetization can be assessed, but also the effect to the transient short-circuit process and demagnetization current under different i_d, i_q, ψ_f and other parameters can be compared.

9.3 Transient Short-Circuit Simulation Analysis Based on the Actual Operation Condition

We have analyzed the three-phase transient short-circuit in the last chapter, which gives a analytical expression of i_d, i_q short circuit current. From the expression, it can be found that the changing process of the transient short-circuit is related to motor dq -axis inductance, permanent magnet flux and other motor parameters, and also will be effected by the speed and the initial value of $i_d i_q$ current at the moment of short-circuit state. Ignore the magnetic saturation, and assume that the motor paraments do not change in this process. The transient short-circuit time is very

short during the actual vehicle moving, considering the vehicle inertia and other factors, the simulation process can be approximated that the motor speed is constant before and after the short circuit. The operating condition at the moment of short-circuit determine the initial value of $i_d i_q$ current. Next, combining the electric vehicle common conditions, the three-phase short-circuit transient current will be simulated.

MTPA (maximum torque current ratio) of Electric vehicle PMSM is achieved by vector control. During the actual using, regardless of the flux weakening region or the non flux weakening region, the basic principle of motor control algorithm is realizing MTPA control by adjusting the $i_d i_q$ current ratio to increase the magnetic reluctance torque. PMSM torque equation is:

$$T_e = 1.5 \times P_n \times [\psi_f i_q + (L_d - L_q) i_d i_q] \quad (9.16)$$

Motor system working conditions is related to the requirement of the electric vehicle's dynamic performance closely. And the requirements of hybrid electric vehicles and pure electric vehicle are very different [6]. For embedded PMSM, usually have:

- (1) Drive motor converts electrical power into mechanical energy to provide a driving force. Positive torque is corresponding to the vehicle's acceleration and climbing condition, and the q-axis current is positive, and d-axis current is negative, so the motor output torque is positive. Figure 9.2 shows, along with the MTPA curve, i_d increases, i_q decreases, positive torque increases.
- (2) Q-axis current is negative, d-axis current is also negative, the motor output torque is negative, which is corresponding to power generating, braking energy recovery and other conditions. Figure 9.2 shows, i_d and i_q both increase, negative torque increase.

Use MTPA to simulate the changing process of the $i_d i_q$ current at the moment of transient short-circuit. The parameters of the star-connection motor used for simulating and testing are as follow.

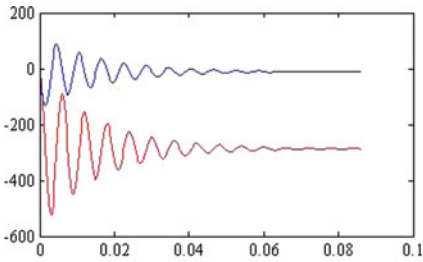
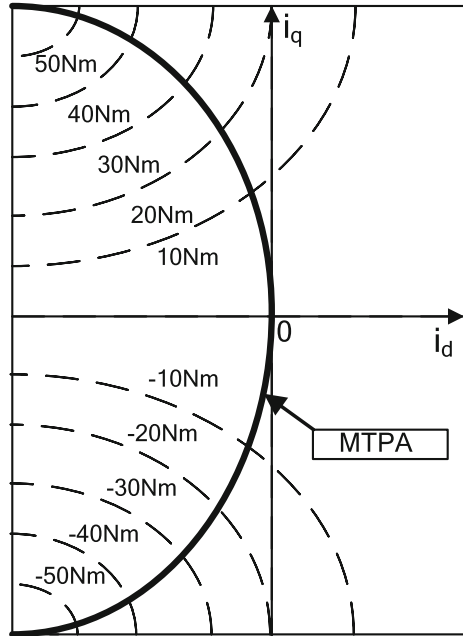
Under motor system follow-up working conditions, which is without load ($i_d = 0, i_q = 0$), compare the short-circuit current at 1000, 2000, 3000, 4000 rpm, as shown in Fig. 9.3.

Compare the transient short-circuit current of different working condition at 1000 rpm. There are low-speed accelerating condition, $i_q = 200$ A, $i_d = -100$ A (142 Nm), low-speed climbing condition, $i_q = 300$ A, $i_d = -250$ A (291 Nm), low-speed braking energy recovery, $i_q = -200$ A, $i_d = -100$ A (-142 Nm), low-speed emergency braking, $i_q = -300$ A, $i_d = -250$ A (-296 Nm). Compare the transient short-circuit current of high-speed accelerating and high-speed braking energy recovery simultaneously (Figs. 9.4 and 9.5).

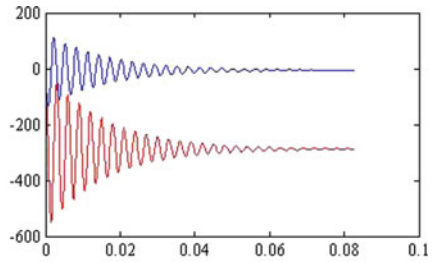
From the above simulation we can see that:

- (1) At the different speed, without load short-circuit, with the higher speed, the more oscillation periods of dq -axis current appear. But the transient process

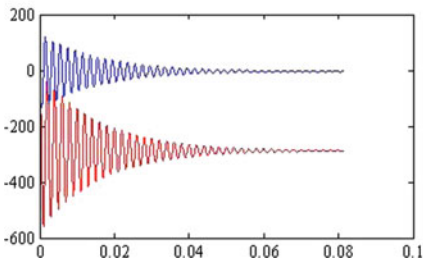
Fig. 9.2 MTPA stator current vector trajectory



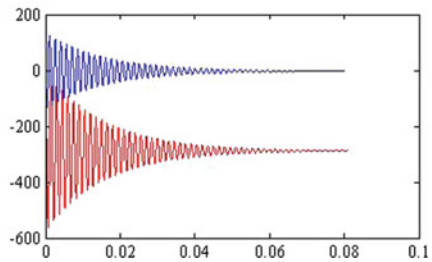
(a) 1000rpm on-load transient short-circuit current



(b) 2000rpm on-load transient short-circuit current



(c) 3000rpm on-load transient short-circuit current



(d) 1000rpm on-load transient short-circuit current

Fig. 9.3 Transient short-circuit current simulation charts at different speed

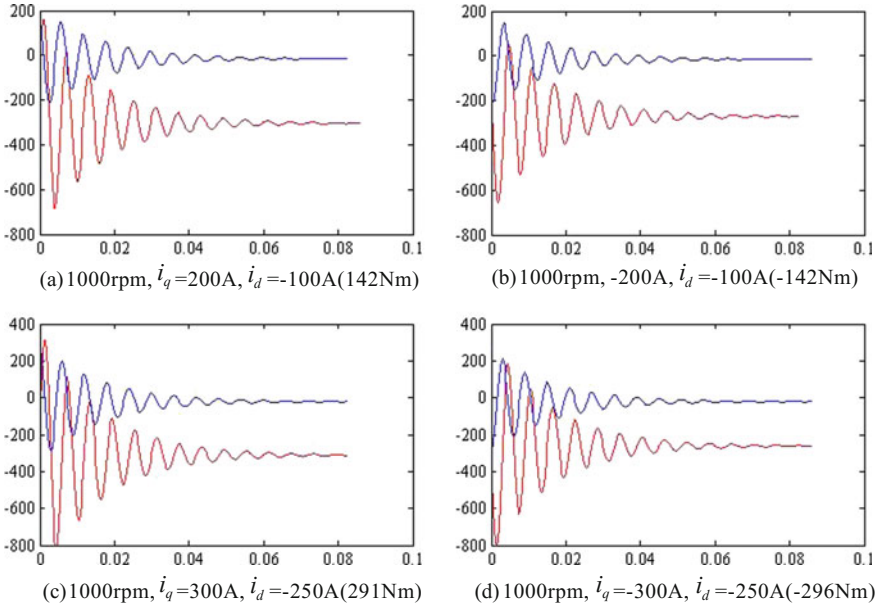


Fig. 9.4 Transient short-circuit current simulation charts at different torque

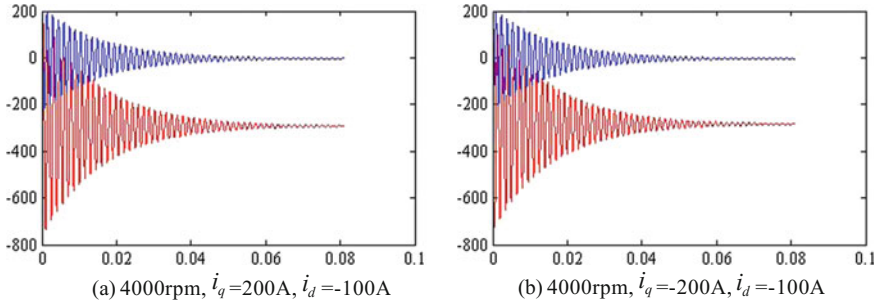


Fig. 9.5 Transient short-circuit current simulation charts at high speed

time is almost the same, the maximum demagnetization-current is almost the same too.

- (2) At the same speed, with load short-circuit, regardless of driving or generating condition, with the load increasing, the demagnetization-current increases, the transient process time is almost the same.
- (3) Under the same load, at different speed, with the higher speed, the demagnetization-current increases, and the more the oscillation periods appear.

9.4 Test Platform Design and Test Results Analyze

In order to verify the correctness of the analysis of PMSM transient three-phase short-circuit model theory in Chap. 2, and support the simulation in Chap. 3, this paper has completed the design of transient short-circuit test platform and the transient short-circuit test on the test platform. The unit under test (UUT) is a C-level hybrid vehicle permanent magnet synchronous motor (IPMSM). The parameters of the UUT are shown in Table 9.1, in Chap. 3.

By the above two chapters' analyzing we know the process of transient short-circuit is very complex and short. Transient current shock will make the motor torque shock and also has some destructive effect. So we need to consider the high response speed and stability to resist the impact of destruction during test platform designing.

Figure 9.6 shows the test platform, which includes dynamometer, battery simulator, elastic shaft, torque sensor, resolver and position acquisition devices, dq -axis current calculating unit, the tested motor and inverter, execution unit of three-phase transient short-circuit. The dynamometer as the test load should be set in speed mode during the test and the speed can be changed. The tested motor and inverter are running in torque mode by controlling the inverter's dq -axis current to change the output torque. A flexible coupling is installed between the tested motor and the dynamometer for eliminating the shock of the system running speed caused by the transient short-circuit torque. Compared to the tested motor, a larger inertia dynamometer is selected, in order to reduce the effect of the shock to the system stability.

The three-phase transient short-circuit execution unit mainly contains a high-power IGBT and its drive hardware circuit. The three-phase synchronous short-circuit process is triggered by hardware. The current and the position signal acquisition unit is consist of several high-response, high-precision sensors. The current and the angle signal is delivered to the dq -axis current calculation unit in real time, of which the output dq -axis current operation rate is 50 kHz. The tested

Table 9.1 The parameters of PMSM tested unit

Parameter	Value
Nominal voltage U_N/V	360
Nominal power P_N/kW	30
Nominal torque T_N/Nm	160
Peak torque T_p/Nm	320
Nominal speed n/rpm	1800
Maximum voltage n_{max}/Nm	4200
Phase resistance $R_s/m\Omega$	13
d -axis inductance L_d/mH	14
q -axis inductance L_q/mH	30
Pole pairs p	10
Flux linkage ψ/Wb	0.456

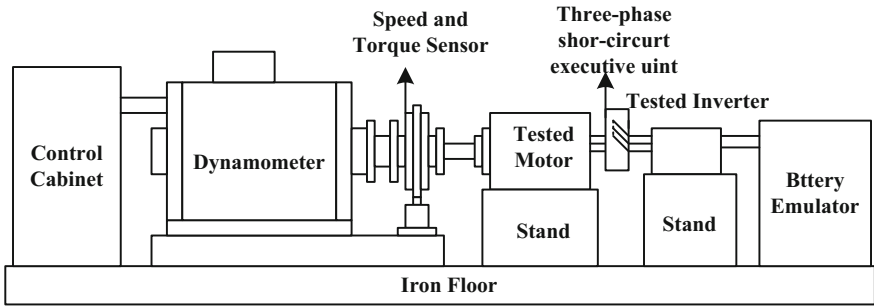


Fig. 9.6 The structure of the torque fluctuation detection system

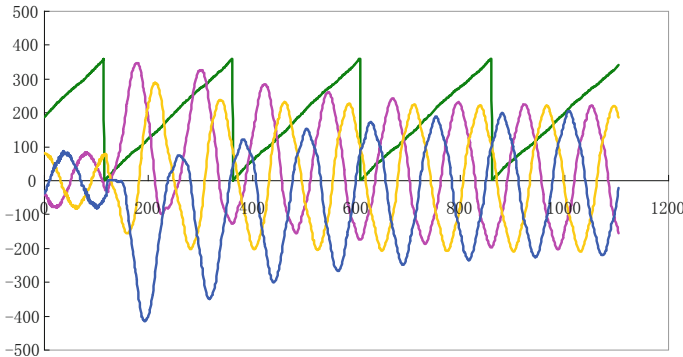


Fig. 9.7 Phase current waveform and the motor resolver position signal waveform after transient short-circuit

inverter must have over-current protection to prevent the IGBT over burning caused by the over-current in the process of the transient short-circuit.

The dynamometer is set to 1000 rpm, Fig. 9.7 is the phase current waveform and the motor resolver position signal waveform during transient short-circuit. The pole pairs of the resolver is the half of the tested motor's. The current has a great shock in the process of short-circuit, but the resolver signal is linear well, which proves the speed of the test system has no significant change during the shock, and the actual speed is consistent with simulation conditions before and after the transient short-circuit. As the current and rotor position is known, the dq -axis current can be calculated by Clark park in real time.

In this paper, in order to verify the correctness of the theoretical analysis and compare the simulated data and the actual test data, the following three conditions have been selected, 1000 rpm @56 Nm ($i_d = -35$ A, $i_q = 95$ A), 2000 rpm

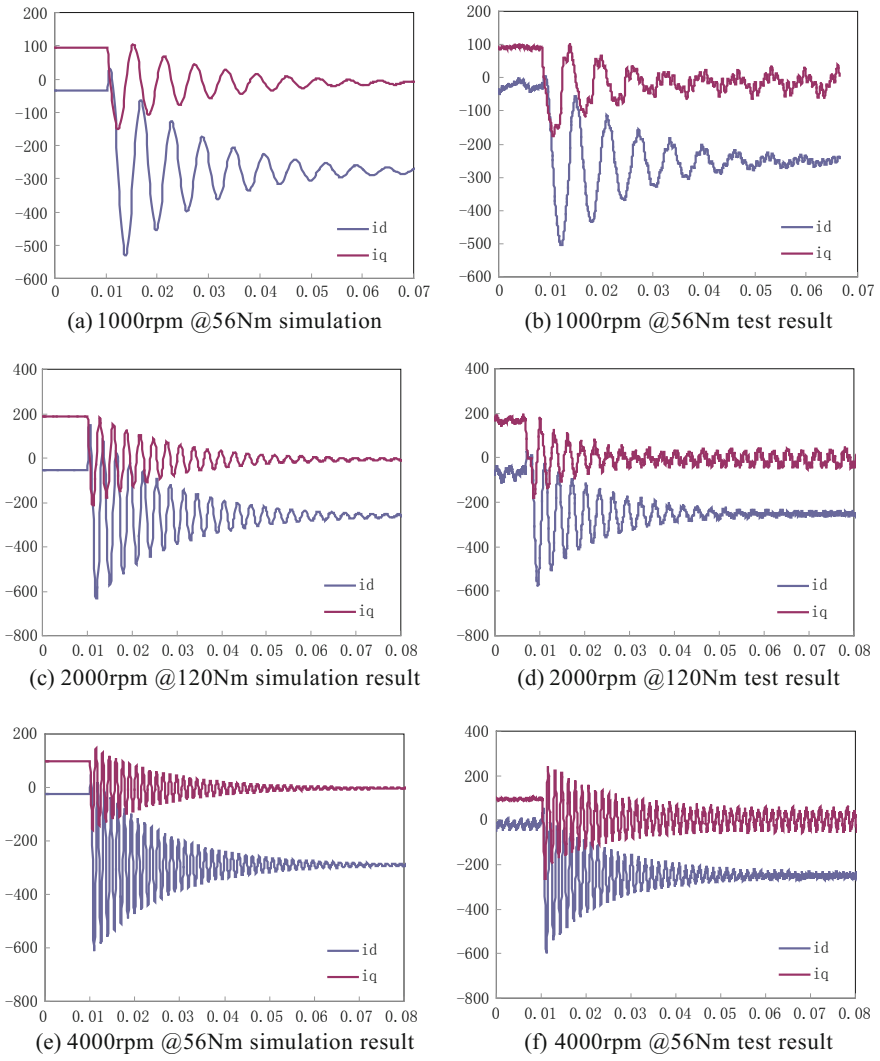
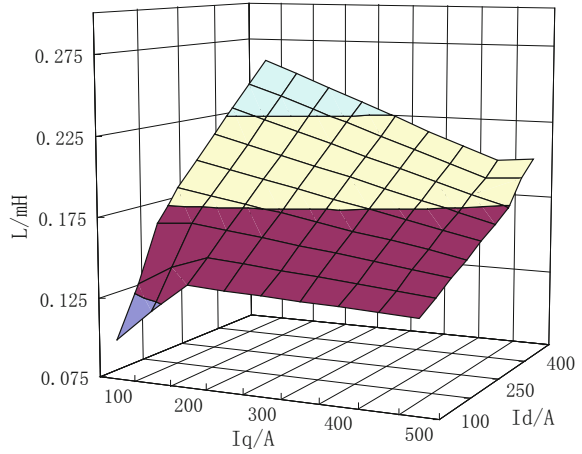


Fig. 9.8 The comparison charts of the simulation results and the test results under different conditions

@120 Nm ($i_d = -55$ A, $i_q = 195$ A), 4000 rpm @56 Nm ($i_d = -35$ A, $i_q = 95$ A). The comparison charts of the simulation results and the test results under different conditions is shown in Fig. 9.8.

By comparing the simulated waveforms and the measured waveform of the above three conditions, the consistency of simulated and actual i_d , i_q current

Fig. 9.9 Inductance variation curve with i_d , i_q



transient response is very high, the simulated steady-state time and the oscillation process are very consistent with the actual situation, and the maximum instantaneous value of the negative i_d current is also consistent basically. In these three conditions, the maximum simulation values of the simulation are: -522.4 , -616.2 , -613.7 A, the maximum measured values are: -499.8 , -597.7 , -600 A. The deviation of the maximum demagnetization current is within 5%. The motor after the test has no abnormal changes of mechanical and electrical characteristics. There is no demagnetization phenomenon after confirming the back EMF of the motor without load.

Next we will analyze the reason for the deviation of the simulation and the measurement, we can find that even the short-circuit process has been steady, the current also has obvious oscillations of d , q -axis (shown in Fig. 9.8) during the actual test. There are two main reasons as follows.

- (1) Since the simulation has assumed the permanent magnetic field induces a sine wave of electromotive force in the phase windings and the three-phase steady-state short-circuit current is fully sinusoidal current. But actually, in addition to the fundamental wave the induced electromotive force also contains a certain amount of harmonics, and the three-phase steady-state short-circuit current also has certain amount of harmonics, so there is current oscillation during the actual test. Non-sinusoidal induced electromotive force will have some impact on the simulation of the transient process.
- (2) There is a cross-saturation effect of permanent magnet synchronous motor inductance, which the parameters of L_d , L_q , ψ_f are influenced by the current actual value of i_d , i_q , as shown in Fig. 9.9. Because the test temperature is difficult to keep constant during the test, the resistance parameters and flux parameters are also influenced by temperature. Dynamic change of motor parameter will influence both the transient state and the steady state.

9.5 Conclusion

The following conclusions can be got from this paper by analyzing an simulation.

- (1) Three-phase transient short-circuit analysis is very important to PMSM. The simulation analysis based on dq -axis models shows that the oscillation of the dq transient short-circuit dq -axis current gradually decays to steady short-circuit condition. The $-i_d$ current during the oscillation process may cause the demagnetization of permanent magnets. Simulation method can be used for fast calculating the dynamic process with the known parameters' motor and assessing the risk of demagnetization, and also for comparing the effect to the transient short-circuit process and demagnetization current under different L_d , L_q , ψ_f and other parameters.
- (2) The PMSM maximum $-i_d$ current at the time of the transient short-circuit is larger than the steady-state short-circuit. The maximum $-i_d$ current and dq -axis current dynamic process is related to the operating conditions (the initial value of $-i_d, i_d$) and the speed at the time of transient short-circuit. The simulation results show that a higher motor speed and a greater load will cause a greater short-circuit i_d current.
- (3) The transient short-circuit test bed designed in this paper can maintain the speed stability with the transient impact during the test. And the synchronization of each channel's signal is good. The tests show dq -axis current transient response simulation is consistent with test results, with the exact parameters of the motor, the current simulation method is applicable to PMSM transient short-circuit analysis.
- (4) The transient changes of there EMF harmonic, L_d , L_q , and ψ_f will affect the short-circuit process and the steady-state value. Nest, further analysis of transient dq inductance will help to analyze the dynamic process and demagnetization risk accurately.

References

1. Rosero J, Espinosa AG, Cusido J, et al (2008) Simulation and fault detection of short circuit winding in a permanent magnet synchronous machine (PMSM) by means of fourier and wavelet transform. In: Instrumentation and measurement technology conference proceedings, 2008. IMTC 2008. IEEE. IEEE, 2008, pp 411–416
2. Jie B, Huichao Z, Xiuhui D et al (2014) Steady-state characteristic analysis and application of PMSM for electric vehicle with symmetrical three-phase short-circuit. *Small Spec Electr Mach* 42(3):17–20
3. Hongmei L, Tao C, Hongyang Y (2013) Mechanism, diagnosis and development of demagnetization fault for PMSM in electric vehicle. *Trans China Electrotech Soc* 28(8): 276–284

4. Chunhong Z, Xin S, Wenming T et al (2009) Calculation and measurement of transient reactance of permanent magnet synchronous motor. *Electr Eng* 4:14–17
5. Eilenberger A, Schrod M (2010) Sudden short-circuit analysis of a salient permanent magnet synchronous machine with buried magnets for traction applications. In: 14th International of power electronics and motion control conference (EPE/PEMC), 2010. IEEE, T9-117-T9-120
6. Mingming H, Xinjun G, Chenghu Z et al (2013) A novel wide speed-range driving system design for electric vehicle. *Trans China Electrotech Soc* 28(4):228–233

Chapter 10

Based on an Improved Sliding Mode Observer for Position Estimation of PMSM

Su Zhou, Daxiang Zhu and Zhe Hu

Abstract To reduce the chattering problem resulted from signum function in conventional sliding mode observer (SMO), a sensorless speed controller based on an improved SMO is proposed for permanent magnet synchronous motor (PMSM), where signum function is substituted for sigmoid function and the stability of the proposed SMO is verified using the Lyapunov method, the influence of different tilt parameters on position estimation is analyzed as well. To reduce phase delay in position estimation in conventional SMO, a new observer which has the structure of an extended Kalman filter is designed for back electromotive force estimation, which is expected to decrease estimation error of improved SMO. Based on improved SMO position sensorless control is modeled in MATLAB/SIMULINK, and result of simulation demonstrates correctness of improved SMO.

Keywords Position estimation · SMO · EKF · Chattering problem

10.1 Introduction

PMSM has been widely used in electric vehicle systems for its many advantages Compared with induction motor. Vector control is mainly used as a control method for PMSM [1], its core idea is that alternating stator current in stator reference frame is divided into exciting current component and torque current component in rotating coordinate system through coordinate transformation, so accurate rotor position is needed. The reliability of the position sensor is greatly reduced under poor and complex work environment of automobile motor, so sensorless control is expected. The position and speed of the rotor can be estimated using some electrical signals related to the motor windings through appropriate means. Several different

S. Zhou · D. Zhu (✉) · Z. Hu
School of Automotive Studies, Tongji University, Shanghai, China
e-mail: zdx_93@163.com

S. Zhou
CHDK, Tongji University, Shanghai, China

sensorless techniques have been developed, these techniques can be divided into several categories: an injecting-signal method utilizing motor space saliency has been used to detect the rotor position of the PMSM in low speed and standstill [2, 3]. This injecting-signal method is not affected by the motor speed and load. By suitably choosing a high-frequency stator voltage signal or current signal, the rotor position and speed can be precisely obtained. This method, however, needs a high-frequency signal generator. In addition, a band-pass filter is required to process and detect the signal which is related to the rotor position. The second is state observer method, directly or indirectly extracted from the motor back-EMF position information [4, 5], which is mostly used in surface mount and buried permanent magnet synchronous motor for excellent dynamic performance.

The sliding mode controller for improving the robustness of the controllers has been proposed for some time. While in the sliding mode, these controllers are insensitive to parameter variations and disturbances. Therefore, the sliding mode observer has been presented as a robust estimation method. To reduce the chattering problem of sliding mode control resulted from signum function, reaching law has been presented, besides, filter and phase compensation element is reduced [6]. The cascade control method has been proposed for the achievement of an accurate tracking performance under an unknown motor and load parameter [7]. Signum function has been substituted for sigmoid function and the chattering problem has been effectively weakened by selecting a reasonable boundary layer thickness, but the speed estimation and close-loop control haven't been further studied [8]. Non-linear system state observation has been implemented by combining high-gain observers with sliding mode control under disturbance [9]. Sliding mode observer combining with software PLL has been proposed to achieve sensorless drive for a PMSM, estimated induced EMF is used as input of software PLL to estimate position and speed, but rotor in still position can't be estimated [10]. On the basis of the literature [10], the adaptive control algorithm has been proposed to estimate the rotor angle estimation error at different speeds through the implementation of adaptive coefficients [11].

Depending on the theory of variable structure, an improved sliding mode observer is designed based on sigmoid function and the Kalman filter. In a conventional sliding mode observer, a low-pass filter and an additional position compensation of the rotor used to reduce the chattering problem are commonly found in SMO using a signum function. Currently, a sigmoid function is used for the SMO as a switching function. Use of LPF in conventional SMO leads to phase delay during computing rotor position. To solve this problem, a Kalman observer is designed to extract the back EMF, so rotor position estimation error can be decreased. This paper proposes a new sensorless control algorithm based on the improved SMO for SPMSM and the superiority is proved by comparing with the conventional SMO through simulation. The Schematic of improved SMO is shown in Fig. 10.1.

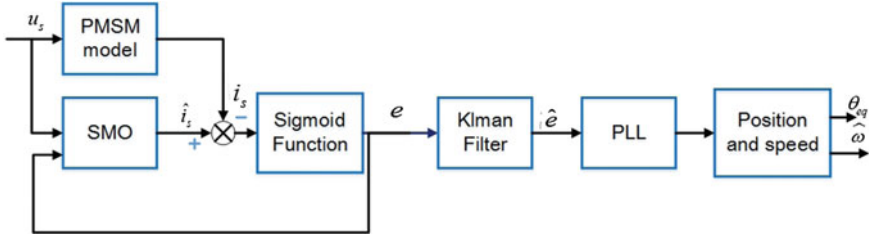


Fig. 10.1 Schematic of improved SMO

10.2 Sliding Mode Observer

10.2.1 Improved Sliding Mode Observer

For PMSM sensorless control, the rotor position is estimated so the stator equations can be used to model the system. The state equations, where the stator current is a state variable of the stationary frame voltage equation, can be represented as

$$\begin{aligned} \frac{di_\alpha}{dt} &= -\frac{R}{L}i_\alpha + \frac{1}{L}u_\alpha - \frac{1}{L}e_\alpha \\ \frac{di_\beta}{dt} &= -\frac{R}{L}i_\beta + \frac{1}{L}u_\beta - \frac{1}{L}e_\beta \end{aligned} \quad (10.1)$$

where i_α, i_β represent the stator current for each phase, u_α, u_β is the stator voltage of each phase, e_α, e_β is the electromotive force of each phase and R, L represent the stator resistance and inductance respectively. The electromotive force for each phase can be represented in the stationary frame as

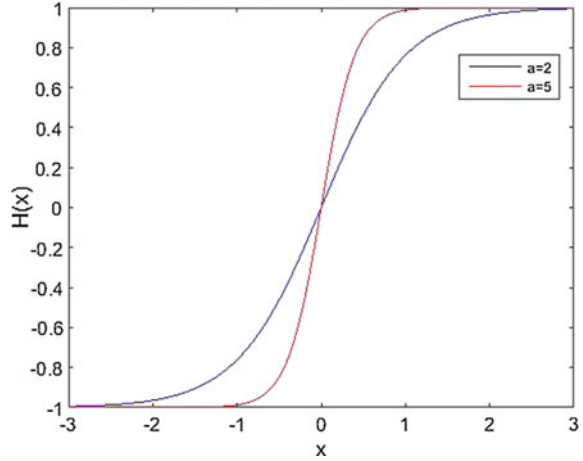
$$\begin{aligned} e_\alpha &= -\omega_e \psi_f \sin \theta \\ e_\beta &= \omega_e \psi_f \cos \theta \end{aligned} \quad (10.2)$$

where ψ_f, ω_e and θ represent the magnetic flux of the PM, the electric angular velocity, and the rotor angle, respectively. It is inferred from Eq. (10.2) that permanent magnet synchronous motor rotor position and speed can be extracted from back-EMF, thereby sensorless control can be realized.

To eliminate the undesirable chattering, sigmoid function is adopted in this research as the switching function. The improved sliding model observer equation in the stationary reference frame as follows:

$$\begin{aligned} \frac{d\hat{i}_\alpha}{dt} &= -\frac{\hat{R}}{\hat{L}}\hat{i}_\alpha + \frac{1}{\hat{L}}u_\alpha - \frac{K_s}{\hat{L}}H(\hat{i}_\alpha) \\ \frac{d\hat{i}_\beta}{dt} &= -\frac{\hat{R}}{\hat{L}}\hat{i}_\beta + \frac{1}{\hat{L}}u_\beta - \frac{K_s}{\hat{L}}H(\hat{i}_\beta) \end{aligned} \quad (10.3)$$

Fig. 10.2 Relationship between slope and tilt parameter



where \hat{i}_α , \hat{i}_β represent the estimated stator current for each phase, \hat{R} , \hat{L} is the estimated value of R , L respectively. $\bar{i}_\alpha = i_\alpha - \hat{i}_\alpha$, $\bar{i}_\beta = i_\beta - \hat{i}_\beta$ denotes the estimation errors of the stator current. The new SMO resolves the problems of the conventional SMO by using a sigmoid function as the switching function. The sigmoid function is represented as

$$H(x) = \frac{1 - e^{-ax}}{1 + e^{-ax}} \quad (10.4)$$

where parameter a is used to change the slope of sigmoid function. Figure 10.2 shows how the slope is changed depending on the tilt parameter.

When $\hat{R} = R$, $\hat{L} = L$, estimation errors of the stator current equation can be configured

$$\begin{aligned} \frac{d\bar{i}_\alpha}{dt} &= -\frac{R}{L}\bar{i}_\alpha + \frac{1}{L}e_\alpha - \frac{K_s}{L}H(\bar{i}_\alpha) \\ \frac{d\bar{i}_\beta}{dt} &= -\frac{R}{L}\bar{i}_\beta + \frac{1}{L}e_\beta - \frac{K_s}{L}H(\bar{i}_\beta) \end{aligned} \quad (10.5)$$

10.2.2 Stability Analysis

The sliding surface $S(x)$ can be defined as functions of the errors between the actual current, i.e., i_α and i_β , and the estimated current, \hat{i}_α and \hat{i}_β , for each phase as follows:

$$S(x) = [\bar{i}_\alpha \quad \bar{i}_\beta]^T = [\hat{i}_\alpha - i_\alpha \quad \hat{i}_\beta - i_\beta]^T \quad (10.6)$$

When sliding mode is reached, i.e. estimation errors are on the sliding surface, estimation errors become zero. At that moment, the sliding surface becomes $S(x)$ and the observer becomes robust against the system parameters variation and disturbances. The Lyapunov function can be defined as

$$V = \frac{1}{2}S(x)^T S(x) = \frac{1}{2}(\bar{i}_\alpha^2 + \bar{i}_\beta^2) \quad (10.7)$$

Taking the time derivative of (10.14), and substitute (10.13) into

$$\dot{V} = -\frac{R}{L}(\bar{i}_\alpha^2 + \bar{i}_\beta^2) + \frac{1}{L}(e_\alpha \bar{i}_\alpha - K_s \bar{i}_\alpha H(\bar{i}_\alpha)) + \frac{1}{L}(e_\beta \bar{i}_\beta - K_s \bar{i}_\beta H(\bar{i}_\beta)) \quad (10.8)$$

where the observer gain can be derived to satisfy the inequality condition as:

$$K_s > \max(|e_\alpha|, |e_\beta|) \quad (10.9)$$

10.2.3 Kalman Observer

The system behavior can be examined by apply equivalent control method. The back EMF can be expressed in the form derived from $S(x) = \frac{ds(x)}{dt} = 0$

$$e_\alpha = (K_s H(\bar{i}_\alpha))_{eq}, \quad e_\beta = (K_s H(\bar{i}_\beta))_{eq} \quad (10.10)$$

The back EMF is high frequency switch signal, a first order LPF is used to obtain smooth back EMF in conventional SMO, which leads to phase delay during computing rotor position. To solve this problem, a Kalman observer is designed to extract the back EMF, so rotor position estimation error can be decreased [12]. The state equation is as follows:

$$\begin{aligned} \frac{d\hat{e}_\alpha}{dt} &= -\hat{\omega}_e \hat{e}_\beta - K_l(\hat{e}_\alpha - z_\alpha) \\ \frac{d\hat{e}_\beta}{dt} &= -\hat{\omega}_e \hat{e}_\alpha - K_l(\hat{e}_\beta - z_\beta) \\ \frac{d\hat{\omega}_e}{dt} &= (\hat{e}_\alpha - z_\alpha)\hat{e}_\alpha - (\hat{e}_\beta - z_\beta)\hat{e}_\beta \end{aligned} \quad (10.11)$$

K_l is an observer gain.

The motor speed changes slowly comparing with electrical signals, since the motor mechanical time constant is much greater than the electrical time constant, a reasonable assumption that motor speed is constant can be made. The model of these induced back EMF is

$$\dot{e}_\alpha = -\omega_e e_\beta, \quad \dot{e}_\beta = -\omega_e e_\alpha \quad (10.12)$$

equations as follow derivate from (10.11), (10.12),

$$\begin{aligned} \frac{d\bar{e}_\alpha}{dt} &= \omega_e e_\beta - \hat{\omega}_e \hat{e}_\beta - K_I(\hat{e}_\alpha - e_\alpha) \\ \frac{d\bar{e}_\beta}{dt} &= \omega_e e_\alpha - \hat{\omega}_e \hat{e}_\alpha - K_I(\hat{e}_\beta - e_\beta) \\ \frac{d\bar{\omega}_e}{dt} &= (\hat{e}_\beta - e_\beta)e_\alpha - (\hat{e}_\alpha - e_\alpha)e_\beta \end{aligned} \quad (10.13)$$

where $\bar{e}_\alpha = \hat{e}_\alpha - e_\alpha$, $\bar{e}_\beta = \hat{e}_\beta - e_\beta$, $\bar{\omega}_e = \hat{\omega}_e - \omega_e$ are observer errors. The Lyapunov function is defined as

$$V = \bar{e}_\alpha^2 + \bar{e}_\beta^2 + \bar{\omega}_e^2 \quad (10.14)$$

Taking the time derivative of (10.14), and substitute (10.13) into

$$\dot{V} = -K_I(\bar{e}_\alpha^2 + \bar{e}_\beta^2) \leq 0 \quad (10.15)$$

It is proved that the estimates \hat{e}_α and \hat{e}_β tend to e_α and e_β asymptotically by Lyapunov stability theory.

10.2.4 Position Estimation

Chattering problem arises when SMO enters sliding mode, the estimated back EMF is high frequency switch signal. Chattering problem can't be eliminated in rotor angle estimation based on arctangent function. Thus, the method of rotor angle estimation based on Phase Locked Loop (PLL) for PMSM is proposed in this paper, which has some advantages in application of rotor angle estimation. Method of rotor angle estimation based on PLL has a simple structure and is easy to implement, furthermore, it has higher speed astringency, which could satisfy the requirement of high real time characteristic for PMSM driving system.

From Eq. (10.2),

$$-e_\alpha \cos \theta = e_\beta \sin \theta \quad (10.16)$$

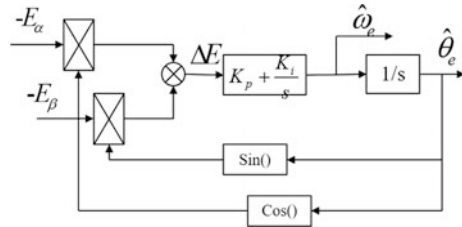
rotor angle can be derived from estimated back EMF and integration of speed estimated by PLL. Define the error as:

$$\varepsilon = -e'_\alpha \cos \theta' - e'_\beta \sin \theta' \quad (10.17)$$

Table 10.1 Parameters of the PMSM

Rated power/kW	3	Stator resistance/ Ω	2.875
Rated line-to-line voltage/V	300	d-axis stator inductance/mH	8.5
PM flux/Wb	0.175	q-axis stator inductance/mH	8.5
Pole pairs	4	Rotor inertia/ Kg^*s	0.001

Fig. 10.3 Schematic of PLL



Estimated electrical rotor speed is obtained by PI regulator and estimated rotor angle is integration of estimated electrical rotor speed. Figure 10.3 demonstrates the principle of PLL.

10.3 Simulation Results

Based on field orientation control (FOC) and SVPWM technology, PMSM sensorless speed controller has been modeled in MATLAB/SIMULINK. To control the PMSM, the three-phase coordinates need to be transformed into rotational synchronous coordinates, which are a part of the vector control. As a result of the vector control, a reference current is generated and passed to the stator of the motor through the inverter. Using the error between the command and estimated velocities, the PID control law is implemented. The PID control is also used for the current control. To meet the current loop and speed loop dynamic and steady-state performance, set the current loop PI regulator parameters $K_p = 9.35, K_i = 140$ and the speed loop PI regulator parameter $K_p = 0.14, K_i = 7$. The SMO, using the sigmoid function as a switching function, estimates the rotor angle from the back EMF. The parameters of a 3 kW PMSM used are given in the Table 10.1.

10.4 Results Analysis

The steady-state performance of the SMO is important, since the reduction of the chattering is a critical factor for the SMO. Therefore, the steady-state performance of the two SMOs are compared at 209 and 628 rad/s with no load, which represents low speed and high speed. As shown in Fig. 10.4, the improved sliding model observer achieve good results in wide speed range that estimated rotor speed is

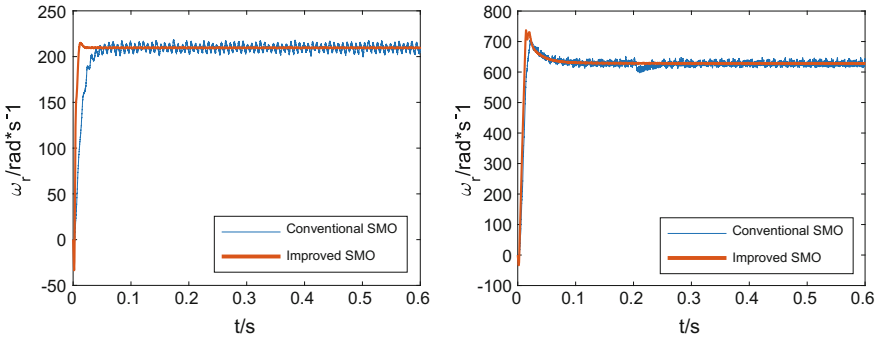


Fig. 10.4 Comparison of conventional and Improved SMO

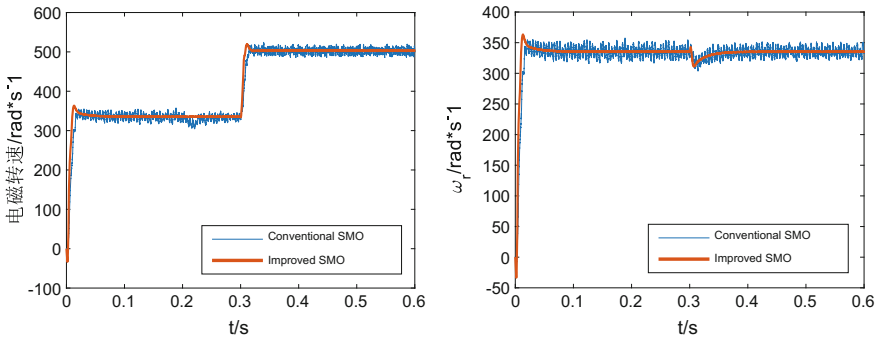


Fig. 10.5 Performance of improved SMO in change of operation conditions

quickly converge to the given speed in high and low speed where speed error is about ± 5 rad/s, however, estimated speed of conventional SMO is ripple obviously and phase delay is inevitable. Improved SMO can well follow the actual speed and effectively reduce the chattering, while the speed ripple greatly in conventional SMO, it can be inferred that performance of improved SMO in speed tracking is superior to conventional SMO.

To study the performance of improved SMO in change of operation conditions, position estimation simulation result has been analyzed under the conditions that speed and torque changes abruptly. The first operation is when t equals to 0.3 s, rotor reference speed changes from 335 to 502 rad/s with no load, the second operation is that rotor reference speed is 335 rad/s and when t equals to 0.3 s, torque changes from 0 to 10 Nm. Figure 10.5 shows that the speed estimation error is substantially zero apart from zero speed nearby, which imply that improved SMO is still able to fast track the actual speed of the rotor under the given operation conditions. Traditional sliding mode observer also implements tracking speed, but the estimated speed still chatters obviously.

Slope of sigmoid function is changed depending on the tilt parameter. To analyze how tilt parameter effects improved sliding mode observer, set tilt parameter that a equals to 2 and 5 respectively. Figure 10.6 shows chattering problem is effectively reduced when the tilt parameter is small. On the contrary, estimated back EMF contains more high frequency information, increasing location estimation chattering.

To verify the improved SMO performance of resistance to parameter variations disturbance, motor parameters variation simulation is modeled. The motor stator resistance changes to $R = 2.5 \Omega$ at the reference speed is 600 rad/s, the load is 5 Nm. As shown in Fig. 10.7, the rotor position estimated by improved SMO has no significant chattering, which indicates improved SMO is still able to accurately

Fig. 10.6 Sensorless speed control using the sigmoid function at $a = 2$, $a = 5$

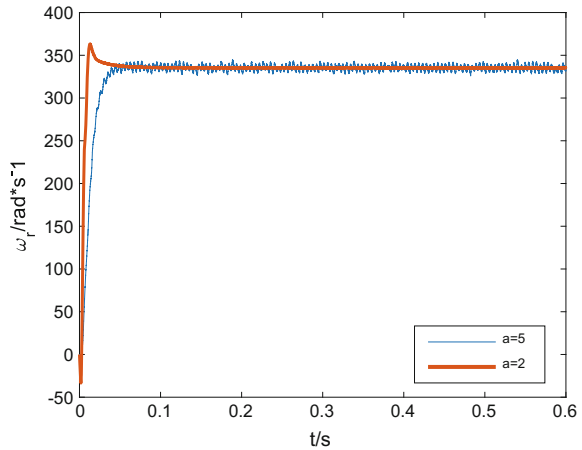
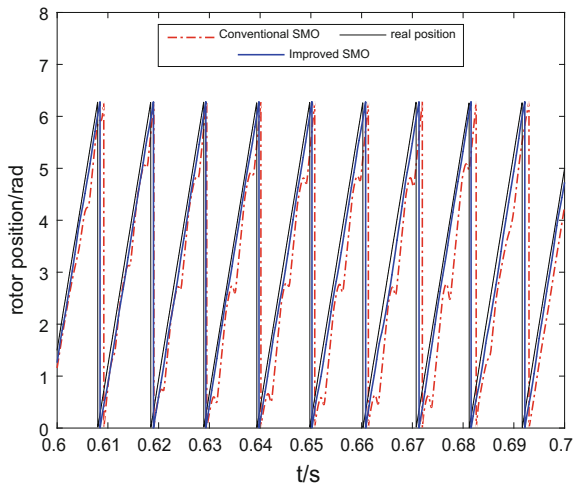


Fig. 10.7 Position estimation when stator resistance changes



estimate the rotor position after the parameters change. However, the rotor position estimated by traditional sliding mode observer fluctuates and is not accurate.

10.5 Conclusion

Depending on the theory of variable structure, an improved SMO is designed in which a sigmoid function is used as a switching function instead of signum function and a Kalman filter is used to extract back-EMF observer to eliminate phase delay. A PMSM position and speed estimation model is built in MATLAB/SIMULINK based on improved sliding mode observer. The corresponding simulation results show that:

- (1) Tilt parameter has influences on improved SMO, chattering problem is effectively reduced when the tilt parameter is small;
- (2) with respect to the conventional SMO, improved SMO can effectively reduce the chattering problem in position estimation;
- (3) when the operation conditions changes, improved SMO can quickly and accurately track changes in speed;
- (4) when the motor electromagnetic parameters change, improved SMO is still able to accurately estimate the rotor position.

References

1. Pillay P, Krishnan R (1991) Application characteristics of permanent magnet synchronous and brushless dc motor for servo drive. *IEEE Trans Ind Appl* 27(5):986–996
2. Zhou S, Jia W, Zhong J (2015) Startup strategy and simulation of vehicle brushless DC motor. *Chin J Automot Eng* 5(2):151–152
3. Miao X, Li Y, Xiao X (2007) Speed sensorless of PMSM with high-frequency signal injection. *Electr Drive* 37(3):11–14
4. Zhao D, Zhang C, Hao L (2006) A robust sliding-mode control strategy of a speed sensorless induction machine. In: *Proceedings of the CSEE*, vol 26, Issue no 22, pp 122–127
5. Zhou S, Wang M, Chen F (2012) Torque servo control for vehicle BLDCM based on feedback linearization. *J Wuhan Univ Sci Technol* 35(5):392–396
6. Zhu X, Li Y, Zhang J (2010) Sensorless control of PMSM based on a novel sliding mode observer. *Power Syst Prot Control* 38(13):6–10
7. Pisano A, Davila A, Fridman L, Usai E (2008) Cascade control of PM DC drives via second-order sliding-mode technique. *IEEE Trans Power Electron* 55(11):3846–3854
8. Lu W, Hu Y, Huang W, Chu J (2008) A hybrid approach of Sensorless rotor position self-sensing for brushless DC motor. *Trans China Electrotechnical Soc* 23(9):70–75
9. Veluvolu KC, Sanda YC (2009) High-gain observers with sliding mode for state and unknown input estimations. *IEEE Trans Power Electron* 56(9):3386–3393
10. Wang H, Xiao F, Ma W et al (2011) Sensorless control of PMSM based on sliding mode observer and software phase locked-loop. *Electric Mach Control* 15(1):49–54

11. Lu W, Hu Y, Du X et al (2010) Sensorless vector control using a novel sliding mode observer for PMSM speed control system. In: Proceedings of the CSEE, vol 30, Issue no 33, pp 78–83
12. Elbuluk M, Li C (2003) Sliding mode observer for wide-speed sensorless control of PMSM drives. Industry Applications Conference, 2003. 38th IAS Annual Meeting

Chapter 11

Simulation Analysis and Research of C70GB Fuel Cell Vehicle

Ping Chen, Chen Liang, Jiangqiu Li and Hongliang Jiang

Abstract Due to long endurance mileage and short fueling time, fuel cell vehicle had became the main development direction of range extend electric vehicle. In order to improve the service life and tech-characteristics, many departments carried out research related to the fuel cell and control system of fuel cell vehicle. In this study, the power systems, fuel cell systems, power battery systems and other simulation systems were constructed and tested for C70GB model, and calculate the power, energy consumption and other aspects of the calculation. The simulation results show that the fuel cell can effectively improve the energy power battery vehicle system dynamic and climbing performance, equipped with two 70 MPa cylinders can effectively extend the mileage of the vehicle, and ensure daily using demand.

Keywords New energy vehicle · Fuel cell · Power system · Simulation analysis · Research

Because of its long endurance mileage and short fueling time, in the process of extending the mileage and promote the technology of new energy vehicles, the fuel cell vehicles had became the main direction in mileage of more than 300 km electric vehicles. The research and exploration of fuel cell, main parts and entire electric vehicle have been carried out by many vehicle enterprises and research institutions [1].

P. Chen (✉) · J. Li · H. Jiang
State Key Laboratory of Automotive Safety and Energy, Tsinghua University,
Beijing 100084, China
e-mail: chenping@bjev.com.cn

P. Chen · C. Liang
Beijing Electric Vehicle Co., Ltd., Beijing 102606, China

11.1 Current Situation of Fuel Cell Vehicle

Fuel cell has been applied to many fields such as aerospace, mobile power station and new energy automobile etc., also, fuel cell vehicles have been researched and demonstratively applied for several times. But currently, because of the bottleneck problem such as high cost, short service life, etc., there is still a long way to go before commercializing the technology for the civil use [2, 3]. In order to fully realize the advantages of fuel cell, moderately reduce their application cost and improve their service life, various technical routes and plans have been designed and applied for fuel cell vehicles. Especially, with growing attention paid to plug in hybrid electric vehicle (PHEV) in recent years, many vehicle enterprises and research university have been doing plenty of R&D work on PHEV models on which took fuel cell as range extender [4–6].

Tang et al. [7] developed a lightweight field vehicle by using a 2 kW proton exchange membrane fuel cell and lead-acid battery. And tested DC-DC's and cell stacks' voltage, current, input & output temperatures and pressures of anode, also carried out the real road tests. The results showed that the vehicle system can meet the demand of people daily use. Kang et al. [8] built a fuel cell hybrid electric vehicle simulation model based on the FTP-75 cycle, and, simulated and calculated the energy consumption and other vehicle performance parameters. Guo et al. [9] built a hybrid-drive type vehicle model and a pure fuel cell type vehicle model on the ADVISOR platform which is based on MATLAB/Simulink environment. The results showed that the fuel cell and lithium battery in the hybrid-drive model can work efficiently and safely, and that the power fluctuation of fuel cell was very small, which can prolong the fuel cell's service life and improve the utilization ratio of the energy in the system. In addition, many scholars and research institutions, both domestic and abroad, had carried out experiments and simulation researches on the fuel cell stack and control logic of fuel cell vehicles, which prolonged the service life of the fuel cells and improved the control accuracy and operational performance of the whole vehicle [10–15].

This research based on C70GB prototype vehicle, added the fuel cell system and established the simulation platform, calculated its economical efficiency, power and energy consumption ETC., aimed to provided reference and safeguard for the latter real car transformation.

11.2 The Configuration and Parameters of the Vehicle System

11.2.1 Dynamic System Configuration

The voltage-current nature of fuel cell and lithium ion power battery is different: the voltage of fuel cell declines rapidly after outputting a certain amount of current,

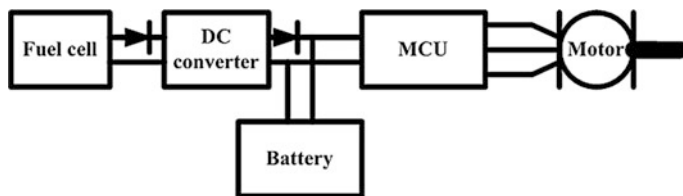


Fig. 11.1 Configuration of power battery direct-connection type and fuel cell hybrid power system

which means that the equivalent inner-resistance is larger, but the voltage of lithium ion power battery changes slightly in the working process, which means the equivalent inner-resistance is small. Taking into consideration of this difference and the features of the vehicle, the researchers installed a DC-DC converter (DC/DC) in front of the fuel cell which was connected to motor controller (MCU), and directly connected the power battery to the MCU. As shown in Fig. 11.1. This configuration could decouple the output power of the fuel cell and the demand of whole vehicle, thereby providing the average steady-state power; at the same time, it ensures that the power battery could provide the system dynamic power and recover the braking energy. This configuration could reserve the driving part of the original pure electric vehicle to the greatest extent, and now becomes the mainstream configuration of domestic and foreign fuel cell vehicles.

11.2.2 Vehicle Parameters

This research takes pure electric car C70GB as the prototype, but retains the original electric powertrain. The Parameters are as follows: vehicle mass 1770 kg, maximum quality 2210 kg, motor peak power 80 kW, maximum torque 255 Nm, the maximum speed 9000 rpm, motor driving efficiency 0.93, the main reduction ratio of transmission system 7.8:1, transmission efficiency 0.95, vehicle accessories power about 0.5 kW, air conditioning power about 2 kW. This research selected the NEDC and other three kinds of conditions as operating conditions, with the average power demand of the vehicle about 10–20 kW, as is shown in Table 11.1.

Table 11.1 Average demand power (kW) under different working conditions, full load and turn on air condition

	Brake energy feedback (Feedback 50%)	Pure mechanical brake
NEDC	10.05	11.86
60 km/h	10.41	10.41
EUDC	15.59	17.91
HWFET	16.44	17.43

In order to ensure that the fuel cell can maintain the average demand power when the vehicle is driving by hybrid power, the researchers selected the 30 kW fuel cell in the simulation study. The power battery used is the energy type (discharge rate 2 C) and the power type (discharge rate 10 C) MnNiCo ternary lithium battery, with the voltage platform 350 V and the hydrogen supply system 70 MPa.

11.3 Construction of the Simulation Model System

According to the vehicle parameters and performance, and in order to verify the hybrid vehicle dynamic performance, economy efficiency, endurance mileage and energy consumption rate of the hybrid vehicle after installing of fuel cell, the research team built a simulation model of the system by MATLAB/SIMULINK dynamic system, including dynamics model of the vehicle, fuel cell model and dynamic power battery model etc.

11.3.1 Analysis of the System Model

The system simulates the driver's behavior, inputting the current vehicle speed and the target vehicle speed, and controlling the vehicle by outputting signal of the acceleration pedal and the brake pedal. Figure 11.2 shows the controller model, which outputs the demand torque of the motor based on its pedal signal and motor rotation speed, and at the same time controls the output power of the fuel cell extender through controlling DC/DC. The system energy distribution formula is:

$$P_{bat} + P_{DC} = P_{motor,e} + P_{aux}$$

In this formula, P_{bat} refers to the battery power, P_{DC} DC/DC output power of the fuel cell, $P_{motor,e}$ the motor power, P_{aux} the attachment power. In addition, some manual input switches, such as the controller, which could change to fuel cell operation and braking energy feedback compulsively, could simulate the control of various special circumstances.

Motor simulation model not only calculates the actual output torque, power, etc. mainly through the motor speed and demand torque, but also determines the power of the fuel cell and lithium battery power source.

Fuel cell model is shown in Fig. 11.3. Its input signal is the output power which determined by DC/DC controller. Its voltage and current are determined by the characteristic curve of fuel cell battery, and its stack energy conversion efficiency and calculation of the hydrogen consumption rate and 100 km hydrogen consumption by the MAP. Respectively, the output power of the fuel cell and the DC/DC controller are:

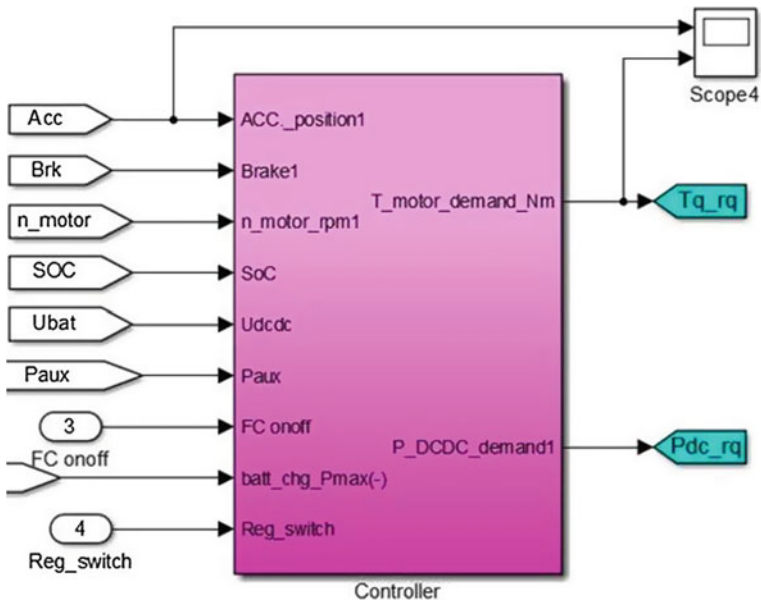


Fig. 11.2 Vehicle controller simulation model

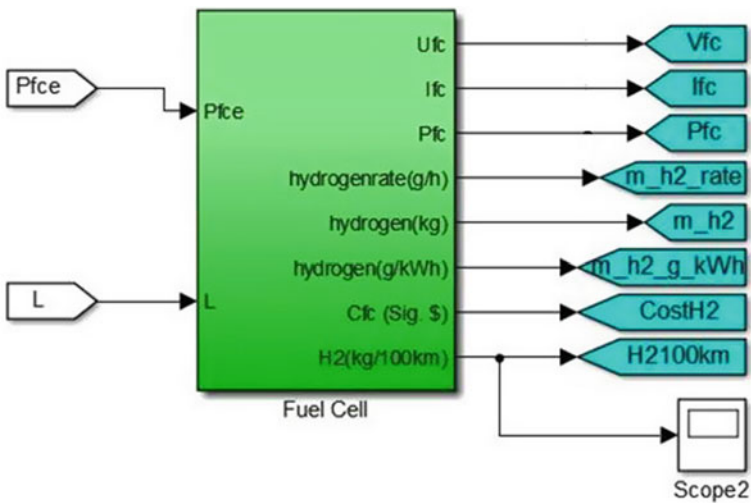


Fig. 11.3 Fuel cell simulation model

$$P_{DC} = \eta_{DC} P_{FCe} \quad P_{FCe} = \eta_{FC,sys} P_{FC} = \eta_{FC,sys} I_{FC} U_{FC}$$

P_{FCe} is the net power of the fuel cell and P_{FC} the total power. $\eta_{FC,sys}$ is the system efficiency, I_{FC} the output current, U_{FC} the output voltage, P_{DC} the output power of the DC/DC controller and η_{DC} the DC/DC efficiency.

In addition, the power battery uses Rint model, and its internal resistance and the open circuit voltage are determined by the battery SOC. The calculation formulas of the battery power and output voltages are:

$$U_{bat} = U_{ocv} - IR \quad P_{bat} = U_{bat}I = U_{ocv}I - I^2R$$

P_{bat} is the power. U_{bat} the output voltage, U_{ocv} the open circuit voltage, I is current and R resistance.

In the simulation process of the whole vehicle system, the motor and the vehicle adopt fixed speed ratio (7.8:1) transmission system model, and the vehicle dynamics model adopt forward calculation model. The calculation of the acceleration resistance and speed follows the formula below:

$$F_{drive} = F_f + F_w + F_\theta + F_{acc} = mgf \cos \theta + \frac{1}{2}CdA\rho_{air}v^2 + mg \sin \theta + ma$$

F_{drive}	Driving force
F_f	Rolling resistance
F_w	Air resistance
F_θ	Climbing resistance
F_{acc}	Accelerating resistance.

11.3.2 Controlling Strategy of Electricity Consumption and Maintenance

CDCS (Charge Depleting Charge Sustaining, namely, power consumption—power sustaining) is been used as the controlling strategy in the energy consumption analysis process. The power battery SOC is consumed constantly in the beginning, and then is maintained 20%. In the early stage, the vehicle takes in pure electric driving mode, and later becomes a hybrid model. The CDCS method can easily evaluate the pure electric power consumption and hybrid equivalent hydrogen consumption of the power system.

(1) Energy provided by the power battery

Assuming that the battery voltage is constant and the capacity reduction is Q_{bat0} , the energy of the power battery supplied to the bus is:

$$E_{bat} = Q_{bat0}V(\lambda_c\lambda_a\lambda_d)$$

In the formula, Q_{bat0} is the electricity that to satisfies the demand of endurance mileage of the pure electric model with ideal power battery. Due to the inconsistency of the monomer battery capacity, the available capacity of the battery group is reduced after package. Therefore, the consistent correction parameter is $\lambda_c = 0.95$. According to the available range of battery, SOC precision correction parameters is $\lambda_a = 0.8$. In general, battery lifetime is defined as the capacity decays to 80% of its initial capacity. Thus, set the performance decline parameter correction $\lambda_d = 0.8$.

(2) Energy provide by Fuel cell

Electricity E_{FC} supplied by m Kg hydrogen from a fuel cell to the bus is:

$$E_{FC} = 1.4 \times 10^8 \cdot m\eta_{FC}\eta_{FCS}\eta_{DCDC}\lambda_d$$

$\eta_{FC} = 0.5$ is the stack efficiency of fuel cell, $\eta_{FCS} = 0.9$ fuel cell system efficiency, $\eta_{DCDC} = 0.9$ is DC/DC controller efficiency, and $\lambda_d = 0.9$ fuel cell decay rate of the whole vehicle life.

Considering the technical parameters of the whole vehicle technical parameters, the simulation is based on 70 L, 70 MPa hydrogen cylinders, gas storage capacity per single cylinder 2.59 and the residual hydrogen amount 0.11 kg. Thus the maximum hydrogen quality that a single cylinder actually could use is 2.48 kg and the output energy of the fuel cell DC/DC controller output terminal is $E_{FC} = 35.1$ kWh.

(3) Endurance mileage

After the fuel cell and power battery are installed, the mileage of the vehicle is:

$$S = S_{bat} + S_{FC} = \frac{E_{bat}}{E} + \frac{E_{FC}}{E}$$

11.4 Analysis of Test Data

11.4.1 Analysis of Acceleration Performance

Figure 11.4 is the vehicle acceleration performance simulation curves which use 50 Ah capacity power battery. The figure shows that the acceleration performance of the vehicles using power type batteries are better than that of the vehicles using energy batteries, no matter in the pure electric mode or battery & fuel cell hybrid mode, and that the power type battery can meet the vehicles' acceleration demand. In addition, for the vehicles which are equipped with energy type power battery, the acceleration time of the hybrid model is shorter than that of the pure electric mode. In the process of acceleration, the power source can output large current in a short

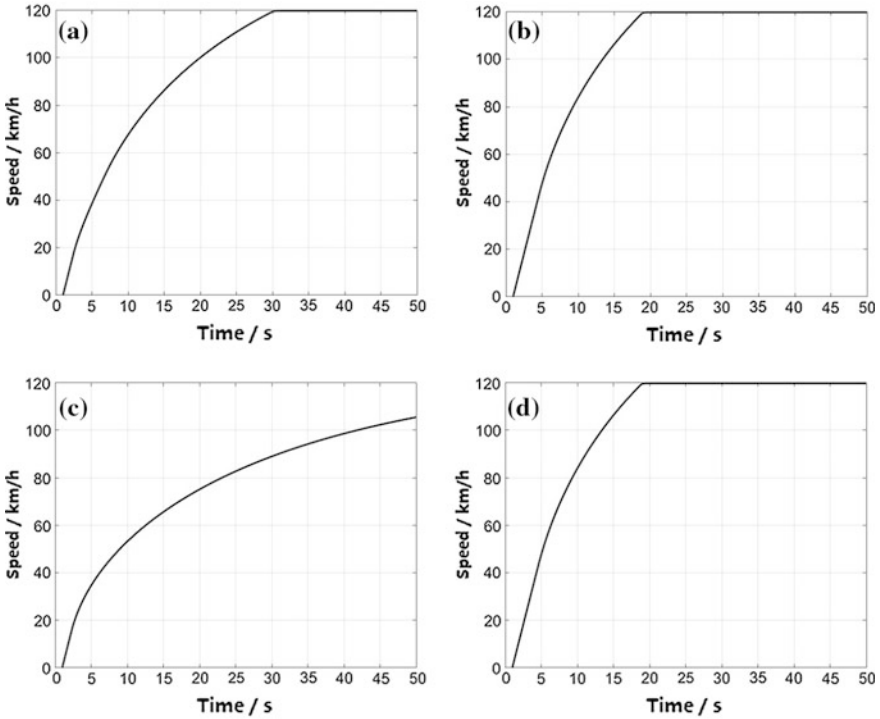
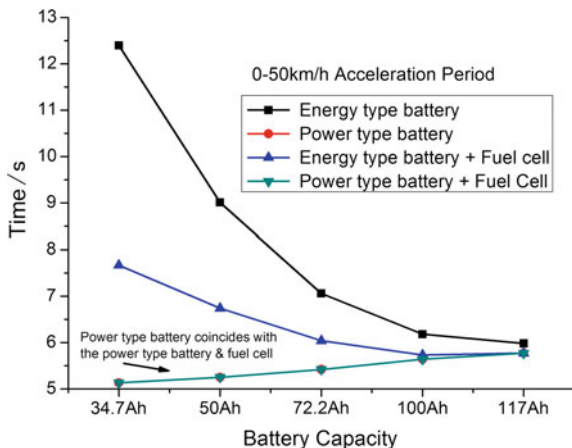


Fig. 11.4 Vehicle acceleration performance curve (50 Ah capacity battery). (a) Energy type battery, hybrid power mode; (b) Power type battery, hybrid mode (c) Energy type battery, pure electric mode; (d) Power type battery, pure electric mode

time so as to meet the demand of high power output. In the simulation process, the discharge rate of power type battery can reach 10 C. Therefore, because of this strong discharge ability, this kind of battery could provide greater power in a short period of time, meeting the demand of output power and fluctuations of vehicle within a short time. In addition, when the energy type power battery is used, whose maximum discharge rate is 2 C, so the fuel cell is needed to support certain power to meet the power demand fluctuation of the driving system in a short time.

Figure 11.5 is 0–50 km/h acceleration simulation curve of whole vehicle. From the chart, it can be seen that the acceleration simulation curve of the vehicles using power type battery coincides with that of the hybrid vehicle using power type battery & fuel cell, and shows a slight upward trend. On the contrary, the acceleration simulation curve of vehicles using energy power battery shows a declining trend. Moreover the acceleration time of the battery and fuel cell hybrid power mode is shorter than that of pure electric mode. In the process of acceleration, the power driven system is limited by two factors, “the maximum power of power source (battery and fuel cell)” and “the maximum power of the motor”. For the system which uses power type battery, the maximum output power of the battery is

Fig. 11.5 0–50 km/h acceleration time

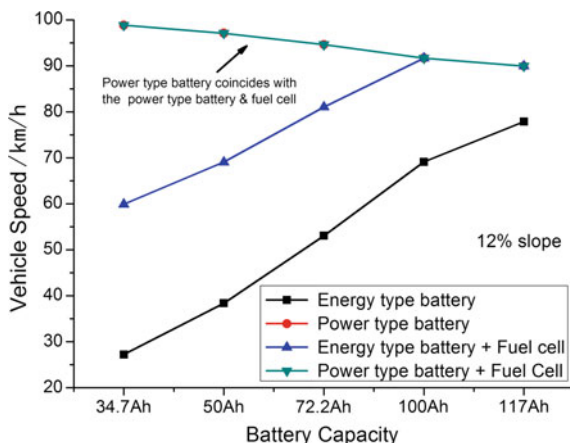


greater than the peak power of the motor, and thus it leaves no working requirement for fuel cell. However, the acceleration time is limited by the effect of “motor peak power”, its acceleration time is prolonged With the increasing battery capacity and the vehicle quality. For the system which uses energy type battery, the battery maximum output power is smaller than the maximum power of motor. Its acceleration time is limited by “power source (batteries + fuel cell) maximum power”, the participation of fuel cell could improve the vehicle acceleration performance. Though the increase of the battery capacity leads to the increase of the vehicles quality, it will also improves the overall peak output power of the power battery. Thus, the acceleration time is shortened with the increase of the power battery capacity as well as the participation of fuel cell.

11.4.2 Climbing Performance Analysis

Figure 11.6 is the simulation curve of the vehicle with maximum speed under 12% slopes. As is shown in chart, in a certain slope, the maximum stable speed of the vehicle using the hybrid model (energy type power battery + fuel cell) is higher than that of the vehicle using pure energy type power battery. Nevertheless, its simulation curve is coincident with that of the vehicle using the power type battery + fuel cell. In addition, when the battery capacity is greater than 100 Ah, all the other three simulation curves demonstrate a declining trend except that of the pure energy type power battery. This is consistent with the change of acceleration curve. For the simulation system of the power type battery, the maximum output power of battery is greater than the maximum output power of the motor, so the power supplied by the fuel cell system has no influence to the entire system. But with the increase of the capacity of the battery, the whole vehicle weight increases, so the maximum stable speed decreases; For the energy type power battery

Fig. 11.6 Vehicle maximum stable speed under 12% slope



simulation system, the maximum power output of the battery is less than motor peak power, thus starting the fuel cell will improve the overall power output. Although increasing battery capacity will increase the weight, the output power of the power battery will increase much more. So the climbing performance is improved. When the battery capacity is more than 100 Ah, the power source output power is higher than the peak power of the motor, so the overlapping and downward trend is presented.

11.4.3 Energy Consumption Analysis

According to the CDCS strategy to do the simulation analysis of the energy consumption, 5 NEDC cycles calculation is carried out to reduce the error of single calculation. Figures 11.7 and 11.8 are, respectively, the electricity consumption curve and endurance mileage simulation curve. In the CD mode, power consumption and endurance mileage increase as the battery capacity increase. The power consumption is in the 18–26 kWh/100 km range, and endurance mileage increases from 50 to 130 km. In CS mode, the power consumption of the battery remains at the 1.5 kWh/100 km and change tightly. But the endurance mileage declines a little with battery capacity increase, which is mainly because of vehicle quality improvement. In addition, the endurance mileage of the vehicle which equipped with two hydrogen cylinders is almost twice as far as the vehicle equipped with single hydrogen cylinder, which near 320 km maximum in CS mode. And combining with CD mode pure electric mileage, the total endurance mileage of the vehicle could reach 400 km. In the analysis of power consumption and endurance mileage, the final simulation results are less affected by the power battery type.

Fig. 11.7 Power consumption simulation curves

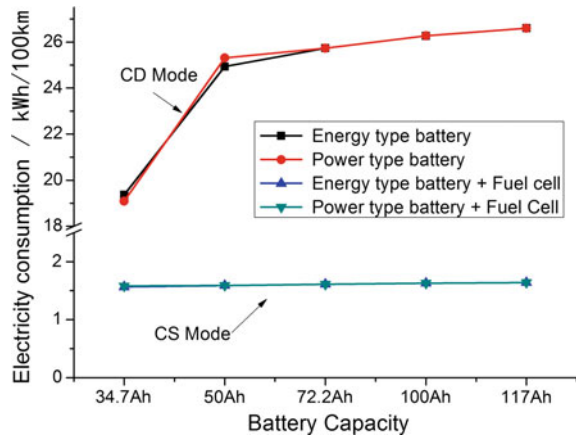
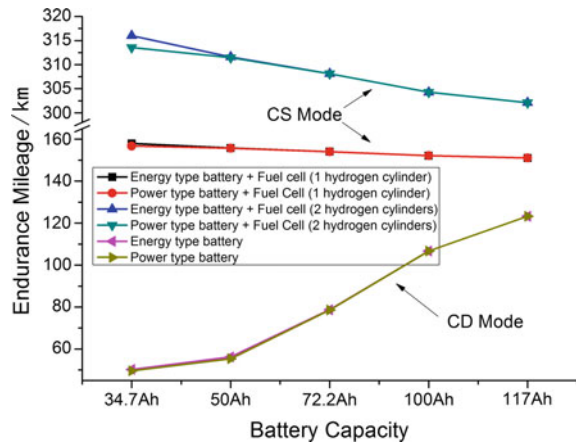


Fig. 11.8 Mileage simulation curves



11.5 Conclusions

- (1) For the system of energy type power battery, fuel cells can effectively improve the vehicle's dynamic performance and climbing performance, and ensure the output power of the whole power system.
- (2) Using the power type battery can effectively protect the power output of the vehicle, and meet the power needs of the vehicle system in a short time, which improve the vehicles' acceleration performance and climbing performance.
- (3) Through the analysis of the energy consumption and the endurance mileage comparison of the vehicle, the equipment of two 70 MPa cylinders can extend the mileage of the vehicle effectively, to ensure the vehicles' daily use and demand.

References

1. Li J, Fang C, Xu L (2014) Research status and development of fuel cell vehicle. *J Automobile Saf Energy Conserv* 1(5):17–29
2. Hou M, Yi BL (2012) Current status and prospect of fuel cell technology development. *Electrochemistry* 1(18):1–13
3. Wang Y, Chen KS, Mishler J, Cho SC, Adroher XC (2011) A review of polymer electrolyte membrane fuel cells: technology applications, needs and on fundamental research. *Appl Energy* 88:981–1007
4. Hwang JJ, Chang WR (2012) Characteristic study on cell/battery fuel hybrid power system on a light electric vehicle. *J Power Sources* 207:111–119
5. Aghaei J, Nezhad AE, Rabiee A, Rahimi E (2016) Contribution of plug in hybrid electric vehicles power system uncertainty management. *Renew Sustain Energy Rev* 59:45–458
6. Ryu J, Park Y, Sunwoo M (2010) Electric powertrain modeling of a fuel cell hybrid electric vehicle and development of a power distribution algorithm based on driving mode. *J Power Sources* 195:5735–5748
7. Tang Y, Yuan W, Pan M, Wan Z (2011) Experimental investigation on the dynamic performance of a hybrid PEM fuel cell/battery system for lightweight electric vehicle application. *Appl Energy* 88(1):68–76
8. Kang S, Min K (2016) Dynamic simulation of a fuel cell hybrid vehicle during the federal test procedure-75 driving cycle. *Appl Energy* 161:181–196
9. Guo B (2015) Design and research of hybrid power system of fuel cell electric vehicle which using vehicle-mounted hydrogen producer. Zhejiang University
10. Zhang J, Lu Q, Wang L (2001) Performance simulation of the pure hydrogen fuel cell vehicle. *Automot Eng* 23(6):365–368
11. Jin Q (2003) Research of system integrated design and system control algorithm development for the power system of fuel cell electric vehicle. Tongji University
12. Kang S, Min K, Yu S (2012) Dynamic modeling of a proton exchange membrane fuel cell system with a shell-and-tube gas-to-gas membrane humidifier. *Int J Hydrogen Energy* 37:5866–5875
13. Li Q, Chen W, Liu Z, Li M, Ma L (2015) Development of energy management system based on a power sharing strategy for a fuel cell-battery-super capacitor hybrid tramway. *J Power Sources* 279:267–280
14. Odeim F, Roes J, Wulbeck L, Heinzl A (2014) Power management optimization of fuel cell/battery hybrid vehicles with experiment validation. *J Power Sources* 252:333–343
15. Guo F, Zeng HJ, Xu SC (2015) Research of thermal management system of fuel cell vehicle. *Automot Eng* 8(37):959–963

Chapter 12

Electrochemical-Thermal Coupled Model of Lithium-Ion Batteries for Low Temperature Charging

Peng Wu, Jan Romberg, Hao Ge, Yakun Zhang and Jianbo Zhang

Abstract To study the low temperature charging performance of lithium-ion batteries, the electrochemical-thermal coupled model is developed. Some key parameters in the model are measured, which includes the kinetic related parameters and the thermal properties. The model is validated with the charging curves at different temperatures with two thermal boundary conditions and several C-rates. Using this model, the voltage loss during low temperature charging is broken down to electrolyte voltage loss, electrode interfacial kinetic loss and solid particle concentration polarization loss. Results show that the negative electrode intercalation kinetic loss is the dominant during low temperature charging.

12.1 Introduction

Lithium-ion batteries have been widely used in electric vehicles. However, the deterioration of low temperature performance, especially the poor charging performance, has been severely impairing the usability of the electric vehicles in regions where there is long winter with sub-zero temperature.

A lot of work has been conducted to study the low temperature performance of lithium-ion batteries through experiments and models. Most of them are focusing on the discharging performance, not the charging performance. However, the charging issues are as important as discharging for the low temperature usability of lithium-ion batteries. Here, to study the low temperature performance and develop

P. Wu (✉) · J. Romberg
BMW China Services Ltd, 19th Floor, Tower a, Gateway Plaza, no. 18 Xia Guang Li,
Chaoyang District, Beijing 100027, People's Republic of China
e-mail: peng.wu@bmw.com

H. Ge · Y. Zhang (✉) · J. Zhang
State Key Laboratory of Automotive Safety and Energy Department of Automotive
Engineering, Tsinghua University, Automotive Building A 109, Haidian District,
Beijing, China
e-mail: zhangyakun@mail.tsinghua.edu.cn

low temperature charging protocols, an electrochemical-thermal coupled model for low temperature charging of lithium-ion batteries is developed. The model is validated with the charging experiments with different conditions. Using this model, the voltage loss is broken down to analyze the major limiting factors of low temperature charging. The work belongs to the cooperative research project between BMW and Tsinghua University.

12.2 Electrochemical-Thermal Coupled Model

The governing equations of the electrochemical-thermal coupled model are listed below [1].

The diffusion equation in the spherical particle in the electrodes:

$$\frac{\partial c_s}{\partial t} = \frac{1}{r^2} \frac{\partial}{\partial r} \left(D_s r^2 \frac{\partial c_s}{\partial r} \right) \quad (12.1)$$

The potential in the solid phase of the electrodes is governed by Ohm's law:

$$i_s = -\sigma_{eff} \nabla \phi_s \quad (12.2)$$

The potential in the solution phase is given by the modified Ohm's law considering the concentrated solution theory:

$$i_l = -\kappa_{eff} \nabla \phi_l + \frac{2\kappa_{eff} RT}{F} (1 - t_+) \left(1 + \frac{d \ln f_{\pm}}{d \ln c_l} \right) \nabla \ln c_l \quad (12.3)$$

Mass balance at the solution phase writes as:

$$\varepsilon \frac{\partial c_l}{\partial t} = \nabla \cdot (D_{eff} \nabla c_l) + (1 - t_+) \frac{\nabla \cdot i_l}{F} \quad (12.4)$$

The coupling at the solid/liquid interfaces, which represents the electrochemical reaction rate, is described by the Butler-Volmer equation:

$$j_p = j_0 \left[\exp \left(\frac{\alpha_a F}{RT} \eta \right) - \exp \left(-\frac{\alpha_c F}{RT} \eta \right) \right] \quad (12.5)$$

The exchange current density writes as:

$$j_0 = Fk \left(\frac{c_l}{c_{l,ref}} \right)^{\alpha_a} c_{s,surf}^{\alpha_c} (c_{s,max} - c_{s,surf})^{\alpha_a} \quad (12.6)$$

The over-potential can be written as:

$$\eta = \phi_s - \phi_l - U_e - \Delta\phi_{film} \quad (12.7)$$

U_e is the equilibrium potential, and $\Delta\phi_{film}$ is the potential drop at the SEI film, which can be expressed as:

$$\Delta\phi_{film} = [j_p + C_{dl}^p \frac{\partial(\phi_s - \phi_l)}{\partial t}] R_{film}^p \quad (12.8)$$

The applied current can be divided into i_l , the current density in the solution, and i_s , the current density carried by the solid phase.

$$\nabla \cdot i_l + \nabla \cdot i_s = 0 \quad (12.9)$$

$$\nabla \cdot i_l = \alpha_p j_p + \alpha_p C_{dl}^p \frac{\partial(\phi_s - \phi_l)}{\partial t} \quad (12.10)$$

The heat generation can be divided into reversible heat and irreversible heat:

$$q = q_{rev} + q_{ir} \quad (12.11)$$

The irreversible heat can be written as:

$$q_{ir} = a_p j_p \eta - i_l \nabla \phi_l - i_s \nabla \phi_s \quad (12.12)$$

The reversible heat can be written as:

$$q_{rev} = a_p j_p T \frac{\partial U_e}{\partial T} \quad (12.13)$$

The heat equilibrium equation adopting a lumped thermal model can be written as:

$$mc \frac{dT}{dt} = S \int_0^{l_e} q dx - hS(T - T_\infty) \quad (12.14)$$

The model is implemented in COMSOL Multiphysics V5.0.

12.3 Model Parameters

The sample cell is a laminate cell with NCM cathode and graphite anode. The nominal capacity is 25 Ah. The parameters and variable names of the lithium-ion battery model are summarized in the Table 12.1. The structure parameters of the

Table 12.1 Parameters of the lithium-ion battery model

Variable	Value and dimension	Physical meaning	Source
rp_neg	6.375e-6 (m)	Particle radius Negative	a
rp_pos	4.889e-6 (m)	Particle radius Positive	a
epss_pos	0.518	Solid phase vol-fraction Positive	a
eps_l_pos	0.34	Electrolyte phase vol-fraction Positive	a
epss_neg	0.54923	Solid phase vol-fraction Negative	a
eps_l_neg	0.386	Electrolyte phase vol-fraction Negative	a
L_neg	57e-6 (m)	Thickness of negative electrode	a
L_sep	30e-6 (m)	Thickness of separator	a
L_pos	49e-6 (m)	Thickness of positive electrode	a
L_neg_cc	12 (um)	Negative current collector thickness	a
L_pos_cc	22 (um)	Positive current collector thickness	a
csm_max_neg	31,542 (mol/m ³)	Max solid phase concentration Negative	a
csm_max_pos	49,668 (mol/m ³)	Max solid phase concentration Positive	a
cl_0	1000 (mol/m ³)	Initial electrolyte salt concentration	a
Thickness	0.0082 (m)	Thickness of the cell	a
k_neg	1.12e-10 (m/s)	Reaction rate coefficient Negative	b
k_pos	9.32e-11 (m/s)	Reaction rate coefficient Positive	b
Eact_k_neg	109,560 (J/mol)	Activation energy of k_neg	b
Eact_k_pos	96,360 (J/mol)	Activation energy of k_pos	b
Cp	1243 (J/kg/K)	Specific heat capacity	b
rou_b	2300 (kg/m ³)	Density of the cell	b
OCV-neg	$f(x) = 0.1505 + 0.9762 * \exp(-46.98 * x) + 0.4346 * \exp(-659.9 * x) - 0.8282 * \exp(38.05 * x - 39.32) - 0.03063 * \operatorname{atan}(26.02 * x - 4.684) - 0.01314 * \operatorname{atan}(28.98 * x - 15.17)$		b
OCV-pos	$f(x) = 26.213 * \operatorname{pow}(x, 5) - 97.432 * \operatorname{pow}(x, 4) + 136.29 * \operatorname{pow}(x, 3) - 87.751 * \operatorname{pow}(x, 2) + 24.155 * x + 2.1108$		b

a: given by manufacture; b: measure in experiments

electrodes as well as the geometric parameters are given by the manufacture. The electrochemical reaction rates and the activation energy of them are measured with electrochemical impedance spectroscopy (EIS) experiments. The solid phase diffusivities and the activation energy are measured with potentiostatic intermittent titration technique (PITT) methods. The thermal related parameters are also measured with experiments [2, 3].

The SOC related parameters are summarized in the figures below.

Figure 12.1a, b show the entropy coefficients of two electrodes. Figure 12.1c, d show the normalized solid phase diffusion coefficient values and Fig. 12.1e, f show the normalized activation energy values. Keeping the SOC dependency, the normalized values are calculated from the results divided by the value on $x = 1$. The solid diffusion coefficient value and activation energy value in this model are scaled from the normalized values by multiplying factors, which are shown in the subtitles below each subfigure.

12.4 Model Validation

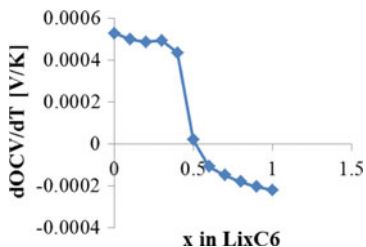
The model was validated by the charging experiments of different temperature, C-rates and thermal boundary conditions. The temperatures are: -20 , 0 and 25 °C. The C-rates are changed from 0.15 to 1.2 C. The charging method is CC-CV. The two thermal boundary conditions are with and without warm-keeping box. The box is shown in Fig. 12.2. The heat transfer coefficients are 8 and 40 W/m²/K separately.

12.4.1 Room Temperature Charging Without Warm-Keeping Box

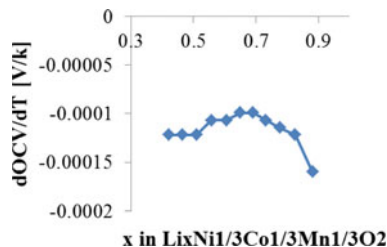
Figure 12.3 shows the validation results of room temperature charging with 0.3 and 1 C. The voltage of CV charging is 4.15 V and cut-off current of the CV stage is 0.03 C.

12.4.2 Low Temperature Charging Without Warm-Keeping Box

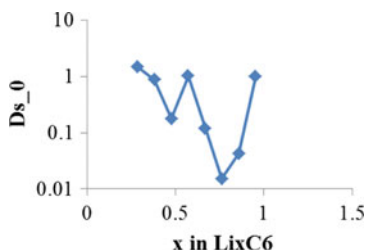
The validation results of low temperature charging at 0 and -20 °C without warm-keeping box are shown in Fig. 12.4. For -20 °C, the charging rates are 0.3 and 0.15 C; for 0 °C, the charging rates are 0.3 , 0.6 and 1.2 C.



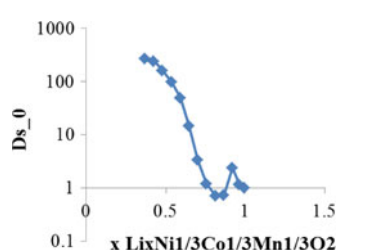
(a) Entropy coefficient of negative electrode



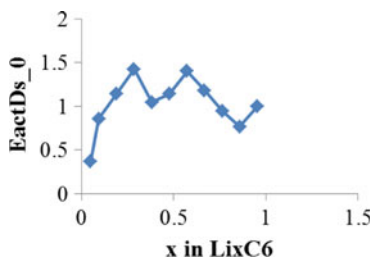
(b) Entropy coefficient of positive electrode



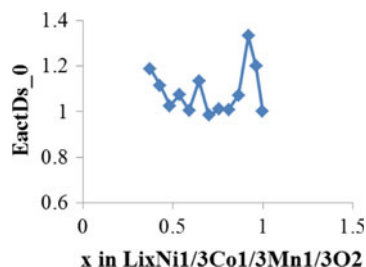
(c) The normalized solid phase diffusion coefficient Ds_0 of negative electrode, while the solid phase diffusion coefficient in this model is $Ds=Ds_0*5.72e-15$ (m^2/s)



(d) The normalized solid phase diffusion coefficient Ds_0 of positive electrode, while the solid phase diffusion coefficient in this model is $Ds=Ds_0*7.05e-15$ (m^2/s)



(e) The normalized activation energy $EactDs_0$ of solid phase diffusion in negative electrode, while the activation energy value is $EactDs=EactDs_0*30.75$ (kJ/mol)



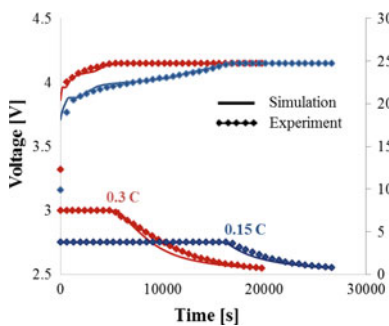
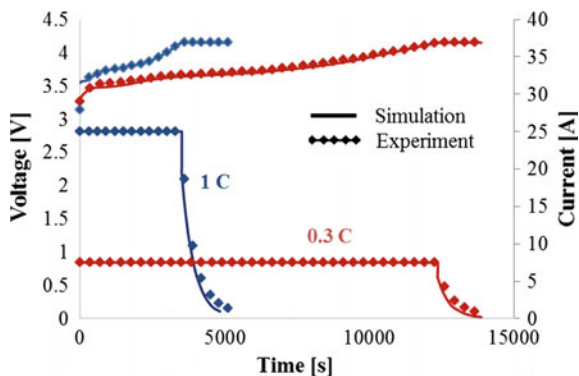
(f) The normalized activation energy $EactDs_0$ of solid phase diffusion in positive electrode, while the activation energy value is $EactDs=EactDs_0* 13.54$ (kJ/mol)

Fig. 12.1 The SOC related parameters

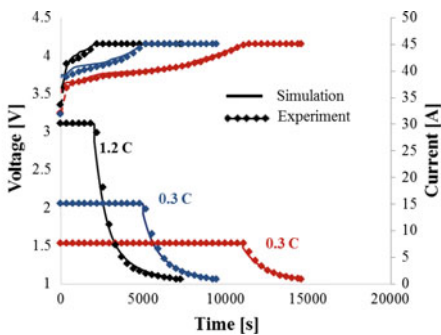


Fig. 12.2 The warm-keeping plastic box

Fig. 12.3 Validation results of room temperature charging



(a) -20 °C



(b) 0 °C

Fig. 12.4 Low temperature charging at 0 and -20 °C without warm-keeping box, $h = 40 \text{ W/m}^2/\text{K}$

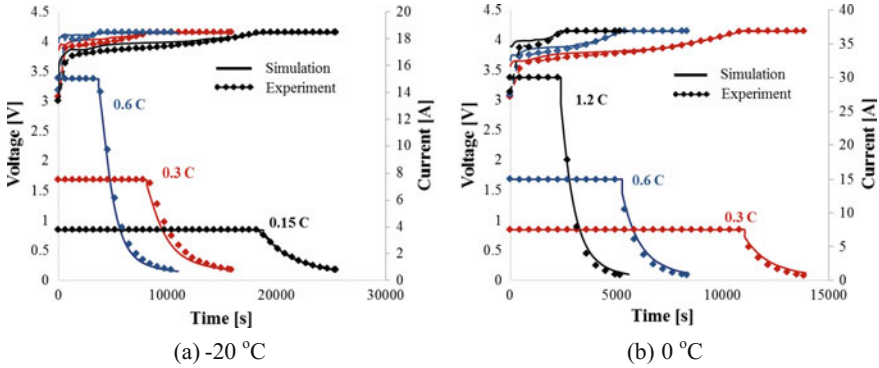


Fig. 12.5 Low temperature charging at 0 and $-20\text{ }^{\circ}\text{C}$ with warm-keeping box, $h = 8\text{ W/m}^2/\text{K}$

12.4.3 Low Temperature Charging with Warm-Keeping Box

The validation results of low temperature charging at 0 and $-20\text{ }^{\circ}\text{C}$ with warm-keeping box are shown in Fig. 12.5. For $-20\text{ }^{\circ}\text{C}$, the charging rates are 0.15, 0.3 and 0.6 C; for $0\text{ }^{\circ}\text{C}$, the charging rates are 0.3, 0.6 and 1.2 C.

12.4.4 Validation of Temperature During Charging

The validation of temperature curves at several conditions are shown in Fig. 12.6. These conditions are $-20\text{ }^{\circ}\text{C}$ with box: 0.3 C, 0.6 C; and $0\text{ }^{\circ}\text{C}$, 1.2 C: with and without box. In the experiments, six thermal couples are used to detect the temperature distribution of the large format cell. The locations of the thermal couples are shown in Fig. 12.6b. In the validation, the experiment curves are set as the $T_{average}$ which are considered as the average temperature of the core. The expression of the average temperature is defined by:

$$T_{average} = \frac{\frac{T_3 + T_4}{2} + T_5 + T_6}{3} \quad (12.15)$$

The simulation and experiment results show good agreement in the charging voltage and current curves as well as the temperature curves.

12.5 Voltage Loss Breakdown

The voltage loss is defined as the extra voltage beyond the equilibrium OCV when cell is charged. The voltage loss has four components: (1) Electrolyte, ionic resistance and concentration polarization in electrolyte; (2) Interfacial, charge transfer kinetics on the active material-electrolyte interface; (3) Solid particle, concentration polarization inside active material particles; (4) Electrical resistance in electrode and current collector, which is very small and can be neglected. Using the model, the voltage loss at $-20\text{ }^{\circ}\text{C}$ 0.3 C charging condition is shown in Fig. 12.7. Results show that for low temperature charging, the dominant voltage loss is the negative electrode interfacial kinetic loss, taking about 50% of all the voltage loss.

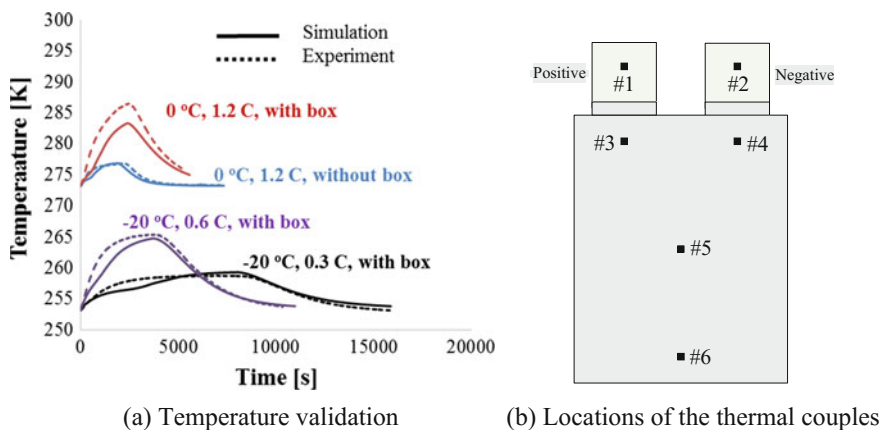
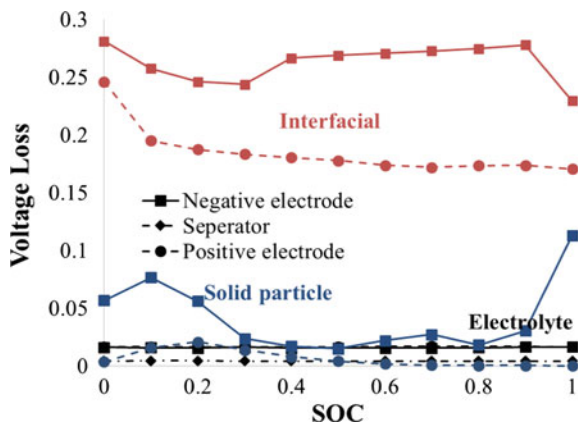


Fig. 12.6 Validation results of temperature during charging

Fig. 12.7 Voltage loss breakdown at different SOCs during charging



12.6 Conclusion

This paper presents the cooperative research between BMW and Tsinghua University. The electrochemical-thermal coupled model of lithium-ion batteries is developed. The model is validated with the charging curves at different temperatures with different thermal boundary conditions and several C-rates. With the help of the model, the voltage loss during low temperature charging can be broken down to electrolyte voltage loss, electrode interfacial kinetic loss and solid particle concentration polarization loss. Results show that the negative electrode intercalation kinetic loss is the dominant during low temperature charging. Future work may focus on developing the low temperature charging protocols for lithium-ion batteries.

References

1. Doyle M, Fuller TF, Newman J (1993) Modeling of galvanostatic charge and discharge of the lithium/polymer/insertion cell. *J Electrochem Soc* 140(6):1526–1533
2. Huang J, Li Z, Liaw BY et al (2015) Entropy coefficient of a blended electrode in a lithium-ion cell. *J Electrochem Soc* 162(12):A2367–A2371
3. Zhang J, Wu B, Li Z et al (2014) Simultaneous estimation of thermal parameters for large-format laminated lithium-ion batteries. *J Power Sources* 259:106–116

Chapter 13

Research on Low Frequency Torque Ripple of In-wheel Motor of Four Wheel Independent Drive

Zhe Li, Zheng Ling, Yue Ren, Yinong Li, Ke Wang and Zhenfei Zhan

Abstract In-wheel motor is a key power element for four wheel independent drive electric vehicle. It can supply accurate driving force control and achieve energy saving in electric power vehicle. Switched Reluctance (SR) motor has become an ideal candidate due to high output torque and reliable performance. However, huge output torque ripple in operation, which affects the comfort and handling stability of electric vehicle, limits its application in vehicle. In this paper, some factors behind low frequency noise and torque ripple of SR motor are investigated from a view of energy consumption including magnetic flux path pattern in SR motor and current imbalance. Furthermore, phase current balance control strategies to improve output torque ripple in operation are proposed. Results show that low frequency noise and torque ripple can be eliminated by applying the proposed current balance control strategy. It provides a good design method for SR motor to achieve excellent comfort and handling performance in four wheel independent drive vehicle.

Keywords Four wheel drive · Switched reluctance motor · Torque ripple · Control

13.1 Introduction

Four-wheel independent drive electric vehicle with in-wheel motors has cancelled the traditional mechanical transmission system. It has integrated wheel motor as power source, reduce the quality of the chassis, makes convenient arrangement possible. Additional, Acceleration Slip Regulation (ASR), Anti-Lock Braking system (ABS) and Electronic Stability Program (ESP) can be integrated easily and controlled due to an accurate driving/braking force control. It has become one of the future development direction of electric vehicle [1].

Z. Li · Z. Ling (✉) · Y. Ren · Y. Li · K. Wang · Z. Zhan
State Key Laboratory of Mechanical Transmission, College of Automotive Engineering,
Chongqing 400044, China
e-mail: zling@cqu.edu.cn

Switched Reluctance Drive (SRD), as one of the optimal schemes of motor drive system for electric vehicle, has a series of competitive advantages. SRD system is composed of switched reluctance motor, power converter, motor controller and position detector. SR motor is the actuator of the SRD system. SR motor has doubly salient structure of rotor, composed of silicon steel laminations and without any form of winding, permanent magnet, slip ring. The stator of motor has simple concentrated winding, and end of the winding is short, So SR motor has the advantages of high reliability, simple structure and low maintenance. The operation principle of the SR motor is followed the magnetic flux along the minimum path closure, the output reluctance torque is irrelevant to current direction. Because only unidirectional current excitation is needed in operation, in theory, each phase winding of a power converter can be connected in series with a main switching device. This makes the power converter has the advantages of simple circuit, high reliability, prohibit the shoot-through state of the inverter bridge. SRD system has similar series characteristic of direct current contact motor. By controlling phase current amplitude, opening angle and the conduction angle, the controller can obtain the mechanical characteristics and is easy to implement the four quadrant operation. The power, torque-speed and efficiency characteristics of SRD system are very suitable for the motor drive system of electric vehicles. In addition, phases of SR motor are independent each other, can still run reliably under the condition of lack of phase, which makes the driving system has strong fault tolerance ability, above mentioned characteristics is not only crucial for driving system of four-wheel independent electric vehicle but also is an important advantage of SRD system relative to other drive systems.

Due to the impact of power supply current harmonic component, stator and rotor doubly salient characteristics, eccentric rotor, stator and rotor magnetic circuit saturation and error factors on motor control system measurement, driving motor of four-wheel drive electric vehicle is in operation of a certain range of torque ripple. The vibration and torque ripple will directly effect on tires and suspension, caused impact and fluctuation of longitudinal and vertical force between tire and ground, which can affect longitudinal driving performance of the vehicle, cause vertical vibration problem. If the wheel motor's torque ripple is too large, it may also lead to vehicle suspension resonance, located in its front and rear direction. Therefore, it is an important task for SR in-wheel motor drive system to study mechanism of torque ripple of driving motor and to use effective measures to eliminate the torque ripple.

For the moment, there are two methods to reduce the torque ripple of switched reluctance motor. One is in motor operation stage. By means of control methods such as Direct Torque Control (DTC), Current Chopper Control (CCC) and Angle Position Control (APC) to optimize output torque curve [2, 3]. The second is in motor design stage, by improving the structure of stator and rotor pole, to obtain the desired output torque curve. Finite element method (FEA) was used by Li [4] and Emmanuel [5] to analyze influence of the design parameters of SR motor, such as rotor and stator yoke height, air gap and pole arc on torque ripple. Mohammad [6], Zhang [7] used Search Optimization Approach (SOA), Genetic Algorithm (GA) and Ordinary Kriging (OK), to optimize the key parameter design of SR

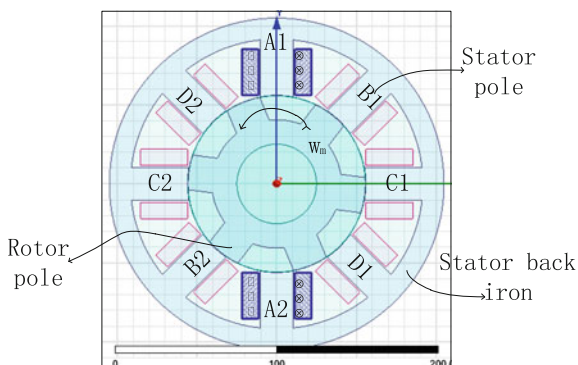
motor through design parameters of the switched reluctance motor as the optimization variables, output torque as the boundary condition, output torque ripple as optimization objectives. Lee [8] researched on SR motor flux distribution and effect of edge flux on torque ripple. The influence of different rotor pole shape on torque ripple of SR motor is studied by Dadpour [9], and the analysis results are verified by simulation. Hur [10] designed vacuum groove along the direction of magnetic circuit in stator pole, rotor pole and yoke of the motor respectively, achieved improvement of SR motor torque ripple by reducing radial magnetic flux density of the motor. Choi [11], Ozoglu [12], Tsuyoshi [13] change the first and second air gap of the motor, as a result, inductance/motor position curve was improved, torque ripple of the SR motor is partial eliminated.

Compared with the first method, the second focused on improving original output characteristics of the motor, which can fundamentally improve motor output characteristics and eliminate torque ripple. Most of the current researches focus on the problem of output torque ripple from control level, and the method of eliminating the torque ripple is not put forward from the design level. In this paper, the finite element model of SR motor is established, and the mechanism of low frequency noise and torque ripple of SR motor is studied from view of energy conversion, method of eliminating torque ripple is proposed and verified by two-dimensional finite element simulation. The research has laid a solid theoretical foundation for the application of SR motor drive system in electric vehicle.

13.2 Basic Operation Principles of SR Motor

Main drive system of independent drive electric vehicle is SR-motor which magnetic flux is in long flux path (LFP) pattern which phase windings are placed on opposite stator poles. Typical long magnetic path excitation 8/6 SR motor is shown in Fig. 13.1, in which, A2, A1 are stator poles.

Fig. 13.1 Typical LFP structure SR motor



In an LFP-SRM, the mutual inductance effect between the windings is negligible. Thus, for a given phase, phase voltage of each is determined by the respective corresponding phase current as

$$v_a = r_a i_a + \frac{d\lambda_a(i_a, \theta)}{dt} = r_a i_a + N \frac{d\phi_a(i_a, \theta)}{dt} \text{ or } v_a = r_a i_a + l_a \frac{di_a}{dt} + e_a \quad (13.1)$$

Which, $l_a = \partial\lambda_a(i_a, \theta)/\partial i_a$ is the A phase winding inductance, $e_a = w\partial\lambda_a(i_a, \theta)/\partial\theta$ is rotational electromotive force of Phase A. Each phase of the motor is excited by independent current. For A phase winding excitation, electromagnetic co-energy is

$$W'_a(i_a, \theta) \triangleq \int_0^{i_a} \lambda_a(\zeta, \theta) d\zeta \quad (13.2)$$

Each phase of winding is excited and produced torque separately, is a function of the electromagnetic co-energy. A phase output torque is

$$T_a(i_a, \theta) = \frac{\partial W'_a(i_a, \theta)}{\partial \theta_m} = P_r \frac{\partial W'_a(i_a, \theta)}{\partial \theta} \quad (13.3)$$

For a four-phase machine operates at a specific time periods, the output torque is produced by all separate phases. The output torque is

$$T = T_a(i_a, \theta) + T_b(i_b, \theta) + T_c(i_c, \theta) + T_d(i_d, \theta) \quad (13.4)$$

13.3 Low Frequency Torque Ripple

Figure 13.2a is typical phase current waveforms of one 8/6 SRM during unipolar excitation. As shown in that diagram, each phase currents are unidirectional. Since self-excitation is not possible, operation of the motor in this mode needs the input current and bus voltage to feed enough power to every phase in excitation. When operate at high rotation rate, motor has a short time to form sufficient magnetic flux. Thus, the excitation interval it expanded, and increases the conduction angle. In an electric cycle, phenomenon of multi-phase excitation occurred in the presence of the adjacent two-phase winding current is observed at the same time. Since electrical phase shift between consecutive phases is smaller than conduction angle, as Fig. 13.2a shows, and a significant overlap between each phase currents can be observed, what is the reason of two consecutive phases conduct current simultaneously in one subinterval of corresponding electrical cycle. During the period, the adjacent phase flux linkage and inductance are all non-zero. As shown in Fig. 13.2b, in overlap region, D phase flux linkage drops while A phase flux rises.

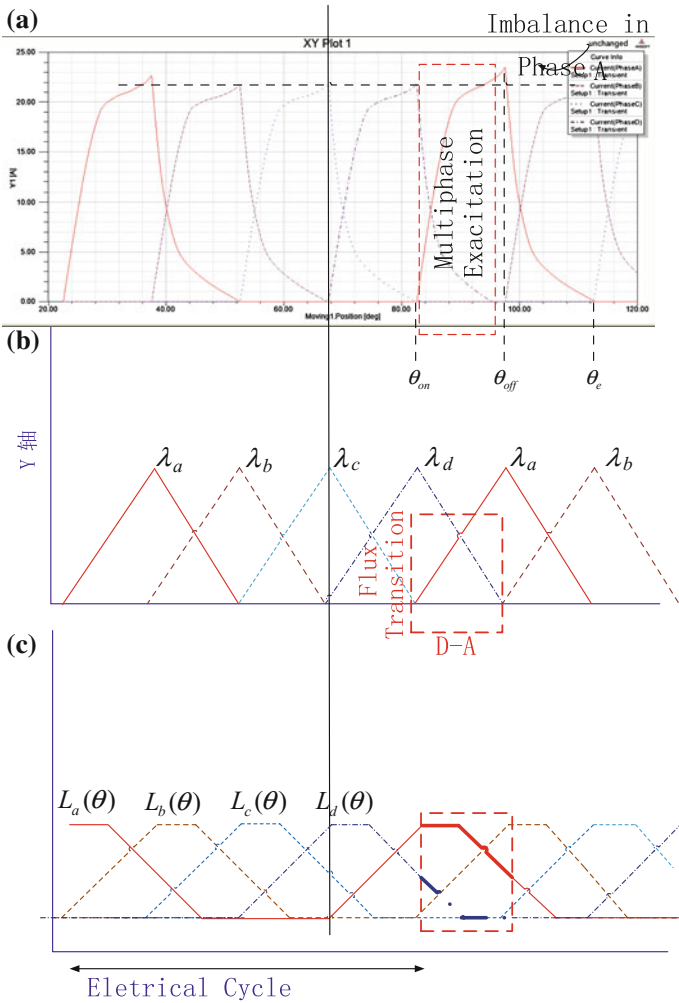


Fig. 13.2 Current/flux/inductance waveform

At the same time, each phase current appears over-lapping, the amplitude of A phase current waveform is higher than that of other phases.

13.3.1 Magnetic Flux Path Pattern of Motor

The distribution of magnetic intensity, flux density isodynamic lines of the prototype is illustrated in Fig. 13.3. Figure 13.3a shows relationship between induction flux polarity of each phase and winding mode.

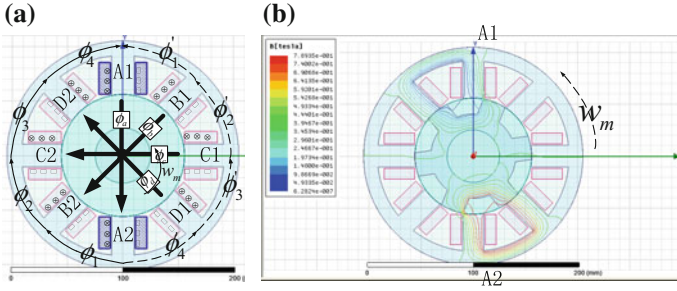


Fig. 13.3 Direction of induced magnetic flux

At a given moment ($\phi_d = \phi_a$) the magnetic flux density distribution of SR motor is shown in Fig. 13.3b, it can be seen that the motor magnetic circuit of short flux path excitation (SFPE) compared with LFPE, is much shorter. Such flux transitions happened four times in one electric cycle as shown in Fig. 13.2b.

$X \rightarrow Y$ indicate magnetic flux from X phase transfer to Y phase. $A \rightarrow B, B \rightarrow C, C \rightarrow D$ form LFPE while, $D \rightarrow A$, forms SFPE. This is because in the process of $D \rightarrow A$, A, D phase induction flux polarity direction is not consistent. That leads to changes in internal magnetic field and direction of the magnetic circuit of SR motor. It also changes magnetic induction intensity of SR motor. In addition, under the multi-phase excitation, the excitation mode of each phase is unbalanced. There exists at least one SFPE in SR motor with unipolar excitation during one electrical cycle.

In practice, even if each phase winding in a consistent and independent way to stimulate, the amplitude of each phase current is not identical. As shown in Fig. 13.2a, compared actually same current waveform of B, C, and D with A phase, the latter current amplitude is slightly higher than the other three. This inconsistent phase current waveform can cause the output torque $T = T_a + T_b + T_c + T_d$ and dc bus current i_{dc} ripple. Because the unbalance phase current only affects one phase of the motor. Therefore, the torque ripple and the motor bus current ripple caused by unbalance phase current is $1/n$ (n is the number of motor phase) times of the torque ripple when motor is running. That pulse is defined as low frequency torque ripple caused by phase current unbalance.

13.3.2 Current Imbalance Analysis

The induction magnetic flux polarity of typical four phase 8/6 SR motor is shown in Fig. 13.3a, stator yoke is divided into 8 sectors on average to determine the direction of the induced magnetic flux polarity. The axial symmetry of the magnetic flux is equal to the size of each part of the magnetic flux, such as the formula (13.5), each phase flux and the stator yoke of the various sectors of the magnetic flux as shown in Fig. 13.4.

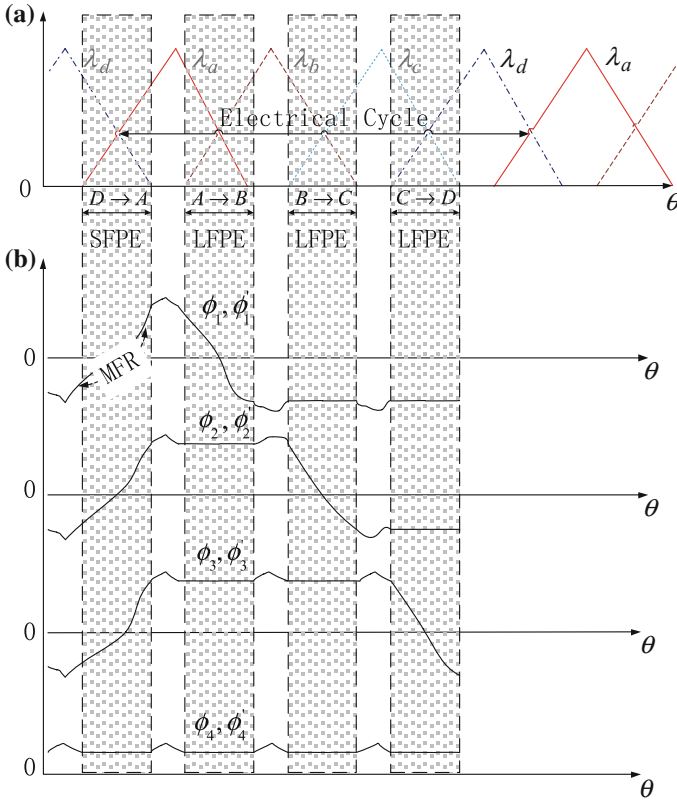


Fig. 13.4 Sector flux waveforms

$$\begin{aligned}
 \phi_1 = \phi'_1 &= \frac{1}{2N} (\lambda_a - \lambda_b - \lambda_c - \lambda_d) \\
 \phi_2 = \phi'_2 &= \frac{1}{2N} (\lambda_a + \lambda_b - \lambda_c - \lambda_d) \\
 \phi_3 = \phi'_3 &= \frac{1}{2N} (\lambda_a + \lambda_b + \lambda_c - \lambda_d) \\
 \phi_4 = \phi'_4 &= \frac{1}{2N} (\lambda_a + \lambda_b + \lambda_c + \lambda_d)
 \end{aligned}
 \tag{13.5}$$

Impact of rotor and stator poles on saturation affects is for all phases which do not the reason of unbalanced currents. Mutual inductance is usually ignorable in SRM of long flux path. Moreover, in order to attenuate mechanical vibrations, back iron of SRM is usually designed thickly in order to form a solid structure. Therefore, without causing saturation in rotor and stator poles, magnetic flux has enough space in the back iron to any consecutive phases to cross over. Accordingly, mutual inductance effect result of saturation in back iron also be neglected since it

impacts all phases identically and does not cause the unbalanced currents. As shown in Fig. 13.4b, the magnetic flux polarity ϕ_1 reversal (MFPR) during the flux transition moment $D \rightarrow A$. There will be six MFPRs in the whole period $D \rightarrow A$, but only two times during the period $A \rightarrow B$, $B \rightarrow C$ and $C \rightarrow D$.

Under same conditions, core loss of long magnetic path is larger than that excitation in short path. The magnetic flux polarity reversal (MFPR) of the stator yoke in the whole SFPE mode is $n-1$ times of that in LFPE. So the core loss in SFPE mode of the stator yoke and whole motor is much larger than in LFPE mode. As in practice, more power is needed to deliver to phase through the phases involved in SFPE to supply the extra core loss. So, SFPE needs windings to provide additional energy to compensate more core loss of the motor. The imbalanced phase reveals a little higher peak current. Thus, iron core loss of the stator yoke section is the cause of the motor phase current imbalance and low frequency torque ripple.

The developed torque, phase current waveform, bus current and the phase inductance of unipolar exciting 12/8 three-phase SR motor without the current balancing technology are shown in Fig. 13.5, in an electric cycle, each phase excitation power in sequence, flux transition occurs in the overlap interval of the adjacent two-phase current. The current of three phases is placed in the same phase position as shown in Fig. 13.5b, A phase current is observed to have a higher amplitude, which is not balanced in the other two phases. The motor bus current and each phase winding inductance curve in Fig. 13.5c, d. Low frequency current ripple and the output torque ripple mark in Fig. 13.5c, e, can see the effect of phase current imbalance on the motor operation.

For three-phase SR motor, three flux transitions occur in an electric cycle, respectively as $A \rightarrow B$ (LFPE), $B \rightarrow C$ (LFPE) and $C \rightarrow A$ (SFPE). In $C \rightarrow A$, A phase winding inductance is much larger than that of in C phase. At this point, A phase winding is required to provide additional energy to motor to meet additional core loss caused during the flux transition of SFPE. A phase is carried unbalanced phase current, which is reflected in Fig. 13.5a, b, has higher peak value and larger amplitude compared with other two phases. Figure 13.5e shows that output torque is affected by imbalance of phase current. The torque of srm is $T_e = \frac{1}{2} i^2 \frac{dL}{d\theta}$, proportional to the square of the current, makes effect of unbalanced current on the output torque curve is more obvious.

13.4 Phase Current Balance Control

Based on the above discussion, unbalanced phase current caused low frequency output torque ripple of the motor and fluctuation of the bus current. In order to eliminate this kind of fluctuation, this paper develops a kind of phase current balancing method, by changing the coil winding mode or the power switch tube topology, LFPE mode during magnetic flux transition is converted into SFPE mode. This balancing technology regulates phase current direction to ensure similar

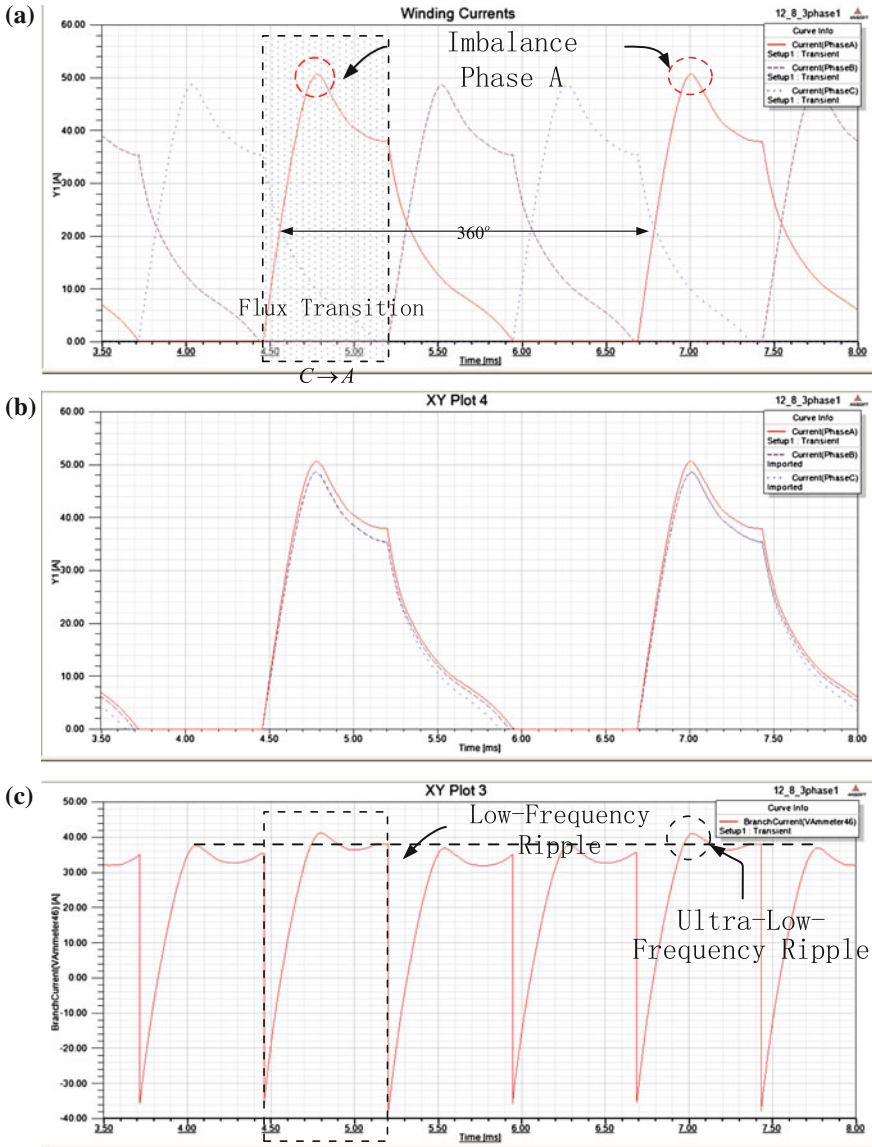


Fig. 13.5 SR motor output curve without current balancing strategy

magnetic flux path pattern for adjacent phases, is applicable to 3 phase and 4 phase SR motor.

Unipolar excitation SR induction flux polarity can be arbitrarily selected, traditional 12/8 three-phase and 8/6 four-phase switched reluctance motor in each coiling winding mode and induced polarity as shown in Figs. 13.6 and 13.7.

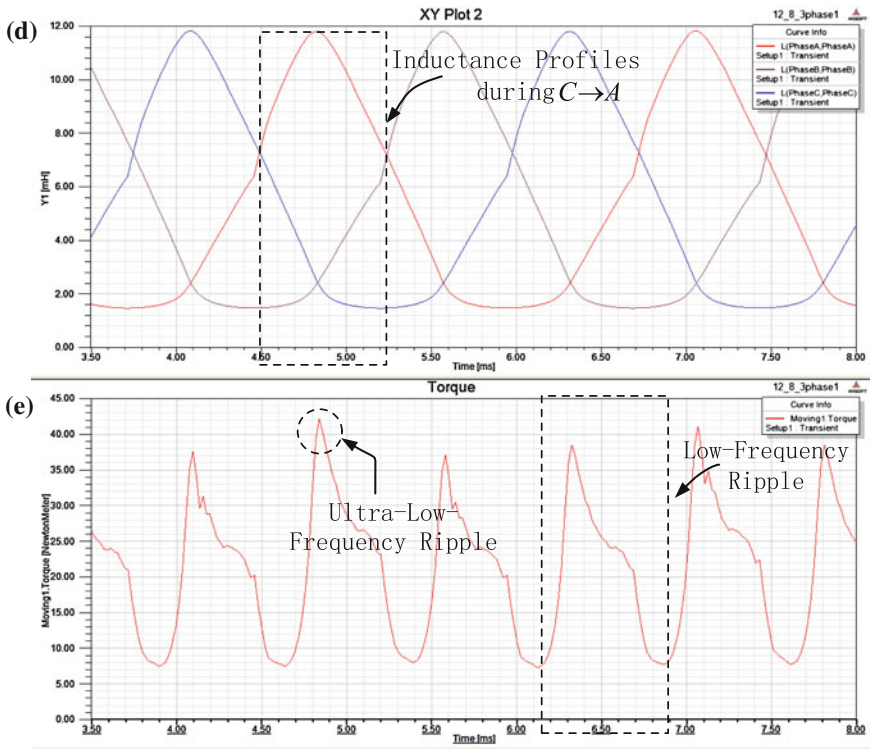


Fig. 13.5 (continued)

Fig. 13.6 6/4 induced polarity

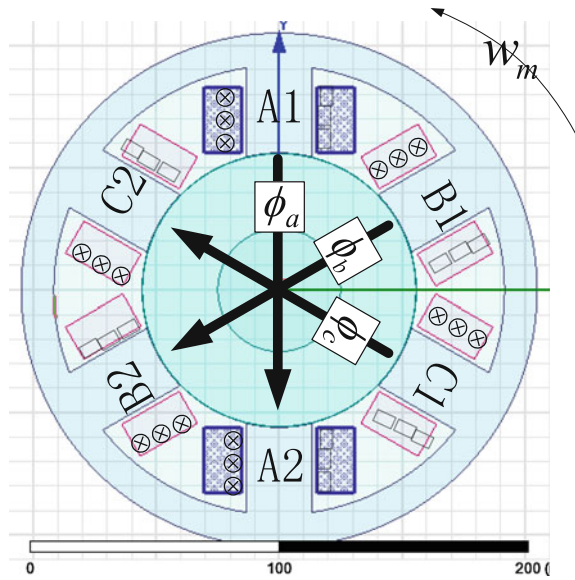
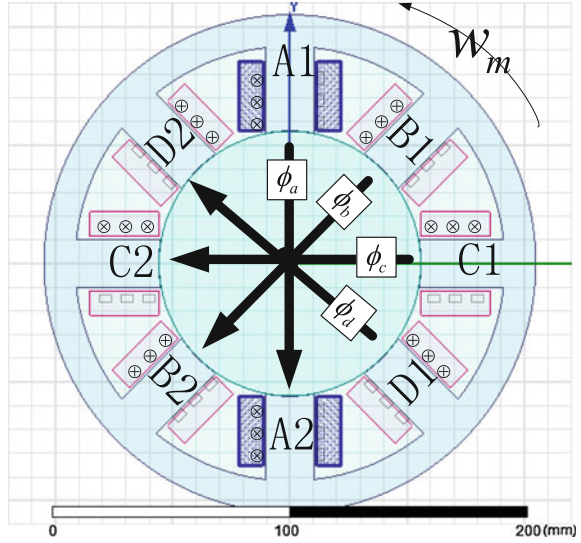


Fig. 13.7 8/6 induced polarity



13.4.1 Motor Current Balancing Strategy with Odd Phase

Induced flux polarity of switch reluctance motor is determined by coiling winding mode. Current direction and induced flux polarity in all phases of SRM can be arbitrarily set up. But, as current direction is assigned, it will be fixed when the machine is under operation. As shown in Fig. 13.6, flux polarity of motor from top to bottom is NNNSSS, in transition period between two adjacent phases when one phase cut and the next phase conduction, $N \leftrightarrow N$ formed LFPE and $N \leftrightarrow S$ formed SFPE, that inconsistency caused unbalanced current. As shown in Fig. 13.8, by

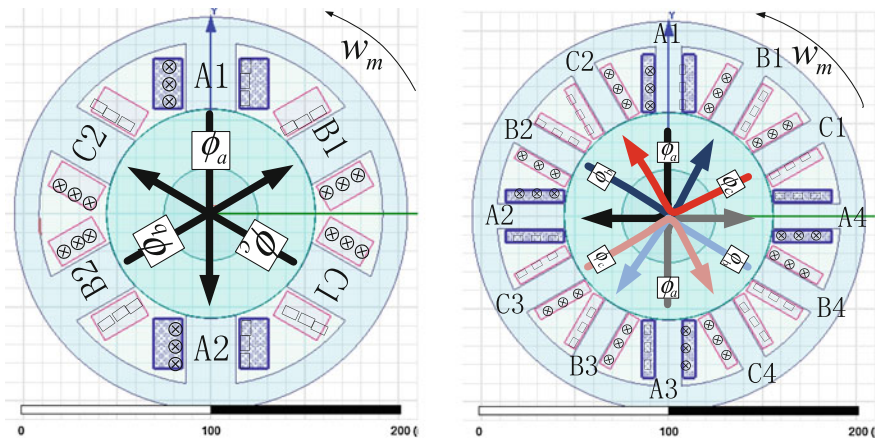


Fig. 13.8 Change the magnetic flux polarity by winding

changing the B phase winding coiling mode to change the current direction, and B phase induced magnetic flux polarity reversal. This motor stator poles formed NSNSNS. Only exists SFPE during flux transition, phase current waveform balance, low frequency torque ripple can be eliminated. This method is only applicable to the switched reluctance motor with odd phase.

The obtained phase current, bus current and output torque waveforms by two-dimensional finite element simulation are shown in Fig. 13.9. As can be seen, ripple of bus current and motor output torque is eliminated and phase currents are balanced.

13.4.2 Motor Current Balancing Strategy with Even Phase

For the even phase of the switched reluctance motor, 8/6 pole four phase switched reluctance motor coiling winding mode and induced magnetic flux polarity is shown in Fig. 13.7, induction flux polarity of stator pole from top to bottom in turn, NNNSSSS. In order to make magnetic flux path pattern during flux transition only in SFPE or LFPE mode, change a single phase current direction is not feasible. In order to solve this problem, adds a control path in each phase of the motor power converter, the motor in the period of two adjacent electric cycles is excited by current with direction of one positive and one negative which have the same absolute value and waveform. So the magnetic flux polarity of the motor is changed to NSNSNSNS, and the magnetic flux path pattern of SFPE is formed. As rotation direction and output torque direction of the switched reluctance motor are not related to the direction of excitation current, this method will not affect the output power and torque of the switched reluctance motor. The excitation voltage of A phase switched reluctance motor with conventional unipolar excitation and current balancing strategy are shown in Fig. 13.10.

The single phase and the whole power converter topology of the power converter are shown in Fig. 13.11, adding a loop on each phase power switch tube circuit. During the operation of the motor, the switching frequency of each circuit is half of the original configuration.

Phase current, bus current and motor output torque waveforms by two-dimensional finite element simulation are shown in Fig. 13.12. It can be seen that the phase currents are balanced. Low frequency torque ripple of bus current and motor output torque ripple is also eliminated.

The output torque is put in the frequency domain as shown in Fig. 13.13a, b. It can be seen from Fig. 13.13a the harmonic frequency of producing output torque ripple frequency of switched reluctance motor is 350 Hz, which is caused by the switching of each phase, is determined by phase number of motor and motor speed. In the 1/4 of the torque ripple frequency, low frequency torque ripple caused by the phase current unbalance is observed. Compared with Fig. 13.13a, b, the balance strategy has a good effect on the elimination of low frequency torque ripple of motor output torque.

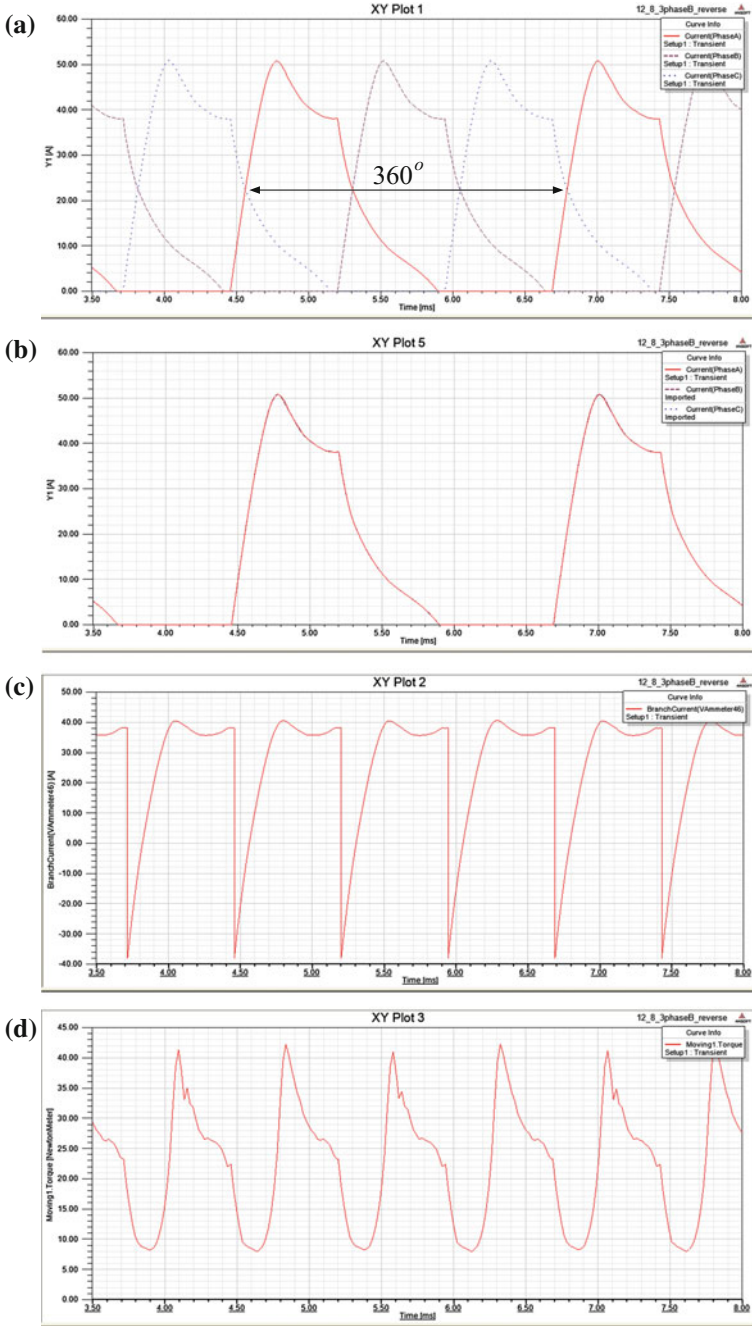


Fig. 13.9 Phase current/bus current/output torque curve

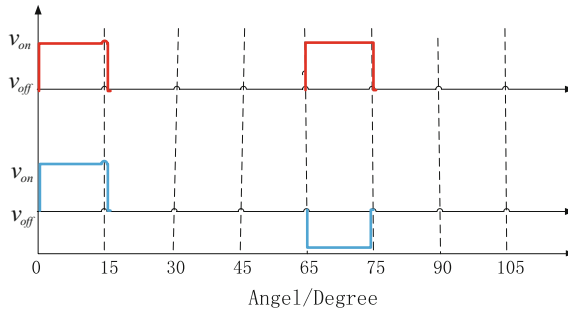


Fig. 13.10 Current excitation mode

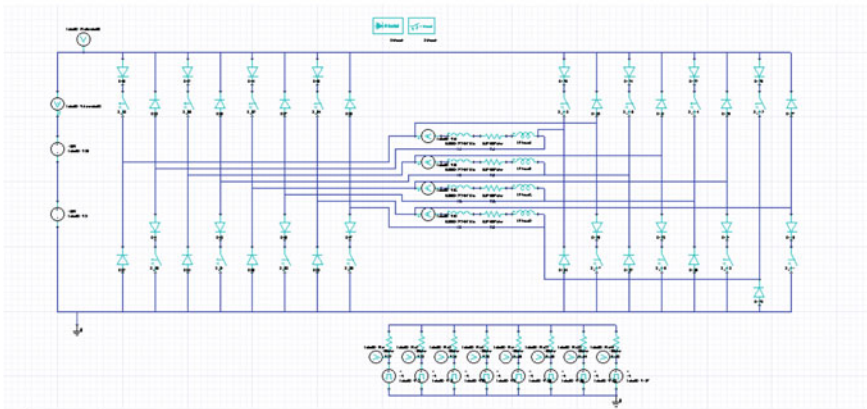
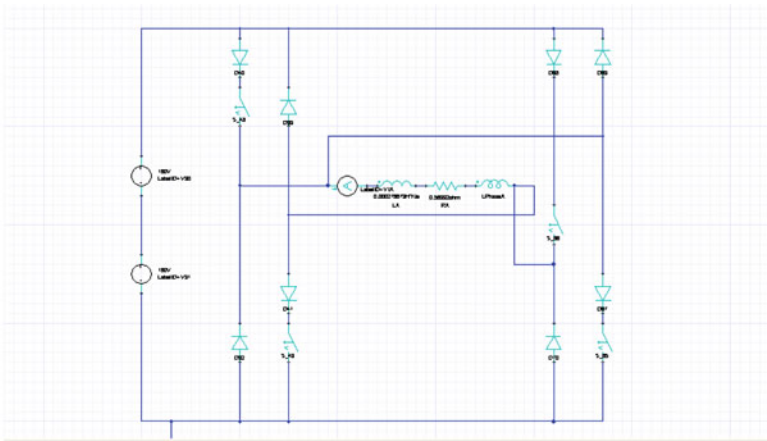


Fig. 13.11 Topology of power converter

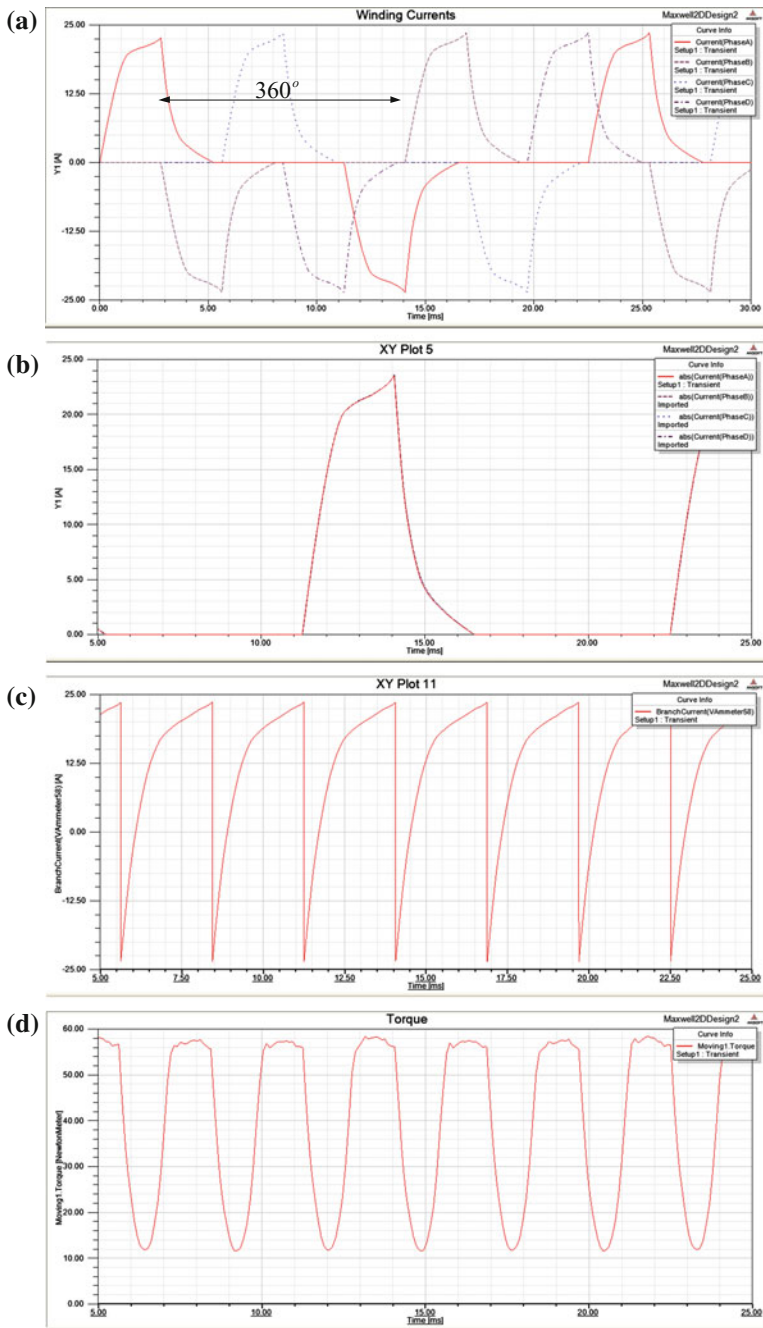


Fig. 13.12 Performance output curve of even phase SR motor

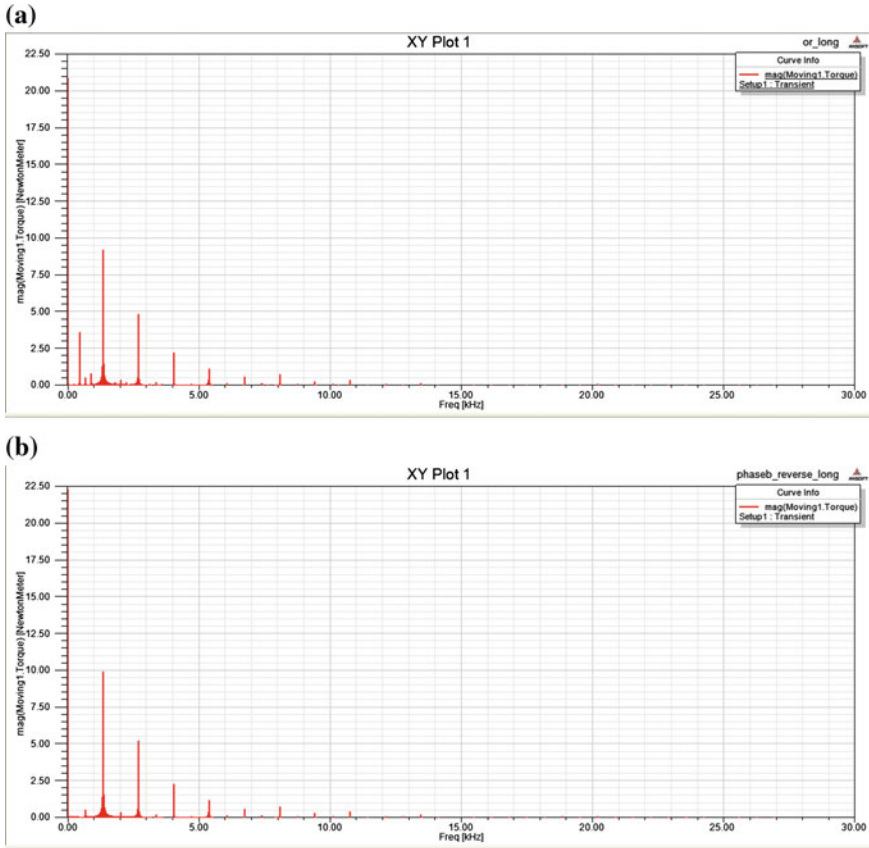


Fig. 13.13 Frequency domain of output torque

13.5 Conclusion

In this paper, problem of low frequency torque ripple of in-wheel-motor is analyzed in detail from energy viewpoint. An elimination of the current balancing strategy is developed, and the main conclusions are as follows:

- (1) Unipolar excitation switch reluctance motor exist different magnetic flux polarity reversal (MFPR) during flux transitions, due to the MFPR directly in part of the energy distribution of core. This difference, results phase currents unbalanced, that one phase has higher or lower peak current amplitude, leads to the emergence of low frequency torque ripple.
- (2) A phase current balancing strategy is proposed, this technique changes current direction of each phase for even phase machine and changes winding coiling mode for odd machine to ensure similar magnetic flux path pattern for adjacent phases, which exhibits a wonderful current balancing performance for not only

3 phase but also 4 phase machines, and low frequency torque ripple can be eliminated which can significantly alleviate the motor output torque ripple, improve motor performance. Thus, improve vertical and longitudinal driving performance of the four wheel drive electric vehicle.

Acknowledgements This paper is supported by the Key Project of Natural Science Foundation of Chongqing (Grant No. cstc2015zdcy-ztx30001) and the Key Technology Innovation Project of Chongqing (Grant No. cstc2015jcyjBX0097).

References

1. Song Y, Jin G (2004) Types and characteristics of electric wheel. *Urban Public Transp* 4:16–18
2. Cajander D, Le-Huy Hoang (2006) Design and optimization of a torque controller for a switched reluctance motor drive for electric vehicles by simulation. *Math Comput Simul* 71:333–344
3. Ohyama K, Naguib M, Nashed F, Aso K, Fujii H, Uehara H (2006) Design using finite element analysis of a switched reluctance motor for electric vehicle. *Power Electron* 6(2):163–171
4. Li G, Ojeda J, Hlioui S, Hoang E, Lecrivain M, Gabsi M (2012) Modification in rotor pole geometry of mutually coupled switched reluctance machine for torque ripple mitigating. *IEEE Trans Magn* 48(6)
5. Suhaili N, Singh RK (2014) Analysis of variation in torque ripple in switch reluctance motor with design. 978-1-4799-5912-9/14/\$31.00 ©2014 IEEE
6. Navardi MJ, Babaghorbani B, Ketabi A (2014) Efficiency improvement and torque ripple minimization of switched reluctance motor using FEM and seeker optimization algorithm. *Energy Convers Manage* 78:237–244
7. Zhang Y, Xia B, Xie D, Koh CS (2015) Optimum design of switched reluctance motor to minimize torque ripple using ordinary Kriging model and genetic algorithm. *Fuel Energy Abs* 56(5):388–457
8. Lee JW, Kim HS, Kwon BI, Kim BT (2004) New rotor shape design for minimum torque ripple of SRM using FEM. *IEEE Trans Magn* 40(2):754
9. Dadpour A, Ansari K (2013) Conversion of shaded-pole induction motor to switched reluctance motor and effects of pole shoe and notch on SRM noise. In: 2013 IEEE XXXIII international scientific conference electronics and nanotechnology (ELNANO)
10. Hur J, Kang GH, Lee JY, Hong JP, Lee BK (2004) Design and optimization of high torque, low ripple switched reluctance motor with flux barrier for direct drive. In: *Industry Applications Conference, 2004. 39th IAS Annual Meeting. Conference Record of the 2004 IEEE*
11. Higuchi T, Ueda T, Abe T (2010) Torque ripple reduction control of a novel segment type SRM with 2-steps slide rotor. In: *The 2010 international power electronics conference*
12. Choi YK, Yoon HS, Koh CS (2007) Pole-shape optimization of a switched-reluctance motor for torque ripple reduction. *IEEE Trans Magn* 43(4):1797
13. Ozoglu Y, Garip M, Mese E (2002) New pole tip shapes mitigating torque ripple in short pitched and fully pitched switched reluctance motors. In: *Conference record of the 37th IAS annual meeting industry applications conference, vol 1, pp 43–50, 18 Oct 2002*

Chapter 14

Relaxed Static Stability for All-Wheel-Drive Electric Vehicle Based on Yaw Moment Control

Jun Ni and Jibin Hu

Abstract All-wheel-drive electric vehicles have been widely focused, which provides the possibility for advanced control technology. In this chapter, a novel control theory for automobile will be proposed-Relaxed Static Stability (RSS), which could also lead to new overall configuration concept. The basic idea of RSS is that the lateral dynamic system of the vehicle could be designed inherent static unstable (oversteer) to improve overall configuration flexibility, and be closed-looped stable based on pole assignment with external yaw moment provided by the independent motors. In this chapter, the basic schematic control strategy of RSS is described. Finally, a nonlinear dynamic model is used to verify the performance of RSS control. The results show that the handling performance of the vehicle could be significantly improved and adjusted to satisfy different handling demand based on adjusting desired pole locations.

Keywords Relaxed static stability · Electric vehicle (EV) · All-wheel-drive · Independent motor · Direct yaw moment control (DYC)

14.1 Introduction

All-wheel-drive electric vehicles have been widely investigated and proved to be with better driving performance and handling performance than conventional vehicles [1, 2]. All-wheel-drive technology provides convenience to achieve advanced vehicle dynamics control, such as Traction Control (TC), Anti Brake Skid (ABS), Direct Yaw Control (DYC) or the integrated control systems [3, 4]. Moreover, all-wheel-drive technology makes the acting torque on each wheel available which boosts the investigations of tyre-road condition or vehicle behavior observation [5, 6]. Among the dynamics control technologies of all-wheel-drive

J. Ni (✉) · J. Hu

National Key Lab of Vehicular Transmission, Beijing Institute of Technology, Beijing,
People's Republic of China
e-mail: nijun_bit@163.com

electric vehicle, DYC is one of the most concerned topics [7, 8]. Y. Shibahata firstly proposed the basic principle of DYC system [9]. M. Nagai proposed a MMC controller to control the vehicle to follow the desired 2 DOF dynamic model with the feedback of yaw rate and side slip angle [10]. Y. Hori proposed a robustified MMC controller. He further claimed that, the research should focus on how to calculate the external yaw moment to make the vehicle follow the desired vehicle model [11]. Like Y. Hori stated, the following researchers mainly putted their focus on the control method to calculate the yaw moment. A. Goodarzi investigated the performance of optimal control on yaw moment generating [12]. Yu proposed an optimal controller with real-time online estimation of the tyre cornering stiffness [13]. Hedrick used sliding mode control during the process of the yaw moment generating [14]. To deal with the DYC control system in high nonlinear maneuver condition, Hori proposed a controller based on body slip angle fuzzy observer [15], and he further proposed a slip angle estimation block using the lateral tire force sensors [5]. Moreover, some researchers such as Wang have also made great achievements in AFS/DYC integrated control system [16, 17].

Above authors' work have made significant contributions to the vehicle dynamics control. But in DYC's basic principle, the desired vehicle lateral dynamics behavior is always calculated by 2 DOF dynamic model with inherent understeer characteristics [9]. As Wang stated in [17], the main problem of DYC mainly focuses on how to generate the desired moment which is indeed the most researchers focus on. In this chapter, based on our previous work of all-wheel-drive electric vehicle [18–20], a novel dynamic control principle-Relaxed Static Stability (RSS) will be proposed.

14.2 Pole Location Discussion of Vehicle Lateral Dynamic System

The state-space of 2 DOF dynamic model is expressed as:

$$\dot{x} = Ax + B\delta \quad (14.1)$$

$$B = \begin{bmatrix} -\frac{C_f}{mu} \\ -\frac{aC_f}{I_z} \end{bmatrix} \quad (14.2)$$

$$A = \begin{bmatrix} \frac{C_f + C_r}{aC_f - bC_r} & \frac{aC_f - bC_r}{a^2C_f + b^2C_r} - 1 \\ \frac{mu}{I_z} & \frac{mu^2}{I_z u} \end{bmatrix} \quad (14.3)$$

The pole location of the lateral dynamic system of several typical type vehicle will be discussed. Table 14.1 shows the specifications of a conventional front-drive passenger car. It is typical with ICE at front of the vehicle and a front C.G location. It can be easily concluded understeer characteristics.

Table 14.1 Conventional passenger car specifications

Specification	Value
m	900 kg
L	2.54 m
I_z	1138 kg*m ²
C_f	-57000 N/rad
C_r	-42000 N/rad
a	0.89 m
b	1.65 m

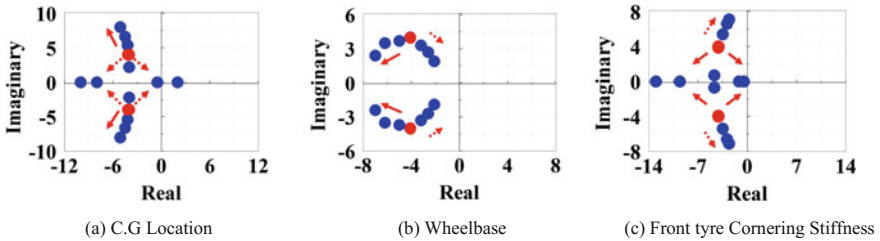


Fig. 14.1 Pole locations distribution with vehicle specifications change (vehicle speed as 30 m/s)

Figure 14.1a shows the case when C.G location changes. The original pole location is conjugate complex values $(-4.1, \pm 4)$ which is noted by red points. With C.G location moves forward to 90%: 10% (red solid arrows), the distance from poles to the origin becomes larger. And they are still conjugate complex values which shows under damped characteristics. With C.G location moves backward to 40%: 60% (red dash arrows), the dynamics system becomes over damped, and the poles become double negative real poles. When the C.G location is 40%: 60%, it can be seen that a positive real pole occurs which indicates the system is unstable. With C.G location continues to move backward, the system will be unstable. Actually, in conventional vehicle overall configuration theory, forward C. G location has to be assured to obtain inherent understeer. For all-wheel-motor-drive vehicle, back C.G location is almost inevitable. It is easy to make the vehicle unstable with back C.G location. Taken the vehicle shown in Table 14.1 as example, the C.G location configuration arrange is constraint in the range from 100%: 0% to 40%: 60%. In Fig. 14.1c the pole locations with front tyre cornering stiffness changes is shown. The red solid arrow show the movement direction when the stiffness increases, and the dash arrow shows the stiffness decreases. When cornering stiffness of front tyres increases, the system goes over damped and double negative real poles occur. When the cornering stiffness of front tyres is higher than certain value (150% as origin), a positive real pole occurs which indicates an unstable characteristics. For conventional vehicle with front-drive, the traction force acting on front tyres makes front tyres' stiffness lower than rear tyres. That makes a

more stable tendency. But for all-wheel-drive vehicle, the traction force also acts on rear tyres which makes the stiffness much lower, so that it's much easier to be unstable than conventional vehicle.

14.3 Basic Hierarchical Control Strategy of RSS

In this section, the basic overall control strategy of RSS will be proposed. With yaw moment M considered as control input, the dynamics model can be expressed as:

$$\dot{x} = Ax + B\delta + CM \quad (14.4)$$

Consider M as feedback according to state vector x :

$$M = Fx \quad (14.5)$$

Then Eq. (14.9) can be expressed as:

$$\dot{x} = (A + CF)x + B\delta \quad (14.6)$$

The pole locations of the new dynamic system are determined by $A + CF$. Consider f_1 and f_2 as feedback coefficients. Through the manipulation with the characteristics matrix, the expression of the closed-looped pole location can be expressed as:

$$p_{1,2} = \frac{I_z(C_f + C_r) + m(a^2C_f + b^2C_r) + f_2mu \pm \sqrt{\Delta_2}}{2I_zmu} \quad (14.7)$$

where:

$$\Delta_2 = [I_z(C_f + C_r) - m(a^2C_f + b^2C_r) - f_2mu]^2 - 4I_zm[mu^2 - (aC_f - bC_r)][(aC_f - bC_r) + f_1] \quad (14.8)$$

It can be seen that the closed-looped pole locations of the vehicle is determined by both vehicle specifications $m, L, I_z, C_f, C_r, a, b$ and parameters f_1 and f_2 . That can be totally considered the CCV concept. The pole locations can be adjusted according to f_1 and f_2 . According to desired target pole locations, feedback vector F can be solved, and the value of M can be determined. According to above basic discussion, the basic strategy of RSS can be expressed (Fig. 14.2).

In RSS, the desired pole locations should be determined first, which indicates the desired vehicle handling response. Figure 14.3 shows the desired pole locations in 'Stable Mode' and 'Agile Mode'. In 'Stable Mode', the desired pole locations are indicated by red hollow circles. It can be seen that they are conjugate complex

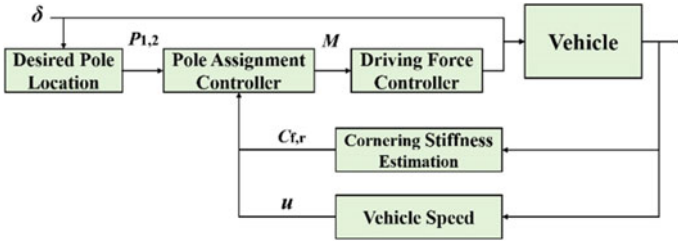
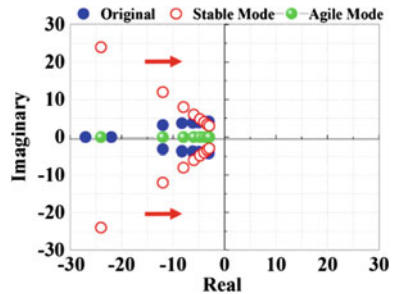


Fig. 14.2 Control schematic diagram of RSS

Fig. 14.3 Desired pole locations



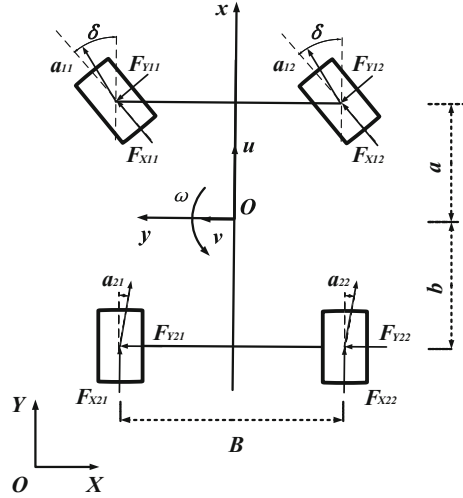
values arranged in straight lines which divide 2nd and 3rd quadrants. That shows an optimal damping ratio as 0.707 which is proved to be the optimal transient response. The moving direction of the pole locations when vehicle speed increases is shown by arrows. According to the passenger car case, it becomes under damped when vehicle speed exceeds 5 m/s. Moreover, the damping ratio becomes lower with vehicle speed increases. Based on that, the desired vehicle handling response is assumed to be with constant optimal damping ratio during the whole speed range, which could significantly increase the handling stability. Green shadow circles indicate the desired pole locations in ‘Agile Mode’. In each speed case, the desired pole locations are assumed to be one single real value which indicates critical damped. According to Ref. [21], neutral steer vehicle has greatest handling mobility, which is also the reason why Formula 1.1 race car is always designed to be neutral steer.

14.4 Simulation Verification

A 7 DOF vehicle nonlinear dynamic model is used here (Fig. 14.4).

The dynamic equation of the vehicle body expressed in (o, x, y) coordinate frame can be written:

Fig. 14.4 7 DOF vehicle dynamics model



$$\begin{cases} m(\dot{u} - v\omega) = (F_{x11} + F_{x12}) \cos \delta + F_{x21} + F_{x22} - (F_{y11} + F_{y12}) \sin \delta \\ m(\dot{v} + u\omega) = (F_{y11} + F_{y12}) \cos \delta + F_{y21} + F_{y22} \\ I_z \dot{\omega} = a(F_{y11} + F_{y12}) \cos \delta - b(F_{y21} + F_{y22}) + (F_{x22} + F_{x12} - F_{x21} - F_{x11})B \end{cases} \quad (14.9)$$

where v is the lateral speed of the vehicle. δ is the front wheel angle. F_{xii} , F_{yii} is the traction and lateral force of 4 tires as figure shown. Rotational dynamic equation of each wheel can be expressed:

$$T_i - F_{xi}R_t = I_w \dot{\omega}_i \quad (14.10)$$

where T_i ($i = 1-4$) is the input torque of the motor acting on 4 wheels respectively. ω_i is the rotation speed of the 4 wheels respectively. RSS concept provide the possibility for the vehicle to be designed as inherent unstable, and to be closed-looped stable with pole assignment. That has great significance for the future vehicle such as all-wheel-motor-drive vehicle with heavy battery package, or other configured vehicle which is inherent unstable according to traditional handling stability theory. In this section, this case will be discussed. If a vehicle is configured as inherent unstable, how RSS control improves the handling performance will be analyzed. The distance from C.G to front and rear axles (a , b) in Table 14.1 is changed to 1.6 and 0.94 m which is inherent unstable (oversteer) configured.

Figure 14.5 show the simulation results in ‘Stable Mode’ in a 100 km/h J-turn with inherent oversteer vehicle. Through Fig. 14.5, it can be seen that the vehicle without control loses stability and spins after 15 s when steer angle is inputted. The lateral acceleration of uncontrolled vehicle peaks about 0.6 g, and the yaw velocity peaks about 0.6 rad/s. The large side slip angle (-0.8 rad) indicates an extreme spin

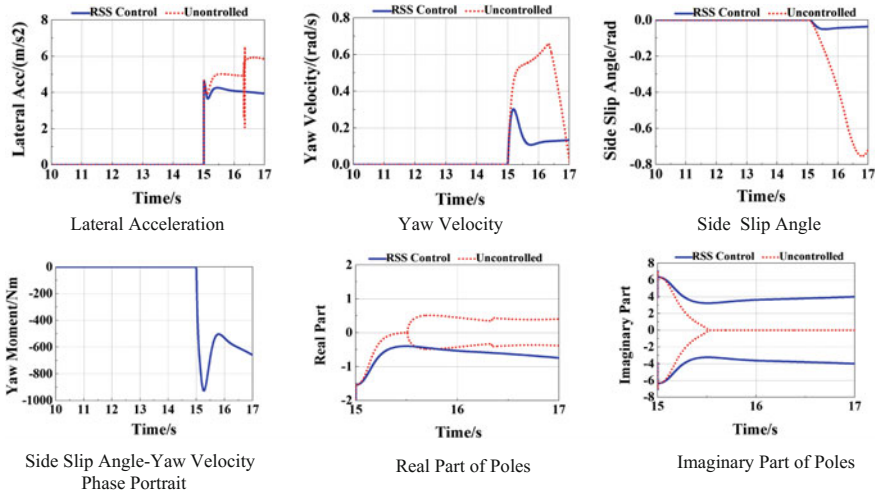


Fig. 14.5 Simulation in 100 km/h J-turn (Stable mode, inherent oversteer)

behavior of the uncontrolled vehicle. In comparison, the vehicle under RSS control is stable after the large steer angle is inputted. The lateral acceleration, yaw velocity and side slip angle remains a stable value after overshoot which indicates the vehicle behaves well under RSS control. Figure 14.5 shows the yaw moment demand for RSS control which peaks about -900 N m. Figure shows the comparison of real and imaginary part of the real-time pole of the vehicle. For uncontrolled vehicle, it can be seen that, in 15.5 s positive real part occurs which indicates the dynamic system of the vehicle becomes unstable. After 15.5 s, the poles of dynamic system of uncontrolled vehicle remains two real values with a positive pole. It indicate the vehicle is unstable during this time. The phenomenon matches the reality reflected by other figures. For the vehicle under RSS control, it can see that the poles remain two conjugate complex values which indicates the dynamic system is under damped, and it matches the control goal of ‘Stable Mode’.

14.5 Conclusion

In this chapter a novel concept-RSS is proposed which could be considered as CCV concept used in ground vehicle field. Different with existing DYC, RSS concept can be considered as a novel overall concept for ground vehicle which combines the mechanical and control systems. RSS control has two major advantages as following.

Firstly, RSS allows the vehicle to be designed as inherent static unstable which could significantly improves the overall configuration flexibility of vehicle. That has great significance for new-type configured vehicle, such as

all-wheel-motor-drive vehicle with back heavy battery package and separate independent motors and controllers, as well as future advanced vehicle.

Secondly, based on pole assignment concept, RSS could significantly improve the handling performance of the vehicle. Moreover, it provides the possibility to easily define different handling performance demand according to the desired pole location determination. The ‘Stable Mode’ and ‘Agile Mode’ discussed in the paper give meaningful examples.

References

1. Chan CC (2008) The state of the art of electric and hybrid vehicles. *IEEE Trans Ind Electron* 55(6):2237–2245
2. Ivanov V, Savitski D, Shyrokau B (2015) A survey of traction control and antilock braking systems of full electric vehicles with individually controlled electric motors. *IEEE Trans Veh Technol* 64(9):3878–3896
3. Shibahata Y (2005) Progress and future direction of chassis control technology. *Annual Rev Control* 29:151–158
4. Chen Y, Wang J (2012) Design and evaluation on electric differentials for over-actuated electric ground vehicles with four independent in-wheel motors. *IEEE Trans Veh Technol* 61(4):1534–1542
5. Nam K, Fujimoto H, Hori Y (2012) Lateral stability control of in-wheel-motor-driven electric vehicles based on sideslip angle estimation using lateral tire force sensors. *IEEE Trans Veh Technol* 61(5):1972–1984
6. Kim J, Park C, Hwang S, Hori Y (2010) Control algorithm for an independent motor drive vehicle. *IEEE Trans Veh Technol* 59(7):3213–3221
7. Hori Y (2004) Future vehicle driven by electricity and control research on four wheel motored UOT electric March II. *IEEE Trans Ind Electron* 51(5):954–962
8. Chen Y, Wang J (2012) Design and evaluation on electric differentials for over-actuated electric ground vehicles with four independent in-wheel motors. *IEEE Trans Veh Technol* 61(4):1534–1542
9. Shibahata Y, Shimada K, Tomari T (1993) Improvement of vehicle maneuverability by direct yaw moment control. *Veh Sys Dyn* 22:465–481
10. Nagai M, Hirano Y, Yamanaka S (1997) Integrated control of active rear wheel steering and direct yaw moment control. *Veh Sys Dyn* 27:357–370
11. Sakai S, Hori Y (1998) Robustified model matching control for motion control of electric vehicle. *IEEE AMC’98*
12. Goodarzi A, Mohammadi M (2014) Stability enhancement and fuel economy of the 4 wheel drive hybrid electric vehicles by optimal tyre force distribution. *Veh Sys Dyn* 52(4):539–561
13. Xiong L, Yu ZP, Wang Y (2012) Vehicle dynamics control of four in-wheel motor drive electric vehicle using gain scheduling based on tyre cornering stiffness estimation. *Veh Sys Dyn* 50:831–846
14. Chen Y, Hedrick K, Guo K (2012) A novel direct yaw moment controller for in-wheel motor electric motors. *Veh Sys Dyn* 51(6):925–942
15. Geng C, Mostefai L, Hori Y (2009) Direct yaw moment control of an in-wheel motored electric vehicle based on body slip angle fuzzy observer. *IEEE Trans Ind Electron* 56(5):1411–1419
16. Shuai Z, Zhang H, Wang J, Li J, Ouyang M (2014) Combined AFS and DYC control of four-wheel-independent-drive electric vehicles over CAN network with time-varying delays. *IEEE Trans Veh Technol* 63(2):591–602

17. Zhang H, Wang J (2016) Vehicle lateral dynamics control through AFS/DYC and robust gain-scheduling approach. *IEEE Trans Veh Technol* 65(1):489–494
18. Ni J, Hu J (2016) Handling performance control for hybrid 8-wheel-drive vehicle and simulation verification. *Veh Sys Dyn* doi:[10.1080/00423114.2016.1169303](https://doi.org/10.1080/00423114.2016.1169303)
19. Ni J, Hu J, Li X (2015) Dynamic Modeling, Validation and Handling Performance Analysis of Skid Steered Vehicle. *Proc Inst Mech Eng Part D J Automobile Eng* 232:1–13
20. Ni J, Hu J (2016) Dynamic modeling and experimental validation of a skid steered wheeled mobile robot on pivot steer condition. *Proc Inst Mech Eng PartD: J Automobile Eng*
21. Milliken WF, Milliken DL (1994) Race car vehicle dynamics. Warren Michigan, SAE
22. Esmailzadeh E, Goodarzi A, Vossoughi GR (2003) Optimal yaw moment control law for improved vehicle handling. *Mechatronics* 13:659–675
23. Ni J (2012) The suspension optimization of FSAE race car based on virtual prototyping technology. FISITA 2012 World Congress

Chapter 15

Test Study on Characteristics of Multi-Hole Injector for Gasoline Direct Injection Engine

Jujiang Liu, Hong Chen, Sicong Lin, Yuhuai Li, Lin Ye and Shuang Zhang

Abstract By means of High speed camera and CCD camera, combining with high energy laser device, spray characteristics test of multi-hole injector for gasoline direct injection engine have been done on the constant volume chamber bench. The variation laws of spray penetration, spray angle and spray target were studied under different injection pressures, different injection pulses and different injection background pressures. Also the variation tendency for spray penetration of different injector flow ranges have been tested and analyzed. The results indicate that injecting pressure boosting can strengthen the initial penetration developing of spray plume, fuel atomizing becoming better, resulting in increasing of spray angle. The effects of changing background pressure on spray angle and target are not obvious. And spray target coordinate is mainly determined by the injector hole layout. Under the same injection pressure and flow quantity, injector having the larger flow range has shorter penetration than that of smaller flow range.

Keywords Gasoline direct injection engine · Multi-hole injector · Spray characteristics · Test study

15.1 Introduction

With passenger vehicle fuel consumption regulations being more and more stringent and serious environmental protection pressure, it is of great importance to develop energy saving and emission reduction gasoline engine. Gasoline direct injection engine has good power, economic performance and better transient characteristics, which has been becoming the mainstream of modern gasoline engine [1, 2]. The function of engine is to convert the fuel combustion energy into the output of mechanical energy. And this process is carried out by engine combustion system, which is a core system of the engine. Spray characteristics and

J. Liu · H. Chen (✉) · S. Lin · Y. Li · L. Ye · S. Zhang
GAC Automotive Engineering Institute, Guang Zhou, Guang Dong, China
e-mail: chen hong@gaei.cn

spray target design in GDI cylinder have significant effects on combustion chamber structure layout and piston crown shape design [3, 4]. Reports can be seen at present that research has been done on spray matching and its characteristics [5–7]. Spray penetration has close relationship with interaction between spray plume and cylinder liner, playing important roles on HC emission and oil dilution phenomenon. Spray target design is one of the main factors which should be taken into consideration when designing piston crown shape. Meanwhile, injector structural parameters, injection pressure and the interaction of spray plume and air flow will determine the Sauter mean diameter. And all factors above will have effects on engine combustion performance.

On the basis of the discussion and analysis above, spray characteristics testing of GDI multi-hole injector has been done on a constant volume chamber bench in this chapter. Variation laws of spray penetration and angle are investigated under different injector pressures, different background pressures. And spray targets under different flow quantities and injection pressures are tested and analyzed. Also research has been done on spray penetration changing trends of injectors whose flow ranges are different.

15.2 Testing Systems and Methodologies

15.2.1 Testing System

Systematical parameters of the adopted constant volume chamber in this chapter are shown in Table 15.1, which is composed of constant volume chamber block, water cooling system, high pressure fuel supplying pipes system, intake pipes, exhaust pipes and injector controlling and monitoring systems. Optical devices include Nd: YAG pulsed UV laser (60 mJ@266 nm), CMOS high speed camera (20 kHz@1024 × 1024 pixel), CCD camera (2048 × 1024 pixel), diffuser and program timing unit. Spray tests results can be post processed by DaVis post processing software.

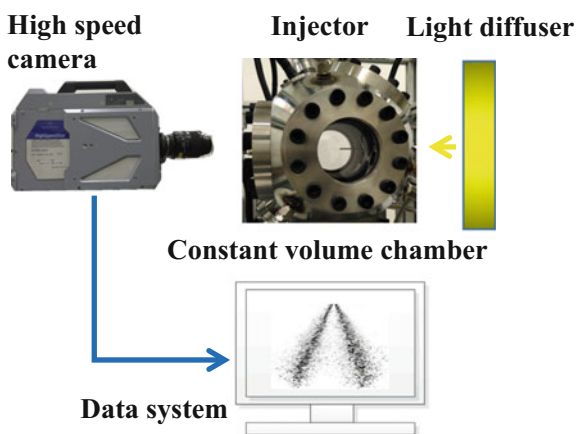
15.2.2 Testing Methodologies

Decompressing lower nitrogen source, whose pressure is 15 MPa, is applied as the background gas of spray injection, and higher 20 MPa nitrogen source is used for the supplying source of injector pressure accumulator. Water cooling circulation system can control the temperature of injecting fuel. In the controlling and testing system of constant volume chamber bench, injection pulse will be controlled by means of inputting the driven current curves of injector. When injection happens, the TRIG signal of injecting starting is produced at the same time, which will be synchronized with camera and laser signal through PTU timing unit, guaranteeing the right spray picture can be captured.

Table 15.1 Constant volume chamber structure and its main parameters

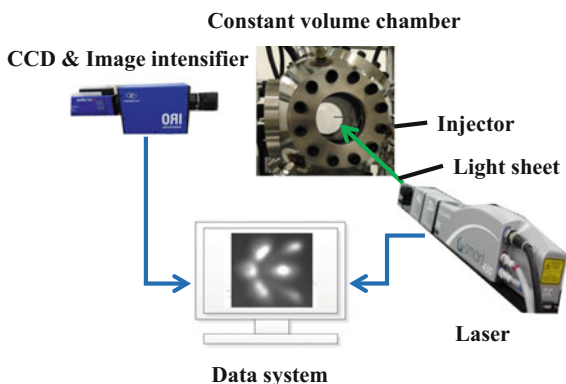
Constant volume chamber structure	Window diameter: $\Phi 100$; angle: $90^\circ, 120^\circ/150^\circ, 180^\circ$	Window	UV transmittance
Temperature limit	0–800 K	Pressure limit	6000 kPa
Temperature fluctuating range	Chamber variation: $<+5^\circ\text{C}$, test zone: $<+3^\circ\text{C}$	Test range	Temperature: 0–1000 K; Pressure: 0–8 MPa; Humidity: 2–98% RH
Seal performance	Pressure drop $\leq 1\%/10\text{ min}$	Fuel temperature controlling	-20 to 90°C
Vacuum degree controlling accuracy	$+1\text{ kPa}$	Test accuracy	Temperature: $\pm 1^\circ\text{C}$; Pressure: 0.1% FS; Humidity: $\pm 2\%$ RH
Vacuum degree pressure range	10 kPa–1 bar	Pressure fluctuating range	$\pm 1\%$
Fuel pressure controlling	0.4–20 MPa	Pressure controlling accuracy	0.1% of maximum pressure
Injector voltage and current	0–120 V; 0–25 A (0–200 μs)	Injection pulse	0–10 ms

Fig. 15.1 Optical layout of shadow method



Shadow method is adopted to test the macro spray shape, spray angle and penetration of the injector. The beam of high energy laser is distributed uniformly through a diffuser, which is taken as background light. Developing process of macro spray shape will be photoed through high speed camera. Spray picture data will be post processed by DaVis software, from which spray angle and penetration are achieved. Optical layout of shadow method is shown in Fig. 15.1.

Fig. 15.2 Optical layout of laser induced fluorescence



Injection spray target can be tested by laser induced fluorescence method. Sheet optic element can convert the laser beam into light sheet, which is used to illuminate Z30 plane, perpendicular with the injector axis, and the laser energy is 60 mJ@266 nm. The 300–400 nm fluorescence, which is induced from gasoline can be captured by CCD camera mounting image intensifier. Spray target can be achieved by means of DaVis post process software. Optical layout of laser induced fluorescence is shown in Fig. 15.2.

15.3 Research on Macro Spray Characteristics

15.3.1 Effects of Different Injection Pressures

On the constant volume chamber, setting the injection pressure as 5, 10 and 18 MPa, the injection back pressure is 0.1 and 0.2 MPa, while the injection pulse is 1.5, 3 and 6 ms, and the macro spray characteristics are tested respectively. The fuel temperature and environmental temperature are both 25 °C. The post processing sketch of spray picture is indicated in Fig. 15.3. And the macro developing process of spray is shown in Fig. 15.4.

Fig. 15.3 Sketch of spray post processing

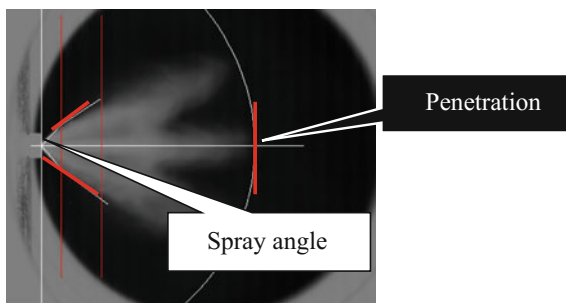


Fig. 15.4 Macro developing of spray with 10 MPa injection pressure and 0.1 MPa injection pulse

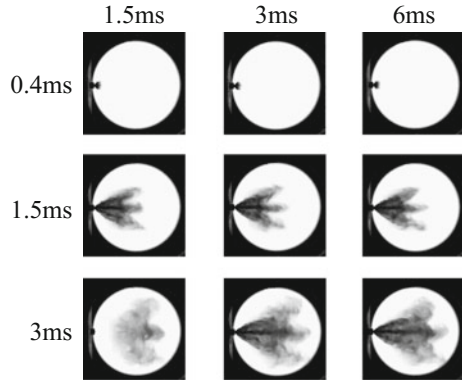
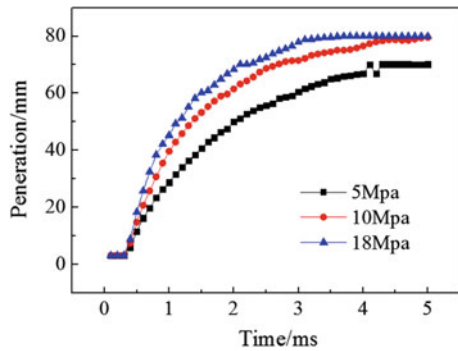


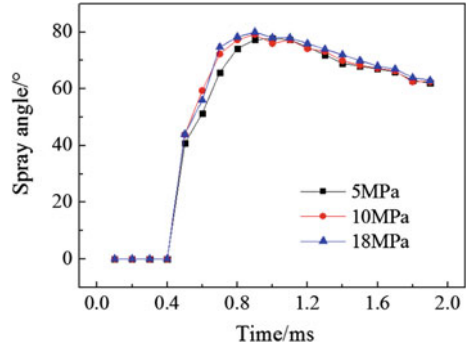
Fig. 15.5 Penetration developing under different injection pressures



It can be seen from Fig. 15.4 that after fuel ejected from nozzle, spray plume is formed, developing along with the flow passage direction of injector hole. Spray plume interacts with air continuously, with emerging of entrainment, diffusion, atomization. The periphery of front tip plume is relatively smooth, while the end of the plume takes on strong fluctuating because of long time interaction with air in the chamber, and this phenomenon will promote atomization and mixing of plume and air.

Figure 15.5 indicates effects of different injection pressures on penetration of spray plume, and the spray background pressure is 0.1 MPa. From Fig. 15.5, it can be known that at the beginning of spray plume forming, bigger injection pressure will produce quick development of penetration, while with the continuous development of spray plume, the increasing trend of penetration is suppressed. Analysis shows that initial injection speed of spray is determined by the fuel injection pressure. At the beginning of spray plume developing, larger injection pressure will produce bigger initial injection velocity, resulting in initial penetration increasing, while with deep development of the plume, the edge fuel of the plume will gradually atomize, make the relative density of the air around increase, leading to the resistance on the plume boosting, so the penetration of the plume is hindered.

Fig. 15.6 Spray angle developing under different injection pressures



Spray angle developing process with time under different injection pressures is figured in Fig. 15.6. The results indicate that injection pressure has minor effects on spray angle, and the spray angle is mainly determined by internal flow passage and injector hole layout. Increasing injection pressure can strengthen the atomization of spray plume, so spray angle takes on boosting trend with the increasing of injection pressure.

15.3.2 Effects of Injection Background Pressures

Developing trends of spray angle and penetration of injection pulse 1.5 ms, injection pressure 10 MPa under different injection background pressures are shown in Figs. 15.7 and 15.8.

The reason of changing tendency for the spray angle in Fig. 15.7 can be explained furtherly that spray angle is up to the injector hole layout position, and hardly influenced by the injection pressure and background pressure. From Fig. 15.8, penetration is becoming shorter with the increasing of background pressure, which results from the resistance of spray plume developing is strengthened with injection background pressure increasing.

Fig. 15.7 Spray angle developing under different background pressures

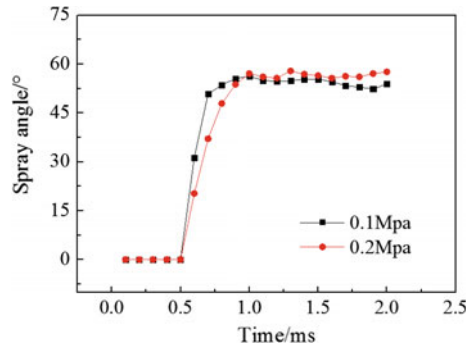
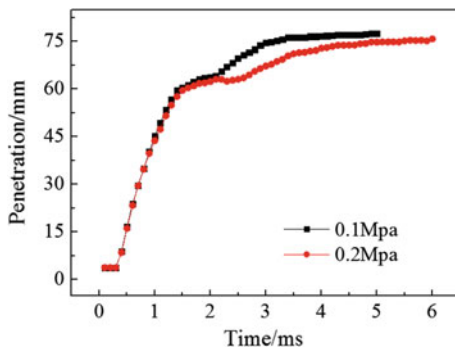


Fig. 15.8 Spray penetration developing under different background pressures

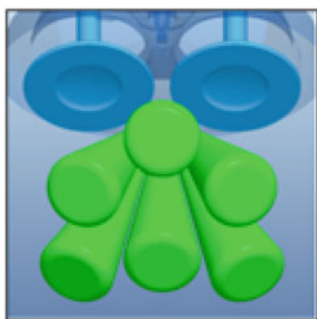


15.4 Research on Injector Spray Target

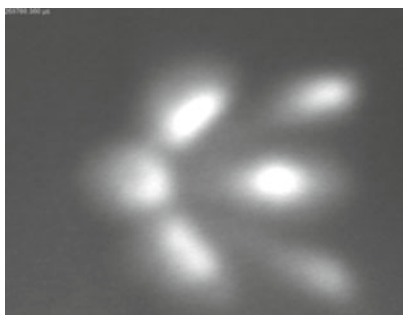
Setting the injection pressure as 10, 15 and 18 MPa, and the injection pulse is 1.5 ms, the spray targets are tested respectively. Also spray targets are tested in turn when injection pulse is 1.5, 3 and 6 ms, under 10 MPa injection pressure. Fuel temperature and environmental temperature are both 25 °C, and background pressure is 0.1 MPa. Laser induced fluorescence picture, when injection pressure is 10 MPa, and injection pulse is 1.5 ms, is displayed in Fig. 15.9, while spray target post processing picture is depicted in Fig. 15.10.

Figures 15.10 and 15.11 have shown the effects of different injection pressures and injection pulses on spray target coordinate. It can be deduced that spray target position has very minor changes with the boosting of injection pressure. When injection pressure boosts from 10 to 18 MPa, spray target has little variation, which is mainly because spray angle increases, resulting from atomization strengthening.

The spray target position in Fig. 15.11 illustrates that different injection pulses almost have no effects on spray target coordinate. Once again, confirmation can be made that spray target position is up to the injector hole layout.



(a) CAD design of spray target



(b) Laser induced fluorescence picture

Fig. 15.9 Laser induced fluorescence picture of injection pulse 1.5 ms under 10 MPa injection pressure

Fig. 15.10 Spray coordinate layout under different injection pressures

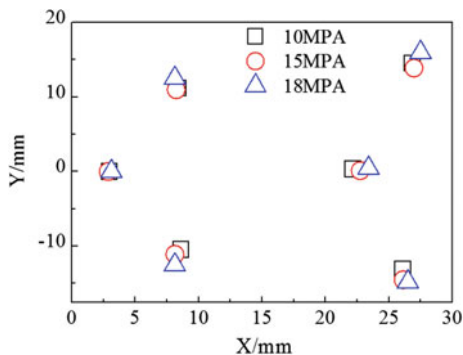
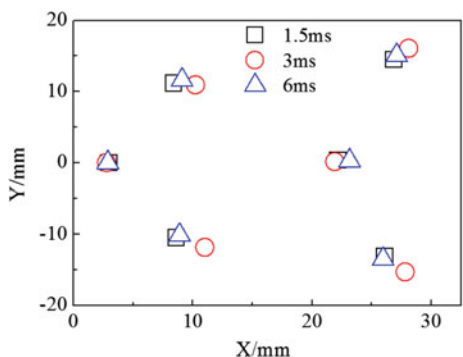


Fig. 15.11 Spray coordinate layout under different injection pulses



15.5 Research on Effects of Injector Flow Range on Penetration

Penetrations of different injector flow ranges are tested respectively when the same quantities are ejected. The results are described through curves in Figs. 15.12 and 15.13.

Testing results of Figs. 15.12 and 15.13 illustrates that under the same injection pressure and same fuel ejecting quantity, larger flow range injector produces smaller penetration, which is beneficial to alleviate oil dilution in the cylinder of GDI engine. It is believed that larger flow range injector uses bigger injecting hole, forming bigger spray angle plume, which is apt to penetration reducing, but designing larger flow range injector should take the possibility of ballistic flow area into consideration.

Fig. 15.12 Penetrations of different flow range injector with the same injection quantities under 10 MPa injection pressure

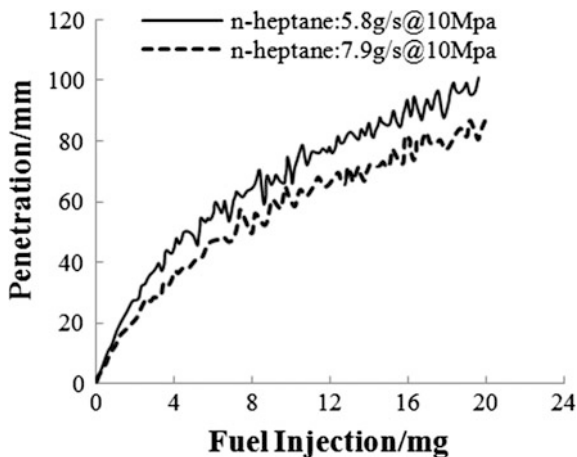
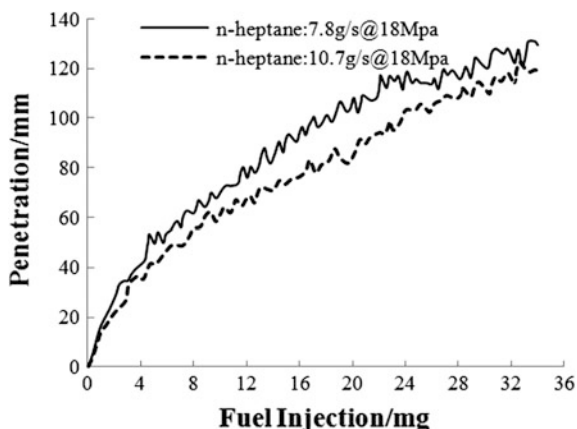


Fig. 15.13 Penetrations of different flow range injector with the same injection quantities under 18 MPa injection pressure



15.6 Comprehensive Analysis of Constant Volume Bench Testing Results

From spray characteristics testing results and comprehensive analysis process above, conclusions can be drawn that four main factors, including initial injection velocity, spray background media, mixing speed between atomized fuel and air, injector flow range, can account for the spray penetration development. Spray angle and target is mainly up to the internal flow and hole layout of the injector. Increasing injection pressure can accelerate atomization speed, spray angle boosting slightly. Under the condition of injection pressure and ejected fuel quantity, injector having bigger flow range is apt to achieve smaller spray penetration.

Therefore, reasonable design of spray target of multi-hole injector is the key point to the matching between spray plume and combustion chamber. Using high

injection pressure system is beneficial to control the spray penetration, while the spray itemization quality is also improved. In order to reduce the risk of oil dilution, and taking flow quantity ballistic area of injector into consideration, large flow range injector can be used to obtain shorter spray penetration, which can also shorten the injection pulse, resulting in much longer time for the mixture forming in cylinder.

15.7 Conclusion

Firstly, development speed of initial spray penetration will accelerate with increasing of injection pressure, while the case of that will be suppressed later because of resistance strengthening.

Secondly, spray angle is mainly determined by internal flow passage direction and hole layout of injector, and is not remarkably influenced by spray background pressure and injection pressure variation. With increasing of injection pressure, single plume atomizing strengthened, resulting in spray angle boosting slightly.

Thirdly, injection pressure and pulse do not have obvious effects on spray target coordinate. Spray target position is also determined by internal flow and hole layout of the injector.

Fourthly, under the same injection pressure and flow quantity, larger flow range injector will produce shorter spray penetration.

References

1. Santavicca DA, Zello JV (2001) Gasoline direct injection (GDI) engines-development potentialities. SAE paper. In: 2001 SAE world congress Detroit, Michigan: 2001-01-1926
2. Wang X, Zhan Z, Yu X et al (2014) Experimental study on injector spray pattern optimization for a turbocharged GDI engine combustion system. SAE paper. In: 2014 SAE world congress Detroit, Michigan: 2014-01-1439
3. Jiang Deming (2006) Advanced vehicle internal combustion engine principle. Xian Jiaotong University Press, Xian
4. Yang Jialin (2006) Combustion system development of vehicle gasoline engine. Machinery industry press, Beijing
5. Zhang M (2014) Study of the mixing process of multi-hole GDI fuel sprays under superheated conditions based on advanced optical diagnostic tools. Shanghai Jiaotong University
6. Wang X, Zhan Z, Yu X, Hu T, Qiao Y, Zhu Y (2014) Experimental study on injector spray pattern optimization for a turbocharged GDI engine combustion system. SAE paper. In: 2014 SAE world congress Detroit, Michigan: 2014-01-1439
7. Zhang M, Xu M, Zhang Y, Zeng W (2011) Flow-field evaluation of superheated fuel sprays using high-speed PIV. JSAE paper. In: 2011 9217 JSAE World congress Detroit, Tokyo: 20119217

Chapter 16

Integrated Exhaust Manifold Type Cylinder Head Structure Design for Gravity Casting Process

Ming Chen, Wenlei Yang, Tianyu Zhang, Donghang Liu
and Hanqing Song

Abstract This chapter aimed at the problem of casting defects during the trial manufacture of a certain engine cylinder head. Combined with the structural characteristics of the internal integrated exhaust manifold, the structure design optimization of gravity casting process introduced in detail. Through the process simulation analysis and trial production verification and other means, reaching the production scrap rate control objectives.

Keywords Cylinder head · Integrated exhaust manifold · Gravity casting · Structure design · Process simulation

16.1 Introduction

In recent years, the design concept of internal integrated exhaust manifold for cylinder head has gradually become a mainstream trend, which applied maturely in international companies, and the optimization of engine thermal management, the improvement of the reliability and advantages of contribution to the fuel consumption recognized in the industry. This design concept is not universal in the domestic at present; the main reason is that its complex structure has increased much more difficulties for casting process and structure design.

The FAW group applied the design concept of internal integrated exhaust manifold for cylinder head in a development project of 1.0 L gasoline engine (hereinafter referred to as 1 L engine). But this kind of cylinder head presented the problem of high scrap rate in the trial manufacture phase. The reason is the casting defects led to the abandonment of cylinder head, statistics of scrap rate [1] showing in Table 16.1.

M. Chen (✉) · W. Yang · T. Zhang · D. Liu
R&D Center Engine Department, CHINA FAW Co., Ltd, Chang Chun, China
e-mail: jluchenming@163.com

H. Song
Non-Ferrous Foundry T&D Department, FAW Foundry Co., Ltd, Chang Chun, China

In these scraped cylinder head, the casting defects are the shrinkage, shrinkage cavity, and the casting flying edge in some key position, showing in Fig. 16.1.

The statistics and inducts results [1] of the defect form and position of all scraped cylinder head showing in Fig. 16.2.

We can see in Fig. 16.2 that shrinkage porosity, shrinkage cavity and flying edge is the main existing form of casting defects, the area around the guide hole and the cylinder head bolt hole is main existing position of shrinkage cavity, the inside of water jacket is main existing position of flying edge. The generation of shrinkage cavity and flying edge influence by multiple factors like casting process and cylinder head structure, etc. Table 16.1 shows that the improvement of the casting process in the second round trail manufacture has not fully solve the problem of high scrap rate, which results in the judgment that the structure of cylinder head itself more leads to the production of casting defects. Therefore, the optimization design of cylinder head structure is very necessary, which is primary measures to ensure mass production feasibility of cylinder head.

Table 16.1 Scrap rate statistics of cylinder head

Scrap rate of cylinder head				
	Total	Qualified	Scrap	Scrap rate (%)
1st trail manufacture	35	20	15	43
2ed trail manufacture	52	40	12	23
Total	87	60	27	31

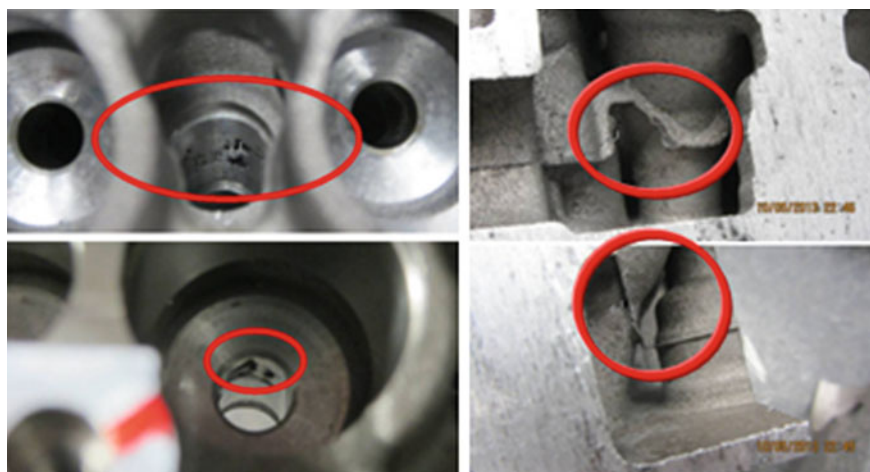


Fig. 16.1 Casting defects of scrap parts

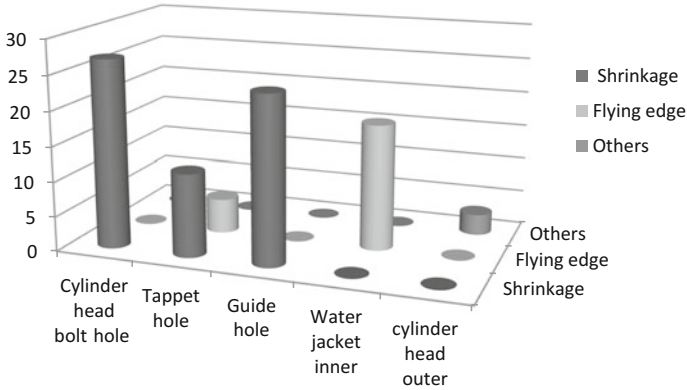


Fig. 16.2 Defects position statistic

16.2 Mass Production Casting Process

The material of 1 L engine cylinder head is AlSi10 Mg (Cu), with T6 heat treatment, which can obtain mechanical properties required high detonation pressure and high load, also is one of commonly used material of aluminum alloy [2] cylinder head. Combining with the material properties and structural characteristics of cylinder head, the mass production process choosing tilting gravity casting process, the characteristics summarized as follows:

- long mould life, low relatively cost;
- process is relatively simple;
- castings can be heat treatment, and obtain a higher intensity;
- suitable for complex structure non-thin wall castings;

Mass production stage has high demands on the casting scrap rate, in terms of gravity casting process, at present, on the scrap rate control, domestic level can reach 3–5%, and the international level can reach 1–3%, the outstanding can control within 1%. The control goal of scrap rate for 1 L engine cylinder head is very clear, is to reach the international level preliminarily.

16.3 Structure Design Optimization

Due to the internal integrated exhaust manifold, 1 L engine cylinder head is more complicated than traditional structure, greatly increases the difficulty of casting, which is also a new challenge for the structure design. To solve the problems during its trail manufacture phase, we should focus on optimizing the structure of the area around the valve guide hole, the cylinder head bolt hole, and the interior of water jacket, these structure distributed in the different modules of cylinder head, so the structure optimization design of cylinder head are divided into three aspects.

16.3.1 Water Jacket Structure Design Optimization

Based on the requirements of the integrated exhaust port structure, cylinder head cooling concept and the engine thermal management, 1 L engine cylinder head water jacket used the full surround type structure. in order to realize exhaust port sand core setting, the water jacket was break up into upper and lower two chips design, which as well as conducive to assembly and positioning of water jacket cores and exhaust port cores. Plan for water jacket and exhaust port showing in Fig. 16.3.

In combination with the main structure characteristics of water jacket, and considering the casting process has occurred or may encounter problems include the following aspects.

Because of the complex structure of water jacket core, local irregular shape lead to non-smooth flow of aluminum water, it will also lead to poor aluminum water filling, which easily produce the casting defects such as cold shut.

In the joint surface of upper and lower water jacket, it is easy to come into being the casting flying edge.

The upper and lower water jacket are thin-walled structure of large area, which bears bigger aluminum water buoyancy in the pouring process, so the sand core stress deformation is bigger also, gaps between the sand core is difficult to control and eventually lead to uneven thickness of cylinder head.

Water jacket cores have large volume, as well as gas evolution when pouring heated, if the gas can't be discharged out of the cylinder head successfully, casting defects such as shrinkage cavity, shrinkage, etc. will occur.

For the above casting defects, the casting technology itself alone is difficult to solve, more reasonable structure design become the key to solve the difficulty.

For the non-smooth flow and poor filling of aluminum water, water jacket cores should focus on optimizing the shape which influence the aluminum water flow, and add the necessary process structure.

For the problem of casting flying edge, complex shape design in combined location should be avoided, and cooperated with the necessary technical measures;

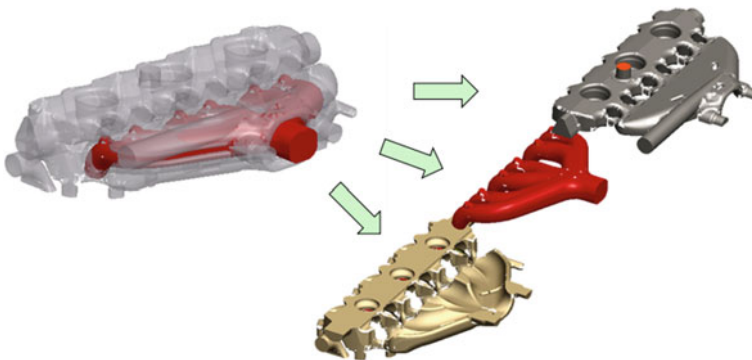


Fig. 16.3 Water jacket and exhaust port

For water jacket cores stress deformation problem, the buoyancy on sand core local should be reduced, the structure of water jacket should be optimized, necessary support core head should be designed to restrain the force deformation.

For the question of the sand cores heated degas, the core head structure should be design, cooperated with the vacuum system of casting process.

Based on the above principle, the structure optimization of water jacket should carried on, comparing the development state and final state of water jacket structure, the main program is showing in Figs. 16.4 and 16.5.

In Fig. 16.4, the water jacket structure optimization consists of the following two aspects.

Number ① express the optimization of water jacket intake side shape, the structure makes the wall thickness around the guide hole more uniform [2], which can inhibit the local heat section, at the same time, the structure is more advantageous to the flow and filling of aluminum water, and can prevent casting defects such as cold shut and shrinkage, etc.

Number ② express the optimization of the joint surface location and shape of upper and lower water jacket, according to the principle that the shortest linear distance between two points, choosing the right combination of location, the cross section in the vertical direction of the joint surface for a short straight line, this design can avoid complex shape of the joint surface of upper and lower water jacket, which can make sand core assembly more accurate, simple and convenient, can effectively reduce the production of casting flying edge, avoid the casting flying edge problems in the trail manufacture phase.



Fig. 16.4 Main structure optimization scheme of water jacket

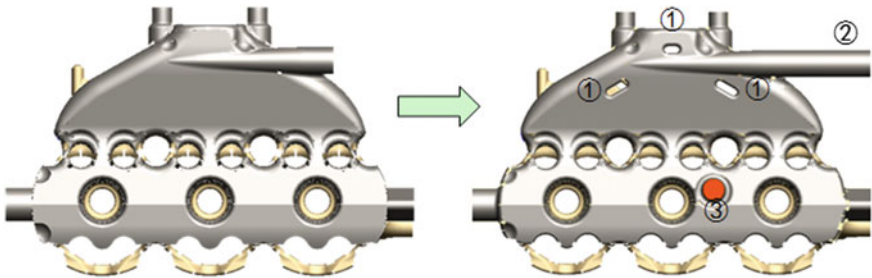


Fig. 16.5 Main structure optimization scheme of water jacket

In Fig. 16.5, structure optimization of water jacket including the following three aspects.

Number ① express that in the water jacket thin-wall large area design some hole, this design can reduce the aluminum water impact force and buoyancy sustained by water jacket cores in the casting process, effectively restrain stress deformation of water jacket cores, at the same time, the design of this structure is advantageous to the aluminum water flow and filling.

Number ② express that the outlet of the sand core extend to the outer mould, which connected with the vacuum system, and easy degas for the sand core during the casting process, reduce the risk of the shrinkage and porosity of casting defects.

Number ③ express that to design a process support core head on the upper water jacket, the structure connected with the oil channel and riser sand core above, better degas for water jacket sand core during the casting process, and restrain stress deformation of the sand cores.

16.3.2 Oil Channel Structure Design Optimization

The main function of oil channel and camshaft housing in the cylinder head is to guide the oil return flow, so the main structure is generally used in traditional combination structure, this kind of structure is easy to shape, and meet the requirements of the oil return area, and also convenient for the assembly and location of the sand cores. On the joint surface of the sand cores of the oil channel and the camshaft housing, casting flying edge will arise, so the combination of position should be in easy cleaning area, obviously the area around the tappet hole and the cylinder head bolt hole is a good choice. The camshaft housing in the casting model often with the riser sand core design as a whole, this can increase the strength of sand core, and make the gas from the heated sand core exhaust from the riser core above. The middle part of the structure of the oil channel in the design also connected to the riser core, which has the same benefits (Fig. 16.6).

Oil channel sand core is one of the most complicated structures of cylinder head, the volume is the same size as the volume of water jacket sand core, based on its complex structure and huge volume, there are much more difficulties in casting around it. The complex shape of the oil channel sand core will affect the flow of aluminum water largely, so the shape design of the oil channel should be smooth and avoid the irregular shape. Because of that during the flow process of aluminum water, loose sand may washed down from the surface of the sand core. Although the number of these sand is less, but if the flow to the main functional areas, that will generate damage to the tools and the cylinder head itself in machining process. So some design of the structure should be done in the relevant position of the oil channel, which can hold the floating sand, these structures can be removed by rough machining, do not affect the structure and function of the finished cylinder head. In addition, the position of the guide hole and the cylinder head bolt hole concentrated in the oil channel is the cylinder head local wall thickness over large area. The

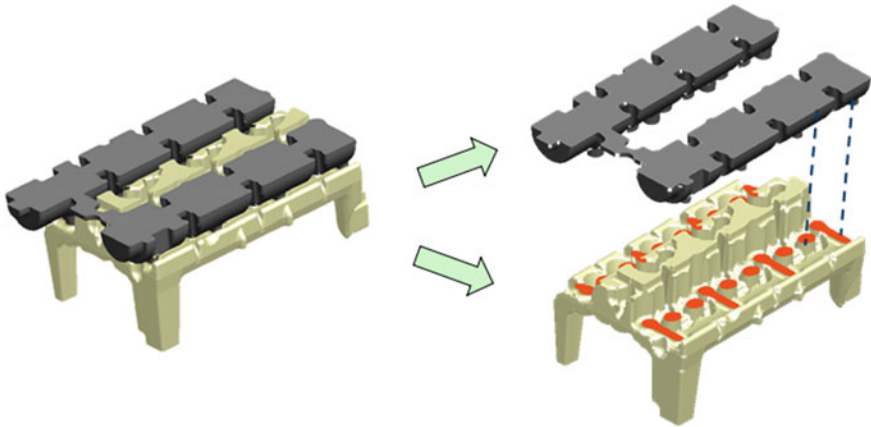


Fig. 16.6 Assembly of oil channel and camshaft housing

cooling speed of which is slowest in the cooling process, these areas will produce shrinkage and other casting defects, this is the root cause of shrinkage and other casting defects mentioned in the previous paper.

Based on the difficulties in the casting process above, the structure of the oil channel optimized, and the main scheme is showing in Fig. 16.7.

Number ① and ② respectively express that design feeding channel for the area around the guide hole and the cylinder head bolt hole, this structure can provide enough aluminum water compensation to eliminate the risk of shrinkage in the area, which can effectively solve the problem of casting defects encountered in the 1st round of trial manufacture.

Number ③ express that design structure to hold the floating sand, the function of the structure as its name implies, and can be removed in the Initial machining stage.

16.3.3 Outer Model Structure Design Optimization

After the inner sand core structure optimized, the outer model structure should optimized. Cylinder head of outer model include the module in four directions. On each module, the thick flange, bolt boss and other characteristics is local wall thickness over large area, the region is the main area of local hot spot distribution, and shrinkage porosity and other casting defects in high incidence area, the design should consider aluminum water compensation in these areas. Figure 16.8 express the outer model structure optimization scheme, green arrows show the direction of the aluminum water compensation. Arabic numerals show specific optimization structure, can be seen that using the characteristics of cylinder head to do the aluminum water compensation is the most simple and effective method, if the characteristics can not provide aluminum water compensation for certain positions,

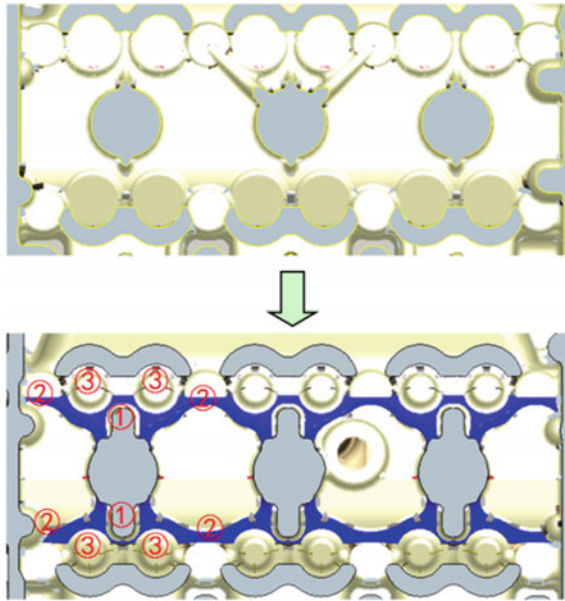


Fig. 16.7 Main structure optimization scheme of oil channel

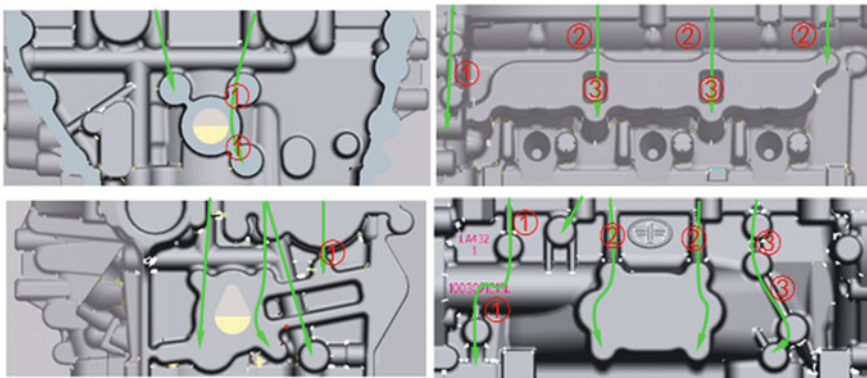


Fig. 16.8 Outer model structure optimization scheme

can design new feeding channel structure to do aluminum water compensation, in order to prevent casting defects generated.

Figure 16.9 shows the assembly of the inner core, the outer mold head in four directions and the cylinder head blank.

The cylinder head blank is completed, should carry out process simulation analysis, to evaluate the feasibility of casting production.

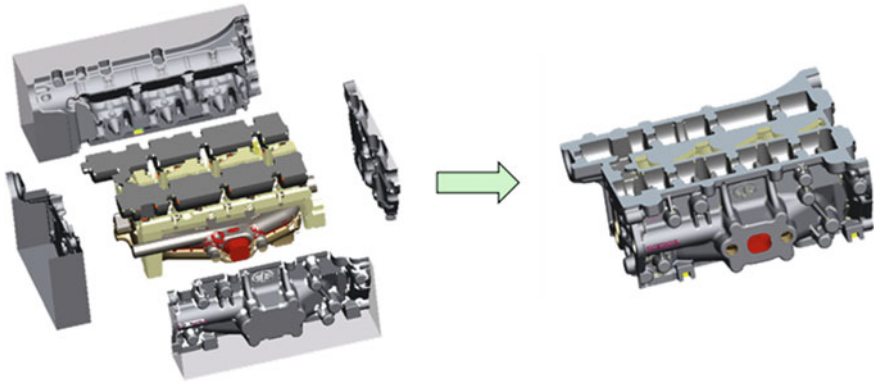


Fig. 16.9 Cylinder head outer model, inner core and blank

16.4 Process Simulation Analysis

In the design and development of 1 L engine cylinder head, using process simulation analysis [3] as an evaluation method, this method is widely used in the world, has the advantage is high accuracy, and can greatly save time and cost [3]. Simulation software selection MAGMA, its advantages are simple mesh; the calculation time is short, the simulation results and the actual high degree of agreement.

Simulation calculation parameters of initial conditions and analysis process is set in accordance with the actual tilting casting process, including initial temperature of mold, mold movement and the cooling time, the total cycle is 360 s, as specified in Table 16.2.

Simulation analysis process is based on the cylinder head model; the cylinder head structure is optimized based on the results of the simulation analysis, they two mutual references. It normally takes after 2–3 rounds of repeated simulation and optimization in order to determine the final optimization scheme, mainly around the tilting process, solidification process, and internal heat section distribution three aspects to do the simulation analysis and evaluation, to highlight key content we just list the final optimization simulation and analysis of the results.

16.4.1 Tilting Process Simulation

From Table 16.2, we can see that the tilting process is in the initial stage of the casting process, the duration time is 16 s, the mold tilting action by -108° to 0° , for this process, the speed of the aluminum water flow and filling is very important. Simulation and analysis results show that in the tilting process, aluminum water

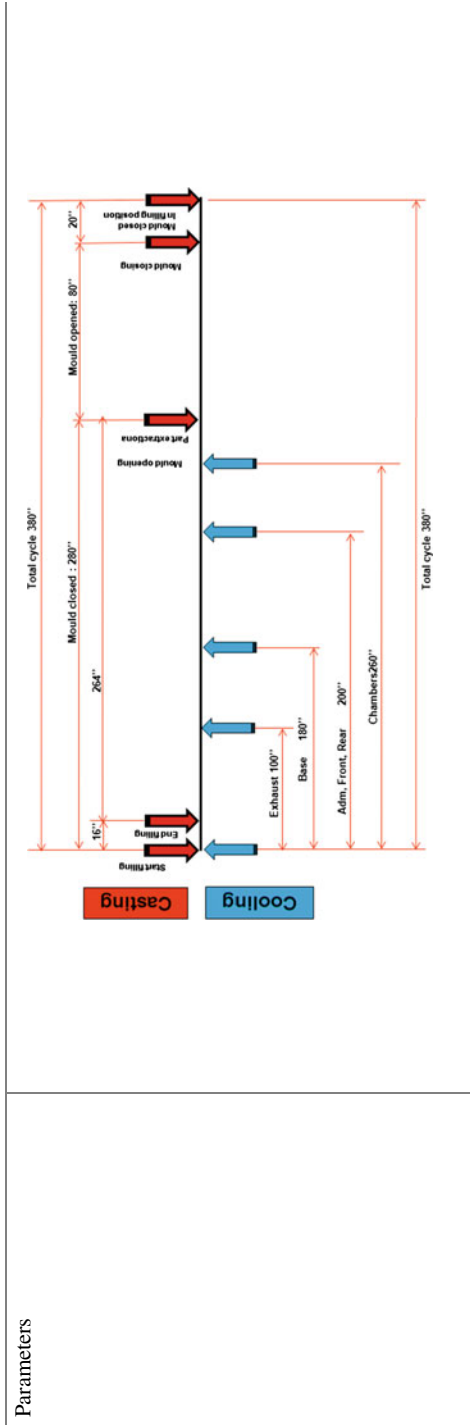
Table 16.2 Simulation conditions of tilting casting process

Aluminum temperature	700 °C				
Mould initial temperature	300 °C				
Chambers material	Densimet 185				
Cores initial temperature	20 °C				
Water average temperature	30 °C				
Aluminum composition	Cu: 0.03%	Ni: 0.03%	Sr: 0.02%		
	Fe: 0.40%	Si: 10.00%	Mg: 0.30%		
	Ti: 0.10%	Mn: 0.30%	Zn: 0.08%		
Mould movement	0 s	-104°			
	4 s	-84°			
	12 s	0°			
Thermal transmission coefficient	1600 W/m ² K				
Geometry					

(continued)

Table 16.2 (continued)

Parameters



velocity is relatively stable; the filling process is very smooth that the structure design of the cylinder head and the riser are reasonable (Fig. 16.10).

16.4.2 Solidification Process Simulation

Table 16.2 shows, the solidification process after the end of the tilting process, the duration time of which is a total of 264 s, and in the mean time, to different parts carry on demand cooling, the solid fraction and solid phase continuity is the main evaluation index of the solidification process. Simulation results show that during the cooling process, the aluminum water from outside to inside, from bottom to top uniform continuous solidification, solid phase rate can reach 100%, no hot spot and other defects appeared, that throughout the cylinder head structure are uniformly and each module cooling time control is very accurate and reasonable (Fig. 16.11).

Cooling solidification simulation results around the area of cylinder head bolt hole show that during the solidification process from bottom to top, the aluminum water into the upper feeding channel has not stopped, solid phase continuity is better, that here the feeding channel structure design to good effect (Fig. 16.12).

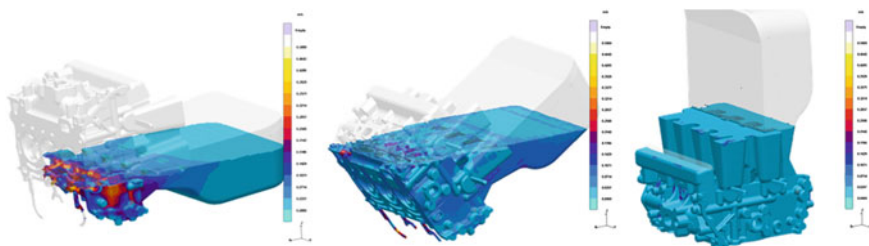


Fig. 16.10 Cylinder head tilting process simulation

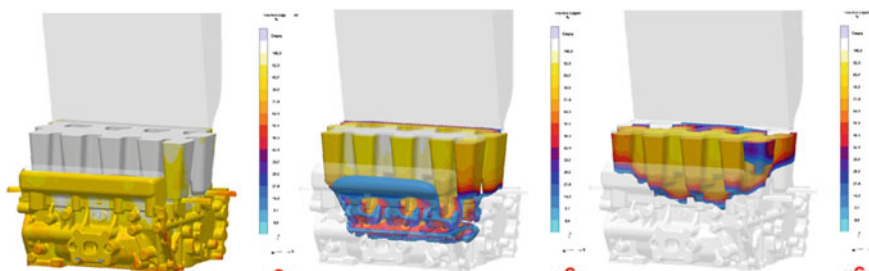


Fig. 16.11 Cylinder head solidification simulation

16.4.3 Internal Thermal Section Simulation

Internal thermal section simulation process is simulation of casting slice scanning, similar to the actual process of industrial CT scanning, and used to find the shrinkage porosity and other casting defects of the inner part of the cylinder head; integrity is the main evaluation index. From Fig. 16.13 slices of simulation analysis results can be found, inside the cylinder head has no obvious hot spot distribution. The part integrity nearly 100%, that means the cylinder head structure matched with the tilting pouring process design is reasonable, the 1 L engine cylinder head structure can meet the casting process requirements.

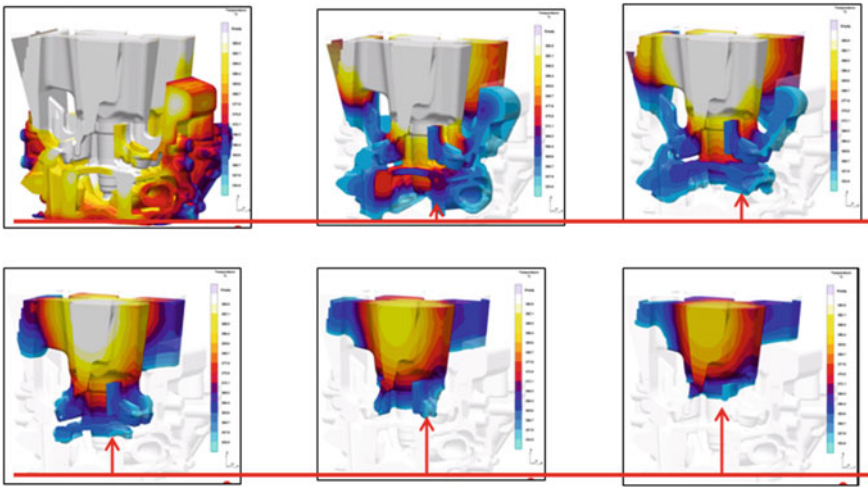


Fig. 16.12 Solidification simulation around the area of cylinder head bolt hole

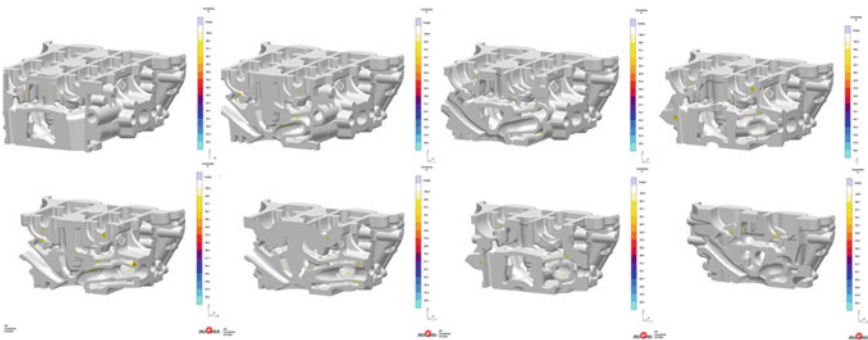


Fig. 16.13 Cylinder head internal thermal section simulation

Through the analysis of the simulation results, we can see, from the tilting process to solidification process are reasonable, can meet the requirements of the casting process. Through the analysis of the internal section can also be found that, there is no hot spot appears around the area of the guide hole, the tappet hole and the cylinder head bolt hole, theoretically can eliminate the risk of the shrinkage and other problems, the cylinder head has the feasibility of production.

16.5 Trial Production Verification

420 cylinder heads cast after the 1 L engine cylinder head mold debugging completed, including 100 of the first round casting, 320 of the second wheel casting. Carry out sampling anatomical examination on some of the castings, and do whole-body CT scan on all castings. Results show that there is no shrinkage in the area around cylinder head bolt hole, valve guide hole and tappet hole of all cylinder castings, no flying edge in the area of the water jacket either. However, due to mechanical damage and other reasons, individual parts obsolescence, including first round 5, the second round 8 (Fig. 16.14).

Statistics show that the scrap rate of the second round of the casting already controlled within 3%, to achieve control objectives. According to previous production experience, the scrap rate of mass production phase can control lower than trial production stage, so estimates, the scrap rate of 1 L engine cylinder head in the production stage will expect much lower, closer with the international advanced level (Figs. 16.15 and 16.16).

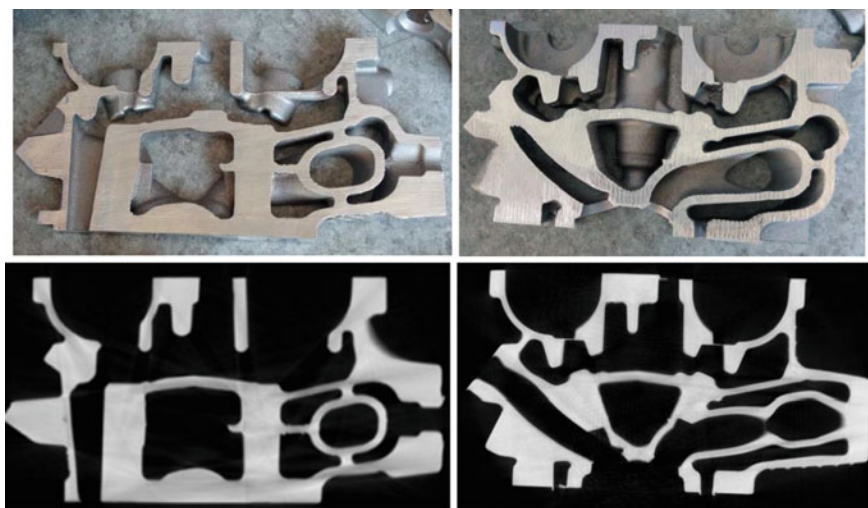


Fig. 16.14 Cylinder head anatomy and CT scan

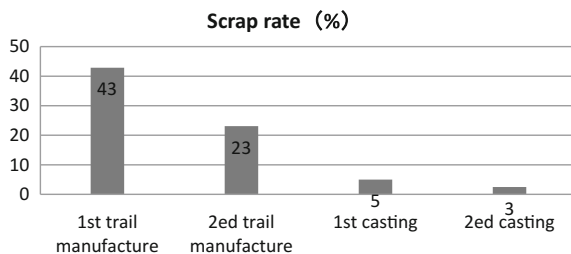


Fig. 16.15 Scrap rate statistics of cylinder head



Fig. 16.16 Qualified cylinder head of trail manufacture stage

16.6 Conclusion and Outlook

This chapter is a summary that according to the practical experience of the cylinder head structure optimization design process, although cylinder integrated exhaust manifold design make the cylinder head structure becomes more complex, but the reasonable structure of the cylinder head design can reduce the casting process difficulty and reduce scrap rate.

The structure optimization scheme of the 1 L engine cylinder head, successfully eliminated the casting defects such as shrinkage cavity, flying edge and so on, and also prevented the occurrence of other defects.

The result of process simulation is in agreement with the actual casting result, it shows that the accuracy of this technique is very high which can apply in the country.

The 1 L engine cylinder head trail production result is ideal, the scrap rate can control within 3%, and a further reduction of expectations, has reached the international level.

References

1. Liu Y (2014) Quality improvement of the 4GC automobile engine aluminum alloy cylinder head. *Automotive Technol Mater* 08:26–29
2. Yuan Z (2008) *Design of internal combustion engine*, 1st edn. China Machine Press, pp 158–174
3. Chen J (2014) Based on numerical simulation analysis aluminum alloy cylinder head low pressure die casting process optimize. In: *Chong Qing Foundry annual meeting (Collection of papers)*, Chong Qing

Chapter 17

Experimental Research on Macroscopic and Microscopic Characteristics of Ethanol-Fatty Acid Methyl Ester Blends Sprays

Junge Li, Xiaocao Yu, Bin Liu, Tiegang Hu and Xibin Wang

Abstract Spray characteristics of Ethanol-Fatty Acid Methyl Ester Blends under common-rail injection condition were experimental investigated, by the high speed photography and particle/droplet image analyses (PDIA). The results show that spray cone angle and project area is increased with the increase of ethanol percentage and ambient pressure. Sauter mean diameter (SMD) increases with the increased axial distance at the same radial distance. SMD sharply decreases with the increased injection pressure, the average amplitude is 2 μm . SMD of Fatty acid methyl ester (FAME) decreases about 3 μm after mixing ethanol. Spray characteristics of Ethanol-Fatty Acid Methyl Ester Blends and diesel are similar, thus the engine is rarely modified while fueled with FAME/Ethanol blends.

Keywords Fatty acid methyl ester · Ethanol · Particle/droplet image analyses · Spray characteristics

Since the advent of the car, automobile industry has been making great contributions to economic development and human progress for a hundred years [1]. Meanwhile, the extensive use of car accelerates the consumption of energy, and leads to serious environmental pollution.

As a clean and renewable fuel, biodiesels' physical property is similar to diesel. The characteristics of fuel spray and mixture formation have great efficient on combustion process and emission characteristics [2]. It's very necessary to investigate the spray characteristics of biodiesels. Li et al. [3] and Agarwal et al. [4] studied the macroscopic spray characteristics of diesel/biodiesel using different

J. Li (✉) · X. Yu · B. Liu · T. Hu
Powertrain R&D Institute, Changan automobile co., Ltd,
Chongqing 401120, China
e-mail: Zhangxy2@changan.com.cn

X. Wang
State Key Laboratory of Multiphase Flows in Power Engineering,
Xi'an Jiaotong University, Xi'an 710049, China

methods, the results show that spray characteristics are mainly determined by fuel viscosity, density and surface tension. Wang et al. [5], Zhijun et al. [6] and Guan et al. [7] investigated droplet velocity, SMD and droplet distribution of diesel/biodiesel, using Phase Doppler particle analyzer (PDPA), particle image velocimetry (PIV) and PDIA.

Since PDIA was rarely used to study spray characteristics of FAME blending with alcohol, the writer investigated the spray characteristics of FAME/ethanol blends on common rail system, using high speed photography and particle/droplet image analyses.

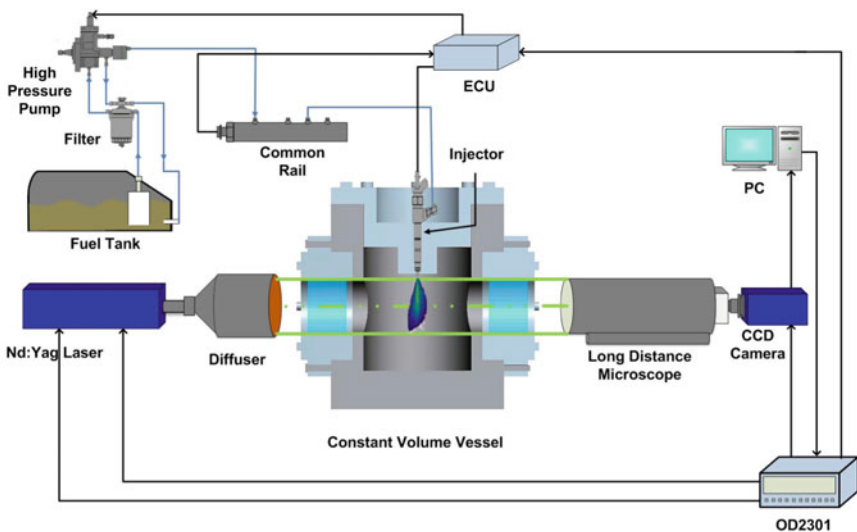
17.1 Experimental Setup and Procedure

17.1.1 Experimental Setup

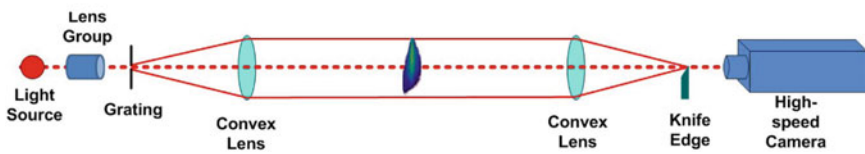
Figure 17.1a shows the sketch of visualization apparatus based on common rail system. It includes injection system, control system, data acquisition system and constant volume vessel. The high pressure pump, common rail, injector and sensors form the injection system. The injector has a single-hole nozzle with 0.2 mm orifice diameter. The controller OD2301 can simulate diesel ECU to realize electrical signal synchronization of injector and data acquisition system. The high pressure constant chamber is filled with nitrogen gas, which the ambient pressure can be changed from 1 to 45 bar by adjusting intake and exhaust valves. The data acquisition system consists of macroscopic and microscopic system. In macroscopic system (as shown in Fig. 17.1b) a Xenon lamp was used as light source and two magnifying lens were used to produce parallel light, a high-speed camera (Phantom V611) was employed to record the spray images with the imaging speed at 10,000 frames/s and resolution of 752×752 pixels. In microscopic system Nd:YAG laser, diffusor, long distance microscope (Queststar QM1), calibration plate and CCD camera with 2456×2058 pixels are equipped.

17.1.2 Experimental Procedure

The ambient temperature is 295 K, and the ambient pressure is 10 and 20 bar. The injection duration is 1.5 ms under all conditions. Injection pressures P set to 600, 800 and 1000 bar in macroscopic experiment, while 400, 600 and 800 bar in microscopic experiment. Experiments mainly investigated the spray characteristics of FAME, FAME/ethanol blends (10, 20 and 30% by mass ethanol in FAME/ethanol blends), and made a comparison with spray characteristics of diesel. Table 17.1 shows the main physical properties of the fuels in 20 °C.



a) Visualization apparatus



b) Schematic of the schlieren method

Fig. 17.1 Sketch of experimental apparatus

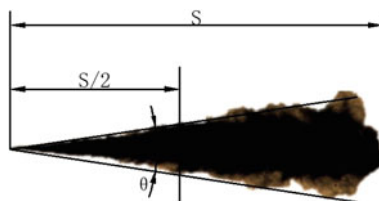
Table 17.1 Main properties of fuels [8]

Fuel property	D100	FAME	Ethanol	E10	E20	E30
Density/(g/L)	830.5	880.5	789	864.7	856.5	848.3
Viscosity/(mPa s)	4.60	9.192	1.17	6.00	4.75	3.22
Surface tension/(mN/m)	28.5	31.2	22.3	30.1	29.3	28.3

17.2 Experimental Results and Analysis

Due to the limited camera speed, the real start time of the injection is earlier than the first spray image. Actually the start time is between the first image and the previous one. It is generally accepted that spray tip penetration is linear to the elapsed time during the early stage of spray development [9]. So the linear extrapolation was

Fig. 17.2 Definition of penetration and spray cone angle



used to calculate the actual start time of injection. Figure 17.2 shows the definition of macroscopic spray characteristics. The penetration(S) is defined as the vertical distance from nozzle tip to the top of the spray, the spray angle measured at half of the S is defined as spray cone angle (θ).

SMD in this experiment was processed by software DaVis 8.0. It was calculated by the following correlation,

$$D_{32} = \frac{\sum_{i=1}^N \frac{D_i^3}{p_i}}{\sum_{i=1}^N \frac{D_i^2}{p_i}} \quad (17.1)$$

where the D_{32} is the mean diameter of all the detected droplets, D_i is the diameter of all the detected droplets, p_i is the detected probability of droplet i .

17.2.1 Spray Cone Angle Under Different Conditions

Figure 17.3 presents the spray cone angle of various fuels at injection pressure of 600 bar and ambient pressure of 20 bar. The result shows that spray cone angle are stable in a small range after initial stage. So the following article will present the averaged spray cone angle instead of spray angle.

Figure 17.4 gives averaged spray cone angle of the test fuels under different conditions. The averaged spray cone angle range from 14.9° to 17.5° at ambient pressure of 10 bar, while 16° to 20.6° when ambient pressure is 20 bar. With the increase of ethanol blending ratio, the averaged spray cone angle is slightly increased. The reason is the low viscosity and surface tension of ethanol decreases the viscosity and surface tension of the blends, leading to the increase of spray cone angle. The spray angle increases significantly with the increase of ambient pressure for the high ambient gas density inhibits the spray from axial orientation by strength resistance. The result also shows that the spray angle of diesel is similar to E20 and E30, this is because their physical properties are very close. The averaged spray angle is little affected by injection pressure, for it increase less than 1° with the increase of injection pressure.

Fig. 17.3 Spray cone angle evolution

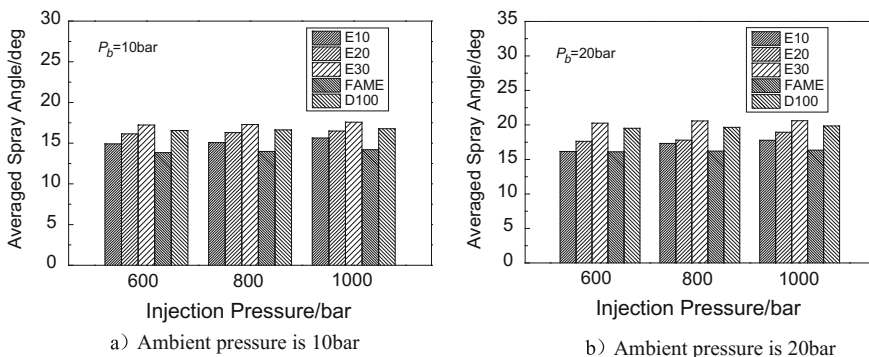
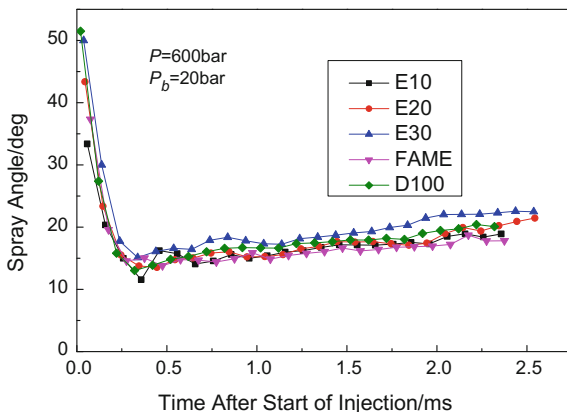


Fig. 17.4 Averaged spray angle of test fuels under different conditions

17.2.2 Projected Spray Area

Figure 17.5a–d presents the projected spray area of test fuels versus spray penetration at different injection pressure and ambient pressure. A literature points out that the projected area quantifies the atomization of spray and the quality of ambient gas mixture [10]. The penetration was used as x-axis to eliminate the effect of injection time. The result shows that E30 has the largest projected spray area under all conditions. And the followings are E20, E10 and FAME. The projected spray areas are increased with the increase of ambient pressure, and also the differences of various fuels are decreased. This is consistent with the change of spray angle induced by ambient pressure. It is also found that the projected area of diesel is similar to E20, which means blending ethanol in FAME improve the atomization significantly.

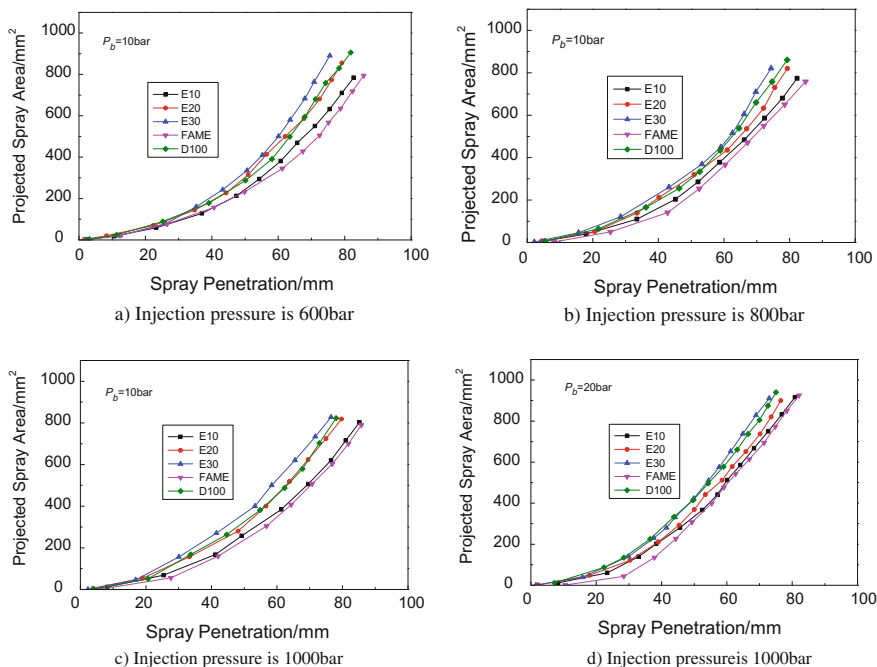


Fig. 17.5 Projected spray area of test fuels under different conditions

17.2.3 Microscopic Results and Analysis

In this experiment SMD and the distribution of droplets were investigated in both axial (distance to inject nozzle is 40, 50 and 60 mm) and radial (distance to axis of spray is 6 mm) directions. Due to the high droplets density at the central of spray that attenuate the illumination light, the droplets on the focal plane can't be measured [7]. A large distance to the axis of spray is selected. The measurements were conducted at 1.5 ms after the start of injection energizing while the spray shows quasi-steady period.

17.2.3.1 Sauter Mean Diameter

Figure 17.6a–b depicts the SMD results under different conditions. Figure 17.6a presents SMDs of test fuels at different axial distances from the injector nozzle. After blending ethanol to FAME, the SMD of FAME is significantly decreased and the average is 3 microns. But the differences of SMD among blends are very small. This is mainly due to the higher viscosity and surface tension of FAME which leads to a small Weber number, but the differences of viscosity and surface tension

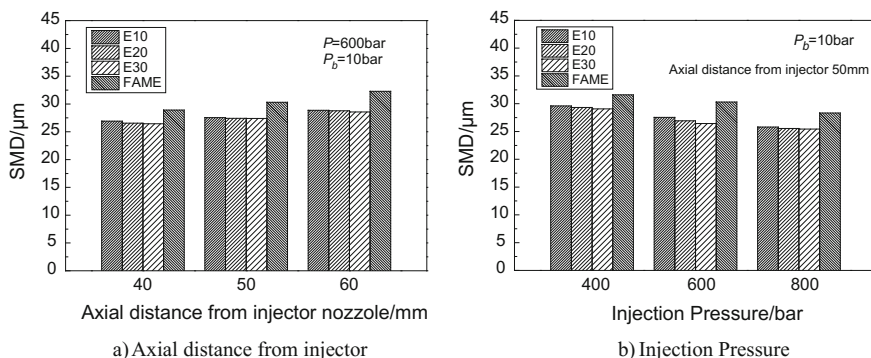


Fig. 17.6 SMD variations under different parameters (radial distance: 6 mm)

among blends are small. The experiment shows the same results with literatures that SMDs increase with the increase of distance between the measuring point and inject nozzle [11]. The reason is that the momentum losses along the penetration development [12]. Figure 17.6b gives SMDs of test fuels under different injection pressures, the ambient pressure is 10 bar and the distance between the measuring locations and inject nozzle is 50 mm. The result shows that SMDs averaged decrease 2 μm with the increase of injection pressure for all the test fuels. This is because a higher injection pressure leads to a larger jet velocity that makes a larger Weber number and higher momentum.

17.2.3.2 Distributions of Droplets

The quantities, diameters and distributions of detected droplets can be obtained by statistic analyzing the experiment results. These parameters represent the quality of spray and atomization. The results show that the atomization of all the blends is generally similar, so the distribution of E10 is illustrated.

Figure 17.7a presents the distribution of E10 at different axial distances from the injector nozzle while injection pressure is 600 bar and ambient pressure is 10 bar. The result shows that maximum frequency of 40 mm occurs at 20 μm, while maximum frequency of 50 mm occurs at 15 μm. However the diameter above 30 μm at 50 mm shows a much higher frequency than that at 40 mm, which leads a higher SMD. The maximum frequency of 60 mm is nearly twice time than that of 50 mm, however the peak distribution of droplets between them is just 3 μm. All of these reasons together lead to a bigger SMD of 60 mm.

Figure 17.7b gives the distribution of E10 at different injection pressures while the axial distance is 50 mm and ambient pressure is 10 bar. It is observed that the distributions of test fuel in all the injection pressures are similar. The frequency decreases with the decrease of injection pressure when the diameter is smaller than

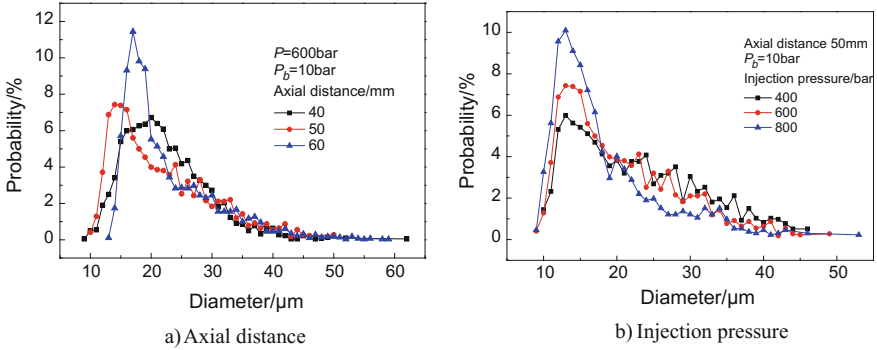


Fig. 17.7 Distribution of droplets under different parameters (E10, radial distance: 6 mm)

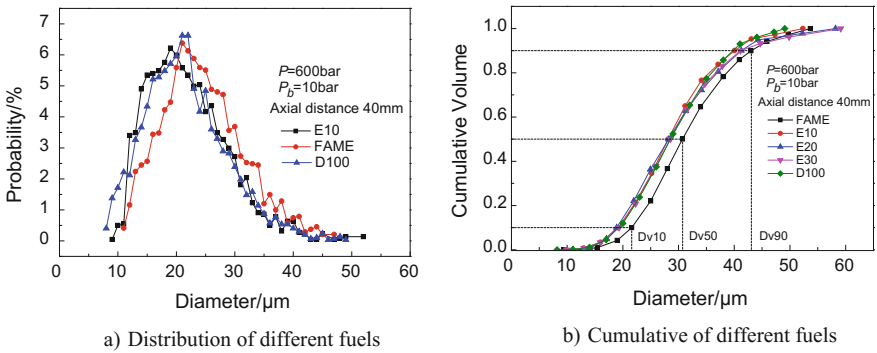


Fig. 17.8 Distribution and cumulative of different fuels (radial distance: 6 mm)

20 μm , frequency increases with the decrease of injection pressure when the diameter is bigger than 20 μm . So the SMD decreases with the increase of injection pressure which is in accordance with the above results.

In order to further study the atomization quality of FAME after mixing with ethanol, the distributions and cumulative of test fuels under injection pressure of 600 bar and ambient pressure of 10 bar were investigated. The distance between the measuring point and injector nozzle is 40 mm. The SMD of FAME, E10, E30 and D100 is 28.92, 26.92, 26.44 and 26.57 μm . Figure 17.8a presents the distribution of FAME, E10 and D100. It is observed that distribution of test fuels have the same trend, but droplets of FAME mainly distribute in the area of large diameter. The droplets of E10 and D100 are mainly distributed in the area that diameter is smaller than FAME, and the maximum probability of E10 and D100 are nearly the same. Figure 17.8b gives the cumulative of various fuels. The result shows that FAME has the largest diameter when the cumulative is the same.

The differences between blends and diesel are small. So the spray and atomization quality of FAME is significantly improved by mixing with ethanol, and the spray characteristics of blends are similar to diesel.

17.3 Conclusions

1. The spray projected area is mainly affected by spray cone angle, and increases with the increase of ambient pressure. Spray projected area of FAME increases with the increase of blending percentage of ethanol, and the projected area of E20 is similar to that of diesel.
2. In this experiment, the SMD of FAME is significantly decreased with the increase of injection pressure. Under the same radial distance, it also increases with the increase of axial distance between the measuring points and inject nozzle. The SMDs of various blend fuels have little difference and nearly the same with that of diesel.
3. The droplet distribution and cumulative of blends are similar to that of diesel. The atomization qualities of blends are in the same level with diesel. The FAME/Ethanol blends can be used in the engine without changing combustion system.

References

1. Chen J, Zhang J, Gao Y et al (2009) Construction of automobile. China Machine Press, Beijing
2. Wen H (2004) Multi-dimensional numerical modeling of spray mixing process in diesel engines based on CFD. Huazhong University of Science and Technology, Wuhan
3. Li L, Wang Z, Xv G et al (2011) Analysis on spray characteristics of diesel engine fueled with diesel and biodiesel. *Trans CSAE* 27(1):299–303
4. Agarwal AK, Chaudhury VH (2012) Spray characteristics of biodiesel blends in a high pressure constant volume spray chamber. *Exp Thermal Fluid Sci* 42:212–218
5. Wang Q, Zhang C, He Z et al (2013) Experiment on spray characteristics of soybean oil methyl ester and diesel blends. *Trans CSICE* 31(5):414–419
6. Zhijun W, Zhiyong Z, Zhen H (2006) An experimental study on the spray structure of oxygenated fuel using laser-based visualization and particle image velocimetry. *Fuel* 85 (10/11):1458–1464
7. Guan L, Tang C, Yang K et al (2015) Effect of di-n-butyl ether blending with soybean-biodiesel on spray and atomization characteristics in a common-rail fuel injection system. *Fuel* 140:116–125
8. Park SH, Yoon SH, Suh HK et al (2008) Effect of the temperature variation on properties of biodiesel and biodiesel-ethanol blends fuels. *Oil Gas Sci Technol* 63(6):737–745
9. Hiroyasu H, Arai M (1990) Structures of fuel sprays in diesel engine. SAE, Detroit Michigan
10. Delacourta E, Desmet B, Besson B (2005) Characterization of very high pressure diesel sprays using digital imaging techniques. *Fuel* 84:859–867

11. Labs J, Parker T (2006) Two-dimensional droplet size and volume fraction distributions from the near-injector region of high-pressure diesel sprays. *Atomization Spray* 16(7):55–843
12. Deshmukh D, Madan Mohan A, Anand TNC et al (2012) Spray characterization of straight vegetable oils at high injection pressures. *Fuel* 97:879–883

Chapter 18

An Ultra-High Power Ignition System for EGR-Diluted GDI Engine

Haifeng Lu, Liguang Li, Yintong Liu, Han Gao and Jiyu Shen

Abstract An innovative ignition system was evaluated for its suitability for EGR-diluted GDI engine. The energy measurements showed the ultra-high power ignition system could provide about 12 kW power and generated a strong shock wave captured by a high-speed photography. The 2000 r/min@0.44 MPa BMEP engine test showed a 10% EGR ratio limit extension and the enhanced flame kernel and flame propagation helped to raise the thermal efficiency by 5.5% relatively.

Keywords Ultra-high power ignition · Spark ignition · EGR dilution · GDI · Combustion stability

18.1 Introduction

The diluted combustion (air dilution or EGR dilution) is a highly effective way to achieve both clean and efficient combustion in modern piston engine. Meanwhile, Three-way catalytic converters (TWC) is still a strong assurance to keep the gasoline low-cost and maintenance-easy advantages under the extremely stringent emission standard, which contributes to the increasing interest of EGR-diluted stoichiometric combustion. However, the combustion inhibition effect of EGR brings the demand for the ignition system to provide a more reliable and repeatable ignition process.

To combat this challenge, a number of new ignition concepts have been created in order to provide more stable operation in engines under dilution conditions [1]. Multi-spark ignition system (also called continuous discharge ignition) is a comparatively simple and convenient method to enhance the energy or duration of the spark. The faster flame propagation and COV of IMEP improvement have been reported by engine and combustion vessel test [2, 3]. The other effective way is pre-chamber torch ignition systems (also called flame jet ignition system). The

H. Lu · L. Li (✉) · Y. Liu · H. Gao · J. Shen
School of Automotive Studies, Tongji University, Shanghai 200092, China
e-mail: liguang@tongji.edu.cn

basic principle of this system is to create partially combusted hot reactants in a small pre-chamber and then use the jet of reactive species to initiate the main chamber combustion [4–6]. Although this kind of system has a significant performance in the lean burn condition, the complex structure restricts its application (only in some huge natural gas engines). Moreover, cold plasma (also called non-equilibrium plasma) has also been applied to improve the ignition process. There are many different types of cold plasma, such as corona, nanosecond pulse discharge, microwave, radio-frequency discharge [7, 8]. They share some common characteristics, like low current discharge and comparatively large spatial non-uniform discharge. However, these technologies are still not mature enough, especially in some high-pressure conditions.

On the other hand, the enhanced airflow movement is also used to optimize the air/fuel mixing process and speed up the combustion duration, like tumble or swirl management in GDI engine. But this kind of high-speed flow has a negative effect on the flame core generation stage, especially combined with a diluted situation. Some recent researches indicated that enough thermal effect is needed to stabilize a flame in a high-speed flow [9]. Thus, it is worthwhile to explore an effective approach, which can rapidly and efficiently deliver the limited energy to the flame core.

In this work, an ultra-high power ignition system (UHPI) [10] was developed to study the ignition characteristics in an EGR-diluted GDI engine. The delivered energy was calculated by the microsecond-based voltage and current measurement and the difference was compared with a normal ignition system. The ignition delay, combustion stability and cyclic variability were used to evaluate the ignition system in the engine application.

18.2 Experimental Setups

18.2.1 *Ultra-High Power Ignition System*

An ultra-high power ignition system was built to enhance the ignition process in this experiment. The discharge process could be divided into two stages: a normal inductive discharge stage and a high power capacitive discharge stage. The schematic of the system is shown in Fig. 18.1 and two current paths were presented. During a UHPI event, a voltage of thousands volts is delivered by the ignition transformer and breakdowns the spark gap (path “a”). After that, the plasma channel forms a low-resistance discharge path across the spark gap, which makes the high power discharge stage possible (path “b”).

Due to the modern ignition system usually supplies a negative high voltage to the central electrode of the spark plug, the current in the schematic is started from the ground, across the spark gap, and then back to the ignition coil. This is because in the high temperature combustion chamber, a hotter central electrode is easy to

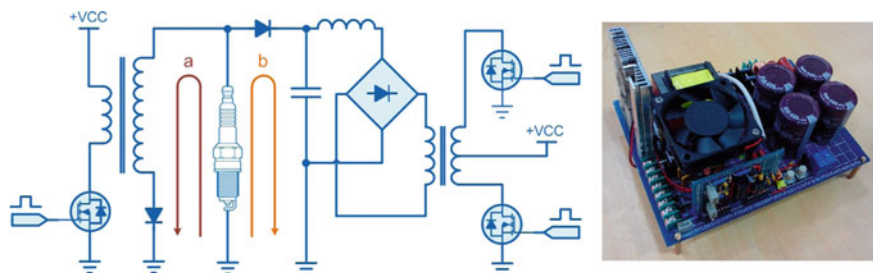
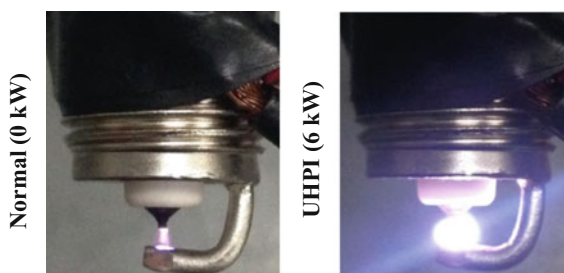


Fig. 18.1 Schematic diagram of UHPI and a picture of partial circuit

Fig. 18.2 Photos of normal and UHPI spark



generate electrons and breakdown the spark gap in the high-density environment. The left-side pulse generator was used to control the spark timing and the two right-side pulse generators were used to control the energy level of the high power ignition stage. All the pulse generators were managed by a self-designed MCU controller, which communicated with the PC by CAN bus. Figure 18.2 shows the conventional photography of a normal spark and the UHPI spark in atmosphere. The average power of UHPI stage is about 6 kW and the details of the energy calculation will be discussed below.

18.2.2 Engine Test Bench

A schematic of the engine layout is shown in Fig. 18.3. The experiments were performed on a single cylinder GDI engine, which was modified from a four cylinders engine. A low-pressure EGR loop was chosen in this experiment, in which the EGR was diverted from downstream of the exhaust tail and introduced upstream of the throttle. There was a tumble control valve in the inlet port and all the experiments showed in this paper were under the strong tumble mode.

By means of a closed loop control with the λ feedback, injection duration was further adjusted to maintain A/F ratio close to stoichiometry ($\lambda = 1$). Two gas sample points were used to analyze the concentration of CO_2 , through which the

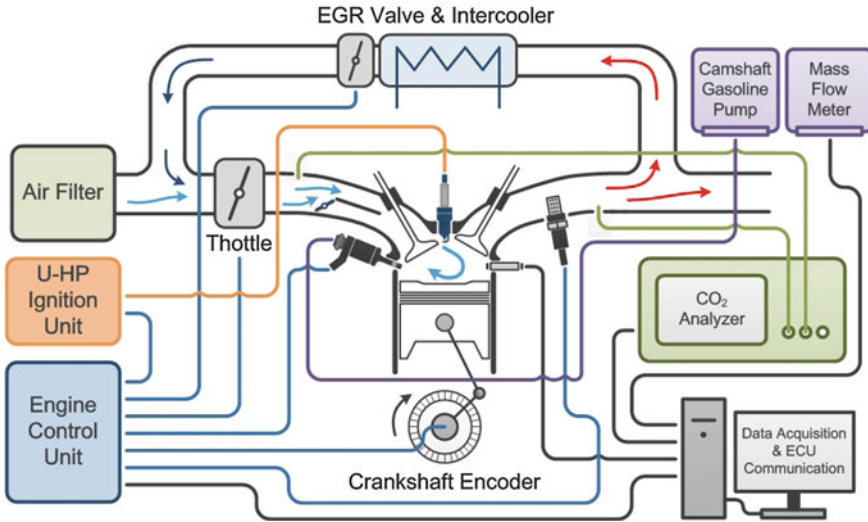


Fig. 18.3 Schematic of the engine layout

Table 18.1 Parameters of test bench

Displacement	496 cc per cylinder	Fuel	RON 92 gasoline
Bore	82.5 mm	Fuel temperature	25 ± 0.5 °C
Stroke	92.8 mm	Inlet air temp	25 ± 1 °C
Compression ratio	11.5	Injection pressure	12 MPa
Number of valves	4	Induction mode	Naturally inspired
Pressure sensor	Kistler 6052C	Fuel meter	AVL 735S/753C
Data acquisition	NI PCI 6250	Coolant conditioning	KAMA SHW160
Camshaft control	VVT of both side	Coolant temperature	88 ± 3 °C
Dynamometer	KAMA ED CJ160	Wideband lambda	Bosch LSU 4.2
Gas analyzer of EGR	Fofen FGA4100	Encoder resolution	720 PPR
Oscilloscope	TDS1012C-SC	Spark timing	MBT for normal spark
Spark plug gap	1.0 mm	Resistance of SP	0.5 Ω
SP heat rating	NGK scale 8	High voltage probe	Tektronix P6015A
Resistance of secondary coil	9170 Ω	High frequency current sensor	Cybertek CP312 & CPA300
Material of central electrode	Iridium	Material of ground electrode	Platinum

volume fraction of EGR rate is determined. Other experimental parameters are shown in Table 18.1.

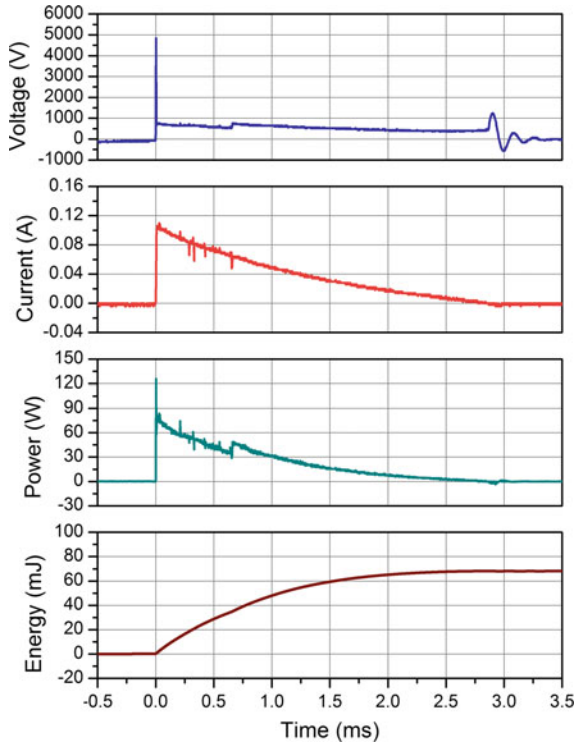
18.3 Results and Discussions

18.3.1 Energy and Transient Power Calculation

The spark discharge process was characterized by measurement of the discharge voltage and current profiles. The tests were conducted at ambient pressure and temperature. Although the higher pressure in the cylinder environment would change the peak voltage, the general characteristics were similar. The discharge voltage was measured by a high-voltage probe, which connected to central electrode of the spark plug. The current was measured by a non-contact DC/AC current probe, which based on the active transformer action principle.

Figure 18.4 shows the voltage and current trace of a normal spark. At 1 atm pressure, breakdown voltages were in the range of 4–6 kV. The voltage drop associated with breakdown itself occurs on a time scale about 10 ns [11]. This is

Fig. 18.4 Power calculation of normal spark



faster than the time resolution of the current sensor and the current pulse peak at about 0.12 A was observed. It turns out that the maximum power is about 120 W and the total energy is about 60 mJ.

Figure 18.5 shows electrical traces of a UHPI event. This discharge process showed a clear two-stage characteristic: a normal inductive discharge process, which was overlapped by a high power capacitive discharge. In other words, the inductive discharge was separated by the capacitive discharge. After the thousands of volts peak touched down the spark gap, the high power discharge was released. The current reached a peak about 160 A and lasted for about 20 μ s (in green box). It should be noticed that the plateau of the voltage curve (about 1700 kV) is not the really value of voltage peak. It is because the signal became out of range when it was amplified for the details. The total energy of an UHPI event was calculated by the sum of the high power stage (in green box) and the normal discharge stage (in

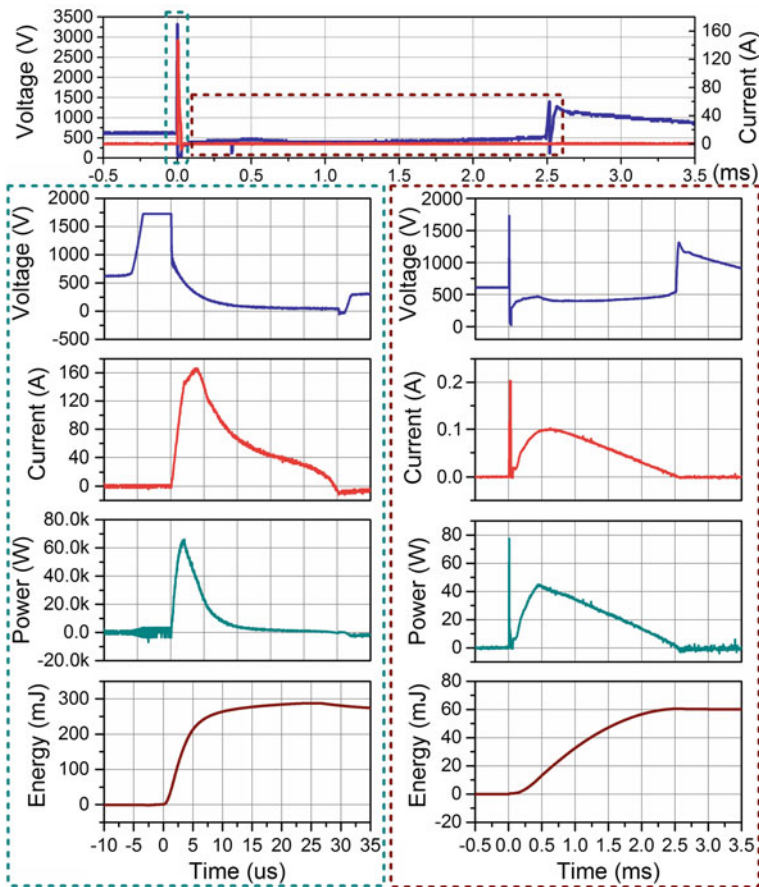


Fig. 18.5 Power calculation of UHPI (average power of U-HP stage = 12 kW)

Table 18.2 Calculation results of energy and power

Pattern	Delivered energy (mJ)	Peak power (kW)	Average power of U-HP stage (kW)
Normal	60	0.12	0
U-high 1	138	11.5	3.2
U-high 2	170	18.1	4.6
U-high 3	210	26.9	6.2
U-high 4	280	44.3	9.2
U-high 5	350	64.4	12.1

brown box). Figure 18.5 shows the high power stage delivered about 290 mJ energy, the normal stage delivered about 60 mJ and the total is about 350 mJ, which is also listed in Table 18.2.

Table 18.2 lists the calculation results of energy and power in different spark patterns, which were applied to the engine test. The curves in Fig. 18.5 is the last case in the table (U-high 5). For simplicity, the cases of normal spark and UHPI will be named as 0, 3, 4, 6, 9 and 12 kW in the following paragraphs.

Figure 18.6 shows the comparison of a normal spark and the 12 kW UHPI under the high-speed photography. The development of sparks were recorded by a shadowgraph imaging system. The high-speed camera was set at 12,500 frames per second and the exposure time of 6 μs. The test was conducted at atmosphere and

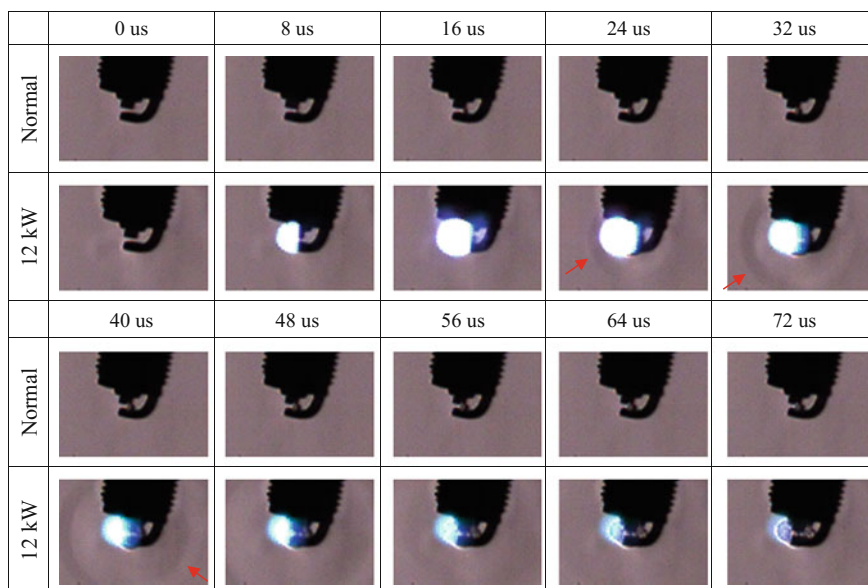


Fig. 18.6 Spark development of normal and UHPI under high speed photography

without any combustion. The pictures include the first 72 μs of the spark events, which cover the high power discharge stage of the UHPI. It is obvious that the bright glow phase of UHPI discharge leads to the over exposure of the photos, which form a great contrast with the normal spark. In addition, because of the ultra-high power, the spark also generated a strong shock wave at the time about 20 μs . Actually, all the spark can generate a shock wave, but for most of the time, they are too weak to be captured by any imaging system. However, the strong shock wave is easy to be seen.

18.3.2 Engine Test Results

The results of 2000 r/min@0.44 MPa BMEP testing are shown in Figs. 18.7, 18.8, 18.9 and 18.10. Since only one cylinder was kept running and the others were shut down, the BSFC data is not available and the BMEP was estimated from FMEP of the engine cranking test. The ignition timing was set to MBT of the normal ignition system and kept the same when that was switched to UHPI system.

These results show a significant improvement over the normal ignition system. Figure 18.7 shows the COV of IMEP in different EGR rate. With the normal ignition system, the cyclic variation began to deteriorate when the EGR rate was higher than 15%. However, with the help of UHPI system (12 kW), the EGR tolerance could be extended to 25% at least. This is because the UHPI system could provide a faster flame initiation and kernel development, which are reflected by the ignition delay and combustion duration shown in Figs. 18.9 and 18.10. The contribution of EGR for fuel efficiency was primarily due to heat loss reduction, increasing of ratio of specific heats and pumping losses reduction in this cases. But the combustion inhibition effect of too much EGR would also offset the positive gains. With the UHPI and more EGR rate, the indicated thermal efficiency could be improved from 36 to 38% (5.5% relative optimization). The data is shown in Fig. 18.8.

Fig. 18.7 COV of IMEP

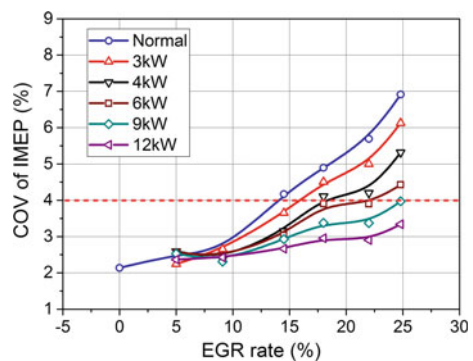


Fig. 18.8 Indicated thermal efficiency

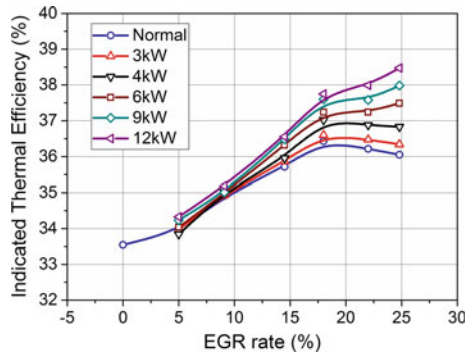


Fig. 18.9 Ignition delay (spark to CA10)

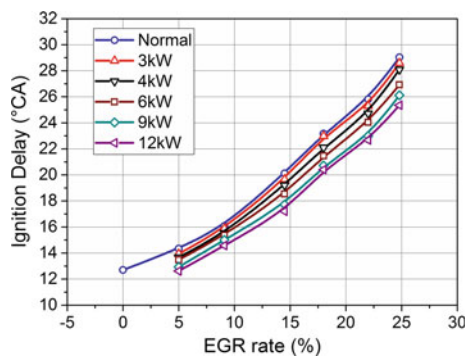
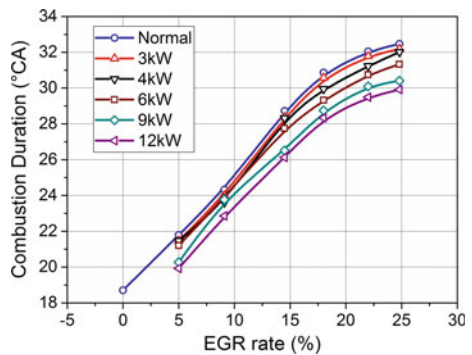


Fig. 18.10 Combustion duration (CA10–CA90)



18.4 Conclusions

An innovative ignition system was developed to extend the dilution limit of GDI engine. Energy measurements showed the UHPI system could provide about 12 kW power during the first 20 μ s of the spark, which help to generate a strong shock wave simultaneously. In the testing condition, the EGR tolerance could be

improved by at least 10% EGR ratio through a more robust flame kernel generated by the UHPI system.

References

1. Briggs T, Alger T, Mangold B (2014) Advanced ignition systems evaluations for high-dilution SI engines. *SAE Int J Engines* 7(4):1802–1807. doi:[10.4271/2014-01-2625](https://doi.org/10.4271/2014-01-2625)
2. Alger T, Gingrich J, Mangold B, Roberts C (2011) A continuous discharge ignition system for EGR limit extension in SI engines. *SAE Int J Engines* 4(1):677–692. doi:[10.4271/2011-01-0661](https://doi.org/10.4271/2011-01-0661)
3. Yu S, Han X, Xie K, Wang M, Li L, Tjong J, Zheng M (2013) Multi-coil high frequency spark ignition to extend diluted combustion limits. In: *Proceedings of the FISITA 2012 World Automotive Congress, 2013. Lecture Notes in Electrical Engineering*, vol 1, pp 217–227
4. Maxson J, Hensinger D, Hom K, Oppenheim A (1991) Performance of multiple stream pulsed jet combustion systems. SAE Technical paper 910565, 1991. doi:[10.4271/910565](https://doi.org/10.4271/910565)
5. Kojic A, Hathout J-P, Cook D, Ahmed J (2005) Control of auto-ignition timing for homogeneous combustion jet ignition engines. 2005: United States Patent No. PCT/US2004/029613
6. Attard W, Kohn J, Parsons P (2010) Ignition energy development for a spark initiated combustion system capable of high load, high efficiency and near zero NO_x emissions. *SAE Int J Engines* 3(2):481–496. doi:[10.4271/2010-32-0088](https://doi.org/10.4271/2010-32-0088)
7. Starikovskiy A, Aleksandrov N (2013) Plasma-assisted ignition and combustion. *Prog Energy Combust Sci* 39(1):61–110. ISSN 0360-1285. doi:[10.1016/j.pecs.2012.05.003](https://doi.org/10.1016/j.pecs.2012.05.003)
8. Ju Y, Sun W (2015) Plasma assisted combustion: dynamics and chemistry. *Prog Energy Combust Sci* 48:21–83. ISSN 0360-1285. doi:[10.1016/j.pecs.2014.12.002](https://doi.org/10.1016/j.pecs.2014.12.002)
9. Matsubara Y, Takita K, Masuya G (2013) Combustion enhancement in a supersonic flow by simultaneous operation of DBD and plasma jet. *Proc Combust Inst* 34:3287e94
10. Li L, Lu L et al (2013) Ultra-high energy spark ignition system: CN. Patent CN103423061A. 2013-12-04
11. Lee M, Hall M, Ezekoye O, Matthews R (2005) Voltage, and energy deposition characteristics of spark ignition systems. SAE Technical paper 2005-01-0231, 2005. doi:[10.4271/2005-01-0231](https://doi.org/10.4271/2005-01-0231)

Chapter 19

Experimental and Simulated Study on the Cylinder Deactivation of Vehicle Gasoline Engine

Shuhai Yu, Xingxing Ma, Zhigang Ma, Rui Liu and Dongxian Song

Abstract Cylinder deactivation performance in vehicle gasoline engine is investigated by experimental and simulated methods, this technology is implemented by adjusting the valve system, and furthermore, a simulated model is built in GT-power. The results show that, in cylinder deactivation mode, the overlap degree of naturally aspirated and effective region is highly, it can be considered that the cylinder deactivation engine just operates in naturally aspirated state. At 2 bar@2000 rpm, BSFC of cylinder deactivation is 312.7 g/kW h, the fuel efficiency is improved 12.6% than normal state. With the reduced engine speed, fuel efficiency becomes better, however, with the increment speed, engine NVH characteristic has been deteriorated.

Keywords Cylinder deactivation · Gasoline engine · Fuel efficiency · Torsional fluctuation · Simulated study

19.1 Introduction

In recent decades, the technology of high efficiency vehicle gasoline engine had been greatly developed, such as cylinder deactivation (CDA), this technology is achieved by closing some cylinders during low load operation, and to insure the entire power output remain unchanged, the active cylinders run in higher fuel efficiency mode [1–3]. Consequently, this technology increases fuel efficiency and decreases emissions from deactivated cylinders. In most instances, the technology of cylinder deactivation is applied to relatively large displacement engines that are particularly inefficient at low load.

S. Yu (✉) · X. Ma · Z. Ma · R. Liu · D. Song
Technical Center, Great Wall Motor Co. Ltd., Baoding 071000, China
e-mail: yushuhai@tju.edu.cn

S. Yu · X. Ma · Z. Ma · R. Liu · D. Song
Hebei Automobile Engineering Technology and Research Center, Baoding 071000, China

First vehicle engine with cylinder deactivation system was designed in 1981 on Cadillac's 6.0L V8-engine. After that, Honda, Nissan, Volkswagen, Chrysler et al. had been performed related research about this technology to improve fuel efficiency.

In this study, the cylinder deactivation mode has been achieved by adjusting the valve system in a six-cylinder gasoline engine, the operating range and fuel efficiency between cylinder deactivation mode and normal engine mode (full-cylinder state) are compared, furthermore, 1-D engine performance simulation software GT-power has been used to investigate the cylinder deactivation engine in depth.

19.2 Experimental Setup

The test engine is designed for a 3.0L six-cylinder gasoline direct injection engine with dual-turbochargers. The implementation of cylinder deactivation is cut off fuel and air simultaneously in the deactivated cylinder. To the fuel-way, the fuel injectors of deactivated cylinders should be stopped. To the air-way, the rocker arms in the deactivated cylinder are removed thus the valve systems of corresponding cylinders become invalid. For the various engine operating conditions, oil pressure range in oil pipe is about 0.8–5 bar, thus after the remove of rocker arms, the corresponding hydraulic tappets should be fixed to avoid oil push out them.

Figure 19.1 shows the schematic of the adjusted valve system in cylinder deactivation engine, the metal clip in Fig. 19.1a provides a fixation of tappet after rocker arm removed, Fig. 19.1b is the cylinder head after adjustment, the deactivated cylinders are 1st, 2nd and 3th cylinder (three cylinders on the left side in this figure), in these three cylinders, the six valves on the intake and exhaust side are stopped; the active cylinders are 4th, 5th and 6th cylinder (three cylinders on the right side), the valve systems of these cylinders remain unchanged. The firing order is 1-5-3-6-2-4, thus all the firing interval angles are maintained 240°CA in cylinder deactivation mode, the identical angle is beneficial for the torque output evenly.

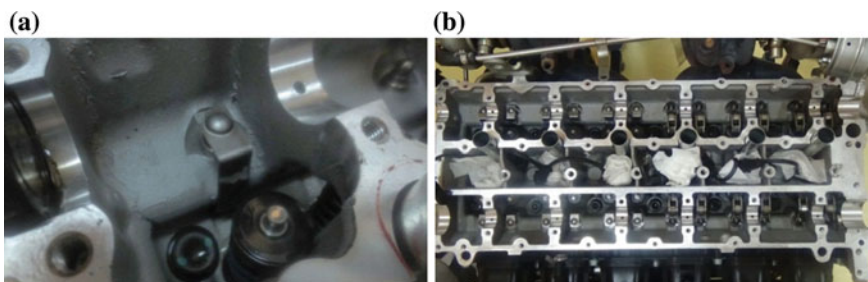


Fig. 19.1 Schematic of valve system in CDA engine. **a** Metal clip; **b** cylinder head after adjustment

Figure 19.2 shows the comparison of brake specific fuel consumption (BSFC) between cylinder deactivation mode (the left figure) and normal mode (the right figure), in the low load region (smaller than 100 Nm), fuel efficiency is improved obviously by cylinder deactivation, in the middle load region (100–120 Nm), fuel consumption is equal to normal engine, in the high load region (larger than 120 Nm), due to the decreased air-fuel ratio, fuel consumption is increased slightly. Therefore, how to determine an appropriate operating region for cylinder deactivation mode is a significant issue of the technology development.

Figure 19.3 shows the comparison of load characteristics between cylinder deactivation and normal mode, three conditions are considered such as the cylinder deactivation mode under naturally aspirated state, cylinder deactivation mode with turbocharger and normal engine mode. It can be seen that, with regard to the cylinder deactivation mode, the operating region can be divided into effective region and invalid region, in the effective region, the fuel consumption is less than normal engine, in the invalid region, the fuel consumption is greater than normal engine. According to the turbocharged state, the operating region can be divided into naturally aspirated region and turbocharged region, in the naturally aspirated region, engine operates without turbocharger and the opening angle of throttle valve increases gradually from minimum. As shown in Fig. 19.3, the overlap degree of naturally aspirated and effective region is high, it can be considered that cylinder deactivation mode just operates in naturally aspirated state, if the power output is insufficiently, the engine should switch into normal mode directly. The more accurate calibration experiment is necessary to find the precise boundary of the effective/invalid region and make this technology more effective. Additional, other load characteristics under various speed are experimented as well, such as 1500, 2000, 2400, 3200, 4000, 4500 rpm, these trends are similar as the 1000 rpm condition and not explained here. At the frequently-used operating point

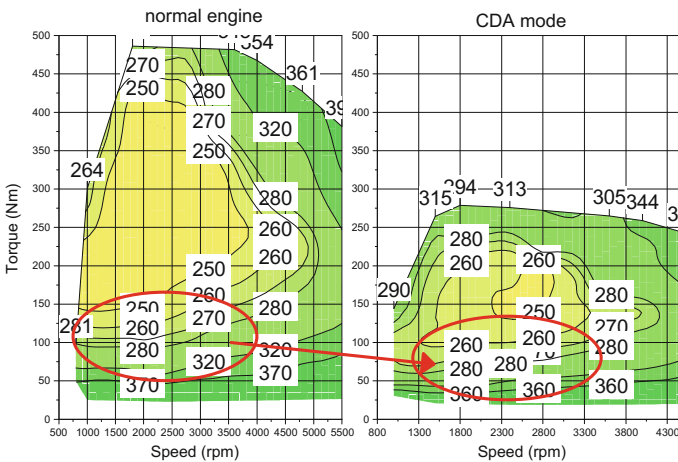
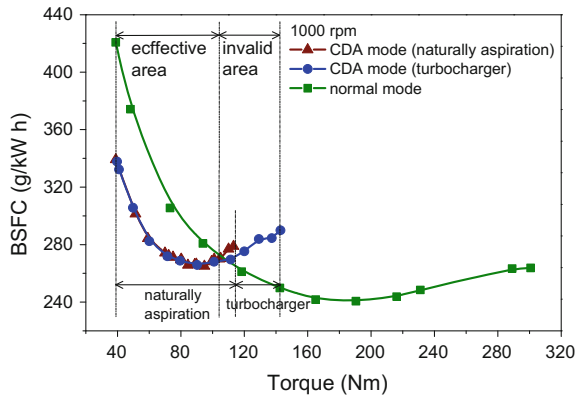


Fig. 19.2 The comparison of BSFC between CDA and normal mode

Fig. 19.3 The load characteristics comparison of CDA and original mode

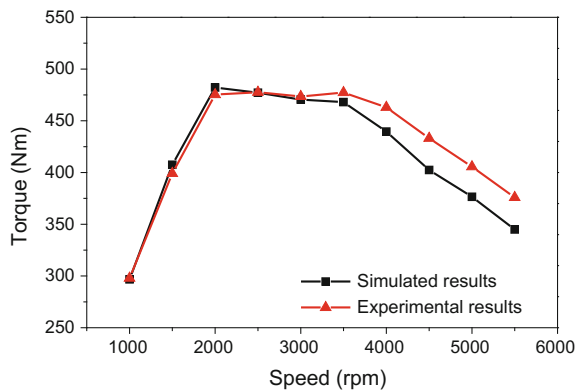


2 bar@2000 rpm, which equals to 48.3 Nm@2000 rpm, BSFC of cylinder deactivation is 312.7 g/kWh, and the fuel efficiency is improved 12.6% than normal state.

19.3 Simulated Model

The GT-power software is used to simulate the engine performance. In this study, first of all, the basal normal engine model has been built and be carefully calibrated by the experimental data in full load region, Fig. 19.4 shows the comparison of experimental and simulated results, a good agreement between these two curves were obtained, especially in low-middle speed region. The CDA model is adjusted into the basal model, these adjustments include: (1) fuel injectors of deactivated cylinders are removed thus their fuel injection is stopped; (2) intake and exhaust valve lifts are defined into zero thus the motion of intake and exhaust valves are stopped; (3) ignition and combustion of deactivated cylinders model are stopped.

Fig. 19.4 Comparison of experimental and simulated results



19.4 Simulated Results

Based on the 1-D model as mentioned above, the simulated results are distributed into two aspects, which are (1) the comparison of various cylinder deactivation mode; (2) the comparison of various cylinder deactivation operating conditions in same mode.

19.4.1 Effect of Cylinder Deactivation Mode

The specific cylinder deactivation mode is determined by the number of deactivated cylinders. Figure 19.5 shows the comparison of maximum pressure under various cylinder deactivation mode, the engine speeds are maintained at 3000 rpm, these modes include stop 1 cylinder, stop 2 cylinders, stop 3 cylinders and stop 4 cylinders, and the difference are analyzed among them. It can be noticed that, the operating range is reduced with the increasing deactivated cylinders; furthermore, the cylinder pressure has a linear relation with engine load under all the CDA modes.

One other thing to note is the region above dotted line, namely the nearly full load region, cylinder pressure of cylinder deactivation mode is higher than normal engine (the rightmost curve), and this phenomenon lead to a risk of knock and pre-ignition which should be avoided in practical. Maximum cylinder combustion temperature is increased with the increasing pressure as well and this phenomenon deteriorated NO_x emission and thermal stress of the engine.

Figure 19.6 shows the reduction of fuel consumption under various mode, it can be seen that, fuel efficiency become better with the increasing deactivated cylinders, the reason is that to maintain power output, opening angle of throttle valve should be increased which lead to a less pump loss and a higher gas-filled efficiency; otherwise, the operating range becomes narrow and the maximum power output

Fig. 19.5 Comparison of maximum pressure under various CDA mode

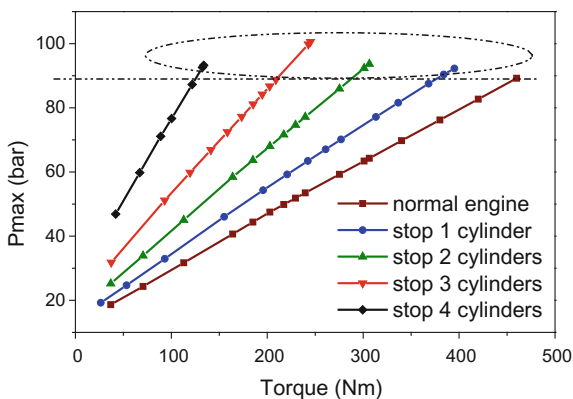
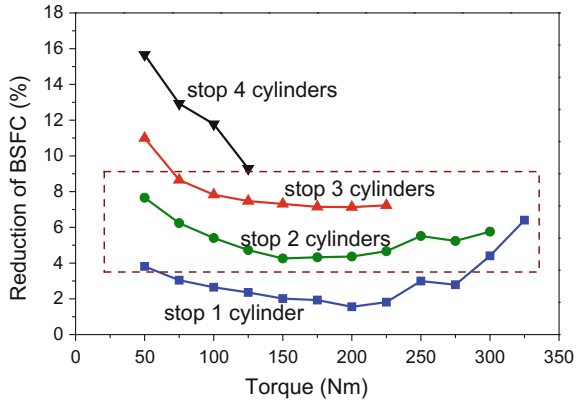


Fig. 19.6 The reduction of fuel consumption under various CDA mode



become lower with the increasing deactivated cylinders. Generally speaking, with regard to a six-cylinder engine, stop 2 cylinders or 3 cylinders is an appropriate choice to consider performance and operating range of cylinder deactivation comprehensively. To stop 2 cylinders condition, the maximum power output is 300 Nm approximately and the reduction of fuel consumption is 4–8%; to stop 3 cylinders condition, the maximum power output is 230 Nm approximately and the reduction of fuel consumption is 7–11%.

Torsional vibration characteristic of crankshaft system is an important research field in engine dynamic analysis which has a great significance on the improvement of vehicle reliability and NVH characteristics [4, 5]. Figure 19.7 shows the torsional vibration for various cylinder deactivation mode at 100 Nm@3000 rpm, the

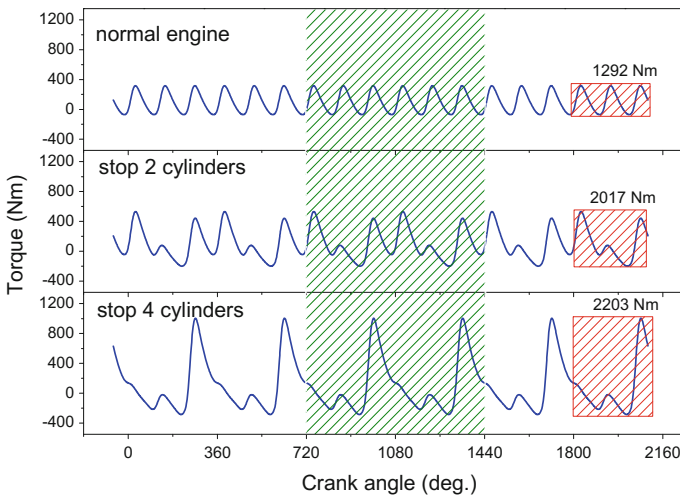


Fig. 19.7 Torque variation under various CDA mode

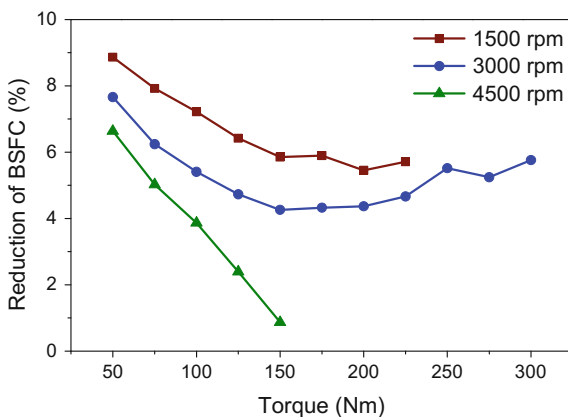
upper, middle and lower sub-figure represent normal mode, stop 2 cylinders and stop 4 cylinders modes, respectively. In this figure, the torsional vibration of three continuous working cycles are represented, in cylinder deactivation mode, the fire interval angles increase and vibration frequencies decrease compare with normal mode, the low vibration frequency is close to the intrinsic frequency of engine body, this phenomenon lead to a increasing vibration amplitude. When some cylinders are deactivated, the positive peak value of torque in one operating cycle will be equal to the number of active cylinders, the active cylinder load will be increased to insure the entire power output remain unchanged, thus the positive peak value of torque in cylinder deactivation mode is greater than normal engine. The vibration amplitude is 2017 Nm in normal engine operating condition, and these values are 2017 and 2203 Nm in stop 2 cylinders and stop 4 cylinders modes, respectively. Therefore, from Fig. 19.7, with the increasing deactivated cylinder, torsional vibration amplitude increases and the frequency decreases.

19.4.2 Effect of Cylinder Deactivation Operating Condition

With regard to the effect of cylinder deactivation operating conditions on the engine performance, take the good effective stop 2 cylinders mode (the 2nd and 5th cylinders are deactivated) as example, the load characteristics are compared under 1500, 3000 and 4000 rpm, these speeds are represented low, middle and high speed conditions, respectively.

Figure 19.8 shows fuel consumption reduction under various engine speed, to the full load condition at 1500 rpm, the fuel reduction reaches upwards of 6–9% approximately, to the full load conditions at 3000 and 4500 rpm, these reductions are 5–8% and 1–7%, respectively. It can be found that, with the decreased engine speed, the effect of cylinder deactivation is improved, in the high speed/load region, the performance is reduced.

Fig. 19.8 Reduction of fuel consumption under various engine speed



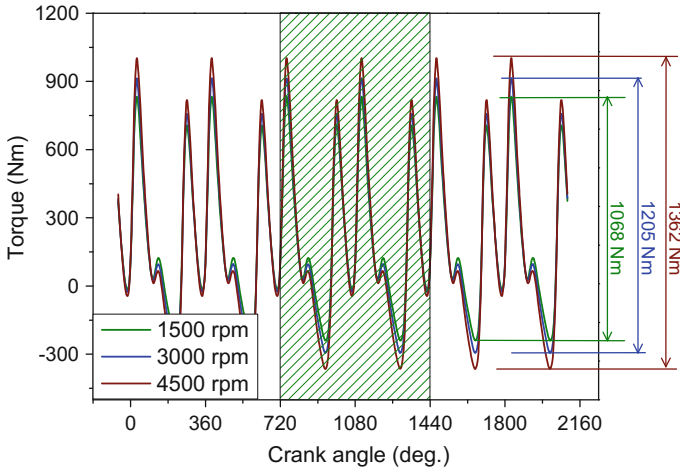


Fig. 19.9 Torque variation under various engine speed

Figure 19.9 shows the torsional variation under various engine speed, the variation amplitude under 1500 rpm is 1068 Nm, and these amplitudes are 1205 and 1362 Nm under 3000 and 4500 rpm conditions. It can be found that, with the increasing speed, variation frequency remains unchanged and negative peak value increases obviously, this phenomenon leads to the increment of variation amplitude, and affects the engine NVH characteristic adversely.

19.5 Conclusion

In this study, the cylinder deactivation performance in vehicle gasoline engine is investigated by experiment and simulation, the following are some findings from this work,

1. In cylinder deactivation mode, the overlap degree of naturally aspirated and effective region is highly, it can be considered that cylinder deactivation engine just operates in naturally aspirated state, if the power output is insufficiently, the engine should switch into full-cylinder mode directly.
2. At the frequently-used operating point 2 bar@2000 rpm, BSFC of cylinder deactivation is 312.7 g/kW h, the fuel efficiency is improved 12.6% than normal state.
3. To consider the performance and operating range comprehensively, stop 2 cylinders or 3 cylinders is an appropriate choice for 6-cylinder engine. With the reduced engine speed, fuel efficiency becomes better, however, with the increment speed, negative peak value of torque increases obviously, this phenomenon leads to the increment of variation amplitude, and affects engine NVH characteristic adversely.

References

1. Zhang D, Yuan Y, Cui Y (2007) Technology of cylinder deactivation of automotive gasoline engine. *Small Intern Combust Engine Motorcycle* 36(6):89–93
2. Paimon A, Jazair W, Rajoo S (2013) Parametric study of cylinder deactivation and valve deactivation for unthrottled operation. *Adv Mater Res* 614:525–528
3. Kwon M, Lee M, Kim J et al (2011) Transient air-fuel ratio control of the cylinder deactivation engine during mode transition. *Trans Korean Soc Automot Eng* 19(2):26–34
4. Yang S, Zhang F, Zhang C et al (2011) Study on torsional vibration characteristics of crankshaft in variable displacement diesel engine. *Acta Armamentaria* 32(09):1047–1052
5. Huang S, Zhang F, Huang Y (2011) Cylinder deactivation on dynamic performances of internal combustion engine motion mechanisms. *Trans Chin Soc Agric Mach* 42(9):8–13

Chapter 20

Study on Effects of Multiple Injection at Intake Stroke on Combustion and Emissions of GDI Engine Under Warm Up Conditions

Wei Dong, Chaojie Pu, Yao Sun, Litao Qiu and Bin Ma

Abstract An experimental investigation on multiple injection at intake stroke under warm up conditions was performed in a GDI engine. With a constant excess air ratio, the effects of multiple injection strategy at intake stroke on combustion and emissions were studied. The results showed that, compared to single injection, with the increase of injection times and coolant water temperature, cylinder pressure increased and its corresponding crank angle was advanced for multiple injection at intake stroke, while the peak transient heat released rate increased, but its occurrence timing was slightly advanced. Meanwhile, THC emissions decreased obviously for multiple injection, but NO_x emissions increased. The particle number concentration under warm up conditions of multiple injection at intake stroke reduced, which also decreased with the increase of coolant temperature. However, when at low coolant temperature, the size of particle number concentration showed bimodal distribution of nucleation mode and accumulation mode. With the increase of coolant temperature, the peak size of particle number concentration behaved as a unimodal distribution. Comparing to the third injection timing at three different injection modes, it showed that, with the advance in injection timing, the peak cylinder pressure and the maximum transient heat released rate increased, while their corresponding crank angle were advanced. Meanwhile, NO_x emissions increased, THC emissions and the particle number concentration decreased.

Keywords GDI · Warm up · Multiple injection · Combustion · Emissions

W. Dong (✉) · C. Pu · Y. Sun · L. Qiu · B. Ma
State Key Laboratory of Automotive Simulation and Control, Jilin University,
Changchun, China
e-mail: dwei@jlu.edu.cn

© Springer Nature Singapore Pte Ltd. 2017
Society of Automotive Engineers of China (SAE-China), *Proceedings of SAE-China Congress 2016: Selected Papers*, Lecture Notes in Electrical Engineering 418,
DOI 10.1007/978-981-10-3527-2_20

217

20.1 Introduction

Warm up stage of the engine means that the engine in cold start should not immediately increase the load. The engine generally waits the coolant temperature to rise to 60 °C at idle condition, and then turns to the normal running process. Thus, the study showed that the CO and HC emissions during start-up phase occupied 60–80% of the total emissions testing phase [1]. In the warm-up process, the low cylinder temperature makes evaporation atomization deteriorated, resulting in a wet wall phenomenon. And part of the mixed gas in cylinder incomplete or did not participate in the combustion, which resulted in the increased THC emissions. In addition, the temperature of the air intake system of the engine and the cylinder wall were low, when the piston upwardly compressed air at the compression stroke, and radiation heat loss is increased while the mixed gas burned incompletely [2]. With the coolant temperature rises, the THC emissions can be reduced. Therefore, improving the problem of the emission in warm-up condition is mainly to shorten the durations of water temperature rising time and improve the heat transmission efficiency. Then the improvement quality of atomization and combustion of fuel and decrease THC and particulate emissions.

For the study on the coolant temperature impact to the exhaust emissions of a diesel engine by Zhang et al. [3], it showed that diesel engine coolant temperature had great impact on CO, HC and particulate matter (PM) emissions. On the engine test bench, the reduced coolant water temperature fluctuation range can stabilize the scope of emission of pollutants. As with another study on the impact of three-way catalyst (TWC) in cold-start and warm-up conditions on particulate emissions of a four-cylinder direct-injection gasoline engine by Whelan et al. [4] the experimental result showed that TWC could reduce the total number of particles concentration by 65%, for size of less than 23 nm nucleate particles can be reduced by 95%, particle number concentration of the particle size over 50 nm increased. And the total particulate concentration increased, geometric mean particle diameter increased by 300%. Kim et al. [5] studied the influence of the control strategy in cold start and warm-up conditions particulate emission in a direct-injection natural gas engine. It showed that single injection brought larger particle number than double injection, which was caused by the wet wall phenomenon. Ketterer and Cheng [6] studied the emission characteristics at low temperature and high idle speed conditions during the direct injection gasoline engine warm-up process. The results showed that the high particle number concentration was brought by compression stroke injection, which was mainly because that the mixed gas mixing time was short, and evaporation atomization was poor.

Currently, related researches put less emphasis on effects of multiple injection at intake stroke on combustion and emission of a GDI engine under warm up condition. In order to further improve the study on combustion and emission characteristics of the GDI engine at warm-up stage, this paper focused on the effects of multiple injection at intake stroke on combustion and emissions in a GDI engine

under warm up conditions. A 1.8L, in-line 4 cylinder GDI engine was used in the experiment.

20.2 Experimental Equipment and Method

Test bench is produced by Volkswagen 1.8T engine with turbocharged and direct injection, which has two intake and two exhaust valves in each cylinder. The main technical parameters are shown in Table 20.1.

Figure 20.1 shows an engine bench testing platform general schematic diagram. The engine was controlled by the model of Simulink, while precise control of engine fuel injection pulse width, fuel injection pressure, injection timing and ignition timing and other operating parameters were realized by rapid prototyping tool dSpace. The dynamometer is Luoyang Nanfeng of CW160, and emissions testing equipment is HORIBA, which was used for conventional engine emissions. The lambda equipment, ETAS, is LAMBDA.LA4, and wide-range oxygen sensor LSU4.2 were used to monitor the air-fuel ratio. Japan Ono Sokki Company's DS 9100-type combustion analyzer, Kistler angle standard instrument and AVL company's spark plug type cylinder pressure sensor were used to monitor the combustion process. Furthermore, particles were measured by TSI Model 3090 engine particulate emission spectrometer, which consists of 22 sections, and particle size measurement range was 5–560 nm. Since the engine exhaust gas has quite high particle number, it must be diluted before the measurement. However, related studies show that dilution sampling conditions have a significant impact on the measurement accuracy of the measuring of particles in particular nucleate particles (≤ 30 nm) [7, 8]. Therefore, the GDI engine exhaust particulate secondary dilution sampling device used in the paper can realized the precise control on the dilution ratio, diluted temperature, residence time diluted and so on, which were the key parameters of exhaust dilution process. The dilution ratio of 180 was selected and dilution temperature was fixed at 200 °C after preliminary tests to ensure a high test repeatability and test accuracy.

Experiments mainly study on the effects of injection strategy at intake stroke on the combustion and emission characteristics under warm up conditions. The excess air ratio, fuel injection pressure, ignition timing and the speed were kept constant to get reliable result. By changing the injection frequency and fuel injection timing,

Table 20.1 Specification of test engine

Engine type	In-line
Displacement (cc)	1798
Bore (mm)	82.5
Stroke (mm)	84.2
Compression ratio	9.6:1
Number of valves	4

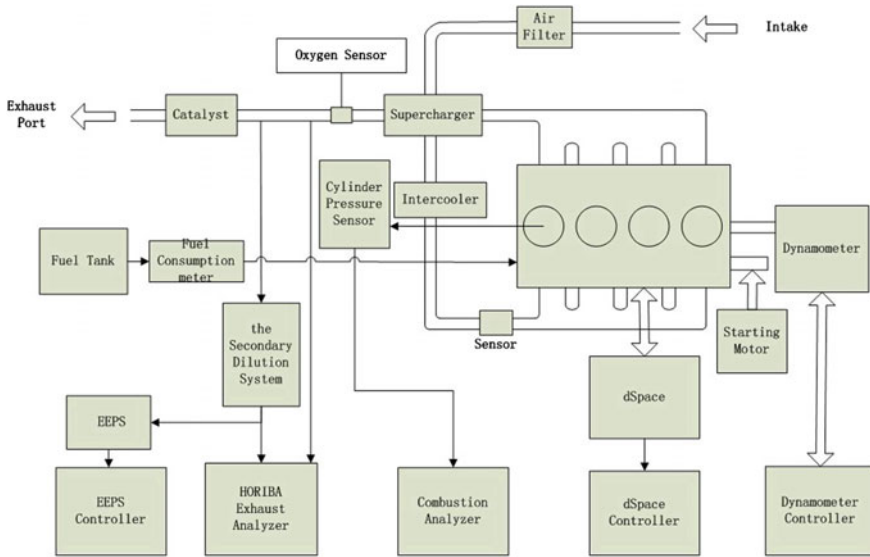


Fig. 20.1 Schematic diagram of experimental equipment

Table 20.2 Experimental parameters in the engine bench test

Injection strategy	Speed (r/min)	Excess air ratio	Injection pressure (MPa)	Ignition timing (°CA BTDC)	Injection timing (°CA BTDC)	Fuel injection pulse width (ms)
Single	1200	0.9	8	20	290	8
Twice	1200	0.9	8	20	290	5
					260	3
Thrice	1200	0.9	8	20	290	5
					260	2
					230, 210, 190	1

the coolant temperature increased from 30 to 80 °C. Specific parameters are adjusted as described in Table 20.2.

20.3 Experimental Results and Discussions

20.3.1 In-Cylinder Combustion Analysis

Figures 20.2 and 20.3 show the impact of multiple injection at intake stroke under warm up conditions on cylinder pressure and transient heat released ratio. As can be seen from the figures, when the air-fuel ratio and fuel injection quantity are fixed,

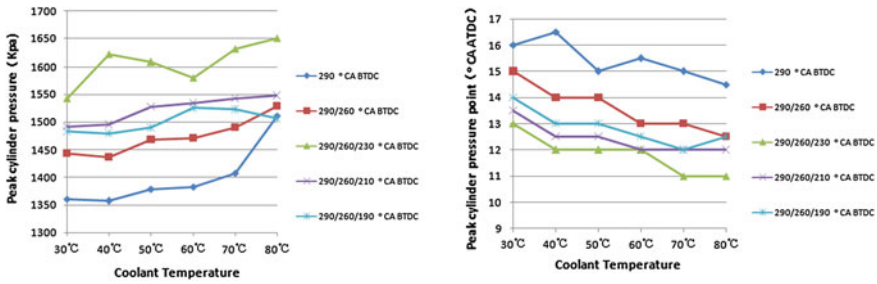


Fig. 20.2 Effects of multiple injection under warm up condition on cylinder pressure and its corresponding crank angle

with the increase in injection times at intake stroke, peak cylinder pressure gradually increased and its corresponding crank angle was advanced. Meanwhile, the peak transient heat released rate of multiple injection was increased than single injection, likewise its occurrence timing was advanced. With the increase of coolant temperature, cylinder pressure increased and its corresponding crank angle was advanced, while the peak transient heat released ratio and peak phase changed lightly. Comparing to the third injection timing for three different injection modes, it showed that, when the third injection time was set at 230°CA BTDC, cylinder peak pressure and the peak transient heat released ratio were higher than other modes. With the advance in the third injection time, the peak cylinder pressure and the maximum transient heat released rate gradually increased, but the corresponding point decreased. The reasons of above phenomenon are as follows. (1) When the total quantity of fuel injection and excess air ratio constant, multiple injection shortens each fuel injection pulse width, spray penetration distance is shortened, the wall fuel film is decreased, and the possibility of fuel from the jet hits the piston is reduced, which is more beneficial for fuel atomization evaporation [9]. (2) With the increase of temperature of cooling water, the cylinder wall temperature rises, a degree of atomization of the fuel is high, mixture gas is more evenly distributed, resulting in higher the combustion efficiency. (3) With the third injection timing advanced, fuel mixing time before ignition lasts longer, the mixed gas distribution is more uniform and combustion state is better.

20.3.2 Emission Characteristics

Figure 20.4 shows the effects of multiple injection on THC emissions during warm up process. As can be seen from the figure, with the increase of coolant temperature, THC emissions decreased gradually and then stabilized. While THC emissions of multiple injection below single injection, and three times injection is lower than the twice. By comparing with the third injection timing for three different injection modes, it shows that, with the advance in injection time, THC emissions increased

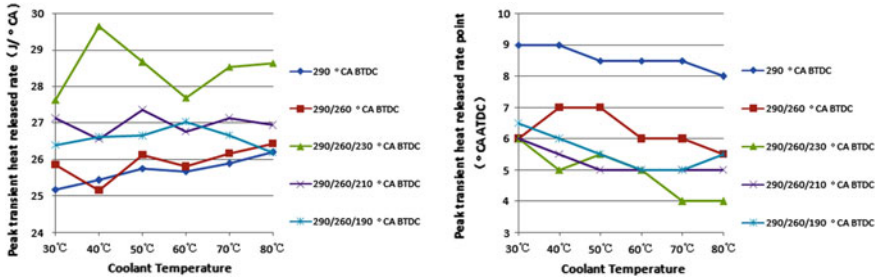


Fig. 20.3 Effects of multiple injection under warm up condition on the peak transient heat released rate and its occurrence timing

gradually. When the third injection time was set at 230°CA BTDC, THC emissions was the lowest. There were some reasons for these phenomena as following. Firstly, THC emissions mainly came from surface quenching. However, during the warm-up period, wall temperature was increased, reducing the quenching layer on the cylinder wall. While the mixture temperature rose, the combustion became more complete. Secondly, in certain the total injection pulse width, multiple injection shortened each injection pulse width, so that the spray penetration distance was shortened, leading to reducing the wall and the film formation on the piston top, so that quenching layer of the cylinder wall reduced, improving the in-cylinder combustion efficiency [10, 11]. Thirdly, with the third injection timing advanced, interval time of fuel injection became shorter. While, the mixed time became longer, which led to more complete fuel atomization and evaporation. More uniformal mixture resulted in better combustion in the cylinder.

When the coolant water temperature was 30 °C, THC emissions concentration of a single injection was 1335 ppm and THC concentration when the third injection was fixed at 230°CA BTDC was 893 ppm. So THC emissions concentration of multiple injection decreased by 33% from a single injection. When the coolant water temperature was 8 °C, THC emissions concentration of a single injection was 933 ppm, and THC concentration was 698 ppm when the third injection was fixed at 230°CA BTDC. Compared to a single injection THC emissions concentration of multiple injection decreased by 25%. Obviously, the multiple injection could reduce THC emissions during warm-up period. With the increase of coolant temperature, THC emissions of a single injection was reduced by 30%, THC emissions of two injections were reduced by 24%, THC emissions of three injections decreased with the range from 16 to 22%. Experimental results showed that, with the increasing of coolant water temperature, THC emissions can be significantly reduced. Although a single injection largely reduced amplitude, but three injections THC emission initial value was lower than the single injection. Therefore, multiple injection was more conducive to reducing the THC emissions during warm-up process. Comparing to the third injection timing for three different injection modes, it shows that, throughout the warm-up process, with the third injection timing

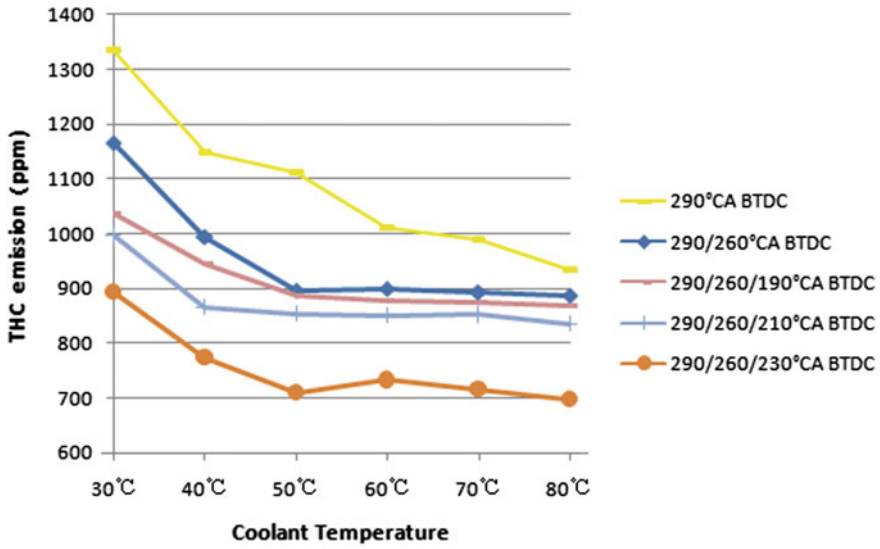


Fig. 20.4 Effects of multiple injection condition on THC emission during warm up process

advanced, THC emission decreased, THC emissions was the least when the third injection time was at 230°CA BTDC.

Figure 20.5 shows the multiple injection impacts on THC emissions during warm up. As can be seen from the figure, NO_x emissions of multiple injection during the warm-up was higher than the single injection. Comparing to the third

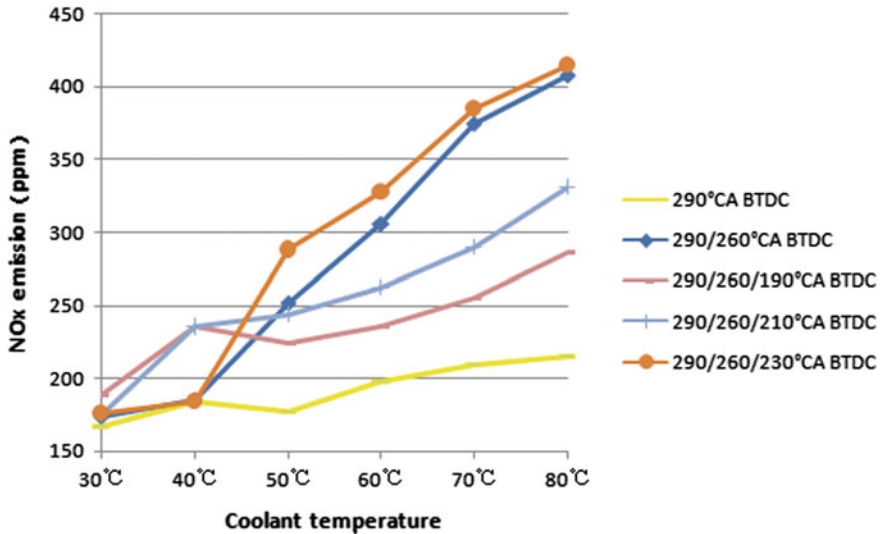


Fig. 20.5 Effects of multiple injection condition on NO_x emission during warm up process

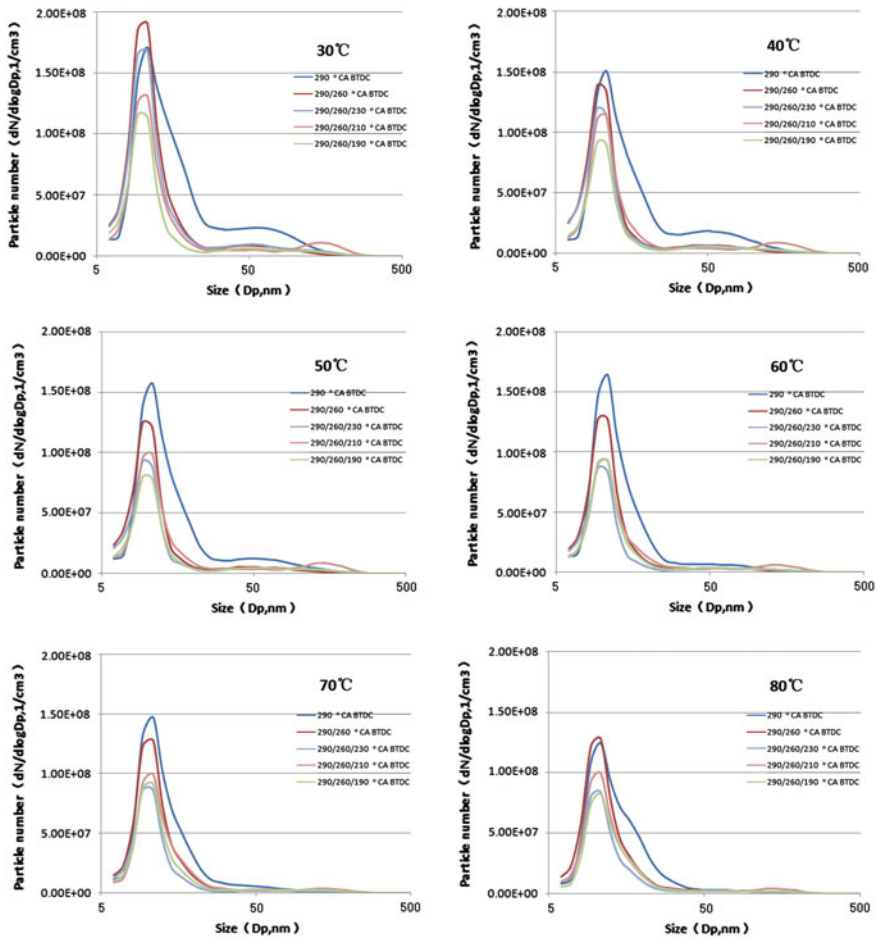


Fig. 20.6 Particle number concentration variation of particle size distribution under warm up conditions with different injection times

injection timing for three different injection modes, it showed that, NO_x emissions was highest when the third injection was set at 230°CA BTDC. With the coolant temperature rose, NO_x emissions increased. NO_x emissions are produced by high temperature, oxygen-enrichment and at long temperature residence time. Multiple injection made fuel mixture more homogeneous, combustion process was better than the single injection, and in-cylinder combustion maximum temperature was higher than the single injection. So NO_x emissions of multiple injection was relatively higher. With the third injection timing advanced, fuel mixture timing was prolonged, which made NO_x emissions gradually increased.

Figures 20.6 and 20.7 shows the effects of different injection times at intake stroke on particle number concentration and particle size distribution change during

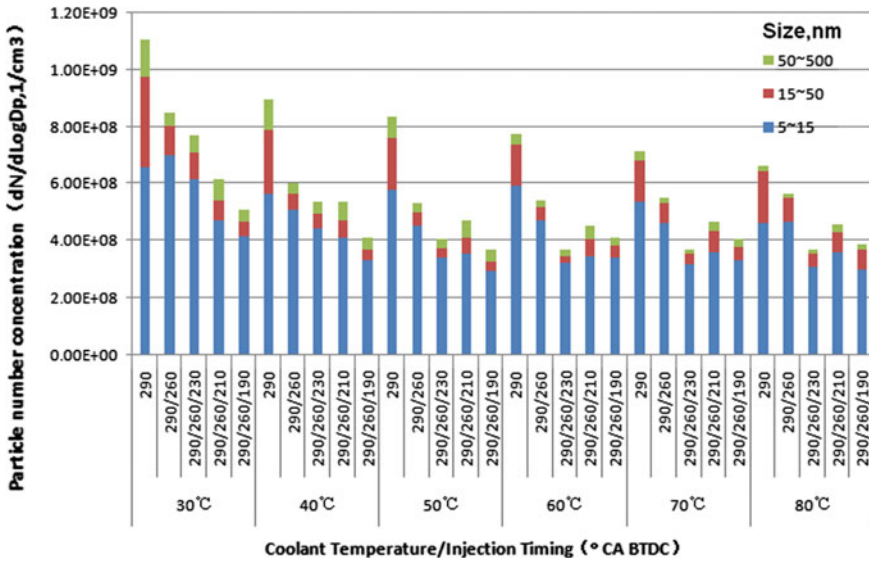


Fig. 20.7 Effects of different injection times on particle number concentration variation of particle size distribution during warm up process

the warm-up process. The particle number concentration decreased with the increase of coolant temperature. With coolant temperature increased from 30 to 40 °C, the particle number concentration sharply decreased. After 50 °C, the particle number stabilized. When the coolant temperature was at 30 °C, the size of particle number concentration behaved as bimodal distribution of nucleation mode and accumulation mode. Accumulation mode particle number concentration increased with the decreased coolant temperature. It is mainly because that accumulation mode particles consisted of soot and HC which through condensation adsorbing other substances to form large particle agglomerates [12]. When the coolant temperature was 30 °C, the in-cylinder combustion status was relatively poor. Due to the wall quenching, THC and soot emissions became higher. With the increase of coolant temperature, the size of particle number concentration performed as unimodal distribution of nucleation mode, and its peak concentration concentrated at 5–15 nm. The peak concentration of accumulation mode was lower than nucleation mode, which was not obvious. However, the peak concentration of nucleation mode showed a decreasing tendency. With the increase of coolant temperature, exhaust temperature rose, which was beneficial for oxidizing unburned HC in the exhaust and accumulation mode particles, so that accumulation mode particles reduced. Comparing to the third injection timing for three different injection modes, it showed that, the number of particles was least when third injection was at 230°CA BTDC. With the third injection timing advanced, injection interval time was shortened, fuel and gas mixing time was prolonged. As more uniform mixture improved particulate emissions. In addition, contrast to the single

injection, the multiple injection not only improved the THC emissions, but also reduced particulate emissions. Due to the fact that multiple injection shortened each injection injector pulse width, reduced the fuel beam penetration distance, which reduced the fuel film formation on the top of the piston and the possibility of the spray hitting on the wall. As multiple injection was more conducive to spray evaporation diffusion, combustion state was better than that of the single injection, unburned HC and soot relative reduced, more nucleation mode particles was formed.

20.4 Conclusions

- (a) The multiple injection at intake stroke has a great influence on cylinder pressure and the transient heat released rate. With the increase of injection times and coolant temperature, cylinder pressure increased and its corresponding crank angle was advanced for multiple injection at intake stroke. While the peak transient heat released rate increased, but its occurrence timing was slightly advanced.
- (b) The THC emissions of multiple injection has decreased than the single injection, the same to NO_x emission. With the coolant temperature increase, THC emissions decreased gradually and then stabilized. However, NO_x emissions gradually rose.
- (c) Multiple injection at intake stroke reduced particle number concentration under warm up conditions, and the particle number concentration decreased with the increase of coolant temperature. However, when at low coolant temperature, the size of particle number concentration performed as bimodal distribution of nucleation mode and accumulation mode. The peak size of particle number concentration behaved as a unimodal distribution with the increase of coolant temperature.
- (d) Comparing with the third injection timing for three different injection modes, it showed that, with the advance in injection time and the shorten in injection interval time, when the third injection time was at 230°CA BTDC, the peak cylinder pressure was the highest, the combustion condition was the best, THC emissions was the lowest and NO_x emissions was the highest.

References

1. Gumus M (2009) Reducing cold-start emission from internal combustion engines by means of thermal energy storage system. *Appl Therm Eng* 29(4):652–660
2. Yao C et al (2003) Study on unburned hydrocarbon emissions from diesel engine during warm-up period. *J Tianjin Univ* 36(5):557–561

3. Zhang D et al (2010) Influence of coolant temperature on diesel engine emissions. *Trans CSICE* 28(6):510–513
4. Whelan I, Smith W, Timoney D et al (2012) The effect of engine operating conditions on engine-out particulate matter from a gasoline direct-injection engine during cold-start. SAE Technical paper, 2012
5. Kim J, Lee JS, Rew SH et al (2014) Comparative evaluation of engine control strategy on regulated emissions and nano-particle characteristics of LPG direct injection (LPDI) vehicle during the cold start and the hot phases in the FTP-75 cycle. SAE Technical paper, 2014
6. Ketterer JE, Cheng WK (2014) On the nature of particulate emissions from DISI engines at cold-fast-idle. *SAE Int J Engines* July 2014 7(2):986–994 (2014-01-1368)
7. Montajir RM, Kawai T, Goto Y et al (2005) Thermal conditioning of exhaust gas: potential for stabilizing diesel nano-particles. SAE Technical paper, 2005
8. Kayes D, Hochgreb S (1998) Investigation of the dilution process for measurement of particulate matter from spark-ignition engines. SAE Technical paper, 1998
9. Chung J, Kim N, Choi H et al (2016) Study on the effect of injection strategies on particulate emission characteristics under cold start using in-cylinder visualization. SAE Technical paper, 2016
10. Kim Y, Kim Y, Jun SY et al (2013) Strategies for particle emissions reduction from GDI engines. SAE Technical paper, 2013
11. Choi K, Kim J, Ko A et al (2011) Evaluation of time-resolved nano-particle and THC emissions of wall-guided GDI engine. SAE Technical paper, 2011
12. Whitaker P, Kapus P, Ogris M et al (2011) Measures to reduce particulate emissions from gasoline DI engines. *SAE Int J Engines* 4:1498–1512 (2011-01-1219)

Chapter 21

Study of Start-Stop Technology on a GDI Engine

Jin Li, Weifei Yu, Peng Zhou, Jianrui Zhang, Tao Chen,
Pengyuan Sun and Hua Li

Abstract This paper has developed a start-stop control system on a GDI engine, studied effects on the rate of ignition for expansion cylinder and the start-stop performance without a starter. The experimental results showed a total rate of a successful ignition of the expansion cylinder beyond 70% when the lambda value ranges from 0.6 to 0.7. A multiple fuel injection could improve the rate of ignition with the case of single injection compared, the rate of ignition can be increased by averaged 4% for two times fuel injection, a four times fuel injection can increase the rate of ignition by averaged 5%. When the exhaust valve opening timing was retarded to 160 °CA ATDC increased success rate of engine starting. It will be 0.62 s for engine start by a start-stop starter, however 0.39 s by direct injection start-stop.

Keywords GDI engine · Expansion cylinder · Lambda · Fuel injection times

21.1 Introduction

As the fuel consumption regulations and emission regulations gradually upgrade, the requirements for passenger car of energy saving and emission reduction are increasing strictly. Traffic jams cause the car working at idle speed condition for long time, consuming more fuel, producing higher emissions. Idling Start-stop technology will contribute to stop the engine when the car is running at the idle speed mode for long time, and start the engine quickly, reduce vehicle fuel consumption and emission, which is employed more and more widely [1, 2]. At present, the technology of the idle start-stop scheme mainly has three ways as follows: Independent of the starter and generator scheme, integrated starter generator

J. Li (✉) · W. Yu · P. Zhou · J. Zhang · H. Li
R&D Center Engine Department, FAW Group Co., Changchun, China
e-mail: lj20050986@163.com

T. Chen · P. Sun
R&D Center Automotive Electronics Department, FAW Group Co., Changchun, China

scheme, direct injection start-stop scheme [3–5]. In the world, Mazda automobile manufactures use direct injection start-stop scheme and obtain the relatively good effect. The direct injection start-stop scheme could results in more quiet and quick engine start, less cost and more effective advantages of fuel saving and emission reduction. In this paper, a direct injection gasoline engine is applied as the prototype, a direct injection start-stop control system is developed, the effect of λ and injection time on rate of ignition for the expansion cylinder is mainly studied, without considering emissions, compared the direct injection starting performance to starting with starter auxiliary performance.

21.2 Start-Stop Technology Research

21.2.1 Prototype Engine Parameters

A GDI engine of FAW serves as prototype engine in this paper. The engine information is specified in Table 21.1.

21.2.2 Development of Start-Stop Control

The logical architecture of start-stop control system is shown in Fig. 21.1. When engine starts successfully, and start-stop control system exits automatically, engine will entry the normal working mode.

21.2.2.1 Engine Stop Position Detection

To determine engine stop position accurately, three hall speed sensor is applied to replace the ordinary crankshaft speed sensor. The sensor can detect engine reverse in the engine stopping process, so ECU can judge the direction of engine rotation, and calculate the actual number of teeth passing through and stop position degree. Due to crank shaft of prototype have 58 teeth, 6 °CA each tooth, so stop position

Table 21.1 Main engine information

Contents	Parameters
Displacement (L)	1.995
Cylinder numbers	4
Bore × stroke (mm)	84 × 90
Firing order	1-3-4-2
Compression ratio n	10.3
Valve type	VVT

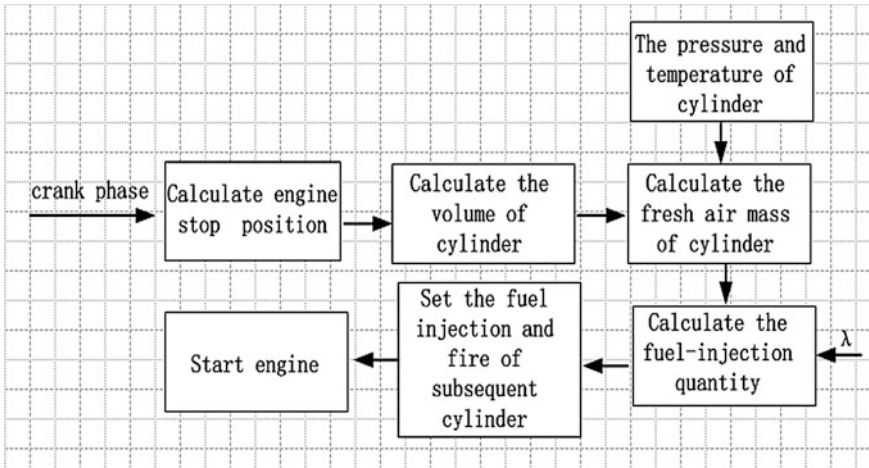
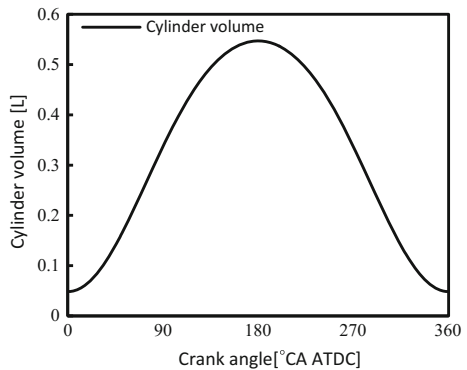


Fig. 21.1 Logical architecture of start-stop control system

Fig. 21.2 Cylinder volume



error is in the range of plus or minus 6 °CA. According to the engine crankshaft angle, the expansion and compression cylinder, stop position angle is identified, and TDC is regarded as 0 °CA.

21.2.2.2 Cylinder Volume Calculation

Cylinder volume is calculated by parameters of engine stop position crank degree, engine displacement, compression ratio, stroke, length of connecting rod. Due to the model involve the cosine and sine angle calculation which is not suitable for running in the ECU, the cylinder volume along with the change of the crankshaft angle is calculate as shown in Fig. 21.2, the precision is 0.5 °CA and stored in the ECU.

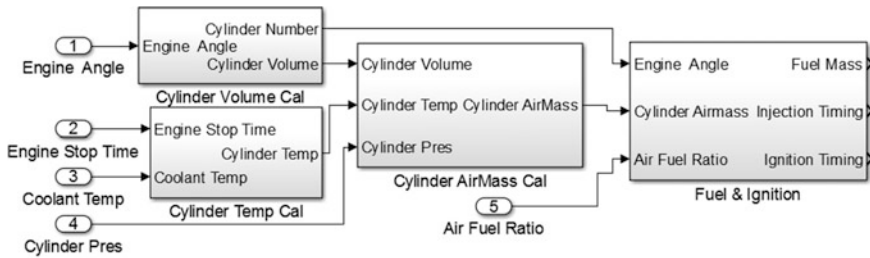


Fig. 21.3 Fuel injection quantity calculation

21.2.2.3 Fuel Injection Quantity Calculation

Firstly, fresh air in the expansion cylinder and compression cylinder is calculated according to the volume of cylinder. And then fuel injection mass is calculated according to Lambda, the calculation model is shown in Fig. 21.3. For subsequent experimental study on the effect of multiple injections on the rate of ignition for expansion cylinder, the control function of two times injection and four times injection is developed which also support the function of manual multiple times engine ignition. At the same time, when engine stop, the parameter of fuel injection and ignition cannot be calculated based on crank shaft angle, so those parameters are calculated based on time scale.

21.2.2.4 Test Bench Development

For the realization of the engine start-stop control functions, the original engine wiring harness needs to be changed. The starter is controlled by key and CANape software independently, and can be set the starter working mode and duration of gear mesh. The prototype on test bench is mounted cylinder pressure sensor for each cylinder in order to record and analyze each cylinder pressure through combustion analyzer when the engine is working.

21.3 Experimental Result Analysis

21.3.1 Factors of the Rate of Ignition for Expansion Cylinder Analysis

In order to study factors of the rate of ignition for expansion cylinder fully in this paper, the rate of ignition into ignition is divided into the first time ignition which ignite by the command of ECU automatic after fuel injection time interval and the second time igniting which ignite for the second time through CANape control

interface manually in case of the ignition for the first time failed. Other parameters are given by constant values on experience. Throttle Valve angle will be set at 11%. The angle range of expansion cylinder stop position is in the range of 96–120° ATDC. The effects of Lambda, injection times on the rate of ignition for expansion cylinder are mainly studied.

21.3.1.1 Lambda Influence on the Rate of Ignition for Expansion Cylinder

When the engine is in stop condition, there is no severe air flow in the cylinder, and lambda value plays an important role on the rate of ignition. The influence of lambda value on the total rate of ignition for expansion cylinder is shown in Fig. 21.4. We can conclude that as the lambda value increase, the tendency of the total rate of ignition which include the rate of first time ignition and second time ignition increase firstly and then decrease. When the lambda = 1, the total rate of ignition is 40% which is the lowest. When the lambda = 0.7, the total rate of ignition is 80%, which is the highest. When the lambda is in range of 0.6–0.7, the total rate of ignition is all above 70%. The influence of lambda value on the rate of first time ignition and second time ignition is shown in Fig. 21.5. We can conclude that as the lambda value increase, the tendency of the rate of first time ignition increase firstly and then decrease. The rate of second time ignition has almost no change, which is at about 10%. When the lambda is in range of 0.6–0.7, the rate of first time ignition is high which was all above 60%. This is mainly because as the gradual increase of lambda, the mixture concentration in cylinder is increasing, and the rate of ignition mainly depends on the concentration of the mixture near the spark plug, the concentration range in cylinder is only in appropriate range which can be ignited, if the concentration is too thick or too thin, which cannot be ignited, cause ignition failure. When the lambda values is in range of 0.6–0.8, the total rate of ignition is more than 50%.

Fig. 21.4 The influence of lambda value on the total rate of ignition

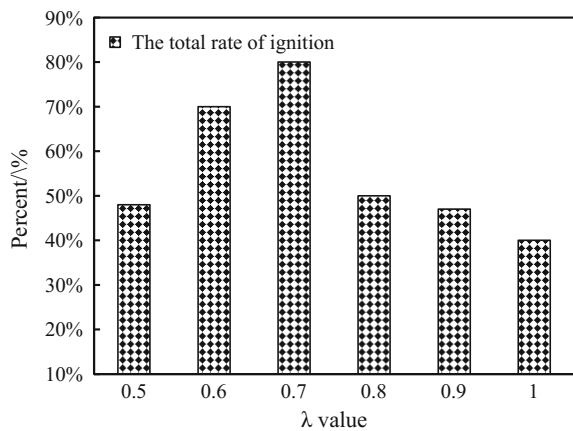
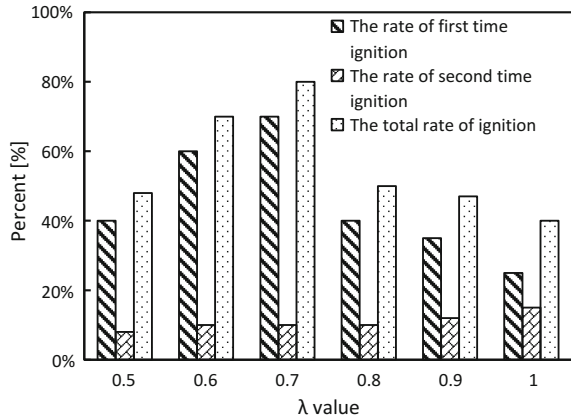


Fig. 21.5 The influence of lambda on the rate of first time ignition and second time ignition



and at other lambda value, the total rate of ignition is low. With the influence of the number of times of the rate of ignition follow-up study, the lambda value is fixed between 0.6 and 0.8 for expansion cylinder.

21.3.1.2 Influence of Injection Times on the Rate of Ignition for Expansion Cylinder

Multiple injections can improve the uniformity of the mixture in cylinder, increase the rate of ignition. Lambda value is fixed between 0.6 and 0.8, and the injection interval is fixed by 50 ms, and fuel injection quantity is constant. The influence of injection times value on the total rate of ignition is shown in Fig. 21.6. We can conclude that in addition to lambda = 0.7, as injection times increase, the total rate of ignition increase compared with single injection. On average, the total rate of ignition for two times injection increase by 4%, and the total rate of ignition for four times injection increase by 5%. When lambda = 0.7, compared with a single injection, the total rate of ignition under reduce for both two times injection and four times injection, two times injection reduce by 26%, four times injection reduce by 30%. The influence of multiple injections on the rate of first time ignition and second time ignition for expansion cylinder are shown in Figs. 21.7 and 21.8. We can conclude that generally, multiple injections can increase the rate of first ignition, compared with single injection, on average, the rate of first ignition for two times injection can increase by 2.5%, the rate of first ignition for four times injection can increase by 15% from Fig. 21.7. When lambda = 0.7, compared with single injection, the total rate of ignition under the two times injection and four times injection reduce. As the Fig. 21.8 shown, compared with single injection, two times injection and four times injection have smaller influence on second time ignition. This is largely depend on the fact that the fuel pressure of high pressure fuel rail is very high during idle shutdown time, the fuel injection pressure of a single injection is high, which makes fuel easy go to the

Fig. 21.6 The influence of injection times on the total rate of ignition

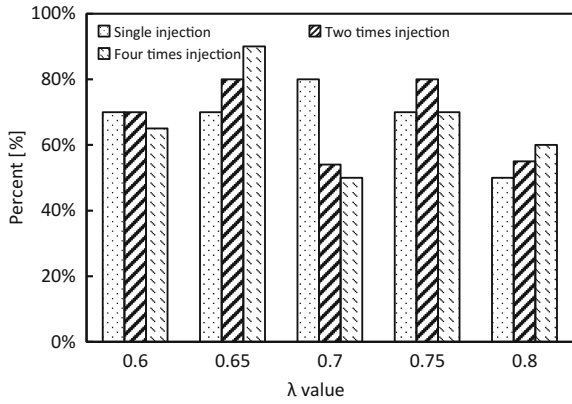


Fig. 21.7 The influence of multiple injections on the rate of first time ignition

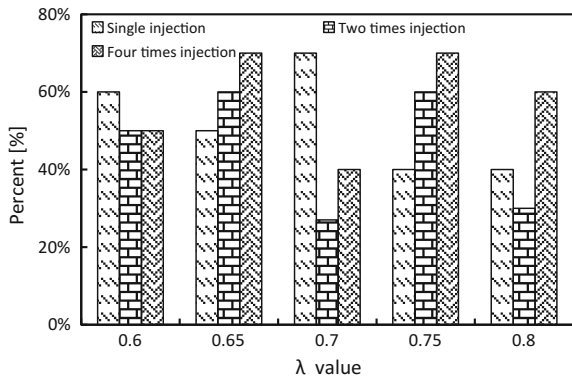
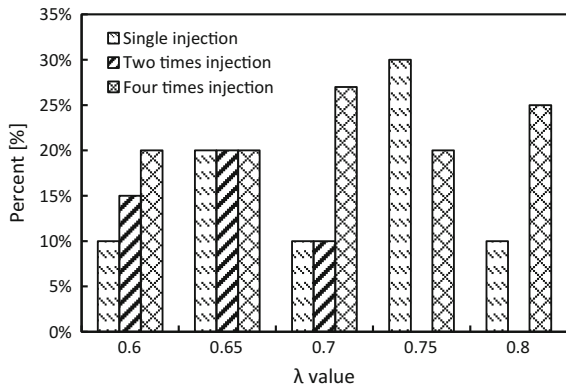


Fig. 21.8 The influence of multiple injections on the rate of second time ignition



cylinder wall and reflect, results in spark plug wet, reduces ignition efficiency. Multiple injections can decrease the energy of each injection, improve the effect of fuel wall reflection and the uniformity of the mixture in cylinder, cause the mixture near the spark plug more conducive to ignition.

21.3.2 Engine Starting Performance Research

21.3.2.1 The Opening Time of Exhaust Valve Influence on the Engine Starting Performance

The opening time of exhaust valve has a greater influence on the performance of engine power, the maximum angle which expansion cylinder can arrive after injection and ignition of the original opening time of exhaust valve at different engine stop position angles is shown in Fig. 21.9. The maximum angle which expansion cylinder can arrive after injection and ignition is mainly less than 180 °CA, causes engine fail to pass through the BDC, leads to the failure of engine starting. The combustion pressure of cylinder at the 120 °CA ATDC for expansion cylinder is shown in Fig. 21.10. It can be found that the cylinder pressure of the expansion cylinder have two different falling gradient in the process of decline. Considering the lift curve of exhaust valve, the exhaust valve is opened too early, which leads to the pressure in cylinder decrease quickly and reduces the duration of power stroke for the expansion cylinder. In order to improve the efficiency of engine, the exhaust valve opening angle is delayed to 160 °CA in this paper. The maximum angle which expansion cylinder could arrive for the exhaust valve opening angle at 160 °CA is shown in Fig. 21.11. It can be concluded that retarding the exhaust valve opening angle appropriately can increase the rate of engine successful start.

Fig. 21.9 Maximum angle of expansion cylinder

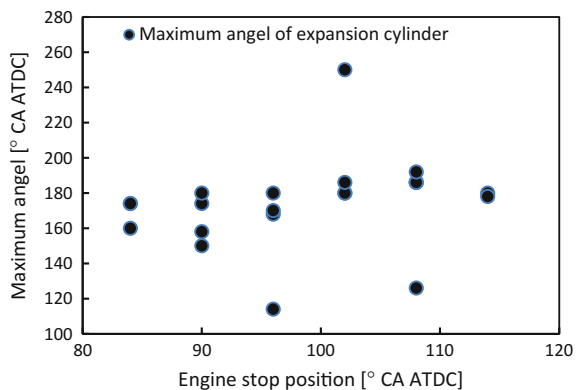


Fig. 21.10 Combustion pressure at the 120 °CA ATDC

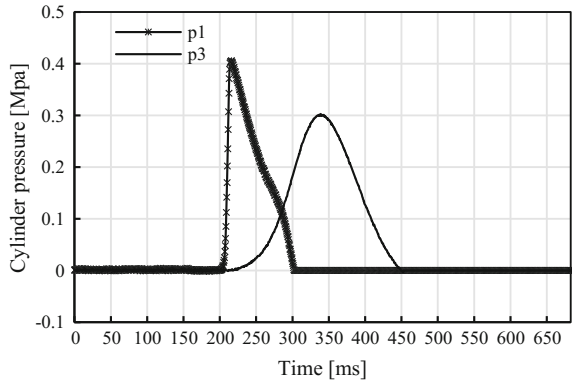
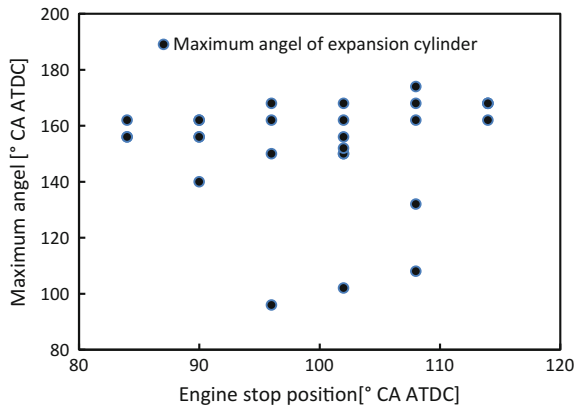


Fig. 21.11 The maximum angle of expansion cylinder



21.3.2.2 The Performance of Starting Result Contrast

Based on the previous experiment research in this paper, a preliminary study is done on the performance of direct injection starting engine, the success of engine starting is defined that engine speed accelerates from 0 to 800 r/min. Without considering the effect of emissions, contrast the direct injection starting performance with starting with starter auxiliary performance. The cylinder pressures in the process of the direct injection starting and starting with starter auxiliary are shown in Figs. 21.12 and 21.13. 0.39 s is needed for the engine speeds by 0–800 r/min in the process of direct injection starting, and 0.62 s for the starting with starter auxiliary. Consider the time of preparing for injection and ignition for the direct injection starting, generally, the two kinds of starting engine above cost about the same time in the start process. Compared to the starting engine with starter auxiliary, noise and vibration of the direct injection starting is much smaller, and has no effect on the starter working life.

Fig. 21.12 The cylinder pressure in the progress of the direct injection starting

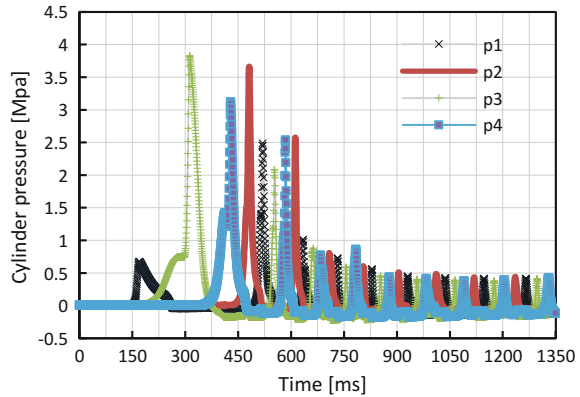
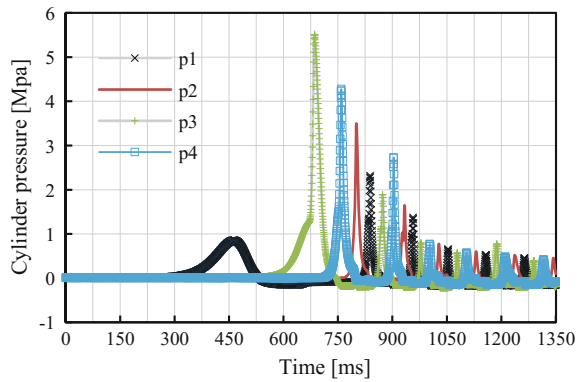


Fig. 21.13 The cylinder pressure in the progress of the starting with starter auxiliary



21.4 Conclusions

The main conclusions are summarized as follows: (1) the developed start-stop control strategy meets the requirements of the direct injection of start-stop system. (2) As the lambda value increase, the total rate of ignition increases firstly and then decreases. When the lambda is in range of 0.6–0.7, the total rate of ignition is all above 70%. (3) As the injection times increase, the total rate of ignition increases compared with single injection. On average, the total rate of ignition for two times injection increases by 4%, and the total rate of ignition for four times injection increase by 5%. On the whole multiple injections can improve the rate of first ignition. (4) Putting off the exhaust valve opening angle to 160 °CA can improve the efficiency of engine. It need 0.39 s that the engine speeds by 0–800 r/min in the process of direct injection starting, and need 0.62 s for the starting with starter auxiliary.

References

1. Guo X, Liu L, Wei C, Ge W (2016) The development and research of the fuel economy standards for passenger vehicles in China. *Small Intern Combust Engine Vehicle Tech* 45 (01):93–96
2. Pei Y, Ji T (2012) Research on engine start-stop technology *auto engineer* 2012(7):17–19
3. Bishop J, Nedungadi A, Ostrowski G et al (2007) An engine start/stop system for improved fuel economy. *SAE Paper 2007-01-1777*, 2007
4. Gao B, Svancara K, Walker A (2009) Development of a BSG micro hybrid system. *SAE Paper 2009-01-1330*, 2009
5. Zhao Y, Chen J, Zhu Z, Le Z, Zhao F (2012) Development status and analysis of start-stop technology in automotive manufacturers in china. *Auto Eng* 5:26–30

Chapter 22

The Study of Friction and Wear Capability of Piston Ring Coatings

Wenping Li and Yun Lu

Abstract The friction and wear capabilities of four coatings piston ring which Chromium, PVD, PCVD and GDC were studied with simulated way. The results indicate that GDC coating shows the minimum wear rate and the lowest friction coefficient, while the Chromium coating shows the worst friction and wear capability. The wear rate of GDC ring is only 15% of Chromium ring.

Keywords Piston ring coatings · Friction and wear

22.1 Introduction

The piston assembly (piston ring and cylinder bore) is one of the key parts of the internal combustion (IC) engine [1]. Its performance will directly determine the performance of the whole engine. It is reported that the piston assembly is responsible for 45% of the total engine energy loss due to friction in IC engines [2].

Coating technology is one of the effective ways to improve wear resistance of engine critical friction pair. With the development direction to high speed and load, the traditional coating technology can no longer meet the demand for the development of low friction and low emissions in modern automobile industry.

In this paper, the tribological properties of PVD, PCVD, and GDC coatings were compared with Chromium coating. The friction and wear capabilities of piston rings with different coatings were studied and the wear mechanisms were analyzed. For saving cost, the tribological properties of piston ring and cylinder bore were studied with simulation method generally [3].

Therefore, the friction and wear behavior of piston ring coatings were simulated on laboratory in this paper. Because the first ring undress the worst condition [4], so this paper selected the first ring as the study object.

W. Li (✉) · Y. Lu
China FAW Corporation Limited R&D Center, Changchun 130011, China
e-mail: liwenping@rdc.faw.com.cn

22.2 Experimental

22.2.1 Tribotests and Materials

Tribotests were conducted on a UMT high temperature reciprocating tribotester, where the schematic diagram of the tribology test is shown in Fig. 22.1. Four kinds of coated piston rings were taken as the upper specimen. The coatings are Chromium, PVD, PCVD, and GDC, respectively. The lower specimen was cut from cast iron cylinder bore.

22.2.2 Test Parameters

Table 22.1 lists the test parameters. The friction and wear test repeat three times with the same standard. The lubricating oil which volume is 0.5 ml was added before test. The class of lubricating oil is CI.

The wear resistance of piston ring and cylinder bore evaluated by wear rate. The wear volumes of piston ring and cylinder bore were measured with 3D Profiler.

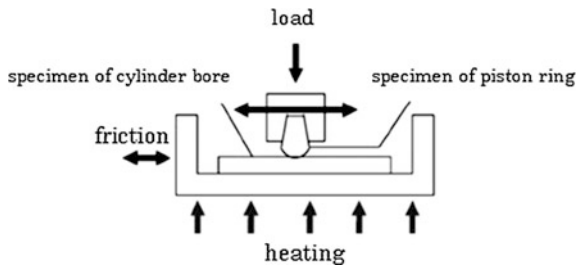


Fig. 22.1 The schematic diagram of the tribology test

Table 22.1 Test parameters

	Load (N)	Temperature (°C)	Time (min)	Remarks
Running step	50	25	5	Frequency: 15 Hz Amplitude: 4 mm Velocity: 0.24 m/s
Test step	200	180	240	

22.3 Results and Analyze

22.3.1 Material Inspection

The material inspection of piston ring listed in Table 22.2. The hardness of cast iron cylinder bore is 220 HBW.

Figure 22.2 shows the section morphology of piston ring coatings.

Table 22.2 The material inspection of piston ring

No	Coating	Matrix hardness (HBW)	Coating hardness (HV0.1)	Surface roughness (Ra)
1	Chromium	341–352	821–836	0.1894
2	PVD	360–372	1217–1246	0.2385
3	PCVD	241–245	794 –813	0.2938
4	GDC	401–413	865–878	0.0796

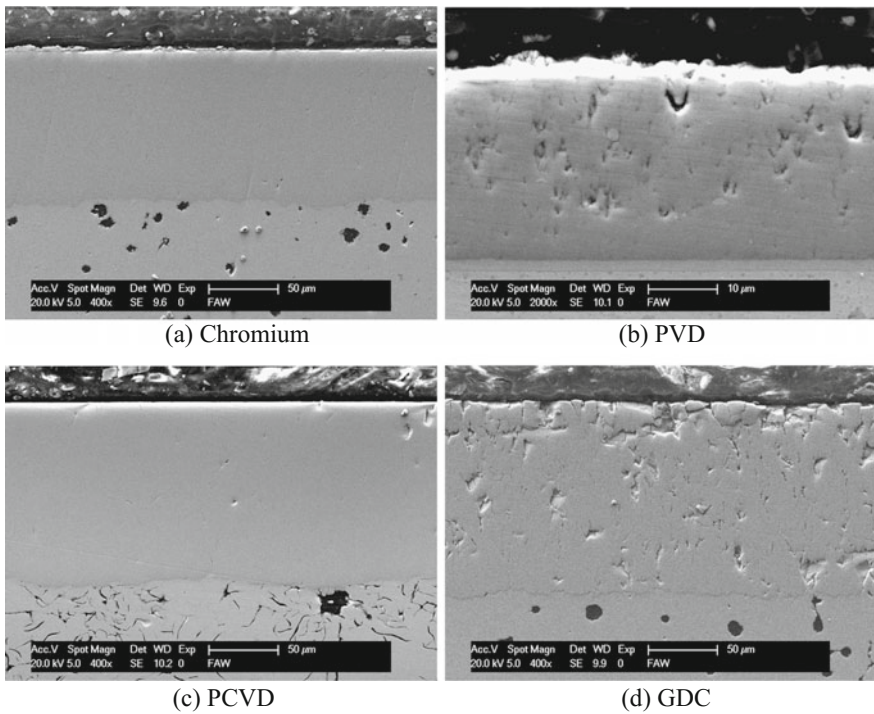


Fig. 22.2 The section morphology of piston ring coatings

Table 22.3 Friction coefficient

No	Coating	Friction coefficient
1	Chromium	0.1258
2	PVD	0.1154
3	PCVD	0.1136
4	GDC	0.1033

22.3.2 Friction Coefficient

Table 22.3 shows the friction coefficient of the four kinds of coated piston rings while sliding against the same cast iron cylinder bore material lubricated with CI-15W-40 oil. The lowest friction coefficient is GDC coating.

22.3.3 Wear Rate

The results of wear rate shows in Fig. 22.3. The wear rate of GDC coating is lowest whereas Chromium coating is highest. The wear rate of GDC coating is 15% of Chromium coating.

22.3.4 SEM Analyses of Wear Tracks

Figures 22.4 exhibit the SEM images of the wear tracks on the Chromium piston ring (upper specimens) and its counterpart (lower specimens). It is obvious that the wear areas of piston rings and cylinder bore were ploughed along the sliding direction. It can be seen that some holes resulted in plastic deformation in the worn area of cylinder bore, and some cracks extended in local area. The wear mechanisms of Chromium piston ring and its counterpart are abrasive wear and fatigue wear.

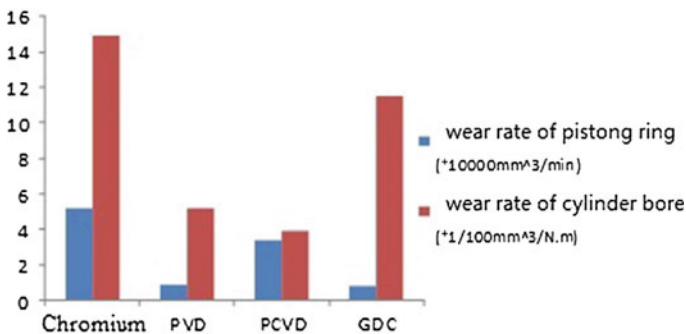


Fig. 22.3 The wear rate of piston ring and cylinder bore

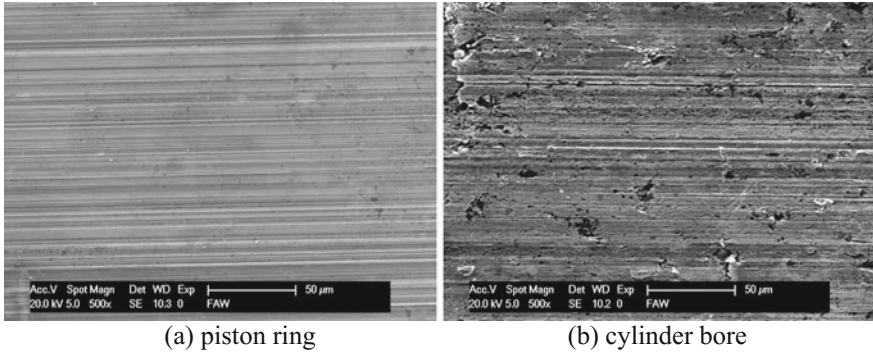


Fig. 22.4 The SEM images of Chromium piston ring and its counterpart (cylinder bore)

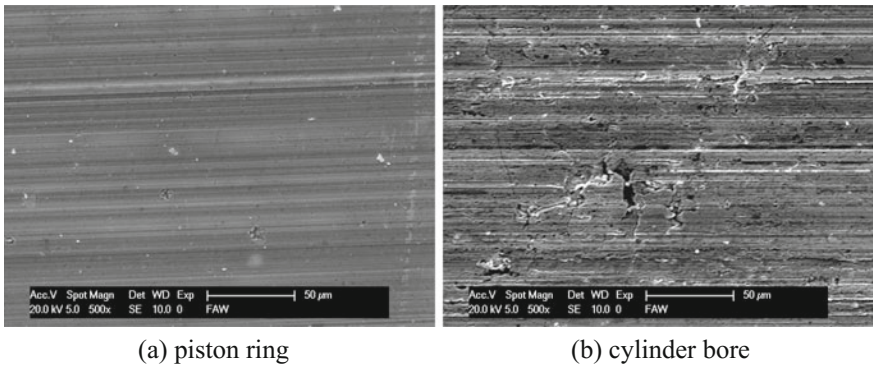


Fig. 22.5 The SEM images of PVD piston ring and its counterpart (cylinder bore)

The SEM photographs of the wear tracks on the PVD piston ring and its counterpart were shown in Fig. 22.5. It is seen that some furrows and holes on worn surface of piston ring. The wear mechanisms of PVD piston ring are abrasive wear and fatigue wear. It is note that many holes which formed with plastic deformation on the worn surface of cylinder bore, and some cracks can be seen. The wear mechanism of cylinder bore is fatigue wear.

Figures 22.6 show the SEM images of the wear tracks on the PCVD piston ring and its counterpart (cylinder bore). It is seen that many furrows on worn surface of piston ring. The wear mechanisms of PCVD piston ring is abrasive wear. It can be seen that many furrows, holes and pits on the surface of cylinder bore. The wear mechanisms of cylinder bore are fatigue wear and abrasive wear.

Figures 22.7 show the SEM images of the wear tracks on the GDC piston ring and its counterpart (cylinder bore). It is obviously that the initial honing traces can

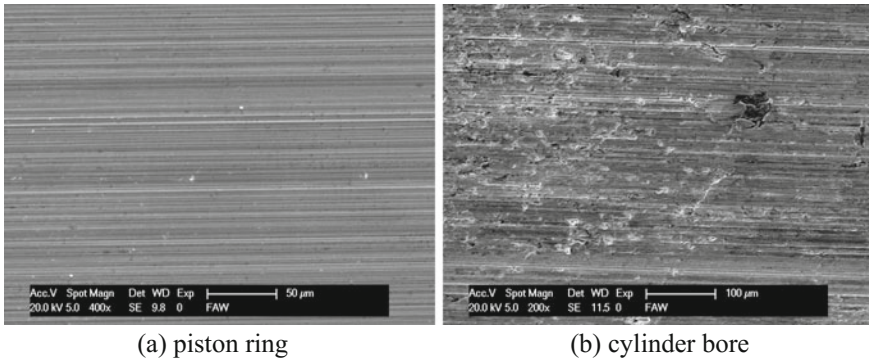


Fig. 22.6 The SEM images of PCVD piston ring and its counterpart (cylinder bore)

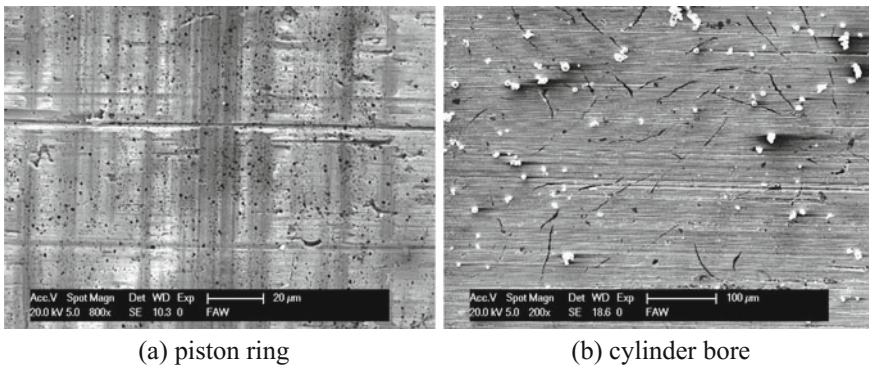


Fig. 22.7 The SEM images of GDC piston ring and its counterpart (cylinder bore)

be seen on worn surface of GDC piston ring. The wear furrows evenly shallower than the honing traces. It can be seen some tiny furrows on worn surface of cylinder bore. The wear mechanisms of piston ring and cylinder bore are abrasive wear.

22.3.5 Discussion

There are many factors influenced the tribological properties of piston ring and cylinder bore, such as hardness, surface physical chemical properties, etc. In this paper, CrN coating was deposited with PVD technology. The wear rate of PVD ring is just higher than GDC ring. The EDS results show that some Calcium, phosphorus and sulfur can be seen on surface of PVD ring and its counterpart. The nitrogen, chromium and oxygen on PVD ring react with upper elements, and the protective film was generated [5]. The high hardness and low roughness of CrN ring make the

cylinder bore deformed in the initial running stage. Therefore, the cylinder bore and CrN ring form the ideal counterpart. The wears of this counterpart decreased.

The surface infiltration of composite ceramic technology was used in PCVD ring. Because the ceramic particles reach the Nano scale, the ceramic morphology is hardly to observe by SEM. The high hardness of ceramic particles improves the wear resistance of piston ring.

The wear rate of GDC ring is the lowest among four samples. However, the wear rate of cylinder bore which paired with GDC ring is slightly greater.

22.4 Conclusions

The friction coefficient and wear rate of GDC piston ring is the lowest. However, the wear rate of cylinder bore paired with GDC ring is slightly greater. The wear rates of Chromium piston ring and its counterpart are the highest. The improvements of PVD, PCVD and GDC technologies were attributed to the hard particles were deposited on surface of piston ring.

References

1. Zhang Y, Lu Y (2002) The friction problems and its countermeasures of piston ring. *Automobile Technol Mater* 2:1–5
2. Zhao W (2005) Tribological performance of chromium nitrided piston ring coating. *Lubr Eng* 2:59–62
3. Tung SC, Schwartz SE, Borgan KB (2000) Assessment of correlation between bench wear test results and engine cylinder wear, Short-Trip Service. SAE Tech Pap Ser 1:2947–2953
4. Lu Y, Han Z (2004) The study of tribological properties of piston ring on diesel engine. *Mater Prot* 37(07B):49–53
5. Liu Y, Meletis EI (1997) Evidence of graphitization of diamond like carbon films during sliding wear. *J Mater Sci* 13:3491–3495

Chapter 23

Direct Injection Start-Stop Piston Final Stop Position Modelling and Analysis

Peng Zhou, Jin Li, Jianrui Zhang, Weifei Yu, Qingtao Si
and Tuozhou Yu

Abstract When it comes to GDI ‘start-stop’ technology, the control of final stop crank angle can never be neglected. The probability distribution of this final angle could be obtained via repetitious engine stop experimental method, the principle of which however, could not. As a result it seems impossible to get a concise control on the engine stop process. Dynamic model ‘engine stop’ has been established, simplified and modified in order to identify the key factors that have an effect on engine stop. The model was verified by related experiment to address the simulation demands. The analysis on simulation results provide us several essential conclusions that the factors, specifically heat transfer and leakage as well as the initial speed in compression top dead center of final stroke, will cause a strongly different piston final position. The engine final position will be relatively located in the range 0–10°CA, 60–90°CA ATDC.

Keywords Piston final stop position · Modeling · Key factors

23.1 Introduction

Vehicle is frequently operating in idle condition when driving in large mount of vehicle or traffic jam urban area. For one thing idle condition results in unnecessary fuel consumption, for another idle condition bring about excessive emission problem. Engine start-stop technology has been gradually becoming the standard configuration of passenger cars. Sophisticated start-stop technology contributes to vehicle emission and fuel consumption decrease [1]. One of the key factors of this technology is start period. It is essential whether the engine could start to idle condition in short period. In 48 V start-stop system, BSG motor can provide extra torque in acceleration and start condition, which enable the finish of start in 250 ms [2, 3]. Besides direct injection assisting start could alleviate the motor burden and utilize a certain torque

P. Zhou (✉) · J. Li · J. Zhang · W. Yu · Q. Si · T. Yu
Engine Department, FAW Group Co. R&D Center, Changchun, China
e-mail: zhoupeng@rdc.faw.com.cn

produced by combustion of fuel injection. Regarding the BSG motor start or direct injection assisting start, only the piston is located in proper position, can the engine start smoothly and quickly. For one thing three hall sensor contributes to record the crank overturn and final phase when engine stop. For another the final crank phase is controllable via adjusting the idle speed and throttle opening. There exist a series of research on the crank final stop phase via experiment method, which can roughly identify the piston stop position and analysis the distribution regularity. Nevertheless experiment method is inevitably limited by the experiment times. Start-stop process is time consuming and experiment cannot analyze essential factors and universal regularity concerning crank stop phase. A detailed dynamic model is based on experiment data and simulation data [4]. The model consists of speed, charge efficiency, heat transfer, leakage and friction torque based on crank angle and other related factors. According to the calculation results, final stop position and effect factors are analyzed in detailed.

23.2 Engine Stop Process Modeling and Analysis

Torque that produced by cylinder charge, friction, crank speed in the dead center of final stroke have effects on piston location when engine stop from idle. Although friction torque is frequently related with engine speed and engine temperature, it is strongly relevant to crank angle in low speed condition. Cylinder pressure results from adiabatic compression and expansion process and heat transfer, leakage process. The research is based on an in-cylinder direct injection engine, 2.0 L, four cylinders, bore 84 mm, stroke 90 mm, compression ratio 10.3, and nominal power 145 kW, ignition order 1-3-4-2.

23.2.1 Engine Stopping Process Modeling

The motoring cylinder pressure can hardly be obtained by bench test when speed ranges from 0 to 600 r/min due to the resonance. Extrapolation and prediction of GT-POWER is applied for the calculation of intake manifold pressure and cylinder curve in very low speed which is calibrated via experiment. The relation between speed and cylinder pressure is shown in Fig. 23.1 that speed ranges from 0 to 100 r/min, and throttle closes to 0 after fuel cutting off. Cylinder pressure falls with the decrease of speed.

Cylinder pressure varies with the change of cylinder volume, heat transfer and leakage during the dynamic process of engine stop. Heat transfer depends on temperature difference and relevant period. There is little change with intake manifold pressure when engine speed is low that stay in approximate 1 bar during the last stroke, which results in little change with the air input of cylinder. Longer heat transfer period causes lower cylinder pressure, the curve of which is close to

isothermal process. In contrast the curve is close to adiabatic process in high speed condition. Usually the highest speed of last stroke is not more than 400 r/min. the cylinder pressure in the compression top dead center with speed from 0 to 500 r/min is shown as Fig. 23.2. The highest cylinder pressure exists in the speed 200–300 r/min due to combined action of inertia and pump loss. The actual cylinder pressure would locate between certain boundaries of speed-cylinder pressure with deceleration as shown in Fig. 23.3. Besides the Fig. 23.3 illustrates one conclusion that theoretically the smallest resultant resistance in stop process follows the lower line in the picture and the upper line represents the highest resultant resistance condition. Here the highest and smallest ones are described as highest resistance and lowest resistance respectively. It is impossible that the cylinder pressure of compression top dead center at the end of one stroke is beyond the one at the start. According to analysis on the smallest speed that enables the piston to move to below dead center in different engine speed condition, some conclusions can be drawn. It notes that the research object is aimed at the cylinder during the last expansion stroke and 0° angle crank is given by compression top dead center. The modeling and analysis is based on the final stroke before stop in order to simplify the problem. The initial crank angular velocity of the final stroke should be given from 0 to ω , ω serves as the critical value that enable the piston to

Fig. 23.1 Relation between low level speed and cylinder pressure

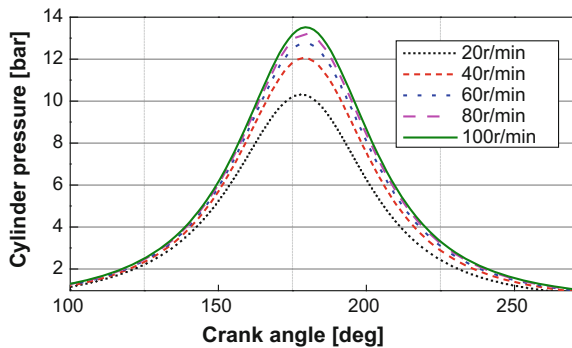


Fig. 23.2 Relation between engine speed and compression top dead center cylinder pressure

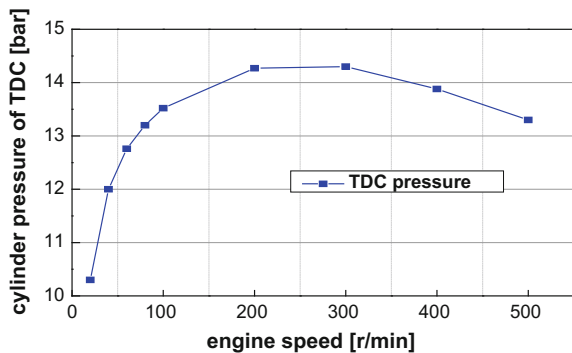
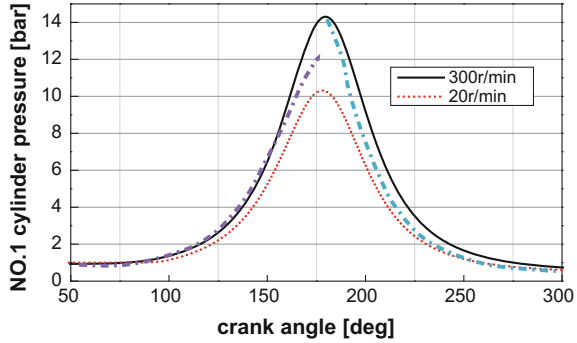


Fig. 23.3 Transient cylinder pressure in engine stop process



move from TDC to BDC, which is calculated based on energy. From the highest resistance to lowest one, the longest distances the piston could reach are calculated in the condition of different cylinder pressure, different initial crank angular velocity of final stroke. Where, the cylinder pressure varies with the crank angle and the influence from air valves is taken into account. In the process of engine stop, fuel is cut off and throttle is fully closed. The friction and pump resistance results in the engine deceleration. Friction torque is correlated with crank angle, engine speed and temperature. The friction torque based on crank angle is measured by torque wrench and the coolant temperature is permanent. The friction torque in common speed is obtained by dynamometer motoring. The cylinder pressure in compression and expansion stroke are simulated via GT-POWER and the moment of inertia is calculated via related software. where $P_1(\alpha)$, $P_2(\alpha)$ is the cylinder pressure of compression and expansion based on crank angle, $T_g(\alpha)$, $T_f(\alpha)$ is the air resultant torque and friction torque, respectively. E_{k0} is work resulting from the resultant torque from TDC to BDC [5].

$$\left\{ \begin{array}{l} E_{k0} = \int_0^{180} [T_g(\alpha) + T_f(\alpha)]d\alpha \\ T_g(\alpha) = T_{gcomp}(\alpha) + T_{gexpan}(\alpha) \\ T_{gcomp}(\alpha_1) = \frac{P_1(\alpha_1)\sin(\alpha_1 + \beta_1)\Gamma}{\cos\beta_1} \\ T_{gexpan}(\alpha_2) = \frac{P_2(\alpha_2)\sin(\alpha_2 + \beta_2)\Gamma}{\cos\beta_2} \\ \alpha_2 - \alpha_1 = \pi \\ \omega = \sqrt{\frac{2E_{k0}}{I}} \end{array} \right. \quad (23.1)$$

23.2.2 Model Solving

It is complex and difficult to obtain the analytic solutions of higher order differential equation, thus by means of writing program, by 0.2–1° of crank angle step

Fig. 23.4 Initial angular velocity enabling piston to reach BDC

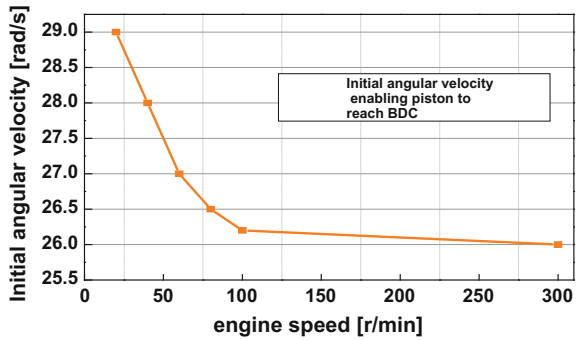
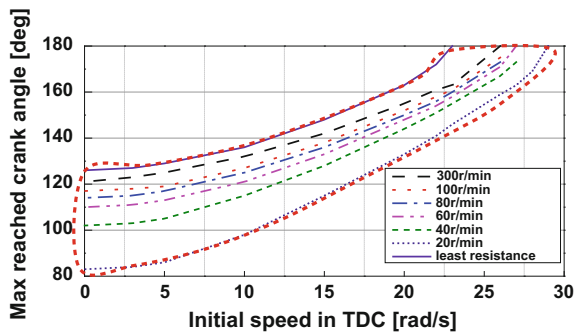


Fig. 23.5 Maximum crank angle the piston could reach



discretizes continuity equation and obtains the numerical solution. The engine speed, indicated torque, friction torque based on crank angle are obtained with leakage and heat transfer process included and experimental verification. As Fig. 23.4 shown, lower initial speed of final stroke demands more energy to reach the BDC and the maximum crank angle the piston could reach in different initial speed is shown in Fig. 23.5. Basically the piston speed is changing continuously, as a result, it is quite complex to identify the heat transfer, leakage, cylinder pressure and speed of any given degree. The red dash circles region where all possible occasions is concluded.

23.2.3 Model Simplification and Modification

If crank speed is 0–60 r/min, no matter accelerate or decelerate, the distance crank goes won't be beyond 6° in this velocity range. Hence the problem could be simplified when the stop process is separated into two parts.

- (1) When engine speed is beyond 60 r/min, one mean value serves as the cylinder pressure input due to the little difference of pressure curve in 60–400 r/min.

- (2) When engine speed is below 60 r/min, crank won't pass more than 6°. The cylinder pressure varies from heat transfer and leakage. Here the pressure drop rate approximately depends on cylinder pressure and is given by the experimental data and linear regression. The pressure varying from volumetric change is calculated as adiabatic process.

When engine speed is quite low, the heat transfer and leakage would have a strong effect on resultant torque as well as final stop position of piston. If these two factors are not considered, the resultant torque is solely related with crank angle. As a result, the crank stop phase would locate in a certain range when the air torque is smaller than friction torque. In fact this certain range should be broadened. Entire engine stop process solving flow is shown in Fig. 23.6. One of the crank reverse processes in final stroke is shown Fig. 23.7. The reverse occurs in crank angle 134° and piston stop in crank angle 67°.

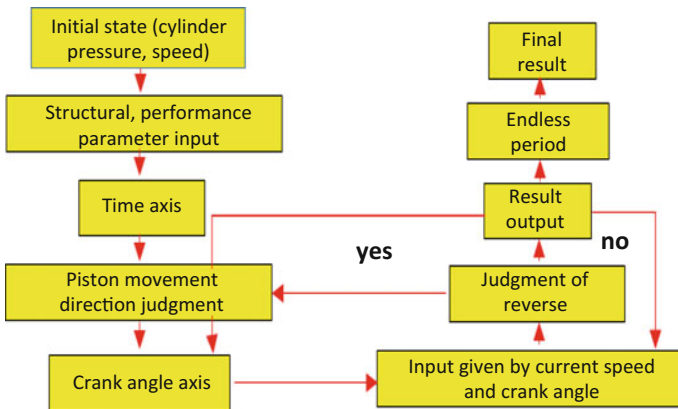
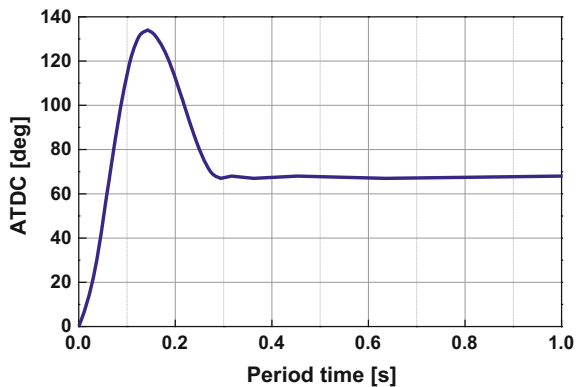


Fig. 23.6 Solving flow of stop process

Fig. 23.7 Crank reverse process



23.2.4 Experimental Verification of Model

The experiment applied for verification of modeling is carried through in the condition of throttle opening 12%. Related experiment bench is shown in Fig. 23.8. Besides the engine would reverse due to the resultant torque affect, thus the cylinder pressure in combustion analyzer should be recorded based on time. A fragment of cylinder pressure happens to reflect the engine stop process as Fig. 23.9 shown. Cylinder pressure is measured via experimental bench and a similar cylinder pressure curve is given by GT-POWER simulation.

Solving the dynamic simulation program, there exist a little difference in the results between calculation and experiment but could address the purpose by means of this modeling method yet as shown in Fig. 23.10. What’s more, concerning the condition that reverse occurs, the reverse position could be reflected exactly as well as the reverse time.

Fig. 23.8 Related experiment bench

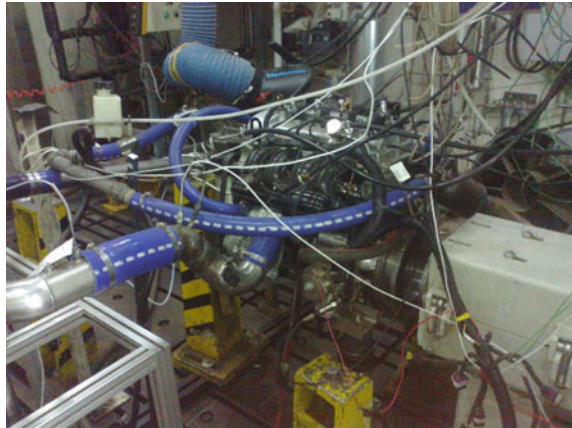
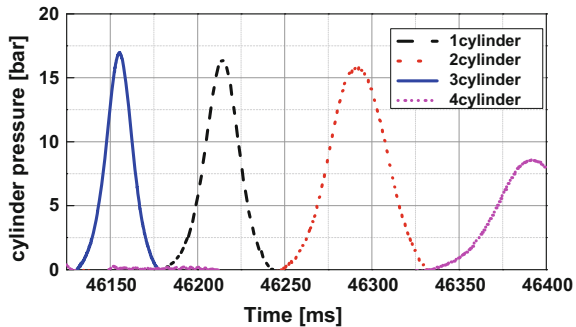


Fig. 23.9 Combustion analyzer time-dependent



23.2.5 Stop Position Calculation via Simulation Experiment

In the vicinity of dead centers, the piston could hardly escape from the dead centers for the friction torque effect when speed is below a limit. As Fig. 23.11 shown suppose five cases from 1.2 to 3 rad/s initial speed, angular speed 1.2 rad/s will result in the piston stopping in the 4° ATDC but 1.5 rad/s gives a different result. The resultant torque imposing on the system is varying with crank angle when piston heads for BDC. The piston is caught when speed is below 1.6 rad/s during 0–8° nearby BDC. To simulate certain stopping process, Monte Carlo method is applied to generate random numbers from 0 to 1 and initial speed. The sample number is given by 1000 to get a similar result with the actual condition. The position of 60–90° ATDC is occupied by more than half of the cases given in Fig. 23.12. It is unreasonable to simply consider the initial speed a random object. Thus three normal distribution of initial speed is applied by expectation of 5, 15 and 25 rad/s (TDC initial speed of final stroke ranges from 0 to 30 rad/s) and variance 2 rad/s. As shown in Fig. 23.13 that several distribution function comparison,

Fig. 23.10 Comparison of time-dependent cylinder pressure experimental calculation

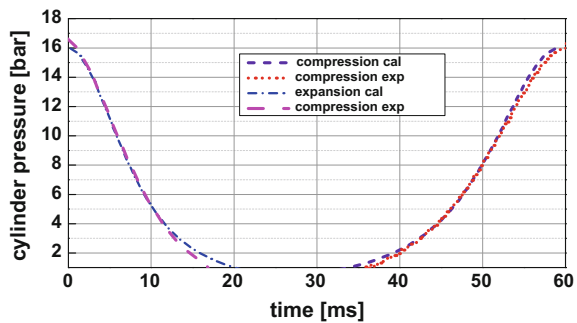
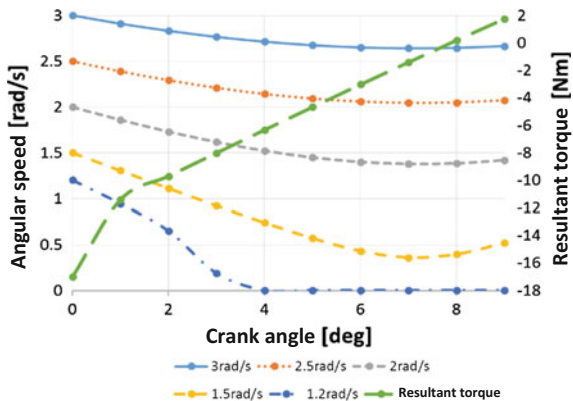


Fig. 23.11 Case piston escapes from vicinity of TDC



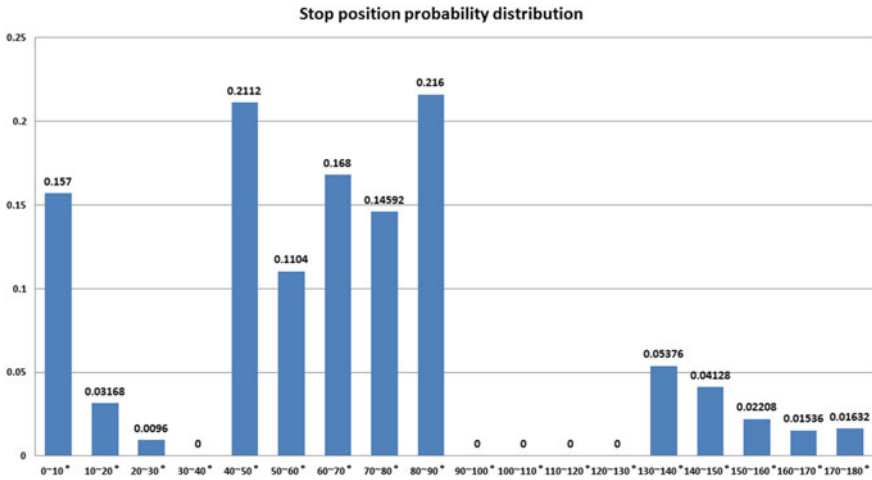
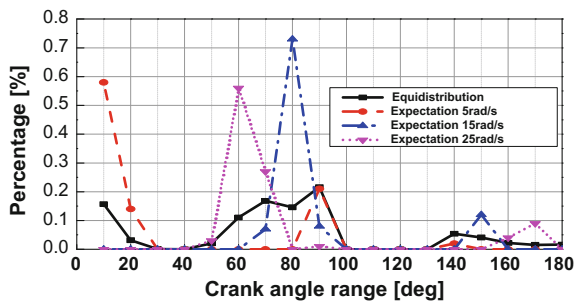


Fig. 23.12 Stop crank distribution of random initial speed

Fig. 23.13 Stop position of different distribution functions

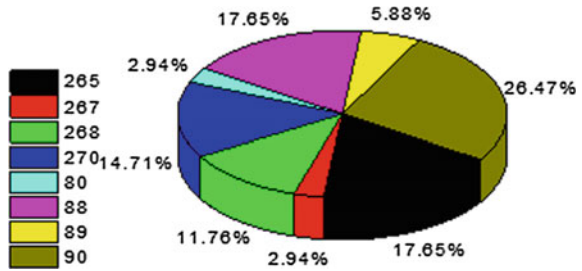


stop position locates in 50–90 and 0–10° ATDC in uniform condition. The expectation of normal has great effect on stop position and results in the vicinity of 50–80 and 0–10° ATDC.

23.2.6 Simulation Experiment Result Validation Application

Basically piston stop position locates in 80–90 or 260–270° ATDC (the same position in fact), which has a similar results with the calculated one. As for this engine, the stop position is fixed in certain range and initial speed of final stroke has great effect on final stop position (Fig. 23.14).

Fig. 23.14 250 rpm engine bench experiment stop position



23.3 Conclusions

The modeling on engine stopping process contributes to the bench experiment limit. Key factors that influence the stop process are identified and the cost is lower. Main points of conclusion are put as following.

- (1) Heat transfer and leakage have great effects on resultant torque when speed is low. It thus affects final stop position;
- (2) As for this type of engine, the engine cannot escape from vicinity of TDC when initial speed is lower than 1.2 rad/s and as is also the case in BDC.
- (3) In the range 0–10, 60–90° locates the final stop position for this engine.

References

1. Bishop J, Nedungadi A, Ostrowski G et al (2007) An engine start/stop system for improved fuel economy. SAE paper 2007-01-1777
2. Uhl M, Wüst M, Christ A, Pörtner N, Trofimov A (2013) Electrified powertrain at 48 V—more than CO₂ and comfort. In: 22nd aachen colloquium automobile and engine technology, pp 975–994
3. Hackmann W, Klein B, Götte C, Schmid R, Pujol F (2013) 48 V—the way to a high volume electrification. In: 22nd aachen colloquium automobile and engine technology, pp 1009–1030
4. Giordano FR, Fox WP, Horton SB, Weir MD (2009) A first course in mathematical modeling. 4th edn. Cengage Learning
5. Merker GP, Schwarz C, Teichmann R (2009) Combustion engines development. Vieweg & Teubner, Wiesbaden

Chapter 24

Study on the Impact of Communication Imperfections on Forward Collision Warning and Avoidance Based on V2V Communications

Minghan Zhu, Hongmao Qin, Jianqiang Wang, Manjiang Hu, Keqiang Li and Zhouwei Kong

Abstract Vehicle-to-vehicle communications bring new opportunities to ADAS, as it allows the vehicles to acquire more information of the environment and extends the range of perception. However, V2V communications have their limits, which could not operate perfectly in all conditions nowadays. This study analyzes the impact of communication imperfections on the performance of Forward Collision Warning and Avoidance based on V2V communications (Connected FCW/FCA) through simulation. Packet drop, time delay and limited communication distance are investigated as parameters of communication imperfections. The conclusion of this study provides supports for improving forward collision warning and avoidance to be accommodated to communication imperfections.

Keywords Forward collision warning/avoidance · V2V communications · ADAS · Packet drop · Time delay

These authors contributed equally to this work.

M. Zhu · J. Wang (✉) · M. Hu · K. Li
Department of Automotive Engineering,
Tsinghua University, Beijing 100084, China
e-mail: wjqlws@tsinghua.edu.cn

M. Zhu
Department of Mechanical Engineering,
University of Michigan, Ann Arbor 48109, USA

H. Qin
School of Transportation Science and Engineering, BUAA,
Beijing 100191, China

Z. Kong
ChongQing Changan Automobile CO.LTD, Chongqing, China

24.1 Introduction

Advanced Driver Assistance Systems (ADAS) is widely applied in vehicles today to improve the safety and comfort of vehicle by making up for the limitation of drivers. Forward Collision Warning and Avoidance System (FCW/FCA) is a critical subsystem in ADAS as an effective technology to reduce and mitigate collisions. This system acquires the information of the vehicle and the environment through information and sensing technology to recognize potential dangers and provide driver with warning signals. When the situation is judged emergency, the system will apply an automatic braking to avoid or mitigate impending collision. However, most FCW/FCA today acquire environment information through sensors like radar and camera, while these sensors have some common limitations. Firstly, the sensing range is relatively small. Secondly, the information that could be acquired is limited. Thirdly, it is possible that the targets are mistakenly recognized. Nevertheless, the development of communication technology brings new opportunities to intelligent vehicles. Vehicle-to-Vehicle (V2V) and Vehicle-to-Infrastructure (V2I) communication make it possible for all vehicles and infrastructures to be connected and to exchange information. Information of vehicles in the environment could be acquired by a vehicle more thoroughly, more accurately and in real time, which brings about a new field for development of Connected FCW/FCA, which is FCW/FCA based on V2V communications.

Most collision warning and avoidance algorithms for vehicle following scenarios judge whether a warning signal or automatic braking should be launched with a distance or time model. HONDA, MAZDA and Berkeley models are representative distance models for collision warning and avoidance [1]. These models define a threshold of warning and braking distance considering speed of both vehicles and the distance between them. Warning or braking is triggered when the distance between two vehicles are less than the threshold. Time models define time-related parameters to judge whether warning and braking should be activated. A TTC (time to collision) strategy was utilized to design the forward collision warning-avoidance algorithms in Wang et al. [2]. Pei et al. [3] proposed a new parameter *Tbuffer* to establish its warning strategy, which is a modification of TTC taking acceleration of both vehicles into consideration. Data of drivers' following and braking behavior was collected and analyzed in Wang et al. [2] and Pei et al. [3] to provide reference for deciding the threshold in the time models. Wang et al. [4] improved collision avoidance algorithms based on VANets by allocating acceleration to both the leading and following vehicles through V2V communications. Wang et al. [5] applied sliding mode control in cooperative active collision avoidance algorithms with V2V communications and avoided hard braking in collision avoidance.

The development of dedicated short-range communication (DSRC) prompt the development of new technologies applying V2V communications. The DSRC devices are based on IEEE 802.11p standard, which is also called the Wireless Access in the Vehicular Environment (WAVE) as a message protocol mainly designed for Intelligent Transportation System. It was found that the effective

communication distance of DSRC between two vehicles is 250 m in a vehicle following scenario, and the distance is slightly shorter in an intersection scenario [11]. Another study found that vehicles in the vicinity of 300 m could have effective communication [12]. It is found that the probability of successful message reception deteriorates from about 80% at 0 m to about 50% at around 250 m [12]. In the scenario set by another study, a vehicle node achieves successful message reception only at a ratio of 14% in the worst case when the sensing range is 1000 m. WAVE has a typical delay of 50 ms [13]. In Tang and Yip [11], the delay of the V2V communication is modeled to be between 25 and 300 ms. The updating interval of DSRC is typically 100–1000 ms [11], while [14] used updating rates up to 20 Hz in its study on V2V communication using IEEE 802.11p standard.

Many studies were conducted to evaluate the effect of different FCW/FCA strategies. Lee and Peng [6] evaluated the performance of four forward collision avoidance distance models: MAZDA, HONDA, JHU and JAGUAR models by utilizing identified “threatening” and “safe” data sets. Mcgehee et al. [7], Werneke and Vollrath [8] and Yan et al. [9] conducted experiments to investigate the influence of human factors on the timing of collision warnings in vehicle following or intersection scenario. The development of V2V communication extended the topic in collision warning and avoidance systems. Some research studies the stability of control system under communication uncertainties like stochastic delays [10], in which a zero-order hold is used to when packet drop occurs. Tang and Yip [11] investigated on the timing of collision avoidance for the DSRC-based vehicles, which analyzed all steps in a collision avoidance maneuver with V2V communications. However, few studies focused on the impact of V2V communication on the performance of collision warning and avoidance strategies, which is the objective of this study. The remainder of this article will be displayed as follows. The strategies for FCW/FCA used for investigation will be proposed in the next chapter. The scenarios and parameters of vehicle dynamics and V2V communications for the simulation will be described in the third part. Then results of the simulation and the analysis is displayed. At last, the conclusion of the impact of communication imperfections on the collision warning and avoidance strategies will be given.

24.2 Forward Collision Warning and Avoidance Strategies

In the situation where one car is following another car running in the same direction, a collision warning algorithm is helpful to alert the driver in the following car to take actions when the leading car brakes to decelerate. If the driver does not take actions when a rear-end collision is impending, the collision avoidance system could interfere with the control of the vehicle to brake automatically. The result could be an escape from or a mitigation of a collision. This paper applies a collision warning and avoidance algorithm proposed by researchers in the University of California,

Berkeley [1]. The algorithm is based on distance model of warning and braking. The proposed warning distance is:

$$d_w = \frac{1}{2} \left(\frac{v^2}{\alpha} - \frac{(v - v_{rel})^2}{\alpha} \right) + v \cdot \tau + d_0 \quad (24.1)$$

where v is the velocity of the host vehicle (namely, the following vehicle), v_{rel} is the velocity between vehicles, α is the maximum deceleration of both vehicles. τ accounts for the system and driver delays, and d_0 is a headway offset. The braking distance is defined as:

$$d_{br} = v_{rel} \cdot (\tau_{sys} + \tau_{hum}) + 0.5 \cdot a_2 (\tau_{sys} + \tau_{hum})^2 \quad (24.2)$$

where τ_{sys} represents the system delay and τ_{hum} is the human response time. a_2 is the assumed deceleration of the leading vehicle. Seller et al. [1] set that $\tau = \tau_{sys} + \tau_{hum}$, and $a_2 = \alpha$. The value of the parameters are selected as following: $\tau_{hum} = 1$ s, $\tau_{sys} = 0.2$ s, $\alpha = 6$ m/s², $d_0 = 5$ m. When the distance between the leading and following vehicle is less than d_w , the warning signal is triggered to alarm the driver. When the distance comes to d_{br} , the vehicle start to apply automatic braking to avoid the collision.

24.3 Simulation Settings

24.3.1 Description of Vehicle Following Scenario in Simulation

In this scenario there are two vehicles running in the same direction. They are assumed to only have 2-D movement and they have the same lateral position (i.e. they are running in the same straight lane and not allowed to change lane). The scenario described above is typical for FCW/FCA applications, and automatic steering for collision avoidance has not been commonly applied in ADAS yet.

The host vehicle is following the target vehicle with a distance h . The two vehicles have the same initial speed v_0 . The target vehicle applies a constant-deceleration a_1 braking starting at $t = 0$ until it comes to stop. The host vehicle will run at a constant speed until the condition for collision avoidance is satisfied and then it will apply emergency braking with its maximum deceleration $a_2 = a_{max-}$. Before the automatic braking, the collision warning signal will be triggered if the warning condition mentioned in the algorithm is satisfied. The selection of the parameters mentioned above is $h = 150$ m, $v_0 = 60$ or 100 km/h, $a_1 = 2$ or 6 m/s², $a_{max-} = 6$ m/s².

The value of initial speed is set considering the limit of vehicles' speed on highway in China which is from 60 to 120 km/h. The deceleration of target vehicle is set to 2 m/s^2 as a moderate braking and 6 m/s^2 as a hard braking. The maximum deceleration of host vehicle is set according to Seller et al. [1].

24.3.2 Parameters Concerning V2V Communications

The information of the other vehicle's speed and location needed for the collision warning and avoidance algorithms is gathered via vehicle-to-vehicle communications.

To study the impact of communication deterioration on the FCW/FCA algorithms, the parameters of communication deterioration, including time delay, packet drop ratio and communication distance is manually set to be relatively larger, and communication distance limitation is manually set to be smaller, than those in usual situations, so as to make the effect more apparent. In this paper, time delay is set to be between 0.1 and 1 s; packet drop ratio is set to vary from 20 to 80%; the limitation of communication distance is between 50 and 100 m. The updating rate of message is 10 Hz. The V2V communication includes information of a vehicle's position and speed. The position information is added with noise subject to normal distributions of which the standard deviation is 0.5 m. The velocity information is added with noise subject to normal distributions of which the standard deviation is 0.5 m/s. These values are set referring to former researches [11–14], which have been introduced in Chap. 1.

24.4 Simulation Results

All simulations are taken under four dynamic conditions: ① $v_0 = 60 \text{ km/h}$, $a_1 = 2 \text{ m/s}^2$; ② $v_0 = 60 \text{ km/h}$, $a_1 = 6 \text{ m/s}^2$; ③ $v_0 = 100 \text{ km/h}$, $a_1 = 2 \text{ m/s}^2$; ④ $v_0 = 100 \text{ km/h}$, $a_1 = 2 \text{ m/s}^2$. Each group of conditions are simulated for 200 times for statistic information. Figure 24.1 shows the simulation time and relative distance when the warning and avoidance action are triggered under ideal condition, which means that the communication has no delay, no packet drop and no sensing range restriction, and that the position and speed information is exactly accurate. The first dark blue bar represents the warning time and the second represents the time when automatic braking was activated. The light blue bars represents the distance between two vehicles when warning signal (first bar) and automatic braking (second bar) are activated. The information in Fig. 24.1 is used as a reference. Situations under communication imperfection are analyzed in compare with the ideal situation.

24.4.1 Single Factors

Packet drop. It brings about uncertainties in the measurement of surrounding vehicles' states. Consequently, the variance of the time when warning or braking is initialized increases with the growth of packet drop ratio. The standard deviation of warning and braking time under different packet drop ratio is shown in Fig. 24.2. The highest standard deviation of warning time and braking time is 0.13 and 0.16 s when the packet drop ratio reaches 0.8. Assuming the deviations obey normal distribution, the maximum deviation of warning and braking time from the ideal value is about 0.4–0.5 s, which could have a significant impact on the result of collision avoidance. However, packet drop does not show obvious influence when the ratio is below 0.4. The mean time of warning and braking does not show clear trends with the growth of packet drop ratio, so the figures are omitted here.

Time delay. The deviation of warning and braking time shows no obvious trends concerning different delay time, but the mean time shifts slightly earlier in

Fig. 24.1 Warning and braking time and distance under ideal conditions

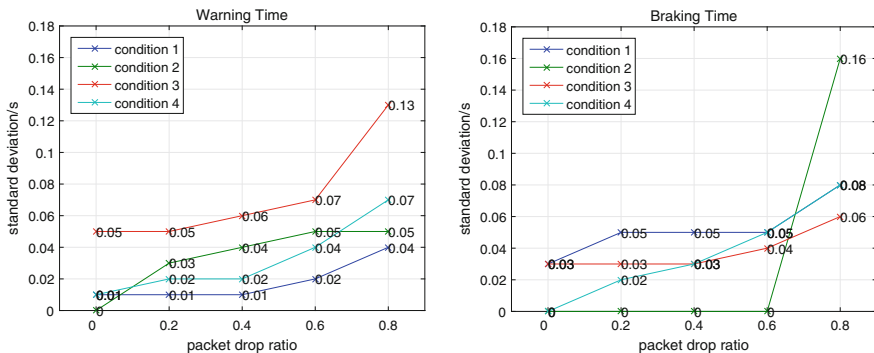
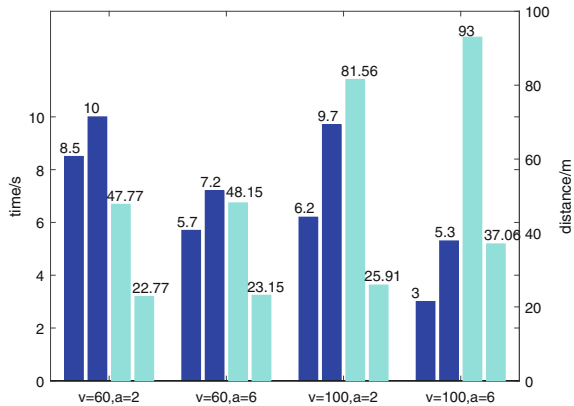


Fig. 24.2 Standard deviations of warning time and braking time with packet drop

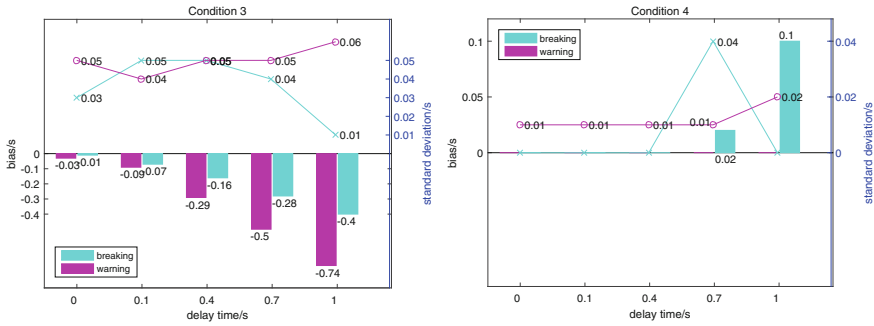


Fig. 24.3 Mean bias from ideal situation (bars) and standard deviation (lines) of warning time and braking time in condition 3 and 4 with delay in V2V communications

condition ③ and later in condition ④ (Fig. 24.3). The time stays steady in condition ① and ② (figure omitted). The impact of time delay on the time of beginning warning and braking has two aspects. On the one hand, the observed position of target vehicle is closer to host vehicle than it truly is under time delay, which makes the collision warning and avoidance actions easier to be triggered. On the other hand, the observed speed of decelerating target vehicle is higher than its real speed under time delay, which reduces the relative speed of host vehicle, hence reducing the threshold of warning and braking distance according to (24.1), (24.2). It delays the activation time of warning and automatic braking. The two factors affects against each other. The deceleration of target vehicle is lower in condition ③ than in condition ④, and the speed of target vehicle is higher in ③ than in ④ when the host vehicle is at the same distance from target vehicle. It makes the first factor more important in ③ and the second factor more important in ④. Consequently, the activation time of warning and braking is put forward in ③ and delayed in ④ with the growth of time delay. There is no impact of time delay in condition ① and ②, because the target vehicle has already come to stop when the warning or avoidance action is about to be triggered.

Communication distance restriction. In low-speed conditions ① and ②, no obvious differences are found in the mean and the variance of warning and braking time with different communication distance from 50 m to infinity. However, the warning time is delayed dramatically with the decrease of communication distance in high-speed conditions ③ and ④ (the left part of Fig. 24.4). The latency of warning time is mainly because the original warning distance is beyond the limitation of communication distance in ③ and ④. It could be proved by the right part of Fig. 24.4 which illustrates the distance between two vehicles when warning and braking are activated. The difference of warning distance roughly equals the difference of corresponding communication distance. However, the braking distance is shorter than the warning distance, and the corresponding distance is shorter in low-speed conditions than in high-speed ones. Therefore, no similar trend is found in conditions ① and ② and in braking time in condition ③ and ④.

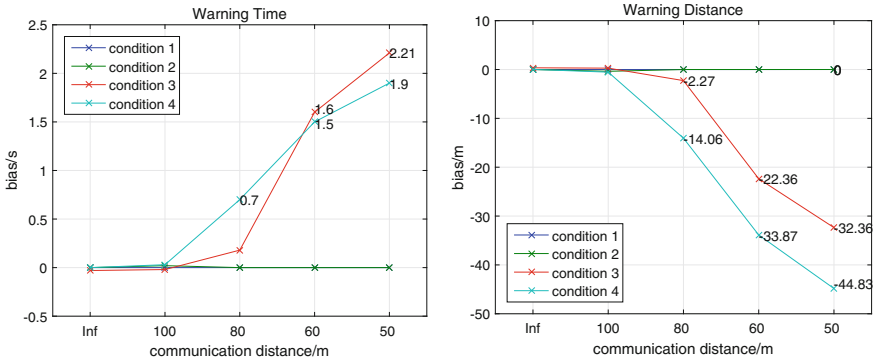


Fig. 24.4 Mean bias of warning time and distance from ideal situation with communication distance restriction

24.4.2 Combination of Different Factors

In reality, the delay of V2V communication consists of basic broadcasting and transmission time and extra latency caused by packet drop. Combining delay and packet drop together better reflects the real situation. More precisely, packet drop ratio is changing when the distance between vehicles is different. An exponential model (24.3) is applied to imitate the packet drop ratio’s changing concerning the communication distance [15].

$$PDR(x) = 1 - \exp(x/CD \cdot \ln 0.05) \tag{24.3}$$

where $PDR(x)$ is packet drop ratio at certain distance (see Fig. 24.5), CD is the communication distance where the packet drop ratio is 0.95, and x is the real distance between vehicles. By tuning delay time and CD , all the three factors discussed above are included.

The simulation results when factors are combined are consistent with the findings in former paragraphs. Figure 24.6 shows the mean and standard deviation of the time when warning and braking is activated. First, CD affects the standard deviation in all four conditions, because it determines the packet drop ratio. Second, delay time has opposite impact in condition ③ and ④, and do not have remarkable impact in condition ① and ②, which has been explained in 0. Third, smaller CD puts off the warning time in condition ③ and ④, because CD reflects the communication distance.

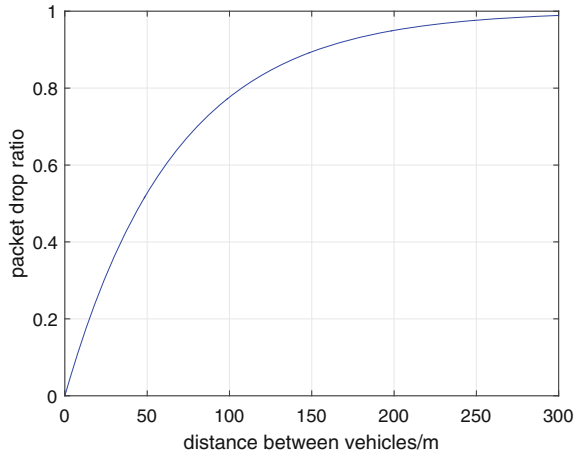


Fig. 24.5 An example of the curve of packet drop ratio when CD = 200 m

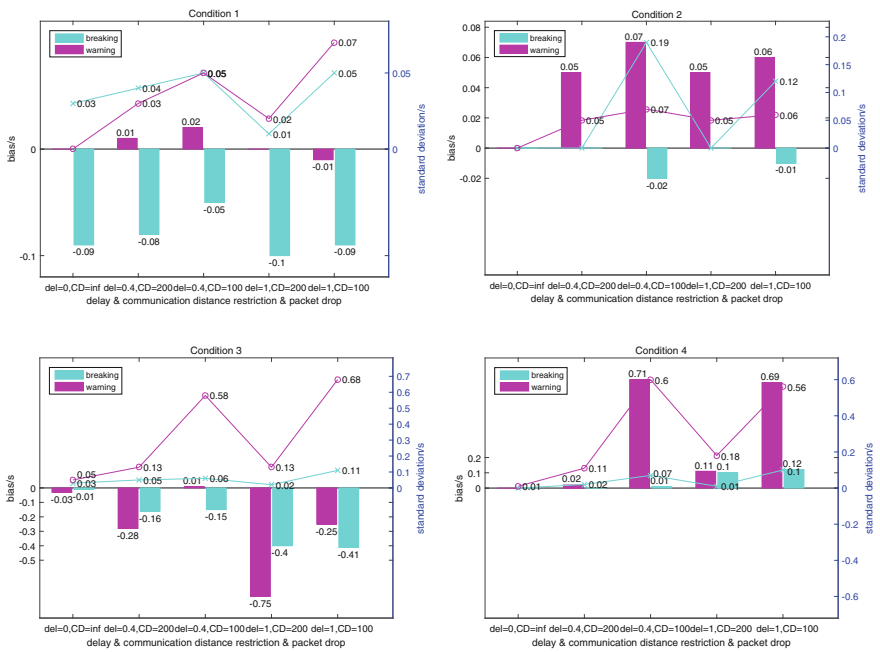


Fig. 24.6 Mean bias from ideal situation (bars) and standard deviation (lines) of warning time and braking time with multiple factors

24.5 Conclusion

The uncertainty of warning and braking time increases with the growth of packet drop ratio. Meanwhile, packet drop may result in delayed or advanced warning and braking because of filter's properties, but this impact is slight.

Time delay has few impact on the uncertainty of warning and braking time, but it results in shorter observed distance and higher observed speed of target vehicle. The mean time could be delayed or advanced according to the applied algorithms for warning and braking. For the algorithms applied in this paper, time delay results in latency if the deceleration of target vehicle is high, and results in advanced warning and braking if the target vehicle's speed is high.

Communication distance affects the warning or braking time significantly when the distance limit is smaller than original warning or braking distance. Moreover, different communication distances determines different start points of observation and filtering, which could result in slight difference on the filtered value of observed status and hence result in slight bias on warning and braking time.

The analysis of combined communication parameters shows accordant results to those found in simulations for individual parameters in both scenarios. The impact of the basic communication parameters on the performance of Connected FCW/FCA algorithms is analyzed through simulation. The conclusions above provide instruction for the development of Connected FCW/FCA algorithms to better accommodate to communication imperfection. Quantitative analysis could be the next step of the research to define the critical demands on the communication quality to ensure the Connected FCW/FCA systems to function properly.

Acknowledgements The research was supported by the Jiangsu provincial key laboratory of new technology application on road delivery vehicle (NO: BM20082061501), the Research fund of Ministry of Education & China Mobile (NO: MCM20150302), Colleges and Universities in Jiangsu Province plans to graduate research and innovation (NO: KYLX16_0882) and the National Natural Science Foundation of China under Grant 51505247.

References

1. Seller P, Song B, Hedrick JK (1998) Development of a collision avoidance system. *Automot Eng Int* 106(1–2):94–102
2. Wang J, Chi R, Zhang L et al (2009) Study on forward collision warning-avoidance algorithm based on driver characteristics adaptation. *J Highw Transp Res Dev*
3. Pei XF, Zhi-Quan QI, Wang BF et al (2014) Vehicle frontal collision warning/avoidance strategy. *J Jilin Univ*
4. Wang Y, Wang P, Yu G et al (2012) Study on cooperative active collision avoidance algorithm based on VANets. In: *CICTP 2012: multimodal transportation systems—convenient, safe, cost-effective, efficient*. ASCE, pp 1156–1167
5. Wang P, Yu G, Wang Y et al (2014) Cooperative active collision avoidance algorithm based on sliding mode control. *J Beijing Univ Aeronaut Astronaut* 40(2):268–273

6. Lee K, Peng H (2005) Evaluation of automotive forward collision warning and collision avoidance algorithms. *Veh Syst Dyn* 43(10):735–751
7. Mcgehee DV, Brown TL, Lee JD et al (1803) The effect of warning timing on collision avoidance behavior in a stationary lead-vehicle scenario. *Transp Res Rec J Transp Res Board* 2002(1803):1–7
8. Werneke J, Vollrath M (2013) How to present collision warnings at intersections?—A comparison of different approaches. *Accid Anal Prev* 52C(2):91–99
9. Yan X, Zhang Y, Ma L et al (2015) The influence of in-vehicle speech warning timing on drivers' collision avoidance performance at signalized intersections. *Transp Res Part C Emerg Technol* 51:231–242
10. Qin WB, Gomez MM, Orosz G (2014) Stability analysis of connected cruise control with stochastic delays. In: American control conference. IEEE, pp 4624–4629
11. Tang A, Yip A (2010) Collision avoidance timing analysis of DSRC-based vehicles. *Accid Anal Prev* 42(1):182–195
12. Jiang D, Taliwal V, Meier A et al (2006) Design of 5.9 GHz DSRC-based vehicular safety communication. *IEEE Wirel Commun* 13(5):36–43
13. Farahmand AS, Mili L (2009) Cooperative decentralized intersection collision avoidance using extended Kalman filtering. In: Intelligent vehicles symposium, IEEE, pp 977–982
14. Khairnar VD, Kotecha K (2013) Simulation based performance of Mumbai-pune expressway scenario for vehicle-to-vehicle communication using IEEE 802.11p. *Transp Telecommun* 14(4):300–315
15. Yim R, Ye F, Roy S et al (2010) Effect of transmission parameters on efficiency and reliability of V2V networks. In: Its world congress

Chapter 25

Wavelet-Based Demodulation Design for Vehicular Communication Network

Yao Ge, Zhan Shu and David Daut

Abstract Wavelet-based Software-defined radios (SDRs), have become very important in both commercial as well as military applications that demand high Quality of Service (QoS) in hostile physical and spectral conditions. It could also be utilized in the vehicle to vehicle communication networks. This WD-based SDR is compose of a AMR and a modulation. This paper focus on the development of the WD-based Demodulation, which enables of obtaining original signal information by demodulation in the wavelet-domain without an inverse transform of a signal to its time-domain form. The development is proven analytically herein. Extensive Monte Carlo simulations also show that the Bit Error Rates (BERs) obtained from wavelet-based demodulation are very comparable with the optimal case of matched filter-based demodulation. The results of this work show the ability of wavelet transforms to enable the demodulation of communications signals in a single processing sequence by solely using the computationally-friendly mathematics of the Discrete Wavelet Transform.

Keywords Vehicular network · Reconfigurable radio · Wavelet-based demodulation · Digital communication · Discrete wavelet transform

Y. Ge (✉) · D. Daut (✉)

Department of Electrical and Computer Engineering, Rutgers University
New Brunswick, Piscataway, NJ 08854, USA
e-mail: yaoge@scarletmail.rutgers.edu

D. Daut

e-mail: daut@ece.rutgers.edu

Z. Shu (✉)

Department of Civil and Environmental Engineering,
New Jersey Institute of Technology, Newark, NJ 07102, USA
e-mail: zs34@njit.edu

25.1 Introduction

An agile radio system was designed for the vehicular communication system, which has the ability to automatically classify the modulation scheme used in a received signal and then automatically demodulate the signal. To better illustrate the idea, an agile radio system is designed automatically classifying the modulation scheme, which can be utilized in a received signal, and with the capacity of automatically demodulating the signal. To specify this agile radio transceiver system, a detailed block diagram will demonstrate core features of the that is composed of its core features as shown in the Fig. 25.1, which is a wavelet-based platform composed of four major components:

1. Channel Estimation [1]: This process enables Electrical characterization of the medium through which a signal is transmitting. Besides, in order to improve the performance, channel estimation also performs to restore signal features prior to the WT-based AMR and demodulation processes.
2. Channel Equalization [2]: This step is to eliminate unwanted channel effects carried by received signals. The reduction of unwanted channel effects present in received signals is a desirable signal conditioning step before invoking the AMR process.
3. AMR: This is a key component of this Wavelet-based transceiver Platform, which automatically identifies the modulation scheme of the received signal.
4. Demodulation: Second to AMR in importance is the automation demodulation of this Wavelet Platform.

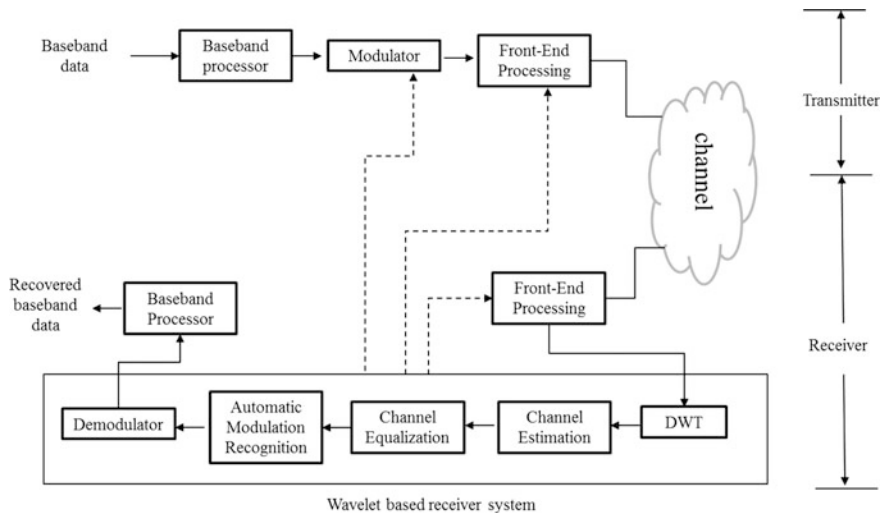


Fig. 25.1 System-level block diagram of an agile radio transceiver based on the wavelet platform

In Fig. 25.1, it shows that a wavelet-based transceiver is consisted of a transmitter and a receiver as majority parts of the receiver which is implemented in the context of the Wavelet Domain. In this transceiver, the transmitter operation is partially controlled by the Wavelet Platform. The dashed lines indicate that sub-systems in the transmitter take feedback provided by the Wavelet Receiver, which could carry information to alter transmission characteristics such as the modulation scheme, carrier frequency, etc., as needed. This function also enables the feature of agility of the wavelet-based transceiver. The WT-based AMR and Demodulation processes both use the Discrete Wavelet Transform (DWT).

Two DWT-based AMR algorithms were described and validated in [3, 4], and it is now necessary to develop the techniques for demodulation in order to complete the baseband processing system on the WD Receiver Platform. After properly classifying the unknown modulation scheme employed by a received communication signal, an appropriate demodulation process must be activated in order to recover the information-bearing signal to the baseband data.

The motivation of designing the WD-Demodulator is to achieve this WD system architecture’s optimization. As shown in the system-level block diagram of Fig. 25.2, although employing a contemporary demodulation system followed by the WD-AMR could fulfill the baseband processing such as the information recovery function, this system is inefficient in its redundant algorithm and a high cost in circuit complexity.

For the implementation shown in Fig. 25.2, the input signal, sampled by the ADC, is a digitally modulated signal at zero IF. The data sequence output by the ADC is accumulated in a memory location (the input signal storage). After sufficient signal samples are stored, the processing engine decomposes the digital-domain IF signal using different wavelets and the output data are stored in a second memory location (the processing signal storage). Next, the processor compares the decomposed signal with pre-existing wavelet signatures that are available in a Look-Up Table (LUT) and makes the modulation recognition decision. This decision is then released to the digital switches through the control unit.

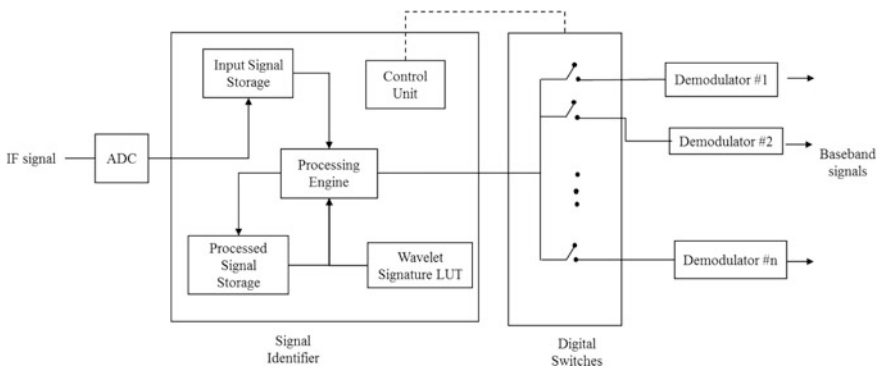


Fig. 25.2 Baseband processor using WD-based signal identification and classical demodulation

The control unit, which operates switches connected to the correct external contemporary demodulator, can be used to recover the baseband data. However, the system shown in Fig. 25.2 is not reconfigurable because each modulation scheme still requires its own unique carrier signal and, correspondingly, its own specific demodulation circuit. Also, there are computational redundancies that can be refined. First, the received signal is transformed to the wavelet domain for the WD-AMR algorithm. It is then transformed in reverse back to the time domain to match with the corresponding classical demodulator. Hence, the system could be improved in two aspects: reduce the computational complexity and lower the circuit design cost. An improved system is introduced as shown in the Fig. 25.3.

The completed baseband processor for the combined processes of signal identification and demodulation is illustrated in Fig. 25.3. The main difference between the two processors is a processor implemented as a universal demodulator in the wavelet domain to detect and recover a signal. This wavelet-based demodulator can directly receive, analyze and make decisions upon the signals' wavelet domain expression without transferring back to the time domain. Besides, by employing the wavelet-based AMR and wavelet-based demodulation jointly, a reconfigurable baseband processor platform is completed and implemented.

The rest of this chapter consists of three parts. Firstly, it focuses on illustrating how this new modulator is derived from the contemporary demodulation technology. Secondly, the architecture of this WD-baseband processor and its general algorithm will be developed. Lastly, the performance of the demodulation techniques is evaluated and BER curves are plotted for cases of signals corrupted with AWGN. The communications signals considered in this case are BASK, 4-ASK, BFSK, 4-FSK, BPSK, QPSK, 8-PSK, 4-QAM (also denoted as $\pi/4$ -QPSK), 16-QAM. The corruption results in SNR values range from -5 dB to 10 dB.

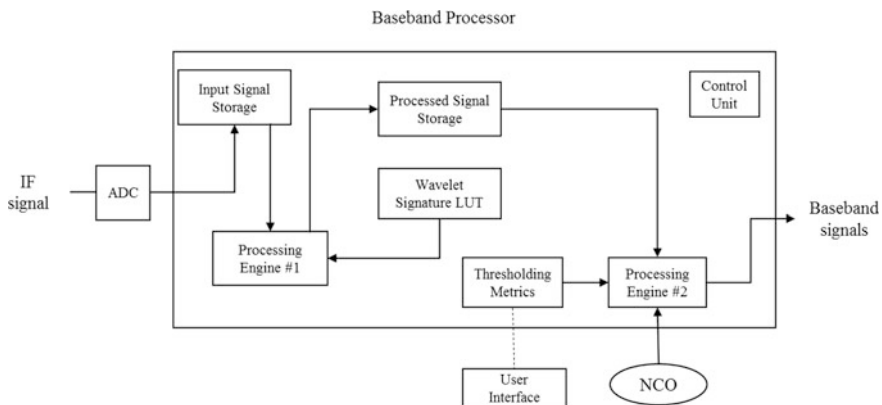


Fig. 25.3 Baseband processor using WD-based signal identification and demodulation

25.2 Development of the WD-Based Demodulation

The contemporary demodulation techniques for digitally modulated communications signals are developed based on the MAP/ML being the best decision strategy. In the classical receiver, the correlation between received signals and noise-free symbols with a known modulation type is a key part of the decision. These correlation outputs are compared and the largest value is selected. Based on the comparison result, the data bit sequence can then be demodulated. Figure 25.4 illustrates the system block diagram for this classical correlation-based demodulation procedure. In this case, the variable η_m is usually treated as a known constant parameter.

In short, the best decision rule of the optimal classical demodulation is known as the maximum a posteriori (MAP/ML) probability rule [6] $\hat{m} = \arg \max_{1 \leq m \leq M} (\eta_m + (r, s_m))$. The variable η_m consists of the signal power, the variance of the Gaussian white noise, and the signal prior probability, all of which are usually either constant values or known variables. Hence, the correlation is the key part of the decision.

In the time domain receiver system, two inputs of the correlator are the received signal and the noise-free symbols employ the same modulation scheme as the received signals. In a wavelet-based receiver platform, the output of the WD-based AMR is the wavelet expression of received signals with a known modulation scheme and the templates signals are also wavelet transformed. It is significant to note that the inputs in the time domain and wavelet-based receiver systems are similar, which warrant further investigation into how the WD correlation is related to the regular correlation.

To research the WD correlation, it must start from the definition of the DWT. As introduced in [5], for an arbitrary function $f(t)$, the correlation results in the decomposition of $f(t)$ into two orthogonal parts:

$$f(t) = f_j(t) + w_j(t) \quad f_j(t) \in V_j, w_j(t) \in V_j^\perp, f_j(t) \perp w_j(t) \quad (25.1)$$

The spaces V_j have a special structure; it is defined as a linear space of the scaled and translated replicas of a single function, called the scaling function, or the father wavelet. Its scaled/translated replicas are defined for any integer of j, n by: $\phi_{jn}(t) = 2^{j/2} \phi(2^j t - n)$. The functions $\phi_{jn}(t)$ are orthonormal for each fixed j , and form a basis of space $V_j \cdot (\phi_{jn}, \phi_{jm}) = \delta_{nm}$.

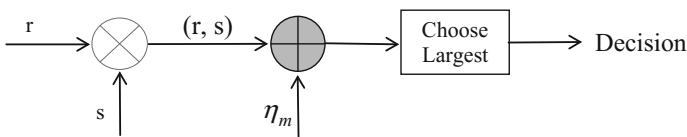


Fig. 25.4 The contemporary correlator based demodulation

Now the projection of an arbitrary signal $f(t) \in L^2(\mathbb{R})$ onto the subspace V_j is defined by the following expansion in the ϕ_{jn} basis:

$$f_j(t) = \sum_n c_{jn} \phi_{jn}(t) = \sum_n c_{jn} 2^{j/2} \phi(2^j t - n) \tag{25.2}$$

Another wavelet function $\psi(t)$ and its scaled and translated replicas actually span the orthogonal complement V_j^\perp of V_j with respect to $L^2(\mathbb{R})$. Note that $\psi_{in}(t) = 2^{i/2} \psi(2^i t - n)$, $i \geq j$, which are orthogonal to $\phi_{jn}(t)$, and are also mutually orthonormal, $(\psi_{in}, \psi_{i'n'}) = \delta_{ii'} \delta_{nn'}$, $(\phi_{jn}, \psi_{in}) = 0$, $i \geq j$.

The component $w_j(t)$ from Eq. (25.1) is referred to as the ‘‘detail’’ and incorporates the details of $f(t)$ at all the higher resolution levels $i \geq j$, or finer time scales $2^{-i} \leq 2^{-j}$. It is spanned by the ψ -basis expansion:

$$w_j(t) = \sum_{i \geq j} \sum_n d_{in} \psi_{in}(t) = \sum_{i \geq j} \sum_n d_{in} 2^{1/2} \psi(2^i t - n) \tag{25.3}$$

Hence, taking (25.2) and (25.3) into (25.1) to complete forming the multi-resolution decomposition analysis of $f(t)$,

$$\begin{aligned} f(t) &= f_j(t) + w_j(t) = \sum_n c_{jn} \phi_{jn}(t) + \sum_{i \geq j} \sum_n d_{in} \psi_{in}(t) \\ f(t) &\xrightarrow{\text{DWT}} \sum_n c_{jn} + \sum_{i \geq j} \sum_n d_{in} \end{aligned} \tag{25.4}$$

The right-hand coefficients in (6.4) are:

$$c_{jk} = (f, \phi_{jk}) = \left(\sum_n c_{j+1,n} \phi_{j+1,n}, \phi_{jk} \right) = \sum_n c_{j+1,n} (\phi_{j+1,n}, \phi_{jk}) \tag{25.5}$$

$$d_{jk} = (f, \psi_{jk}) = \left(\sum_n c_{j+1,n} \phi_{j+1,n}, \psi_{jk} \right) = \sum_n c_{j+1,n} (\phi_{j+1,n}, \psi_{jk}) \tag{25.6}$$

According to the Eq. (25.1), in the time domain the correlation of two signals $f(t)$ and $f'(t)$ could be re-defined as:

$$\begin{aligned} (f, f') &= (f_j + w_j, f'_j + w'_j) \\ &= (f_j, f'_j) + (f_j, w'_j) + (w_j, f'_j) + (w_j, w'_j) \\ &= (f_j, f'_j) + (w_j, w'_j) \end{aligned} \tag{25.7}$$

Because the f and w are two orthogonal parts of a signal, their correlation is 0.

Based on the discrete wavelet transform definition (25.2) and (25.3), the two components in the output of (25.7) could be reformatted in the wavelet domain in the following way. The first part of function (25.7) is re-written:

$$(f_j, f'_j) = \left(\sum_n c_{jn} \phi_{jn}(t), \sum_n c'_{jn} \phi_{jn}(t) \right) = \sum_n c_{jn} c'_{jn} (\phi_{jn}, \phi_{jn}) = (c_{jk}, c'_{jk}) \quad (25.8)$$

The scalar property of correlation and the orthonormal basis function feature are applied to the above expression equation.

Following the similar strategy, the second component of (25.7) could be expressed by wavelet coefficients.

$$\begin{aligned} (w_j, w'_j) &= \left(\sum_{i \geq j} \sum_n d_{in} \psi_{in}(t), \sum_{i \geq j} \sum_n d'_{in} \psi_{in}(t) \right) \\ &= \sum_{i \geq j} \sum_n d_{in} d'_{in} (\psi_{ik}, \psi_{ik}) = \sum_{i \geq j} (d_{ik}, d'_{ik}) = \left(\sum_{i \geq j} d_{in}, \sum_{i \geq j} d'_{in} \right) \end{aligned} \quad (25.9)$$

Now combine (25.8) and (25.9) together, then apply the scalar property of correlation and the orthogonality property of basis function, the WD correlation equation can be reformatted as:

$$\begin{aligned} (c_{jk}, c'_{jk}) + \left(\sum_{i \geq j} d_{in}, \sum_{i \geq j} d'_{in} \right) &= (c_{jk}, c'_{jk}) + 0 + 0 + \left(\sum_{i \geq j} d_{in}, \sum_{i \geq j} d'_{in} \right) \\ &= (c_{jk}, c'_{jk}) + \left(c_{jk}, \sum_{i \geq j} d'_{in} \right) \\ &\quad + \left(c'_{jk}, \sum_{i \geq j} d_{in} \right) + \left(\sum_{i \geq j} d_{in}, \sum_{i \geq j} d'_{in} \right) \\ &= (c_{jk}, c'_{jk} + \sum_{i \geq j} d'_{in}) + \left(\sum_{i \geq j} d_{in}, c'_{jk} + \sum_{i \geq j} d'_{in} \right) \\ &= (c_{jk} + \sum_{i \geq j} d_{in}, c'_{jk} + \sum_{i \geq j} d'_{in}) \end{aligned} \quad (25.10)$$

Another direction to develop the WD correlation (25.10) is to link the wavelet coefficients to its function in the time domain with the help of (25.7),

$$\begin{aligned} (c_{jk}, c'_{jk}) + \left(\sum_{i \geq j} d_{in}, \sum_{i \geq j} d'_{in} \right) &= (f_j, f'_j) + (w_j, w'_j) \\ &= (f_j + w_j, f'_j + w'_j) = (f, f') \end{aligned} \quad (25.11)$$

Through comparing the two expressions (25.10) and (25.11), a new equality is presented in the (25.12): The correlation of two signals in the time domain is the same as the correlation of their discrete wavelet transformed coefficients,

$$(f, f') = (c_{jk} + \sum_{i \geq j} d_{in}, c'_{jk} + \sum_{i \geq j} d'_{in}) = (DWT(f), DWT(f')) \tag{25.12}$$

25.3 The Architecture Design of the WD-Receiver System

Upon the conclusion of the last section, the correlator component can be preserved in the WD demodulation system from the contemporary receiver system. Its system block diagram is plotted in the Fig. 25.5.

As shown in Fig. 25.5, the basic construction of the WD Demodulation has not changed much from the classical demodulator system, except for two input signals that are wavelet transformed. The reason is that the correlation in the time domain generates the same correlation as it does in the wavelet domain, so the underlying decision rules for both systems are the same as well.

Since both inputs of the correlator are wavelet-transformed signals, they are the same as the outputs of the WD-AMR. Hence, this WD-Demodulation system could be further updated to the WD-Receiver platform by combining the WD-AMR processor into the system as stated in the Fig. 25.6.

This WD-Receiver system can enable both modulation recognition and demodulation. Also, it achieves two improvements compared to the contemporary receiver:

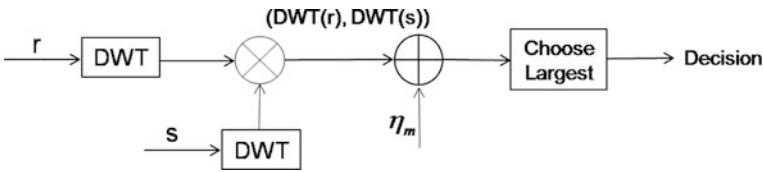


Fig. 25.5 Wavelet based-demodulation system

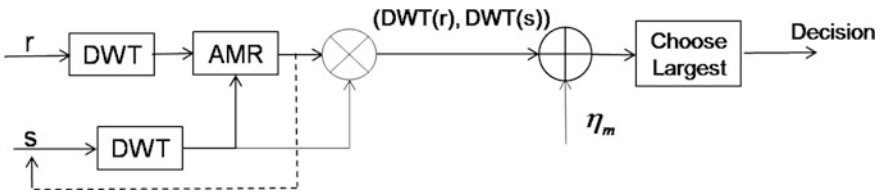


Fig. 25.6 Wavelet-based receiver platform

1. Avoid transferring signals back and forth between the wavelet domain and the time domain. This WD demodulator is designed to follow after the WD-based AMR processor to complete the receiver system within the wavelet platform. The wavelet-based demodulation has proved that it is capable of directly processing the output of the WD-AMR; it can employ wavelet expressions of the received signal at its input without having to transfer the WD signals back to the time domain. Hence, the computation of this algorithm is low in redundancy.
2. This wavelet-based Receiver is a reconfigurable radio system. Signal “r” was received with unknown modulation type first, then the WD-AMR detects the modulation scheme and feeds this decision back the templates signal storage “s”. The template signal “s” will employ the same modulation technology, go through the discrete wavelet transformation, and join the following WD-Demodulation procedure. Instead of utilizing a distinct demodulation system for different modulated signals, this universal system design could fulfill the baseband process for multiple types digital transmitted signals. This feature of the WD-Receiver system highly reduces the circuit design complexity.

The general algorithm of this wavelet-based reconfigurable receiver system is illustrated by below:

1. After going through the channel, the received signals “r” are wavelet transformed with an unknown modulation type.
2. The template signals are wavelet transformed and stored at the “s” end.
3. As shown in Chaps 4 and 5, the wavelet expressions of “r” and “s” are analyzed.
4. After the ARM process, its outputs contain two useful pieces of information for the following WD-demodulation system:
 - (a) The detected modulation scheme decision employed by the received signal. This information is transmitted to the template signal “s” end to control the modulation type for input of the correlator.
 - (b) The other result of the AMR is the wavelet expression of the received signal “r” with detected modulation scheme, which will be sent to the correlator as well.
5. Two wavelet components from 4a and 4b are correlated in the WD demodulator.
6. The comparator selects the largest WD correlation and the corresponding symbol that generates the largest correlation value becomes the demodulation result.

Even if the digital communication receiver is designed in the wavelet domain, the correlator-based optimal demodulation system still preserves its main circuit structure. This is because the important features proved in (25.12) shows that the correlation of two signals in the time domain is equal to their correlation in the wavelet domain.

25.4 Simulation Experiments and Results

In this section, there are two experiments tested to verify the WD correlation and TD correlation equality. In the first experiment, the two vectors for the two signals are discrete wavelet transformed. Their wavelet coefficients correlation and also their time domain correlation are both calculated as follows:

1. We have two vectors in time domain:

$$X = [1\ 2\ 3\ 4\ 5\ 6\ 7\ 8], \quad Y = [6\ 7\ 8\ 1\ 2\ 3\ 4\ 5]$$

2. After applying discrete wavelet transformations on X and Y through MATLAB, their WD expressions are calculated as below:

$$\begin{aligned} W_X &= [12.7279 - 1.4794 - 4.4090\ 2.2467\ 0\ 0 - 3.7938\ 0.9654] \\ W_Y &= [12.7292 - 2.9484\ 4.8818 - 1.5166 - 0.1147\ 0.2818\ 0.6614] \end{aligned}$$

3. Now the correlation in the wavelet domain shows:

$$(W_X, W_Y) = 143.991, \quad (W_X, W_X) = 203.997$$

And the correlation in the time domain and

$$(X, Y) = 144, \quad (X, X) = 204$$

Hence, $(X, Y) = (DWT(X), DWT(Y))$

The first experiment numerically proved that the correlation values could be preserved even after being discrete wavelet transformed. This theorem can be explained from the matrix calculation's point of view. Since the DWT is an orthogonal transformation, that is, the DWT can be written:

- (a) Linear transformation $WX = W * X$,
- (b) The DWT matrix W is orthogonal,
- (c) $W' * W = I$

This guarantees the preservation of the correlation value.

The second experiment will solely focus on the simulation of the WD-demodulation part. Also, it would be more meaningful to compare the performance of the WD demodulator with the regular demodulation system but exclude the AMR processor from the comparison. This is because when two receiver systems operate under the assumption of the same test environment, such as the same known modulation type, the same noise channel, and so on, the test results are more comparable.

In following content, the algorithm developed in this chapter shows itself using the MATLAB simulation. All of the signals involved in this study have been corrupted by zero-mean AGWN resulting in SNR values in the range of -5 to -10 dB. The WD Demodulator performance has been evaluated based on 10^5 Monte-Carlos trials wherein each simulation experiment consists of 192 bits per frame for ASK, FSK and PSK signals, and 1024 bits per frame for M-ary QAM signals. In order to maintain a high degree of resolution in the WD scalogram, the signal, which corresponds to the carrier frequency, is oversampled by a factor of 16 over the Nyquist rate. Here, the key parameter assumed for the demodulation process is that of perfect symbol timing with no timing offset.

Each received, noisy signal has been demodulated using the WD demodulator. Each set of demodulator performance results presented in Figs. 25.7, 25.8, 25.9, 25.10, 25.11, 25.12, 25.13 and 25.14 contains two types performance curves. One curve corresponds to the theoretical performance of the traditional correlation receiver demodulation [6]. The other curve is the simulation results for the WD Demodulators developed in this dissertation. It has been observed that the probability of error is almost the same between these two systems. This result actually meets the expectation. This is because the classical correlation based demodulator is designed upon the theoretical best decision rule MAP/ML that was proven to produce the optimal detection accuracy with the AWGN channel digital signal communication system. In the WD demodulation system, although signals are wavelet transformed and processed in the wavelet domain, the communication

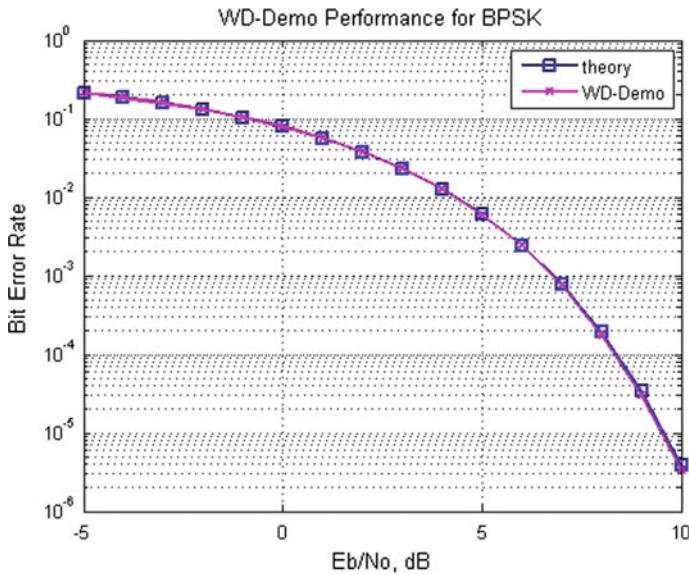


Fig. 25.7 BPSK BER curve comparison

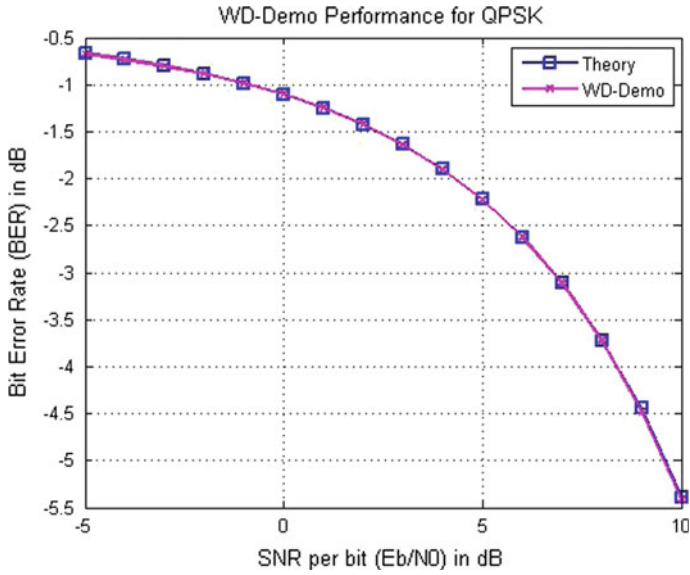


Fig. 25.8 QPSK BER curve comparison

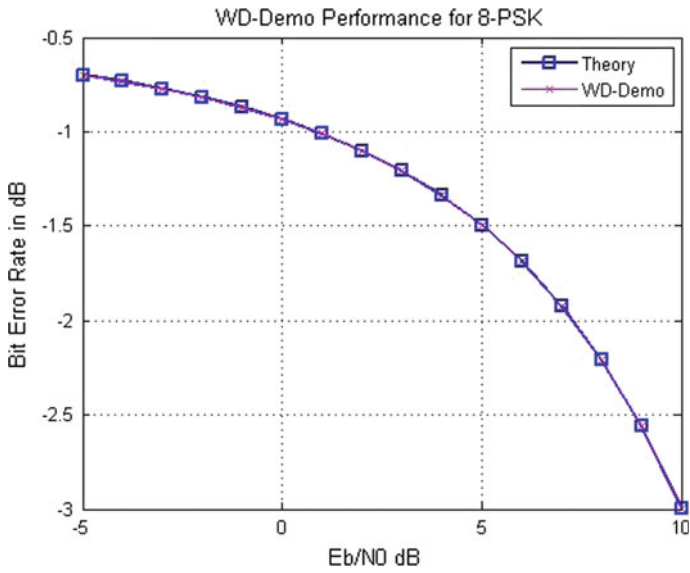


Fig. 25.9 8-PSK BER curve comparison

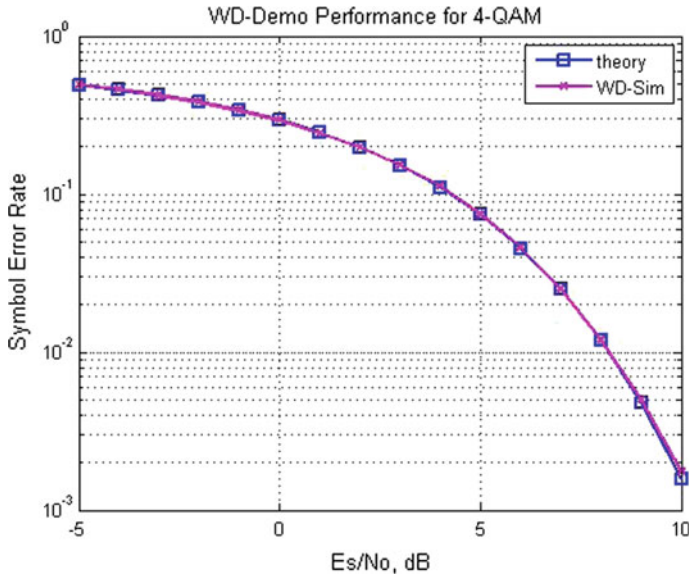


Fig. 25.10 4-QAM SER curve comparison

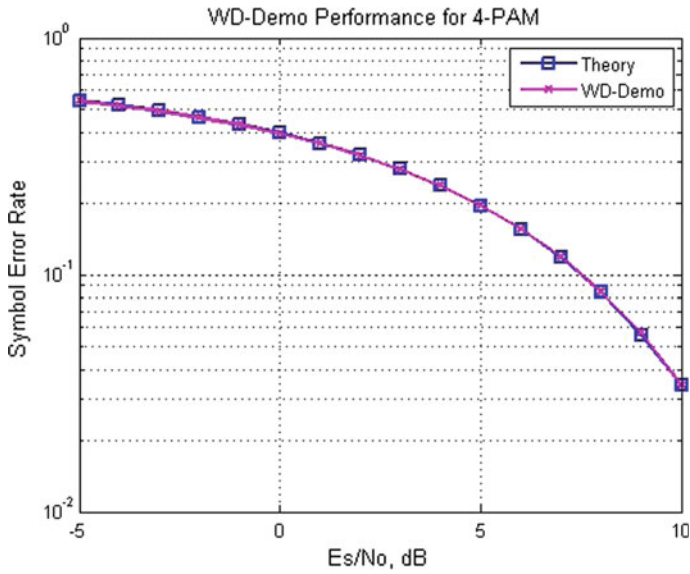


Fig. 25.11 4-PAM SER curve comparison

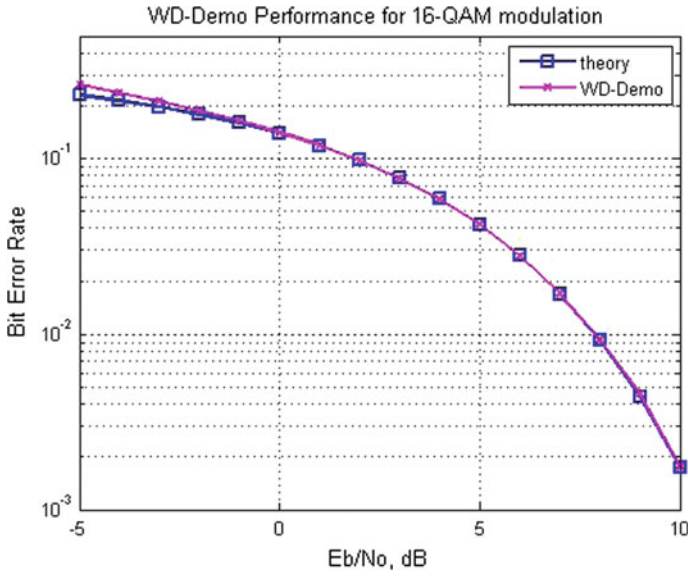


Fig. 25.12 16-QAM BER curve comparison

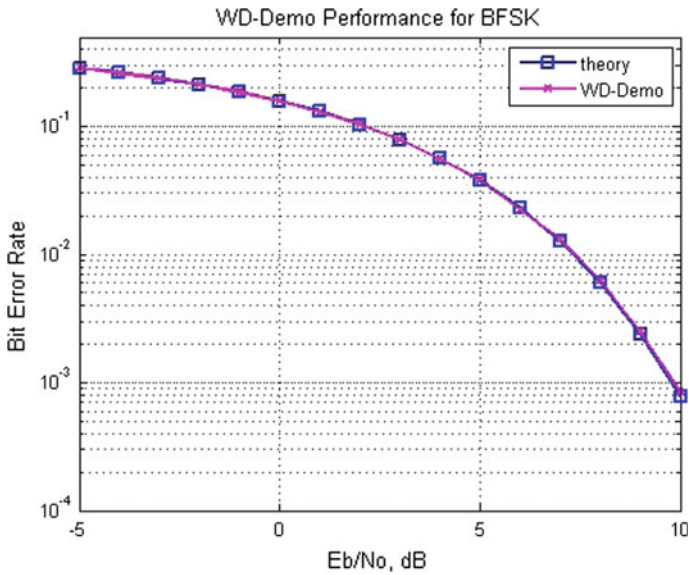


Fig. 25.13 BFSK BER curve comparison

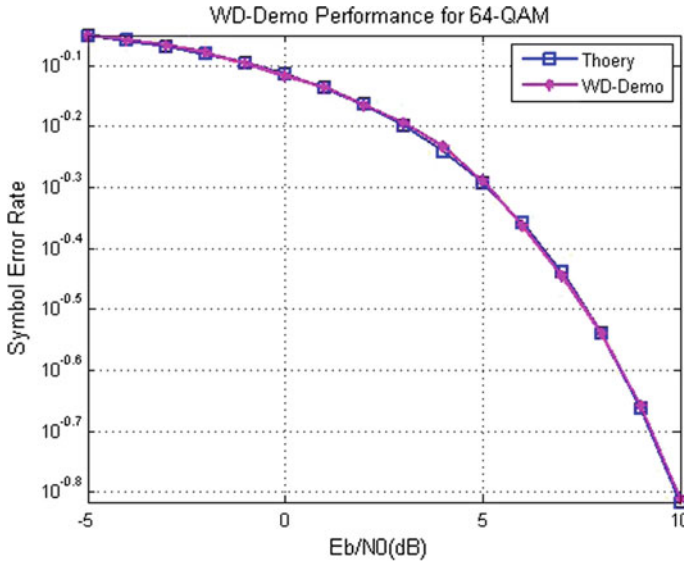


Fig. 25.14 64-QAM SER curve comparison

channel and the whole environment did not change. Hence, its performance will not proceed beyond the best performance boundary given by the classical system.

Besides, the performances obtained through simulating both the WD Demodulation techniques and the TD (correlation-based) Demodulation mentioned in this chapter are also compared and showed in details in Appendix B.

25.5 Discussion of Results

In conclusion, for the test modulation signals considered in this dissertation going through the same AWGN channel system, the wavelet-based demodulation performance is, at most, as good as the contemporary optimal correlation-based demodulator. Its BER performance is also simulated and compared with the contemporary receiver. For every modulation scheme considered in this dissertation, the WD Demodulation methodology performed comparably with the traditional correlator-based demodulation system. This observation is based on comparing the BER performances obtained using both types of demodulators.

Moreover, the WD Receiver system has been devised in a manner such that automatic demodulation of a communications signal from the wavelet domain is possible after the WD AMR processor has recognized the modulation scheme. This feature, which ensures that a signal-specific demodulator can adapt and work automatically, is advantageous for the development of agile radio receivers. It allows the WD-based demodulation system to adhere to the wavelet-transformed

signal perfectly from the WD-AMR. This is another advantage, which improves the computational efficiency and saves time by eliminating the transfer of signals between the time and wavelet domains. Although the final detection result is in the time domain, a complete analysis is finished in the wavelet domain. There is no domain transfer computation at all during the whole process. This improvement keeps the computational complexity as low as possible. Overall, the development of the wavelet-based Demodulation and the wavelet-based AMR make the utilization of the SDR technology in the vehicular communication network possible, practical and realist.

Appendix A: Algorithm Computational Complexity Comparison

Comparing with the CWT, another improvement of using the DWT is reduction of the computational complexity as the different fundamental of the CWT [7, 8] and the DWT technologies. The overall WD-AMR method's computational complexity consists of: Generation of WD templates; Transformation of received signals into the WD; Correlation of WD-templates and WD-received signals; and Decision procedure.

If the CWT was used in the instantaneous featured template AMR process, a test signal has a length of L bits, and there are N samples for each bit. The template size is set at M samples, $M \leq N$. So the size of the CWT domain based template would be a $M * M$ matrix and the computation cost of a CWT-template generation is $O(M^2)$. The next computation is to continuously wavelet transform received signals, whose complexity could up to $O(N^2)$. The third step is correlation of the WD template matrix with the WD received signal matrix. In the instantaneous featured template method, the size of template is usually shorter than or equal to the signal bit size. So the WD signal matrix $N * N$ will be fragmented to $M * M$. Hence the complexity of their correlation is $O(M^2)$. Thus, the summation this three term lead the overall complexity to $O(N^2)$.

For the CWT statistical featured template AMR process, a test signal has a length of L symbols, and there are N samples for each symbol. The template size is N samples per symbol as well. Hence, followed by similar analysis as above, the overall complexity is $O(N^2)$.

For the DWT Instantaneous featured template AMR process, by defining the same signal size as in the CWT case, a test signal has a length of L bits, and there are N samples for each bit. The template size is set at M samples. So the size of one WD template would be a $M * (\log_2 M)$ matrix and the computation cost of a DWT-template generation is $O(M \log_2 M)$. The next computation is to discretely wavelet transform received signals, which complexity could up to $O(N \log_2 N)$. The third step is correlation of the WD template matrix with the WD received signal matrix. In the instantaneous featured template method, the size of template is

Table 25.1 CWT-based and DWT-based algorithm complexity comparison

Algorithm	Complexity
CWT instantaneous featured templates AMR	$O(M^2)$
CWT statistical featured templates AMR	$O(N^2)$
DWT instantaneous featured templates AMR	$O(M\log_2M)$
DWT statistical featured templates AMR	$O(N\log_2N)$
CWT-based demodulation	$O(M^2)$ or $O(N^2)$
DWT-based demodulation	$O(N\log_2N)$

usually shorter than the signal bit size. So the WD signal matrix $N * \log_2N$ will be fragmented to $M * \log_2M$. Hence the complexity of their correlation is $O(M\log_2M)$.

For the DWT Statistical featured template AMR process, a test signal has a length of L bits, and there are N samples for each bit. The template size is set at N samples as well. Similarly, the overall complexity is $O(N\log_2N)$.

In CWT-based Demodulation algorithm [9], because it basically adheres from two CWT-AMR methodology. Hence it also contains the same complexity as the AMR. In DWT-based Demodulation system developed in this dissertation, it has proved that the DWT-based correlation and the regular correlation deliver the same output. Hence, in the DWT-based demodulation system, the DWT-based correlator replaced the regular correlation was used in the contemporary correlation based receiver. So the overall complexity is the same as the DWT-based correlation complexity, which is $O(N\log_2N)$.

In summary, there are two points could be pointed through the comparisons:

1. The DWT-based AMR algorithm cost less computation effort than the AMR CWT-based algorithm;
2. Although the statistical featured templates AMR algorithm costs higher computational complexity than the instantaneous featured templates AMR algorithm, the statistical feature-based algorithm is able to process more multiple modulation signal types than the instantaneous feature based algorithm.
3. Although the instantaneous feature-based AMR algorithm remains higher efficiency, but it can only work with binary modulation signals (Table 25.1).

Appendix B: WD-Demodulator and TD-Demodulator Performances Comparison

Under the same experimental environment as setup in the Chap. 6, another set of comparison tests were implemented in MATLAB. Each received, noisy signal has been demodulated using the WD demodulator, and the same each received, noisy signal has been also demodulated using the TD (correlation-based) demodulator. Correspondingly, their two performance curves of two demodulators performance results were presented in Figs. 25.15, 25.16, 25.17, 25.18, 25.19, 25.20, 25.21 and 25.22. One curve corresponds to the simulated performances of the TD

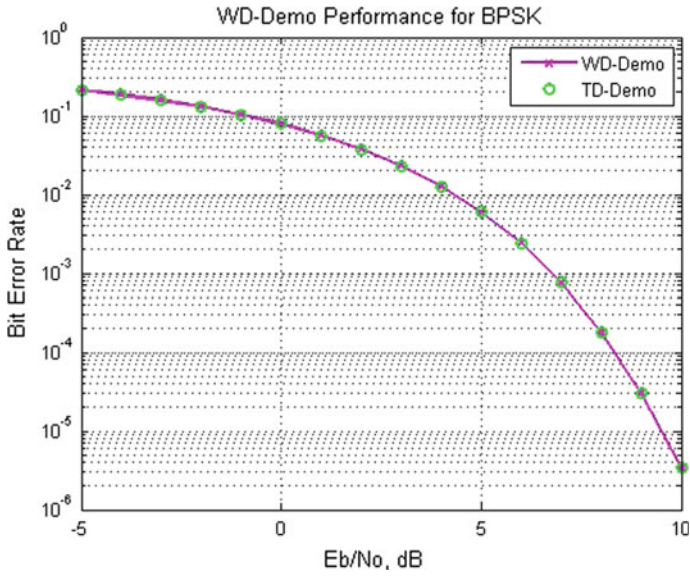


Fig. 25.15 BPSK BER curve comparison

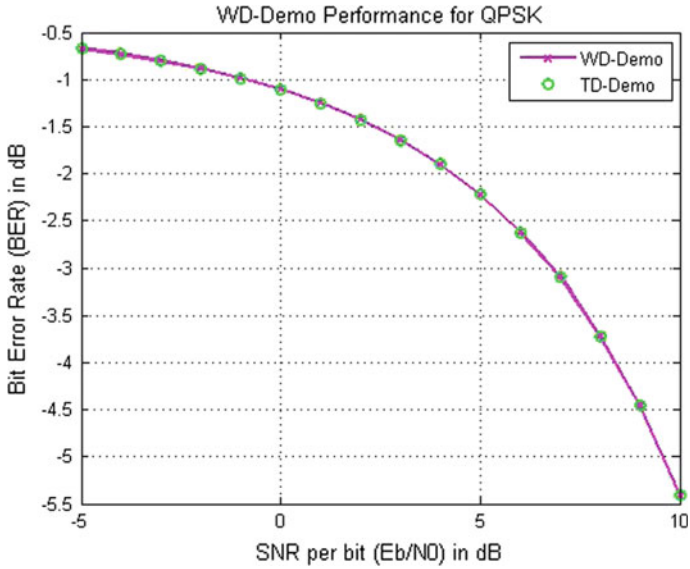


Fig. 25.16 QPSK BER curve comparison

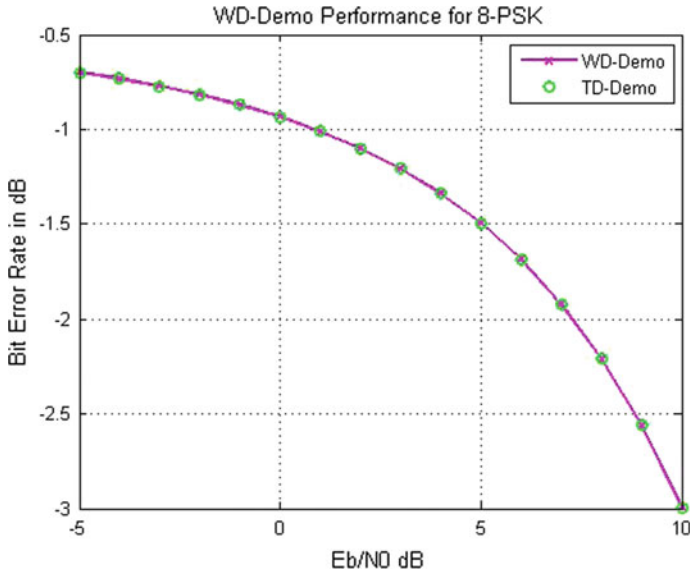


Fig. 25.17 8-PSK BER curve comparison

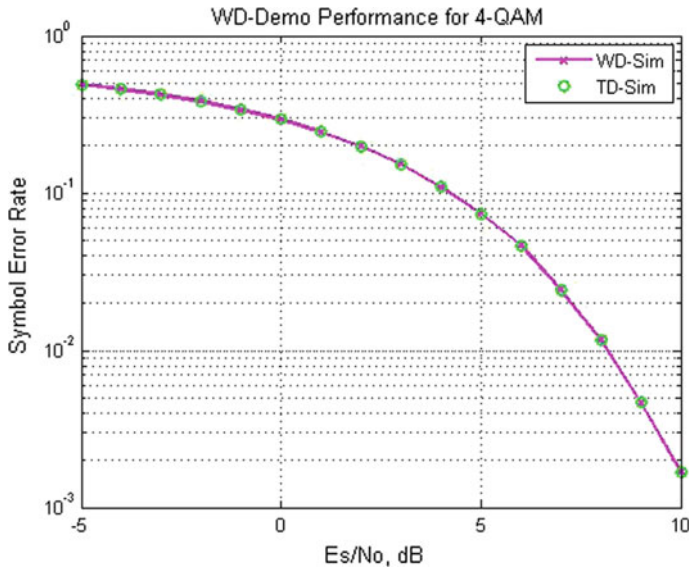


Fig. 25.18 4-QAM SER curve comparison

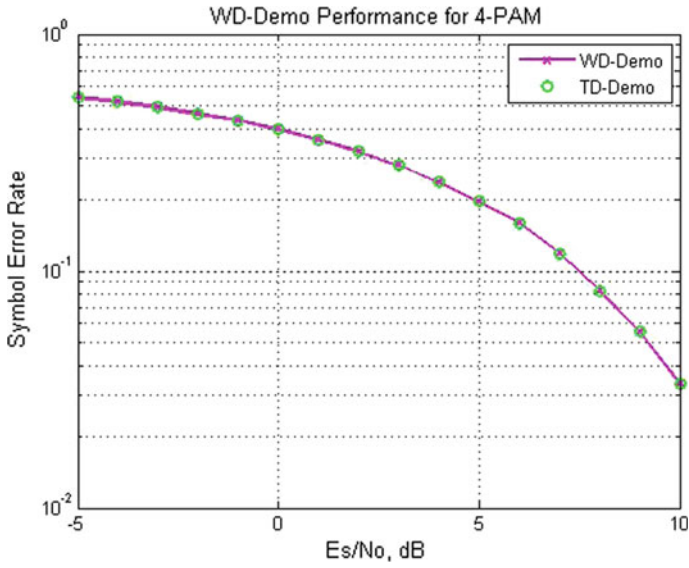


Fig. 25.19 4-PAM SER curve comparison

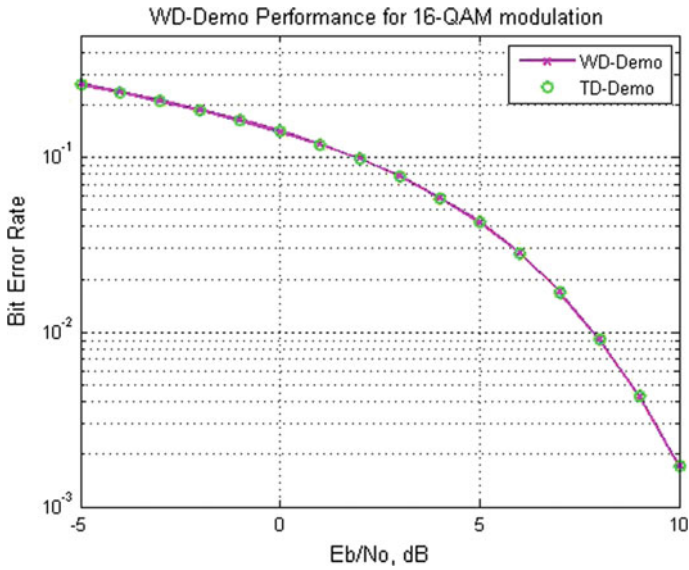


Fig. 25.20 16-QAM BER curve comparison

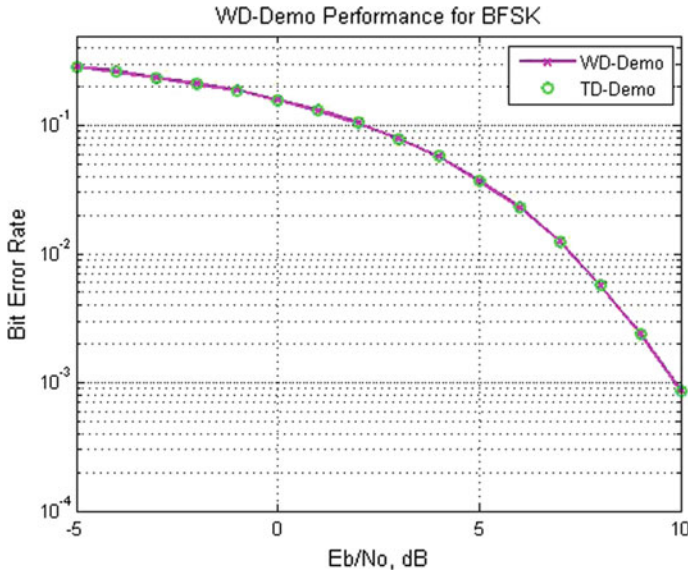


Fig. 25.21 BFSK BER curve comparison

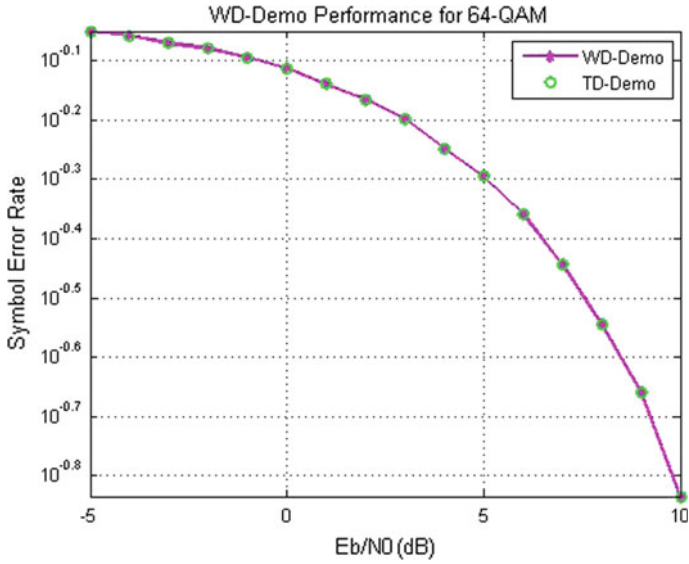


Fig. 25.22 64-QAM SER curve comparison

(correlation-based) Demodulation introduced in Chap. 6. The other curve is the simulation results for the WD Demodulators developed in this dissertation.

References

1. Vaz C, Yao Ge, David D (2013) Estimation of communications channel using discrete wavelet transform-based de-convolution. *IEEE Trans Comm* 61(10):4186–4195
2. Vaz C, David DG (2012) Communications receivers employing wavelet-domain zero-forcing equalization of multipath fading channels, In: 75th vehicular technology conference, May 2012
3. Yao Ge, David DG (2013) Automatic modulation recognition using the discrete wavelet transform. *IEEE SDR-WInnComm*
4. Ho KM, Vaz C, Daut DG (2008) Improved demodulation of phase shift keyed signals using wavelet thresholding. In: *Proceedings 2008 Sarnoff symposium*, Princeton, NJ, 28–30 April 2008
5. Orfanidis SJ (2010) *Introduction to signal processing*. Pearson Education, Prentice Hall, pp 427–451
6. Proakis JG (2001) *Digital communications*, 4th edn. McGraw-Hill, New York
7. Ho KM, Vaz C, Daut DG (2009) A wavelet-based method for classification of binary digitally modulated signals. In: *Proceedings 2009 Sarnoff symposium*, Princeton, NJ, March 2009
8. Ho KM, Vaz C, Daut DG (2010) Automatic classification of amplitude, frequency, and phase shift keyed signals in the wavelet domain. In: *Proceedings. 2010 Sarnoff symposium*, Princeton, NJ, April 2010
9. Ho KM (2010) Automatic recognition and demodulation of digitally modulated communications signals using wavelet-domain signatures. Ph.D. dissertation, Department of Electrical and Computer Engineering, Rutgers, The State University of New Jersey, New Brunswick, USA
10. Yao G (2015) Feature-based automatic modulation recognition design for vehicular network communication. In: *Proceedings 2015 Society of Automotive Engineering*, December 2015
11. Vaz C (2010) Estimation and equalization of communications channels using wavelet transforms. Ph.D. dissertation, Department of Electrical and Computer Engineering, Rutgers, The State University of New Jersey, New Brunswick, USA

Chapter 26

Research on Static Viscoelastic and Tribological Properties of PP-EPDM, PP-GF30 and ABS in Automobile

Xiaojia Zhang, Lei Den, Changyong Lin and Bo Liu

Abstract To establish the relationship between the static viscoelastic and the tribological properties, creep and friction experiments were performed on PP-EPDM, PP-GF30 and ABS through a UMT-II multi-functional micro-friction test machine. Results showed that PP-EPDM has the smallest creep rate and the better dimensional stability. This was related to the more complicated internal net structure, and the local slip and diffusion were more difficult than PP-GF30 and ABS under load. The Simulation Study of Burgers model founded that the viscosity coefficients of PP-EPDM was the smallest and the stiffness coefficient was the biggest, which exhibited a more apparent viscosity performance. The friction coefficient and wear depth of PP-EPDM were smaller than those of PP-GF30 and ABS, therefore, it has better wear resistance. Higher viscosity performance is favourable for friction coefficient improvement, and this goes against improving the wear resistance. Under the same conditions, PP-EPDM will be a better choice.

Keywords Engineering plastics · Creep · Friction and wear · Static viscoelastic properties

26.1 Introduction

With automobiles developing towards lighter weight, lower emission and lower energy consumption, the application of engineering plastics as decorating parts in interior and exterior trim has continuously extended to functional parts. The proportion of engineering plastics in complete vehicle was going up year by year. As one of the most prevalently used general plastics, PP-EPDM, PP-GF30 and ABS were widely used in automobile engine room parts field in China and abroad. The results showed that the fiber reinforced PP and ABS have excellent mechanical, low temperature tolerance, and anti-fatigue performance and so on. Meanwhile, wear

X. Zhang (✉) · L. Den · C. Lin · B. Liu
Changan Auto R&D Center, Changan Automobile Co, Ltd., Chongqing 401120, China
e-mail: zhangyw1@changan.com.cn

resistance of the materials significantly increased [1–3]. At present, scholars had conducted many studies on PP-EPDM, PP-GF30 and ABS, and they mostly focused on the single performance instead of the relationship of these properties.

In this paper, the creep and tribological properties of three materials commonly used in automobile, namely, PP-EPDM, PP-GF30 and ABS, are tested and compared. Meanwhile, the effects of the static viscoelastic on the tribological properties are analysed. The objective of this study is to provide experimental basis for the three materials (PP-EPDM, PP-GF30 and ABS) in engineering application.

26.2 Experiments

26.2.1 Materials

The three materials used in this experiment are three commercialized engineering plastics, namely, PP-EPDM, PP-GF30 and ABS (produced Chongqing, China). These materials are widely used in interior and exterior trim industry in China and abroad.

26.2.2 Creep Performance Test

The creep performance test was conducted to study the strain variations of the materials over loading time under a certain stress. This experiment was performed on the UMT-II multi-functional micro-friction testing machine. The rationale behind the test was demonstrated in Fig. 26.1. The experimental parameters were shown in Table 26.1. The dimensions of the samples were 20 mm × 20 mm × 20 mm. The creep rate could be calculated as Eq. (26.1):

$$\eta = \frac{J_1 - J_2}{J_2} \times 100\% \quad (26.1)$$

Fig. 26.1 Schematic diagram of creep properties test

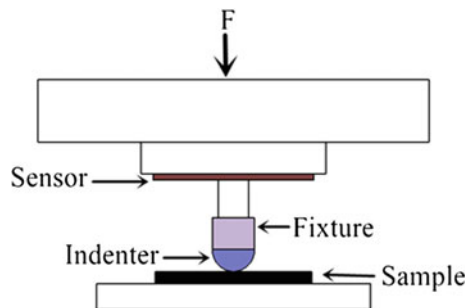


Table 26.1 Parameters of creep experiments

Parameter	Value
Pressure (N)	20
Indenter radius (mm)	5
Sampling interval (s)	0.02
Time (min)	60
Surrounding temperature (°C)	Room temperature

Table 26.2 Parameters of friction experiments

Parameter	Value
Pressure (N)	20
Sliding speed (mm/s)	10
Sliding time (min)	60
Surrounding temperature (°C)	Room temperature

Where η is creep rate, %; J_1 is final creep compliances (7200 s), $\mu\text{m}^2/\text{N}$; J_2 is initial creep compliances (600 s), $\mu\text{m}^2/\text{N}$.

In addition, Burgers model was selected in this study to analyse the creep properties of the three materials. Burgers model was connected in series by Maxwell and Kelvin model, which could analyse the viscoelastic properties under creep experiment. The creep compliances satisfied the Eq. (26.2) [4]:

$$J(t) = \frac{1}{G_0} + \frac{1}{G_1} \left[1 - e^{-\left(\frac{G_1 t}{\eta_1}\right)} \right] + \frac{t}{\eta_0} \quad (26.2)$$

G_0 and G_1 represent the elastic modulus (Pa), whereas η_0 and η_1 the viscosity coefficients (Pa·s).

26.2.3 Tribological Performance Test

The tribological properties of three materials were tested with UMT-II multi-functional micro-friction test machine. The dimensions of the samples were 20 mm × 20 mm × 2 mm. The matching part was a spherical indenter (10 mm) made of 45[#] steel and the radius was 5 mm. The movement mode was reciprocating sliding. The experimental parameters were shown in Table 26.2. Moreover, wear depth was measured by JB-4C roughness tester, and evaluated the anti wear property of three materials based on it.

26.3 Results and Discussion

26.3.1 Static Viscoelastic Properties

Creep test curves showed that within the first 500 s, the depths of indentation of PP + GF30 and PP + EPDM increased rapidly over time and then later increased gradually (Fig. 26.2a). However, the depths of indentation of ABS increased quickly all along. Because of the maximum elastic modulus of PP + EPDM, it was difficult to deform and was easily to maintained a same strain among three materials, therefore, so the depths of indentation of the same load is the least. Research showed that the change of creep performance of polymer materials results from gradual conformational changes or displacement change of internal macromolecular segment under external loads [5]. Figure 26.3 showed that the creep rates of PP + GF30 and PP + EPDM were 31.09 and 24.14% respectively, which were

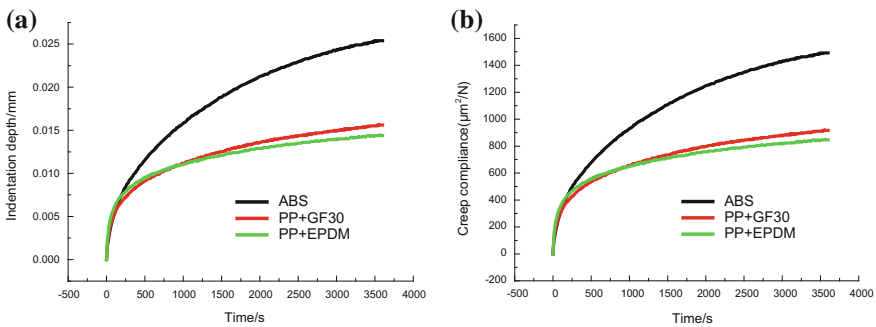
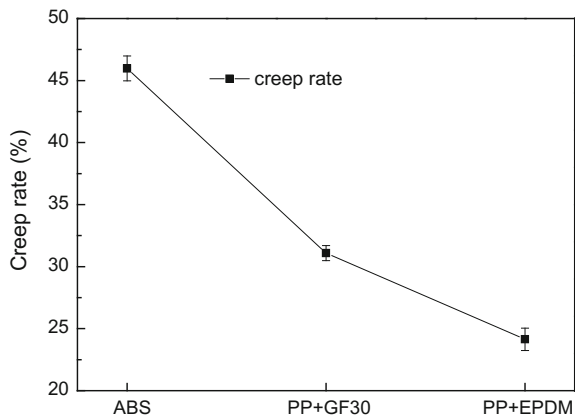


Fig. 26.2 Creep performance curves for ABS, PP + GF30 and PP + EPDM. **a** Creep curve. **b** Creep compliance

Fig. 26.3 Creep rates for ABS, PP + GF30 and PP + EPDM



significantly less than ABS (45.98%). This was mainly because PP + GF30 and PP + EPDM were compounded by EPDM and GF30 with matrix material (PP), respectively. And Sea island special structures were respectively formed by glass fibers, rubber particles and matrix material [6]. Slippage and displacement were more difficult between internal molecular chains and added inorganic particles. And this made their internal net structures more complicated and molecular linkages stronger. So under the same conditions, PP + GF30 and PP + EPDM had apparently smaller creep rates than ABS. However, as the internal net structure of ABS was simpler, local slip and diffusion were more likely to occur, and the change of chain angle and length and the extension of molecular chain were more active. Therefore, ABS had the highest creep rate.

In addition, the matrix material (PP) of PP + GF30 and PP + EPDM was Semi-crystalline plastic, but ABS was amorphous plastic. Research showed that crystallization was similar to cross linking, which could obviously decrease the creep rate of material. So the creep resistances of PP + GF30 and PP + EPDM were higher than ABS, which led to the dimensional stability properties of the materials were superior to ABS. Therefore, PP + GF30 and PP + EPDM were priority selections for structural and functional parts of automobile engine room parts.

Burgers model was selected to analyse the static viscoelastic properties and the fitting curves and model parameters of three materials that were obtained by Eq. (26.2) to perform the nonlinear fitting of creep compliances were showed in Fig. 26.4 and Table 26.3. The coefficients of determination R^2 of the fitted curves were separately 0.997, 0.992 and 0.986, which indicated that the Burgers model can properly reflect the creep performance of three materials. Table 26.3 showed the viscosity coefficient and stiffness coefficient of ABS were higher and smaller than PP + GF30 and PP + EPDM, separately. Study demonstrated the material which had larger viscosity coefficient of burgers model would display more apparent viscosity property than others. Therefore, these results proved that ABS had stronger viscosity properties than PP + GF30 and PP + EPDM.

26.3.2 Tribological Properties

The friction coefficient and depth of wear scar curves of ABS, PP + GF30 and PP + EPDM under the same conditions over time were showed at Figs. 26.5 and 26.6, separately. It showed that PP + EPDM had the smallest friction coefficient and depth of wear scar (0.13 and 12.6 μm), whereas ABS had the biggest friction coefficient and depth of wear scar (0.27 and 18.4 μm), which was 1.5 times that of depth of wear scar of PP + EPDM. PP + GF30 was in between (0.15 and 14.2 μm). So PP + GF30 and PP + EPDM exhibited superior wear resistance than ABS. This was because glass fiber (GF30) and ethylene propylene diene monomer (EPDM) were added to matrix material (PP) and this would form Sea island special structures in internal structure. The modulus and hardness of the materials would be

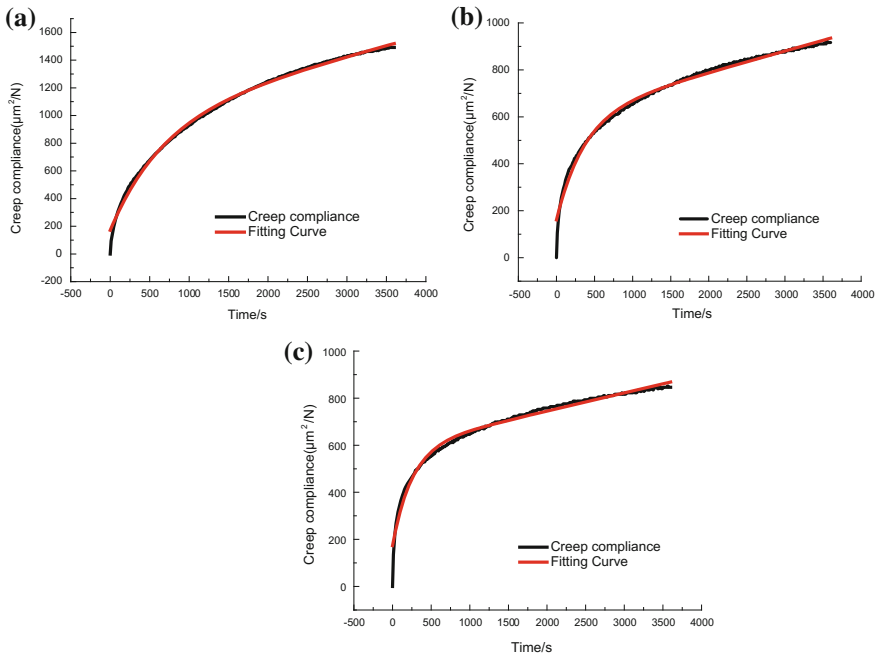


Fig. 26.4 Creep fitting curves for ABS, PP + GF30 and PP + EPDM **a** ABS **b** PP + GF30 **c** PP + EPDM

Table 26.3 Burgers model parameters for ABS, PP + GF30 and PP + EPDM

Material	Parameter		
	G_1	η_1	R^2
ABS	0.00125	0.8356	0.997
PP + GF30	0.00225	0.8145	0.992
PP + EPDM	0.00240	0.6053	0.986

increased evidently with this structure. In the actual process of friction, the effective contact area was reduced obviously, and the phenomenon of adhesion wear and deformation would be reduced. Meanwhile, most of the load was firstly loaded on the added GF30 and EPDM, which would cause the process of friction was occurred on the wear resistant materials (GF30 and EPDM) [7]. Therefore, the wear of polymer materials was reduced. Furthermore, the friction coefficients and depth of wear scar were less than ABS and the wear resistance property was improved.

Moreover, the volatility of friction coefficient curves of PP + GF30 and PP + EPDM were bigger than ABS. This was mainly because strong sticky points were formed on the contact peak point of contact surface and these points would not be damaged easily. During the relative sliding process between friction pair, the repetitive models of adhesion-break-adhesion which were caused by adhesive wear were intensified. And then the stability of friction coefficient was lower than ABS.

Fig. 26.5 Friction coefficient curves for ABS, PP + GF30 and PP + EPDM

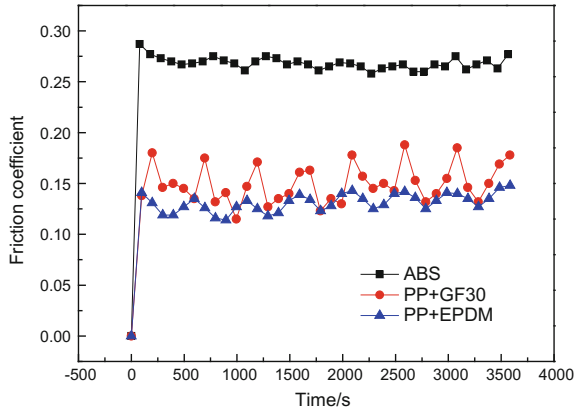
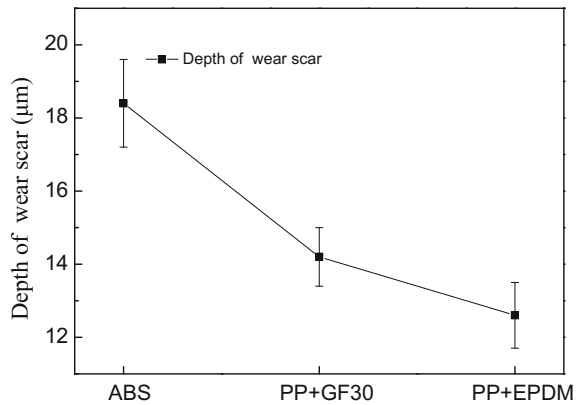


Fig. 26.6 Depth of wear scar for ABS, PP + GF30 and PP + EPDM



26.3.3 Relationship Between Static Viscoelastic Properties and Friction Performance

The relationships among average friction coefficient, creep rate, viscosity and stiffness coefficient were showed in Fig. 26.7. When PP + GF30, PP + EPDM and ABS were selected as structural and functional parts of automobile engine room parts, such as engine room guard plate, plastics parts should satisfy the strength requirement, meanwhile, they should have excellent anti wear property. A few creep deformations would be happened on the surface of parts caused by sustained loading of nuts under working. If the deformation was excessive, the parts would occur structure invalidation and lead to economic losses, and even happen major safety accidents.

Figure 26.7 showed that the friction coefficients of three materials were significantly positive correlation with creep rate and viscosity coefficient, and obviously negative correlation with stiffness coefficient. It was showed that the viscous

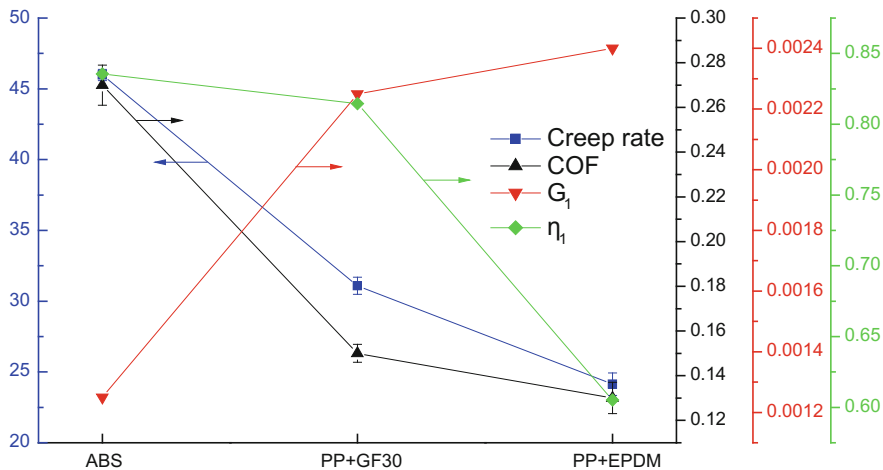


Fig. 26.7 Relation between viscoelastic properties and friction performance

property of the material enhanced with increase of creep rate and viscosity coefficient would lead to friction coefficient increase, which would go against the enhancement of anti wear property. This was because the material which had larger viscosity coefficient would display more apparent viscosity property and cause creep rate increased. With the same load, the bigger creep rate, the quicker the motion of the chain segment, and the adhesion on the contiguous micro-bulge peak was constantly intensified. As the adhesive force was intensified, the friction coefficient increased. Therefore, PP + GF30 and PP + EPDM were priority selections for structural and functional parts of automobile engine room parts.

26.4 Conclusions

The internal net structure of PP + EPDM was more complex than PP + GF30 and ABS. Under the same conditions, slippage and displacement were more difficult between internal molecular chains and added inorganic particles. Meanwhile, the change of chain angle and length and the extension of molecular chain were more difficult. So PP + EPDM had the smallest creep rate and the optimal dimensional stability properties. The simulation result of Burgers model showed that the viscosity and stiffness coefficient of PP + EPDM were smaller and higher than PP + GF30 and ABS, separately. Therefore, PP + EPDM exhibited the smallest viscosity property.

Because friction process was firstly occurred on the wear resistant materials, the friction coefficient and depth of wear scar of PP + EPDM were smaller than PP + GF30 and ABS. It had the best wear resistance property.

Higher creep rate was favorable for friction coefficient improvement and viscosity property. But it went against the enhancement of wear resistance property. In the same condition, PP-EPDM should be first selected.

References

1. Yang H, Li B, Wang K et al (2008) Rheology and phase structure of PP/EPDM/SiO₂, ternary composites. *Eur Polymer J* 44(1):113–123
2. Liang JZ (2002) Toughening and reinforcing in rigid inorganic particulate filled poly (propylene): A review. *J Appl Polym Sci* 83(7):1547–1555
3. Li P (2011) Research development and application in polypropylene materials in automobile. *China Plast Ind* 39:26–29
4. Zhan XL (2007) Research on the viscoelastic properties of asphalt using DMA. Harbin Institute of Technology, Harbin
5. Liu QH, Wang QL, Shen H et al (2010) Static viscoelastic properties of bionic UHMWPE cartilage material. *J Med Biomech* 25(5):369–374
6. Jiang J, Zou F, Lin L et al (2008) Application of dynamic vulcanization EPDM/PP in auto parts. *Eng Plast Appl* 36(11):50–52
7. Zhang SH, Chen G, Cui C et al (2006) Friction and wear behavior of glass fiber reinforced MC-nylon composites. *Tribology* 26(05):452–455

Chapter 27

Study of the Design and Torsion Performance for Carbon Fiber Composite Material Automobile Drive Shaft

Jiancai Liu, Yingguo Xian, Du Cao, Jianbo Su, Wei Liao, Mingde Ding and Zhong Su

Abstract Based on the classical laminate theory, the stacking structure and its joining structure of a carbon fiber composite drive shaft are designed with the carbon fiber epoxy resin as the substrate. The static torsional performance and its fatigue performance of the drive shaft are analyzed using the finite element method. It is showed that the experiment results are consistent with the CAE results in substance, and the drive shaft meets the requirements of the static torque performance and the fatigue performance simultaneously.

Keywords Lightweight · Drive shaft · Composite · Carbon fiber · Design

Research shows that the car weight per reduction of 10%, can reduce fuel consumption by 6–8%, reduce emissions by 5–6%. Lightweight is the most effective way to reduce fuel consumption, and is also an important measure to realize the national strategy of “energy saving and emission reduction” [1]. The automobile drive shaft is a very important part in the automobile, which is composed of the drive shaft tube and the two end flange connection. The outer diameter, wall thickness and inner diameter of the shaft tube are determined according to the conditions of the maximum working torque and the maximum working speed by the drive shaft.

Most of the automobile drive shaft is a steel drive shaft, which has the advantages of good toughness and high yield strength, but also has some disadvantages such as heavy weight, poor corrosion resistance and so on. Compared with steel, carbon fiber composite material has many advantages, such as high strength, high specific modulus, light weight, good anti fatigue performance and excellent vibration reduction performance. At present, Carbon fiber reinforced composites drive shaft (referred to as CF drive shaft) in BMW, Audi, Toyota and other models have been a mature application. Global CF drive shaft has been used more than 900 thousand, but some enterprises for confidentiality of core technology, without the

J. Liu (✉) · Y. Xian · D. Cao · J. Su · W. Liao · M. Ding · Z. Su
Changan Auto R&D Center, Changan Automobile Co., Ltd., Chongqing 401120, China
e-mail: liujc1@changan.com.cn

application of external publicity of the CF drive shaft, such as driving performance is superior to that of Acura MDX models.

The application of carbon fiber reinforced composites in China has not been applied in a wide range, which is mainly used in aerospace and other high end fields. In the civil field, Wuhan science and engineering, Donghua University, Harbin Institute of glass and Steel Research Institute jointly with Chery, Geely, Beijing automobile, SAIC and other car companies to carry out the research work of carbon fiber transmission shaft [2–7].

The project is based on the existing metal drive shaft of a certain type of vehicle, the CF drive shaft is developed through the use of carbon fiber composite material shaft tube instead of the original metal axle tube. Based on the classical laminated plate theory, the structure of the drive shaft of the carbon fiber composite was designed by using the carbon fiber epoxy resin as the base material. The static torsion property and fatigue property of the carbon fiber composite drive shaft are analyzed by using the finite element method. The preparation of carbon fiber shaft winding process, static torsion test and fatigue test of prototype trial, and compared with the theoretical calculation results.

27.1 Structure Design

27.1.1 Axial Dimension Requirement

Existing model of a two section type structure of the drive shaft includes at both ends of the metal shaft, two metal shaft pipe and the middle couplings, as shown below. On the basis of the structure of the metal drive shaft, the project uses the carbon fiber composite material to replace the two metal axle tubes. This can be achieved in the light of the drive shaft, while ensuring the future of the existing models can be directly replaced. One end of the carbon fiber shaft tube is connected with the cross shaft through a shaft pipe fork, and the other end is connected with a spline coupling. In order to ensure the assembly and function of the drive shaft assembly, the length of the carbon fiber tube should be consistent with the length of the metal tube. According to the boundary condition and performance of original products, the static torsional strength is ≥ 1800 N m, and tube body wall thickness

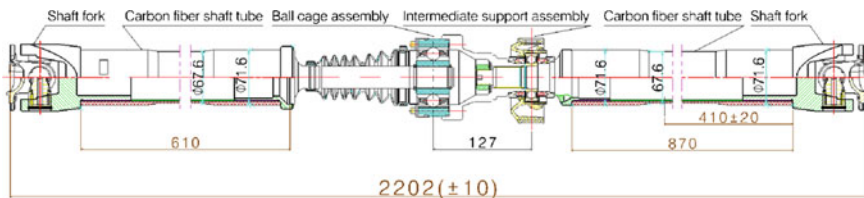


Fig. 27.1 Schematic diagram of carbon fiber transmission shaft assembly

Table 27.1 Comparison of the dimensions and weight of the carbon fiber shaft tube of the transmission shaft with the metal tube

	Internal diameter (mm)	External diameter (mm)	Tube wall thickness (mm)	Pipe length (mm)	Weight (kg)
The metal front axle	61.2	63	1.8	570	1.5
Carbon fiber front axle	62	67.6	2.8	610	0.85
Metal rear axle	74.2	76	1.8	840	2
Carbon fiber rear axle	62	67.6	2.8	870	1.2

Table 27.2 performance of raw materials

	Tensile strength (MPa)	Tensile modulus (GPa)	Fiber density (g/cm ³)
T700 carbon fiber	≥ 4200	≥ 170	1.78–1.80
Epoxy resin	80	3.73	1.23

through the strength calculation optimization proceeds. The initial size of the tube is shown in Fig. 27.1 and Table 27.1.

27.1.2 Material Selection and Process

The carbon fiber tube is made of T700 carbon fiber and high performance epoxy resin, and its mechanical properties are shown in Table 27.2. The properties of carbon fiber composite material prepared by T700 carbon fiber and high performance epoxy resin are shown in Table 27.3.

27.1.3 Layer Design

The design of CF drive shaft is based on the conditions of use and performance requirements, to meet the requirements of strength, minimum frequency and buckling performance, by adjusting the winding angle, stacking sequence, product geometry and material properties. Layer design is the design of the composite layer, layer sequence and layer number. The best results were calculated by the static torsional strength of the carbon fiber, the average longitudinal winding angle of the

Table 27.3 Properties of single layer plate of CF

Longitudinal tensile strength (MPa)	Longitudinal tensile modulus (GPa)	Transverse tensile strength (MPa)	Transverse tensile modulus (GPa)	Longitudinal compressive strength (MPa)	Longitudinal compression modulus (GPa)	Transverse compressive strength (MPa)	Transverse compressive modulus (GPa)
1830	133	37.7	10.4	615	118	137	10.4

carbon fiber axis is 26° , the thickness of the longitudinal winding layer is 2.0 mm, and the circumferential winding layer is 0.8 mm. In order to ensure the performance of the composite pipe fittings, we need to make appropriate adjustments to the filament winding layer, and to meet the following criteria in the design process [4, 5]:

- a. In order to avoid tension bending coupling and prevent warping deformation in the process, the whole laminate paving layer to be symmetric to the neutral surface and should follow the principle of balance, such as every 45° shop layer corresponds to a 45° layer.
- b. The number of layers in any direction is at least 10% of the total amount of the layers. This criterion is in many aspects to consider: first consider vertical in the main by the direction of the force on the Poisson effect and other loads acting directly on the substrate, the second is considering damage tolerance, and finally should also take into account the future may need to repair of the connecting bolt.
- c. In order to avoid the stress concentration and internal micro cracks, it should be as far as possible to the different layers of the spread of the whole layer thickness, to prevent the same angle ply continuous laying.
- d. Adjacent layer should be less than 60° , this is in order to reduce the inter layer shear, and to avoid fatigue problems.
- e. In order to get the two solidified layer, the layer near the curing position should avoid the vertical stress direction, which is to enhance the strength of the connection.
- f. Whenever there is a change in the thickness of the layer, it should change the layer by layer (adjacent layer interval transition), and at the same time to meet the requirements of the slope angle (10°). Special attention is paid to the phenomenon of the glue rich phenomenon in the process of the transition region, as well as the prevention of stress concentration and fatigue.

According to the above principles, to determine the final laying order of carbon fiber composite material shaft tube is $45^\circ/-45^\circ/90^\circ/15^\circ/-15^\circ/90^\circ/15^\circ/-15^\circ/90^\circ/60^\circ/-60^\circ/90^\circ$, a total of 12 layers, with a total thickness of 2.8 mm.

27.1.4 Design and Check of the Static Torsion Strength of the Shaft Tube

- (1) CAE analysis of the length of 870 mm carbon fiber tube, the stress distribution of the tube is shown in Fig. 27.4. When the stress value is 151.4 MPa, the carbon fiber shaft tube is damaged, so the static torque strength of the pipe is:

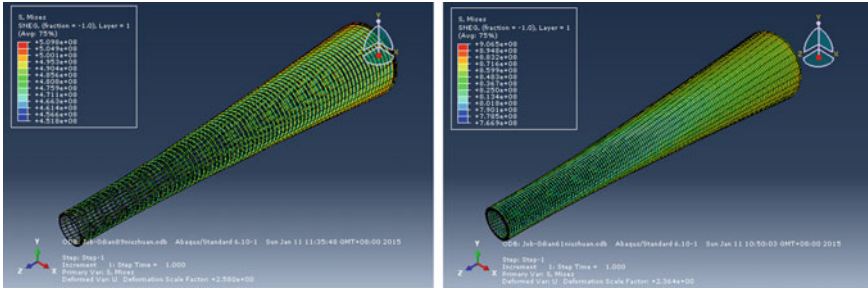


Fig. 27.2 The distribution of the static torsion stress of carbon fiber shaft tube (left length 870 mm, right 610 mm)

$$[T] = [\tau] \cdot S \cdot R = 151.4 \times \frac{\pi}{4} \times (67.6^2 - 62^2) \times 0.031 = 2675.5 \text{ (N m)}$$

Because the design value $[T]_{designvalue} = 1800 \text{ N m} < [T] 2675.5 \text{ N m}$, so the length of 870 mm carbon fiber tube to meet the requirements of the static torsion strength.

- (2) CAE analysis of the length of 610 mm carbon fiber tube, the stress distribution of the tube is shown in Fig. 27.5. When the stress value is 156.5 MPa, the carbon fiber shaft tube is damaged, so the static torque strength of the pipe is

$$[T] = [\tau] \cdot S \cdot R = 156.5 \times \frac{\pi}{4} \times (67.6^2 - 62^2) \times 0.031 = 2765.7 \text{ (N m)}$$

Because the design value $[T]_{designvalue} = 1800 \text{ N m} < [T] 2765.7 \text{ N m}$, so the length of 610 mm carbon fiber pipe fittings to meet the requirements of the static torsion strength (Fig. 27.2).

27.1.5 Connection Design

27.1.5.1 Connecting Structure

The carbon fiber shaft pipe and the flange shaft pipe fork are connected through interference fit and glue, the connection structure see Fig. 27.3. In the preparation process, 40 Cr spline embedded carbon fiber pipe fittings 40 mm. By theoretical analysis, it can be known that the spline connection can transmit the torque is 48,280 N m; Aluminum flange fork spline embedded carbon fiber 60 mm pipe, can transfer torque of 32,243 N m, is greater than the required value (1800 N m) of the static torque required by the car.

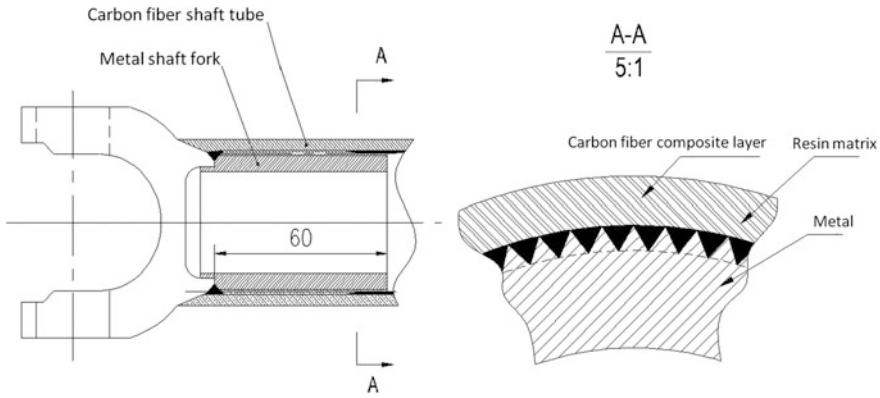


Fig. 27.3 Schematic diagram of the connection structure of carbon fiber shaft pipe and flange

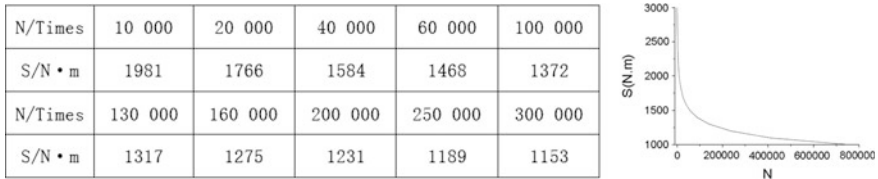


Fig. 27.4 Analysis data and fatigue life curve of the residual strength of the carbon fiber drive shaft

27.1.5.2 Fatigue Analysis

CAE analysis of the fatigue strength of the CF drive shaft, we obtain cycles respectively for 10 000, 20 000, 40 000, 60 000, 100 000, 130 000, 160 000, 200 000, 250 000 and 300 000 times the residual strength values. The least square method is used to fit, then $A = 1.12 \times 1025$, $m = 6.39$, the analysis results are shown in Fig. 27.4. When the torque is less than 2000 N m, the life span of the CF drive shaft is greatly increased; When the torque is less than 1000 m N, the fatigue life is almost unaffected by the torque. Therefore, the design requirements of the torsional fatigue 300 N m fatigue life value of more than 300 000 times can be achieved. It shows that the connection design of the carbon fiber shaft tube and the flange shaft tube cross through the interference fit with glue is designed to meet the design requirements.

27.2 CF Drive Shaft Prototype and Experimental Verification

27.2.1 Winding Process and Prototype

Two section CF drive shaft manufacturing process is divided into four parts, Carbon fiber composite material parts manufacturing, metal parts manufacturing, composite parts and metal parts assembly connection, and the two section of the drive shaft assembly welding. According to the process requirement, the mould of the CF drive shaft is mainly used for the forming process of the composite pipe fitting, that is, the winding part of the carbon fiber shaft tube. The section carbon fiber shaft tube was prepared by adjusting the low cost wet winding forming process, and the two section of carbon fiber was prepared by adjusting the gel content, winding tension, winding speed and other key winding process parameters. The carbon fiber shaft tube is connected with the metal cross fork and the shaft through the interference and bonding of the spline shaft, and the final assembly is assembled into two sections of the transmission shaft.

27.2.2 Static Torsional Strength Test

According to the installation requirements of CF drive shaft, the test fixture was made. The carbon fiber drive shaft is fixed on the test equipment through the clamp, as shown in Fig. 27.5. The test method and basis for static strength of CF drive shaft are QC/T523-1999 “vehicle transmission shaft assembly bench test method”: One end of the transmission shaft is fixed, and the other end is slowly applied to the 1800 N m by the MTS hydraulic torque cylinder, then check whether the transmission shaft assembly has cracking, failure and other phenomena.

The results show that: (1) under the torque of 1900 N m, the drive shaft assembly is no crack, failure and other phenomena, to meet the design requirements. In the 2600 N m torque, the CF shaft tube is not damaged, but the use of a

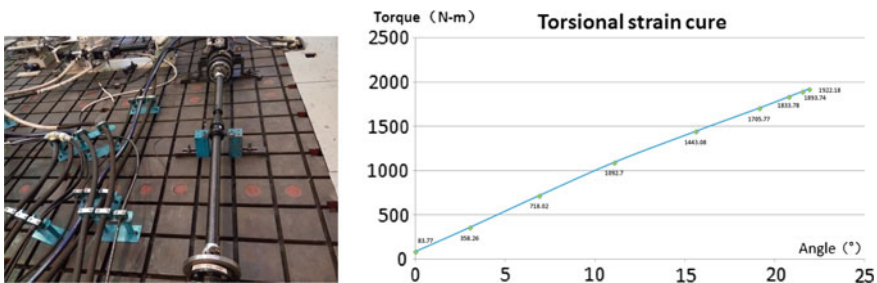


Fig. 27.5 Test device and results of static torsion strength of carbon fiber transmission shaft

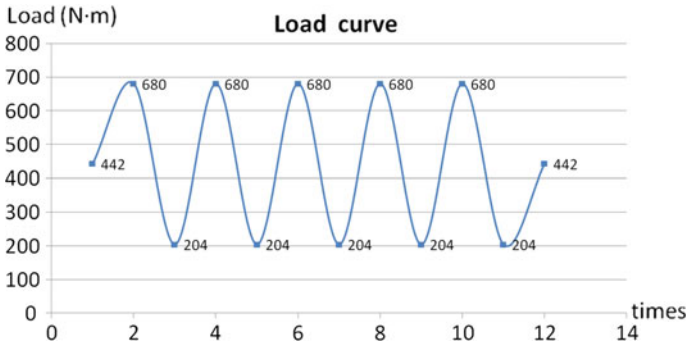


Fig. 27.6 Results of endurance test

cross (cross fork) cracking. This result is equivalent to the CAE analysis results 2675.5 N m, the static torsion strength of the CF drive shaft meets the design requirements.

27.2.3 Durability Test

Durability test method based on QC/T523-1999 “automobile transmission shaft assembly bench test method”. One end of the drive shaft is fixed, and the other end is clamped on the MTS hydraulic torsion cylinder and is applied for 30 000 times of the alternating torsion load, then check whether the transmission shaft assembly has cracking, failure and other phenomena. Figure 27.6 results show that, according to the requirements of the completion of 30 000 times of alternating torsion load, check the drive shaft assembly did not find cracking, failure and other phenomena, to meet the requirements. At the same time, the axial tube in the static torsion up to 2600 N m fatigue test is still in good condition, The results are consistent with the theoretical analysis, Under the condition of less than 1100 N m, the fatigue performance of the carbon fiber transmission shaft is almost not affected.

27.3 Conclusions

The torsion performance of CF drive shaft has a great relationship with the spread angle, the thickness of the layer and the connection structure. For the two section type CF drive shaft were overlay structure and connection structure design, and through the finite element analysis and test on the performance of the prototype was verified. The results show that the test results are consistent with the CAE analysis results. The drive shaft of carbon fiber composite material can meet the requirements of torsional strength and fatigue performance. This shows that the design

method of this paper and CAE analysis method is correct and reliable, and this is for the Chinese brand automobile development and application of CF drive shaft forming technical reserves.

Acknowledgements The authors acknowledge the financial supported by program for science and technology talent training in Chongqing (cstc2014kjrc-qncr60003)

References

1. China Automotive Engineering Society (2015) China automobile lightweight technology innovation strategic alliance, China's first automotive Limited by Share Ltd technical center. China automotive lightweight development-strategy and path. Beijing Institute of Technology Press, pp 2–10
2. Xiao W, He Z, Dong Q (2012) Study of design and manufacture technology on carbon fiber reinforcement composite driveshafts. *Glass Fiber Reinf Plast Compos* S1:232–235
3. Yuan T, Zhou L, Tan C, Zheng W (2012) Research on key technologies of design and fabrication for composite drive shaft. *Manufact Technol Mach Tools* 10:159–163
4. Zhou Z (2012) Study of composite drive shaft for an automobile. Donghua University
5. Hong B (2012) Design of CF transmission shaft. Wuhan University of Technology
6. Hu J, Li X, Zhang T, Han H (2009) Design optimization on torsion property of carbon-fiber composite drive shaft. *Acta Mater Compos Sin* 06:177–181
7. Cui G, Xiao W, Wang P (2014) The study on the torsional properties of the carbon fiber composite drive shaft. *Glass Fiber Reinf Plast Compos* 07:74–77

Chapter 28

Effect of Solution Treatment on Structure and Mechanical Properties of Fe–Mn–Al–Si Light Steel After Cold Rolling

Liang Yao and Wen Shi

Abstract The solution treatment of three different components of Fe–Mn–Al–Si light steel after cold rolling are carried out at 1050 °C and the time is 1 h, 30 min, 10 min. The microstructure and mechanical properties of steel is investigated by using optical microscopy, drawing machine, XRD and SEM. Results shows that with the increasing of heat treatment time, the tensile strength of No. 1 and No. 2 reduces and the elongation of No. 1 and No. 2 firstly increases after an initial decrease; the tensile strength and elongation of No. 3 decreases with the heat treatment time increasing. The microstructure of three different components of steels are always austenite + ferrite and the content of retained austenite increases with the heat treatment time increasing. There is no phase transformation and Transformation Induced Plasticity occurs during the deformation of the tested steel.

Keywords Fe–Mn–Al–Si · Light cold-rolled steel · Solution treatment · Mechanical properties · Microstructure

28.1 Introduction

With the development of society and the progress of science and technology, energy saving and emission reduction has become an important standard of automobile design. Relevant research [1] showed that in the other conditions remain unchanged, with the vehicle weight reduce by 10%, fuel consumption decrease by 8–10%. Furthermore, Automobile lightweight will reduce CO₂ emissions. Steel accounts for 55–70% of the total vehicle weight, so we must optimize and upgrade the automotive steel plate, develop high strength and ultra high strength automotive steel plate used in automobile manufacturing.

L. Yao · W. Shi (✉)

School of Materials Science and Engineering, Shanghai University,
Shanghai 200072, China
e-mail: shiwen@shu.edu.cn

Fe–Mn–Al–Si TRIP/TWIP Steel is one of the new generation of automotive steel with great potential, which has high yield strength and tensile strength, ductility, stamping forming ability, and can be used to reduce the weight and the fuel consumption. In addition, the steel has high energy absorption ability, can resist the plastic deformation in impacting and improve the safety level of the car significantly. Mn in the steel is mainly to expand the region of the austenite. But when the content is too high, it will produce banded microstructures [2] and decrease the welding performance significantly [3]. Al in the steel is to lose weight because some scholars [4] studied that with the content of Al increases by 1%, the weight of the steel plates decrease by 1.3% compared with traditional steel plates. But if the content is too high, it will promote the formation of ferrite and reduce thermal cracking resistance of weld metal. Therefore, the actual designed Al content can not be too high. Si is also a ferrite forming element, but its solid solution strengthening effect is strong, and can play a role in inhibiting the precipitation of carbides [5, 6].

In order to further reduce the weight of the steel plate, this paper designs three different component of Fe–Mn–Al–Si light cold rolling with high Al content. Moreover it designs several kinds of solid solution treatment process and studies the effects of solid solution treatment on mechanical performance and microscopic organization of Fe–Mn–Al–Si light cold rolling steel.

28.2 Experimental Materials and Methods

The composition of the experimental steel which is smelted by the vacuum induction melting is given in the Table 28.1. Firstly, the cylindrical ingot is heated to 1150 °C for 30 min and quenches in air after being forged into about 20 mm thick steel plate. Secondly, the steel plates start to be rolled at the temperature of 1150 °C and stop at the temperature of 880 °C. After hot rolling, the steel quenches in air and the thickness is 2.8 mm. Finally, the steels are pickled and the thickness becomes the 1.5 mm after cold rolling.

The three experimental steel after cold rolling are processed into 10 × 10 mm small sample and tensile specimen with a gauge of 30 mm which be treated with solid solution treatment at 1050 °C for 1 h, 1050 °C for 30 min, 1050 °C for 10 min and quenches in water.

The samples are corroded with alcohol solution containing 6% of nitric acid, and the microstructure is observed by metallographic microscope Nikon LV150 300. Microstructure and tensile fracture morphology of the samples are observed by Tungsten Filament SEM of Hitachi SU-1500. The phase analysis and the content of

Table 28.1 Chemical composition of specimen (%)

Steel	C	Mn	Al	Si	Fe
1#	0.8	15	9.5	0.5	Bal
2#	0.8	15	8.5	1.5	Bal
3#	0.8	15	7	3	Bal

retained austenite are used by the 18KW D/MAX2200 PC type XRD. Tensile test at room temperature is performed on the CMT5105 electronic universal testing machine, and the tensile rate is 2 mm/min.

28.3 Experimental Results and Analysis

28.3.1 Mechanical Property Analysis

The stress-strain curve of three specimens after solution treatment at 1050 °C for 1 h, 1050 °C for 30 min, 1050 °C for 10 min are shown in Fig. 28.1. Three experimental steel tensile curves are very smooth and display the characteristics of continuous yield and no obvious yield platform. After the start of the deformation, stress increases soon with the strain increases and elastic deformation only existence in small strain range. But the stress increases slowly during plastic deformation stage. It can be drawn the conclusion that the mechanical property of the steel after three different solution treatment is well as shown in Fig. 28.1 and Table 28.2. The tensile strength is in 850–1100 MPa, the elongation is at 33–55%.

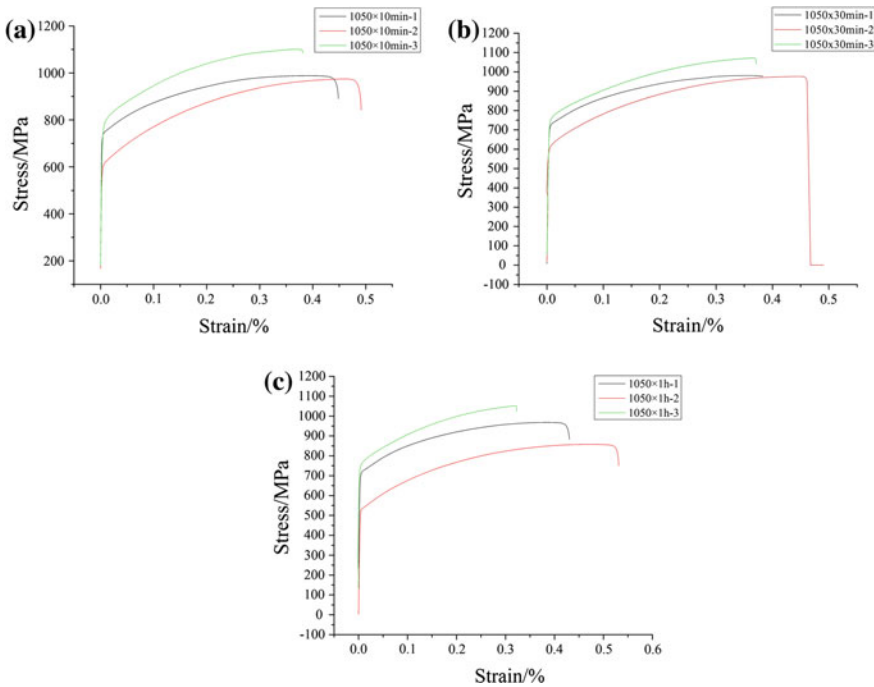


Fig. 28.1 Stress-strain curve of three specimens after solution treatment for different time **a** 1050 °C × 10 min **b** 1050 °C × 30 min **c** 1050 °C × 1 h

Table 28.2 Mechanical properties of three specimens after solution treatment for different time

Specimen		Tensile strength (MPa)	Elongation (%)	Strength-ductility (MPa%)
1050 × 1 h	1	968.25	41.7	40,376.03
	2	857.96	55.9	47,959.96
	3	1051.56	32.8	34,491.17
1050 × 30 min	1	981.21	37.87	37,158.42
	2	976.52	47.07	45,964.80
	3	1072.07	37.93	40,663.62
1050 × 10 min	1	988.58	44	43,497.52
	2	974.98	50.1	48,846.50
	3	1100.99	38.7	42,608.31

The product of strength and plasticity is generally greater than 40,000 MPa%, and the best is close to 50,000 MPa%. The best tensile strength is No. 3 steel after solution treatment at 1050 °C for 10 min and can reach 1100.99 MPa; the best elongation is No. 1 steel after solution treatment at 1050 °C for 1 h and can reach 55.9%; the best product of strength and plasticity is No. 2 steel after solution treatment at 1050 °C for 10 min and can reach 48,846.50 MPa%. With the solid solution heat treatment time increases, the tensile strength of the No. 1 and No. 2 steel is on the decline, and elongation shows a trend from decline to rise; with the solid solution heat treatment time increases, the tensile strength and elongation of No. 3 steel decrease, as shown in Figs. 28.2 and 28.3. This is because that with the solid solution heat treatment time increases, organizations grow up, resulting in elongation and tensile strength decrease. But with the solid solution heat treatment time continues to increase, C and Mn enters in microstructure, reducing the pinning effect, decreasing the tensile strength, increasing the elongation. The different of No. 3 steel may be due to the $Al_{0.7}Fe_3Si_{0.3}$ after the solid solution treatment which can grown up with the solid solution treatment time increases and decrease the tensile strength, elongation.

It can be found that integrated mechanical property of No. 2 steel is the best at the same solid solution treatment. Although its tensile strength is the worst, its

Fig. 28.2 Effect of heat treatment time on tensile strength

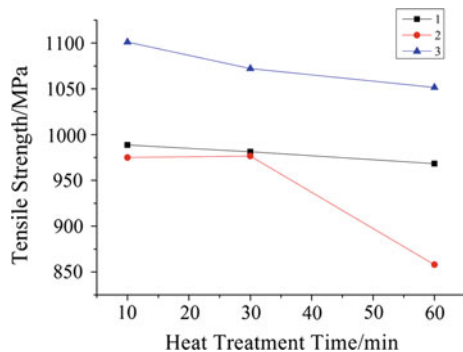
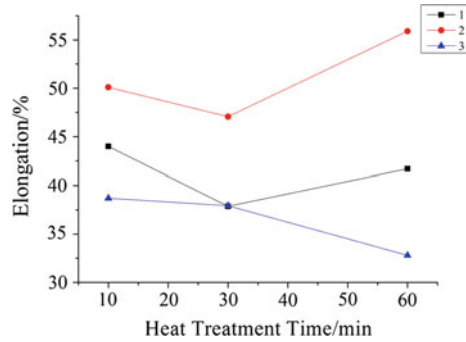


Fig. 28.3 Effect of heat treatment time on elongation



product of strength and plasticity is the best because its elongation is the best. Because the plasticity of No. 3 steel is very bad, its product of strength and plasticity is not good in spite of the good tensile strength. It may be due to the content of Al and Si in the steel. Al and Si all have solid solution strengthening effect, but the effect of Si is better than Al. So No. 3 steel has good tensile strength and bad plasticity. Hamada et al. [7] and the others find that adding a certain amount of aluminum in steel can significantly improved heat deformation resistance, delay the dynamic recrystallization and refine the austenite grain after dynamic recrystallization which may explain why the plasticity of No. 2 steel is so good.

28.3.2 Microstructure Analysis After Heat Treatment

Microstructure of three substrate specimens after solution treatment for different time are shown in Fig. 28.4. From Fig. 28.4, it can be found that the microstructures of all the three kinds of experimental steel are strip shape. It is because that the sample is cold-rolled specimens. After heat treatment, some microstructures recovery and recrystallize into the spherical structure, but most of microstructures are still strip shape. Figure 28.5 is the XRD result of three substrate specimens after solution treatment for different time. It can be drawn the conclusion that the main microstructure of the three kinds of experimental steel are ferrite + austenite without carbide although the heat treatment time is different from Fig. 28.5. In addition, there is a small amount of $Al_{0.7}Fe_3Si_{0.3}$ in No. 3 steel, which may be because the content of Si in No. 3 steel is 3%, far more than No. 1 and No. 2 steel. The ferrite phase is a white phase, and the austenite phase is a gray phase in Fig. 28.4. The gray phase can be defined as austenite phase because there are obvious twin structures in it. The existence of $Al_{0.7}Fe_3Si_{0.3}$ is not found in all the metallographic pictures maybe because the content of $Al_{0.7}Fe_3Si_{0.3}$ is too small. Although the microstructure is ferrite + austenite, but the morphology is still different for the different heat treatment time. The microstructure of the specimens with heat treatment for 10 min is significantly flatter than that of the specimen with

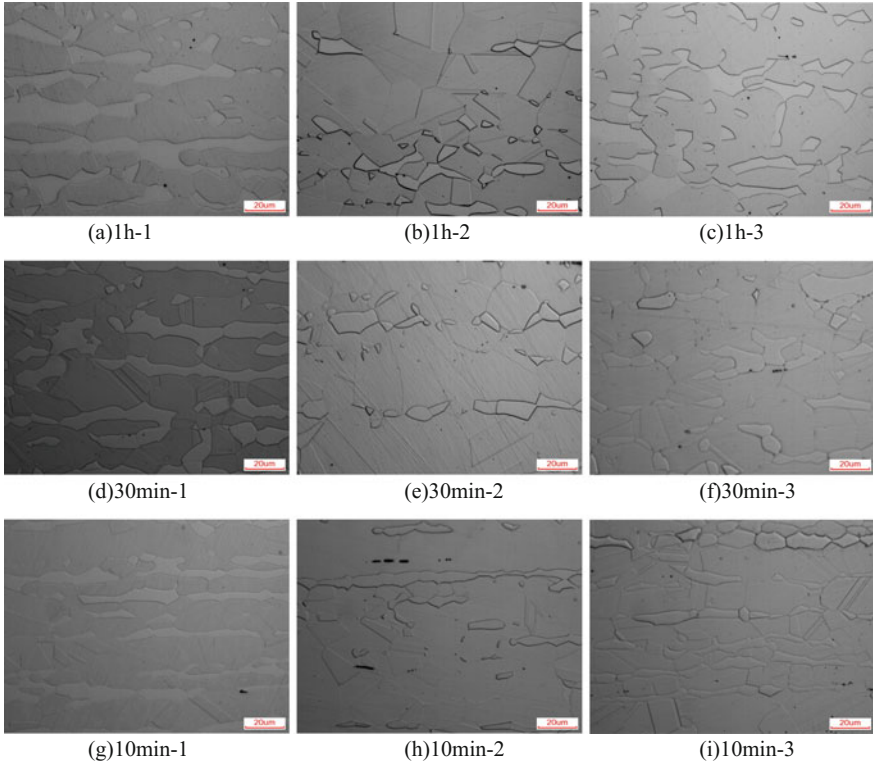


Fig. 28.4 Microstructure of three substrate specimens after solution treatment for different time

heat treatment time for 1 h. It is because that the broken grains have recrystallized after longer heat treatment. This phenomenon is most obvious in No. 2 steel which may explain why the plasticity of No. 2 steel is the best.

In order to explore the relationship between the content of retained austenite and mechanical properties, this paper analyzes and calculates the content of retained austenite by X-ray diffraction method. According to the principle of X-ray diffraction [8], the cumulative intensity of X-ray diffraction of phase increases with the relative content of the phase increases in the sample. So according to the Chinese People Republic of ferrous metallurgy industry standard [9], the cumulative intensity of ferrite phase and austenite phase diffraction line should be put into the formula (28.1) to calculate the volume fraction of retained austenite phase in steel.

$$V_A = \frac{1 - V_C}{1 + G \frac{I_{F(hkl)}_j}{I_{A(hkl)}_j}} \quad (28.1)$$

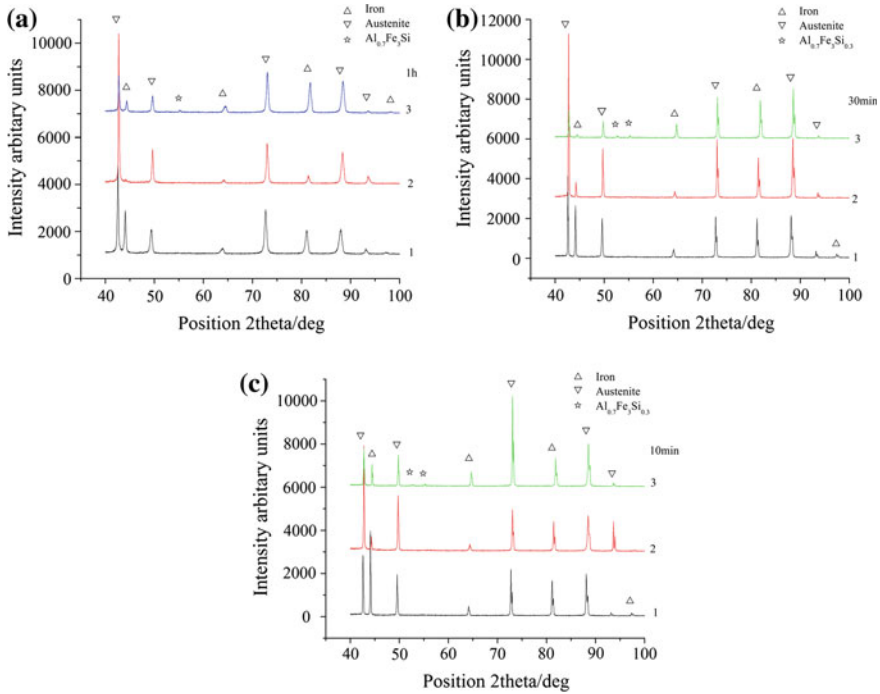


Fig. 28.5 XRD result of three substrate specimens after solution treatment for different time

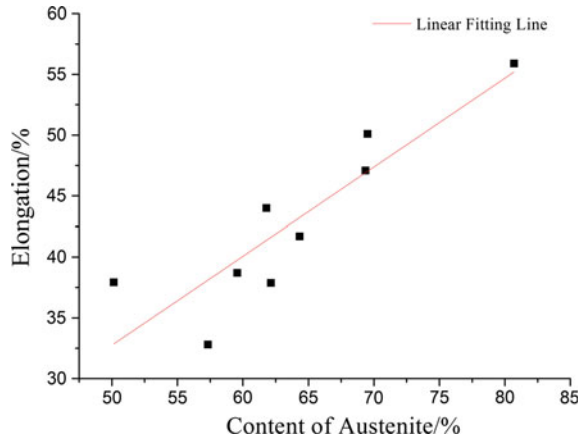
Table 28.3 Volume fraction of austenite in three substrate specimens after solution treatment for different time

Heat treatment time	Volume fraction of austenite (%)		
	1	2	3
1 h	64.33	76.37	57.34
30 min	62.15	69.36	54
10 min	61.80	69.51	59.58

V_A , V_C , $I_{F(hkl)_i}$, $I_{A(hkl)_j}$ and G show the volume fraction of austenite phase in steel, the volume fraction of carbide in steel, the cumulative intensity of $(hkl)_i$ crystal face of ferrite phase in steel, the cumulative intensity of $(hkl)_j$ crystal face of austenite phase in steel, the ratio of intensity of related factors correspond to $(hkl)_j$ crystal face of austenite phase and $(hkl)_i$ crystal face of ferrite phase, respectively.

The volume fractions of austenite in three substrate specimens after solution treatment for different time are shown in Table 28.3. It can be drawn the conclusion that when Si content is 1.5%, austenite content is the highest and when Si content is 3%, austenite content is the lowest although different heat treatment time from Table 28.3. In addition, the content of austenite decreases with the reduction of heat

Fig. 28.6 The linear fitting of austenite content and elongation of nine substrate specimens



treatment time. Figure 28.6 is the linear fitting of austenite content and elongation of nine substrate specimens. According to the overall analysis, it can be found that there is a linear relationship between the austenite content and elongation. With the increase of the content of austenite, the elongation will increase. The research data show that, no matter how much heat treatment time is, No. 2 steel which has the highest austenitic content has the largest elongation and product of strength and plasticity. Therefore, in order to ensure excellent mechanical properties, it is necessary to make the steel have enough content of retained austenite.

28.3.3 Microstructure Analysis After Tensile Test

In order to explore the microstructure change after tensile test, the microstructure of the fracture surface is analyzed by metallographic examination and XRD analysis as shown in the Figs. 28.7 and 28.8. Because the steel has been stretched, the organization becomes more flat after tensile test as shown in the Fig. 28.8. But there is no new phase, the main organization is ferrite + austenite as before. Figure 28.7 shows that there is no new diffraction peak in tensile fracture specimen after XRD test, which corroborated the results of metallographic observation. Furthermore, austenite content calculated by XRD diffraction analysis do not occur big changes after tensile test although the heat treatment process are different as shown in Table 28.4. According to the experimental results, it can be concluded that although heat treatment time are different, the microstructure of steel is ferrite + austenite after tensile test, which means there is no phase transition occurred in tensile process. In other words, the steel in tensile process do not occur TRIP effect.

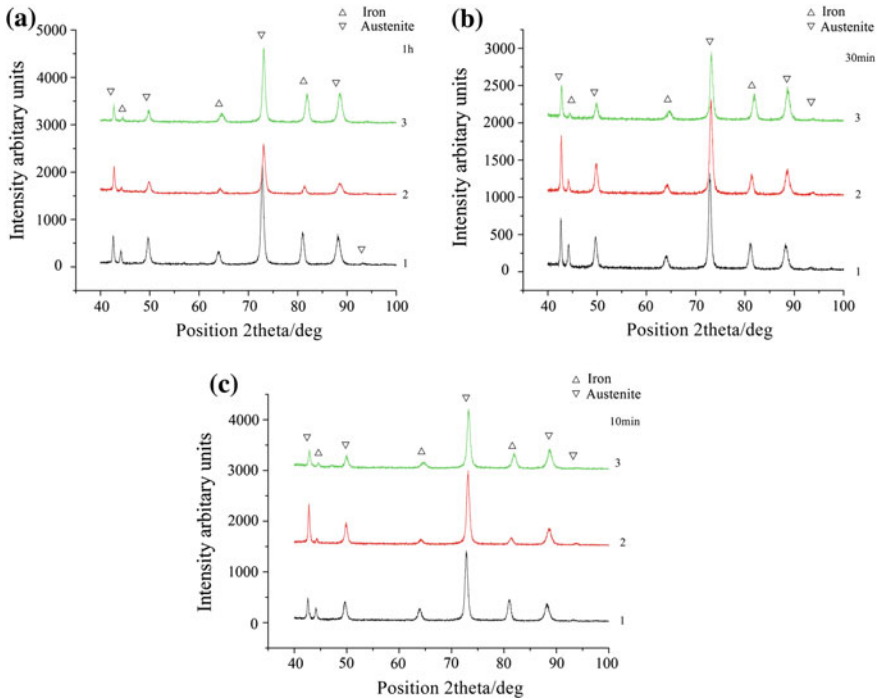


Fig. 28.7 XRD result of three fracture specimens after solution treatment for different time. **a** 1 h. **b** 30 min. **c** 10 min

28.3.4 Fracture Analysis

Figure 28.9 is the SEM results of three fracture specimens after solution treatment for different time. The elongation of No. 3 steel after solution treatment at 1050 °C for 1 h is the worst and is 32.8%. In Fig. 28.9, there are dimples and a large number of tear edges which are the characteristics of quasi-cleavage. This shows that No. 3 steel after solution treatment at 1050 °C for 1 h has mixed-rupture characteristics of brittle rupture and tough rupture. The poor elongation of No. 1 steel and No. 3 steel after solution treatment at 1050 °C for 30 min and No. 2 steel after solution treatment at 1050 °C for 10 min is about 38%. The tensile fracture morphology confirmed that elongation is poor, because there are more dimples and a certain amount of tear ridges on the fracture surface, although the number of tear ridges is less than the number in No. 3 steel after solution treatment at 1050 °C for 1 h. It confirms that their elongation is poor, but is better than the elongation of No. 3 steel after solution treatment at 1050 °C for 1 h. The elongation of No. 2 steel after solution treatment at 1050 °C for 1 h and at 1050 °C for 10 min can reach 55.9 and 50.1% respectively. According to Fig. 28.9b, it can be found that the

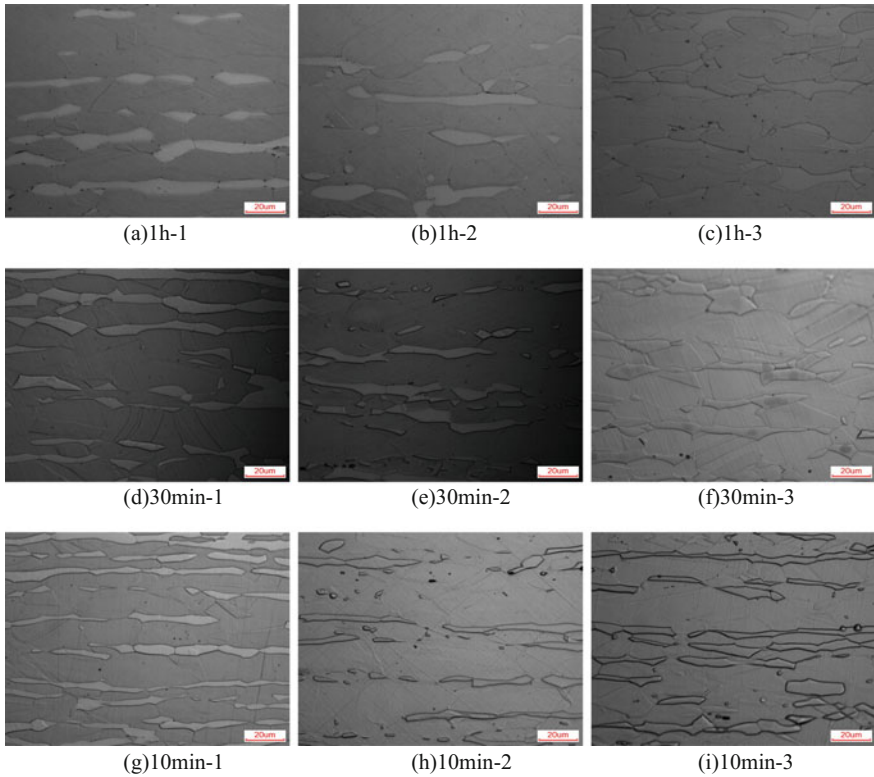


Fig. 28.8 Microstructure of three fracture specimens after solution treatment for different time

Table 28.4 Volume fraction of austenite in three substrate specimens and three fracture specimens after solution treatment for different time

Heat treatment process	Specimen	Volume fraction of austenite in matrix (%)	Volume fraction of austenite after tensile test (%)
1050 °C × 1 h	1	64.33	64.09
	2	76.37	75.75
	3	57.34	55.88
1050 °C × 30 min	1	62.15	61.97
	2	69.36	68.94
	3	54	53.87
1050 °C × 10 min	1	61.80	59.14
	2	69.51	67.98
	3	59.58	59.03

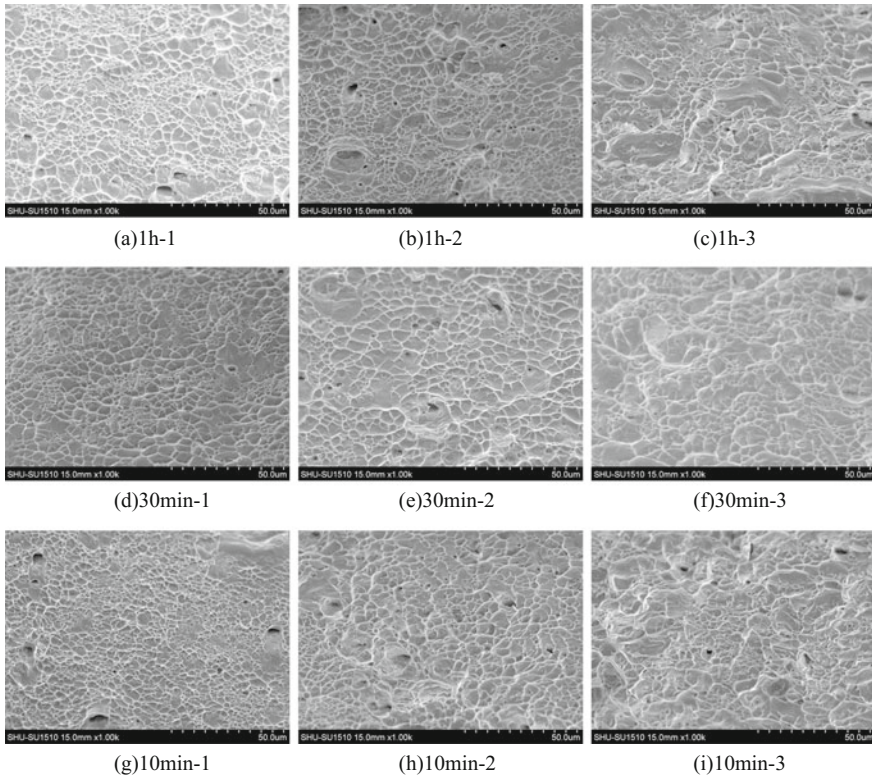


Fig. 28.9 SEM results of three fracture specimens after solution treatment for different time

tensile fracture surface is densely covered with a large number of small and shallow dimples, indicating that the fracture mode is ductile fracture. The elongation of No. 1 steel after solution treatment at 1050 °C for 1 h, No. 2 steel after solution treatment at 1050 °C for 30 min and No. 3 steel after solution treatment at 1050 °C for 10 min can reach 40%. Their elongation are 41.7, 47.07, 44% respectively. The fracture surface has a large number of dimples and a small number of tear edges, so the plastic is not better than the plastic of No. 2 steel after solution treatment at 1050 °C for 1 h and at 1050 °C for 10 min.

In addition, there are some deeper holes in the tensile fracture as shown in Fig. 28.9, which may be caused by the inclusion of the steel. During the tensile test, the matrix and the non-metallic inclusion, the precipitation phase particles will generate the stress concentration which will form a small hole. With the further development of the tension, the small holes grow up, and the adjacent holes will also gather together to form a larger hole until the fracture is produced.

28.4 Conclusion

1. The best comprehensive mechanical properties of the three kinds of experimental steels are No. 2 steel. With the solid solution heat treatment time increases, the tensile strength of the No. 1 and No. 2 steel is on the decline, and elongation shows a trend from decline to rise; with the solid solution heat treatment time increases, the tensile strength and elongation of No. 3 steel decrease. With the solid solution heat treatment time increases, the content of austenite increases.
2. The main microstructure of the three kinds of experimental steels is ferrite + austenite. Because No. 3 steel has 3% Si, there is a small amount of $Al_{0.7}Fe_3Si_{0.3}$ in No. 3 steel.
3. There is a linear relationship between the austenite content and elongation. Therefore, in order to ensure excellent mechanical properties, it is necessary to make the steel have enough content of retained austenite.
4. The microstructure of steel is ferrite + austenite after tensile test, which means there is no TRIP effect in tensile process. And the content of austenite do not occur big changes.
5. The elongation of No. 2 steel after solution treatment at 1050 °C for 1 h is the best. It can be found that the tensile fracture surface is densely covered with many dimples, indicating that the fracture mode is ductile fracture. The elongation of No. 3 steel after solution treatment at 1050 °C for 1 h is the worst. There are some dimples and a large number of tear edges in tensile fracture. This shows that No. 3 steel after solution treatment at 1050 °C for 1 h has mixed-rupture characteristics of brittle rupture and tough rupture. The elongation of the other steel is between the two above-mentioned steels. There are a large number of dimples and a small amount of tear edge in the tensile fracture, so the fracture mode is ductile fracture mainly.

References

1. Joseph C, Benedyk K (2000) Light Metals in automotive applications. *Light Metal Age* 10: 34–35
2. Kim SJ, Lee CG, Choi I (2001) Effects of heat treatment and alloying elements on the microstructures and properties of 0.15 wt pct C transformation-induced plasticity-aided cold-rolled steel sheets. *Metall Mater Trans A V32A*(March):505–514
3. Hu GX, Qian MG (1980) *Metallography*. Shanghai Science and Technology Publishing House, Shanghai, pp 292–301
4. Frommeyer G, Brüx U (2006) Microstructures and mechanical properties of high-strength Fe-Mn-Al-C light-weight TRIPLEX steels. *Steel Res Int* 77:627–633
5. Owen WS (1954) The effect of silicon on the kinetics of tempering. *Metall Trans A* 46(1): 812–829
6. Leslie WC, Rauch GC (1978) Precipitation of carbides in low-carbon Fe–Al–C alloys. *Metall Trans A* 9(2):343–349

7. Hamada AS, Karjalainen LP, Somani MC (2007) The influence of aluminum on hot deformation behavior and tensile properties of high-Mn TWIP steels. *Mater Sci Eng A* 467 (2):114–124
8. Zhou Y, Wu GH (2007) *Material analysis and testing technology*. Harbin Industrial University Press, Harbin, pp 84–94
9. Quantitative determination of retained austenite in steel by X-ray diffraction method. State Standard of the People's Republic of China YB/T5338-2006

Chapter 29

Damping Analysis and Test Research of a Composite Leaf Spring in a Light Bus

Wenku Shi, Chen Qian, Qianqian Song, Bo Gao and Jun Ke

Abstract In order to study damping characteristic and its influencing factors of E glass fiber/polyurethane composite leaf spring, we use finite element simulation method. Give a detailed research method of it: According to the structure semesters of the spring, building 3D models of composite laminate and spring and carrying out the grid division by the finite element software HYPERMESH and the mechanical property parameters of the material were given to the model; making tests of composite laminate and spring and convert the results into simulation semesters of the model; we make analysis by finite element software ABAQUS and compare the simulation results with the experimental results to find out that the mainly influence factors of composite leaf spring damping characteristic are laying angle and longitudinal tensile modulus of materials. Analysis results show that 0 angel layer damping ratio is 0.0074 belongs to small damping system. Above all, our research provides theoretical basis and research methods for studying composite leaf spring damping characteristic.

Keywords Bus · Composite · Leaf spring · Finite element analysis · Damping characteristic analysis

29.1 Introduction

Since twenty-first century, with the rapid development of social science and technology, economy and culture, the car has become a necessity for every household. People's demand for cars is no longer a simple power, comfort, but more safe, more economical and more environmentally friendly. Therefore, the automobile light-weight has become the inevitable trend of the development of the industry. Under the premise of meeting the requirements of the basic mechanics, composite leaf

W. Shi · C. Qian (✉) · Q. Song · B. Gao · J. Ke
State Key Laboratory of Automotive Simulation and Control, Jilin University,
Changchun 130022, China
e-mail: qcjlu@foxmail.com

spring weights less than 40% of the weight of the steel plate spring, and composite leaf spring has the advantage of corrosion resistance and oxidation resistance, the fatigue life of that is two times of leaf spring. At the same time, it has damping characteristics, which has a great contribution to the damping effect of the suspension. At present, fiber reinforced resin based composite material have been widely used in the cars, it is bound to replace the traditional metal materials. However, the domestic research of composite leaf spring damping theory and experiment is less, which is unable to meet the needs of development [1–4].

Therefore, this paper established a composite laminates and spring assembly finite element model: Simulation and experiment of damping characteristics were carried out, the factors which influence the spring damping characteristics were analyzed. And the methods and ideas about spring damping characteristics of composite material research were also provided. The valuable conclusions are obtained, which provide references for similar studies.

29.2 Brief Introduction of Composite Leaf Spring

Resin matrix fiber reinforced composite material is a simple point of the composite formed by the formation of fiber and polymer. This paper studies the spring E glass fiber/polyurethane composite leaf spring just as shown in Fig. 29.1, it has the characteristic of high specific strength, high specific modulus and viscoelasticity. We can see from Table 29.1 that its damping is 10–100 times of ordinary metal materials [5]. Therefore, the damping performance of the resin matrix composites can not only reduce the vibration and noise of the system, but also can extend the structure to bear the time of cyclic loading and impact, and improve the system fatigue life [6].

Therefore, we firstly research on composite leaf spring damping characteristics, predict damping properties of the composites, and reveal the impact of factors, then obtain a composite leaf spring stiffness and damping characteristic curve, finally we

Table 29.1 Common consumption factor for engineering

Material	Loss factor
Glass	$0.6 \times 10^{-3} - 2 \times 10^{-3}$
Steel and iron	$1 \times 10^{-4} - 6 \times 10^{-4}$
Plywood	$1 \times 10^{-2} - 1.3 \times 10^{-2}$
Nonferrous metal	$1 \times 10^{-4} - 2 \times 10^{-3}$
Concrete	$1.5 \times 10^{-2} - 5 \times 10^{-2}$
Plastic	$5 \times 10^{-3} - 1 \times 10^{-2}$
Cork	0.13–0.17
Stone	$5 \times 10^{-3} - 7 \times 10^{-3}$
Viscoelastic material	$2 \times 10^{-1} - 5 \times 10^0$

Fig. 29.1 Composite leaf spring



design the component to meet the practical engineering through the matching design of composite leaf spring and the suspension system, it has important practical significance to meet the need of car to ride and safety demand.

29.3 Simulation Analysis and Experimental Verification of Damping Characteristics of Laminated Plates

29.3.1 E Glass Fiber/Polyurethane Laminate Damping Test

29.3.1.1 Test Method for Damping Properties of E Glass Fiber/Polyurethane Laminates

The damping properties of the composites are related to the anisotropy of the material itself, the viscoelasticity, and the design of the layer. It cannot be calculated or predicted by the simple mathematical model, which must be obtained through the experiment. There are many ways to characterize the damping properties of the composites. In this paper, the damping ratio of the composite component is used to measure the damping characteristic, and the energy dissipation capacity of the system is very intuitive. Reference to national standards [7]. The damping ratio of the component can be obtained through the attenuation vibration test: The damping property of the composite member is much higher than that of the steel plate, but its damping size still belongs to the small damping range. The free attenuation method is accurate, especially for the small damping and low frequency system, so the damping ratio of the component is obtained by designing the attenuation vibration curve of the component.

29.3.1.2 Test Scheme for Damping Properties of E Glass Fiber/Polyurethane Laminates

Considering the sample size and the accuracy of measurement, glass fiber/polyurethane laminate will be used in the modal test will be cut. Because the sample mass and stiffness are much lower than the composite leaf spring,

so the measurement accuracy will decline. The test sample size cannot be too small, the size of the composite laminate is shown in the left of Fig. 29.2, then clip it to the shape shown in the right of Fig. 29.2: The test small sample piece laminate length 300, width 30, thickness of 3.2 (mm), composed of 4 layers of 0°; The test big sample piece laminate length 300, width 100, thickness of 3.2 (mm), composed of 4 layers of 0°.

Based on the natural frequency and damping ratio of automotive suspension system, clamp and fix one end of the test member, and the other end is forced to do the free decay vibration until still, the free attenuation rate was calculated and analyzed by the sensor, the clamping method of laminate is shown in Fig. 29.3.

This test uses the TEST.LAB LMS test system and B&K/PCB company's one-way vibration acceleration sensor, the specimen is subjected to an external force to bend the back side of the specimen, then remove the force, the specimen began free vibration until it reaches a stationary state. By giving the test pieces of different sizes of external force, the free damped vibration curves of specimens under different accelerations are obtained, the test results of the initial acceleration 36 g of the small laminated plates are shown in Fig. 29.4.

Because the peak points in the test data are very close to each other, the error of artificial points is large. In order to improve the accuracy of data processing, the data

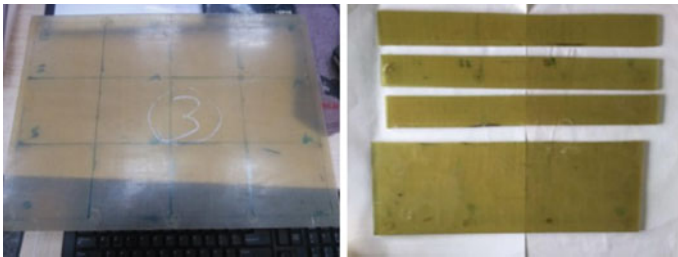


Fig. 29.2 Laminates damping test

Fig. 29.3 Composite laminates clamping method



Fig. 29.4 Decaying vibration curves of large laminates

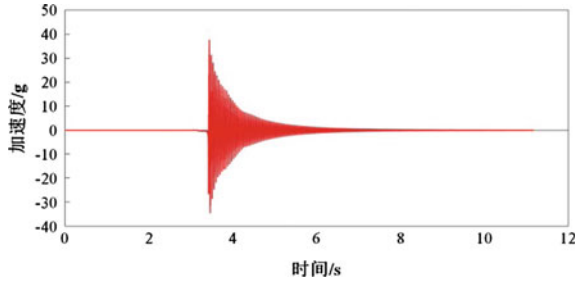


Table 29.2 Results of damping analysis

Acceleration	17	27	36	45	57
Damping ratio	0.0068	0.0074	0.0071	0.0071	0.0073

processing program is compiled by MATLAB software. Based on the principle that the acceleration value of the vibration peak value is greater than that of the adjacent two points, the peak value is extracted. Because of the phenomenon of peak coincidence and missing in the test data, the binomial exponential function $y = a \times e^{bx} + c \times e^{dx}$ is used to fit the change trend of the peak point, the fitting correlation is greater than 0.99. Then, the sine function $y = a \times \sin(bx + c)$ is used to fit the decay period, the attenuation period of test $T_d = \frac{2p}{b}$ data is obtained. The calculation of the initial point is selected as the maximum acceleration of the peak point of the horizontal coordinates, through the fitting function $y = a \times e^{bx} + c \times e^{dx}$ to calculate the peak value of the first point; Then select a transverse coordinate every T_d , and then calculate the peak value of each point in turn. Finally, the peak value is composed of the calculation point set, and the damping ratio is calculated according to the damping ratio of the adjacent peak points.

The free attenuation vibration test data of the sample with different initial acceleration is analyzed, the damping ratios at different initial acceleration are shown in Table 29.2. Due to the initial stage of the attenuation of the sample, the air resistance has a great influence on the damping, and the influence of the air resistance is weakened at the later stage of the damped vibration, so the damping ratio of the damping vibration curve is relatively stable. The damping ratio of the specimen is 0.0068–0.0074 in the Table 29.2, the mean value is 0.007. There are three main factors that affect the damping ratio of the laminated plates: the air resistance, the structure size and the inertia force of the sensor with the vibration of the sample [8]. Consider the above factors, the damping ratio of the E glass fiber/polyurethane laminate is 0.007, which is 1 orders of magnitude higher than that of the spring steel, which shows that the damping performance of the E glass fiber/polyurethane laminate is significantly higher than that of the spring steel. But we should also note that the absolute value of the damping ratio of the E glass fiber/polyurethane laminate is no more than 0.01, indicating that the E glass fiber/polyurethane laminate is a small damping material.

29.3.2 Simulation and Analysis Method of Damping Performance of E Glass Fiber/Polyurethane Laminate

29.3.2.1 Simulation Procedure and Parameter Setting of E Glass Fiber/Polyurethane Laminate Damping Performance

The results obtained by the test of the damping characteristics of the laminated plates: After conversion, the damping ratio is used in the finite element simulation in the form of the parameters. The damping characteristic of the finite element model is obtained by finite element simulation, and the damping ratio is calculated, the results of the two methods are compared to verify the correctness of the parameter setting and simulation method.

First, the three-dimensional model of the laminated plate specimen is established in the ABAQUS software, which is used to define the parts and components. Then, in the Property module, the mechanical properties of the composites are defined. The mechanical properties are defined by engineering constants, and the performance parameters are set according to Table 29.3. Through the composite layup manager dialog box to define the laminate layer parameters, set the parameters as shown in Table 29.4. Then, in the Step module a linear perturbation load step is established which named step 1: Frequency, using the Lanczos method to solve, the frequency range is set to 0–1024 Hz. After step 1, we establish another modal dynamics analysis step which named step 2: in which the Rayleigh damping parameters are set, given the start and end of the calculation of modal order. Then the boundary condition of the laminate specimen is set to one end completely fixed as shown in Fig. 29.5, and applied a concentration F at the other end. After the modal analysis of laminated plates, the force is applied in the analysis step Step 2. The amplitude and direction of the force and the time of action in the edit load

Table 29.3 Mechanical properties of E-glass/polyurethane

Parameter	Parameter value	Parameter	Parameter value
E_{xx} (MPa)	40,978	ρ (g/cm ³)	2.07
E_{xy} (MPa)	14,058	X_T (MPa)	1003
G_{xy} (MPa)	3641	X_C (MPa)	832
ν_{xy} (MPa)	0.31	Y_T (MPa)	84
ν_{xx} (MPa)	0.31	Y_C (MPa)	217
ν_{yy} (MPa)	0.36	S_{xy} (MPa)	51

Table 29.4 Simulation parameters of laminates

Parameter	Lay number	Lay angle	Layer thickness	Lay size
Numerical value	4	0°	0.808 mm	300 × 30 mm

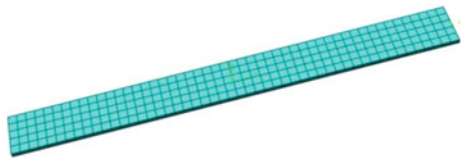
Fig. 29.5 Laminates boundary condition setting



Table 29.5 Amplitude parameters of laminates

	Time/frequency	Amplitude
1	0	0
2	0.01	1
3	0.2	1
4	0.22	0

Fig. 29.6 Laminates meshing method



manager use the “table” way to edit the amplitude, the set parameters as shown in Table 29.5. In the Mesh module partition grid, type of grid is a hexahedral element C3D8R (Fig. 29.6). Finally, the finite element model is submitted to ABAQUS solver calculation.

29.3.2.2 Setting Method of Damping Parameter in Simulation of E Glass Fiber/Polyurethane Laminate Damping Performance

In this paper, the linear combination of the mass matrix and stiffness matrix is used in the finite element simulation software ABAQUS:

$$C = \alpha M + \beta K$$

Among them, the α and β are defined according to the material properties, M and K are the system mass and stiffness matrix. Although the Rayleigh damping model has not yet been fully applied to all complex models, the Rayleigh damping model is reliable in the case of damping values less than 10%; Rayleigh damping can be precisely defined for each mode of the system; And the Rayleigh damping can be transformed into the correlation function of damping ratio in the process of parameter setting. And it greatly simplified calculation, which provides a convenient for the damping matching work, so the damping characteristic of the composite laminated plate is suitable for the use of Rayleigh damping.

The correlation expression for the conversion of Rayleigh damping to the damping ratio is:

$$\xi_i = \frac{\alpha_i}{2\omega_i} + 2\beta_i\omega_i.$$

Among them, α_i is the mass matrix of the first I of Rayleigh damping, which plays the leading role in the low frequency band of the system response. β_i is the first order I stiffness matrix, which plays a leading role in the high frequency band. ω_i represents the natural frequency of the first I mode.

The damping ratio x and the natural frequency ω of the component are obtained by the attenuation vibration curve of the component, after calculating, the damping coefficient of Rayleigh damping is obtained, which can be set up in the finite element simulation. We will be able to get α, β after we take the experiment result into the formula. In the finite element method, the Rayleigh damping coefficient α, β is set up after the modal analysis step, then the simulation is carried out in ABAQUS. Because the main spring modal order are in the range of 500 Hz, When the composite leaf spring is installed on the suspension system, the resonance frequency of the suspension system is general about 20 Hz, also belong to the low frequency vibration, so in the general finite element simulation of Rayleigh damping parameter setting, the stiffness coefficient β can be set to 0. After the modal and damping test results are analyzed, the parameters are set: $\alpha = 2.23, \beta = 0$.

Laminated plate free attenuation curve is shown in Fig. 29.7, we carry on the processing to obtain laminated damping ratio: $x_l=0.0072$.

Comparison of simulation results with experimental results for laminated plates is shown in Table 29.6: The simulation results are smaller than the experimental results, the gap between the two is about 2.8%, and the error can be accepted. Analysis of the causes of errors, mainly in the following two aspects:

- (1) The acceleration sensor and its unidirectional wire bonding on the laminated plates have an influence on the free attenuation vibration of the laminated plates, which makes the damping ratio test values larger than the experimental value.

Fig. 29.7 Simulation decaying vibration curves of laminates

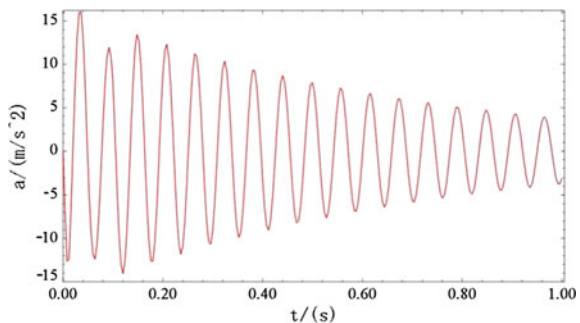


Table 29.6 Comparison of predictive value and test value of damping of laminates

Measurement parameters	Simulation result	Test result	Error
Damping ratio	0.0072	0.007	2.8%

Fig. 29.8 Model of composite leaf spring



(2) Computational analysis methods and testing techniques: the nonlinearity, material properties, amplitude and deformation of damping itself will affect the measurement results of damping ratio.

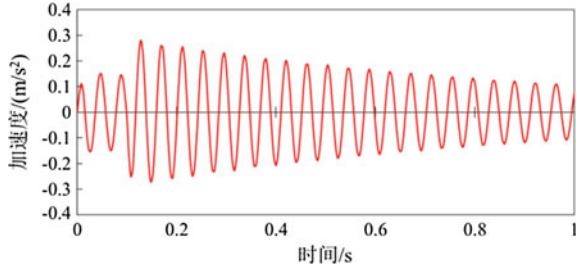
29.4 Simulation Analysis and Experimental Verification of the Damping Characteristics of Composite Leaf Spring

29.4.1 Simulation Analysis of Damping Characteristics of Composite Leaf Spring

29.4.1.1 The Simulation Steps and the Parameters of Damping Properties of Composite Leaf Spring

The finite element model and mesh of composite leaf spring assembly is shown in Fig. 29.8. Refer to the last section: Simulation and analysis method of damping performance of glass fiber/polyurethane laminate. Because the simulation method can be used to laminate simulation, so the method after appropriate modification can also be used in composite leaf spring damping characteristics simulation. Simulation of spring damping characteristics of composite materials is completed in modal dynamics analysis, the mesh of the simulation model is fine in HYPERMSEH, the number of grid is 140,000. Because of the parabolic structure design of composite leaf spring, layer length is different at the place of different thickness, in the division of the grid, the grid painting in different regions are also different, the finite element model is more accurate, the calculation modal calculation and the stiffness of the leaf spring more accurate results, it's more easier to obtain the results of modal calculation and spring stiffness calculation. However, taking into account the need for the calculation of damping characteristics,

Fig. 29.9 Results of damping simulation of composite leaf spring



the viscoelastic properties of composite fibers are mainly reflected in the setting of damping model parameters α , β , so the finite element model can be simplified, each zone of composite leaf spring layer is unified, and the number of grid is reduced. In addition, in order to make the binding mode consistent with the way of loading, we also need to set the boundary conditions on the finite element model of composite leaf spring, the displacement constraint is set at the direction of Y, Z at the two ends of the plate spring lug. A vertical load is applied in the composite leaf spring, load amplitude are shown in Table 29.5, the load is 5000 N. Finally, the finite element model is presented to the ABAQUS solver to calculate.

29.4.1.2 The Prediction Results of Damping Composite Leaf Spring

After calculation, the calculation results are processed by using ABAQUS's post processing module, the damping prediction results are shown in Fig. 29.9.

To deal with the attenuation curve data, the predictive value of composite leaf spring damping ratio is 0.0074.

29.4.2 *Experimental Verification of the Damping Properties of Composite Leaf Spring*

29.4.2.1 Vehicle Test of Natural Frequency and Damping Ratio of Automotive Suspension System

The final performance evaluation of the final composite leaf spring should be carried out under the loading environment, therefore, the composite leaf spring assembly is mounted on the vehicle, the damping characteristics of suspension is further testing by rolling method. The test vehicle is full loaded. In order to eliminate the damping effects on the test results, before the damping test, remove vibration damper of vehicle rear suspension. TEST.LAB LMS test system and B&K/PCB company's three direction vibration acceleration sensor are used in test, the sensors arrange in the frame and the axle which are on the top of leaf spring,

as shown in Fig. 29.10. The rear wheel drive on the road shoulder as shown in Fig. 29.11, in order to test the vibration acceleration response of sprung mass and non sprung mass (Fig. 29.10).

Experimental procedure: ① The car on the shoulder (select 90–120 mm Strapless height), push down the steps by human in a stationary state. (Note: the shoulder should not be too high, ensure that the suspension compression does not exceed its maximum compression stroke) ② The time history of the free decay on the frame is recorded, and every record time is not less than 3 s. In order to ensure the integrity of the vibration attenuation curve, this test has been done for 8 times, take one of the most complete and smooth attenuation vibration curve, as shown in Fig. 29.12. ③ Limit the vibration of the front suspension.

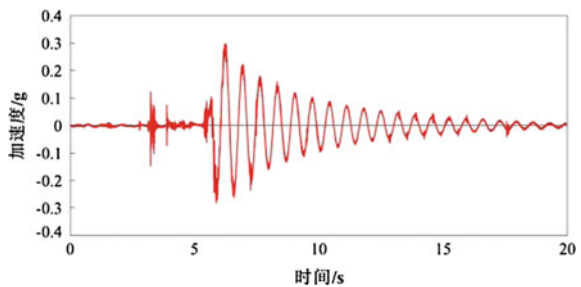
Fig. 29.10 Sensor placement



Fig. 29.11 Rolling method test



Fig. 29.12 The decaying vibration curves of composite leaf spring test



29.4.2.2 Simulation Analysis Results of Damping Characteristics of Composite Leaf Spring Are Compared with the Experimental Results

In order to ensure the accuracy of data processing, the data processing program is compiled by MATLAB software. Different from the free decay curve of composite laminates and the leaf spring, the noise signal in the original data of the loading test is more. First of all, the original data which is useless is removed, and the original data are resampled and processed by light. Then the data are fitted with piecewise polynomial, and the sine function is used to fit the attenuation period, and the method is the same as that of the laminated plates. Vibration acceleration attenuation curve of frame is processed, the damping ratio of composite leaf spring—rear axle—tire is changing with time as shown in Fig. 29.13, which is between 0.025 and 0.034. According to the preliminary test results of the cooperative enterprises, the overall damping ratio of the original vehicle rear suspension is 0.165. After processing the data of stable attenuation section in the vibration acceleration attenuation curve of the rear axle, taking into account the tire damping ratio is 0.023, which is far greater than the damping ratio of composite leaf spring assembly (0.008–0.0025), this shows that the damping of composite leaf spring—rear axle—tire system is mainly composed of tires.

Composite leaf spring finite element simulation completely and vividly simulates the whole process of spring vibration attenuation, it's consistent with the movement of the leaf spring which is in the experiment of damping ratio in suspension system, spring damping ratio is predicted from a theoretical point of view, but it has less reliability; Composite leaf spring damping ratio of the vehicle was affected by many external factors, but the result of the measurement is more real, and the credibility is high. Therefore, the composite leaf spring damping ratio of the finite element simulation analysis and vehicle damping ratio test results can verify each other, and make the appropriate changes, learn from each other according to the error, and ultimately determine the damping ratio of composite leaf spring. The contrast of the error is shown in Table 29.7.

Fig. 29.13 Composite leaf spring rear axle—tire damping ratio changes with time

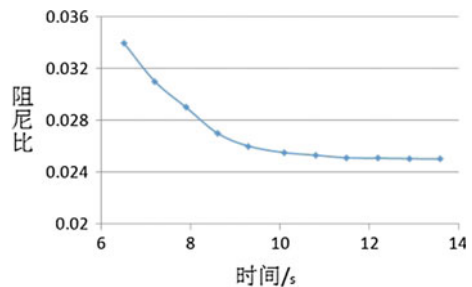


Table 29.7 Comparison of composite leaf spring damping between simulation and test

Parameter	Simulation result	Experimental result	Error
Damping	0.0074	0.008	7.5%

According to Table 29.7 we can see that the error of simulation and experiment is about 7.5%. Thus, the finite element simulation can reflect the real spring damping results, the establishment of finite element model and its parameter setting is basically correct. At the same time, we can think of neglecting the nonlinear properties of the composite materials have little effect on the damping properties of the composite leaf spring calculation. Composite leaf spring finite element simulation analysis is not only earlier than the experimental analysis, it can also prove that the composite leaf spring damping obtains the accurate prediction of sample.

29.5 The Influencing Factors on the Damping Properties of Composite Leaf Spring

In this paper, we study the full 0° in layer, 45 story, 58% fiber volume fraction, parabolic type resin based glass fiber reinforced composite leaf spring damping characteristics. This practical study is limited, the composite leaf spring is not suitable for other different models, it also will affect the practical application of composite leaf spring, leading to a sharp rise in the development cycle and cost, which will affect the vehicle ride comfort and handling stability.

Based on the above reasons, this paper will study the finite element parameters which have great influence on composite materials spring damping properties, on the condition of ignoring the external factors such as temperature, amplitude and frequency of spring, study the influencing factors on the design. When the main structure and size of the composite spring is constant, the quality of composite leaf spring mainly depends on the density of composite materials. Stiffness mainly depends on the ply scheme of the composite leaf spring, including layer angle, fiber volume content and layer number. These influencing factors are embodied in the following aspects of finite element simulation: ① Layer number will affect inter-layer friction and inter layer shearing of spring assembly. ② the setting of laying angle will also affect the friction between the layers and shear. ③ Material selection aspect: Selection of different resin matrix and the reinforcing fiber will greatly influence the damping properties of composite leaf spring, it embodies as the density, elastic modulus and shear modulus of the material in the simulation. Considering the practical engineering, the factors which influence spring damping properties of composite is mainly considered other properties and process conditions of composite leaf spring., only the design variables such as the number of layers, the angle and the volume content of the fiber can be considered separately. The correctness of the finite element model of composite leaf spring damping

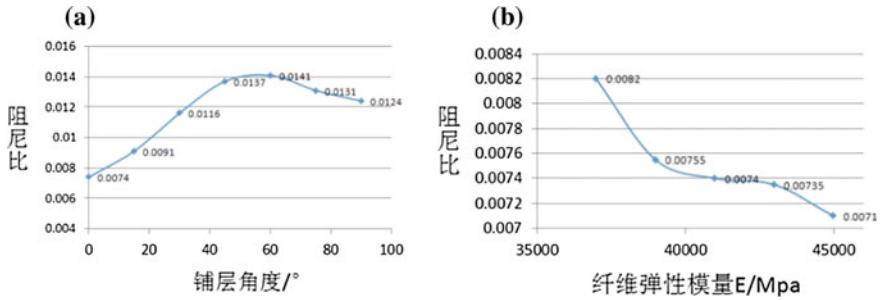


Fig. 29.14 Damping of composite leaf spring changes with parameters

characteristics simulation has been verified by experiment in the above. Therefore, only the ply angle and fiber volume content can be considered separately.

Lay angle of composite leaf spring is changed through dialog composite layup manager, then the damping ratio of the model is calculated separately, and the calculated results are shown in Fig. 29.14a.

In the figure, the horizontal coordinates represent the shop floor, and the longitudinal coordinates represent the damping ratio. From the figure we can see a composite leaf spring damping ratio increases with the angle of layer increased first and then decreased. The maximum damping ratio is between 45° and 75° , it shows that lay angle has a significant effect on the composite leaf spring damping. We can notice that when using 0° , the composite leaf spring damping ratio and the Impact on the performance of the original suspension are smallest. On the other hand, according to the relevant literature research [9], when the fiber orientation is 0° – 15° , the loss factor of the composite structure does not depend on the change of the stress, and the composite material damping performance is linear. When the fiber orientation is 30° – 90° , the loss factor is mainly influenced by the interaction of the fiber/resin matrix, nonlinear effect is appeared with the increasing of stress level. Therefore, the 0° layer can make the loss factor of composite leaf spring as a certain value, and risk of failure of suspension damping match can also be reduced, so it's better to adopt 0° layer in composite leaf spring layer design. The longitudinal tensile modulus of the composite material is changed through the composite layup manager dialog box to reflect the change of the fiber volume content. Then, the damping ratio of the model is calculated when the longitudinal tensile modulus is different, and the calculation results are shown in Fig. 29.14b. According to Fig. 29.14b, with the increase of longitudinal tensile modulus of the composite material, the damping ratio of composite leaf spring is declining, this shows that the composite leaf spring damping ratio decrease with the increase of fiber volume content. Therefore, in order to reduce the risk of failure of the suspension damping match, high fiber volume content should be selected.

29.6 Conclusion

- (1) This paper presents the analysis method and detailed finite element simulation steps of damping composite leaf spring, the correctness of the analysis method was verified through the test, and the parameters of composite laminates and composite leaf spring assembly were obtained.
- (2) According to the analysis result of the damping characteristics of the composite leaf spring, the conclusion could be made that its damping ratio is far less than the car suspension system damping ratio and will not on ride comfort caused adverse effects.
- (3) Through the finite element simulation, we analyzed the factors which affect the damping properties of the composite leaf spring, in which the elastic modulus of the material and the laying angle are the main influencing factors.

References

1. Sun H, Shen G, Hu P et al (2010) Lightweight design of an auto body considering its crash performance. *Mech Sci Technol Aerospace Eng*
2. Merklein M, Geiger M (2002) New materials and production technologies for innovative lightweight constructions. *J Mater Process Technol* 126:532–536
3. Benedyk JC (2000) Light metals in automotive applications. *Light Metal Age* 10(1):34–35
4. Asnafi N, Langstedt G (2000) A new light weight metal-composite-metal panel for applications in the automotive and other industries. *Thin Walled Struct* 36:289–310
5. Chang H (2012) *Viscoelastic damping material*. Defense industry publishing, Beijing, pp 179–180
6. Tian N, Xue ZM, Chen C et al (2009) Advances in damping performance of fiber reinforced polymer-based composite material. *Fiber Reinf Plast/Compos* 26(1):85–88
7. GB/T 18258-2000 “Test method for damping properties of damping materials” [s]
8. Li DZ, Chen SN (1992) Study on the damping test method of composite material and the influence of air damping. *J Vib Shock* (1):128–130 (in Chinese)
9. Li RJ, He AR, Xu C et al (2012) Structural damping determination of carbon fiber reinforced composite. *Aerospace Mater Tech* 42(4):64–67

Chapter 30

Analysis on China's Fuel Consumption Standards and Its Influences on Curb Weight

Xiao Li, Fuquan Zhao, Han Hao and Zongwei Liu

Abstract With the explosive growth of China's vehicle ownership, energy consumption and emissions from passenger vehicles become a major concern. The fuel consumption standards for passenger vehicles play an essential role in addressing such issues. In this study, four most important aspects of China's fuel consumption standards, i.e., evaluation standard, constraint form, basic curb weight and the slope, are investigated. By establishing the database comprising the major characteristics of 2010–2015 new vehicles, the rationale of each aspect and the influences on China's vehicle market and manufacture are analyzed. The results indicate that the evaluation standard and constraint form have strong impacts on the motivation of manipulation and the stress of achieving the standard targets. On the other hand, the basic curb weight and the slope have strong impacts on the change of curb weight and technology friendliness of lightweighting.

Keywords Fuel consumption standards · The standard targets · Curb weight

30.1 Introduction

Facing the increasingly severe challenges of energy crisis and environmental degradation, China began to implement fuel consumption standards as from 2005, including four phases of year 2005–2008, 2009–2012, 2012–2015 and 2016–2020 [1], as is shown in Fig. 30.1. Among them, phase I and phase II regulate fuel consumption limits according to the curb weight, but there is no actual statistics, constraint or punishment. From phase III, China introduced the concept of CAFC

X. Li · F. Zhao · H. Hao · Z. Liu (✉)

State Key Laboratory of Automotive Safety and Energy, Tsinghua University,
Beijing 100084, China
e-mail: zw.liu@gast-group.com

X. Li · F. Zhao · H. Hao · Z. Liu

Tsinghua Automotive Strategy Research Institute, Tsinghua University,
Beijing 100084, China

© Springer Nature Singapore Pte Ltd. 2017

Society of Automotive Engineers of China (SAE-China), *Proceedings of SAE-China Congress 2016: Selected Papers*, Lecture Notes in Electrical Engineering 418,
DOI 10.1007/978-981-10-3527-2_30

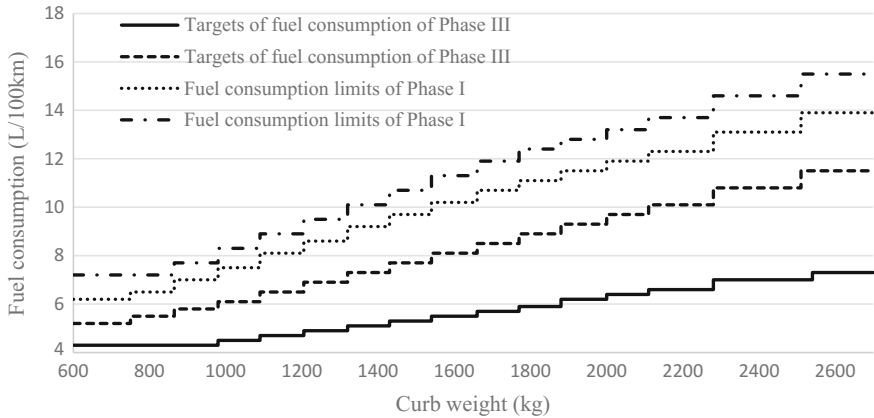


Fig. 30.1 Four phases of China’s fuel consumption standards



Fig. 30.2 Development processes of the world’s CAFC standards

(Corporate Average Fuel Consumption), and relevant departments set up the targets for the average fuel consumption of passenger car corporations [2]. Ministry of Industry and Information Technology (MIIT) of China began to make statistics and notifications of the CAFC targets of various Chinese corporations. The corresponding monitoring scheme Management Measures of the CAFC would be issued. China’s CAFC standard is gradually playing an essential role in energy saving and emission reduction.

The setup of CAFC standards in China is not groundless, the US, Europe and Japan all issued their fuel consumption standards ahead of China. Figure 30.2 describes the development of the CAFC standards worldwide. The US formulated the stringent CAFE standard during the first oil crisis period at 1975. Till 1985, the average fuel economy of passenger car in the US increased from 13.5 to 27.5 mpg [3], and the doubled fuel economy during a decade had profound impacts to the world’s automobile manufacturing industry. Entering into the new century, global warming becomes increasingly serious, with world’s focuses on carbon emission control problem. Various countries begin to issue a next round of standards, with general formation of two phases of A and B, with 2015 and 2025 as time nodes.

Since 2012, China’s fuel consumption standards has entered into Phase III, MIIT of China required all corporations to report their targets and actual performances, and publicize them. Table 30.1 is the condition of reaching the target of CAFC standard by corporations. As can be seen, the target of Phase III is implemented smoothly. Though MIIT of China does not publicize the statistics of CAFC in 2015,

Table 30.1 Implementation of CAFC standard in China in 2014 [4]

Type of enterprise	Target of CAFC (L/100 km)	Actual performance (L/100 km)	Proportion of the actual performance to the target (%)
Indigenous enterprise	7.40	7.10	96.0
Joint venture	7.29	7.15	98.0
Import enterprise	9.20	8.76	95.2

the average fuel consumption in China reduces by 4% every year. It is predicted that the target of Phase III can be achieved successfully.

In 2015, MIIT of China noticed 1448 new models passenger cars, and the situation of reaching the target by different models refers to Fig. 30.3. Among them, there are 870 models that reach the target of Phase III, accounting for 60% of the total noticed models. There are 30 models that reach the target of Phase IV, accounting for 2% of the total noticed models. Combined with specific models, models that have heavier curb weight are in poor condition to reach the target, however, A-class and B-class models that occupy the market mainstream are in good conditions to reach the target. The models that reach the targets of Phase IV are mainly hybrid electric vehicles.

This paper conducts detailed description and argumentation for the contributing factors of passenger car fuel consumption standards at Phase IV. Combined with the data of actual models, this paper analyzes the impacts of fuel consumption standards.

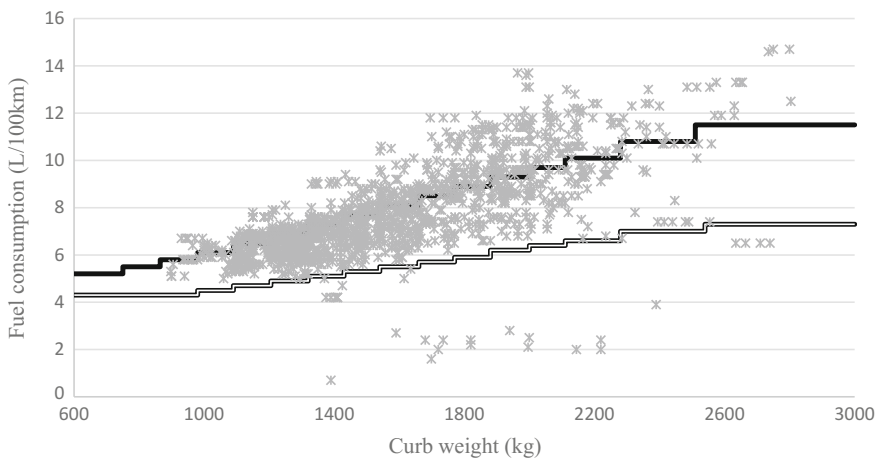


Fig. 30.3 The condition of reaching the targets of Chinese new models in 2015

30.2 The Evaluation Standard and Constraint Form of China's CAFC Standard

30.2.1 Causes of the Evaluation Standard and Constraint Form

China's fuel consumption standards regard passenger car curb weight as the evaluation standard, and give out limits or targets for fuel consumptions of passenger cars at different weight ranges with the step-shaped constraint form, which is similar to that of the Japanese standards. Table 30.2 shows the evaluation standards and constraint forms of fuel consumption standards in different countries.

Except North America, other regions in the world mainly adopt curb weight as the evaluation standard. Relevant studies have compared different evaluation standards such as curb weight, footprint and power, and results show that compared with footprint, fuel consumption standards that take curb weight as the evaluation standard has poor friendliness to the application of automotive energy saving technologies [5, 7]. However, when designing fuel consumption limits, we shall not only consider the advantages and disadvantages of the evaluation standards themselves, but also consider the test method for fuel consumption, therefore, most countries in the world adopt curb weight as the evaluation standard. The fuel consumption test methods in regions like China, Japan and the European Union have profound historical origins with the standard formulated by UNECE (United Nations Economic Commission for Europe). Among them, China adopts *Test Methods for Fuel Consumption of Light-Duty Vehicles* (GB/T 19233-2008), and basically follows the standard by UNECE. China categorizes the vehicle reference mass according to weight ranges, and set the corresponding equivalent inertia and dynamometer resistance coefficient according to weight ranges. The reference masses of passenger cars are categorized into 22 weight ranges, and every reference mass has its corresponding equivalent inertia, absorbed power and load and

Table 30.2 Evaluation standards and constraint forms of fuel economy standards in major countries and regions in the world [5, 6]

Country	Constraint unit	Constraint form	Evaluation standard	Test cycle
China	Fuel consumption per hundred kilometers (L/100 km)	Step-shaped	Curb weight (kg)	NEDC
Japan	Fuel economy (km/L)	Step-shaped	Curb weight (kg)	JC08
EU	Carbon emission CO ₂ (g/km)	Linear	Curb weight (kg)	NEDC
North America (including Canada and Mexico)	Fuel economy (mpg)	Linear	Footprint (ft ²)	CAFE

Table 30.3 Correspondings set methods for dynamometers at different curb weight ranges [8, 9]

			Set of dynamometer (80 km/h)		Coefficient	
Curb weight (kg)	Basic weight (kg)	Equivalent inertia (kg)	Power (kW)	Load (N)	Curb weight (kg)	Basic weight (kg)
750–865	850–965	910	5.6	252	5.7	0.0385
865–980	965–1080	1020	6	270	6.1	0.0412
980–1090	1080–1190	1130	6.3	284	6.4	0.0433
1090–1205	1190–1305	1250	6.7	302	6.8	0.046
1205–1320	1305–1420	1360	7	315	7.1	0.0481
1320–1430	1420–1530	1470	7.3	329	7.4	0.0502
1430–1540	1530–1640	1590	7.5	338	7.6	0.0515
1540–1660	1640–1760	1700	7.8	351	7.9	0.0536
1660–1770	1760–1870	1810	8.1	365	8.2	0.0557
1770–1880	1870–1980	1930	8.4	378	8.5	0.0577
1880–2000	1980–2100	2040	8.6	387	8.7	0.0591
2000–2110	2100–2210	2150	8.8	396	8.9	0.0605
2110–2280	2210–2380	2270	9	405	9.1	0.0619
2280–2510	2380–2610	2270	9.4	423	9.5	0.0646
>2510	>2610	2270	9.8	441	9.9	0.0674

resistance coefficient, which explains that vehicles at the same reference mass will obtain the same resistance from the dynamometers. Chinese standards describe vehicle reference mass as “adding 100 kg to vehicle curb weight”. Table 30.3 gives out the setting method for dynamometers combined with the set of dynamometers and the weight ranges in China's CAFC of appendix 1 CB1 of *Limits and Measurement Methods for Exhaust Pollutants from Light-Duty Vehicles* (GB 18352.3-2005, test method for fuel consumption refers to this standard). Table 30.3 shows for vehicles at the same weight ranges, the set of dynamometer is fair, and it is reasonable that China's fuel consumption standards regard curb weight range as the evaluation standard, and step-shape as the constraint form to design fuel consumption limits and targets.

30.2.2 *The Influence of Evaluation Standard and Constraint Form*

According to the resistance coefficient set for the dynamometers, it is reasonable to take curb weight as the evaluation standard, and step-shape as the constraint form for vehicle with different weights at the same weigh ranges. But China's fuel consumption test method does not strictly implement look-up table, and the *Test*

Methods for Fuel Consumption of Light-Duty Vehicles (GB/T 19233-2008) points out that, “the driving resistance curve is provided by automobile manufacturers, and manufacturers shall provide test reports, calculation reports and other relevant materials, which shall be confirmed by inspection agencies”, and “if automobile manufacturers request, driving resistance can be selected by the look-up table” [9]. Different models have different driving resistance curves, and the changes of curb weights have direct impacts on this. If test resistance curves are provided by automobile manufacturers, and under the same weight ranges, with other variables remaining the same, models of light weight have certain advantages compared with models of heavy weight, making the step-shaped standard lose its fairness.

If the resistance curves are provided by enterprises, adding a little weight to the vehicles with comparatively heavier weight in small weight ranges can make vehicles enter into the next weight range under the condition of no big impact to resistance curves, thus the target is loosened. While models at this weight range can reduce curb weight to gain better resistance curves, with unchanged target. Therefore, the 10% before curb weight enters into the weight range reduces the difficulties to achieve the target to some extent, and define the models with curb weight that is 10% ahead of weight range as the “manipulation” models [10]. This study further analyzes the “manipulation” phenomenon based on previous studies.

Figure 30.4 shows from 2013 to 2015, the proportion of “manipulation” models remains at 18%, which is obviously higher than other model types. This shows that some enterprises adopt the “manipulation” method to cope with the fuel consumption standards of passenger cars in China. However, this phenomenon is not universal, and has no trend of further improvement. Figure 30.5 describes the manipulation of new models from 2013 to 2015 in China. View from different enterprise types, indigenous brands have obvious “manipulation” phenomenon, with the use of “manipulation” method by over 20% of models. While joint ventures do not have obvious “manipulation” behavior. There are mainly two reasons for this. First, the major market of indigenous brands is China, and indigenous brands consider to meet the CAFC standard at the initial design stage. Besides, indigenous brands are poor in energy saving technology, compelling enterprises to adopt “manipulation” to reach the targets. Second, the products of joint ventures are

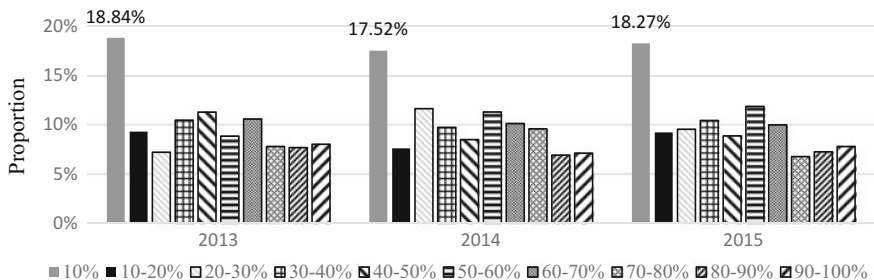


Fig. 30.4 Distribution proportion of new models in the corresponding weight ranges from 2013 to 2015 in China

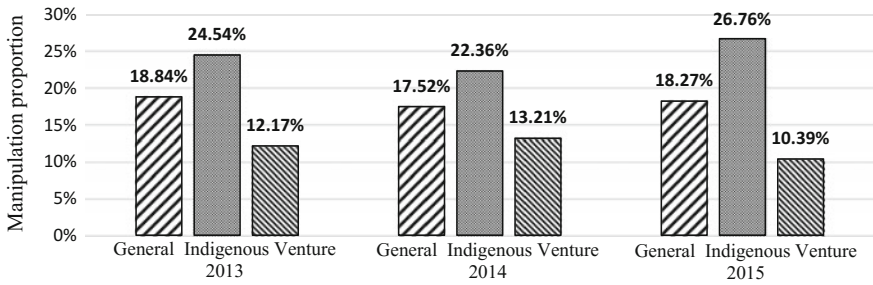


Fig. 30.5 Manipulation of new models from 2013 to 2015 in China (according to enterprises’ types)

most foreign models that are introduced to China, and the models are not specially designed to meet the China’s CAFC standard. Joint ventures have high levels in energy saving technologies, and do not need “manipulation”.

CAFC standard adopts curb weight as the evaluation standard and step-shape as the constraint form. When models at different curb weight ranges begin lightweighting to reach the next weight ranges, they will face different pressures in reaching the target. Define the pressure in reaching the target as Eq. 30.1:

$$P = \frac{\frac{\Delta F}{F} * 100\%}{\frac{\Delta M}{M} * 100\%} \tag{30.1}$$

P is the pressure in reaching the target, F is the fuel consumption target of this weight range, ΔF is the difference in fuel consumption targets of two weight ranges, M is the weight of the vehicle, ΔM is weight reduction from this weight range to the next weight range. The physical significance of pressure in reaching the target is the fuel consumption reduction proportion to divide the weight reduction proportion. The bigger the pressure in reaching the target of the corresponding weight range means more fuel consumption reduction is required for the model to enter into the next weight range through lightweighting.

Analyzing the CAFC standard of Phase III and Phase IV, Fig. 30.6 describes the pressures in reaching the targets of different weight ranges and the “manipulation” proportion of the corresponding weight range in 2015. With the increase of curb weight, there is a trend of increase for the pressure in reaching the target comprehensively. The pressure in reaching the target shows a saltus at 2000–2110 kg for Phase III, and at 1880–2000 kg for Phase IV. Combined with the “manipulation” phenomenon, year 2015 is at Phase III of the CAFC standard, and the weight range of 2000–2110 kg that saltus occurs in the pressure of reaching the target has high “manipulation” proportion, which means the “manipulation” behavior is closely related to the pressure in reaching the target. The overly high pressure in reaching the target enhances the motivation for enterprises’ “manipulation”. Thus we can infer that by 2020, the weight range with the highest “manipulation”

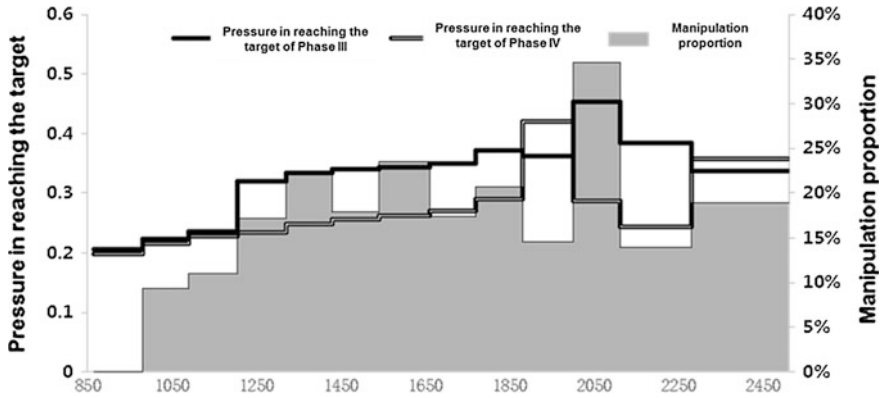


Fig. 30.6 Relationship between the pressure in reaching the targets of Phase III and Phase IV and the “manipulation” phenomenon

proportion will move left to 1880–2000 kg of Phase IV standard that fuel consumption reduction pressure saltus. Besides, Fig. 30.6 shows weight ranges of 1320–1430 kg and 1540–1660 kg have strong “manipulation” phenomenon and these two ranges cover the best-selling A-class and B-class vehicles in the Chinese market. Though the pressure in reaching the target is not strong, the high sales volume has high weight in the calculation of CAFC target. “Manipulation” behavior is beneficial for reducing the difficulties for enterprises in reaching the target.

30.3 Changes of the Slope of China’s CAFC Standards and Its Influence

30.3.1 Changes of the Slopes of Fuel Consumption at Phase IV in China

The fuel consumption standards are categorized according to the constraint forms in China. Phase I and Phase II are limits and Phase III and Phase IV are targets. However, view from time nodes, the fuel consumption standards meet the categorization methods of Fig. 30.2. Among them, Phase I and Phase II are transition stages, and Phase III is Phase A. Achieve the target of 6.9 L/100 km by 2015. Phase IV and Phase V in future will be Phase B, and achieve the target of 5 L/100 km at Phase IV by 2015; Phase V has not been released yet, and it is projected to take year 2025 as the time node, which is similar to most countries in the world. Details refer to Table 30.4.

Analyze China’s fuel consumption standards according to this trend. Figure 30.7 describes the reduction change of fuel consumption standards during the first three

Table 30.4 Fuel consumption targets according to phases in major countries of the world [11]

Country	Phase A (2015)	Phase B (2020)
China (L/100 km)	6.9	5.0
Japan (km/L)	16.8	20.3
EU (g/km)	130	95
US	36.2 mpg (2017)	56.2 mpg (2025)

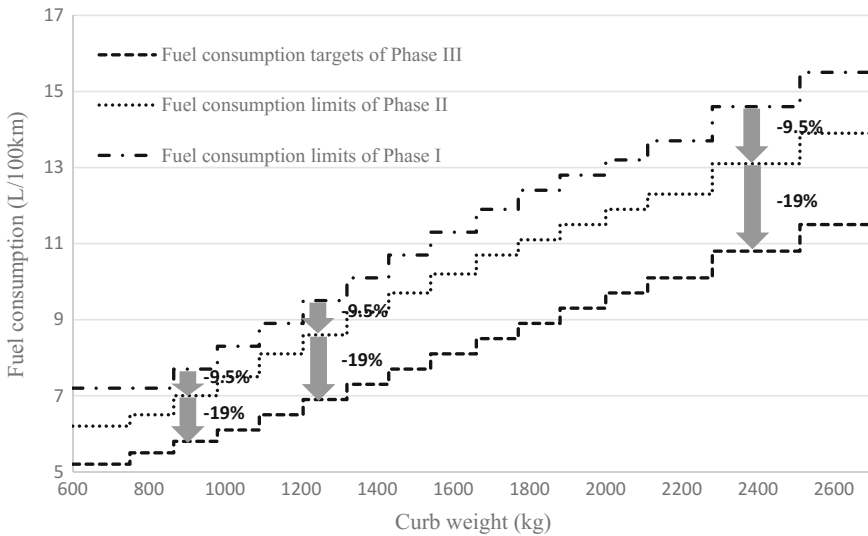


Fig. 30.7 Changes of China’s fuel consumption standards in the first three phases

phases. Among them, the reduction of fuel consumption reaches to 9.5% at Phase II, and that of Phase III reaches to 19%. Every weight range calculates the limits and targets according to the reduction of the former phase directly. These three phases all regard the weight range of 1250–1320 kg as “base”, meaning the average weight range of the passenger cars under this phase. The corresponding limits or targets are the overall limits and targets of passenger cars under this phase.

The slope of CAFC standard at Phase IV in China has changes, and is no longer the single equal proportion reduction. Figure 30.8 describes the formulation steps of the standard of Phase IV. To make better understanding, Fig. 30.8 takes the line of linear regression and slope change to describe the formulation steps:

- ① Determine the reduction, and the corresponding weight reduction proportion, namely $(6.9 - 5.1) / 6.9 = 26\%$
- ② Choose the basic weight range, and adjust the basic weight range of CAFC standard at Phase IV to 1320–1430 kg, and move the standard right
- ③ Take basic weigh range as the pivot point, and multiply the slope of ② by 70%.

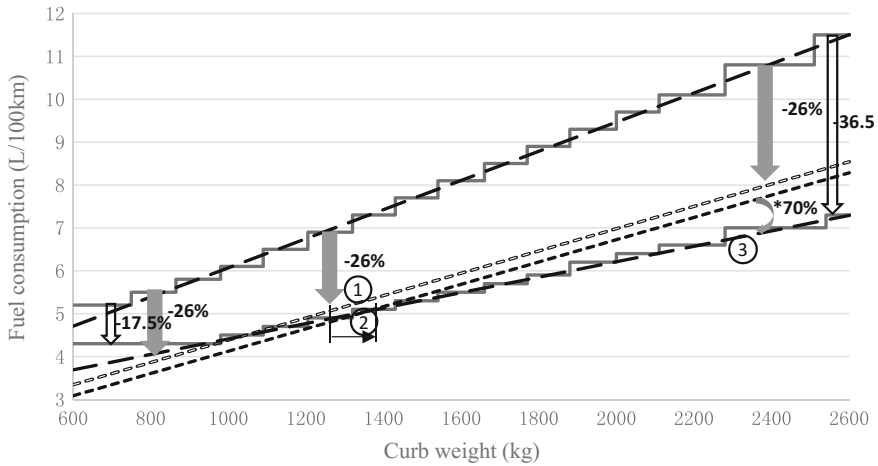


Fig. 30.8 Changes of China’s fuel consumption standards at Phase III and Phase IV

The rotating line has different standard formulation compared with the first three phases. The CAFC standard of Phase IV is more mature, which is shown in two aspects. First, increase the basic weight range to 1320–1430 kg, and fully consider the reality of the increase of curb weight of passenger cars in China; second, rotate the constraint line of target, and models with different weights face unequal reductions from 17.5 to 36.5%, which is more suitable for the application laws of energy saving technologies.

30.3.2 The Influence of the Change of Slope of Fuel Consumption Standard at Phase IV in China to Curb Weight

The average curb weight of passenger car is the weighted average with sales as the weight. Table 30.5 is the change of average curb weight released by MIIT of China. The curb weight of passenger car in China at Phase III increases continuously. Figure 30.9 makes statistics of the proportion of noticed models at all weight ranges in the noticed models of that year, and the new noticed models with the largest proportion changes from 1090–1205 kg to 1205–1320 kg gradually, confirming the phenomenon of curb weight increase.

Table 30.5 Change of average curb weight of passenger car in China [11, 12]

Year	2nd half of 2012	2013	2014
Average curb weight	1339	1355	1371

As is known to all, lightweighting is an effective approach to improve vehicle fuel economy [13–15]. In recent years, Chinese and foreign enterprises attach importance to lightweighting, making lightweighting become a commonly automotive technology trend recognized by the industry. However, view from Table 30.5 and Fig. 30.9, under the comparatively stringent standard restrictions of Phase III, the weight of passenger cars in China increases rather than reduces, and the reason for this is complex. On the one hand, this correlates with the high growth rate of market shares of SUV and MPV, and on the other, this correlates with the increasingly rich configurations of passenger cars. However, under stringent CAFC standard, there is still room for growth, which correlates with the constraint of standards themselves. Section 2.1 of this study introduces the slope changes of CAFC standards in China, and it can be seen that the constraints for the first three phases all reduce in proportion, and when vehicles with different weights face the targets of fuel consumption reduction with same proportion, there is no special constraints for vehicles with comparatively heavy weight. The data shows, when vehicle weight is reduced by 100 kg, the corresponding fuel consumption will be reduced by 0.35 L–0.64 L/100 km, and the numerical value is the result of the linear regression of passenger car curb weight and fuel consumption [14]. Constrained by CAFC standard, the linear relation between passenger cars and fuel consumptions is similar to the standard slope in China. Figure 30.10 conducts the linear regression to new models in 2015, and when weight is reduced by 100 kg, the fuel consumption is reduced by 0.37 L/100 km. The regression line basically coincides with the standard of Phase III.

Figure 30.11 shows that if we set up the standard of the next stage with reduction in proportion, the absolute value of fuel consumption required to be

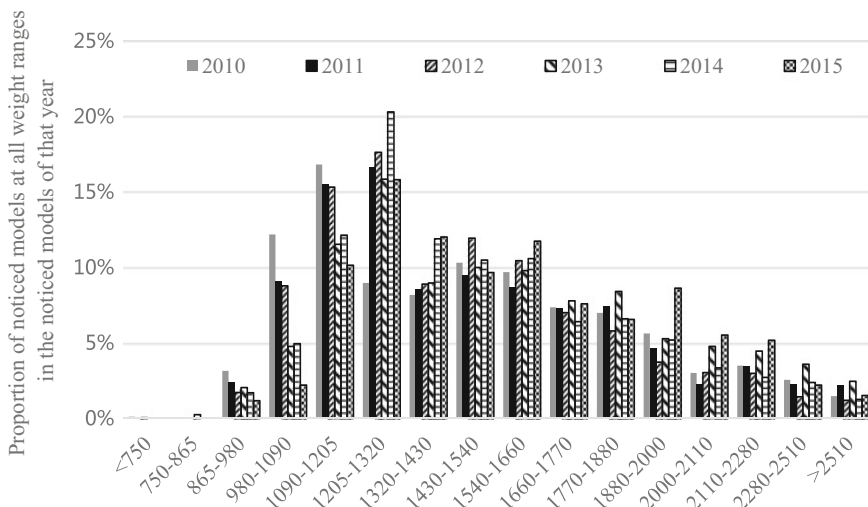


Fig. 30.9 Change of the proportion of noticed models at all weight ranges in the noticed models of that year

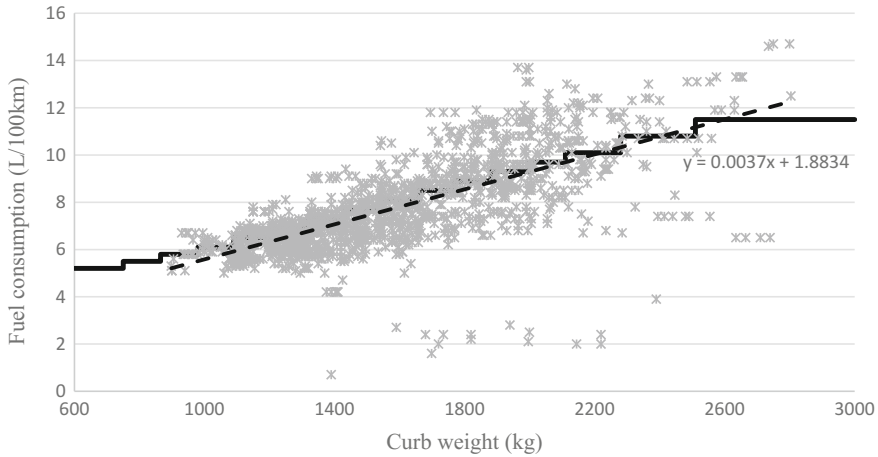


Fig. 30.10 Relationship between China’s CAFC standard of Phase III and new models in 2015

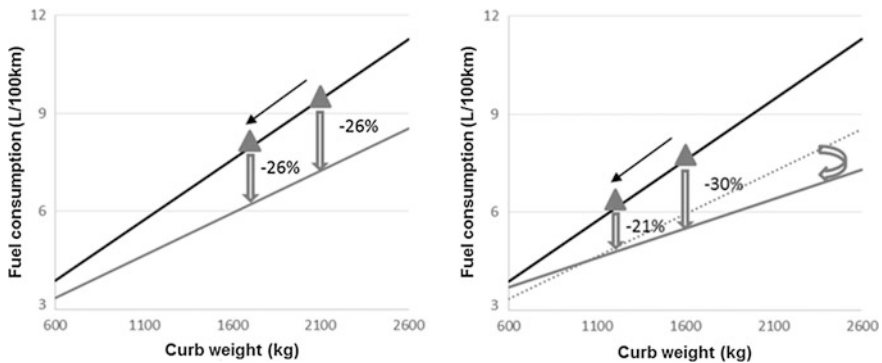


Fig. 30.11 Influence of the change of slope to the motivation of lightweighting

reduced after lightweighting has certain reduction, but the reduction remains unchanged, which counteracts the fuel saving effectiveness to certain degree. If the standard of the next stage conducts the rotation of a certain angle, the fuel consumption reduction required after lightweighting will be reduced. Influenced by the reduction in proportion of fuel consumption standards of the first three phases in China, the fuel saving effectiveness brought by lightweighting is weakened. Chinese passenger car enterprises are not active in the application of lightweighting technologies.

At Phase IV, on the basis of reduction in proportion of China’s CAFC standard, it multiplies the slope by a certain proportion, featuring more friendliness to automotive lightweighting technology. Models with comparatively heavier weight will face more stringent targets, and models with comparatively lighter weight will

loosen the targets, forming the pattern of “constraining the large vehicles while encouraging the small vehicles”. According to the experience of Europe, multiplying the slope by 40–60% has good impacts to the pattern of “constraining large vehicles while encouraging small vehicles”. China selects the proportion of 70%, which is more flexible than Europe. However, considering the differences in auto market structures between China and Europe and it is the first time for China to rotate the slope, this proportion is comparatively reasonable, with further consideration of rotating the slope in the CAFC standard at the successive Phase V to implement the favorable policy guidance of “constraining large vehicles while encouraging small vehicles”.

30.4 Conclusion

- (1) The fuel consumption standard with curb weight as the evaluation standard and step-shape as the constraint form brings certain “manipulation” motivation for enterprises. The proportion of “manipulation” models stabilizes at around 18%, and indigenous enterprises have stronger motivation for “manipulation” than joint ventures.
- (2) The pressure for reaching the target has close relationship with “manipulation”. The high pressure for reaching the target strengthens the motivation for enterprises’ “manipulation”. It is predicted that by 2020, the weight range with the highest “manipulation” proportion in 2020 will be 1880–2000 kg.
- (3) During the implementation period of the first three phases in China, the average curb weight of passenger car increases instead of reducing, which correlates with the reduction in proportion of fuel consumption standards. The improper setting of the slope of CAFC standard counteracts the fuel saving effectiveness of lightweighting technologies.
- (4) The standard of Phase IV in China increases the basic weight, and meanwhile multiplies the slope by 70%, forming the effectiveness of “constraining large vehicles while encouraging small vehicles”, and it is predicted that the average curb weight of passenger cars from 2015 to 2020 will stabilize at the basic weight range, featuring better application of lightweighting technologies.

References

1. National Standards of the People's Republic of China (2014) Fuel consumption limits for passenger cars, GB19578-2014
2. Zhao F, Hao H, Liu Z (2015) Technology strategy to meet China's 502 L/10002 km fuel consumption target for passenger vehicles in 2020. *Clean Technol Environ Policy*
3. Cheah LW (2010) Cars on a diet: the material and energy impacts of passenger vehicle weight reduction in the US. Massachusetts Institute of Technology

4. Feng AN (2015) China passenger vehicle fuel consumption development annual report 2015. Innovation Center for Energy and Transportation, Beijing
5. He H, Yang Z (2013) Incentivizing vehicle mass reduction technologies via size-based passenger car fuel consumption standards in china. ICCT
6. Hao H, Wang S, Liu Z, Zhao F (2016) The impact of stepped fuel economy targets on automaker's light-weighting strategy: the China case. *Energy* 94:755–765
7. Mock P (2011) Evaluation of parameter-based vehicle emissions targets in the EU. ICCT
8. National Standards of the People's Republic of China (2008) Measurement methods of fuel consumption for light-duty vehicles, GB/T19233-2008
9. National Standards of the People's Republic of China (2005) Limits and measurement methods emission from light-duty vehicles, GB 18352.3-2005
10. Hao H, Wang S, Liu Z, F Zhao. Impacts of China's CAFC standards on light-weighting strategy of automotive manufacturers. In: Proceedings of 2015 SAE-China congress 2015, vol 4
11. Department of Equipment Industry, Ministry of Industry and Information Technology (MIIT) of China. Interpretation of fuel consumption of passenger cars at phase IV [EB/OL]. <http://www.miit.gov.cn/n11293472/n11293832/n11294042/n11481465/16423221.html>
12. National Standards of the People's Republic of China (2014) Fuel consumption evaluation methods and targets for passenger cars, GB27999-2014
13. Zhao F-Q, Liu Z (2015) China's 5 L/100 km target in 2020 challenges the growth pattern of self-owned enterprises. *Auto Mobile Sci Technol* 2:1–4
14. SAE-China (2013) Trace research on world automotive technology development lightweight. Beijing Institute of Technology Press, Beijing pp 15–16
15. SAE-China (2015) China automotive lightweight development—strategy and path. Beijing Institute of Technology Press, Beijing, pp 32–33

Chapter 31

Prediction and Study on the Influence of Propeller Shaft to Vehicle Noise Based on BP Neural Network

Yongjun Liu, Chaonan Xu, Weilong Niu, Xiuming Zhang
and Jun Wei

Abstract Propeller shaft is one of main sources to arouse vehicle noise. To decrease development cost and shorten development cycle, BP Neural Network model of influence of propeller shaft to vehicle noise was established using MATLAB software, combined with historical data. Then, the model was trained, results showed that it was stable and credible and the error of this model was between -4 and 4 , which could be acceptable. Last, noise of the developing vehicle in the company was predicted using the model, offering theoretical reference to related people.

Keywords Propeller shaft · Neural network · Vehicle noise · Prediction

31.1 Introduction

Automobile noise directly affects vehicle driving comfort, causing complaints from drivers and passengers. As an important evaluating indicator, it is highly concerned by experts, scholars and engineers. There are lots of exciting sources arousing automobile noise, and the high speed rotating propeller shaft is one of the most important factors [1]. To lower researching cost and shorten developing period, it has significant realistic meanings to predict the influence of propeller shaft to automobile noise based on experienced data.

Since it refers to many irregular factor changes, there has no mature mathematical model yet to work out the influence of propeller shaft to vehicle noise. But, theoretically, BP Neural Network could approach any nonlinear functions at any precision [2, 3]. So, the prediction model of the influence of propeller shaft to vehicle noise was established using BP Neural Network combined with MATLAB

Y. Liu (✉) · C. Xu · W. Niu · X. Zhang · J. Wei
R&D Center of Great Wall Motor Co. Ltd., Baoding, China
e-mail: liuyongjun819@126.com

Y. Liu · C. Xu · W. Niu · X. Zhang · J. Wei
Automotive Engineering Technical Center of Hebei Province, Baoding, China

software. This model can be used to predict the noise caused by propeller shaft for vehicle in research phase under certain conditions, providing theoretical reference for engineers.

31.2 BP Neural Network

31.2.1 BP Neural Network Structure

BP Neural Network is a dynamic training system, which consists of numerous widely connected nodes or neurons. It features error back propagation and multi-layer feed forward. Due to its practical function, it is one of the widest used Artificial Neural Network [4]. BP Neural Network consists of three nodes layer, they are input layer, output layer and hidden layer. Both input layer and output layer have only one layer, and hidden layer includes one layer or more. The nodes in the same layer keep mutual independence, but the every node in one layer connects with all nodes in another layer, and all the nodes can input and output any nonlinear mapping. Related theory shows that a three layer BP Neural Network model can reflect any nonlinear functional relationship between input value and output value at any precision [5, 6], its topological structure is shown as Fig. 31.1.

31.2.2 Algorithm of BP Neural Network

The algorithm of BP Neural Network includes two step, they are forward propagation of signal and back propagation of error [7]. Before sample trained, the weighted value w_{mi} between input layer and output layer and the threshold value Q_i of all hidden nodes are assigned randomly. Through input layer and processed by all hidden nodes, the signal get into output layer forward. If result achieves to expected effect, the training will end. Otherwise, the error will enter back

Fig. 31.1 Topological structure of BP Neural Network

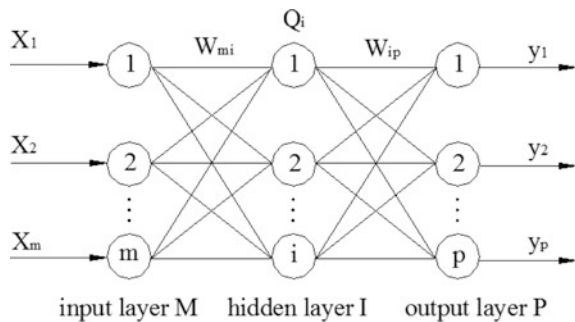
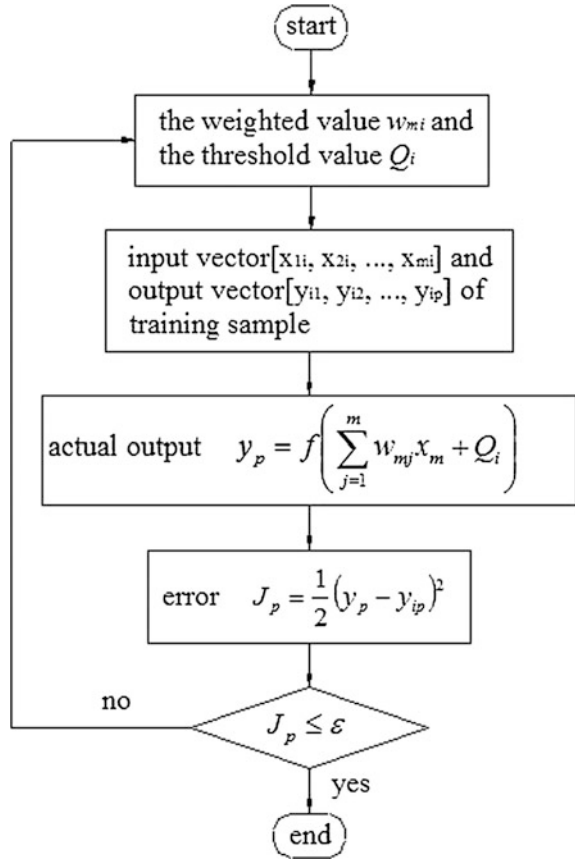


Fig. 31.2 Algorithm of BP Neural Network



propagation procedure, the detailed procedure as follow: first, the error J_p of actual value y_p and output value y_{ip} returns to the start; second, according to the returned error, the weighted value w_{mi} and threshold value Q_i are revised; then the signal get into forward propagation stage again. The back propagation procedure will not stop until error J_p is within the prescribed range ϵ . The algorithm flow chart is shown as Fig. 31.2.

31.3 Sample Obtaining and Preprocessing

Experienced data show that mass, rotary speed and layout angle of propeller shaft have bigger impact to vehicle noise than other factors. Take noise of driver right ear (DRE) as evaluating indicator. The sample data of one SUV vehicle are as follows (Table 31.1).

Table 31.1 Experienced data

Order	Mass/kg	Rotary speed/rpm	Layout angle/°	Decibel
1	10.6654	3000	4.8	66
2	12.1559	4000	3.5	76
3	15.2125	1200	0	70
4	10.5896	600	4.8	89
5	15.4125	4600	4.6	52
6	10.9654	400	1.4	62
7	12.1589	3600	0.5	84
8	10.2654	4400	3.6	64
9	14.4125	1000	3.9	81
10	12.1589	500	4.6	65
11	12.1259	6000	5.5	70
12	10.2654	800	4.4	84
13	15.4125	2000	2.1	73
14	12.1589	1800	1.3	69
15	10.2654	3500	1.5	89
16	12.1589	700	7.1	65

In order to calculate fast and decrease adjustment range of weighted value between input layer and output layer, the sample data was normalized using Formula (31.1).

$$x'_i = \frac{x_i - x_{\min}}{x_{\max} - x_{\min}} \tag{31.1}$$

All sample data are within the range [0, 1] after normalization. When the training is finished, the obtained simulated data should be counter-normalized.

31.4 BP Neural Network Establishment and Prediction

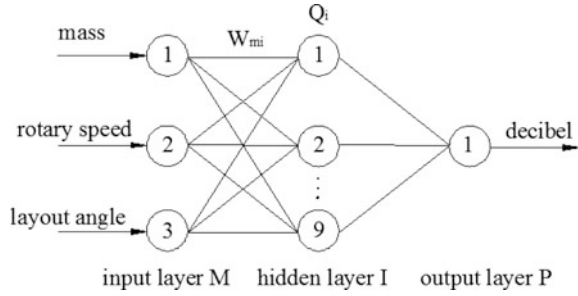
31.4.1 BP Neural Network Model Establishment

Combined training results and sample data, BP Neural Network structure is used in this paper shown as Fig. 31.3.

The sample data input vector after normalization is
 $p = [0.078 \ 0.368 \ 0.961 \ 0.063 \ 1.000 \ 0.136 \ 0.368 \ 0.000 \ 0.806 \ 0.368 \ 0.368 \ 0.000 \ 1.000 \ 0.368 \ 0.000 \ 0.368; 0.464 \ 0.643 \ 0.143 \ 0.036 \ 0.750 \ 0.000 \ 0.571 \ 0.714 \ 0.107 \ 0.018 \ 1.000 \ 0.071 \ 0.286 \ 0.250 \ 0.554 \ 0.054; 0.676 \ 0.493 \ 0.000 \ 0.676 \ 0.648 \ 0.197 \ 0.070 \ 0.507 \ 0.549 \ 0.648 \ 0.775 \ 0.620 \ 0.296 \ 0.183 \ 0.211 \ 1.000];$

Output vector is

Fig. 31.3 Concrete structure of BP Neural Network



$t = [0.378 \ 0.649 \ 0.486 \ 1.000 \ 0.000 \ 0.270 \ 0.865 \ 0.324 \ 0.784 \ 0.351 \ 0.486 \ 0.865 \ 0.568 \ 0.459 \ 1.000 \ 0.351]$

It is known from above that the established BP Neural Network has 3 input layer nodes, 9 hidden layer nodes and 1 output layer node. So, the model can be embodied below with newff() function of MATLAB software.

```
net = newff(minmax(p), [3, 1], {'tansig', 'purelin'}, 'trainlm')
```

- tansig Excitation function of hidden
- purelin Excitation function of hidden
- trainlm Training function

Training parameters are

```
net.trainParam.show = 50
net.trainParam.epochs = 2000
net.trainParam.lr = 0.001
net.trainParam.goal = 0.05
```

After the BP Neural Network of influence of propeller shaft to vehicle noise was established, begin to train it.

31.4.2 Training and Checking of BP Neural Network

Sample data was trained based on the BP Neural Network model of influence of propeller shaft to vehicle noise, and the training process was obtained shown as Fig. 31.4.

It can also be obtained the difference between model prediction value and actual value shown as Fig. 31.5 and the overall error shown as Fig. 31.6.

It can be known from Figs. 31.5 and 31.6 that most errors between sample data prediction value and actual value are in the range from -4 to 4 dB, only one or two errors reaches 8 dB because of small sample size, and model precision can improve

Fig. 31.4 Training process

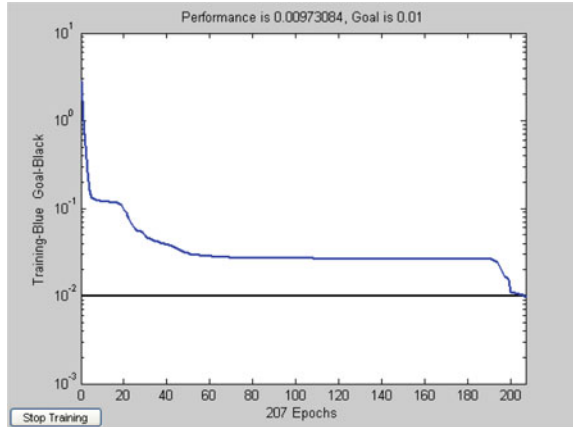
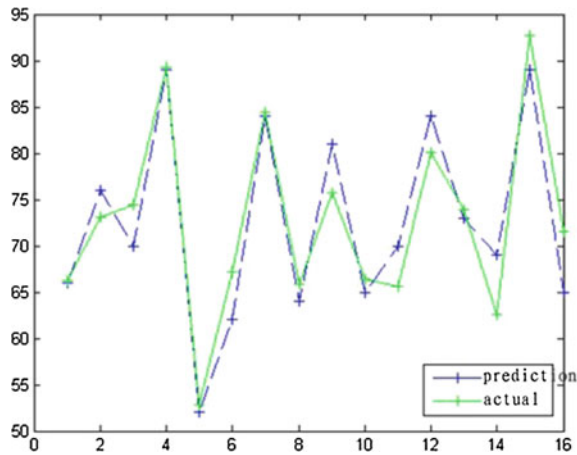


Fig. 31.5 Difference between prediction value and actual value



if increasing the sample size. To sum it up, the training errors are in acceptable range and the model can be used to predict the vehicle noise which is caused by propeller shaft.

31.4.3 Prediction and Application

The noise was predicted for the vehicle in research stage using trained BP Neural Network model, the prediction results are as Table 31.2.

It is necessary to note that the results in Table 31.2 just offer a reference for engineers, and they still need to carry out some tests according to actual situation.

Fig. 31.6 Overall error

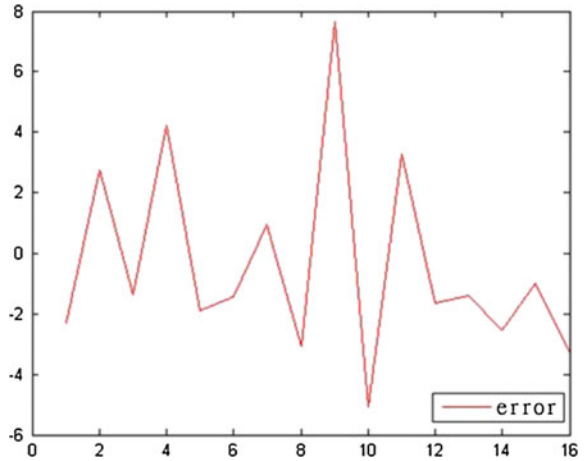


Table 31.2 Prediction results

Order	Mass/kg	Rotary speed/rpm	Layout angle/°	Decibel
1	12.5646	4000	4.5	68
2	11.6254	3200	1.5	55
3	10.8159	1300	5.9	89

31.5 Conclusion

- (1) BP Neural Network model of influence of propeller shaft to vehicle noise was established based on experienced data.
- (2) The BP Neural Network model was trained using MATLAB software, and the error was in the acceptable range.
- (3) The noise was predicted for the vehicle in research stage using the trained BP Neural Network model, providing theoretical reference to engineers.

References

1. Qian Z, Yuekui S, Yue S (2011) Study on automobile noise & vibration of causing by transmission shaft with cross-type universal joint. *J Mech Transm* 35(10):70–76
2. Ma D, Yu Z, Liu Y (2014) Research on application of BP neural network in predicting employment rate of college graduates. *J Jiamusi Univ (Nat Sci Ed)* 32(5):751–753
3. Liu H, Ren XZ, Zhang LP (2006) Prediction on grinding error of inner-bore of bearing ring based on BP neural network. *J Henan Univ Sci Technol Nat Sci* 27(2):13–15
4. Zhou J, Gu B (2006) Lifetime prediction of mechanical seal based on artificial neural networks. *Fluid Mach* 34(3):19–22

5. Kiani MKD, Ghobadian B, Tavakoli T et al (2010) Application of artificial neural networks for the prediction of performance and exhaust emissions in SI engine using ethanol-gasoline blends. *Energy* 35:65–69
6. Lee HH, Lee SK (2009) Objective evaluation of interior noise booming in a passenger car based on sound metrics and artificial neural networks. *Appl Ergon* 40(5):860–869
7. Chen ZY, Li SC, Zhai CY (2008) Application of improved BP network to leak-detecting system of pipeline. *J Henan Univ Sci Technol Nat Sci* 29(3):44–47

Chapter 32

Optimization and Simulation of SUV Sunroof Buffeting Noise

Xu Gong, Jun Wang, Chaoyi Deng, Penghui Wei, Bo Liu and Lin Li

Abstract To solve the buffeting problem of a SUV at low speed, the transient CFD simulation with LES model is run to get the buffeting frequency and Sound Pressure Level (SPL) at the front passenger's ear sitting in the SUV with sunroof full open. The simulation results show that there is buffeting problem for the SUV. Then optimization of the sunroof spoiler is made and CFD simulation shows that SPL at the front passenger's ear decreases by 9 dB. Subjective and objective road tests show that there is no buffeting problem with the optimized sunroof spoiler.

Keywords SUV · Buffeting noise · Sunroof · Road test

32.1 Introduction

Vehicle Sunroof buffeting can be considered as cavity noise. The cabin acts as a cavity when the sunroof window is open. There is unstable shear layer at the front edge of the opening, vortices shed from the front edge and propagate downward with the flow, when impinge onto the rear edge of the opening, the vortices break down and pressure wave is generated and propagates every each way, when the pressure wave reaches the front edge of the opening, it triggers another set of vortex shedding. This process occurs many times per second and causes the shear layer to change with a specific frequency. Resonance occurs when this frequency coincides with the natural frequency of the cabin. This resonance is the so-called Helmholtz resonance. The resonance frequency depends on the flow speed, geometry of the opening, and volume of the cabin and so on [1].

For vehicle sunroof buffeting, the resonance frequency is usually very low (<20 Hz), but the intensity is very strong (>100 dB). It occurs when the vehicle moves with the sunroof opening. Although human's ear cannot "hear" such a low frequency, it can be "felt" as a pulsating wind force that may be very annoying and

X. Gong (✉) · J. Wang · C. Deng · P. Wei · B. Liu · L. Li
Chongqing Changan Automobile Company Ltd., Chongqing, China
e-mail: gongxu@changan.com.cn

fatiguing. As computer becomes stronger and stronger and NVH performance gets more and more attention, more and more study on vehicle buffeting has been done by OEMs around the world since the early 21st century [2–7]. Crouse B. etc. studied the mechanism of sunroof buffeting [2]. An C F and Kanwerdip S focused on SUV's sunroof buffeting reduction. They found the buffeting noise can be reduced by optimizing the spoiler, and the CFD results agreed with experimental results [4]. Hangsheng Hou simulated buffeting noise with spoiler made of meshed fabric material and the simulation results agreed well with experimental results which means CFD is a very effective tool to predict buffeting noise [7]. Therefore, it is necessary to use CFD method to solve buffeting problem at early stage of vehicle design to assure passenger comfort and reduce TGW complaint.

This paper simulates sunroof buffeting of an SUV with sunroof full open by using CFD method, the simulation result shows there is serious sunroof buffeting problem. Based on the project's situation and buffeting mechanism, we tend to solve the buffeting problem by changing the spoiler from a flat bar to a suitable serrated bar. To get the suitable serrated bar, the proper installation angle, the right height of the spoiler and etc., many simulations are run and the final result shows that SPL at the front passenger's ear decreases by 9 dB because the serrated spoiler avoids the vortices break down at the rear edge of the opening. Finally, the subjective and objective road tests show that there is no buffeting problem with the optimized sunroof spoiler.

32.2 Simulation Analysis

32.2.1 Methodology

With the development of computer technology and the improvement of CFD method, numerical simulation has been increasingly becoming an indispensable tool for turbulence research. There are mainly three methods for turbulence simulation: Direct Numerical Simulation (DNS), Large Eddy Simulation (LES) and Reynolds-Averaged Navier-Stokes simulation (RANS).

DNS method directly solves Navier-Stoke equations, without any turbulence model. However, this method requires huge memory and tremendous computing capability, it is impossible to be used for complicate engineering problem with current computing capability. RANS method can robustly simulates mean turbulent flow, it does not require too much memory and is not very CPU time consuming and thus be widely used, but it cannot accurately capture the eddies of various scale. LES method directly solves eddies of big scale and uses sub-grid model to simulate small eddies [8]. There is a mixed model called Detached eddy simulation (DES) which uses LES method for the main flow and RANS method for the boundary flow [9].

Sunroof buffeting process is a transient process, LES model is used to simulate it in this paper.

32.2.2 Geometry

The geometry for the simulation in this paper includes both exterior and interior body with lots of details, the grills, seals, doorknobs etc. are kept for the exterior body, the instrument panel, seats, console, dummies etc. are kept for the interior body and the sunroof itself is full details kept. Complex structures of chassis are simplified on the condition that it makes little influence on flow. The final interior body and sunroof is shown in Fig. 32.1 which shows geometry of the real car is faithfully kept for the simulation.

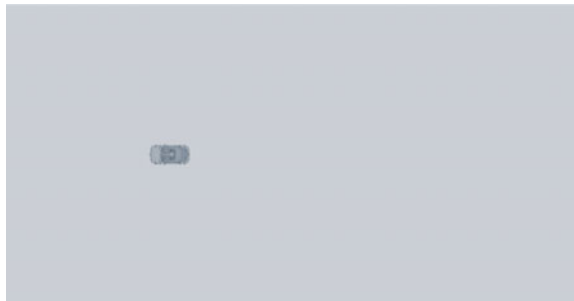
32.2.3 Computational Domain

Figure 32.2 shows the rectangular computational domain for the numerical simulation of the SUV. The SUV is 4100 mm in length (L), 1730 mm in width (W), and

Fig. 32.1 Cabin model of SUV



Fig. 32.2 Computational domain



1635 mm in height (H). The width, height and length of the rectangular computational domain are set to be 12W, 8H and 11L, respectively, as shown in Fig. 32.2. The sensor points are installed at the driver's and first row passenger's ears, the names and coordinates of the points are PDL (1.36, -0.416, 1.11 m), PDR (1.36, -0.264, 1.11 m), PPL (1.36, 0.264, 1.11 m), PPR (1.36, 0.416, 1.11 m) respectively.

32.2.4 Meshing

In this paper, trim mesh is used. For key areas where flow changes fast, smaller surface mesh and volume mesh refinement are implemented. To capture shear layer shedding in the area of sunroof opening, three local volume mesh refinement blocks are used to get proper volume mesh, prism layers are used in the vicinity of car body for wall function.

32.2.5 Boundary Conditions

The boundary conditions used in this paper are shown in Table 32.1.

32.2.6 Simulation Methods

Steady flow is firstly simulated by using Realizable $k-\epsilon$ turbulence model, when the steady flow is converged, transient flow is run with LES model to simulate the buffeting phenomenon, due to the fact that buffeting frequency is about 20 Hz which means the cycle is about 0.05 s, thus the time step is set to be 0.0025 s which means 20 sampling points in a cycle, this is enough for the simulation. The total simulation time is 6 s and static pressure is recorded for every points at each time step. The recorded static pressure is not stable at first, after about 800–1000 time steps, it becomes periodically stable and static pressure after this can be used for post processing.

Table 32.1 Boundary conditions of domain

Location	Boundary conditions
Inlet	Velocity inlet, $v = 45$ km/h
Outlet	Pressure outlet
Ground	Wall (no slip)
Body	Wall (no slip)
Top and sides	Wall (slip)

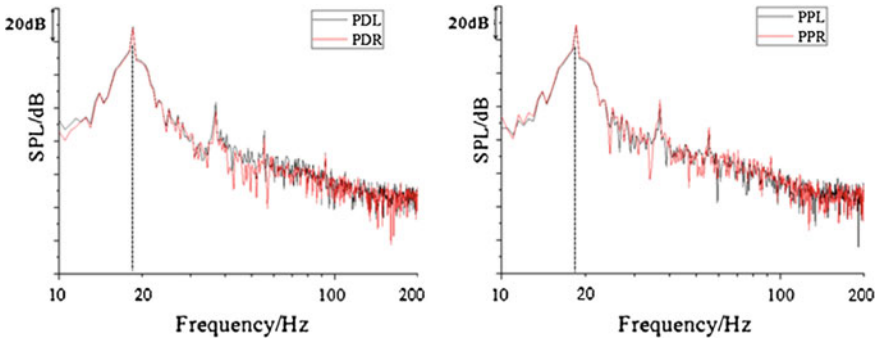


Fig. 32.3 SPL at driver's (*left*) and passenger's (*right*) ears

32.2.7 Analysis

Figure 32.3 shows the simulated results of sound pressure level (SPL) at driver's and passenger's ears for the baseline case. It shows that there is a peak of 130 dB at 19 Hz which means severe buffeting problem occurs for the SUV. The spectrum curves at driver's and passenger's ears almost completely overlap.

As we know from Fig. 32.3 that the buffeting frequency is 19 Hz, thus, the cycle is $T = 1/f = 0.0526$ s. Figure 32.4 shows the static pressure of the $y = 0$ section plane at different time. At $t = 0$, strong vortex with low pressure core occurs at the front of the sunroof opening. At $t = T/4$, the vortex moves downstream and becomes larger. At $t = T/2$, the vortex impinges the rear edge of the sunroof, breaks down and intrudes into the cabin so that the interior pressure decreases significantly. At $t = 3T/4$, the interior pressure starts to increase and a new vortex is about to form at the front edge of the sunroof. At $t = T$, the newly formed vortex with low pressure core sheds from the front edge of the sunroof and moves downstream. Figure 32.4 shows a periodic phenomena, vortex generation, vortex development, vortex crashing, pressure bouncing back and vortex generation again. The periodic phenomena results in the severe buffeting problem of the SUV sunroof.

32.3 Optimization

There are two methods to control sunroof buffeting, active control and passive control. Since there is already prototype for the SUV, to solve the sunroof buffeting problem quickly, effectively and at low cost, we tend to optimize the spoiler to change the vortex structure to solve the buffeting problem.

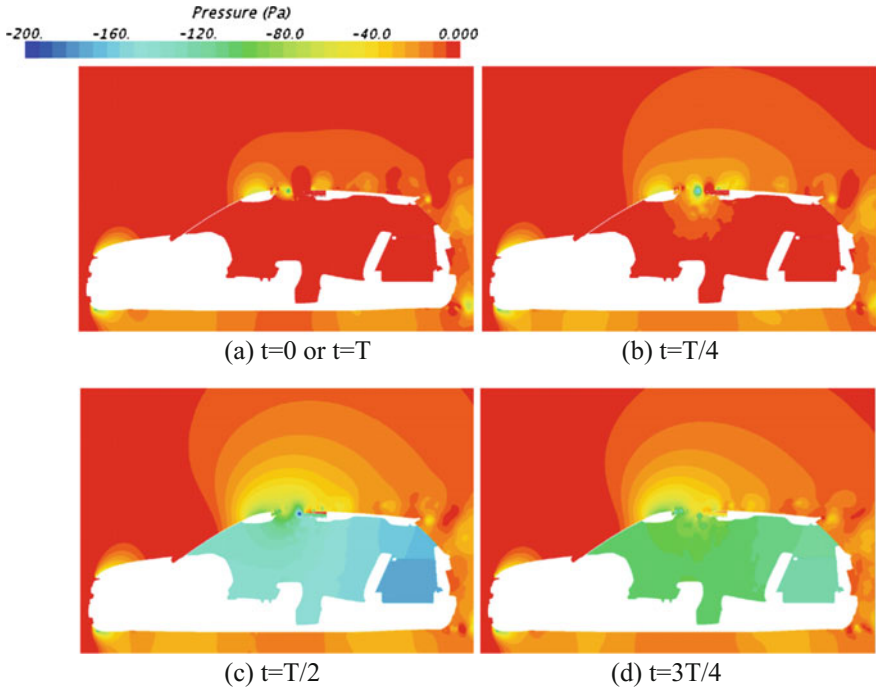


Fig. 32.4 Static pressure of the $y = 0$ section plane

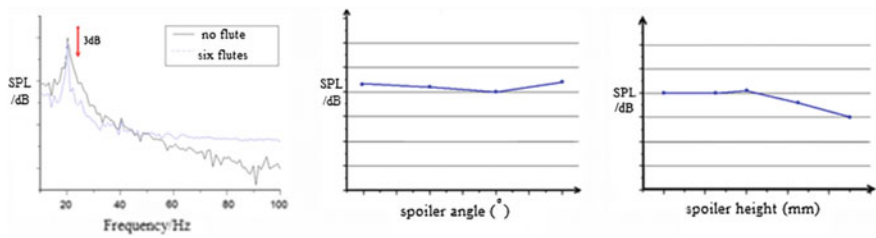


Fig. 32.5 Influence of spoiler style, angle and height

32.3.1 Optimization Plan

The serrated spoiler can control the sunroof buffeting by destroying the vortex periodically shedded at the front edge of sunroof. From Fig. 32.5, it can be seen clearly that spoiler angle and spoiler height are important for buffeting control [10]. Therefore, this paper solves the buffeting problem by changing the flat spoiler to a suitable serrated spoiler which can be gotten by optimizing the spoiler's angle and height.

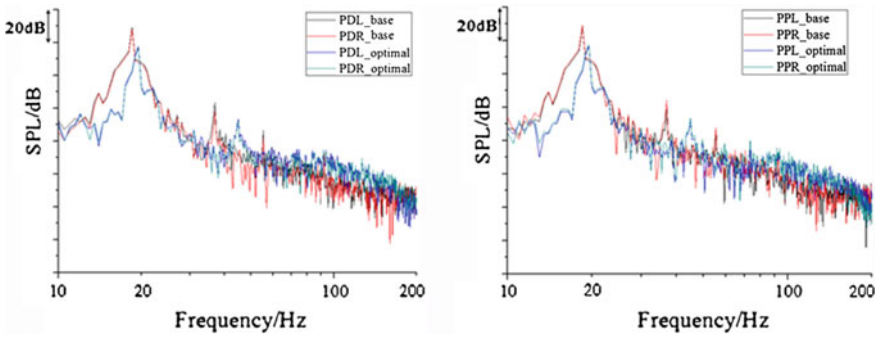


Fig. 32.6 SPL at driver's (left) and passenger's (right) ears

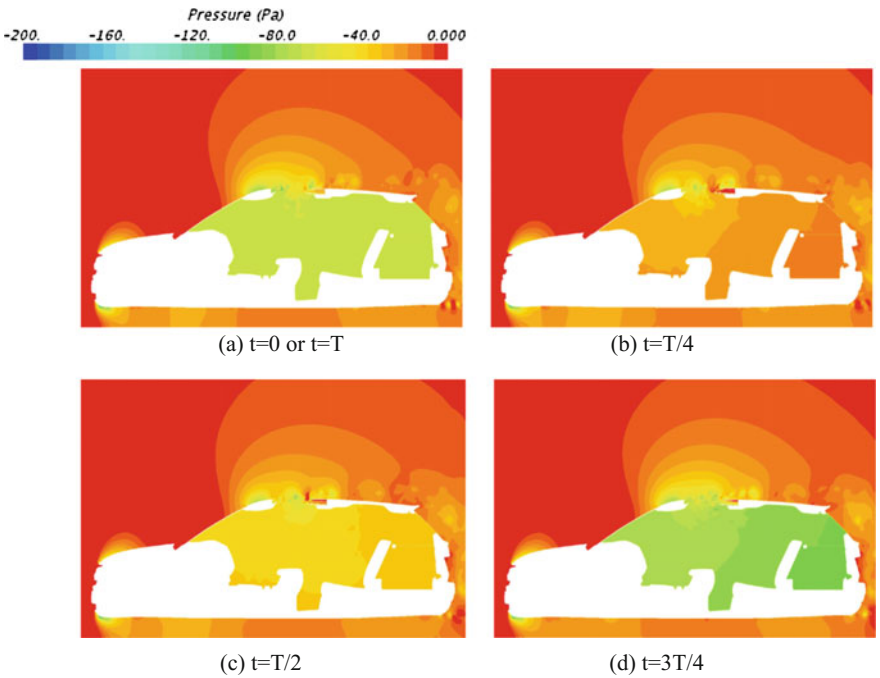


Fig. 32.7 Static pressure of the $y = 0$ section plane

32.3.2 Analysis

Figure 32.6 shows the simulation results of SPL at driver's and passenger's ears for the baseline and optimized case. From Fig. 32.6, it can be seen that the buffeting frequency is about 20 Hz and the peak of SPL at the front passenger's ear decreased by 9 dB for the optimized case.

Similar to the baseline case, a set of 4 frames of static pressure contour within a cycle for the serrated spoiler are shown in Fig. 32.7. It is clearly seen that the change of the interior pressure is slight and the size of the vortex is smaller than that of the baseline case. For the direction of downstream, the vortex does not impinge the rear edge of the sunroof and does not intrude into the cabin. These graphs explain why the buffeting noise is solved in this case, compared to the baseline case.

32.4 Road Test

Based on the optimized data, prototype of serrated spoiler is made and be installed on the SUV for road test and subjective evaluation. The results of road test and subjective evaluation show that the buffeting problem is completely gone with the optimized spoiler installed. Figures 32.8 and 32.9 show the road test results in

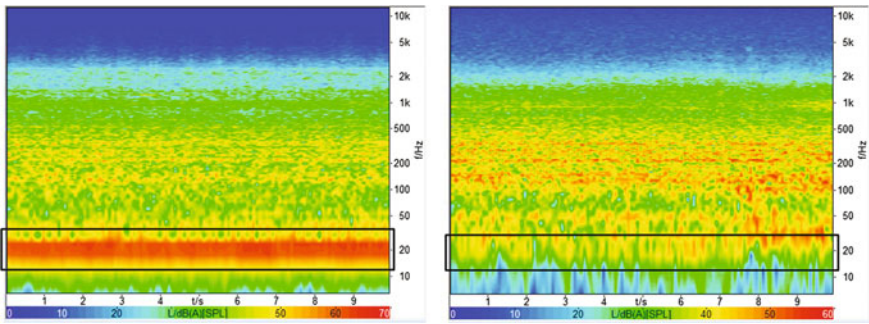


Fig. 32.8 Results of road test: base (left) and optimized (right)

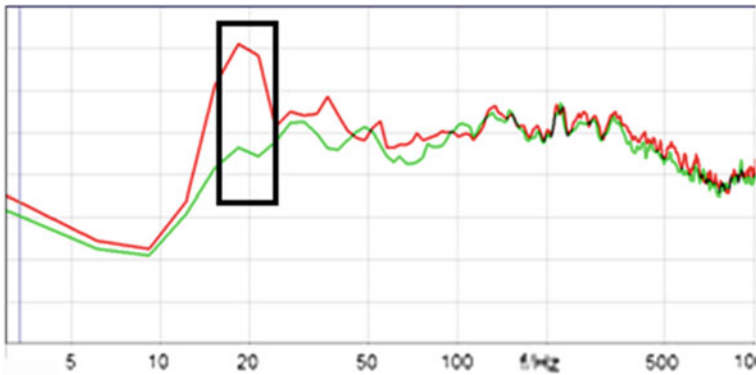


Fig. 32.9 SPL at driver's right ear: base (red line) and optimized (green line) (Color figure online)

detail. It is clearly seen that the results of road test are similar to the results of CFD simulation qualitatively, with more reduction of SPL peak. Since the sunroof is full open, the environmental noise and road noise cannot be excluded for the road test, therefore, only trend is compared for optimization and baseline in this paper.

32.5 Conclusions

- (1) CFD simulation results show there is a peak of 130 dB in the SPL which means severe buffeting problem for the SUV.
- (2) The peak of SPL decreases from 130 to 120 dB by changing the spoiler from a flat bar to a suitable serrated which means an effective way for buffeting control.
- (3) The results of road test and subjective evaluation show that the buffeting problem is completely gone with the optimized spoiler installed, it agrees with the results of CFD simulation qualitatively which means CFD is an effective method for sunroof buffeting prediction and optimization.

References

1. An CF, Alaie SM, Sovani SD et al (2006) Side window buffeting characteristics of an SUV. SAE technical paper 2004-01-0230
2. Crouse B, Senthoooran S, Balasubramanian G, Freed D et al (2007) Computational aeroacoustics investigation of automobile sunroof buffeting. SAE technical paper 2007-01-2403
3. Balasubramanian G, Crouse B, Freed D (2009) Numerical simulation of leakage effects on sunroof buffeting of an idealized generic vehicle. AIAA-2009-3348
4. An CF, Kanwerdip S (2006) Optimization study for sunroof buffeting reduction. SAE technical paper 2006-01-0138
5. Mendonca F, Shaw T, Tran L, Mueller A (2011) Aero-vibroacoustics fully coupled prediction of panel impedance effects in sunroof buffeting. AIAA-2011-2817
6. Mendonca F (2013) CFD/CAE combinations in open cavity noise predictions for real vehicle sunroof buffeting. SAE technical paper 2013-01-1012
7. Hou H (2014) CAA application to automobile wind throb prevention design. SAE technical paper 2014-01-0593
8. Wang F (2004) Analysis of computational fluid dynamics—theory and application for CFD software. Tsinghua University Press, Beijing, pp 117–118
9. Liu X, Wu YZ (2004) The computation of the lateral jet turbulence flow using DES method. *Acta Aeronautica et Astronautica Sinica* 25(3):209–213
10. Wang Y, Gu Z, Yang X, Lin X, Dong G (2010) Numerical simulation and control of automobile sunroof buffeting noise. *China J Highw Transp* 23(6):108–114

Chapter 33

Semi-active Intake Structure Design and Vehicle Validation

Jie Li, Changjun Tan, Donglian Zhang, Shuo Zhang and Liang Yang

Abstract A development idea of dual-mode intake system is proposed and a passive flapper intake valve is designed in this paper. The GT-Power model of intake structure is established, the effect law of valve switch and opening angle on 2nd order intake noise is researched through simulation and test. The dynamic model of passive flapper valve is established by ADAMS software, which analyzes the matching relationship among spring stiffness, valve opening rotation rate and valve opening angle. The test results show that the intake noise and engine power loss are reduced effectively, and vehicle ride comfort and NVH quality are also improved obviously, when the intake valve is opened automatic at 3100 engine speed.

Keywords NVH · Semi-active intake · Valve · Simulation · Matching

33.1 Introduction

Capacity of air cleaner and structure of vehicle intake system play an important role in the intake noise reduction. Generally, the higher the capacity of air cleaner is, the better the noise reduction performance is. However, due to the compact engine compartment, the arrangement of structures is difficult for air cleaner with high capacity. At the same time, to have better noise elimination performance, the intake system, such as Helmholtz mufflers and 1/4 wavelength tubes for different frequency noise, is designed to be complicated, which results in the unsmooth air flow,

J. Li · C. Tan · D. Zhang · S. Zhang · L. Yang
Changan Auto Global R&D Center, Chongqing 401120, China

J. Li (✉) · C. Tan · D. Zhang · S. Zhang · L. Yang
State Key Laboratory of Vehicle NVH and Safety Technology,
Chongqing 401120, China
e-mail: lijiestrive1215@163.com

high intake system back pressure and high engine power loss, or the appearance is not simple and beautiful. On the other hand, even though the air flow is smooth, resistance and engine power loss is low, the noise elimination performance is too weak to satisfy the NVH requirement. Noise reduction and engine power loss reduction are conflicting requirements for intake system. Dual-mode intake system is proposed to effectively solve the contradiction between noise reduction and engine power loss reduction and the contradiction between high capacity of air cleaner and muffler elements and arrangement of structures in engine compartment. To have better NVH performance but not increase the capacity or weight of air cleaner, dual-mode intake system is an ideal choice, and this technology has been extensively applied in Japanese, Korean, European and American medium and high end cars.

Although studies on dual-mode intake system are few, the researches on dual-mode exhaust mufflers are numerous, and the research method on dual-mode exhaust mufflers is applied to study dual-mode intake system in this paper. In 2002, Choi [1] studied the exhaust sound pressure and exhaust temperature of active muffler with valve under given twist spring stiffness. Liu [2] proposed a dual-mode valve to control exhaust flow and studied the relationship between noise reduction and opening angle of valve in 2003. In 2006, Alcini [3] established a GT model of passive exhaust valve and predicted the pressure loss of valve. In 2009, Hill [4] proposed an exhaust valve with high performance, which is better than traditional passive valve, the pressure loss is smaller at high rotational speed and is much closer to the pressure loss of active valve. In 2009, Zhaoxiang [5] studied the performance degradation of a passive exhaust mufflers based on CFD analysis. In 2013, Liu [6, 7] proposed a dual-mode exhaust muffler with valve to increase the quality of exhaust acoustic, especially the order noise at low frequency, and studied the influence of opening angle on the muffler sound characters in 2015 and the test on real car showed that muffler with valve could effectively reduce the order noise. Liu [8] proposed a semi-active muffler of exhaust system for diesel engine, and it can dramatically improve the noise elimination effect during 35–100 Hz.

The paper studies a dual-mode intake system (semi-active intake structure with valve) whose valve is fitted on the intake pipe of air cleaner, proposes a development idea of dual-mode intake system (Fig. 33.1), the content of the paper is divided into three parts: design of dual-mode intake system, simulation of intake system and experimental analysis:

- (1) Design of valve drive structure and determination of the layout of valve.
- (2) Determination of the diameter of valve pipe and normal intake pipe, and research the effect of valve opening angle on intake noise;
- (3) Adaptation of spring stiffness, engine rotational speed and valve opening angle;
- (4) Adaptation design of valve automatic opening considering experimental test.

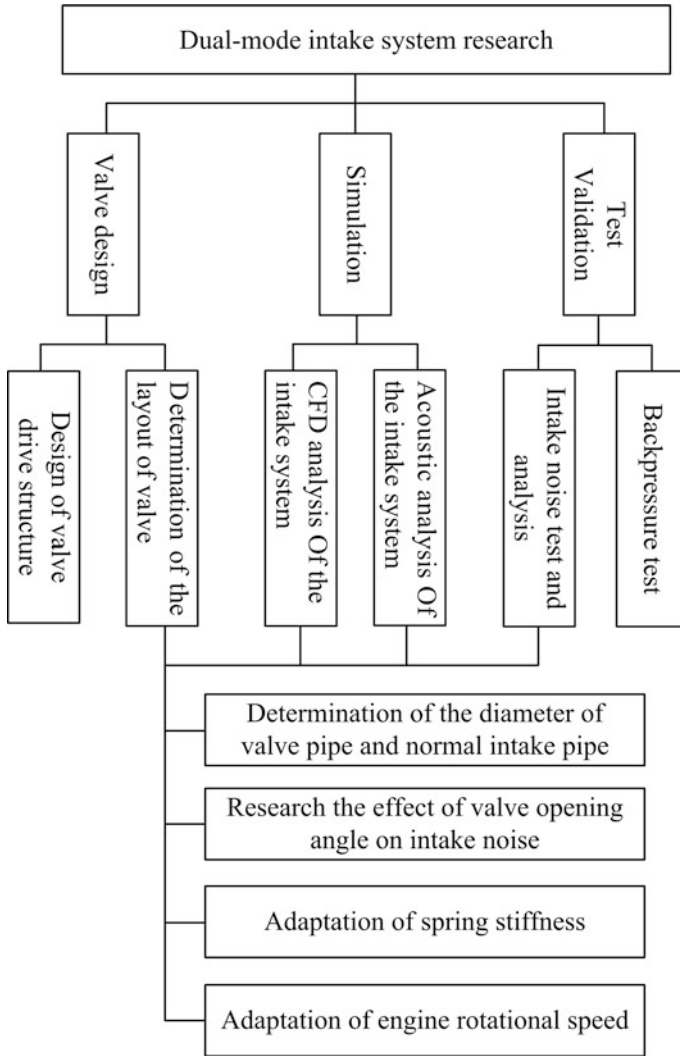


Fig. 33.1 Development idea of dual-mode intake system

33.2 Principle of Semi-active Intake System

From the view point of layout position, semi-active intake structures can be divided into two types: one is the type in which the valves are integrated into the interior of air cleaner; the other is the type in which valves are designed on the intake pipe of air cleaner. The second type is used in the paper, shown in Fig. 33.2, and the differences between this type and traditional structure are: two intake pipes are used in the air cleaner, one normal intake pipe and one valve pipe; to have better NVH

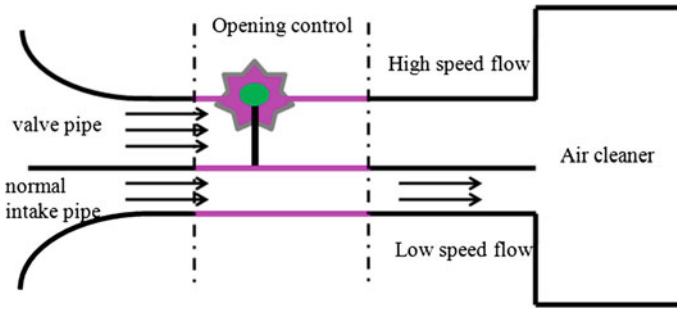


Fig. 33.2 A semi-active intake structure with valve

performance of intake, normal intake pipe is with smaller diameter, valve pipe is with larger diameter, automatic valve is fitted on the valve pipe, and this valve can open or close according to the work condition of engine when intake flow and pressure vary. When vehicle is at low speed or at cruising speed, the rotational speed of engine is low, intake flow is little, so the valve is closed, thus the cross section area of intake is smaller, expansion ratio is larger, transfer loss of air cleaner is large, intake noise is small; When vehicle is at high speed or speeding up, intake flow is large, the valve is opened, and thus the cross section area of intake becomes larger, transfer loss of air cleaner decreases, intake noise is large and power loss decreases. This method can meet the requirement of weak noise at low speed and high power at high speed.

Intake system uses this semi-active valve, intake noise and intake pressure loss experimental analyses, as shown in Fig. 33.3, are carried out under the three conditions: mandatory closing, mandatory opening and automatic opening of the valve.

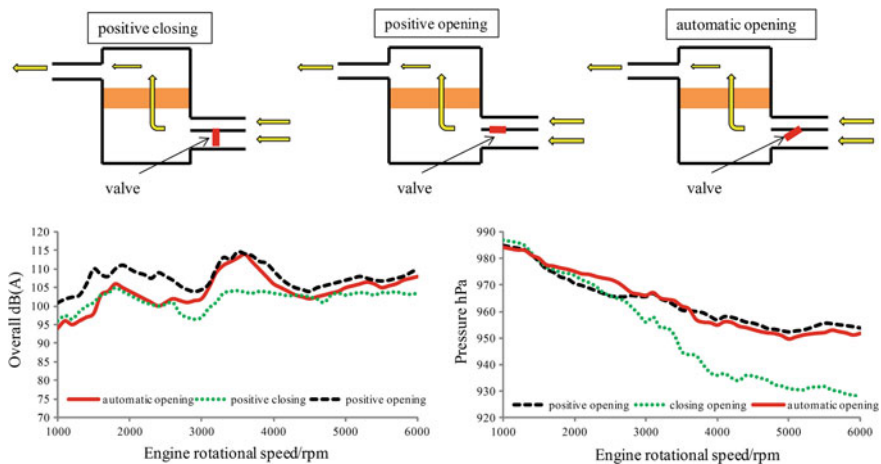


Fig. 33.3 Intake noise and pressure loss analysis of dual-mode intake structure

The result is: when dual-mode intake structure is applied, the intake noise dramatically decreases whereas intake pressure loss varies small at low engine rotational speed, meanwhile, the intake pressures loss dramatically decreases whereas intake noise does not dramatically increase at high speed (shown in Fig. 33.3).

33.3 Determination of the Diameter of Normal Intake Pipe and Valve Pipe

33.3.1 Determination of the Diameter of Normal Intake Pipe

Generally, with smaller diameter of normal intake pipe, intake pressure level of sound and 2nd order noise are lower, but the flow noise at high speed becomes larger. Take intake noise analysis of normal intake pipe of a car as an example, results are shown in Figs. 33.4 and 33.5, at low rotational speed, intake pressure level of sound decreases when the diameter of normal intake pipe becomes smaller; at high rotational speed, the pressure level of sound increase when the flow noise becomes larger, but the 2nd order noise decreases when the diameter of normal intake pipe decreases. The primary task of acoustic simulation of intake system by GT-Power is to determine a reasonable diameter of normal intake pipe, and the initial diameter is 42 mm considering flow noise and order noise.

In order to determine the diameter of normal intake pipe, CFD simulation on the resistance of closed intake system is carried out to see whether intake pressure difference satisfies the requirement (Fig. 33.6). When the diameter of normal intake pipe is less than 42 mm, intake pressure loss increases dramatically (shown in Fig. 33.7). In order not to affect the engine power due to large intake pressure loss, the diameter of normal intake pipe is determined to satisfy the intake resistance requirement (Table 33.1).

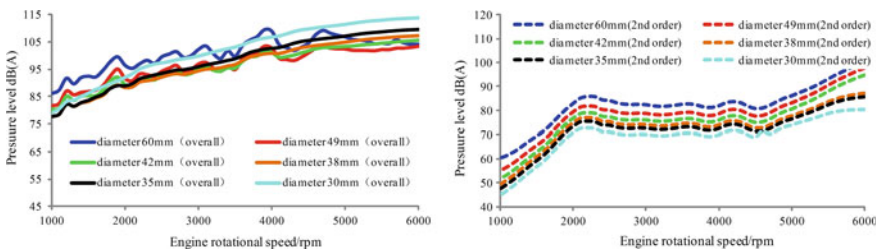


Fig. 33.4 The comparison of the overall and 2nd order intake noise with different diameter of normal intake pipe

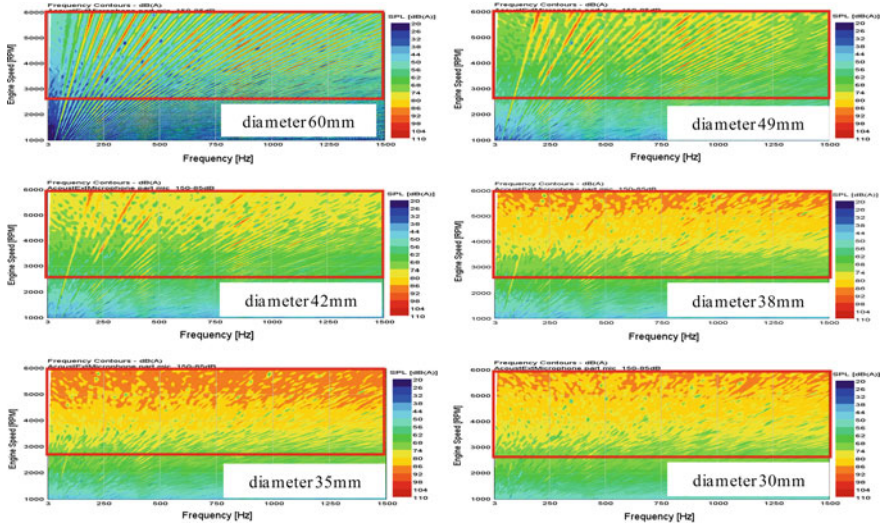


Fig. 33.5 The colmap of intake noise with different diameter of normal intake pipes

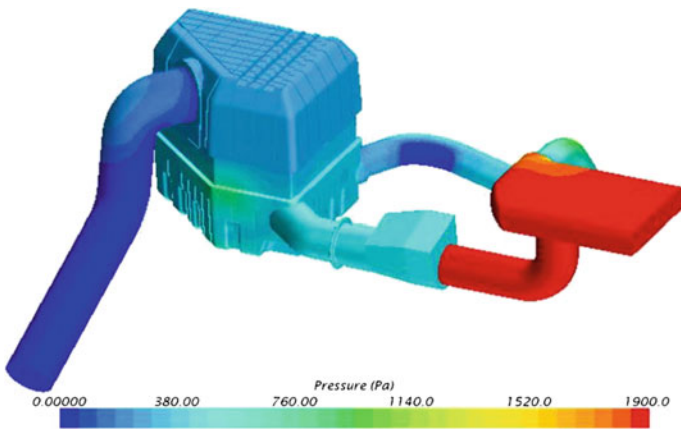


Fig. 33.6 The static pressure distribution of dual-model air cleaner

33.3.2 Research on the Opening Speed of Semi-active Valve and the Determination of the Diameter of Valve Pipe

In GT-Power, semi-active valve is throttle valve, two intake pipes are simulated by bifurcated pipe, as shown in Fig. 33.8, the diameter of normal intake pipe is known, and we will determine the diameter of valve pipe which is not smaller than normal intake pipe. Through the acoustic analysis of normal intake pipe, under the

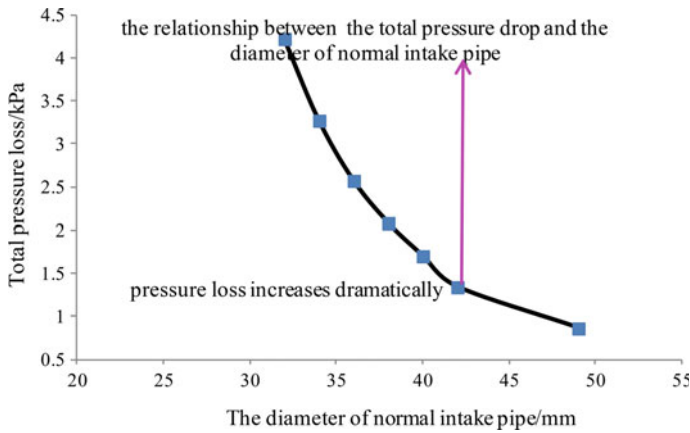


Fig. 33.7 The relationship between the total pressure loss and the diameter of normal intake pipe

Table 33.1 The intake total pressure loss of different diameter of normal intake pipe

Diameter/mm	The total pressure loss/kPa	Pressure difference both ends of the valve/kPa
32	4.22	3.89
34	3.27	2.97
36	2.57	2.31
38	2.08	1.8
40	1.7	1.41
42	1.34	1.07
49	0.86	0.5

condition that flow noise is not obvious, intake pressure level of sound and 2nd order noise do not change with the diameter of pipe, so the initial diameter of valve is the same as that of normal intake pipe and the research on opening speed of valve is carried out based on these conditions. When the opening speed of valve is determined, intake acoustic analysis is carried out to determine the diameter of valve pipe.

In this instance, both diameters of valve pipe and normal intake pipe are 42 mm to study the opening speed of valve. Figures 33.9 and 33.10 are pressure level of sound and 2nd order noise of intake simulation with different opening speed respectively; through overall analysis of pressure level of sound and 2nd order noise under different opening speed of valve, the reasonable opening speed of semi-active valve is determined finally and the intake noise suddenly change has nothing to do with the opening angle. In the following simulation, the valve is set to all open state at relative opening speed.

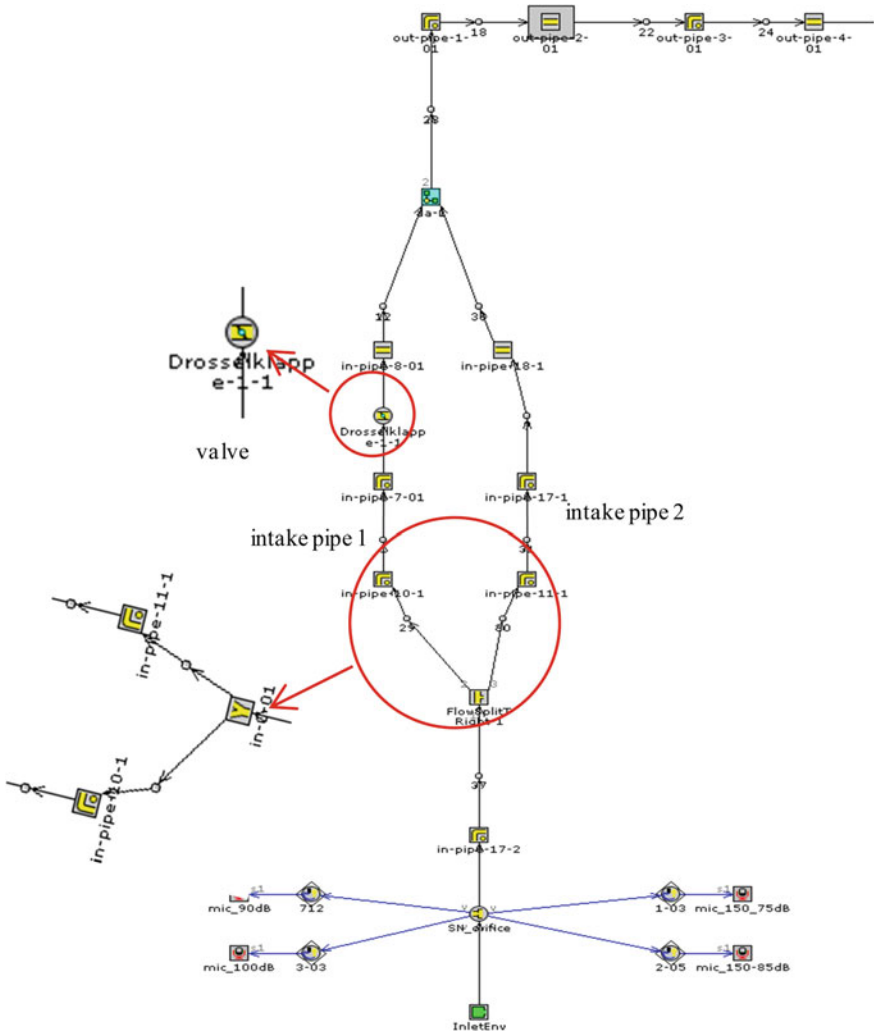


Fig. 33.8 The GT-Power model of the semi-active intake structure

Figures 33.11 and 33.12 are simulation results of intake noise colormap and 2nd order noise, respectively; from these figures, the diameter of the normal pipe is 42 mm, when the diameter of valve pipe varies from 60 to 42 mm, intake flow noise becomes larger; considering the 2nd order noise, the diameter of valve pipe is determined as 49 mm.

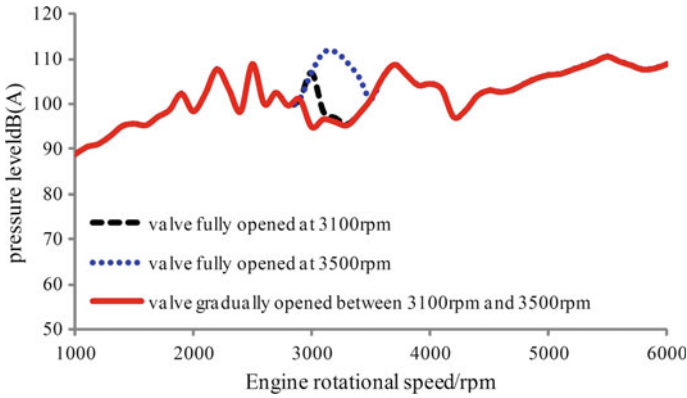


Fig. 33.9 The overall of intake noise when valve opened at different engine rotational speed

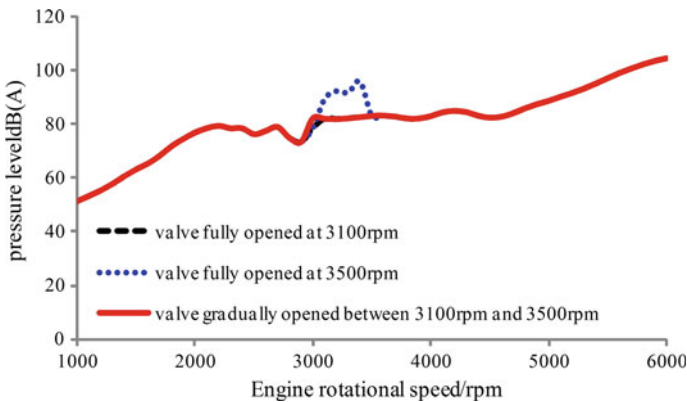


Fig. 33.10 The 2nd order intake noise when valve opened at different engine rotational speed

33.4 Research on Spring Stiffness Matching of the Valve

As shown in Fig. 33.13, Semi-active valve are consists of valve body, valve plate, sealing strip, link, rocker arm and spring. Valve plate and shaft are fixed as a whole, and the valve plate is connected with rocker arm through link. The spring is connected to the link at one end, and at the other end, the spring is fixed on the valve body through spring cup. In order to control the intake noise, the valve is closed when the engine rotating speed is low, with the increase of the intake air velocity, the pressure on valve overcome the spring resistance which passing from the link, and the valve is opened. When the air velocity is reduced to a certain value, the valve is closed again. Due to the rocker arm and link mechanism, a very small air pressure can open the valve and keep the valve open.

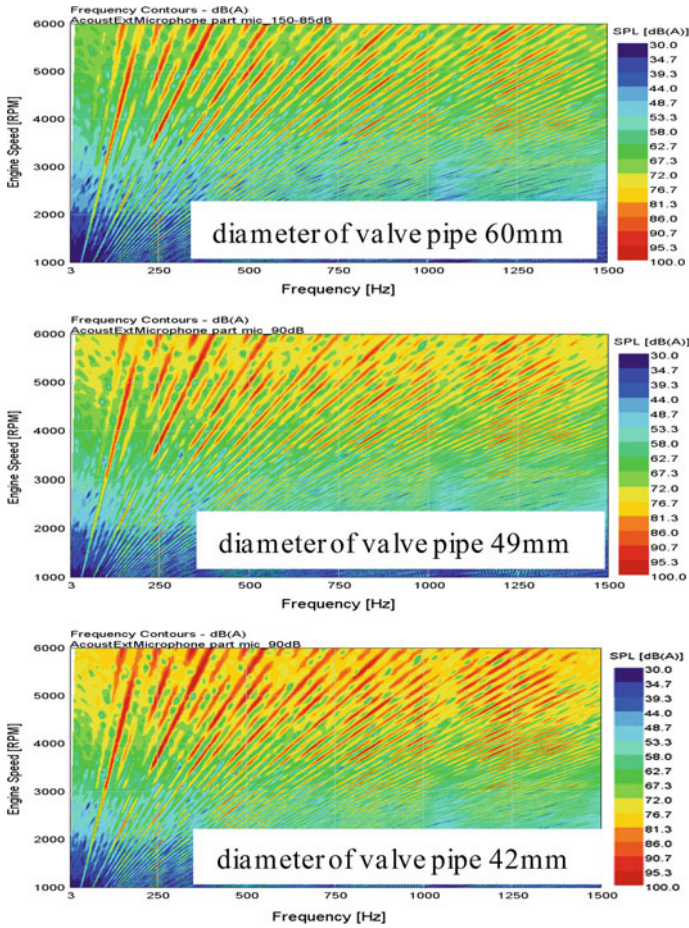


Fig. 33.11 The colormap of intake noise with different diameter of valve pipes

When researching the spring stiffness matching of the valve, the pressure on the valve plate must be received first as the simulation import. So the pressure difference between both ends of the valve will be researched in the next section.

33.4.1 The Simulation of Pressure Difference Between Both Ends of the Valve Based on STAR-CCM+ Software

The pressure difference between both ends of the valve are received through analysis and after-treatment by STAR-CCM+ software, which includes importing

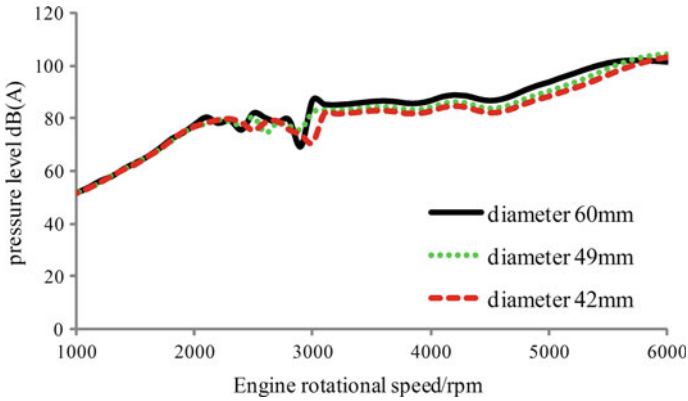


Fig. 33.12 The 2nd order intake noise of different diameter of valve pipes when the valve opened at 3100 rpm

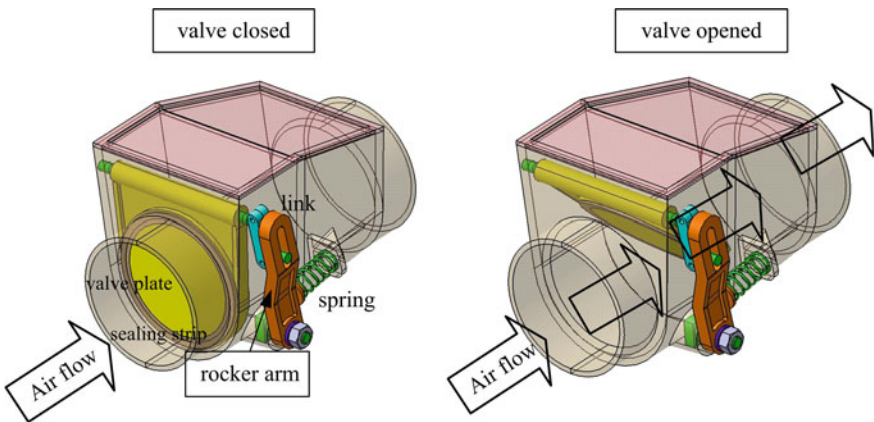


Fig. 33.13 The structure diagram of the Valve

dual-mode air filter model, simplifying model, delimiting boundary conditions after repairing part of the surface, generating mesh, delimiting physical model and so on. The main import parameters of CFD simulation are shown in Table 33.2, which includes engine rotating speed, Throttle pressure loss, and diameter of normal intake pipe and so on. The static pressure distribution of dual-mode air filter is received through the analysis, and the pressure difference between both ends of the valve are gained by analyzing multiple sets of engine rotating speed and the results are shown in Table 33.3.

Table 33.2 Import parameters of CFD simulation

Engine rotating speed (rpm)	2000	2500	3100	3500	4000
Air flow (kg/h)	122.5	164.2	193.9	226	277.8
Throttle pressure loss (kPa)	0.7682	0.81	0.82	1.02	1.4
Diameter of normal intake pipe (mm)	42	42	42	42	42

Table 33.3 CFD simulation results of the pressure difference both ends of the valve

Engine rotating speed (rpm)	Total pressure loss (kPa)	Pressure difference both ends of the valve (kPa)
2000	0.59	0.46
2500	0.99	0.78
3100	1.31	1.07
3500	1.79	1.43
4000	2.64	2.12

33.4.2 Research on Spring Stiffness Matching of the Valve Based on ADAMS Software

33.4.2.1 Mechanical Analysis and Dynamic Model Building of the Valve

As shown in Fig. 33.14, the forces acting on the valve main include airflow static force F_I acting on the valve plate and the spring force F_S acting on the rocker arm. The gravity of valve plate can be negligible because of the plastic material. According to force translational theorem, a moment of force $M_I(O_1)$ is added in order not to change the effect of the force while translating F_I to point O_1 , as shown

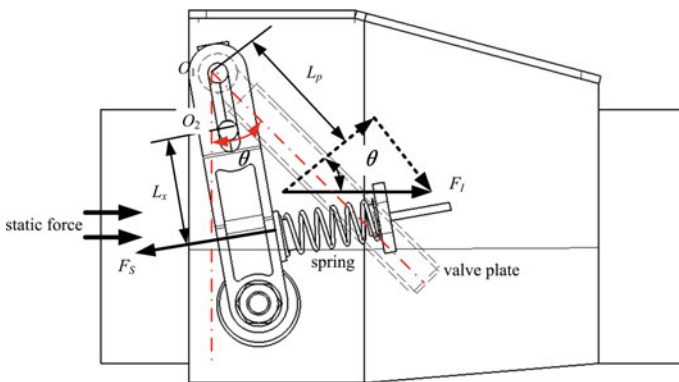


Fig. 33.14 The force diagram of the valve

in Eq. (33.1). The direction is vertical outward. The valve is opened when the torque is balanced, as shown in Eq. (33.4).

$$M_I(O_1) = F_I \cos \theta \cdot L_p \quad (33.1)$$

$$M_S(O_2) = F_S \cdot L_{S2} = K\Delta S \cdot L_{S2} \quad (33.2)$$

$$M_I(O_1) + F_I L_{S1} \cos^2 \theta = M_S(O_2) \quad (33.3)$$

Equation (33.4) can be obtained by expanding Eq. (33.3).

$$F_I \cos \theta (L_p + L_{S1} \cos \theta) = K\Delta S \cdot L_{S2} \quad (33.4)$$

where, $M_I(O_1)$ is the torque achieved by calculating the airflow static force F_I and its arm of force which is relative to the rotation center O_1 . $M_S(O_2)$ is the torque achieved by calculating spring force and its arm of force which is relative to the rotation center O_2 . O_1 is the rotational center of the valve plate. O_2 is connecting point of link rod and rocker arm. θ is the opening angle of the valve. L_p is the distance between the action point of F_I and O_1 . L_{S1} is the distance between O_1 and O_2 . L_{S2} is the distance between the action point of F_S and O_2 . L_{S1} and L_{S2} varies with the opening angle θ , and the sum of L_{S1} and L_{S2} is constant. K is the spring stiffness, ΔS is the pre-compression of the spring.

According to the mechanical analysis of the valve, then the pressure difference between both ends of the valve is converted to a force, which is loaded on the valve plate as the boundary conditions of the spring stiffness matching. Considering the pre-compression of the spring, the constraints among valve plate, axle, link, and rocker arm, a multi-body dynamic model for matching the spring stiffness is built by ADAMS software, as shown in Fig. 33.15.

33.4.2.2 Simulation Results Analysis

As mentioned above, the opening engine speed of valve plate is 3100 rpm according to the intake noise simulation. Based on this conclusion, the multi-body dynamic simulate speeds are set to 2000, 2500, 3100, 3500, and 4000 rpm, and the opening angle is set to 40° which is verified through the experiment.

The maximum spring stiffness and the opening angle under different spring stiffness are gained by changing the spring stiffness K in ADAMS. The pressure acting on the valve is always unchanged at a certain engine rotating speed during the simulation process.

The spring deflection and opening angle of valve under different engine rotating speed are obtained through after-treatment the simulation data. Taking engine rotational speed 3100 rpm as an example, as shown in Fig. 33.16, where, the spring deflection δ is negative when the spring is compressed and the spring deflection δ is positive when the spring is tensioned.

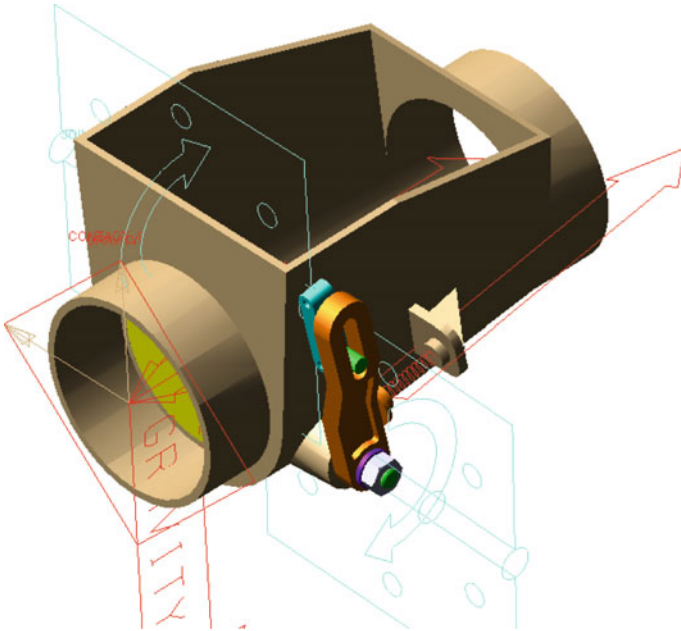


Fig. 33.15 The multi-body dynamic model of the spring stiffness matching

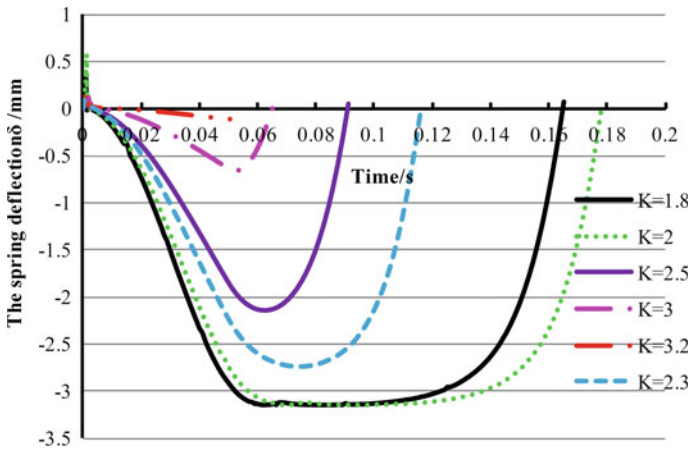


Fig. 33.16 Time domain curve of the spring deflection under 3100 rpm

The spring deflection δ gradually decreases with the increase of the spring stiffness, when the spring stiffness equals 3.2 N/mm, the spring deflection is about 0 mm, it means that the valve is keeping closed, so the maximum spring stiffness is 3.2 N/mm. In the same way, the maximum spring stiffness under other engine

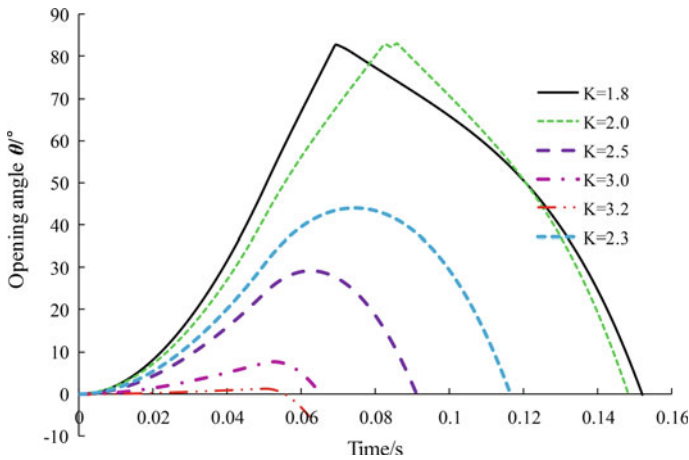


Fig. 33.17 Time domain curve of the opening angle under 3100 rpm

rotating speed is obtained, as shown in Table 33.3. Figure 33.17 shows the time domain curves of the opening angle, it can be seen that the opening angle is larger when the spring stiffness is smaller, in other word, the opening angle rapidly decreases with the increase of spring stiffness. The spring stiffness is 2.3 N/mm when the valve opening angle is 40°. In the same way, the spring stiffnesses under other engine rotating speed are also obtained when the valve opening angle is 40°, shown in Table 33.4.

The relationship between the maximum spring stiffness and engine rotating speed is obtained by fitting the data in Table 33.4, as well as the spring stiffness under $\theta = 40^\circ$, as shown in Figs. 33.18 and 33.19.

Within a certain speed range, the maximum spring stiffness increases linearly with the increase of engine rotating speed.

$$K = 0.00244n - 3.8 \tag{33.5}$$

Within a certain speed range, the spring stiffness under $\theta = 40^\circ$ also increases linearly with the increase of engine rotating speed.

Table 33.4 Spring stiffness K of the valve (N/mm)

Engine rotating speed (rpm)	Maximum spring stiffness (N/mm)	The spring stiffness under $\theta = 40^\circ$ (N/mm)
2000	1.3	0.8
2500	2.3	1.8
3100	3.2	2.3
3500	4.5	3.7
4000	6.3	5.2

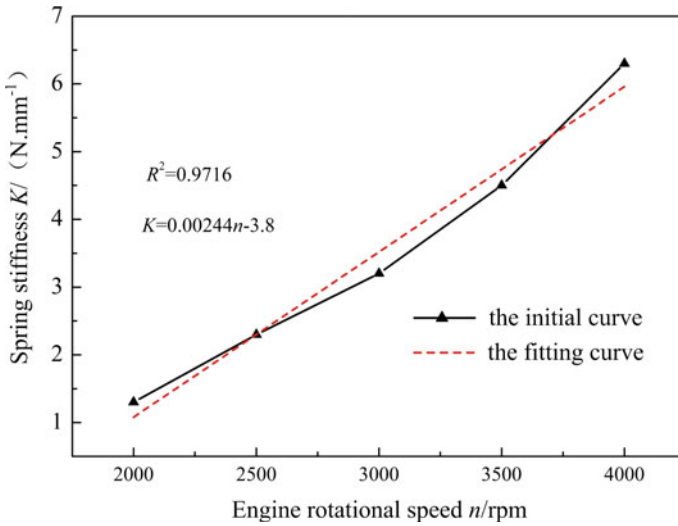


Fig. 33.18 The curve of maximum spring stiffness and engine rotating speed

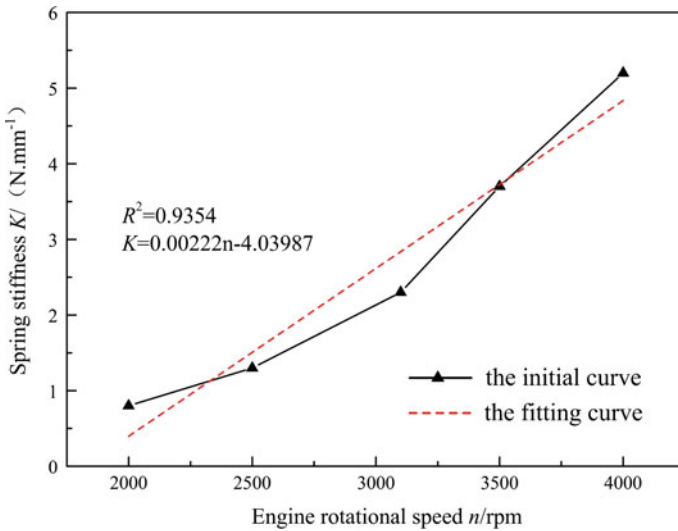


Fig. 33.19 The curve of maximum spring stiffness under $\theta = 40^\circ$ and engine rotating speed

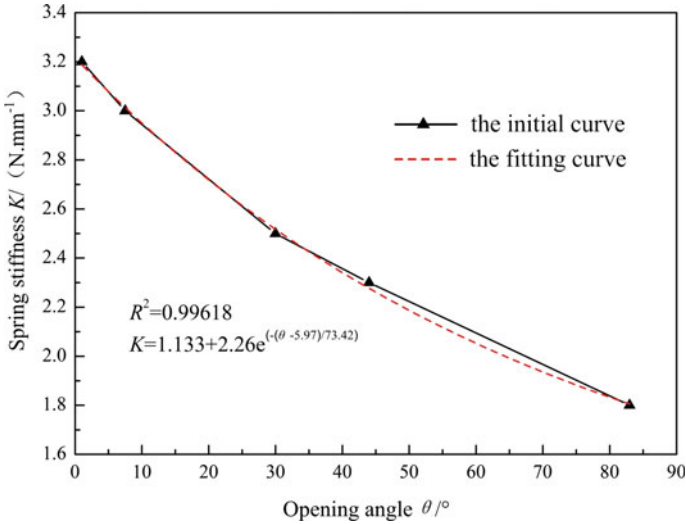


Fig. 33.20 The relationship between spring stiffness and opening angle at 3100 rpm

$$K = 0.00222n - 4.03987 \tag{33.6}$$

In order to research the relationship between spring stiffness and opening angle during the opening process of valve plate, the data of spring stiffness and opening angle is fitted. The relationship is shown in Eq. (33.7).

$$K = 1.133 + 2.26e^{-(\theta-5.97)/73.42} \tag{33.7}$$

It is found that within a certain opening angle range, the spring stiffness exponentially decreased with the increase of opening angle when the engine rotating speed is 3100 rpm (Fig. 33.20)

33.5 Test Validation of Semi-active Intake Structure with Passive Flapper Valve

33.5.1 Test Research of Opening Rotating Speed and Spring Stiffness Matching

Valve opening rotating speed and spring stiffness matching are the important content of vehicle validation. The purpose of vehicle validation is to test and verify the opening rotating speed analyzed in the second part, and the spring stiffness simulated in the third part of this paper.

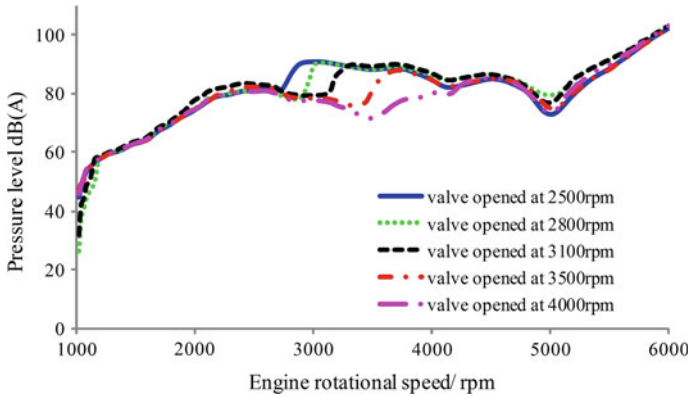


Fig. 33.21 The contrast of 2nd order intake noise of valve opened at different rotating speed

The intake noise is tested and analyzed at engine rotating speed 2500, 2800, 3100, 3500 and 4000 rpm in the vehicle validation according to the simulation conclusions. The results shows that the overall of intake noise is almost equivalent and the 2nd order noise is smoother when the opening rotating speed is higher, as shown in Fig. 33.21. Taking into account the intake resistance and vehicles commonly operating rotating speed, the opening rotating speed of the valve is determined at 3100 rpm. If the opening rotating speed determined in the test is different from the simulation result, the intake resistance should be reassessed. When the opening rotating speed is determined, firstly, the spring stiffness should be selected according to the simulation results, if the valve opened earlier in the actual operation, the spring stiffness should be increased, and on the contrary, the spring stiffness should be reduced until the valve opened at the desired rotating speed. In this case, the matched spring stiffness is 2.4 N/mm which consistent with the simulation result.

33.5.2 Test Research the Relationship Between Intake 2nd Order Noise Mutation and Valve Opening Angle

It can be known that intake 2nd order noise mutation has nothing to do with the valve opening angle according to the intake noise simulation results. In the vehicle validation, the intake noise is tested in the case that the valve is opened at 10°, 30°, 60° and fully opened. It can be seen that the 2nd order noises mutate when the valve is opened, as shown in Fig. 33.22, and the intake 2nd order noise mutation has nothing to do with the valve opening angle.

In order to verify the influence of the sealability of valve on 2nd order intake noise, seal test is also carried out. The test result is shown in Fig. 33.23, which

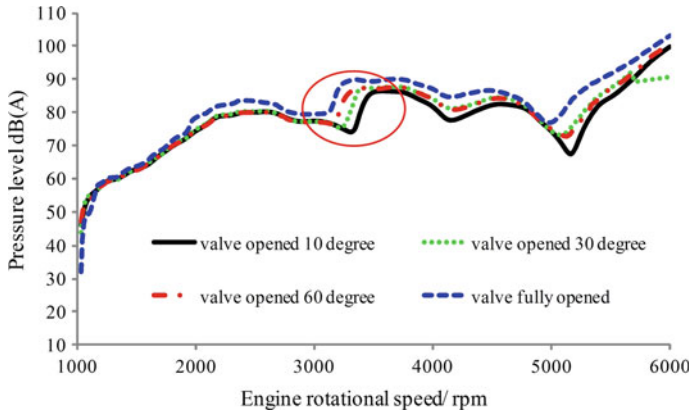


Fig. 33.22 The comparison of the 2nd order intake noise with the valve opening different angles

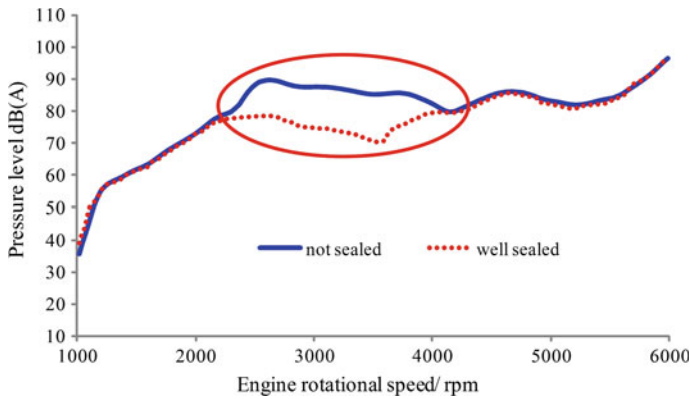


Fig. 33.23 The influence of the valve sealability on 2nd order intake noise

shows that the 2nd order intake noise with not sealed valve is significantly increased comparing with the one with well-sealed valve when the valve is opened at 3500 rpm. It is proved that the sealability is very critical.

33.5.3 The Vehicle Validation Effect of Semi-active Intake

The semi-active control valve can be opened automatically after the simulation and test matching. The vehicle validation effect is shown in Figs. 33.24 and 33.25, it can be seen that the overall of semi-active intake noise with same volume reduced 4–6 dB(A), and the 2nd order noise reduced 8–14 dB(A) compared with the conventional intake structure. The volume of semi-active intake can reduce 3 L and the 2nd order noise can reduce 3–6 dB(A) with the same intake noise level.

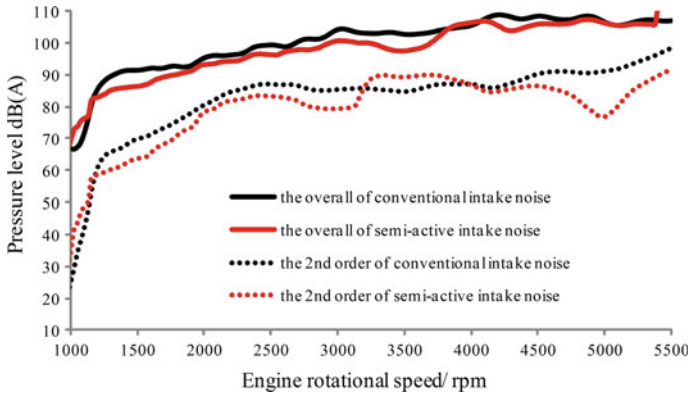


Fig. 33.24 The comparison of semi-active intake noise with same volume

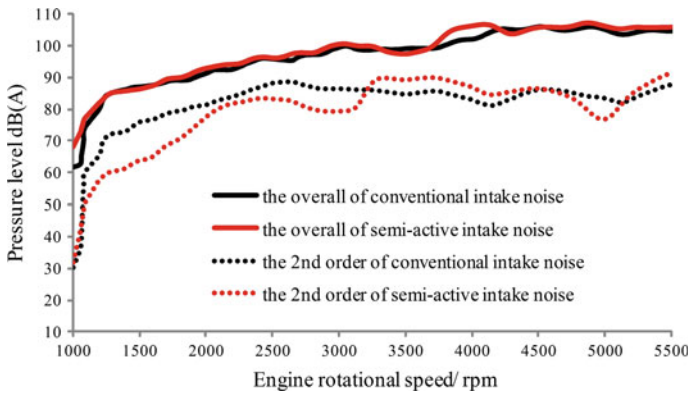


Fig. 33.25 The noise of semi-active intake with decreasing 3 L volume

33.6 Conclusion

A semi-active intake structure is designed; the GT-Power model of this kind of intake structure and the dynamic model of the valve are built; and the spring stiffness of the valve is analyzed using Adams software in this paper. The vehicle matching of this semi-active intake structure and vehicle NVH test are also researched, the conclusions shown as flow.

- (a) A development idea of dual-mode intake system is proposed, A GT-Power model with a throttle, and two bifurcated pipes is simulated.
- (b) In the semi-active intake structure, the 2nd order intake noise mutated when the valve opened, however, the mutation feature has nothing to do with the opening angle, and the sealability of the valve is very critical.

- (c) A semi-active control valve driven by the lever is designed in this paper, the relationship among spring stiffness, valve opening rotating speed and opening angle is obtained. It provides a foundation for the design of the semi-active control valve.
- (d) The vehicle NVH test results shows that the semi-active intake structure put forward in this paper can effectively solve the contradiction between intake noise and engine power loss, and improve the riding comfort and NVH quality.

References

1. Choi SC, Kong TW, Han SC, Jeong HM, Chun YH (2002) The study on effect of exhaust performance according to active muffler valve spring as followed spring constant. *J Therm Sci* 11(4):372–377
2. Liu B, Maeno M, Hase S, Wakamatsu S (2003) A study of a dual mode muffler. SAE technical paper 2003-01-1647. doi:[10.4271/2003-01-1647](https://doi.org/10.4271/2003-01-1647)
3. Alcini WV, West I (2006) GT model for passive flapper exhaust valve. SAE international: 400 commonwealth drive, 2006-01-1373
4. Hill WE (2009) A high performance passive muffler valve. SAE international, 2009-01-2039
5. Zhaoxiang D, Haijun Z, Jie Y, Pan F (2009) Research on attenuation performance of a semi-active exhaust muffler based on CFD. *Neiranji Gongcheng/Chin Intern Combust Engine Eng* 30(5):83–87
6. Liu H, Zheng S, Dan J, Lian X (2013) A study of dual mode muffler for improving sound quality of vehicle exhaust noise. In: 20th international congress on sound and vibration 2013, ICSV 2013, vol 3, pp 2609–2616
7. Liu H, Zheng S, Dan J, Lian X (2015) Acoustic performance analysis of the varying valve opening angle for the muffler with valve and its application. *Jixie Gongcheng Xuebao/J Mech Eng* vol 51(6), pp 135–141, 20 Mar 2015. doi:[10.3901/JME.2015.06.135](https://doi.org/10.3901/JME.2015.06.135)
8. Liu X, Yin C, Wang Y (2014) Design and test research on semi-active muffler system based on the H-Q tube. *Noise Control Eng J* 62(5):322–332

Chapter 34

Calculation and Application of Sound Insulation of the Vehicle Dash Panel

Cheng Peng, Feng Xu, Wei Pan, Min Sun and Yanghui Xu

Abstract In the reverberation chamber and the anechoic chamber, the sound transmission loss (STL) of panel specimens and steel sheets is measured. According to the insulation theory of combination parts, A program named IAS which can be used to calculate the STL of the vehicle inner dash system is compiled with the MATLAB. The calculated results show good correlation with the STL measurements of the inner dash system. In this paper, the key parameters which can effect the STL of the inner dash system are analyzed and the insulation optimization of the inner dash system is conducted and applied based on the calculation of the IAS program.

Keywords Plate STL · Dash insulation · Influence factor · Performance improvement

34.1 Introduction

Sound package which is used as an important sub-system in vehicle has a significant effect on vehicle NVH performance. The inner dash system, as one of the most important parts of the sound package, insulates the engine noise from the passenger cabin. The design of the inner dash system has a critical importance to the vehicle NVH performance.

In order to quickly and precisely predict sound insulation of the sound package, researchers have made lots of study and investigation on vehicle trim parts in the recent decade. Unglenieks [1] developed a simplified porous inner dash SAE model. In this model, the calculation of the sound transmission loss has a good correlation with the test. Musser [2] use the SEA method to analyze the sound response distribution in the vehicle and the insulation of parts.

C. Peng (✉) · F. Xu · W. Pan · M. Sun · Y. Xu
Automotive Engineering Institute, Guangzhou Automobile
Group Co., LTD, Guangzhou, China
e-mail: pengcheng@gaei.cn

Jin in Tongji University [3], by using the SEA method, researched on the inner noise of the vehicle and gave some countermeasures to reduce noise. Li [4] in Huazhong science and technology university predicted the inner noise of the car and got the noise contribution of subsystem from the SAE modal of the commercial vehicle.

34.2 The Theory of the Sound Transmission Loss in Reverberation Anechoic Chamber

The sound transmission loss is defined as the logarithm of the ratio of incident sound power and transmission sound power [5].

$$STL = 10 \lg \frac{W_{in}}{W_{out}} \quad (34.1)$$

The incident sound power W_{in} is defined as below

$$W_{in} = \frac{p^2}{4\rho c} S \quad (34.2)$$

In this formula, p is the effective sound pressure value in the reverberation chamber. S is the surface area of the specimen. ρc is the character impedance of the air.

Scanning the surface of the specimen with the sound intensity probe, we can get the sound intensity I . The transmission sound power is:

$$W_{out} = IS \quad (34.3)$$

According to the formula (34.1), the sound transmission loss is:

$$STL = L_p - L_I - 6 \quad (34.4)$$

In this formula, L_p is the average sound pressure in the reverberation chamber and L_I is the average sound intensity of the specimen.

34.3 The Sound Transmission Loss Measurement in the Reverberation—Anechoic Chamber

34.3.1 The STL Measurement of Steel Sheet and Plate Panel

The steel sheet is fixed in the wall between the reverberation chamber and the anechoic chamber, and sealed around the edges. In general, the sound intensity of

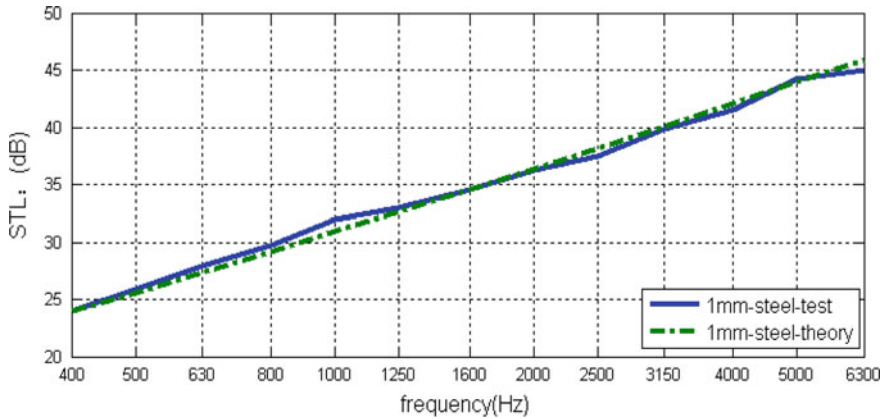


Fig. 34.1 Test and theory of STL of 1 mm steel sheet

the wall should be 10 dB less than the sound intensity of the steel sheet in all 1/3 octave frequency. Simultaneously, the sound intensity of the edge of the steel sheet should be lower than the intensity in the middle of it. In this case, it can be considered that all the sound energy passes only through the steel sheet to the anechoic chamber. On the anechoic chamber side, the surface intensity of the steel sheet is measured and then the steel sheet STL is calculated by formula (34.4). Compared with the theory result, the measurement result is acceptable (shown in Fig. 34.1). According to the comparison, this system and process are validated.

And then, the specimen should be cut as the same size of the steel sheet, and put on the surface of the steel sheet facing to the anechoic chamber. The edge of the specimen should be properly sealed to insure that sound energy only pass through the specimen and steel sheet to the anechoic chamber. Based on this method, the STL results of different combinations of steel sheet and plate specimen are obtained (shown in Fig. 34.2). From Fig. 34.2, the STL of combination of steel and plate specimen become smaller at the resonance frequency. The resonance frequency moves to the lower frequency if the thickness of the plate specimen is increased.

34.3.2 The STL Measurement of Inner Dash System

Usually, the STL of inner dash is measured between the reverberation and anechoic chamber. The high precision is the advantage of this method. But, the dash board should be cut from the body-in-white of the vehicle and used as the base board. The fixing and sealing treatments are more complicated than the treatments of the plate specimen. Because of the heavy workload, it is hard to measure the inner dash STL with this method (Fig. 34.3).

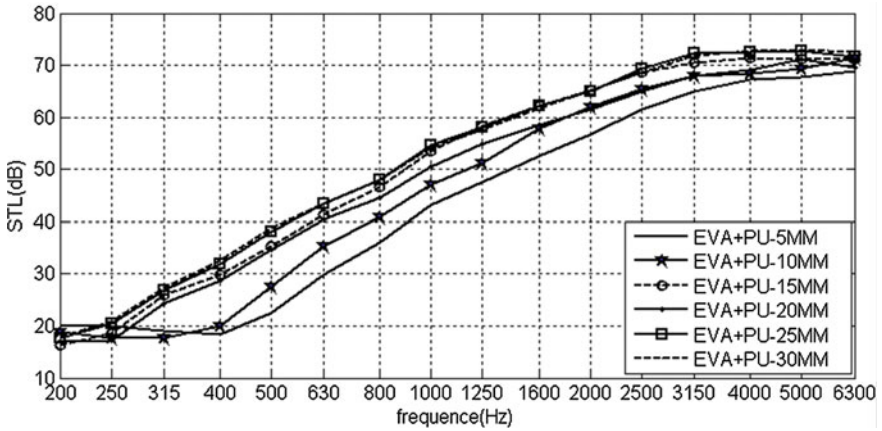


Fig. 34.2 The STL results of different combinations of steel sheet and plate specimen



Fig. 34.3 Inner dash test between the reverberation and anechoic chamber

Instead of the above method, if the inner dash is divided into different blocks (Fig. 34.4), each block can be considered as the combination of the certain thickness steel sheet and plate specimen. The total STL of the inner dash can be calculated with the STL of each block.

34.4 The STL Calculation of the Inner Dash System

When a system consists of different insulation parts, the equivalent transmission loss coefficient [6] τ refers as:

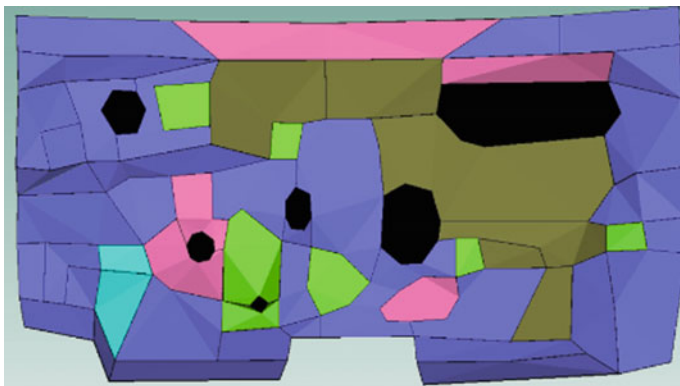


Fig. 34.4 Inner dash grid division

Table 34.1 The thickness distribution of inner dash

Thickness/mm	Bared steel sheet	0-5	5-10	5-15	15-20	20-25	25-30
Equivalent value/mm	0	5	10	15	20	20	30
Area/m ²	0.070	0.150	0.007	0.506	0.142	0.100	0.125

$$\tau = \frac{\tau_1 s_1 + \tau_2 s_2 + \dots + \tau_n s_n}{s_1 + s_2 + \dots + s_n} \tag{34.5}$$

In this formula, $\tau_1, \tau_2, \dots, \tau_n$ means the sound transmission loss coefficient of the different parts respectively. s_1, s_2, \dots, s_n means the distribution area of different parts respectively. So, the sound transmission loss (STL) is calculated as below:

$$STL = 10 \log(1/\tau) \tag{34.6}$$

Based on this method, the vehicle’s inner dash system is divided into multiple blocks. The thickness of steel sheet and inner dash in each block is measured and collected. In fact, the thickness of inner dash is continuous and it is hard to measure the STL of each thickness. In practice, 6 thickness of the inner dash will approximate to represent the real thickness of the inner dash (shown in Table 34.1).

A program named as Insulation Analysis System (IAS) is compiled to calculate the combination STL with Matlab (GUI shown in Fig. 34.5). In the GUI of the IAS, the steel sheet thickness is set 0.8 mm. Then the data from the Table 34.1 are input into the IAS respectively and the STL of the combination is output as fast as possible by the IAS. Compared with the measurement result (Fig. 34.6), the calculated result in the IAS is convinced and validated.

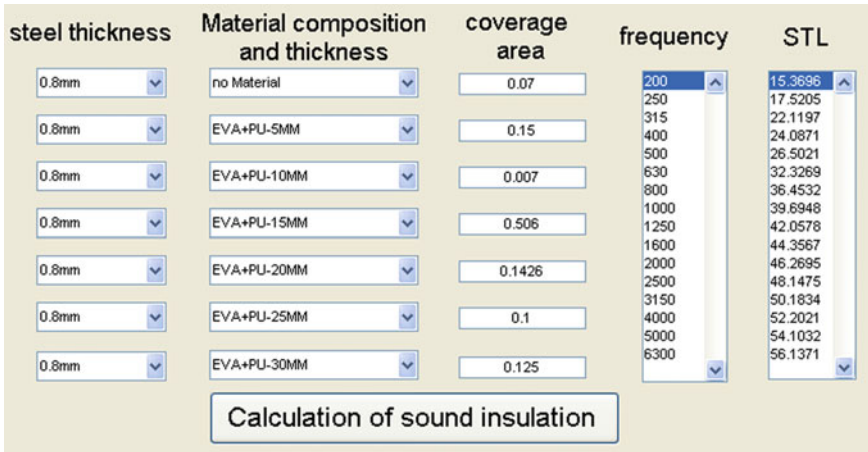


Fig. 34.5 Insulation analysis system interface

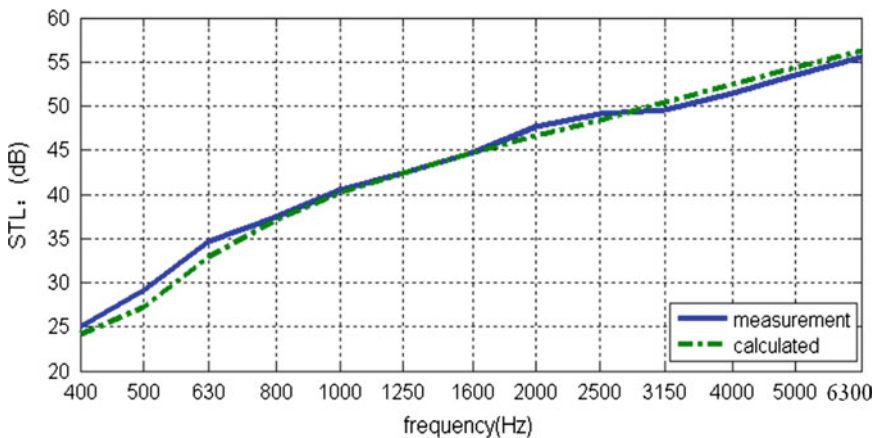


Fig. 34.6 Result of measurement and calculated by IAS

34.5 The Design and Optimization of the Inner Dash

During the development of the inner dash system, if its insulation is checked physically after its tooling is finished, this will probably result in modifying the tooling and therefore delaying the project. Adversely, if STL of the inner dash is predicted in the conception design phase, and the design parameters are optimized based on the analysis results, the tooling modification will be avoided.

The major parameters affect the insulation of inner dash include leakage, area of the bared steel sheet, thickness of steel sheet and average thickness of inner dash. The effects of these parameters will be analyzed respectively in the followed paragraphs.

34.5.1 The Effects of the Leakage and the Bared Steel Sheet

34.5.1.1 The Effect of the Leakage

In the IAS, if the leakage area is increased by 0.0001 m^2 while the other parameters keep the same (Table 34.2), STL of the inner dash will be 1–15 dB lower than the original from 1000 to 6300 Hz and the largest STL value will just reach 40 dB (shown in Fig. 34.7). If the leakage area is up to 0.01 m^2 . The largest STL value will be only 20 dB above 500 Hz. It is concluded that the leakage has a great effect on insulation and should be severely restricted.

34.5.1.2 The Effect of the Bared Steel Sheet Area

In the IAS, if area of the bared inner dash panel is changed while other parameters keep the same, the calculated result of STL of the inner dash is shown in Fig. 34.8. According to Fig. 34.8, the area of bared steel sheet is bigger and the STL of inner dash is lower at high frequency. If the area of bared steel sheet is decreased from 0.07 to 0.01 m^2 , the STL of the inner dash system will be improved about 10 dB above 1000 Hz. It is concluded that the area of bared steel sheet has a great effect on insulation of the inner dash.

34.5.2 The Effect of the Steel Sheet Thickness and Inner Dash Thickness

34.5.2.1 The Effect of the Steel Sheet Thickness

In the IAS, if thickness of the inner dash steel sheet is changed while other parameters keep the same, the result of STL of the inner dash is shown in Fig. 34.9. According to Fig. 34.9, STL of inner dash system will increase with the increased thickness of the steel sheet. STL of inner dash system will be enhanced by 6 dB as

Table 34.2 Different leakage area

	Original	Proposal 1	Proposal 2	Proposal 3
Leakage Area/ m^2	0	0.0001	0.001	0.01
Leakage Percentage/%	0	0.01	0.1	1

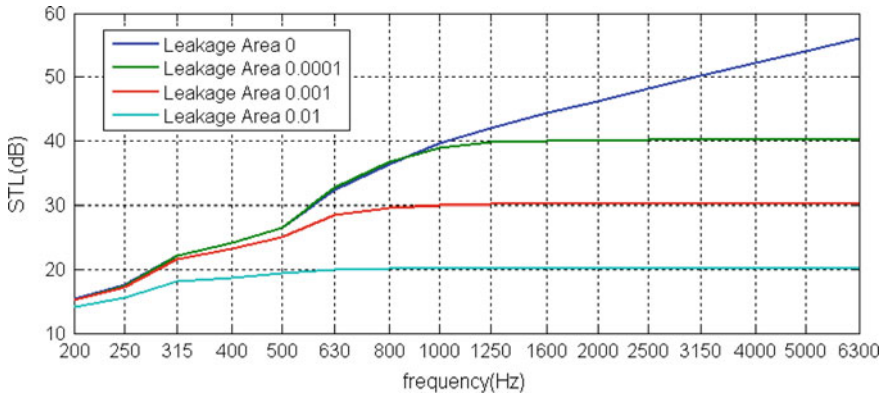


Fig. 34.7 Effect of leakage to STL of inner dash

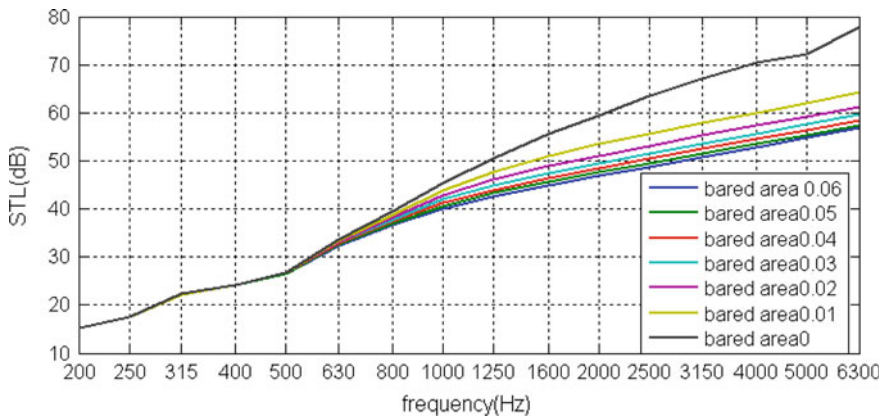


Fig. 34.8 Effect of bared steel sheet area to STL of inner dash

the thickness of the steel sheet is doubled. The trend obeys the mass law. In real situations, the insulation, weight and cost of the inner dash system will be balanced in the design phase. If the weight and cost could be ignored, the thickness of the steel sheet should be as large as possible.

34.5.2.2 The Effect of the Average Thickness of the Inner Dash

In the IAS, if the thickness distribution of inner dash is changed (shown in Table 34.3) while other parameters keep the same, the result of STL of the inner dash system is shown in Fig. 34.10. According to Fig. 34.10, STL of the inner dash system will be enhanced a little at low frequency and remain unchanged at high frequency if the average thickness is increased only.

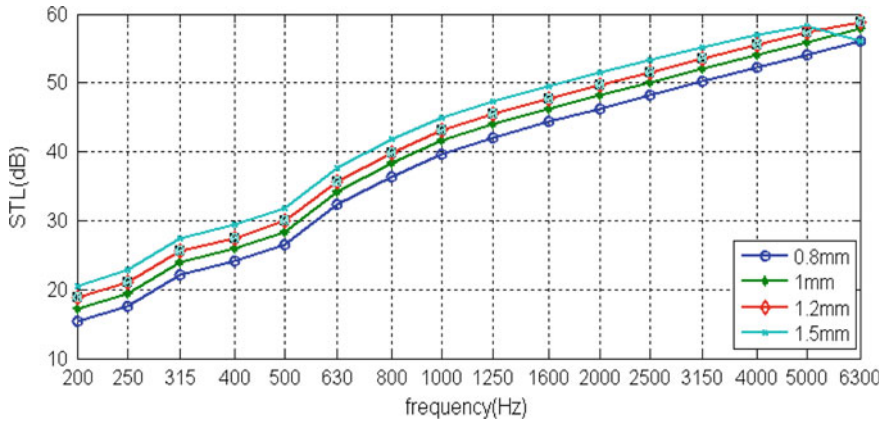


Fig. 34.9 Effect of steel sheet thickness to STL

Table 34.3 The thickness distribution of inner dash

Thickness distribution/mm	0	5	10	15	20	25	30
Original	0.07	0.150	0.007	0.506	0.143	0.100	0.125
Proposal 1	0.07	0	0	0.663	0.143	0.100	0.125
Proposal 2	0.07	0	0	0	0.805	0.100	0.125
Proposal 3	0.07	0.663	0	0	0	0.905	0.125

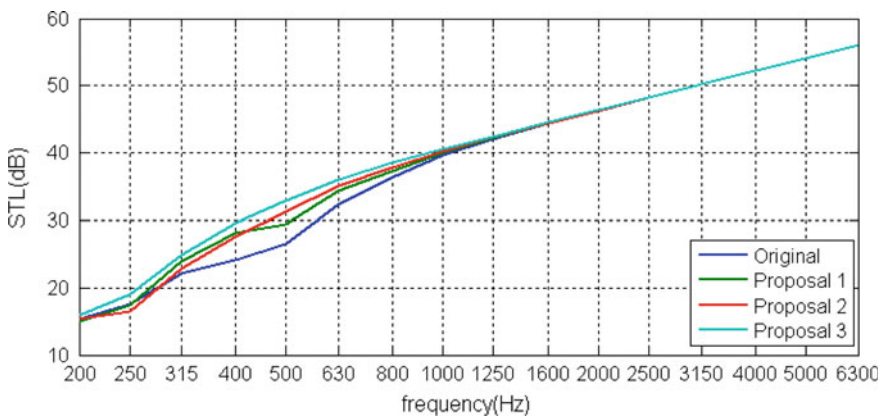


Fig. 34.10 Effect of average thickness of the inner dash to STL

Table 34.4 The optimization proposals of inner dash system

	Thickness of steel sheet/mm	Bared steel sheet area/m ²	Average thickness of the inner dash/mm
Original	0.8	0.07	15.9
Proposal 1	1	0.02	15.9
Proposal 2	1	0.02	24

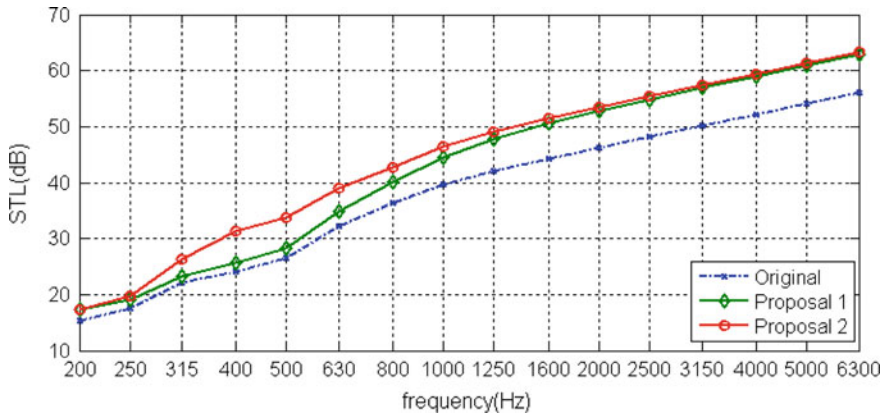


Fig. 34.11 STL of optimization proposal and original proposal

34.5.3 The Insulation Optimization of Inner Dash System

Based on the calculation in the IAS mentioned above, the leakage area of the inner dash system should be severely restricted and the bared steel sheet area should be as small as possible in order to enhance the insulation of inner dash system at high frequency. The thicker the inner dash is, the better insulation it has at middle-low frequency. In addition, if the steel sheet is thicker, the insulation of the inner dash system will be enhanced at the whole curious frequency range. Taking the design of an A-class car’s inner dash system as an example, insulation target is finally achieved by proposing the following countermeasures based on the optimization results by using the IAS. The proposals are shown in Table 34.4, taking account of weight and cost.

The STL of 3 proposals is calculated in the IAS (shown in Fig. 34.11). According to Fig. 34.11, after the thickness of the steel sheet is increased from 0.8 to 1 mm, the bared steel sheet area is decreased from 0.7 to 0.2 m² and the average thickness of the inner dash is improved from 15.9 to 24.0 mm, the STL of the inner dash system is enhanced about 7 dB compared with the original. The optimization result is satisfied.

34.6 Conclusion

- (1) In this paper, the STL of the panel specimen of the inner dash is measured in the reverberation and anechoic chambers firstly. Secondly, based on the theory of the insulation of the combination parts, the inner dash system is divided into different blocks. Finally, the STL of the inner dash system is calculated in the IAS after the panel specimen's STL is input to the IAS. Compared the calculation and the measurement, the IAS reliability is validated.
- (2) In the IAS, the effects of leakage area, bared steel sheet area and inner dash average thickness are analyzed respectively. From the contribution of each parameter, the optimization of the inner dash system is conducted. Based on this method, the STL of one A-class car's inner dash system is enhanced about 7 dB. It is confirmed that the panel specimen database and combination parts insulation method can be useful for inner dash design.

References

1. Unglenieks RJ, Mealman MR (2003) Simplified porous panel subsystem for SEA modeling. In: SAE noise and vibration conference and exhibition, 2003-01-1538
2. Musser C, Manning J, Peng GC (2011) Prediction to vehicle interior sound pressure distribution with sea. In: SAE technical papers, 2011-01-1705
3. Jin X, Ye W, Ding Y (2002) Car interior noise simulation using statistical energy analysis method. *J Tongji Univ* 30(7):867
4. Li X, Huang Q, Huang Y (2005) Optimization design about cab inner noise based on statistical energy analysis. *Noise Vib Control* 3:32
5. Pang J (2015) Automobile body noise and vibration control. China Machine Press, Beijing (2015.1.270-271)
6. Lord H, Gatley WS, Eversen HA (1987) Noise control for engineers. Krieger Publishing Co, Florida, pp 285–286

Chapter 35

The Analysis for Casting Axle Cover Leakage

Jun Chang, Buliang Zhang, Zhiying Liu and Chuanlong Huang

Abstract To solve the problem of oil leakage of connection between casting housing and the rear cover, using finite element method to simulate the position that most probability leak, and then give the advises to the designer. Firstly using Hypermesh to mesh all the part from the axle and set interface and then exports the inp file. Secondly use the Python language to set the load step. Thirdly use the Dos window to invoke the standard of ABAQUS solver to calculate. Compare the calculation results with the actual failure, so as to put forward a more reasonable design change.

Keywords Commercial axle · Rear cover · Finite element · Simulation calculation

35.1 Introduction

Drive axle is one of the important parts in the vehicle. Commercial vehicle axle can hold the vehicle's gravity and transfer to wheel. That means the reaction from wheel including gravity, drive, brake and turn left or right, transfer to suspension and frame using axle [1]. The design of commercial vehicle axle should meet the requirements from customer who using new energy vehicle more and more. As the casting axle can't weld, the connection about housing and cover should use bolts. There will be a possibility oil leakage between housing and cover. Simulate the connection between housing and cover using ABAQUS, and then find out the trend about oil leakage. The simulation results will give some advice to designer to rebuilt the model. At last, use road test to verify the connection.

J. Chang (✉) · B. Zhang · Z. Liu · C. Huang
R&D Center, Dongfeng Dana Axle Co., Ltd., No. 1 Zhongyuan West Road,
Hi-Tech Industry Development Zone, Xiangyang 441057, Hubei, China
e-mail: jun.chang@ddac.com.cn

35.2 Set Up FEA Model

35.2.1 Geometry Introduce and Mesh

The simulation geometry is one drive axle from commercial vehicle, which include housing, carrier, cover, tube and so on. This housing is casting. The BC (boundary conditions) is from laboratory testing. The geometry is shown in Fig. 35.1.

Input the geometry into the hypermesh and get the second order elements [2]. In order to more convenient to simulate using ABAQUS, it should be set up the group and sets. At last, the whole FEA model include 897,991 elements and 1,503,774 nodes. The FEA model is shown in Fig. 35.2.

35.2.2 Material Properties

The different part has different material in axle. The detail is shown in Table 35.1.

35.2.3 Boundary Condition

The boundary conditions follow the test rule. It is holding in spring seat center, and loading in wheel center. Set up the RBE2 in bearing place. The detail is shown in Fig. 35.3.

Fig. 35.1 Geometry

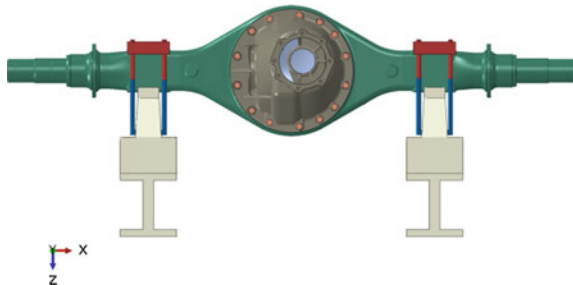


Fig. 35.2 FEA model

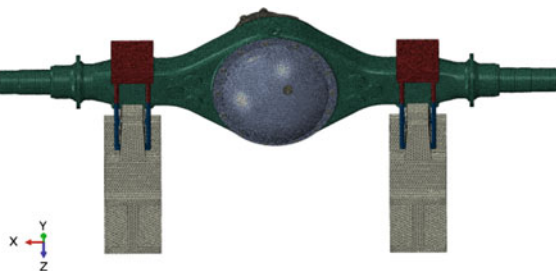
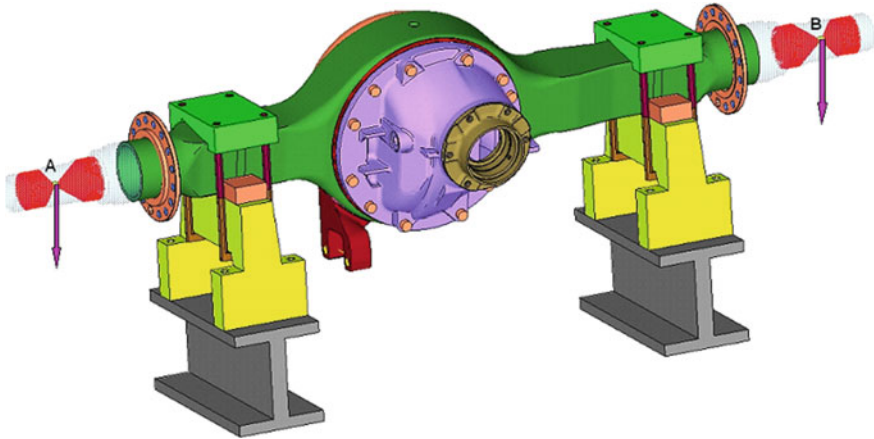


Table 35.1 Materials list

Material name	E (Gpa)	μ
16MnL	212	0.31
Q235	210	0.275
QT450	169	0.257

**Fig. 35.3** Vertical load case

This paper simulates three load cases.

- (a) Vertical load case. Hold at the spring seat center and load the vertically force at the wheel center. The detail is shown in Fig. 35.3.
- (b) Fore and vertical load case. Hold at the spring seat center and load the vertically and fore force at the wheel center.
- (c) After and vertical load case. Hold at the spring seat center and load the vertically and after force at the wheel center.

35.2.4 Set Up the Load Steps

Using ABAQUS script rule and python program language to define material properties and contact surface [3, 4]. Add the material property to part and set up the contact relation. This simulation has eight load steps. The first two steps define the pre-loads of bolts. The third step keeps the system steady. The fourth-sixth steps set up the vertical load case. The seventh step set up the fore and vertical load case. The last steps set up the after and vertical load case. The output file is default.

Using Dos windows to run inp file which includes steps. When the program run, it will call geometry information from another inp file. This method separates the steps and geometry, and it is easy to change something if needed. Such as if you want simulate different axle, you only need to change the geometry inp file and keep the same steps inp file. That is more efficiency.

35.3 Simulate Results

The drive axle includes a lot of parts and the some of the key places mesh should be better. At last, the total elements number is almost 900,000. So it take a long time to get the results.

35.3.1 The Vertical Load Case Results

As noted earlier, the vertical load case only add the force from wheel to tube. Figure 35.4 shows the deformation and it is easy to see the trend is agree with the theory. Figure 35.5 shows the COPEN between housing and cover. If we define the engine is front, we can find the most possible place for oil leakage is the lower right about cover in this case.

35.3.2 Fore and Vertical Results

As noted earlier, the fore and vertical load case means add fore force and proper vertical force. Figure 35.6 shows the deformation in fore and vertical load case. Figure 35.7 shows the COPEN between housing and cover. If we define the engine is front, we can find the most possible place for oil leakage is the lower right about cover in this load case.

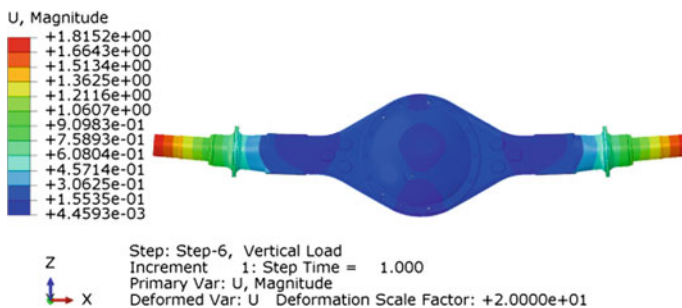


Fig. 35.4 Vertical load deformation

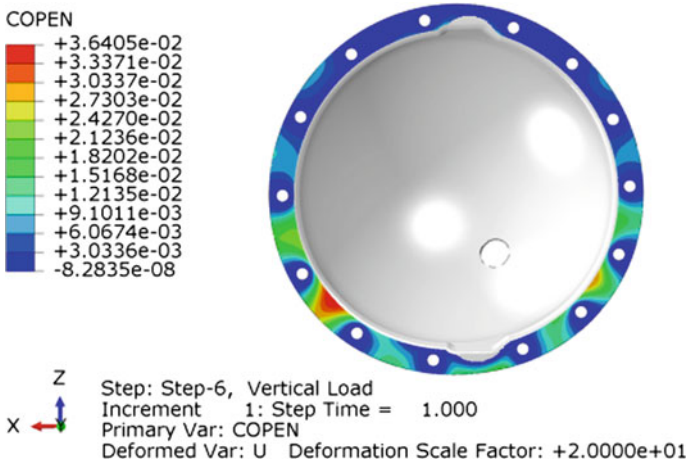


Fig. 35.5 Vertical load leakage

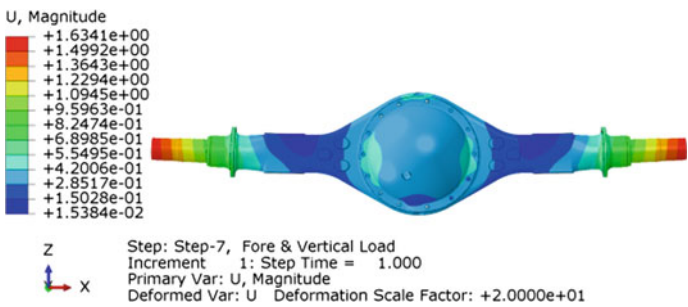


Fig. 35.6 Fore and vertical deformation

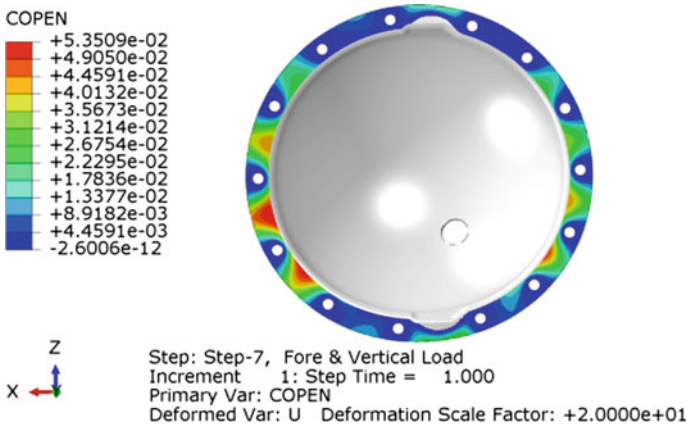


Fig. 35.7 Fore and vertical leakage

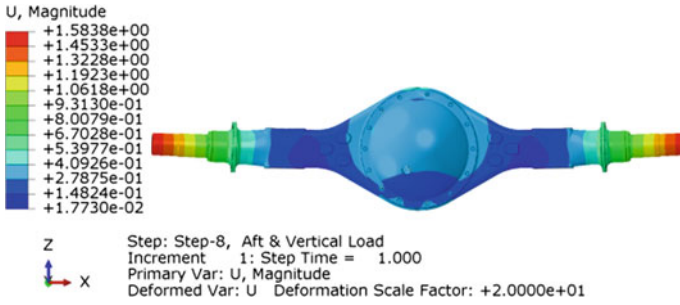


Fig. 35.8 After and vertical deformation

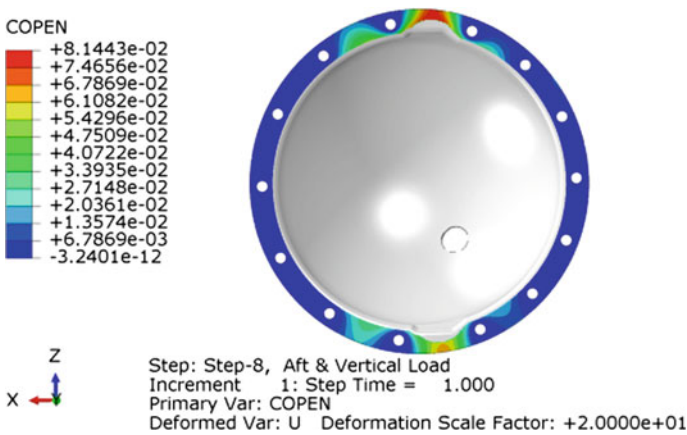


Fig. 35.9 After and vertical leakage

35.3.3 After and Vertical Results

In a similar way, the after and vertical load case means add after force and proper vertical force. Figure 35.8 shows the deformation in after and vertical load case. Figure 35.9 shows the COPEL between housing and cover. If we define the engine is front, we can find the most possible place for oil leakage is the upper about cover in this load case.

Fig. 35.10 Upper oil leakage



Fig. 35.11 Lower right oil leakage



35.4 Conclusions

We can get the conclusion that the most possible place for oil leakage is upper and lower right about cover from the simulate results. It is agree with the failure from markets such as Figs. 35.10 and 35.11. We can consider changer bolt's model or distribute or flange thickness.

This paper achieves that separate geometry inp file and steps inp file. It is easy to keep step inp file all the time and only need to change the geometry inp file when simulate the different axle. The simulate results are agree with failure model, means the simulate method is right.

References

1. Liu W (2000) Automobile design. Tsinghua University Press
2. HyperWorks help document
3. ABAQUS help document
4. Lutz M (2013) Learning python. O'Reilly Media

Chapter 36

The Layout Design of Rearview Mirror Based on Vehicle Ergonomics

Yingying Xu, Hongfang Ling, Fang Qian, Yuyong Wang
and Jianzi Huang

Abstract The installation position of the external mirror, a very significant safety parts of vehicles, directly affects the driver's field of view. To determine the position of the external mirror is a complicated task, factors need to be considered such as styling, ergonomic, safety, engineering design, etc. In the process of vehicle development, the external mirror is often arranged after the modeling schemes is determined. However, it is not easy to get a good visual field and human comfort subject to the constraints of the styling features. Therefore, it is necessary to give out the position of the external mirror and the field of vision in the early stage of modeling. In order to obtain a good view, the ideal position of the outside mirror is packaged considering of ergonomic, and the minimum visible dimension of the mirror is designed on the basis of vision conformance, which avoid the safety hazard and massive amounts of modification caused by improper design of the external mirror.

Keywords External mirror · Styling limit · Vision · Ergonomic · RAMSIS

Technical Paper—Vision problems are often quickly exposed when drives vehicles. Drivers need to observe the road conditions by rearview mirror for left and right and rear side of the vehicles when overtaking, turning and reversing. Therefore, the rearview mirror must provide sufficient scope of vision for the driver to observe the surrounding environment of the cars, and reduce the obstruction of the rear and left and right sides. So the reasonability layout of the rearview mirror affects the traffic safety directly. Due to higher request to ergonomic and security for the vehicles, rearview mirror should be located in a rational position in the early design phases, and the styling of vehicles should be designed rightly on the basis of obtaining a good vision and satisfying the ergonomic comfort.

Y. Xu (✉) · H. Ling · F. Qian · Y. Wang · J. Huang
Guangzhou Automobile Group CO., LTD Automotive
Engineering Institute, Guangzhou, China
e-mail: xuyingying@gaei.cn

36.1 Styling Factors Affecting the Field of View of the External Mirror

Effective sight of rearview mirror that can be obtained depends on the drivers' seating position and external structure of vehicles. Due to the high beltlines, large A pillar, and big mirror housing, driver's field of view would be reduced by increasing the visor obstruction, as shown in Fig. 36.1. If these problems not solved in the early, correction will cost lots of time and money lately, even have a subversive influence on styling. Therefore, the styling factors affecting the rearview mirror's vision need to be analyzed and constrained.

36.1.1 Beltline

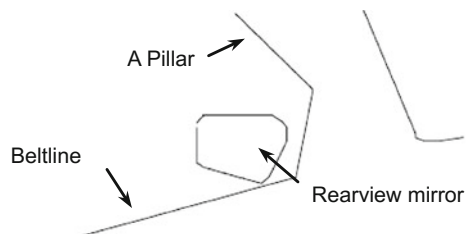
The beltline is not only an important parameter of ergonomic but also a key characteristic of the external modeling. High beltline and narrow side window, making the body styling more solid and fashion, which is the trends of the styling of vehicles. However, high beltline increase the obstruction of the field of view on both sides of the vehicle, which is unfavorable for the driver to observe the children or vehicles on both sides of the vehicle.

The sight cannot be obstructed by beltline when drivers observe the surrounding environment through the rearview mirror. The position of the beltline determines the height of the rearview mirror directly. It is necessary to considered comprehensively of the factor of styling, ergonomic and safety to determine the height of the beltline in CAS stage of modeling.

36.1.2 A Pillar

When turning the vehicles, the driver's sight are easily influenced by A pillar and rearview mirror. If not arranged properly, the A pillar and rearview mirror would form a whole, which would enlarge the obstruction of A pillar. It is difficult for

Fig. 36.1 Modeling factors affecting the view of the outside mirror



driver to discover the pedestrians or vehicles appeared in the obstruction, which would cause the safety accidents more likely.

The position of A pillar tend to be more and more forward. On one hand, the styling is more plump, on the other hand help to increase the internal space of the car. The longitudinal position of the A pillar affects the layout of the rearview mirror, and also influences the obstruction caused by A pillar and rearview mirror.

Figure 36.2 shows the different arrangement forms of the rearview mirror affected by A pillar longitudinal position, and Fig. 36.3 shows the view of the driver from the car with different forms of the outside mirror. As can be seen from Fig. 36.3a, rearview mirror and A pillar joint together as a whole, the obstruction of driver is large, the field of vision is better when there is a gap between A pillar and rearview mirror, that will not generate a obstruction with A pillar (Fig. 36.3b), the vision is widest between A pillar and rearview mirror, and the view is best among these three cases (Fig. 36.3c).

The size of A pillar cross section also influences the field of view between rearview mirror and A pillar. Under the condition that A pillar meets the impact performance, the obstruction caused by A pillar should be minimized. In addition, the angle of inclination for A pillar also influences the vision field between rearview mirror and A pillar, especially for the passenger side. When the angle of inclination for A pillar is small, rearview mirror is easy to form a whole with beltline and A pillar, that will expand the obstruction, and disadvantage to discover pedestrians and vehicles timely in the obstruction at the right turn.

36.1.3 Size of Outside Mirrors

Size of the outside mirrors, directly affect the driver's field of vision. Under the premise of meeting the regulatory requirement of visual field, the size of lens in rearview mirror should be reduced as far as possible, the thickness of the mirror housing along the forward direction should also be as small as possible on condition

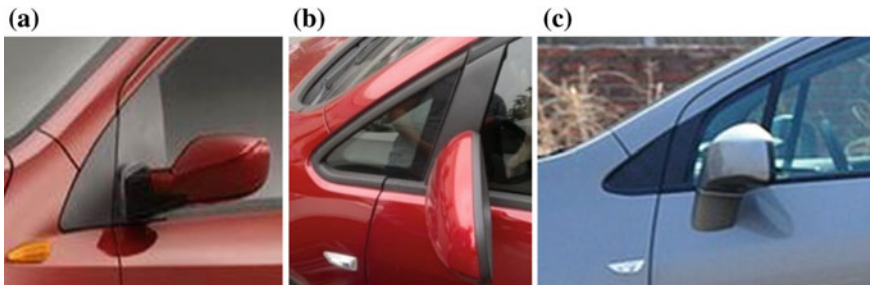
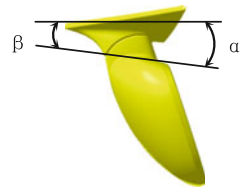


Fig. 36.2 Different arrangement forms of the rearview mirror affected by A pillar longitudinal position



Fig. 36.3 The view of the driver from the car with different forms of the outside mirror

Fig. 36.4 Requirements of the outside mirror housing for improving the wind noise



of satisfying structure of rearview mirror to reduce the obstruction caused by rearview mirror.

Influence of the aerodynamic and wind noise performance by the shape of the outside mirror also cannot be ignored. In order to improve the wind noise performance, the angle between the outside mirror housing and mounting surface along the direction of the car should be increases gradually, that is $\alpha \geq \beta$, as shown in Fig. 36.4. It is recommended a bigger gap between the outside mirror and the mounting surface and a larger thickness of the outside mirror housing along the direction of the car.

It should be noted that improving the aerodynamic drag is a trade-off issue with the mirror field of view as it requires reduction in size of the outside mirrors [1].

36.1.4 Instrument Cluster

Another factor affects the observation of the rear view mirror is the instrument cluster. When driving at night, if the backlight of the instrument cluster, which incidents on the inner surface of the side windows and reflects to the driver's eyes, just coincides with the sight observed by drivers, the driver will be interfered to observe the objects in rearview mirror. The higher the rearview mirror is, the more likely it is to cause reflective problem of instrument cluster. Therefore, the sight of driver and the backlight of the instrument cluster should staggered.

The outside mirror's field of view is closely related to the car's exterior and interior design. The exterior design defines the beltline, A pillar and outside mirror,

while inside design provides the drivers eyes and the location of the instrument cluster. Thus, the exterior and interior design must be closely coordinated in order to ensure that the driver is able to see all the necessary vision to drive safely.

36.2 Package of Outside Mirror Based on Ergonomics

After setting the human body posture, the position of rearview mirror lens could be located initially based on the demands of human comfort and vision.

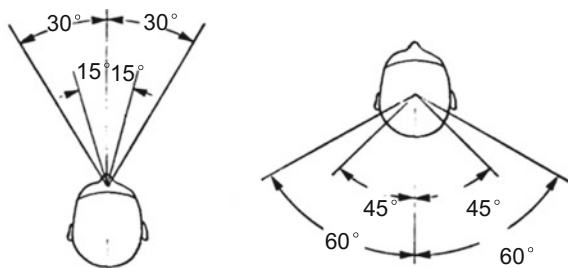
36.2.1 Front and Rear Position

Due to the shrink image caused by the convex mirror, the farther distance from the outside mirror to the human eyes, the harder for driver to judge the actual distance through the mirror. On the other hand, distance too close to the human eyes would cause a sense of oppression. For those older drivers, it is difficult to focus on the close object, even can see double image, the closer distance means more difficult to observation, so the location of the outside mirror should be comprehensive consideration. Distance to the center of the outside mirror lens from driver's eyes along the direction of vehicles is recommended for 590–610 mm.

36.2.2 Horizontal Position

SAE standard J1050 provides the field of eye and head turning. The eye may rotate easily 15° left, 15° right, and a maximum of 30° left, 30° right from straight ahead. The driver's head may easily turn about a vertical axis 45° to the left or to the right and a maximum of 60° to the left or to the right from the straight ahead position, as shown in Fig. 36.5. To satisfy human comfort, driver's eyes and head turning angle

Fig. 36.5 Horizontal rotation of the eyes and head



should maintain in the comfortable range when observing outside mirror, and should not beyond the maximum rotation.

At the same time, position of the outside mirror should meet the requirements of GB 11562. First, the unilateral overhang must not be greater than the maximum width of 250 mm of the vehicles (excluding the outside mirror). Second, the angle between the vertical plane of the connection from the center of the outside mirror by driver's side to the driver's eye point and vertical datum plane is no more than 55° , whereas the front passenger's side no greater than 75° , as shown in Fig. 36.6.

36.2.3 Vertical Position

The outside mirror should be vertically package within the comfortable rotation arrangement of driver's eyes and head. SAE standard J1050 provides the field of eye and head turning. The eyes may rotate easily 15° up, 15° down, and a maximum of 45° up, and 65° down from straight ahead. The driver's head may easily turn about a vertical axis 45° up or down and a maximum of 60° up or down from the straight ahead position, as shown in Fig. 36.7.

In addition, the outside mirror could cause obstruction to direct vision. GB 11562 sets that the projection of the obstacles between planes down to the horizontal of 1° and 4° through V2 point in the area of the "S" region no more than 20%. The rearview mirror should located as far as possible to avoid this area, because the occlusion by A pillar is inevitable, to reduce the obstruction to direct vision. Therefore, the upper edge of the rearview mirror should be placed below the plane which through V2 point and down to the horizontal of 4° .

In general, the distance between the outer edge of the mirror and lens is 15–20 mm, which can defined the peak position of lens. According to the requirements of regulations, the minimum visual size of the mirror lens can be obtained. The sight of driver must be higher than beltline, to avoid the block of the view, especially for the right side mirror. The height of beltline is restricted by the height of the outside mirror.

Fig. 36.6 Comfort range of the outside mirror defined by regulation

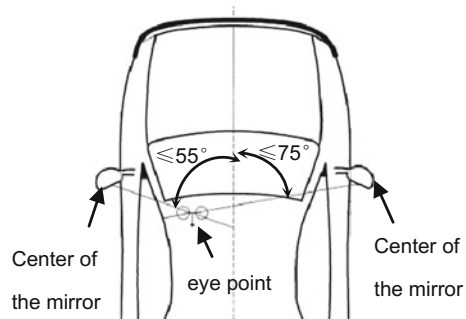
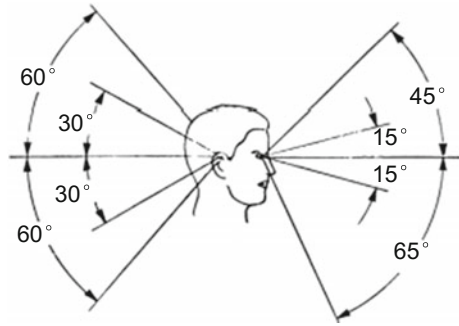


Fig. 36.7 Vertical rotation of the eyes and head



36.3 Minimum Visual Size of the Outside Mirror Based on Visual Field Compliance

In order to minimizing the obstruction caused by the rearview mirror, the size of the lens and mirror housing should minimize as much as possible on the basis of meeting regulatory requirement of the field of view. At the beginning of the design stage, it is necessary to provide the minimum visual size of the rearview mirror lens, in order to constrain the modeling engineer making outside rearview mirror.

36.3.1 Determine the Radius of Curvature

It is seen by the optical principle, a convex mirror image is shrinking. The smaller the radius of curvature is, the smaller imaging and greater visual range it is for the same size of the lens. However the smaller radius of curvature are more easily lead to distortion. In general, the radius of curvature radius of the outside mirror is no less than 1200 mm, and no more than 1400 mm.

36.3.2 Outside Rear View Mirror Installation Angle

Installation Angle of the outside mirror is between the normal line of the mirror center and the direction of the vehicle. General the installation angle of the mirror by driver's side is 14° – 17° , which is smaller than the front passenger's side by 8° – 14° . Usually the adjustment angle of the lens vertically and horizontally no less than 8° , without any interference occurs between the lens and fold axis during regulating. After given the electric adjusting mechanism and the range of size of the folding mechanism, the position of the fold axis can be preliminarily determined, as shown in Fig. 36.8.

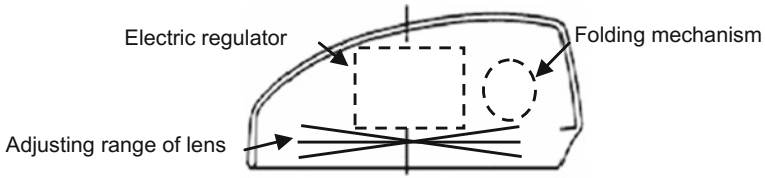
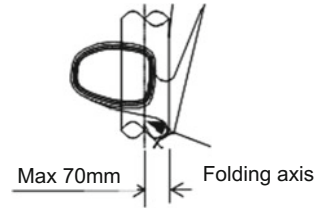


Fig. 36.8 Folding mechanism arrangement of the outside mirror

Fig. 36.9 Regulatory requirements for folding axis of the outside mirror



In addition, GB 15084 requires that a cylinder with a radius of 70 mm, which rotating around the folding axis of the outside mirror, should be at least tangent to the installation surface of the outside mirror, as shown in Fig. 36.9.

36.3.3 *The Lens Minimum Visual Size*

The minimum visual size of the outside mirrors should be designed to meet the field of view requirements specified in GB 15084. The outside mirror should provide a horizontal field of 1 m width at 4 m and 4 m width at 20 m behind the driver at ground level. Figure 36.10 shows the minimum required fields for the outside mirrors for the passenger cars. Take the left mirror to determine the minimum visual size of lens.

- (1) Select the curvature radius for the outside mirror lens, preliminary set the installation angle, then draw the spherical surface of the lens;
- (2) According to the width of the vehicle, draw the triangle area of view defined by regulations after the driver's eyes point at 4 m and 20 m (Fig. 36.11).
- (3) Using the light reflection principle, make the reflection point of each vertex of the triangle area of view on the spherical surface of the lens, the size of the lens at 4 m after the driver's eyes point is obtained, as shown in Fig. 36.12.
- (4) In the same way, the size of the lens at 20 m after the driver's eyes point is also obtained, the quadrilateral region combined with these two vision triangle is the smallest visual size of the outside mirror lenses, as shown in Fig. 36.13.

Fig. 36.10 Outside mirror field required for passenger cars

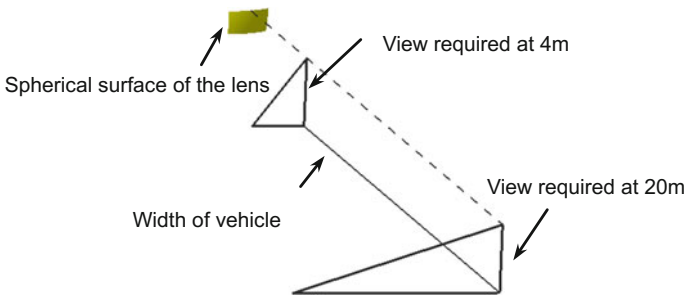
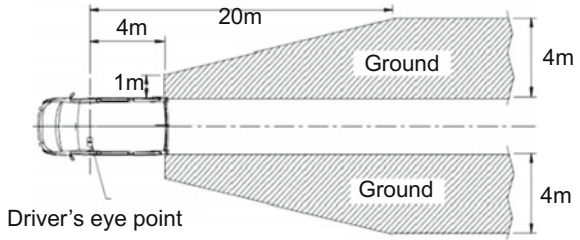


Fig. 36.11 Triangle area of driver's field of view

Fig. 36.12 Mirror size required for the triangle view area at 4 m after driver's eyes

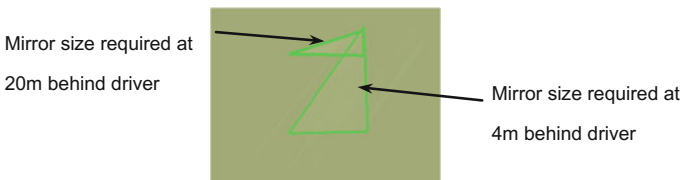
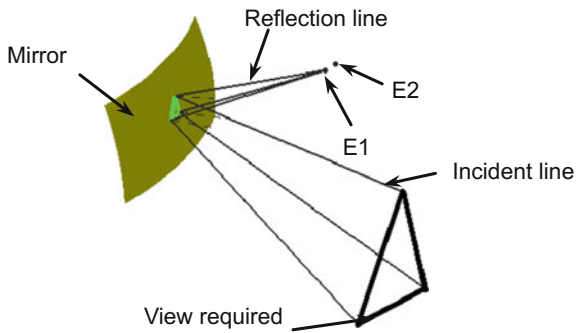
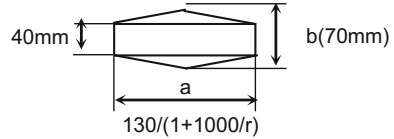


Fig. 36.13 Minimum visual size of the outside mirror

Fig. 36.14 Size requirements of the reflection surface



The minimum visual lens of right mirror that can be obtained by using the same method is larger than the minimum lens of left mirror. The final size of lens should meet the requirements of both sides at the same time.

In addition, as required in GB 15084, a rectangle should be drawn on the reflection surface of rearview mirror, the bottom edge of which is a as high as 40 mm, and a line can be drawn in parallel with the height of rectangular, the length of which is b , for class II rearview mirror, a can be calculated by the formula of $130/(1 + 1000/r)$, and the value of b is 70 mm (see Fig. 36.14). The final size of the lens need to meet the above requirements.

Through the above method, the position of rearview mirror can be packaged initially, constraining the modeling engineer to make the rearview mirror, beltline and the overall model. However, determining the position of rearview mirror is always a complex task, which need to be arranged and checked repeatedly.

36.4 Virtual Test and Verify for Rearview Mirror View Based on RAMSIS

The modeling of rearview mirror need be tested and verified virtually to ensure that the target population of different height does not produce the vision problems of rearview mirror when driving a car in different driving conditions. Serious ergonomic problems need to be verified such as view conformance with regulatory requirement, view occlusion and reflection [2].

The normal driving posture of driver should be defined before any vision analysis with following procedure. 1. Constraint the RAMSIS human body on the seat. 2. Define the backrest angle of seat. 3. Step on the accelerator pedal of one third of position. 4. Put the left foot on resting pedal or carpet. 5. Hold the steering wheel, with the sight straight ahead.

Based on the size of the human body and the defined constraints, the most likely posture of the driver is calculated automatically by RAMSIS, as shown in Fig. 36.15. After the completion of the calculation, the field of view of the outside mirror can be verified based on normal driving gesture.

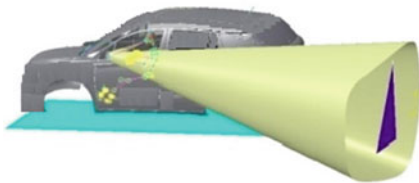
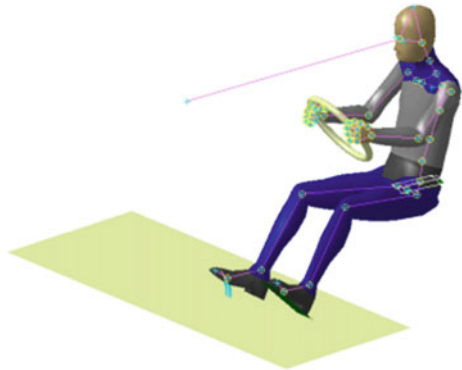
36.4.1 Regulations Vision Validation

The normal driving posture of the 5% female, 50% and 95% male of human body in China are respectively transferred to verify the regulation vision area of the rearview mirror by using the mirror vision analysis function of RAMSIS. As shown in Fig. 36.16.

36.4.2 View Occlusion and Reflection Validation

Defined the sight line to the center of the outside mirror in the tasks, after the normal driving posture of the 5% female, 50% and 95% male of human body in China were set, the vision of mirror seen by the driver of different heights are simulated, as shown in Fig. 36.17.

Fig. 36.15 Normal driving posture set by RAMSIS



(a) Left outside mirror



(b) Right outside mirror

Fig. 36.16 Outside rearview mirror vision compliance verification of the 5% female in China

Outside rearview mirror lenses should not be blocked by any surrounding obstacles, including guide, antenna, beltline, mirror shell, A pillar, etc. In addition, make sure there is a certain gap between the mirror housing of the external mirror and the A pillar, to avoid the mirror housing connected integrally with A pillar, which would increase the obstruction of vision when turning.

Define the instrument cluster as the light source, side window as a reflective surface, the instrument cluster image at the side window is automatically calculated using reflective function of RAMSIS in vision module, as shown in Fig. 36.18.

Whether the lens of the external mirror and the instrument cluster imaging area overlap is judged by using the left and right eye vision function to observe the outside rearview mirror. The instrument cluster can meet the requirements if overlap not happened, as shown in Fig. 36.19.

Fig. 36.17 5% female in China to observe the visual field of the outside mirror



(a) Left outside mirror

(b) Right outside mirror

Fig. 36.18 Side window imaging of the instrument cluster by 95% male

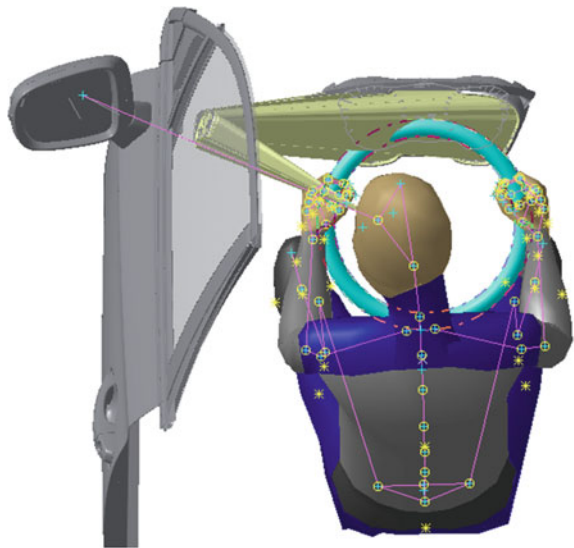
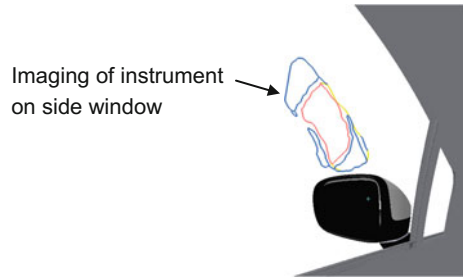


Fig. 36.19 Reflective validation of the instrument cluster by 95% male in China



36.5 Conclusion

External mirror is a very important safety parts of passenger cars. In order to obtain a good field of vision, constraints need to be provided on modeling at the beginning of the design stage. On the basis of setting the parameters of the vehicle, the location of the external mirror is preliminarily arranged from conformity of ergonomic, the minimum visual size of outside rearview mirror is determined from the view of vision, which constraints the styling engineer to make the preliminary model of the outside rearview mirror, beltline and the overall model, so that the outside rearview mirror can not only meet the requirements of modeling but also can satisfy the requirement of human comfort and the vision at the beginning of the design stage.

References

1. Bhise Vivek D (2012) Ergonomics in the automotive design process. CRC Press, New York, p P119
2. Cao L, Guo Y, Xu S (2009) Analysis of exterior mirror layout based on ergonomics [C]. International conference on automotive interior products and new materials

Chapter 37

Research on Curve Safety Speed Warning for Vehicle with Risk Prediction

Xian Qu, Feng Yu and Shu-en Zhao

Abstract Aiming at the driving safety problem on the curve, safety speed warning system with risk prediction is designed as the vehicle drives on the curve. Considering both the static multi-factor such as drivers, vehicles, roads and vehicle dynamics performance, safety speed warning model on the curve based on multiple sources is established. The road curvature is estimated by machine vision technology. Then, the maximum safety speed is computed. Also, the risk state estimation function is introduced to judge vehicle driving state in advance. And, the alarm criteria is determined. Finally, safety speed warning system is developed with LabVIEW. The simulation results shown that it can accurate predict the driving state of the vehicle on the curve and warn for drivers when the vehicles have a safety hidden.

Keywords Vehicle engineering · Machine vision · Curve · Speed · Warning system

Curves are the traffic accident prone sections, especially in the bends and steep mountain road. The dangerous conditions of rollover and side-slip are caused with drivers inattention and speeding easily [1]. Data show that 1 s alarm in advance could reduce the traffic accident by 50–90% [2]. Therefore, it is of great significance to study safety speed warning system on the curve for reducing the traffic accidents.

A lot of researches on the curve driving safety warning had conducted at home and abroad. The achievements were huge. Li et al. [3] developed safety warning system to introduce the transverse longitudinal adhesion coefficient into the safety

X. Qu (✉) · F. Yu
Chongqing Vocational Institute of Engineering,
College of Mechanical Engineering, Chongqing 402260, China
e-mail: 516685355@qq.com

S. Zhao
Chongqing Jiaotong University, School of Mechatronics
and Automobile Engineering, Chongqing 400074, China

speed calculation model. The results showed that it could be used to alarm the traffic status of heavy vehicles in the curve. Lee et al. [4] designed the curve safety warning system with introducing into the driver's behavior influence factor in curve safety speed calculation model. Zhang et al. [5] designed curve anti side-slip speed warning system based on risk prediction for passenger cars. Yu et al. [6] studied curve anti-rollover warning algorithm. It is verified with hardware in the loop simulation. Safety state is usually judged with vehicle current state in above models. However, the driver advance control before the dangerous is seldom considered. Also, few warning algorithm is applied for the early warning.

Therefore, the main contribution is to predict the curvature by machine vision technology and estimate the vehicle curve driving state to predict the risk based on the curve safety speed warning model. The dangerous hints were graded to improve the safety of vehicle. Finally, a vehicle curve safety speed warning system was designed for risk prediction.

37.1 The Curve Safety Speed Warning Model

37.1.1 Calculation of Curve Safety Speed with Lateral Instability

The vehicle would be side-slip in the curve when the friction provided by ground is not enough to balance the lateral force of gravity and centrifugal force.

In general, the critical speed of vehicle side-slip in a super high curve is [7]

$$v_{w-h \max} = \sqrt{\frac{Rg(i_h + \phi_y)}{1 - i_h \cdot \phi_y}} \quad (37.1)$$

where, ϕ_y is lateral adhesion coefficient. i_h is transverse slope value, $i_h = \tan\theta$. θ is pavement cross slope angle. R is steering radius. G is acceleration of gravity.

Also, when the high centroid vehicles drive in a curve, the overturning moment containing centrifugal and lateral force transfer the weight from inner wheel to the outside one. When the inner wheel force is 0, the car would be rolled. The critical speed of vehicle rollover in lateral ultra high road is [8]

$$v_{w-f \max} = \sqrt{\frac{b + 2h_g i_h}{2h_g - b i_h}} gR \quad (37.2)$$

where, B is the wheelbase; H_g is the height of center of mass.

37.1.2 Vehicle Curve Safety Speed Warning Model

The traditional maximum safety speed is derived by the vehicle mechanical analysis. The model is failed to consider effect factors on speed such as the driver characteristics, vehicle parameters and road conditions. If the rollover or side-slip is analyzed separately, it can't get safety speed in a variety of driving conditions with all kinds of models. Therefore, the traditional driving safety speed model is improved. The curve safety speed warning model is

$$v_z = \min \left(K_V K_d \sqrt{\frac{\phi_y + i_h}{1 - i_h \phi_y} R g A_y}, K_V K_d \sqrt{\frac{b + 2h_g i_h}{2h_g - b i_h} R g A_y} \right) \quad (37.3)$$

where, K_V related to tire characteristics, road width and road conditions parameters; K_d related to the driver's age, vision and driving style. K_V, K_d generally took 0.6–0.9; A_y is mainly used to improve the safety factor, desirable 0.3 [4].

37.2 Curvature Estimation Based on Machine Vision

The accurate estimation curvature radius of the front road is the premise to guarantee the reliable work of curve safety speed warning system. Scholars make use of different sensors to measure the curvature of the road in foreign. The speed differences of different wheels are measured with speed sensors [9]. The curvature is solved with speed and yaw rate [10]. GPS and electronic maps [11] are also main technical measures. The above methods have many problems. Such as, complicated calculation process, large measurement error and so on. In recent years, machine vision technology has been used in security assistance system widely because of the simple operation and low cost. In this paper, the front road was identified with machine vision. Then, the identification marking was fitted and curvature is calculated. The process generally includes image preprocessing, lane line segmentation and curvature estimation. Figure 37.1 is the flow chart.

37.2.1 Lane Line Model and Segmentation

Polynomial, convolution and spline curve are commonly used road curvature models [12]. Among them, the polynomial curve model is widely used with high real-time performance and measurement accuracy. Polynomial curve model is

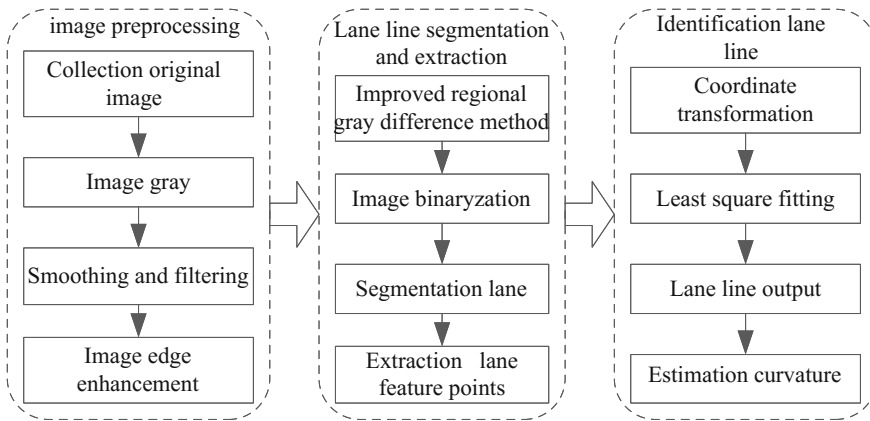


Fig. 37.1 Flow chart of curvature estimation



Fig. 37.2 Mean filter

$$y = a_0x^n + a_1x^{n-1} + \dots + a_{n-1}x + a_n \tag{37.4}$$

where, n is the number of fitting polynomial, a_0, \dots, a_n is the coefficient, x is the derivative direction of road; y is the level direction of road.

The images often have noise which is collected. Due to the noise and signal are intertwined, the inappropriate processing would make the image detail fuzzy and quality decline. The mean filter was used. The filtering result is shown in Fig. 37.2.

The gray scale, filtering and edge enhancement are made here. After the image pre-processing, a lane line is extracted with the improved region growing method. Segmentation lane line is shown in Fig. 37.3.



Fig. 37.3 Lane line is segmented

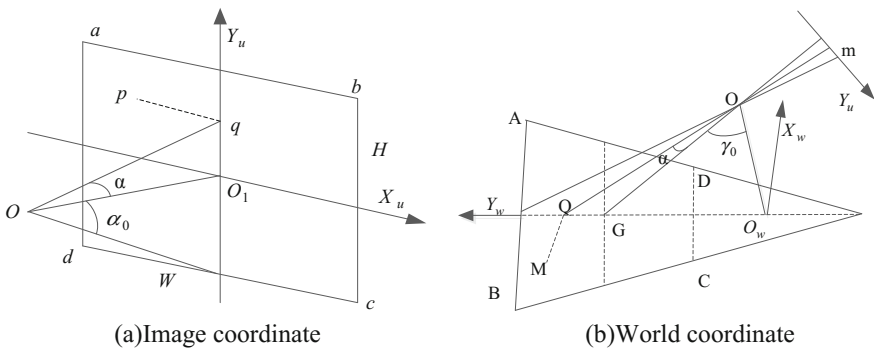


Fig. 37.4 Imaging model of Y axis **a** Image coordinate **b** World coordinate

37.2.2 Coordinate Conversion

In order to realize the accurate estimation of curvature, the points of image coordinates need to be changed to the world coordinates. Pinhole imaging model is an ideal imaging model, which can simplify the derivation process and meet the accuracy requirements. The coordinate conversion formula is established [13]. The Y axis of the imaging model is shown in Fig. 37.4.

Where, O is the camera's optical center, squareness $abcd$ is imaging plane of image, whose width is W and height is H . Squareness $abcd$ corresponding to the road area is trapezoidal $ABCD$. OO_w is the installation height h of camera. The point M is took in the road. Its coordinate is (X, Y) . The point P corresponding to graph is p . Its coordinate is (x, y) . The coordinates transformation from absolute coordinates to image is a conversion from (X, Y) to (x, y) actually. Y axis of the coordinate conversion is

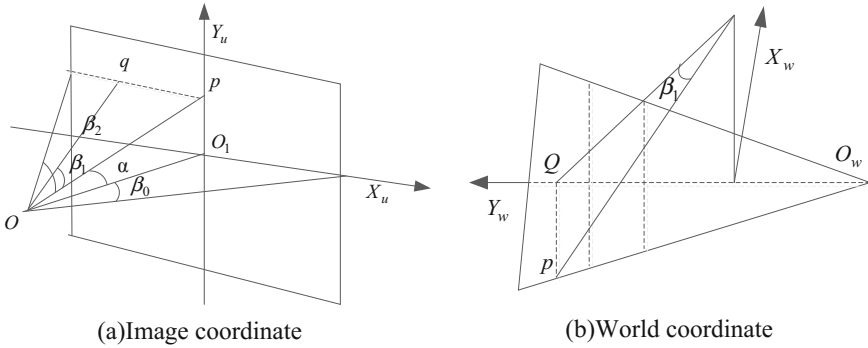


Fig. 37.5 Imaging model of X axis **a** Image coordinate **b** World coordinate

$$\begin{cases} P_y = \frac{h(H \tan \gamma_0 + 2p_y \tan \alpha_0)}{H - 2 \tan \gamma_0 \tan \alpha_0 p_y} \\ P_x = \frac{P_y H - H h \tan \gamma_0}{2P_y \tan \gamma_0 \tan \alpha_0 + 2h \tan \alpha_0} \end{cases} \quad (37.5)$$

Figure 37.5 is the X axis of the image. The meaning of the symbols are same to Fig. 37.4. Similarly, the horizontal relations of the coordinate are derived.

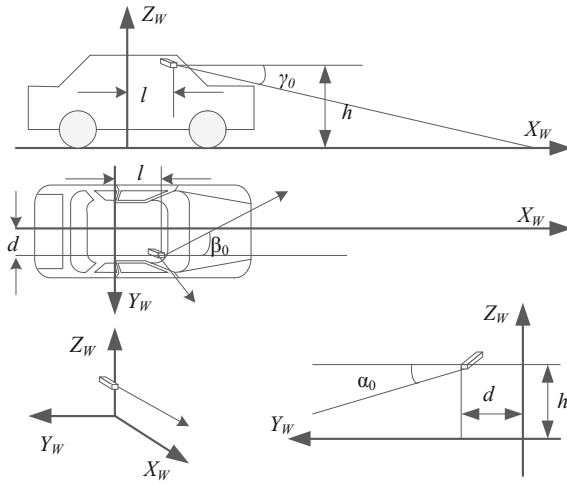
X axis of the coordinate conversion is

$$\begin{cases} P_x = \frac{2p_x \tan \beta_0 \sqrt{h^2 + P_y^2} \cos(a \tan(2p_y \tan \alpha_0 / H))}{W} \\ P_x = \frac{P_x W}{2 \tan \beta_0 \sqrt{h^2 + P_y^2} \cos(a \tan(2p_y \tan \alpha_0 / H))} \end{cases} \quad (37.6)$$

37.2.3 Calibration Installation Position

The fixed focus camera is used on-board cameras. After calibration of its internal parameters, it would not change generally. After mounted, internal parameter is calibrated to have restrictions. So, It can be calibrated online. But, external parameters are calibrated when the camera is installed to the vehicle. Camera internal parameters are calibrated with MATLAB toolbox. Images are put into toolbox. Then, starting left vertex of image, the corner of calibration grid is extracted in a clockwise. After extracting the corner, the camera's internal parameters are calculated with optimized and iterations. By formulas (37.5) and (37.6), external parameters of camera mounting height h , camera pitch angle γ_0 , yaw angle $2\beta_0$ and roll angle (vertical angle) $2\alpha_0$ need to be calibrated. The relationship between body and camera is shown in Fig. 37.6.

According to the three line method calibration theory [14], two parallel lanes need to be collected as the calibration reference at least when the external



(Upper is main view, middle is vertical view, under is left view)

Fig. 37.6 Relationship between body and camera (Upper is main view, middle is vertical view, under is left view)

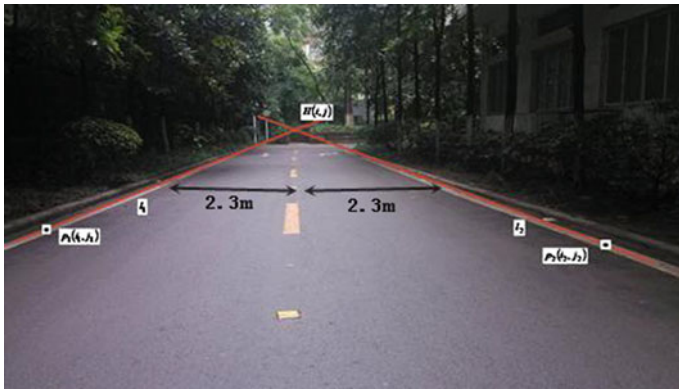


Fig. 37.7 The straight line on a straight highway

parameters are calibrated. The vehicle is parked in the center of the lane line. The distance between two lanes is measured. Two parallel lines L1, L2 are drawn by hand on the image, which is collected by camera. The intersection $H(i, j)$ is found and recorded. The other point (except $H(i, j)$) in every line is took, which the distance from the intersection as far as possible. The pixel coordinates of each point is recorded, as shown in Fig. 37.7.

According to the calibration results of internal parameters, the offset of line relative the longitudinal center of the vehicle and coordinates of line in a pixel coordinate, the external parameters are calculated.

37.2.4 Curvature Estimation

After the coordinate transformation, the lane line is fitted with least square method [15]. The polynomial is used 5times which the effect is good. And, the correlation coefficient is 0.9921. The fitting result is shown in Fig. 37.8.

The fitting curve is

$$y = 2.941 \times 10^{-8}x^5 - 1.636 \times 10^{-5}x^4 + 0.00346x^3 - 0.3478x^2 + 15.64x + 172.5$$

For the curvature ρ of $y = f(x)$ on the P , the calculation formula is

$$\rho = \frac{1}{R} = \left| \frac{(1 + y'^2)^{3/2}}{y''} \right| \quad (37.7)$$

where, ρ is the curvature of point, R is the radius, y' is first derivative, y'' is second derivative.

The point $p_i(x_i, y_i)$ is selected from the image which represent the characteristics of road. The lane line is converted with perspective projection transformation. The point $P_i(X_i, Y_i)$ of lane edge line is got in the world coordinate. The curvature is calculated by formula (37.7) with four close points. Then, the radius is taken with the average value. The vehicle trajectory is collected with GPS data acquisition system. Then, the curvature is calculated. So, the method of curvature estimation is verified. Figure 37.8 is the result of the curvature.

As can be seen from Fig. 37.9, the predicted curvature is consistent with the actual curvature.

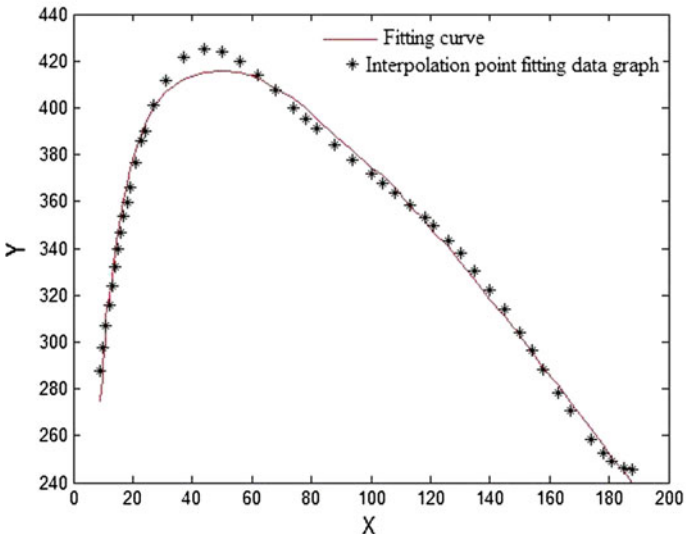
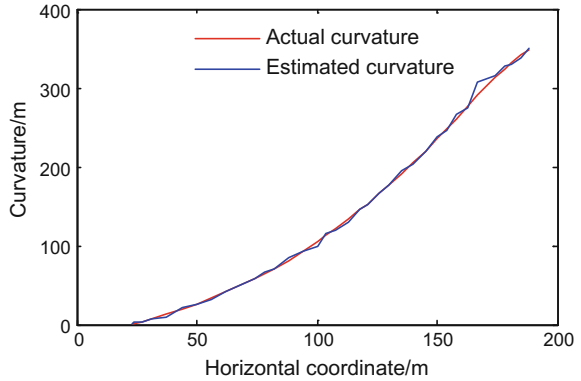


Fig. 37.8 Fitting results

Fig. 37.9 Recognition result of curve radius



37.3 Curve Safety Speed Warning Algorithm Based on Risk Prediction

The risk state estimation function is introduced to judge the vehicle driving safety state which be in the corner or be in the curve.

$$M = \sum_{j=1}^n P_j G_j \tag{37.8}$$

where, n is the number of dangerous events. G is damage degree after the occurrence of hazardous events. It relates to the speed and the roadside environment. In order to simplify the calculation, we argue that harm would be caused as long as the accident happens. So, $G = 1$. P is the probability of risk event occurrence. Aiming to the vehicle curve driving safety, side-slip or rollover is considered to cause by excessive speed when the car is in the curve. Therefore, $n = 1$.

$$M = PG \tag{37.9}$$

When the vehicle is in danger, the driver should always react and control in advance. So, the acceleration of the vehicle and driver estimated time T are introduced. The specific expressions of P is

$$P = \begin{cases} v(T)/v_Z < v(T) < v_Z \\ 1 & v(T) > v_Z \end{cases} \tag{37.10}$$

where, T is the driver estimated time, generally 2–4 s. v_Z is the maximum curve safety speed which is calculated formula (37.3). $V(T)$ is estimated speed after the time T according to the current speed and the acceleration of vehicle.

$$v(T) = v + aT \tag{37.11}$$

According to the level of risk estimated value, the driver can be alarmed. After estimation the driving safety risk state, warning rules are made (Table 37.1) [16].

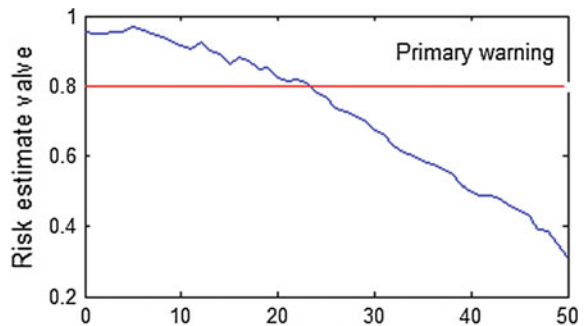
The vehicle dynamics model and identification radius are combined. The actual speed is collected with speed sensor. So, the curve safety speed warning algorithm for vehicle with risk prediction is verified. The results are shown in Fig. 37.10.

As is shown Fig. 37.10, the test result meets the actual operation of the driver basically. In order to confirm the accuracy of warning algorithm, the vehicle curve safety warning software based on LabVIEW is designed.

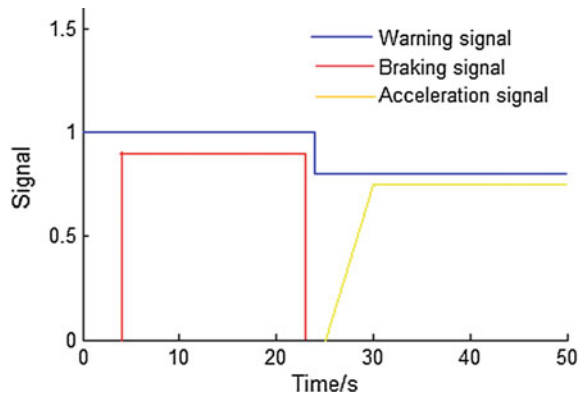
Table 37.1 Warning rules

M	Warning level
$(0, 0.8)$	No warning
$[0.8, 1)$	Primary warning
$[1, +\infty)$	Advanced warning

Fig. 37.10 Experimental results. **a** Risk state estimation. **b** Warning, braking and acceleration signal



(a) Risk state estimation



(b) Warning, braking and acceleration signal

37.4 Vehicle Curve Safety Speed Warning System is Designed with LabVIEW

37.4.1 Project Design of Warning System

Curve safety speed warning system for vehicle with risk prediction mainly includes safety speed calculation module, curvature estimation module, risk state prediction module and human-computer interaction interface. The road images are collected. The lane line is identified and fitted. The curvature of the front road is estimated real-time. Combined with the curvature, vehicle characteristics, road condition and the driver characteristics information, the maximum safety speed is calculated. The current speed is measured with sensor. Combining with risk prediction function, the driving state of vehicle is judged in advance. The risk prediction value is shown on the man-machine interface. The drivers are reminded to make the corresponding measures when it has safety risks. The structure of system is shown in Fig. 37.11.

37.4.2 Warning System is Designed

Combined with the risk prediction function, curve safety warning system for vehicle is designed with LabVIEW. The front panel and block diagram of background process is designed. According to the function, the interface is divided into information input, risk state estimation, classification and warning module. The curvature which is estimated with machine vision is invoked by the MATLAB script of LabVIEW. The driver characteristics, road conditions and other information parameters can be input and adjusted with tester.

The bus is selected as the research object. The weather condition is clear. The road is dry. The physical parameters of road and vehicle are shown in Table 37.2.

Block diagram of warning system is shown in Fig. 37.12.

Warning result when the vehicle is running is shown in Fig. 37.13.

From Fig. 37.13, we can see that maximum safety speed is 31.3 km/h when the radius is 40.87 m. The risk prediction value 0.766 is smaller than the primary alarm

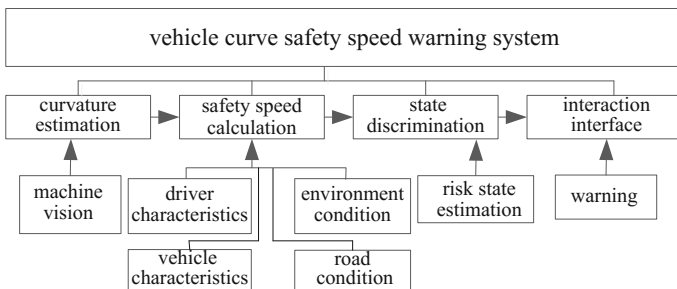


Fig. 37.11 Structure diagram of safety speed warning system

Table 37.2 Main vale of road and vehicle

Physical meaning	Valve
Complete vehicle quality (kg)	6360
High/wide (m)	2.92/2.6
The centroid height/wheel-base (m)	1.2/2.03
Lateral adhesion coefficient (dry)	0.8
Transverse gradient value	0.06

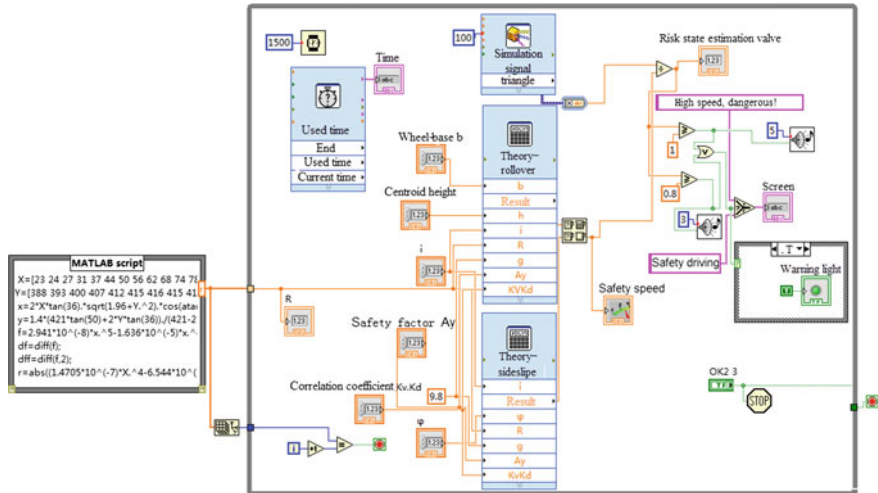


Fig. 37.12 Block diagram of warning interface



Fig. 37.13 Warning results when the vehicle is in normal running



Fig. 37.14 Warning results of vehicle is in dangerous driving

limit value 0.8. Also, warning light does not alarm. The screen is display ‘safety driving!’ The system is working properly. Primary simulation results of dangerous driving is shown in Fig. 37.14.

From Fig. 37.14, we can see that maximum safety speed is 37.2 km/h when the radius is 58 m. The risk prediction value 0.8584 is higher than the primary alarm limit value 0.8. Also, warning light turn red and beeps. The screen is display ‘High speed, dangerous!’ The system can be monitored and alarmed correctly. If the risk estimation value is greater than 1, the warning light and screen display are same as primary warning. But the buzzing sound is more rapidly than the primary warning.

37.5 Conclusions

This work investigates the driving safety on curves by introducing the means of machine vision and curve driving safety model. The Curve safety speed warning algorithm is achieved. And, main conclusion is as follow:

- (1) The curvature radius of front curve is estimated with the machine vision technology. The estimation results are in line with the actual road alignment.
- (2) The vehicle curve safety speed warning algorithm with risk state estimation is proposed. It could be used to determine the traffic status of the vehicle in advance.
- (3) Combining with the risk prediction function, vehicle curve over-speed prevention warning system is designed based on LabVIEW. Simulation results show that the warning system can accurately judge the safety state when vehicle is entering or passing the curve. It ensures the vehicle safety in the corner effectively.

Acknowledgements Authors would like to thank anonymous reviewers and the editor for their valuable comments and Municipal Education Commission Project of Chongqing (KJ1603207). Chongqing Vocational Institute of Engineering Research Project (KJB201511) for their sponsorship.

References

1. Farmer CM, Lund AK (2002) Rollover risk of cars and light trucks after counting for driver and environmental factors. *Accid Anal Prev* 34(11):163–173
2. Parenteau CS, Vianob DC, Shaha M (2003) Field relevance of a suite of rollover tests to real world crashes and injuries. *Accid Anal Prev* 35(3):103–110
3. Li K, Tan HS, Misener JA et al (2008) Digital map as a virtual sensor-dynamic road curve reconstruction for a curve speed assistant. *Veh Syst Dyn* 46(12):1141–1158
4. Lee YH, Deng WW Speed control method for vehicle approaching and traveling on a curve: U.S., US400963B2. 15 July 2008
5. Zhang D, Wang J, Li S et al (2009) Risk prediction based curve anti-sideslip speed warning system. *J Highw Transp Res Dev* 26(S1):44–48
6. Yu G, Li Q, Wang Y et al (2014) Roll stability and early warning of vehicle driving in the curve. *J Beijing Univ Technol* 40(4):574–579
7. Wang C (2010) Study on road traffic safety analysis and countermeasures in curve. Chang'an University, Xi'an
8. Zhou H (2012) Simulation research of vehicle safe speed based on car and road conditions. Chongqing Jiaotong University, Chongqing
9. Li B, Cao Y, Li Z et al (2014) Turn safety of concrete truck mixer based on LabVIEW. *J Chongqing Jiaotong Univ* 33(1):144–147
10. Wang C (2012) Research on several key problems of vehicle lane change warning, vol 6. Chang'an University, Xi'an, pp 69–77
11. Zheng S, Li X, Li K et al (2007) Simulation of vehicle active steering based on digital map information. *J Highw Transp Res Dev* 24(11):154–158
12. Swami A, Zhao Q, Hong Y-W (2003) Wireless sensor networks: signal processing and communications, vol 2, pp 1105–1108
13. Jia L, Luo J (2012) Road curvature estimation based on linear lane model. *J Jiangsu Univ Nat Sci Ed* 33(4):374–378
14. Xie M (2011) Research on active safety technology of vehicle based on monocular vision, vol 5. University of Electronic Science and Technology of China, Chengdu, pp 16–20
15. Southall B, Taylor CJ (2001) Stochastic road shape estimation. In: Proceedings of eighth IEEE international conference on computer vision, vol 1, pp 205–212
16. Zhao SE, Qu X, Shu HB et al (2004) Mountain road traffic safety evaluation based on weighted least squares. *J Math Prac* 44(13):88–90

Chapter 38

Multi Objective Optimization of Vehicle Crashworthiness Based on Combined Surrogate Models

Ling Zheng, Yinan Gao, Yinong Li and Zhenfei Zhan

Abstract Several surrogate models such as radial basis function and Kriging models are developed to speed the optimization design of vehicle body and improve the vehicle crashworthiness. The error analysis is used to investigate the accuracy of different surrogate models. Furthermore, the Kriging model is used to fit the model of B-pillar acceleration and foot well intrusion. The multi-quadric radial basis function is used to fit the model of the entire vehicle mass. These models are further used to calculate the acceleration response in B-pillar, foot well intrusion and vehicle mass instead of the finite element model in the optimization design of vehicle crashworthiness. A multi-objective optimization problem is formulated in order to improve vehicle safety performance and keep its light weight. The particle swarm method is used to solve the proposed multi-objective optimization problem. The simulation results show that the B-pillar acceleration and the foot well intrusion are reduced 4.9, 6.31% respectively. The entire vehicle mass is reduced 4.9 kg. The proposed combined surrogate models and their applications in the optimization design of vehicle crashworthiness provide an important design method.

Keywords Vehicle crashworthiness · Radial basis function · Kriging model · Particle swarm

38.1 Introductions

In recent years, the requirements for vehicle safety becomes more strict than before due to a large amount of vehicle in the road. Vehicle safety includes active safety and passive safety. The accident can be avoided actively by some advanced driving assistant systems or active safety techniques. However, the vehicle should also have

L. Zheng (✉) · Y. Gao · Y. Li · Z. Zhan
Collage of Automotive Engineering, Chongqing University, Chongqing 400044, China
e-mail: zling@cqu.edu.cn

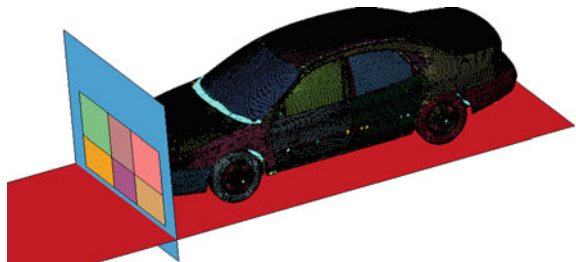
a good passive safety performance that can ensure passenger safety when the accident cannot be avoided. Therefore, the optimization of vehicle crashworthiness becomes an important topic in vehicle design. Although the finite element method is used widely in the vehicle crashworthiness design. However, its computation cost is very huge. How to reduce the computation cost is still a challenge in the optimization design of vehicle worthiness. On the other hand, the dynamic process of vehicle crash is complex and nonlinear. It increases the burden of the computation and often results in simulation failure. Some surrogate models with high accuracy are thus developed to replace the complex finite element model such as the response surface model, Kriging model, radial basis function model and so on.

Forsberg and Nilsson [1] studied the stability and convergence of the iterative optimization by comparing the response surface and Kriging model. Zhu [2] studied the support vector machine regression mathematical model. Kaymaz [3] studied the application of the structural reliability problems of Kriging model and compared them with the response surface model. These researches have shown that the response surface model is incompetence to the nonlinear problem. The Kriging model and radial basis function are relatively easy to obtain ideal fitting results when solving a high degree of nonlinear problem. In this paper, the Kriging model and radial basis function are used to fit the optimization objectives such as acceleration in B pillar and vehicle mass. Their errors are analyzed and the accuracy of the surrogate model is evaluated. In additional, multi-objective optimization model is developed to minimize the acceleration response in B pillar and foot well intrusion and the mass of vehicle body.

38.2 Optimization Design

The Fig. 38.1 is the finite element model of a vehicle frontal crash. The model has a total of 1.06 million elements and 0.94 million nodes. The vehicle impacts rigid barrier in a speed of 56 km/h. The simulation time is set to 150 ms. B-pillar peak

Fig. 38.1 The finite element model of vehicle crashworthiness



acceleration is 35.548 g and foot well intrusion is 0.1418 m and the entire vehicle mass is 1.6349 t in the process of crash.

38.2.1 Optimization Objectives

The structure of vehicle body has an important influence on its passive safety. Usually, structural responses in some important locations should be calculated or measured in order to evaluate its safety. For example, the deformation of the front panel, the peak acceleration of B-pillar, the foot well intrusion and so on. On the other hand, vehicle body mass in total should be limited to a low level to achieve its lightweight. Here, the peak acceleration of B-pillar, the foot well intrusion and vehicle body mass in total are considered as objective functions in optimization design of vehicle crashworthiness.

38.2.2 Design Variable

As shown in Fig. 38.2, the seven components with high energy absorption are selected as design variables. Their total absorption energy is 55.75 kJ. The absorption energy of the vehicle is 173.59 kJ. That means the optimized energy occupies 32.11% of the total absorption energy in vehicle. The initial values of design variable and optimization objective are shown as Table 38.1.

Fig. 38.2 The position of design variable

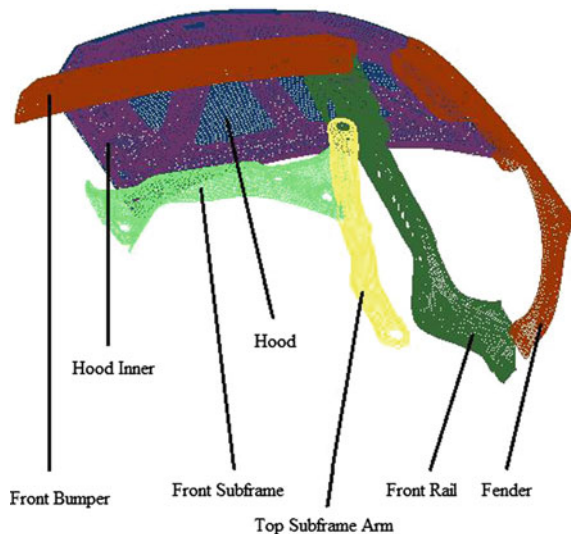


Table 38.1 The initial value of design variable and optimization objective

Design variable and optimization objective	Initial value	Design variable and optimization objective	Initial value
Front rail x_1	1.9 mm	Hood inner x_6	0.8 mm
Top subframe arm x_2	2.25 mm	Hood x_7	0.7 mm
Front subframe x_3	2.25 mm	Mass m	1.6349 t
Front bumper x_4	1.22 mm	B-pillar acceleration a	35.548 g
Fender x_5	0.9 mm	Foot well intrusion s	0.1418 m

38.2.3 Optimize Processes

The optimize processes is shown as Fig. 38.3. First of all, Optimization Objectives and Design Variable are selected. In proposed optimization process, B-pillar peak acceleration, foot well intrusion and mass are selected as optimization objectives the sample points are selected by Latin hypercube design method. The response values of these sample points are calculated by the finite element model for vehicle body. The surrogate model is established accord the responses of these sample points including Kriging model and radial basis function models. Furthermore, particle swarm optimization method is used to solve the proposed multi-objective optimization problem. The optimization scheme is developed according to the demand of designer for safety and lightweight.

38.3 Radial Basis Functions

The surrogate model is a mathematical model which approaches the results of physical experiments or numerical analysis in a small amount of calculation compared with conventional finite element model. It can make optimization interactive calculation easy and high efficiency. Before the surrogate model is established, the sample points in original finite element model have to be decided. It is called experimental design method. Once the results from sample points are calculated and completed, the surrogate model can be developed and used as an approximate model instead of the complex finite element model in optimization process.

38.3.1 Experiment Design

In general, experimental design methods used in the optimization design of vehicle body including orthogonal arrays, Latin hypercube design and so on. In this paper, the Latin hypercube design is used as the experimental design method to obtain the

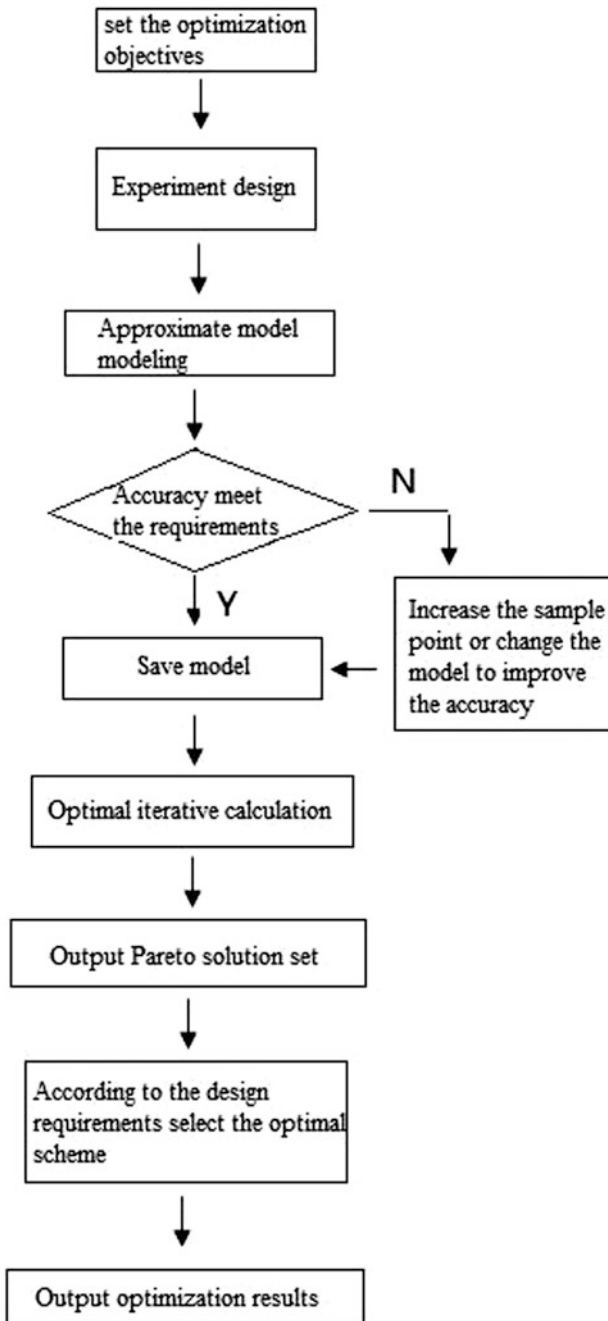


Fig. 38.3 Multi-objective optimization process of vehicle crashworthiness

Fig. 38.4 Full factorial design

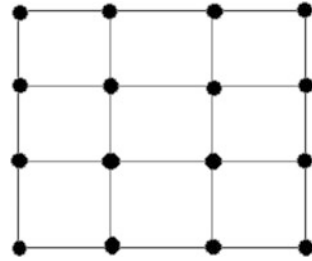
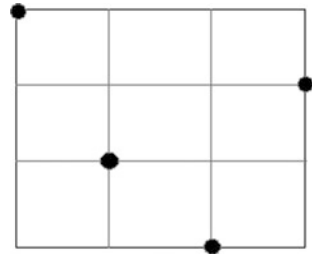


Fig. 38.5 Latin hypercube design



sample points in surrogate models. This method is developed first by M.D. McKay, R.J. Beckman and W.J. Conover. Its principle is that dimensional coordinates of each section $[x_k^{\min}, x_k^{\max}]$, $k \in [1, n]$ is divided into m intervals and each interval is counted as $[x_k^{i-1}, x_k^i]$, $i \in [1, m]$. m points are selected to ensure that each level of a factor is only calculated once. Figures 38.4 and 38.5 are Latin hypercube design with mn sample points in n -dimensional space, in terms of $m \times n$ LHD. It is seen that the different between the full factorial design and Latin hypercube design is obvious, each level of factors are only calculated once by Latin hypercube design. In this way, the amount of computation and cost are reduce greatly.

In the proposed Latin hypercube design, 27 sample points are selected. At the first, the response results such as accelerations and deformations in some special locations are calculated by using conventional finite element model for vehicle body. The response results of all sampling point are shown in Table 38.2.

38.3.2 The Modeling of Radial Basis Functions

The radial basis function is a type of typical surrogate model or function in which the Euclidean distance between the target point and the sample point is selected as the independent variables. Here, a radial function is considered as a basis function, which is in a linear superposition and then configured radial basis function model. As a good surrogate model, the radial basis function model demonstrates its flexibility, simple structure, and high efficiency.

Table 38.2 The response results of sample points

Sample number	B-pillar peak acceleration (g)	Foot well intrusion (m)	Mass (t)
1	35.499	0.1112	1.6429
2	33.938	0.1445	1.6261
3	34.758	0.2193	1.6418
4	35.932	0.1005	1.6371
5	34.739	0.1663	1.6345
6	36.007	0.1902	1.6345
7	36.723	0.0974	1.6339
8	33.584	0.1541	1.6351
9	35.932	0.1717	1.6423
10	35.446	0.1135	1.6345
11	33.326	0.1628	1.6404
12	35.164	0.1652	1.6390
13	34.244	0.1128	1.6388
14	35.011	0.1231	1.6388
15	33.931	0.1822	1.6388
16	34.153	0.1045	1.6394
17	35.554	0.1091	1.6381
18	35.226	0.1908	1.6440
19	35.757	0.1043	1.6362
20	34.707	0.1069	1.6434
21	34.398	0.1912	1.6421
22	34.814	0.1331	1.6197
23	34.448	0.1203	1.6380
24	30.894	0.1972	1.6562
25	34.968	0.1072	1.6341
26	34.507	0.1549	1.6447
27	32.911	0.2167	1.6350

The expression of radial basis function is as follows:

$$f(x) = \sum_{i=1}^n \omega_i \varphi(r^i) = \omega^T \varphi \tag{38.1}$$

$\omega(x) = \begin{bmatrix} \omega_1 \\ \dots \\ \omega_n \end{bmatrix}$, $\varphi = \begin{bmatrix} \varphi(r_1) \\ \dots \\ \varphi(r_n) \end{bmatrix}$, ω_i is the weight coefficient, $\varphi(r)$ is the basis function the Euclidean distance of the target point X and the sample point X_i is $r_i = \|X - X_i\|$. Gauss function, Multiquadric function and inverse Multiquadric function are used as radial functions widely. In this paper, Gauss function and Multiquadric function are selected as the radial basis function.

Gauss function: $\varphi(r) = \exp\left(-\frac{r^2}{c^2}\right)$.

Multi-quadric function: $\varphi(r) = (r^2 + c^2)^{\frac{1}{2}}$.

In order to obtain the prediction model, the following relationship is established

$$f(X_i) = y_i \tag{38.2}$$

y_i is the response value of X_i . Substituting Eq. (38.2) into Eq. (38.1), the follow equation is generated:

$$\varphi\omega = Y \tag{38.3}$$

$$\varphi = [\varphi_{ij}] = [\varphi(\|X_i - X_j\|)], \quad Y = \begin{bmatrix} y_1 \\ \dots \\ y_n \end{bmatrix}. \text{ So the weight coefficient } \omega. \text{ written:}$$

$$\omega = \varphi^{-1}Y \tag{38.4}$$

Generally two methods can be used to determine shape parameter c . First method is from the experience of the designer. Second method is so called cross-validation [4]. Here, cross-validation is used to decide the shape parameter c . Shape parameter c is from 0.005 to 0.2 in the Gauss function. It is from 4 to 5 in the Multiquadric function. Several shape parameters c in Gauss function and in Multiquadric function are selected as shown in Tables 38.3 and 38.4. Then, the fitting errors between the sample points and radial basis function approximation value are calculated. In order to verify the Gauss function or the Multiquadric function, other eight additional sample points by using Latin hypercube design are analyzed and the fitting error are also obtained. Results are shown in Tables 38.3 and 38.4.

This can be seen that Multiquadric radial basis function with shape parameter 4.5 has a small average error of 0.037% for vehicle mass. On the other hand, Gauss radial basis function with shape parameter 0.1 has a small average error of 3.335% for B-pillar peak acceleration and Gauss radial basis function with shape parameter

Table 38.3 The error analysis of Gauss radial basis functions

c	Optimization objectives	Average error (%)
0.1	B-pillar peak acceleration	3.335
	Foot well intrusion	9.359
	Mass	1.204
0.02	B-pillar peak acceleration	3.382
	Foot well intrusion	9.162
	Mass	0.537
0.01	B-pillar peak acceleration	3.921
	Foot well intrusion	8.142
	Mass	0.091

Table 38.4 The error analysis of Multiquadric radial basis functions

C	Optimization objectives	Average error (%)
4	B-pillar peak acceleration	3.343
	Foot well intrusion	9.672
	Mass	0.060
4.5	B-pillar peak acceleration	3.344
	Foot well intrusion	9.973
	Mass	0.037
5	B-pillar peak acceleration	3.345
	Foot well intrusion	66.394
	Mass	0.039

0.01 has a average error of 8.142% for foot well intrusion. These errors are different obviously due to nonlinear of different objectives. It is implied that the mass is kept relative high linearity.

38.4 Kriging Model

The Kriging model is another type of surrogate model. The same sample points as radial basis function model are used to develop Kriging model.

Kriging model is an unbiased estimation model with minimum estimated variance that South Africa geologist Daniel Kriging proposed in 1951. Its advantage is high degree of nonlinearity. It can obtain ideal fitting and high precision for strong nonlinear problem. Because the process of vehicle crash is typical nonlinear, the Kriging model is more suitable than normal models.

If x_1, x_2, \dots, x_n are the sample points around target point x_0 , the response of the sample points are $y(x_1), y(x_2), \dots, y(x_n)$ and then the estimated response of the target point is $\tilde{y}(x_0)$, their relationship can be expressed as follows:

$$\tilde{y}(x_0) = \sum_{i=1}^n \lambda_i y(x_i) \tag{38.5}$$

λ_i is weight coefficient. λ_i needs to meet two conditions. First is unbiased estimation that means the variance of different between estimated values and the real values is minimal.

The relationship of response value and independent variable of Kriging model is expressed as follows:

$$f(x) = g(x) + z(x) \tag{38.6}$$

$g(x)$ is a deterministic part. Usually, it is a constant. $z(x)$ is changed with the measured point. It has the following statistical properties.

$$E[z(x)] = 0,$$

$$\text{Var}[z(x)] = \sigma^2$$

$$E[z(x_i), z(x)] = \sigma^2 R(x, x_i)$$

$R(x, x_i)$ is the correlation function. The Gauss function is selected as correlation function in this paper. It should meet two conditions. First is unbiased estimation, it can be expressed as $E[f^*(x) - f(x)] = 0$ and it also can be expressed as $E[\omega^T Y - f] = \omega^T G - g = 0$, among them $G = (g(x_1), \dots, g(x_n))$. Second is minimum variance, it can be expressed as that:

$$\varphi(x) = E\left[(f^*(x) - f(x))^2\right] = \sigma^2(1 + \omega^T R \omega - 2w^T r)$$

is the smallest,

$$R = [R_{ij}] = \exp\left(-\sum_{i=1}^n \theta_k |x_k^i, x_k^j|^2\right),$$

$$r = [R(x, x_1), \dots, R(x, x_n)]^T.$$

If the variance is the minimum, the weight coefficient is:

$$\omega(x) = R^{-1}\left(r(x) - G(G^T R^{-1} G)^{-1}(G^T R^{-1} r(x) - g(x))\right)$$

Kriging model is established by using the same sample points as the Radial basis functions. As shown in Table 38.5, the parameters θ . the correlation function are obtained.

As shown in Table 38.6, the fitting precision of Kriging model is verified. It can be seen that the complex correlation coefficient of the three objective functions are more than 0.9 and the maximum value is 0.998. The results show that the fitting effect is ideal. Beside the foot well intrusion, the average errors of the other two objective functions are not more than 1%. The average error of the foot well intrusion is only 2.585% because of the fact that a prediction of a sample point value deviates from the response value. Table 38.7 shows the relative error and average error of eight additional points.

Table 38.5 The parameters θ of Kriging model

	x_1	x_2	x_3	x_4	x_5	x_6	x_7
Acceleration	0.3069	1.9929	0.0002	0.1588	0.0031	0.0024	0.0049
Intrusion	0.5408	0.1328	0.0299	0.0562	0.0020	0.0099	0.0059
Mass	0.0477	0.0194	0.0266	0.0497	0.0479	0.0720	0.1403

Table 38.6 Fitting accuracy verification of Kriging model

	R ²	Average error (%)
Acceleration	0.915	0.829
Intrusion	0.987	2.585
Mass	0.998	0.001

Table 38.7 Error analysis of Kriging model

Optimization objectives	Finite element simulation value	Kriging predictive value	Relative error (%)	Average error (%)
B-pillar peak acceleration (g)	35.757	35.423	0.935	3.069
	33.306	34.990	5.057	
	34.313	35.277	2.807	
	32.472	34.073	4.931	
	36.204	35.169	2.857	
	35.920	33.658	6.298	
	33.899	33.927	0.082	
	34.499	33.953	1.583	
Foot well intrusion (m)	0.091	0.100	9.391	5.005
	0.095	0.093	2.318	
	0.109	0.115	5.727	
	0.144	0.136	5.762	
	0.118	0.112	4.832	
	0.181	0.181	0.421	
	0.224	0.216	3.530	
	0.188	0.203	8.060	
Mass (t)	1.6355	1.6360	0.033	0.051
	1.6362	1.6361	0.006	
	1.6353	1.6387	0.207	
	1.6390	1.6382	0.049	
	1.6399	1.6396	0.018	
	1.6407	1.6417	0.058	
	1.6389	1.6389	0.003	
	1.6381	1.6375	0.037	

It can be seen from Table 38.7 that the average error of the mass is the lowest. It is 0.051%. The main reason is that its high linearity. Therefore, the fitting precision is ideal. The average error of B-pillar peak acceleration is 3.069% and the maximum error is 5.057%. The average error of Foot well intrusion is 5.005% and the maximum error is 9.391%. The fact that the errors of some regional will increase in the process of fitting accuracy verification shows that the fitting accuracy will be reduced in some regions. But considering the calculation efficiency will be greatly improved, the accuracy is still acceptable.

38.5 Multi-Objectives Optimization

By comparing the accuracy of two surrogate models, the Kriging model is selected to fit the model of B-pillar acceleration and foot well intrusion and the Multiquadric radial basis function with $c = 4.5$ is selected to fit the model of the entire vehicle mass. The three models are used as approximate surrogate models to replace the complex finite element model in multi-objective optimization of vehicle crashworthiness.

The mathematical model of multi-objective optimization is expressed as follows:

$$\begin{aligned}
 & \text{Min } f_1(x) \\
 & \quad f_2(x) \\
 & \quad f_3(x) \\
 & \text{s.t. } 1 < x_1 \sim x_3 < 3 \\
 & \quad 1 < x_4 < 2 \\
 & \quad 0.5 < x_5 \sim x_7 < 1.2
 \end{aligned}$$

Here,

$f_1(x)$ is B-pillar peak acceleration. $f_2(x)$ is foot well intrusion. $f_3(x)$ is entire vehicle mass. $x_1 \sim x_7$ is the thickness of plates to be optimized. The algorithm of particle swarm optimization is used to solve the multi objective optimization problem and the Pareto optimal solution set for the optimal results is obtained. As shown in Fig. 38.6, in total, 125 Pareto solutions are obtained.

An optimal solution is selected in Pareto optimal solution set as the optimization scheme by consideration of safety and lightweight. Table 38.8 is the results of optimization.

The optimization results are brought into the finite element model and the simulation results are shown in Table 38.9.

Fig. 38.6 Pareto optimal solution set

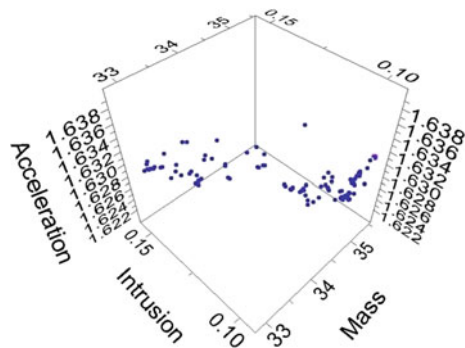


Table 38.8 The result of multi objective optimization

Optimization objectives and design variable	Optimization results
x_1 (mm)	1.76
x_2 (mm)	2.79
x_3 (mm)	1.86
x_4 (mm)	1.83
x_5 (mm)	0.90
x_6 (mm)	0.51
x_7 (mm)	0.64
B-pillar peak acceleration (g)	33.526
Foot well intrusion (m)	0.1215
Mass (t)	1.6323

Table 38.9 The comparison between the predicted value and the simulation value

Optimization objectives	Simulation value	Predicted value	Relative error (%)
B-pillar peak acceleration (g)	33.306	33.526	0.661
Foot well intrusion (m)	0.1282	0.1215	5.226
Mass (t)	1.6300	1.6323	0.141

The relative error between finite element model and predicted model of B-pillar peak acceleration and mass is within 1%. The relative error of foot well intrusion is 5.226%. The mass is changed to 1.63 t after optimization. Compared with the before optimization, the weight reduces 4.9 kg. The B-pillar peak acceleration changes to 33.306 g after optimization. Compared with the before optimization, acceleration reduces 6.31% as shown in Fig. 38.7. The foot well intrusion changes to 0.1282 m after optimization. A 9.6% reduction is obtained as shown in Fig. 38.8, the living space of the passengers is improved obviously after optimization.

Comparing with the B-pillar peak acceleration, the optimization effect of foot well intrusion is more obvious.

Fig. 38.7 Comparison of the B-pillar acceleration before and after optimization

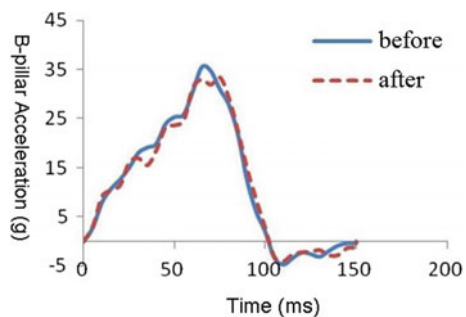
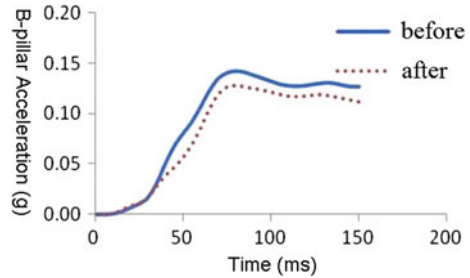


Fig. 38.8 Comparison of the foot well intrusion before and after optimization



38.6 Conclusions

In this paper, the radial basis function model and Kriging model are developed as surrogate models to optimize the vehicle body and achieve a balance of passive safety and light mass. Furthermore, Multi-objective optimization model is described and solved by means of particle swarm method. Some conclusions are summarized:

- (1) Kriging model is used to develop the surrogate model of B-pillar acceleration and foot well intrusion due to their nonlinear in process of vehicle crash. Multiquadric radial basis function is used to develop the surrogate model of vehicle mass due to its linear properties. The error analysis verifies their accuracy as available approximate surrogate models instead of the finite element model in optimization design of vehicle crashworthiness.
- (2) The multi objective optimization is completed by using particle swarm method. The simulation results show that the B-pillar acceleration and the foot well intrusion are reduced 4.9, 6.31% respectively. The entire vehicle mass is reduced 4.9 kg. The proposed combined surrogate models and their application in the optimization design of vehicle crashworthiness provide an important design method.

Acknowledgements This paper is supported by the Key Project of Natural Science Foundation of Chongqing (Grant No. cstc2015zdcy-ztzx30001) and the Key Technology Innovation Project of Chongqing (Grant No. cstc2015jcyjBX0097).

References

1. Forsberg J, Nilsson L (2006) Evaluation of response surface methodologies used in crashworthiness optimization. *Int J Impact Eng* 32(5):759–777
2. Zhu P et al (2012) Use of support vector regression in structural optimization: Application to vehicle crashworthiness design. *Math Comput Simul* 86(3):21–31
3. Kaymaz I (2005) Application of Kriging method to structural reliability problems. *Struct Saf* 27(2):133–151
4. Hou S, Xie J, Han X (2013) Shape parameter selection of radial basis function based surrogate models in vehicle crashworthiness design. *Int J Aerosp Lightweight Struct* 3(1):87–107

Chapter 39

The Influences of Pre-impact Braking Scenarios on Occupant Restraint System During the Full Frontal Impact

Hongyun Li, Chengyue Jiang, Dong Cui, Shugang Xie and Shuang Lu

Abstract The integration of active safety and passive safety has become a critical technical problem. A full frontal simulation model with human model was built up to analyse occupant kinematics and injuries. Human model moved forward and neck & thorax injuries were increased duo to pre-impact braking. Seat belt pretensioner TTF, DAB holes size and tethers length were chosen as optimal parameters of occupant restraint system (ORS) to improve human model injuries by the method of Multiple Factor Variance Analysis (MFVA). Seat belt pretensioner TTF was the most significant factor ($P > 0.8$) on human model injuries while DAB tethers length has little influence ($P < 0.25$).

Keywords Pre-impact braking · ORS · Integrated safety · MFVA

39.1 Introduction

With the development of sensor technology and control technology, automotive active safety systems, such as Electronic Stability Program (ESC), Forward Collision Warning (FCW), Automatic Emergency Brake (AEB), are popularly applied for vehicles [1]. AEB system can reduce the vehicle speed in case of emergency, thereby reduces the impact strength greatly or avoid impact. However, when the vehicle speed is too high (such as 80 km/h), the vehicle still has the possibility of high-speed collision (such as 50 km/h). In such scenario, the occupant restraint system (ORS) starts to work based on occupants in position. However, occupants have moved forward during the working phase of the AEB [2, 3]. The protective effects of ORS for occupants may be discounted. Therefore, the integration of active safety and passive safety has become a critical technical problem.

H. Li (✉) · D. Cui · S. Xie · S. Lu
China Automotive Technology and Research Center, Tianjin, China
e-mail: lihongyun@catarc.ac.cn

C. Jiang
Chongqing University of Technology, Chongqing, China

Based on analysis of occupant kinematics and injuries, the influences of pre-impact braking scenario on ORS during the full frontal impact were studied. Human model injuries were optimized by the method of MFVA.

39.2 Materials and Methods

To assess the effects of pre-braking events on the occupant kinematics and injuries, a pre-impact scenario with the initial speed at 80 km/h, all leading to equal closing speeds (50 km/h, as that of the Full Frontal impact, 50 FF) was introduced.

39.2.1 Simulation Model with Human Model

Vehicle braking deceleration cannot exceed the road coefficient of friction and is accepted to be in the interval of 1.0" g" to 1.3" g" in very rare instances [4]. In this study, accelerations in X direction (without vehicle pitching), were applied on the occupant compartment model to evaluate vehicle braking effects.

The pre-impact braking pulse as in the research of [1], together with the pulse of 50 FF test (shown as Fig. 39.1), was used as the input of the simulation model.

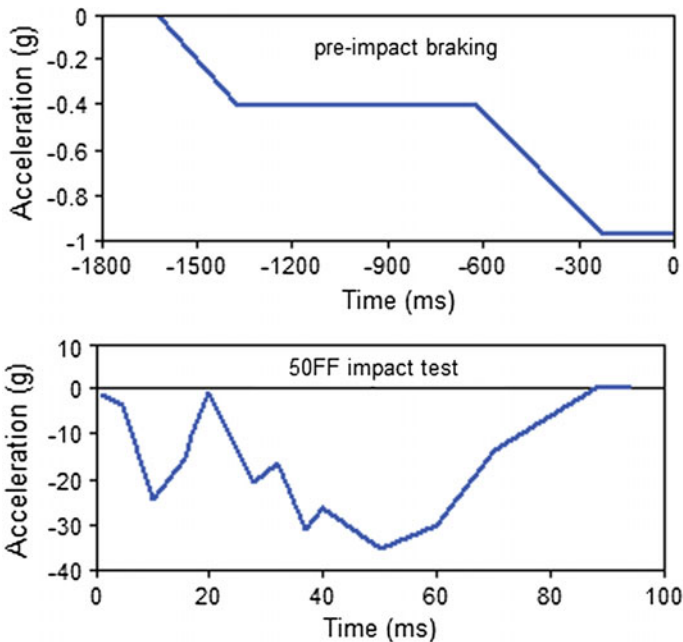


Fig. 39.1 Pulse for the pre-crash scenario (up) and full front impact (down)

Fig. 39.2 Full frontal simulation model

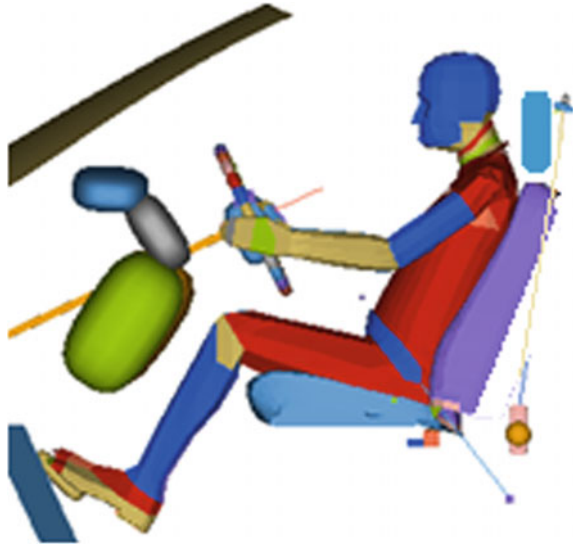


Table 39.1 Parameters of two load cases

No.	Initial velocity (km/h)	AEB system	Impact velocity (km/h)	Initial time (ms)	Compared time (ms)	Posture
CASE1	50.0	Without	50.0	0	0	Initial
CASE2	80.0	With	50.0	-1620	0	Changed

Note In CASE2, initial time is -1620 ms, which means AEB system start to work before 1620 ms vehicle impact and vehicle impact happened at 0 ms

A full frontal simulation model with MADYMO human model was built up, shown as Fig. 39.2. The human body models are more biofidelic than dummy models, which was developed for the evaluation and optimisation of passive and active restraint systems in a wider range of loading conditions than the standard impact tests [5].

This frontal simulation model have been correlated very well with 50 kmph crash test results, including dummy injuries, belt forces and dummy kinematics [6]. So it can be used for the following study on pre-crash braking effects on occupant kinematics.

39.2.2 Comparison of Human Model Posture and Injuries

Following two load cases were compared. The parameters were shown as Table 39.1.

Due to inertia of body, human model moved forward and its posture was changed in CASE2, shown as Fig. 39.3 (The green model is CASE1 and the grey model is CASE2).

Fig. 39.3 Comparison of posture

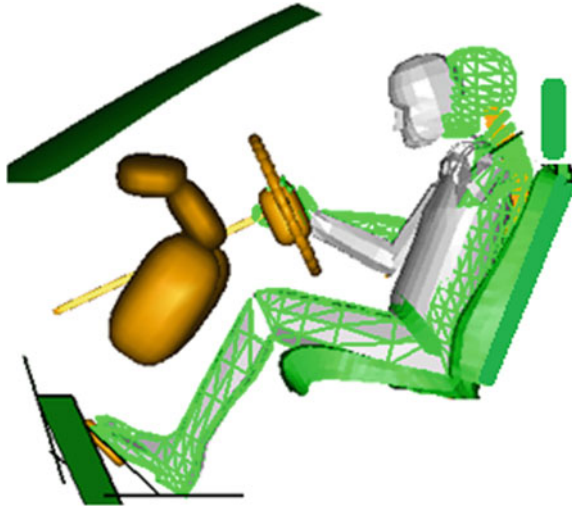


Fig. 39.4 Head acceleration

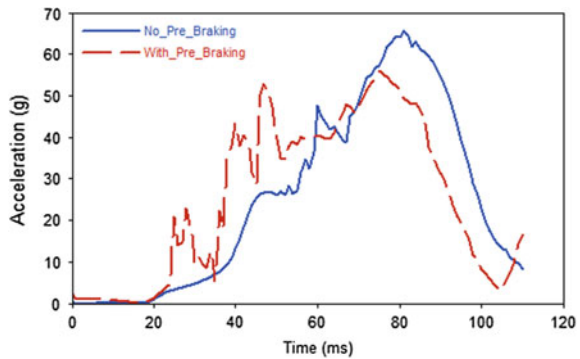


Table 39.2 Human model injuries for US-NCAP

Injury index	HIC15	Nij	Neck Fz (N)	Chest deflection (mm)	RR	Star rating
CASE1	432	0.28	1291	25.1	0.86	★★★★
CASE2	383	0.29	1513	34.03	1.08	★★★

Head forward displacement of CASE2 was about 110 mm from -1620 mm to 0 ms, while chest forward displacement was about 40 mm. Figure 39.4 shows that the head acceleration with pre-braking rises earlier and has lower peak value. This is because distance from head to steering wheel became shorter and head contact airbag earlier.

Besides, human model injuries were also compared CASE1 with CASE2 (see Table 39.2). To make the comprehensive assessment of human model injuries, Relative Risk (RR) was introduced according to US-NCAP regulation [7]. RR is the

ratio between probability of Injury (P_{joint}) and 15%, where P_{joint} is evaluated with Probability of Head Injury (P_{head}), P_{Neck} , P_{Chest} and P_{Femur} . The RR evaluation result is three-star when RR is between 1 and 1.33, while the RR evaluation result is four-star when RR is between 0.67 and 1.

For CASE1, the RR evaluation result is four-star, while the evaluation result of CASE2 is three-star due to the effect of pre-impact braking. CASE2 did not meet the target of four-star and the restrain systems were required to be optimized.

39.3 Results

Multiple factor analysis of variance is one of the basic methods of mathematical statistics to solve value comparison with more than two normal populations [8], which is widely used in many fields, as well as vehicle passive safety field.

39.3.1 Optimization Parameters and Its Levels

For ORS, the optimal parameters include seat belt pretensioner Time To Fire (TTF), Driver Airbag (DAB) holes size and DAB tethers length, which were marked as A, B and C, respectively. A, B and C all have three levels, as shown in Table 39.3.

Seven optimization cases were set up when combining the different levels of the three factors above, as shown in Table 39.4.

Table 39.3 Optimization parameters and its levels

Parameters	Seat belt pretensioner TTF (ms)			DAB hole size (mm)			DAB tethers length (mm)		
	0	9	18	20	25	30	200	300	400
Code	A1	A2	A3	B1	B2	B3	C1	C2	C3

Table 39.4 Seven optimization cases

Num.	Code	Seat belt pretensioner TTF (ms)	DAB hole size (mm)	DAB tether length (mm)
1	A3B2C2	18	2 × 25	300
2	A2B2C2	9	2 × 25	300
3	A1B2C2	0	2 × 25	300
4	A3B1C2	18	2 × 20	300
5	A3B3C2	18	2 × 30	300
6	A3B2C1	18	2 × 25	200
7	A3B2C3	18	2 × 25	400

39.3.2 Influence of Three Factors on Relative RR

Seven optimization cases were simulated with MADYMO model, and injury indexes and relative RR values were shown in Table 39.5.

The simulations’ main target for US-NCAP star rating was lower value of RR in this study. In addition, the minimum distance between head and steering wheel was introduced as simulations’ supplementary target to take into account the contact risk. So the experiment design was a multivariate experimental design. To evaluate the experimental results, the RR values and the minimum distance between head and steering wheel were balanced.

RR is considered as a variable, and three factors are considered as levels. The one dimensional linear multivariate analysis of variance was carried out and P Values were calculated, as shown in Table 39.6.

Seat belt pretensioner TTF was the most significant factor ($P > 0.8$) on human model injuries while DAB tethers length was non-significant factor.

Table 39.6 shows that the p-value of seat belt pretensioner TTF is greater than 80%, which indicates that it has the most significant effect on RR value. While the p-value of DAB tethers length are less than 25%, indicating little influence.

When Seat belt pretensioner TTF was decreased from 18 ms to 0 ms, human model injuries and RR value were also decreased. This is because human model forward displacement was reduced due to earlier pretensioner TTF.

With the increase of DAB hole size, human model injuries were improved and RR value was decreased. The pressure of DAB was decreased with bigger hole size

Table 39.5 Human model injuries for US-NCAP of seven cases

Code	HIC15	Nij	Neck Fz (KN)	Chest deflection (mm)	RR	Distance (mm)
A3B2C2	383	0.29	1513	34.03	1.08	22
A2B2C2	316	0.28	1421	32.13	0.94	26
A1B2C2	280	0.27	1376	29.87	0.83	29
A3B1C2	477	0.32	1531	35.95	1.31	32
A3B3C2	339	0.28	1443	32.38	0.97	17
A3B2C1	428	0.27	1351	34.89	1.16	21
A3B2C3	331	0.38	1956	33.82	1.10	23

Table 39.6 Multiple factor variance analysis for RR values

Num.	Factors	F value	P value
1	Seat belt pretensioner TTF (ms)	2.48	0.81
2	DAB hole size	2.40	0.79
3	DAB tethers length	0.25	0.21

so that contact forces between DAB and human body were also reduced. However, the minimum distance between head and steering wheel was decreased from 22 to 17 mm when hole size changed from 25 to 30 mm (see Table 39.6). So there was a risk of contact between head and steering wheel if DAB hole size was too large.

Shorting the DAB tethers length can decrease neck injury index while the head and chest injury index were increased (see Table 39.6). Contact time between head and DAB was delayed because the DAB deployment height was reduced. Therefore, neck injury was improved. However, the pressure of DAB was increased due to smaller DAB volume, which caused head and chest injury worse.

39.4 Discussions

A scenario of AEB system was selected in this study. The initial velocity of vehicle was 80 km/h, and then velocity of vehicle was reduced to 50 km/h with the help of AEB system, and finally the vehicle impact with rigid barrier. This is only a small part of traffic accidents in our life. Velocity of vehicle may be reduced to 60 or 40 km/h. So more scenarios of AEB system need to be researched to improve the compatibility of current ORS. In addition, current ORS needs to be changed into an adaptive system, whose parameters can be adjusted according to different collision conditions [9]. For example, seat belt pretensioner TTF can be advanced or delayed based on information, such as vehicle velocity from active safety devices.

39.5 Conclusions

With pre-impact braking events, human model moved forward and posture was changed. Injuries of human model were also worse. RR evaluation result changed from four-star to three-star.

Seat belt pretensioner TTF is most significant factor ($P > 0.8$) on RR value while DAB tethers length have little influence ($P < 0.25$). A good way to improve human model injuries was to use earlier pretensioner TTF. Another way is to increase DAB hole size if distance between head and steering wheel was enough. Shorting DAB tethers length can decrease neck injury index while head and chest injury index were increased.

Acknowledgements This project is supported by National Natural Science Foundation of China (Grant No. 51405050) and Chongqing Science and Technology person training program (cstc2013kjrc-qncr60002).

References

1. Lex R (2011) Effect of various pre-crash braking strategies on simulated human kinematic response with varying levels of driver attention. In: Proceedings of the 22nd ESV. Washington, USA
2. Gernot W, Wolfgang S (2014) Influences of pre-crash braking induced dummy—forward displacements on dummy behaviour during EuroNCAP frontal crash test. *Accid Anal Prev* 62 (1):268–275
3. Ejima S, Zama, Y, Ono K et al (2009) Prediction of pre-impact occupant kinematic behaviour based on the muscle activity during frontal collision. In: Proceedings of the 21st ESV. Stuttgart, Germany
4. Bastien C (2010) Investigation into injuries of out-of-position (OOP) posture occupants and their implications in active safety measures. In: Proceedings of ICRASH. Washington, USA
5. TASS. Madymo 7.4, human body model user manual. TASS
6. Jiang C, Liu X, Hu Y et al (2014) Braking effects on occupant kinematics and injury during the full frontal impact simulation using human model. In: Proceedings of the 11st INFATS. Chongqing, China
7. NHTSA (2012) Laboratory test procedure for new car assessment program frontal impact testing. National Highway Traffic Safety Administration
8. Rohr S, Lind R et al (2002) An integrated approach to automotive safety systems. SAE technical paper 2000-01-0346
9. Yuan Z, Zhou J (2012) Multivariate statistical analysis. Science Press, Beijing

Chapter 40

Rear Seat Belt Usage Models Using FARS and Field Data

Yang He, Zhan Shu, Yao Ge and Janice Daniel

Abstract Little research has been performed to evaluate the factors that impact seat belt usage for rear seat occupants. Because of the difficulties to collect rear seat belt data in the field, most researches have to rely on crash data, however, has its limit. Seat belt usage passengers not seriously hurt in a crash would typically not be recorded in the police officer filling report. In this study, Rear seat belt models using logistic regression analysis were performed using both FARS data and observational data. The resulting models were then analyzed to determine differences between using crash data and field data in identifying factors associated with the seat belt usage of rear seat occupants. The research showed both similar and differing results between the models produced using FARS data and field data. All the models using the FARS data showed a strong correlation between the back seat passenger's seat belt usage and the driver's seat belt usage. The research shows there are differences obtained in the factors that influence seat belt usage using field data and FARS data. The research demonstrates that care must be taken in the use of this data with regard to safety research looking at passenger restraint.

Keywords Rear seat belt · FARS

Y. He (✉) · Z. Shu · J. Daniel
Department of Civil and Environmental Engineering,
New Jersey Institute of Technology, Newark, NJ 07102, USA
e-mail: yh38@njit.edu

Z. Shu
e-mail: zs34@njit.edu

J. Daniel
e-mail: daniel@njit.edu

Y. Ge
Department of Electrical and Computer Engineering Rutgers, The State University
of New Jersey, Piscataway, NJ 08854, USA

40.1 Introduction

Seat belt usage is one of the most effective strategies available to avoid death and injury in a crash. Today, however, nearly 40 years since the federal government required all passenger cars to be equipped with seat belts, the nationwide seat belt usage is at 83%. According to a National Highway Traffic Safety Administration [1] report, an estimated 13,250 lives were saved by seat belt use in 2008 [2]. Although the seat belt usage rate in the US increases each year, this usage still lags behind some other developed countries, such as Canada, Australia and some European countries, especially for rear seat belt usage.

Based on the statistics provided by Occupant Restraint Use in 2010 [2], seat belt usage for rear passengers stood at 74% in 2010. In addition, in states where rear seat belt use was not required in 2008, only 66% of adult passengers buckled their seat belts while seating in the back seat [1]. In New Jersey, a study conducted by New Jersey Institute of Technology showed the rear seat usage rate was only 47.9%.

Much research has been performed demonstrating seat belt use by vehicle occupants during crashes can result in lower injury severities with seat belts and airbags the most effective strategies to protect occupants [3, 4]. While most of vehicles are not equipped with back seat airbags; the seat belt seems to be the only protection for back seat passengers. In some cases, the unrestrained rear seat occupants can injure the driver or front seat passenger even if the front seat occupants are buckled. Therefore, using seat belts for rear seat occupants is not only beneficial for protecting rear seat occupants, but also reduces the risk of a second injury for the driver and front passenger.

In 2009, the majority of US states have primary or secondary Seat Belt Laws. Primary state laws allow motorists to be stopped and cited solely for violating a seat belt law, while secondary state laws are applicable when the motorists is stopped for another offense and are found violating the seat belt law. These laws play an important role in increasing seat belt usage and prove to be one of the most effective measures.

The State of New Jersey has a primary Seat belt Law, furthermore, NJ government recently tried to strengthen the state seat belt laws. On January 18, 2010, legislation was signed into law requiring all passenger vehicle occupants, regardless of their seating position, to wear their seat belts (NJS 39:3-76.2f). As a secondary law, the new law allows law enforcement to issue summonses to unbuckled back seat occupants, 18 years of age and older, when the vehicle they are riding in is stopped for another violation.

40.2 Problem Statement and Objectives

Factors influencing seat belt usage have been researched in safety analysis. Most research has focused on factors influencing the seat belt usage for drivers and front seat passengers. Little research has been performed to evaluate the factors that impact seat belt usage for rear seat occupants. In addition, because of the difficulties associated with collecting rear seat belt data in the field, most research in this area has relied on crash data, particularly the Fatal Accident Reporting System (FARS), to obtain seat belt usage data. Crash data, however, has its limits. Seat belt usage for vehicle occupants not seriously hurt in a crash would typically not be directly observed by the police officer filling out the report.

A rear seat belt model using logistic regression analysis was performed using both FARS data and also using observational data. The variables used from the FARS data and the field data, included vehicle type, age of rear seat passenger by seating position, vehicle occupancy and other variables. The resulting models were then analyzed to determine differences between using crash data and field data in identifying factors associated with the seat belt usage of rear seat occupants. In this paper, we analyze the two data sets, show the differences and try to examine whether the FARS data can be used to make a general conclusion of seat belt usage.

40.3 Literature Review

The methodology for collecting rear seat belt usage has not been clearly documented in the literature. However, gathering rear seat belt usage is increasing becoming an important role for safety agencies. Rear seat occupants are difficult to observe on highways due to high speeds on this roadway and visibility is difficult from a distant location. Surveyors are also unable to stand close to the traffic for their own safety and to avoid distracting drivers. Even when vehicles are stopped at an intersection, it is often still difficult to observe seat belt usage for rear seat occupants, especially when many vehicles have tinted windows also made difficult under dark conditions. Another complication is the lack of vehicles with back seat passengers. For this reason crash data is often used to determine seat belt usage in model development.

Data on seat belt usage, both front and rear, is obtained through a variety of methods including: phone interviews, observation and through crash records. NHTSA's *Traffic Safety Facts: Seat Belt Use in Rear Seats in 2008* reports on seat belt usage data collected by sending trained observers to probabilistically sampled intersections controlled by stop signs or stoplights, where vehicle occupants are observed from the roadside. Data is collected between 7 a.m. and 6 p.m. Only stopped vehicles are observed to permit time to collect the variety of information required by the survey, including subjective assessments of vehicle occupants' age and race. Most observational seat belt data collection use similar approaches for

collecting data. Some of data collection use random dialed telephone surveys to report seat belt usage [5], some others conduct questionnaire survey to acquire seat belt usage rate [6, 7].

Research to identify factors that influence seat belt usage has primarily relied on data from crash records, particularly the Fatal Accident Reporting System (FARS) crash database. The Fatal Accident Reporting System (FARS) provides a wealth of data that is usable by researchers to better understand many crash related factors. To be included in FARS, a crash must involve a motor vehicle traveling on a traffic way customarily open to the public and result in the death of a person (occupant of a vehicle or a non-motorist) within 30 days of the crash. Since it only lists those crashes where there is at least one fatality, the problem of sample selection becomes obvious. Sample selection arises because a given individual's seatbelt usage affects his or her probability of death, which in turn influences whether the crash is included in the data [8]. If the death not occurred, the crash would not be recorded in FARS database. Furthermore, the same people may perform different behavior in different situations. For example, people have the awareness of fatal crashes have more chance occurred on highways with high speed, which is reasonable for more occupants choose to buckle up. The same one could be less likely to use seat belt when they are on local road for a quick trip. This affected the observation field seat belt usage data, while not showed from FARS data. Although providing a wealth of information on fatal crashes, obtaining seat belt usage from this data is limited.

FARS provides only those crashes where there is at least one fatality, which may lead to some bias in the sample selection [8]. Research performed by Salzberg and Yamada [9], indicate that FARS data may underestimate seatbelts usage when compared to estimates obtained from observational data. Salzberg et al. [9] investigated differences in seat belt use by the general public and belt us by motor vehicle occupants fatally injured in crashes. The study indicated that seat belt use rates obtained from FARS are much lower than the use rates found in observation surveys. A "straw man" model, describing the empirical relationship between FARS and observed usage rates, was developed. To examine the fit of the model, the state's FARS use rate was compared to the model's predicted rate. Corrections were made to the initial model to provide a more reasonable fit. The study concluded that unbelted occupants are over-represented in fatal collisions because these types of occupants have a greater likelihood of being involved with potentially fatal collisions in the first place, and because they are unbelted, the crash has a greater likelihood of being fatal.

Islam et al. [8] showed that FARS data can be a comparable alternative to the observational annual National Occupant Protection Use Survey (NOPUS) data. NOPUS is an annual survey providing the only probability-based observed data on seatbelt use in the United States. Although NOPUS is considered to be a reliable dataset, the data also has limitations because it is observational and based on the observer's ability to capture seat belt usage in a relatively short amount of time. The study found that NOPUS data can be used in estimating seat belt use once corrected for sample selection bias. Once the sample selection bias was corrected, the corrected FARS data can be applied as a comparable alternative to NOPUS estimates.

Factors influencing seat belt usage has been comprehensively studied. Common factors that have been identified are gender, age, income, time, familiarity of roadway, and geometric factors, such as [10, 11]. Very little work has been done to determine these factors that impact seat belt usage for back seat passengers. Some research reveal that the rear seat occupants' belt usage impact front occupants' injury severity. Mayrose et al. [12] studied the influence of unbelted rear seat passenger on driver mortality; logistic regression model disclosed that the probability of fatality for a belted driver in a head-on crash was 2.27 times greater with an unbelted rear seat passenger than if seated in front of a restrained passenger. However, the study was limited to whether unbelted left rear seat passenger increases the risk of death of belted driver involved in fatal crashes. The author applied FRAS data 1995–2001 involving belted driver with a left rear seat passenger.

40.4 Methodology

In this research, seat belt usage models are developed to examine the contribution of several variables to seat belt usage of back seat occupants in motor vehicles. Separate models were developed for back-left (behind the driver), back-middle and back-right (behind the front passenger) occupants. In these models seat belt usage is the dependent variable and is a binary or dichotomous variable with two categories, usage and non-usage.

Logistic regression was used to develop the seat belt usage models. Logistic regression falls in the class of models called generalized linear models. Generalized models are extensions of general linear models in which the assumptions of normality, linearity, and constant variance (Homoscedasticity) are removed. Maximum likelihood estimation is used after transforming the dependent variable into a logit variable (the natural log of the odds of the dependent variable occurring or not). The logistic function is given by:

$$F(Z) = \frac{1}{1 + e^{-z}}$$

or

$$P = \frac{e^{a + bX}}{1 + e^{a + bX}} \tag{40.1}$$

The “input” is Z and the output is $F(Z)$. The output $F(Z)$ takes values between 0 and 1. The variable Z represents the exposure to some set of risk factors. $F(Z)$ represents the probability of a particular outcome, given a set of risk factors. The variable Z is the measure of the total contribution of all the risk factors used in the model and is known as the Logit. Z is defined as:

$$Z = \alpha + \beta_k X_k \quad (40.2)$$

where α is called the intercept and the β_k are the regression coefficient of the X_k . That is $\beta_1, \beta_2, \beta_3, \dots, \beta_k$ are coefficients of $X_1, X_2, X_3, \dots, X_k$. The intercept is the value of Z when the values of all the risk factors are zero (i.e. the value of Z with no risk factors).

Substituting Eq. (40.2) into Eq. (40.1) yields:

$$F(Z) = \frac{1}{1 + e^{-(\alpha + \beta_k X_k)}} \quad (40.3)$$

Suppose $F(Z)$ is denoted as Y , then Eq. (40.3) becomes

$$Y = \frac{1}{1 + e^{-(\alpha + \beta_k X_k)}} \quad (40.4)$$

Each represents the size of the contribution of that risk factor. A positive regression coefficient implies that the risk factor increases the probability of the outcome, while a negative coefficient implies the risk factor decreases the probability of that outcome. A large regression coefficient implies the risk factor strongly influences the probability of that outcome; while a near zero value implies that the risk factor has little or no influence on the probability of that outcome.

The specific form of the logistic regression model in Eq. (40.1) is

$$\Pi(x) = \frac{e^{\alpha + \beta_1 x}}{1 + e^{\alpha + \beta_1 x}} \quad (40.5)$$

where Eq. (40.5) is transformed by using the natural log to develop a linear relationship between the dependent variable and the independent variables. The transformation of the function is known as the logit transformation:

$$g(x) = \ln \left[\frac{\Pi(x)}{1 - \Pi(x)} \right] = \alpha + \beta_1 x \quad (40.6)$$

The importance of transformation of the logit model (40.5) into (40.6) is that $g(x)$ has most of the properties of a linear regression model. The logit, $g(x)$ is linear in its parameters, may be continuous, and may range from $-$ to $+$.

In logistic regression the slope coefficient, is equal to the difference between the values of the independent variable at $x + 1$ and x , for any value x . That is

$$\beta_1 = g(x + 1) - g(x) \quad (40.7)$$

Therefore the slope coefficient represents the change in the logit for a change of one unit in the independent variable x .

Logistic regression calculates the probability of success over the probability of failure. Results are in the form of odds ratio. Odds ratio is the ratio of an event occurring to the likelihood of not occurring. An odd ratio also provides knowledge of the relationships and strengths among variables.

SPSS version 16.0 Statistical Software is used to develop the seatbelt usage model. In the SPSS result output for a logistic regression, the odds ratio for each independent variable is calculated as the exponential of the coefficient of that variable.

40.5 Data Collection

40.5.1 *Field Data*

Seat belt usage data were collected for drivers, front seat outboard passengers, and rear-seat passengers in passenger motor vehicles. Seat belt usage was obtained separately for three passenger motor vehicle types including: passenger cars, vans and sport utility vehicles (SUVs). Pick-up trucks were no included as these vehicles hardly have rear-seat passengers. For FARS data models, pick-up trucks were also not included to make sure that all models have the same variables.

The rear seat belt data is part of New Jersey “Click It or Ticket” campaign field survey conducted by New Jersey Institute of Technology graduate students in March 2010. NBA Games and pop-star concerts were selected because these events will attract more family members or friends. Two locations were identified to conduct the survey. One is Izod Center, East Rutherford, NJ. Another is Prudential Center, Newark, NJ. The data were collected two hours before the event starts. Eight surveyors divided into four groups, two people per group, one people observe whether the vehicle occupants use seat belt or not; another one recorded what were observed. Surveyors stood at the toll booths of parking decks or parking lots to observe the occupants seat belt usage when the vehicle stopped and rolled the window down to pay toll fees. Stopped vehicles are observed to permit time to collect the variety of information required by the survey. Observers do not interview vehicle occupants, so that the undisturbed behavior of vehicle occupants can be captured.

New Jersey’s Child Passenger Law requires the following:

- Children up to age 8 or 80 lb must ride in a safety or booster seat in the rear-seat of the vehicle. If there is no rear-seat, the child must sit in the front seat secured by a child safety seat or booster seat.
- Children under age 8 who weigh more than 80 lb must wear a seat belt anywhere in the vehicle.
- Passengers age 8–18 (regardless of weight) must wear a seat belt anywhere inside a vehicle.

For this reason, rear-seat passenger data were collected for three types of passengers: adults (older than 18), young (between 8 and 18) and child (under 8 years old). The age of the occupant was determined through observation by the data collector. Data were also collected by seating position of the rear-seat passengers including the left position (behind the driver), middle and right position (behind the front-seat passenger).

A total of 2923 vehicles were observed at two locations in New Jersey. Of these vehicles, 1915 back seat passengers were observed. Of the observe back seat passengers, 657 adults were observed with 178 or 27.09% using seat belts. A total of 516 youths were observed with 209 (40.5%) using seat belts. A total of 742 children were observed with 531 (71.56%) using seat belts. As the data shows, children have the highest seat belt usage and adults have the lowest among other age groups, probably because the safety of teenagers and kids are guarded by their parents. Most of adults go with their friends or adult family numbers who lack of the safety supervision. In addition, the usage rate of left back and right back seat occupants are relatively equal with the usage rate for the middle back seat lower than that of the other two back positions. This may be due to the fact that there almost 4 times more observations for right and left-back seat occupants compared to middle-seat occupants. Also, the seat belt usage of middle back seat passengers is more difficult to observe because for some vehicles, the middle seating position is a lap belt only, not a shoulder belt. In some cases, middle back seat passengers are conditioned to unbuckle when seated in the middle or with other back seat occupants.

40.5.2 FARS Data

Seat belt usage data were pulled out from the Fatality Analysis Reporting System (FARS) from 2004 to 2006 for New Jersey. FARS is a national wide database which contains data for all motor vehicle crashes that result in at least one fatality within 30 days of the crash. The database was created and maintained by the National Highway Traffic Safety Administration (NHTSA). The database records the crash information related to the environment, road conditions, circumstances of the crash, characteristics of the involved vehicles, and data on all related people involved in the crash.

FARS database was selected for this study for the reason that it contains many detail factors during the crash. In addition, it also contains restraint usage information for occupants during the crash. On the other hand, other existing databases, such as the New Jersey Department of Transportation Crash Database, are not suitable because it does not have information on restraint use for all occupants involved in the crash.

Three separate datasets were obtained from FARS database in developing the rear seat belt usage models. The datasets contain crash data factors for back-left, back-middle and back-right occupants in passenger cars, sport utility vehicles

Table 40.1 Model variable description

Variable	Description
Vehicle type	1 if passenger car; 2 if mini-van; 3 if SUV
Driver seat belt usage	1 if belted; 0 otherwise
Front passenger seatbelt usage	1 if belted; 0 otherwise
Left back passenger age	1 if Adult(>18); 2 if Youth (8–18); 3 if Child(<8)
Left back passenger seatbelt usage	1 if belted; 0 otherwise
Middle back passenger age	1 if Adult(>18); 2 if Youth (8–18); 3 if Child(<8)
Middle back passenger seatbelt usage	1 if belted; 0 otherwise
Right back passenger age	1 if Adult(>18); 2 if Youth (8–18); 3 if Child(<8)
Right back passenger seatbelt usage	1 if belted; 0 otherwise
Vehicle occupancy	2 if two people; 3 if three people; 4 if four people; 5 if five people

(SUV) and minivans. Crashes involved in large trucks, pedestrians, bicycles, motorcycles were not included in the study in order to consistent with field data. Variables used in the logistic regression models are obtained from the FARS database. These variables are treated as independent variables in the models. Table 40.1 gives a description of the variables used and how categorized in the models. A total of 10 independent variables are used in the models. The dependent variable—seat belt usage—is derived from the FARS data called “restraint system”.

A total of 1954 vehicles were recorded in New Jersey FARS data from 2004 to 2006. Of these vehicles, 3981 back seat passengers were recorded. Of the FARS data back seat passengers, 1600 adults were observed with 751 or 46.93% using seat belts. A total of 1206 youths were recorded with 687 (56.97%) using seat belts. A total of 1175 children were recorded with 789 (67.15%) using seat belts. As the data shows, all age group have similar usage rate, but children have the highest seat belt usage and adults have the lowest among other age groups which is the same as field data showed.

40.5.3 Data Comparison

Table 40.2 shows the seat belt usage rate comparison between observational data and FARS data. The overall usage rate for field data is 47.94% while the rate for FARS data is 55.94%. The figure below indicates that all FARS data categories have higher usage rate than field data by age groups and rear seat seating positions except children’s usage rate in left back seat. When compared the increase rate between two data sets, the rate of adult and youth have significant increase while the rate of children are in same level. The reason for the difference is the data

collection strategies; FARS data only recorded the accidents that involve death which cannot represent the general seat belt usage in all circumstances. In addition, the sample size should be another reason that has to be considered. In our case, we select similar sample size for both field data and FARS data (BL Field 822 vs. FARS 800; BM Field 225 vs. FARS 274; BR 870 vs. FARS 880, for example, “BL Field 822” means 822 vehicles that have passengers seating in left back seat in field data).

Table 40.2 Usage rate comparison

Back left						
	Adult		Youth		Child	
	Field	FARS	Field	FARS	Field	FARS
Usage rate (%)	26.06	48.83	43.87	57.88	72.09	62.29
Increase rate (%)	87.37		31.95		-13.60	
Back middle						
	Adult		Youth		Child	
	Field	FARS	Field	FARS	Field	FARS
Usage rate (%)	12.28	34.54	23.61	44.08	55.91	58.74
Increase rate (%)	181.24		86.71		5.05	
Back right						
	Adult		Youth		Child	
	Field	FARS	Field	FARS	Field	FARS
Usage rate (%)	30.70	48.51	42.67	63.04	75.54	77.65
Increase rate (%)	58.03		47.74		2.79	

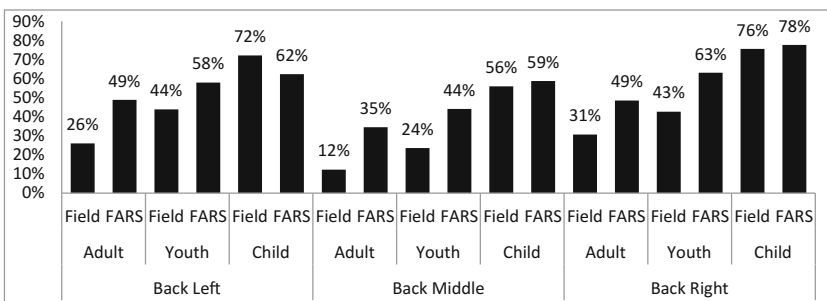


Table 40.3 Rear seat back seat belt usage models developed

Model number	Model description	
1	Field data	Left-back occupant seat belt usage
2	FARS data	
3	Field data	Middle-back occupant seat belt usage
4	FARS data	
5	Field data	Right-back occupant seat belt usage
6	FARS data	

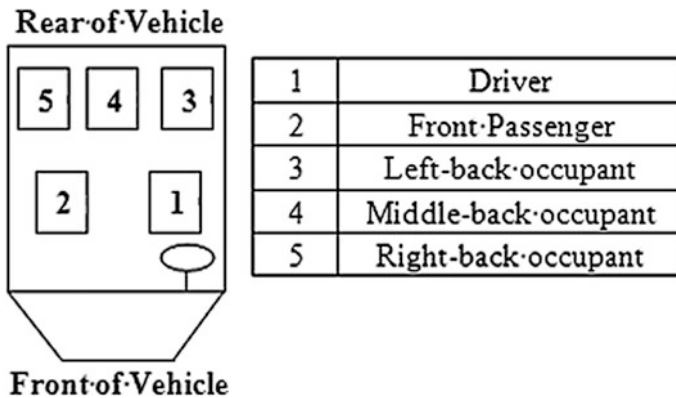


Fig. 40.1 Passenger positions

40.5.4 Analysis

Using the methodology described above for the seat belt usage model, models for left-back, middle-back and right-back seat passenger are developed. Models for each back seat position are developed using both field and FARS data. These models are described in Table 40.3 and Fig. 40.1. SPSS version 16.0 Statistical Software is used to develop the model.

The models examine the contribution of several variables that impact seat belt usage for each back seat occupant in a vehicle. The dependent variable is the back seat passenger seatbelt usage in the six models. Seatbelt usage in these models is a binary or dichotomous variable with two categories: usage and non-usage.

The variables used in the development of the logistic models are obtained from the field survey, and the FARS data variables are selected and coded as the same value of field data. Table 40.1 gives a description of the variables used and how they are coded in the models.

Results from these models are interpreted by examining the odds ratio and *p*-value for each of the model’s independent variable. Table 40.4 provides the coefficients and *p*-values for each model variable. The confidence level for all models is 90%.

Table 40.4 Model coefficients and *p*-values

Field data						
Variables	Left back seat		Middle back seat		Right back seat	
	Model 1		Model 3		Model 5	
	Coeff.	Sig.	Coeff.	Sig.	Coeff.	Sig.
<i>BLAge</i>		0.026		0.095		0.057
<i>BLAge</i> (1)	-3.216	0.013	3.003	0.030	-2.140	0.065
<i>BLAge</i> (2)					-2.476	0.047
<i>BLUsage</i>			4.419	0.000	1.933	0.032
<i>BMAge</i>		0.045		0.040		0.013
<i>BMAge</i> (1)	2.726	0.025	-3.077	0.012	3.046	0.014
<i>BMAge</i> (2)	2.646	0.041				
<i>BMUsage</i>	5.916	0.000			3.019	0.002
<i>BRAge</i>		0.078				0.002
<i>BRAge</i> (1)					-2.999	0.009
<i>BRAge</i> (2)	-3.563	0.025			2.844	0.038
<i>BRUsage</i>			2.873	0.002		
Constant	-2.929	0.001	-5.682	0.001	-1.573	0.005
FARS data						
Variables	Left back seat		Middle back seat		Right back seat	
	Model 2		Model 4		Model 6	
	Coeff.	Sig.	Coeff.	Sig.	Coeff.	Sig.
<i>VehicleType</i>		0.049				0.075
<i>Driver</i>	-1.884	0.068	-1.618	0.061	-2.028	0.072
<i>BLUsage</i>					-3.277	0.000
<i>BMAge</i>		0.001		0.000		
<i>BMAge</i> (1)	3.302	0.001				
<i>BMAge</i> (2)	4.731	0.000	-1.782	0.001		
<i>BMUsage</i>	-4.781	0.001			-2.303	0.000
<i>BRAge</i>		0.000				0.000
<i>BRAge</i> (1)	-3.825	0.001			-1.238	0.000
<i>BRAge</i> (2)	-6.621	0.000			-0.043	0.012
<i>BRUsage</i>			3.062	0.000		
Constant	-35.553	0.998	20.444	0.998	25.588	0.999

Vehicle Type

The vehicle type was found to be an insignificant factor for all models except left and right back passenger seat belt usage models using FARS data. However, when the different levels are considered and compared with the reference level “3” which is SUV, this variable is found to be insignificant as well. The result indicates that people choose to buckle no matter what kind of vehicle he or she is in.

Driver Seat Belt Usage

In this research, the driver's seat belt usage was considered for all back seat occupants using the FARS data. For the left-back occupant using the FARS data, model 2, the odds ratio for the driver seat belt usage is 0.152. Thus the odds of left back seat passenger using a seat belt are 0.152 times less when the drivers are not using their seat belt than when the driver is using a seat belt. For the middle back seat occupant using the FARS data, model 4, the odds ratio for the driver seat belt usage is 0.198 and coefficient estimated as -1.618 . Thus the odds of a middle back seat passenger using a seat belt are 0.198 times less when the driver is not buckled than when they are buckled. The odds of the right back seat passenger using a seat belt are 0.132 times less when the driver is not buckled. The result of FARS data indicates that driver seat belt usage has an impact on whether the back seat occupant will wear a seat belt.

The models developed using field data, however, did not show the same result with the driver's seat belt usage significant only for the middle back occupant model, model 3. Unlike the FARS data, the coefficient for this model is positive, 1.978.

Front Passenger Seatbelt Usage

The Front Passenger Seatbelt Usage variable is insignificant for all models using both FARS and field data. This indicates that the front passenger seat belt use does not have an impact on the whether the back seat passengers use their seat belts.

Back Passenger Age

The back passenger age variable was categorized into three levels: 1 for adult; 2 for youth and 3 for child, with the child level as the reference level. For the Left Back Passenger, age was found to be a significant factor for all the back seat occupant seat belt usage models using field data. This variable was not significant using FARS data. In Model 5, right back seat occupant seat belt model, the level 1 and level 2 coefficients of -2.14 and -2.476 variables are significant with p -values of 0.065 and 0.047, respectively. The odds ratios for these two levels are 0.118 and 0.084, therefore the odds of a middle back adult passenger using seat belt are 0.118 times less than children, while a middle back teenager passenger using seat belt are 0.084 times less than a child. Children have higher seat belt usage rate than adult and youth because children under 12 are required, under law, to be in a booster seat.

The Middle Back Passenger Age variable is significant in all models except for Model 6, right back seat occupant belt usage model. So both the FARS and field data showed this variable to be significant except for the right back seat occupant where the field data showed the middle back passenger age to be significant and the FARS data showed it was not significant. The middle passenger age variable was not significant by level for all the models. For the left back seat usage models, both the FARS and field data were significant at levels 1 and 2 with positive coefficients indicating that the odds for a left back seat occupant using their seat belt is more than a child.

For the middle back seat occupant field data model, Model 3, the odds of a middle back adult passenger using seat belt are 0.046 times less than a child. This is

different to the middle back seat occupant FARS data model, Model 4, which shows that the odds for a middle back seat occupant using a seat belt are more than a child.

The Right Back Passenger Age variable is significant for both the FARS and field data for the left back seat usage models and for the right back seat usage models. In addition, looking at the coefficients for the right back passenger age variable at its levels, the coefficients are generally consistent in sign between the FARS and field data models. For the left back seat model, all of the coefficient variables are negative. For the right back seat models, all but one of the coefficients is negative. For example, the Right Back Passenger Age variable is significant in Model 2 overall and for both levels with the reference level of “child”. For level 1, p -value is 0.001 and an estimate value of -3.825 . The odds ratio is 0.022. This shows that the odds of adult seating in right back side that will buckle seat belt are 0.022 times less than child in the right back seat.

In general, back seat passengers’ age is significantly impact their seat belt usage in most cases in this research. Adults have lower seat belt usage in the back seat than youth and children; this is proved both by the models and the data. Thus, measures that could improve back seat adult seatbelt usage will be considered in the future studies.

Back Passenger Seat Belt Usage

This variable determines whether one back seat passenger using a seat belt will impact the seat belt usage for the other back seat passengers. As the models are predicting the seat belt usage for the back seat passenger, only the remaining back seat belt usage not being predicted is used as independent variables.

The Left Back Passenger Seat Belt Usage variable was found to be significant in Model 3, middle back seat belt usage, and Model 5, right back seat usage, which is both models, developed using field data. In Model 5, the p -value is 0.032 and the coefficient estimate is 1.933. The reference category is the right back occupant being belted. Therefore, the odds of right back occupant being belted are 6.907 times more when the left back passenger is belted than not belted.

The Middle Back Passenger Seat Belt Usage variable was found to be significant in both the FARS and field data left back seat usage models, Models 1 and 2, and in the right back seat usage models, Models 5 and 6. In both the left back seat models and in the right back seat models, the coefficient for the FARS data is negative and the coefficient for the field data is positive. In Model 5, the right back seat model using the FARS data, the p -value is 0.02 and the coefficient estimate is 3.019. The reference category is the middle back occupant being belted. Therefore, the odds of right back occupant being belted are 20.47 times more when the middle back passenger is belted than not belted. A similar result could be found in Right Back Passenger Seat Belt Usage variable. It can be concluded that the seat belt usage of back seat passengers is interact each other if more than one back seat occupants.

Vehicle Occupancy

This variable was found to be insignificant in all of the models and indicates that the number of people in a vehicle will not impact whether a back seat occupant uses their seat belt.

40.5.5 Predicted Logistic Regression Model

The predicted logistic regression model for left back seatbelt usage model using field data, model 1 is given as:

$$\text{Log}\left(\frac{p}{1-p}\right) = -2.929 - 3.216\text{BLA}(1) + 2.726\text{BMA}(1) + 20.646\text{BMA}(2) + 50.916\text{BMU} + 30.563\text{BRA}(2)$$

where,

- p Probability of wearing a seat belt
- BLA(1) Left back seat adult passenger
- BMA(1) Middle back seat adult passenger
- BMA(2) Middle back seat youth passenger
- BMU Middle back seat passenger seatbelt usage
- BRA(2) Right back seat youth passenger

The predicted logistic regression model for left back seatbelt usage model using FARS data, model 2 is given as:

$$\text{Log}\left(\frac{p}{1-p}\right) = -35.553 - 1.884\text{DR} + 3.302\text{BMA}(1) + 40.731\text{BMA}(2) - 4.781\text{BMU} - 30.825\text{BRA}(1) - 6.621\text{BRA}(2)$$

where,

- p Probability of wearing a seat belt
- DR Driver seatbelt usage
- BMA(1) Middle back seat adult passenger
- BMA(2) Middle back seat youth passenger
- BMU Middle back seat passenger seatbelt usage
- BRA(1) Right back seat adult passenger
- BRA(2) Right back seat youth passenger

The predicted logistic regression model for middle back seatbelt usage model using field data, model 3 is given as:

$$\text{Log}\left(\frac{p}{1-p}\right) = -5.682 + 3.003\text{BLA}(1) + 4.419\text{BLU} - 3.007\text{BMA}(1) + 2.873\text{BRU}$$

where,

- p Probability of wearing a seat belt
- BLA(1) Left back seat adult passenger
- BLU Left back seat passenger seatbelt usage
- BMA(1) Middle back seat adult passenger
- BRU Right back seat passenger seatbelt usage

The predicted logistic regression model for middle back seatbelt usage model using FARS data, model 4 is given as:

$$\text{Log}\left(\frac{p}{1-p}\right) = 20.444 - 1.618\text{DR} - 1.782\text{BMA}(2) + 3.062\text{BRU}$$

where,

- p Probability of wearing a seat belt
- DR Driver seatbelt usage
- BMA(2) Middle back seat youth passenger
- BRU Right back seat passenger seatbelt usage

The predicted logistic regression model for right back seatbelt usage model using field data, model 5 is given as:

$$\begin{aligned} \text{Log}\left(\frac{p}{1-p}\right) = & -1.573 - 2.14\text{BLA}(1) \\ & - 2.476\text{BLA}(2) + 1.933\text{BLU} + 3.046\text{BMA}(1) + 3.019\text{BMU} \\ & - 2.999\text{BRA}(1) - 2.844\text{BRA}(2) \end{aligned}$$

where,

- p Probability of wearing a seat belt
- BLA(1) Left back seat adult passenger
- BLA(2) Left back seat youth passenger
- BLU Left back seat passenger seatbelt usage
- BMA(1) Middle back seat adult passenger
- BMU Middle back seat passenger seatbelt usage
- BRA(1) Right back seat adult passenger
- BRA(2) Right back seat youth passenger

The predicted logistic regression model for right back seatbelt usage model using FARS data, model 6 is given as:

$$\begin{aligned} \text{Log}\left(\frac{p}{1-p}\right) = & 25.588 - 2.028\text{DR} - 3.277\text{BLU} - 2.303\text{BMU} - 1.238\text{BRA}(1) \\ & - 0.043\text{BRA}(2) \end{aligned}$$

where,

- p Probability of wearing a seat belt
- DR Driver seatbelt usage
- BLU Left back seat passenger seatbelt usage
- BMU Middle back seat passenger seatbelt usage

- BRA(1) Right back seat adult passenger
- BRA(2) Right back seat youth passenger

40.6 Conclusions

The research showed both similar and differing results between the models produced using FARS data and those produced using field data. All the models using the FARS data showed a strong correlation between the back seat passenger's seat belt usage and the driver's seat belt usage. This may be due to the fact that a large proportion of back seat occupants are children and teenagers who required buckling by the laws which may be why age influences these occupants' seat belt usage. Only the middle back seat usage model developed using the field data showed significance and the results were opposite, different coefficient signs, compared to the coefficients developed using the FARS data.

Mixed results were obtained between FARS data and field data for the back seat occupant age variable. In some cases the results between the models produced by the two data are similar, in other cases it is not. Similar mixed results were also found for the back seat passenger usage as an independent variable. It is also found that back seat occupants' seatbelt usage was influenced by the other back passengers' usage. This indicates the presence of interaction among back seat occupants. The result shows that a single back seat passenger is less likely to be belted than if more than one back seat passenger is belted. In addition, New Jersey passengers are more aware of using their seat belts when seated in the back row due to the secondary state law.

The research shows there are differences in the factors that influence seat belt usage using field data and FARS data. The models developed were limited in the variables used as the primary focus of the field data collection was to obtain the back seat belt usage. Although further research is warranted to understand the limitations of FARS in looking at overall passenger restraint, the wealth of data provided through FARS still makes this data to be a valuable tool for safety research. Care must be taken, however, in the use of this data with regard to safety research looking at passenger restraint. Future studies are needed to find a better approach to obtain back seat belt usage data and to include additional factors not traditionally used in back seat belt usage models that may influence the seat belt usage for back seat occupants.

Acknowledgements This study was funded by the New Jersey Division of Highway Traffic Safety and New Jersey Institute of Technology as a part of the research project Seat Belt Study. The authors would like to thank Mr. Robert Gaydosh who served as the Project Manager.

References

1. National Highway Traffic Safety Administration. Lives Saved in 2008 by Restrain use and Minimum Drinking Age Laws, U.S. Department of Transportation, National Highway Traffic Safety Administration, Washington, DC
2. Pickrell MT, Ye JT, Occupant Restraint Use in 2010: Results from the National Occupant Protection Use Survey Controlled Intersection Study, U.S. Department of Transportation, National Highway Traffic Safety Administration, Washington, DC
3. Cunill M, Gras ME, Planes M, Oliveras C, Sullman MJ (2004) An Investigation of Factors Reducing Seat Belt Use Amongst Spanish Drivers and Passengers on Urban Roads. *Accid Anal Prev* 36(3):439–445
4. Eluru N, Bhat CR (2007) A joint econometric analysis of seat belt use and crash-related injury severity. *Accid Anal Prev* 39(5):1037–1049
5. Strine TW, Beck LF, Boden J, Okoro C, Dhingra S, Balluz L (2010) Geographic and sociodemographic variation in self-reported seat belt use in the United States. *Accid Anal Prev* 42(4):1066–1071
6. Cunill M, Gras ME, Planes M, Oliveras C, Sullman MJ (2004) An investigation of factors reducing seat belt use amongst spanish drivers and passengers on urban roads. *Accid Anal Prev* 36(3):439–445
7. Daniel J, Bladikas A, Curley J (2007) Factors influencing seat belt usage rate for blacks and hispanics. *Transp Res Rec J Transp Res Board* 2009:74–81
8. Islam S, Goetzke F (2009) Correcting sample selection in FARS data to estimate seatbelt use. *J Saf Res* 40(5):389–393
9. Salzberg P, Yamada A, Saibel C, Moffat J (2002) Predicting seat belt use in fatal motor vehicle crashes from observation surveys of belt use. *Accid Anal Prev* 34(2):139–148
10. Boontob N, Tanaboriboon Y, Kanitpong K, Suriyawongpaisal P (2007) Effect of seat belt use on road accidents in Thailand. *Transp Res Rec J Transp Res Board* 2038:84–92
11. Briggs NC, Schlundt DG, Levine RS, Goldzweig IA, Stinson N, Jr, Warren RC (2006) Seat belt use among hispanic ethnic subgroups of national origin. *Inj Prev* 12:421–426
12. Mayrose J, Jehle D, Hayes M, Tinnesz D, Piazza G, Wilding GE (2005) Influence of the unbelted rear-seat passenger on driver mortality: “the backseat bullet.” *Acad Emerg Med* 12(2):130–134

Chapter 41

Study on Dynamic Torque PID Control for Automobile Diaphragm Spring Clutch Based on Kalman Filter

Chen Shao, Xue Bin Wu, Xin Zhang and Hong Wei Chen

Abstract This paper built a power transmission model based on Parallel Hybrid Electric Vehicle (PHEV). Based on this model, the Kalman filtering algorithm which was used to estimate the clutch transmitting torque was derived by the state vector which consist of the engine rotation torque and speed. The PID controller which was built based on the Kalman filtering was used to control the deviation between estimated torque and target torque. And the control errors are analyzed by comparing the controlled values and simulated values of the clutch torque at vehicle starting process by engine-driven. The conclusion show that the PID controller has the sufficient accuracy and response speed. Therefore, the PID controller of clutch transmitting torque are feasible.

Keywords PHEV · Diaphragm spring clutch · Kalman filtering · Torque · PID

41.1 Introduction

To improve the control performance and stability of automobile clutch during the switching process in Hybrid Electric Vehicle, the engine torque and clutch transmission torque must be coordinated. It is particularly important to control the engagement of automated clutch in the various driving cycle. But the clutch friction torque is immeasurable in the driving process. Clutch torque cannot be controlled directly in the process of PHEV mode switch. Many control methodologies of clutch engagement have been discussed through many research activities. Esenovskiy-Lashkovy and Polyak [1] introduced a strategy aiming at controlling the throttle angle and the engine speed. The results show that the control strategy cannot satisfy driver's comfort. It is defective to set the engine information as single basis for clutch engagement law. Glielmo et al. [2] proposed the optimal methods

C. Shao (✉) · X.B. Wu · X. Zhang · H.W. Chen
School of Mechanical, Electronic and Control Engineering,
Beijing Jiaotong University, Beijing 100044, China
e-mail: 15121353@bjtu.edu.cn

based upon the clutch release bearing position, engine speed and main-shaft speed on power transmission system model. The transmission load torque is transferred to the main shaft on this model which is assumed as rigid body.

In this paper, Kalman filter technology is applied to the clutch torque estimation. Based on dynamic analysis on the model of power transmission system, the transmission friction torque in the process of clutch engagement is estimated by Kalman filter. The discrete incremental PID controller of the friction torque is designed based on the control parameters which are made of the estimated torque and the specific torque, so that the clutch torque can be controlled placidly during clutch combination and separation.

41.2 PHEV Powertrain Model

The PHEV powertrain system includes the engine mode, motor model, battery model, clutch model, transmission model, main reducer, mechanical accessories and other electric components. The schematic diagram of coaxial parallel hybrid electric vehicle (PHEV) of powertrain system is shown in Fig. 41.1.

It is clear that the motor is arranged between the automatic clutch and the transmission in this system from Fig. 41.1. The parallel hybrid power system is very close to the traditional automobile power system in the structure, which is good in inheritance and easy to realize industrialization.

When the clutch is in separation/sliding, the powertrain system has two degrees of freedom. The engine is acted by engine torque and clutch transmission torque together. And the input shaft of AMT is acted by motor torque and clutch transmission torque. The dynamic equation is

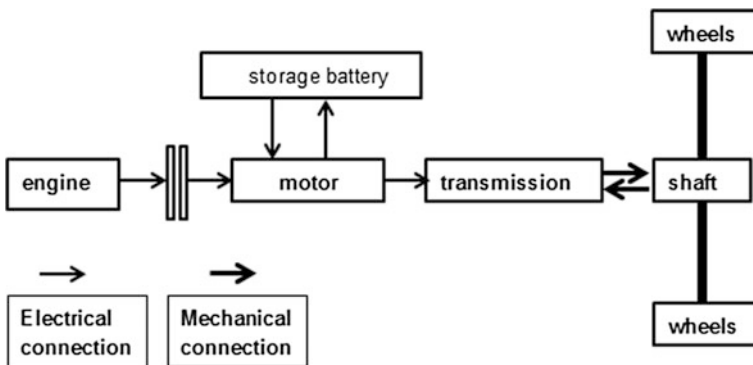


Fig. 41.1 Coaxial parallel hybrid system based on AMT

$$\begin{aligned}
J_e \dot{w}_e &= T_e - T_c \\
J_m \dot{w}_m + J_{veh} \dot{w}_{whl} / (i_g i_0) &= T_m + T_c - T_{load} / (i_g i_0) \\
\dot{w}_m &= \dot{w}_{whl} \times i_g i_0
\end{aligned} \tag{41.1}$$

When the automatic clutch is in fully joint position, the powertrain system has only one degree of freedom. The clutch transmission torque turn into the internal force of the transmission shaft. The shaft is acted by the motor and the engine torque together. The dynamic equation is

$$\begin{aligned}
[J_e + J_m + J_{veh} / (i_g i_0)] \dot{w}_m &= T_m + T_e - T_{load} / (i_g i_0) \\
\dot{w}_m = \dot{w}_{whl} = \dot{w}_e
\end{aligned} \tag{41.2}$$

$$J_{veh} = \frac{mr^2 + \sum_{i=1}^4 J_w(i)}{i_0^2 i_g^2} \tag{41.3}$$

where

- J_e is the rotation inertia of the engine
- J_m is the rotation inertia of the engine
- J_{veh} is equivalent to the transmission shaft rotation inertia
- w_e is the engine angular velocity
- w_m is the motor angular velocity
- w_{whl} is equivalent to the transmission shaft angular velocity
- T_e is the engine torque
- T_m is the motor torque
- T_{load} is equivalent to the transmission shaft resistance torque
- i_g is current gear transmission ratio of gearbox
- i_0 is main speed reducer's ratio
- m is the mass
- r is the tire rolling radius
- J_w is the rotation inertia of the tire

By ignoring the effects of wind speed and driving wheel slip, T_{load} can be calculated as follows:

$$T_{load} = \frac{r\eta}{i_0 i_g} [mg(f + i) + \frac{C_d A}{1.632} (\frac{w_{whl} \times r}{i_0 i_g})^2] \tag{41.4}$$

where: f is rolling resistance factor, I is road slope, A is the windward area, C_d is the wind resistance coefficient.

By Eqs. (41.1), (41.2), (41.3), (41.4), the complete equations of power transmission system can be established. The vehicle parameters are shown in Table 41.1

Table 41.1 Vehicle parameters

Parameters	Value	Units
m (vehicle equipment quality)	15,500	kg
r	0.4643	m
A	6.73	m ²
C _d	0.65	
J _e	0.3	kg m ²
J _m	0.2	kg m ²
f	0.015	
i ₀	6.17	
i _g	3.71	
η	0.85	
J _w	1.1	kg m ²
i	0.018	rad

41.3 Clutch Torque Estimation Model Based on Kalman Filter Arithmetic

The being measured data is taken as the estimator in the soft sensing method based on the state estimation. The principle and application of this method are simple and the measured data can be estimated accurately as long as the measured object’s mathematical model can be reflected precisely. In this paper, Kalman filter technology is based on state estimation.

41.3.1 System State Space Model

Based on the model of vehicle power transmission system, the Kalman filter estimator is used to estimate the transmission torque of the clutch, which is obtained by measuring the angular velocity of the engine and the torque of the engine.

The state space model for Kalman filtering is as follows

$$x_{k+1} = Ax_k + Bu_k \tag{41.5}$$

$$Y = Cx_k \tag{41.6}$$

The state variable in the equation is

$$x_k = \begin{bmatrix} \omega_e(k+1) \\ \omega_e(k) \\ T_c(k+1) \\ T_c(k) \end{bmatrix} \tag{41.7}$$

The control input variable u_k is

$$u_k = \begin{bmatrix} T_e(k+1) \\ T_e(k) \end{bmatrix} \quad (41.8)$$

The measurement output variable Y is

$$Y = [\omega_e(k)] \quad (41.9)$$

where

ω_e is the engine speed

T_c is the Clutch transmission torque

T_e is the engine torque

41.3.2 State Space Model Parameter

After state space model is derived, the parameters that are used in the program of Kalman filter estimation algorithm need be calculated. Dynamic transmission equation can be written as

$$T_e - T_c = j_e \dot{\omega} \quad (41.10)$$

$$\dot{T}_e - \dot{T}_c = j_e \ddot{\omega} \quad (41.11)$$

The discrete equation is

$$\omega_e(k) = \frac{\Delta T}{J_e} [T_e(k) - T_c(k)] + \omega_e(k-1) \quad (41.12)$$

$$\omega_e(k+1) = \frac{\Delta T}{J_e} [T_e(k+1) - T_c(k+1)] + \omega_e(k) \quad (41.13)$$

$$T_c(k+1) = T_e(k+1) - T_e(k) + T_c(k) - \frac{J_e}{\Delta T} [\omega_e(k+1) - 2\omega_e(k) + \omega_e(k-1)] \quad (41.14)$$

$$x_{k+1} = A_1 x_{k+1} + A_2 x_k + B_1 x_k \quad (41.15)$$

$$Y = C x_k \quad (41.16)$$

The coefficient matrix is

$$A_1 = \begin{bmatrix} 0 & 0 & 0 & 0 \\ 0 & 1 & 0 & 0 \\ \frac{J_e}{\Delta T} & -\frac{J_e}{\Delta T} & 0 & 0 \\ 0 & 0 & 0 & 0 \end{bmatrix} \quad C = \begin{bmatrix} 1 \\ 0 \\ 0 \\ 0 \end{bmatrix}$$

$$A_2 = \begin{bmatrix} 0 & 1 & -\frac{\Delta T}{J_e} & 0 \\ 0 & 0 & 0 & -\frac{\Delta T}{J_e} \\ -\frac{J_e}{\Delta T} & \frac{J_e}{\Delta T} & 0 & 1 \\ 0 & 0 & 0 & 1 \end{bmatrix} \quad B_1 = \begin{bmatrix} \frac{\Delta T}{J_e} & 0 \\ 0 & \frac{\Delta T}{J_e} \\ 1 & -1 \\ 0 & 0 \end{bmatrix}$$

The coefficient matrix is

$$A = [I - A_1]^{-1}A_2 \quad (41.17)$$

$$B = [I - A_1]^{-1}B_1$$

The system state space model has been established based on the above equation.

41.3.3 The Simulink Model Based on Kalman Filter

The classical Kalman filter algorithm equation is

$$\begin{cases} \text{time-update-equation} \begin{cases} \hat{x}_{k/k-1} = \varphi_{k,k-1}\hat{x}_{k-1} \\ \hat{P}_{k/k-1} = \varphi_{k,k-1}\hat{P}_{k-1}\varphi_{k,k-1}^T + Q_{k-1} \end{cases} \\ \text{status-update-equation} \begin{cases} K_k = P_{k/k-1}H_k^T / [H_k P_{k/k-1}H_k^T + R_k] \\ \hat{x}_k = \hat{x}_{k/k-1} + K_k[Z_k - H_k\hat{x}_{k/k-1}] \\ P_k = [I - K_kH_k]P_{k/k-1} \end{cases} \end{cases} \quad (41.18)$$

where:

- $\hat{x}_{k/k-1}$ is state of the predicted from the moment $k - 1$ to k ;
- \hat{x}_k is state of the estimated value in the moment of k ;
- K_k is the filter gain matrix on in the moment of k ;
- $\hat{P}_{k/k-1}$ is the covariance matrix of predicted error from the moment $k - 1$ to k ;
- P_k is the covariance of estimated error in the moment of k ;
- Q_{k-1} is the covariance matrix of systematic noise;
- R_k is the measurement noise covariance.

The clutch transmission torque program is written in the Matlab. And the Simulink model is established based on the Kalman filter to estimate the clutch transmission torque at the start process of the engine (Fig. 41.2).

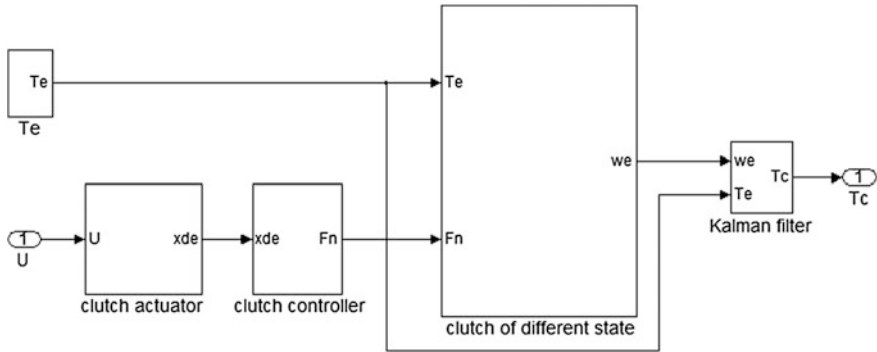


Fig. 41.2 The Simulink model of torque estimation

41.4 PID Controller for Clutch Torque

The PID controller can control the deviation between estimation value and target value of the clutch torque in real time, so that the optimal clutch control can be obtained.

41.4.1 PID Controller Design

PID controller is a linear controller and its control input is the deviation between target value and actual value. The equation is

$$e(t) = r(t) - c(t) \tag{41.19}$$

Clutch torque follow PID control law can be expressed as:

$$u(k) = k_p e(k) + k_i \sum_{j=0}^k e(j)T + k_d \frac{e(k) - e(k - 1)}{T} \tag{41.20}$$

where

$e(k)$ is engine torque deviation; K_p is PID ratio coefficient; K_i is PID integral coefficient; K_d is PID differential coefficient; $u(k)$ is PID output; T is sampling period. Under the Simulink environment, the PID control model of power transmission system is set up on the condition of starting process driven by engine (Fig. 41.3).

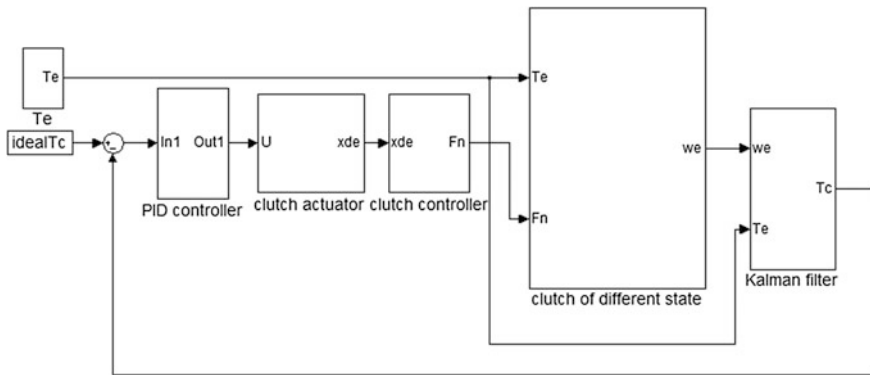


Fig. 41.3 The torque estimation Simulink model of system PID controller

Table 41.2 Regulator experience data sheet for critical proportion method

Regulating law	P (%)	T _I	T _D
P	2 P _m		
PI	2.2 P _m	0.85 T _m	
PID	1.7 P _m	0.5 T _m	0.13 T _m

P_m and T_m can be calculated by the pure proportion
 P_m = 2.432335, T_m = 1.3 ms

41.4.2 Parameters Setting and Analysis of PID Controller

The process of determining the proportional, integral and differential coefficient is called parameters setting of PID controller. The three parameters are closely related to the control effect of the controlled system, which determine the quality of the controlled object.

The critical proportion method (also known as the stability boundary method) is used in the paper. The regulating law is to increase the proportion coefficient ceaselessly based on the pure proportion, and then make the controlled parameter of the system being the steady boundary. And each coefficient can be calculated according to the empirical data of Table 41.2 after measuring the ratio of the amplification factor K_m or the critical ratio P_m and the oscillation period T_m.

And the sampling period of PID is 1 ms. K_i and K_d can be calculated as follows:

$$K_i = K_p \frac{T}{T_i} \quad K_d = K_p \frac{T_d}{T} \quad (41.21)$$

K_i = 6.3615, K_d = 0.7

The PID control effect is shown in Fig. 41.4a.

It can be seen from the figure that the system static error has been eliminated, but the overshoot is larger, and the response time is long, so the PID parameters should be further adjusted on the basis of the above. Finally, the optimal parameters are as

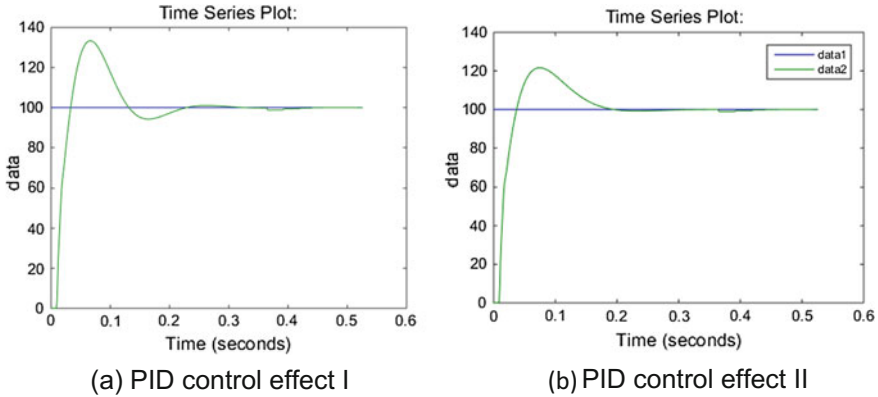
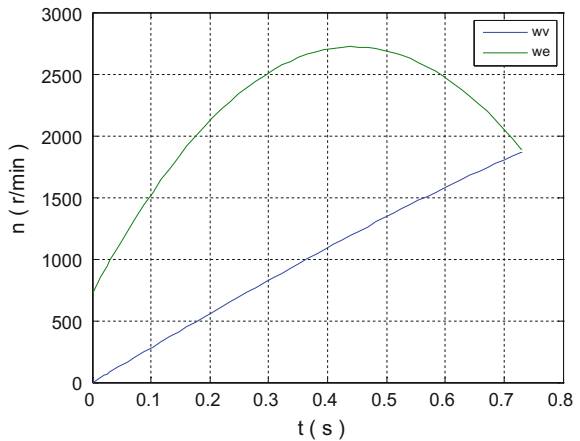


Fig. 41.4 PID control setting

Fig. 41.5 Clutch speed simulation at starting process



follows: $K_p = 5.324$, $K_i = 2241$, $K_d = 0.86$. The PID control effect is shown in Fig. 41.4b.

It can be seen that the PID control error is very small, and the dynamic response speed is relatively fast, so the design of the PID controller can meet the requirements.

41.5 PID Control Simulation and Analysis of Clutch Torque at Starting Process Driven by Engine

Engine torque and DC motor voltage are given: $T_e = 200$ Nm, $U = 24$ V. The figure of the engine speed and the wheel speed at starting process is shown. Where we is engine speed and wv is clutch speed in Fig. 41.5.

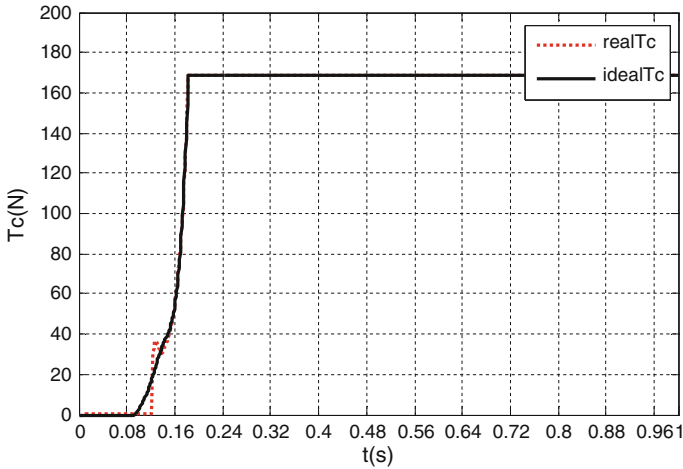


Fig. 41.6 Clutch simulation by PID at starting process

The coefficient of PID can be obtained through the above PID setting process as follows:

$$K_p = 5.324, \quad K_I = 2241, \quad K_D = 0.86$$

According to the established PID control system above, the clutch torque is simulated at starting process driven by engine (Fig. 41.6).

41.6 Conclusion

A parallel hybrid electric vehicles is taken as the research object and the model of powertrain system with automatic clutch is built in this paper.

The discrete state equations and the observation equations for torque estimation of clutch are derived on the starting condition driven by engine. Clutch transmission torque estimation method is designed based on discrete Kalman filter. The estimation value and the target value are taken as two parameters. The PID clutch torque following controller is designed to control the transmission torque of the automatic diaphragm spring clutch in real time.

Through the analysis above, the deviation of Kalman filter estimation is relatively small. And the PID controller can meet the requirements of the torque tracking accuracy and response speed. It can be applied to the control of automatic clutch transmission torque, which can realize the stability of the control performance during the lifetime of the clutch and improve the quality of the switching process of the HEV mode.

References

1. Esenovskiy-Lashkov Y, Polyak D (1996) New concept of automatic control for a passenger car clutch. Proc Inst Mech Eng Part D J Automobile Eng 210(3):227–233
2. Glielmo L, Iannelli L, Vacca V, Vasca F (2006) Gearshift control for automated manual transmissions. IEEE/ASME Trans Mechatron 11(1):17–26

Chapter 42

Research on Parameters Optimization of Transmission System of Military Off-Road Vehicle

Bo Li, Xueyuan Li, Wei Wu, Junjie Zhou and Chaoheng Qin

Abstract The working conditions of Military off-road vehicles are harsh and complex, which put forward higher requirements on vehicle dynamic performance. Parameters of the transmission system obtained by the traditional geometric series division method is usually difficult to achieve good dynamic property and fuel economy. This paper proposed a comprehensive objective function of dynamic property and fuel economy based on weight coefficient method. On the basis of the traditional geometric series division method, considering the dynamic constraint conditions of off-road vehicles, a set of optimal transmission parameters are confirmed using the nonlinear optimization function `fmincon` in Matlab optimization toolbox. Simulation results show that the acceleration time and fuel consumption reduced after optimization, and the military off-road vehicles achieved a better dynamic property and fuel economy.

Keywords Powertrain system · Dynamic property · Fuel economy · Optimization and simulation · Vehicle dynamics

42.1 Introduction

Military off-road vehicles are always working on the harsh conditions such as desert, earthen road and hills. It put forward higher technical and tactical requirements to dynamic property of vehicles. The traditional geometric series division method based on experience is difficult to satisfy the higher requirements on

B. Li · X. Li · W. Wu · J. Zhou · C. Qin
Science and Technology on Vehicular Transmission Laboratory,
Beijing Institute of Technology, Beijing 100081, P.R. China

X. Li (✉)
Beijing Institute of Technology, Room 412, Building 9, Beijing 100081, P.R. China
e-mail: bit_libo@foxmail.com

dynamic property and fuel economy. Generally speaking, there are two effective schemes to improve the vehicle dynamic property: (1) use engines with higher power and larger torque; (2) improve the matching of powertrain systems to exploit the maximum dynamic property of the engine. In the case of the selected engine, the second scheme is usually adopted [1]. In recent years, many researchers have done lots of research on powertrain matching and optimization and proposed some useful methods. Yao et al. established automatic transmission powertrain system optimal model, and developed powertrain parameters simulation programs. Lei built powertrain system model in ADVISOR software, and optimized the vehicle powertrain parameters using genetic algorithm [2]. Wang et al. built joint multi-objective powertrain optimization model on the basis of GT-Drive and GADST direct search toolbox. However, the optimization methods above are complex and need large amount of programs, which cost too much simulation time. To simplify the optimization process, this paper build powertrain model of off-road vehicles based on nonlinear optimization function *fmincon* in Matlab optimization toolbox. The maximum speed, dynamic factors, maximum climbable gradient, and road adhesion are regarded as constraint conditions of extreme driving mode. Main reducer ratio and gear transmission ratios are chosen as design variables. Acceleration time and fuel consumption of six cycle conditions are chosen as objective functions to indicate dynamic property and fuel economy of the vehicles. Weight coefficient method is adopted to allocate proportion of dynamic property and fuel economy. Better dynamic property and fuel economy is achieved after simulation and optimization in Matlab.

42.2 Mathematical Model of Powertrain Optimization

42.2.1 Definition of Design Variables

Powertrain system of vehicles includes engine, gear transmission, main reducer and differential. In the case of the selected engine, total transmission ratios of the powertrain system make a big difference on vehicle dynamic property and fuel economy, that is the product of the main reducer ratio and gear transmission ratio of each level [3]. In the process of the powertrain optimization, this paper neglect the reverse gear and just consider the forward gears. The optimal object is a 5-leveled military off-road vehicles, and the design variables are as follows:

$$x = [x_1, x_2, x_3, x_4, x_5, x_6] = [i_{g1}, i_{g2}, i_{g3}, i_{g4}, i_{g5}, i_0]$$

where i_{gj} ($j = 1, 2, \dots, 5$) is the transmission ratio of j level, i_0 is the main reducer transmission ratio.

42.2.2 Establishment of Objective Functions

The matching and optimization of the vehicle powertrain parameters is a multi-objective problem. It aims at improving the dynamic property and fuel economy at the same time. However, the various objectives of the multi-objective optimization problem in general conflict with each other. Improvement of dynamic property leads to deterioration of fuel economy, the same as the inverse. So it is difficult to objectively evaluate the superiority-inferiority of the solution to a multi-objective optimization problem [4]. One non-domination optimal solution set is obtained in general, elements of which are named Pareto optimal solution. So it is very important to choose a proper weight coefficient between dynamic property and fuel economy to get the Pareto optimal solution.

42.2.2.1 Dynamic Property Sub-objective Function

Vehicle dynamic property includes three indicators: maximum velocity v_{max} , maximum climbable gradient α_{max} and acceleration time t respectively. The first two indicators focus on the extreme driving capability of the vehicles, while acceleration time indicates the comprehensive dynamic property of the vehicles. The continuous shift acceleration time t on the flat pavement is chosen as the dynamic property sub-objective function, while the maximum velocity v_{max} and the maximum climbable gradient α_{max} are regarded as constraint conditions. According to the vehicle driving equation, the acceleration expression is as follows in Eq. (42.1):

$$\frac{du}{dt} = \frac{1}{\delta m} \cdot [F_t - F_f - F_w] \quad (42.1)$$

Then, dynamics sub-objective function $f_1(X)$ is obtained. The mathematical expression is as follows in Eq. (42.2):

$$f_1(X) = t = t_0 + \int_{u_{min}}^{u_i} \frac{\delta \cdot m}{3.6 \times [F_t - F_f - F_w]} du \quad (42.2)$$

where m is the mass of vehicle, kg; δ is the conversion factor of vehicle rotational mass; t is the continuous shift acceleration time, s; F_t is the driving force, N; F_f is the rolling resistance force, N; u is the velocity, km/h; F_w is the air resistance force, N; t_0 is the initial time, s; we usually assume that the vehicle is at a minimum starting velocity in the initial time, and neglect the slipping and friction process of the clutch, that is $t_0 \approx 0$; shift time t_s is regarded as a constant, $t_s = 0.45$ s.

The mathematical expression of F_t is as shown in Eq. (42.3):

$$F_t = \frac{T_{iq} \cdot i_0 \cdot i_{gj} \cdot \eta_T}{r} \quad (42.3)$$

where η_T is the transmission efficiency of powertrain system, the value is 0.85; T_{iq} is the engine output torque, N m; r is the rolling radius of the wheel, m;

The mathematical expression of F_f is as shown in Eq. (42.4):

$$F_f = f \cdot F_N \quad (42.4)$$

where f is the rolling resistance coefficient, $f = 0.03$ in the field environment; F_N is the normal force, N; $F_N \approx G = mg$ in the flat pavement, g is the acceleration of gravity, m/s^2 .

The mathematical expression of F_w is as shown in Eq. (42.5):

$$F_w = \frac{C_d A u^2}{21.15} \quad (42.5)$$

where C_d is the air resistance coefficient; A is the frontal area of the vehicle, m^2 .

42.2.2.2 Fuel Economy Sub-objective Function

Fuel consumption per 100 km at a constant velocity is commonly used as the evaluation index of fuel economy. It doesn't fully characterize the fuel consumption in the actual conditions. This paper adopt the fuel consumption per 100 km in six-cycle conditions as the fuel economy sub-objective function $f_2(X)$. The expression is as shown in Eq. (42.6):

$$f_2(X) = Q_s = \frac{\sum Q}{s} \times 100 \quad (42.6)$$

where $\sum Q$ —total fuel consumption in the whole process, mL; s —total distance, km.

42.2.2.3 Comprehensive Objective Function

Comprehensive objective function of the dynamic property and fuel economy is established using weight coefficient method. The expression is as follows in Eq. (42.7):

$$F(X) = \lambda_1 f_1(X) + \lambda_2 f_2(X) \quad (42.7)$$

where λ_1, λ_2 is the weight coefficient of vehicle performance. Considering the special requirements for the dynamic property of the military off-road vehicles, the value of λ_1 is set as 0.7 while λ_2 is 0.3.

42.2.3 Automotive Engine Model

For the automotive engine model, we adopt the following fitting method to obtain the external and universal characteristic curves of the engine.

- (1) External characteristic equation of engine output torque is as shown in Eq. (42.8):

$$M_e = \sum_{i=0}^k A_i n_e^i, \quad i = (0, 1, 2, 3, \dots, k) \tag{42.8}$$

where:

- M_e engine output torque, N m;
- n_e engine speed, r/min;
- A_i engine external characteristics fitting coefficient;
- k polynomial order, $k \leq 5$, the higher the k value, the higher the fitting accuracy is obtained, $k = 4$ in this paper.

- (2) Universal characteristics fitting equation of engine:

In universal characteristics, fuel consumption rate b_e is regarded as two-variables-function of n_e and M_e . According to the definition, the expression of b_e is as follows in Eq. (42.9):

$$b_e = \sum_{j=0}^s \sum_{i=0}^j A_{[\frac{1}{2}(j+1)(j+2)-j-1+i]} M_e^i n_e^{j-i} \tag{42.9}$$

where:

- b_e fuel consumption rate, g/kWh;
- A coefficient matrix;
- S the order of mathematical model;

The engine data of a certain military off-road vehicle are shown in Table 42.1.

According to the mathematical fitting model and the data above, universal characteristic curves of the engine are obtained as shown in Fig. 42.1.

Table 42.1 Engine external characteristic data of prototype vehicle

T_{max} (N m)	$n(T_{max})$ (r/min)	P_{max} (kW)	$n(P_{max})$ (r/min)
169	4120	82	5100

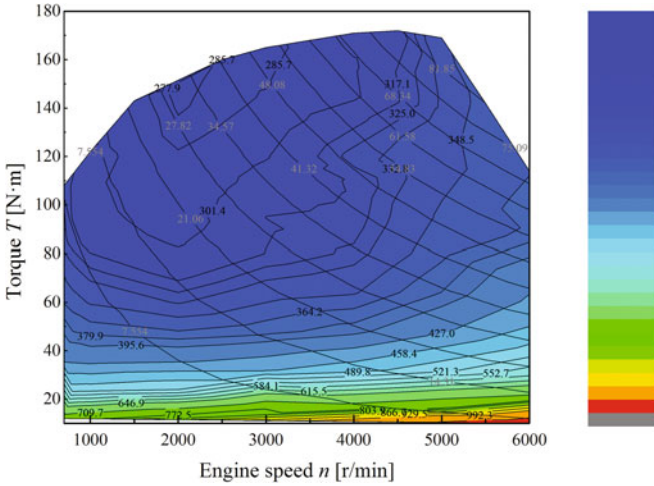


Fig. 42.1 Universal characteristic curves of prototype vehicle

42.2.4 Constraint Conditions

After the establishment of the powertrain optimization mathematical model and objective functions, appropriate constraints of the design variables are needed. The main constraint conditions include the dynamic requirements of the vehicle and the adjacent gear ratio interval of the shift comfort.

a. Constraint conditions of the vehicle dynamic property

(1) The limit of maximum dynamic factor in first gear:

$$\frac{F_{t1} - F_{\omega}}{m \cdot g} \geq D_{1max} \tag{42.10}$$

where D_{1max} is the maximum dynamic factor index of I gear, $D_{1max} = 0.62$ for off-road vehicles; F_{t1} is the maximum driving force of I gear, N.

(2) The limit of maximum dynamic factor in direct gear:

$$\frac{F_{td} - F_{\omega}}{m \cdot g} \geq D_{dmax} \tag{42.11}$$

where D_{dmax} is the maximum dynamic factor index of direct gear, $D_{dmax} = 0.06$ for off-road vehicles; F_{td} is the maximum driving force of direct gear, N.

(3) The limit of minimum stable velocity:

$$\frac{0.377n_{emin} \cdot r}{i_0 \cdot i_{g1}} \leq u_{amin} \quad (42.12)$$

where n_{emin} is the minimum stable RPM of the engine, r/min, the value is 600–800; u_{amin} is the index of the minimum stable velocity, km/h.

(4) The limit of the maximum velocity:

$$\frac{0.377n_{emax} \cdot r}{i_{g5} \cdot i_0} \geq u_{amax} \quad (42.13)$$

where n_{emax} is the maximum RPM of the engine, r/min; u_{amax} is the index of the maximum velocity, km/h, $u_{amax} = 160$ km/h in this paper.

(5) The limit of maximum climbable gradient:

$$\frac{T_{emax} \cdot i_0 \cdot i_{g1} \cdot \eta_T}{r} \geq G(f \cos \alpha_{max} + \sin \alpha_{max}) + \frac{C_d \cdot A \cdot u_n^2}{21.15} \quad (42.14)$$

where T_{emax} is the maximum torque of the engine, N m; α_{max} is the maximum climbable gradient, °, u_n is the climbing velocity, $u_n \leq 15$ km/h.

(6) The limit of road adhesion:

$$\frac{T_{tq} - T_f}{r} \leq F_z \cdot \varphi \quad (42.15)$$

where φ is the adhesion coefficient, determined by the road and tire conditions, for the asphalt pavement, φ is set as 0.7; F_z is the normal force of the driving wheels, N.

b. Constraint conditions of adjacent interval gear ratios

Considering the high utilization rate in high gears and shift comfort, adjacent interval gear ratios is usually limited to 1.7–1.8. The constraint conditions of adjacent interval gear ratios are as follows in Eq. (42.16):

$$\begin{aligned}
 1.7 \leq g_1(x) = \frac{i_{g1}}{i_{g2}} &\leq 1.85 \\
 g_2(x) = \frac{i_{g2}}{i_{g3}} - \frac{i_{g1}}{i_{g2}} &\leq 0 \\
 g_3(x) = \frac{i_{g3}}{i_{g4}} - \frac{i_{g2}}{i_{g3}} &\leq 0 \\
 g_4(x) = \frac{i_{g4}}{i_{g5}} - \frac{i_{g3}}{i_{g4}} &\leq 0
 \end{aligned}
 \tag{42.16}$$

42.3 Model Optimization and Solutions in Matlab

According to the optimization model above, the powertrain parameters of a certain military off-road vehicle is optimized. The vehicle parameters and technical requirements of the military off-road vehicle are as shown in Table 42.2.

Original powertrain parameters of the vehicle are shown in Table 42.3.

Fmincon function in Matlab optimization toolbox specifically to solve the optimization problem of multi-variables with nonlinear constraints [5]. The mathematical model is as follows in Eq. (42.17):

$$\begin{cases}
 \min f(x) \\
 c(x) \leq 0 \\
 ceq(x) = 0 \\
 A \cdot x \leq b \\
 Aeq \cdot x \leq beq \\
 lb \leq x \leq ub
 \end{cases}
 \tag{42.17}$$

where x, b, beq, lb, ub are vectors; A, Aeq are matrix; $c(x), ceq(x)$ are constraint functions.

The original transmission gear ratios are initial conditions, $X_0 = [3.8, 3.72, 2.04, 1.34, 1.0, 0.8]$. When setting the relative parameters, if there is no constraint, the parameters are set as []. According to the methods and conditions above, put the relative parameters into Matlab optimization model and simulate.

Table 42.2 Vehicle parameters and technical requirements of prototype vehicle

Parameters	Value	Parameters	Value
m (kg)	1515	A (m ²)	1.94
C_d	0.32	f_r	0.04
r (m)	0.30	φ	0.7
α_{\max} (°)	32	n_{emin} (r/min)	700

Table 42.3 Original powertrain parameters of prototype vehicle

Parameters	i_0	i_1	i_2	i_3	i_4	i_5
Value	3.8	3.72	2.04	1.34	1.0	0.8

42.4 Simulation Results and Analysis

Comparisons on powertrain parameters before and after optimization are as shown in Table 42.4:

Comparisons on dynamic property and fuel economy before and after optimization are as shown in Table 42.5.

Comparisons on dynamic factor curves, acceleration curves and driving power curves are as shown in Figs. 42.2, 42.3, 42.4, 42.5, 42.6, and 42.7 respectively.

Simulation results show that the acceleration time, fuel consumption and maximum velocity reduced after optimization. As shown in Figs. 42.2–42.5, the

Table 42.4 Comparisons on powertrain parameters before and after optimization

Parameters	Before optimization	After optimization	Rate of change (%)
i_0	3.8	4.98	31.58
i_{g1}	3.72	3.959	6.42
i_{g2}	2.04	2.14	4.90
i_{g3}	1.34	1.339	0.07
i_{g4}	1.0	0.935	-6.50
i_{g5}	0.8	0.751	-6.13

Table 42.5 Comparisons on dynamic property and fuel economy before and after optimization

Parameters	Before optimization	After optimization	Rate of change (%)
0–100 km/h acceleration time (s)	15.2972	14.0168	-8.37
Fuel consumption (L/h km)	7.4939	7.1670	-4.36
Maximum velocity (km/h)	201.19	192.57	-4.28

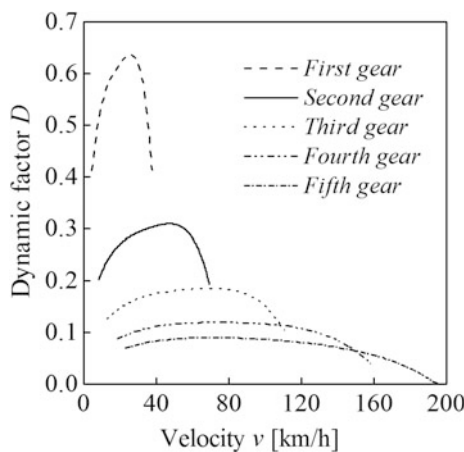


Fig. 42.2 Dynamic factors after optimization

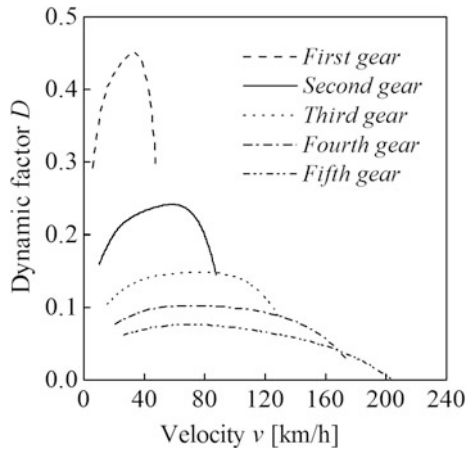


Fig. 42.3 Dynamic factors before optimization

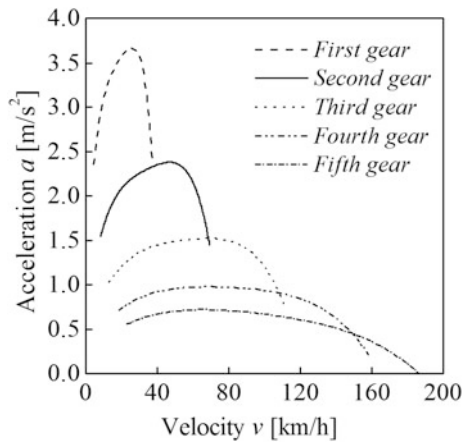


Fig. 42.4 Acceleration after optimization

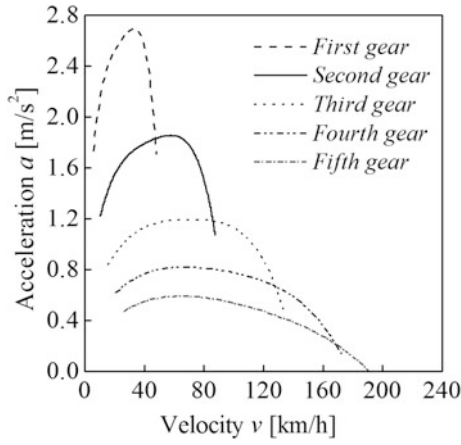


Fig. 42.5 Acceleration before optimization

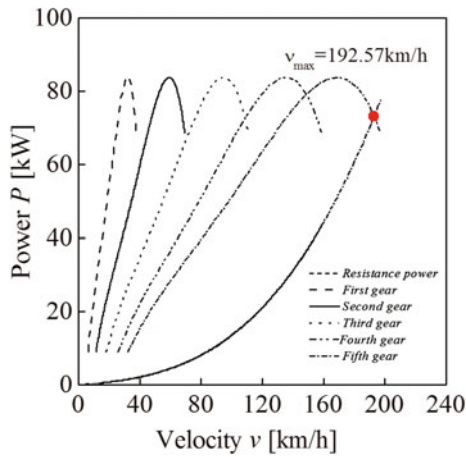


Fig. 42.6 Driving power after optimization

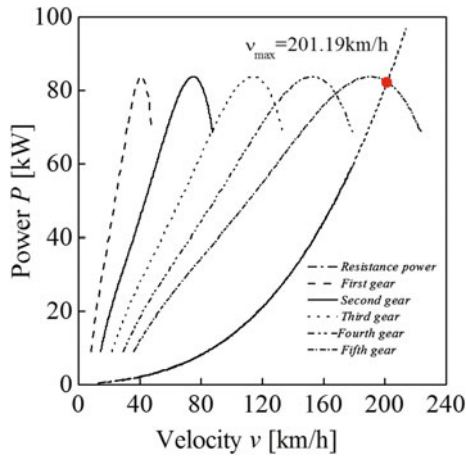


Fig. 42.7 Driving power before optimization

dynamic factors and acceleration increase obviously. Though the maximum velocity decrease 4.28%, the optimization results are relatively ideal in general.

42.5 Conclusion

Powertrain parameters of the military off-road vehicles are optimized in Matlab using nonlinear optimization function *fmincon*. The dynamic property and fuel economy improved obviously compared to the traditional geometric series division method. The simulation process is completely calculated in computer. Optimization time is shortened and efficiency is higher. There is a good practicability and application value to the design of the vehicle powertrain system in the future.

However, the optimization results couldn't be used to design gear transmission directly. In the future work, practical gear design will be considered into the optimization process.

References

1. Wang Z, Zhou P (2014) Multi-objective matching and optimization of the vehicle powertrain based on GT-drive. *Mod Manuf Eng* 10(021):40–44, 142
2. Lei S (2010) Parameters matching and simulation optimization of automobile transmission. Zhejiang University, p 1
3. Xu D (2015) Research of pure vehicle dynamic parameter optimization based on ant colony algorithm. Chang'an University, p 5
4. Pang H et al (2012) Optimization for heavy vehicle transmission ratios based on pareto optimal solution. *Automobile Technol* 02(039):39–43
5. Sup DCS, Sup MGS, Sup MRS (2014) Simulation tool for optimization and performance prediction of a generic hybrid electric series powertrain. *Int J Automot Technol* 1:135–144

Chapter 43

Study on the Program Load Spectrum of the Suspension Fatigue Bench Test and Correlation

Bing Rong, Zhengwen Tan, Pan Xiao, Yuanyuan Ma, Jianwen Zhou and Chaojie Liu

Abstract Based on pseudo damage equivalent principle, converted the wheel transducer force to the program load spectrum, then built a load spectrum for the suspension fatigue bench test, which has the equivalent damage with the durability test in proving ground. To ensure the consistency of the pseudo damage, the component true damage is consistent. First, through rain flow counting, got the relation curve in the double logarithmic coordinate system between amplitude and time for the wheel transducer force, and found a straight line that more or less matches as much as possible the highest part of the curve, then the slope of straight line is as the slope of SN curve for counting pseudo damage, and the intercept of SN curve is not less than the maximum amplitude. Finally, through comparative study of the result of suspension fatigue bench test and proving ground durability test, the fatigue life is found to agree well with each other, which demonstrate the effectiveness of the presented method.

Keywords Pseudo damage equivalent · SN curve · Rain flow counting · Program load spectrum

43.1 Preface

The chassis system is as one of the most important system in vehicle structures, their fatigue performance attracts much attention. From the chassis parts test and chassis systems test in early development stages to the proving ground durability test, the risk of chassis components cracking does not exist. At present, the external dynamic load can be obtained by the wheel force transducer in the early stage of

B. Rong (✉) · P. Xiao · Y. Ma · J. Zhou
Automotive Engineering Research Institute Co., Ltd, Chongqing, China
e-mail: rebe0606@163.com

Z. Tan · C. Liu
BAIC YINXIANG Automobile Limited Company, Chongqing, China

vehicle development, so the engineer can simulate the fatigue damage of the suspension system in the laboratory, according to the dynamic load.

There have two methods for fatigue bench test based on the random load spectrum: First, 24 channels vehicle bench test; Second, 12 channels suspension system bench test. They both require specialized test bench, the cost was expensive, and the utilization ratio of bench is low. According to the principle of linear superposition of fatigue damage, the random load of single direction can be translated into program load spectrum, then time and cost of the bench test are significantly reduced. So this method has been widely used in fatigue bench test. In paper [1], the distribution law of random load spectrum was obtained by rain flow counting, established two dimensional joint probability function of the mean and amplitude, then, compiled and simplified the program load spectrum. In paper [2], by using the geometric mean difference of cumulative cycle times of the two stages, the cycle times of the each amplitude of the eight stage program load spectrum were obtained.

This chapter took someone front suspension system as the research object, the random load spectrum was translated into the program load spectrum under the premise of equivalent pseudo damage. Finally, through comparative the result of suspension fatigue bench test and proving ground durability test, the fatigue life was found to agree well with each other, which demonstrated the effectiveness of the presented method.

43.2 Random Load Spectrum for Proving Ground

43.2.1 Random Load Spectrum Collection

According to the road test specifications, getting the random load spectrum was the basis step to carry out the latter fatigue bench test. In this chapter, the random load spectrum was mainly consisted of two regions in someone proving ground, they were: enhanced pavement area and ramp area as show in Fig. 43.1; Considered the impact of road accident factor and driving habits, must had 9 acquisition samples, three drivers were collected three times. In order to verify the status of the suspension system in the later stage test, the vehicle status must be recorded.



Fig. 43.1 An automobile proving ground

43.2.2 Random Load Spectrum Editing

The random load spectrum from proving ground had a large number of transition sections, and its impact on fatigue damage was very small, so it was necessary to remove the transition section and identify the road conditions. A total of 9 samples were collected, and each one included 19 events in enhanced pavement area and 5 events in ramp area. Road identification was mainly based on the logic of the segmentation signal and acquisition sequence. Then, the signal need to be filtered, to be remove spike and drift etc. the sample screening was particularly important, the methods of sample screening were more and mature [3, 4], In this chapter, we used the Rossow sampling principle (50% survival rate), which was pointed out in the reference paper [4], to screen the samples. Finally, according to the road test specification, the screening samples were combined the target data to prepare the program load spectrum. As show in Figs. 43.2 and 43.3, time for deleting transition

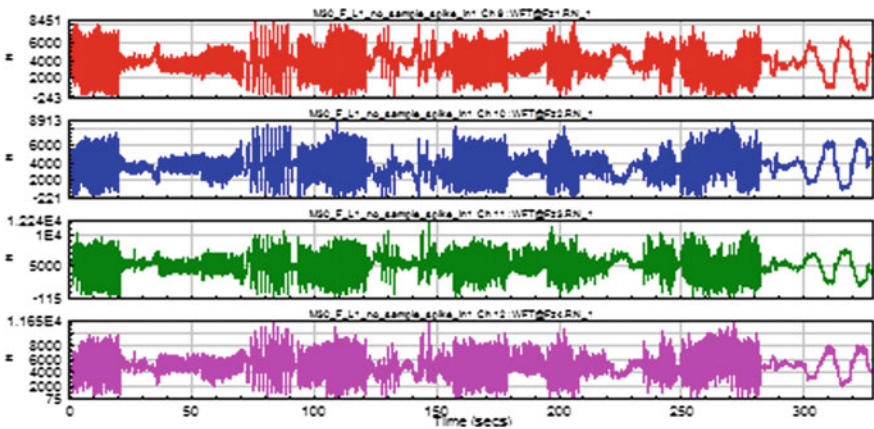


Fig. 43.2 Remove signal transition sections

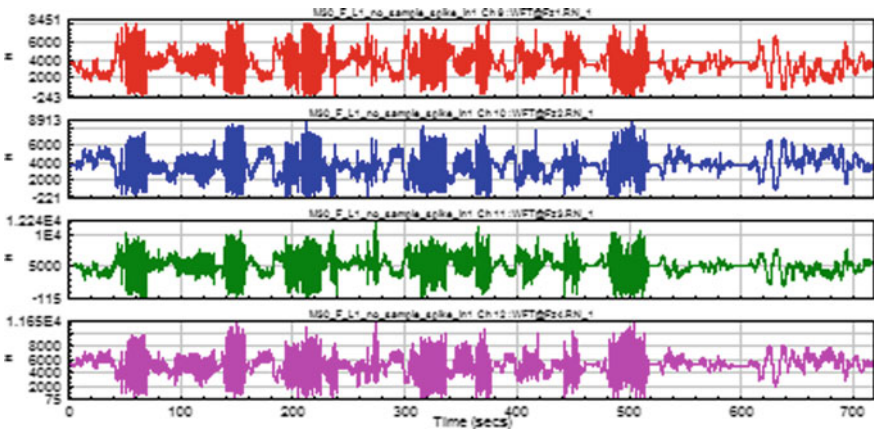


Fig. 43.3 Original signal

section signal was 328 s, compared with time of the original signal, time was reduced by 54%, and pseudo damage was maintained at more than 99.9%.

43.3 Program Load Spectrum Preparation

43.3.1 Defined SN Curve for Pseudo Damage

In double logarithmic coordinates, the relationship between alternating stress S and the number of cycles N to failure is a straight line as show in Fig. 43.4. When determined the slope b and intercept S_0 of the straight line, the SN curve is got, and the slope is calculated by formulas (43.1) and (43.2).

$$b = \frac{1}{m}. \tag{43.1}$$

$$m = \frac{\log(\frac{N_2}{N_1})}{\log(\frac{S_2}{S_1})} \tag{43.2}$$

Based on the fatigue cumulative damage theory, whether the force, moment or strain is considered as the generalized stress on sensor mounting point, the generalized damage or pseudo damage can be obtained by using the SN curve [4]. The premise of random load spectrum to program load spectrum is the equivalent of the pseudo damage, however, after the pseudo damage equivalent, the real damage of structural components is also equivalent, the influence parameters are mainly determined by the choice of the SN curve for calculating the pseudo damage. As shown in Fig. 43.4, and ultimately attributed to the choice of slope b and intercept S_0 are correct or not.

First, rain flow counting was carried out for the target random load spectrum, got the relationship curve in the double logarithmic coordinates between the amplitude and frequency. According to the definition of the SN curve, the curve could be defined as the SN curve to solve the pseudo damage, but due to the relationship curve was not a straight line, it was necessary to do linear fitting. Because of the

Fig. 43.4 Idealized SN curve

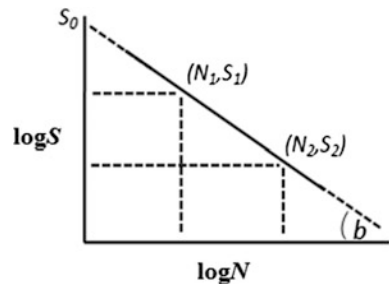
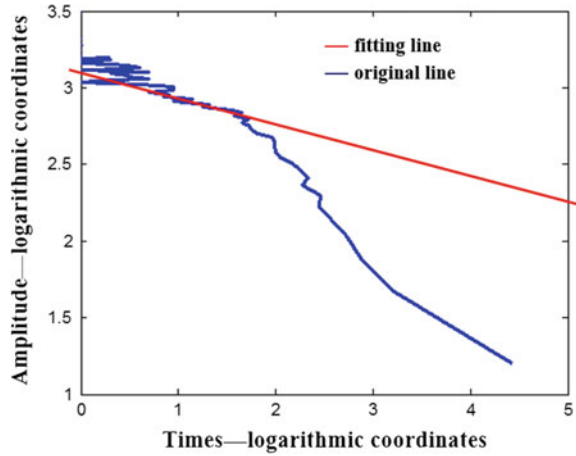


Fig. 43.5 Determined SN curve slope



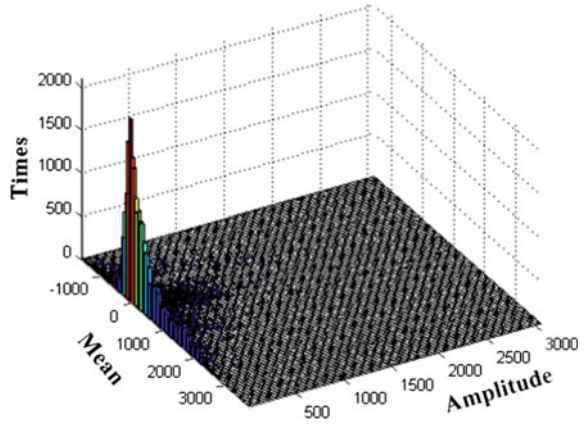
high amplitude area has large contribution to the damage, data for linear fitting only included the high amplitude region, then the slope of the SN curve was the slope of the fitting straight line, and the intercept S_0 must be greater than the maximum amplitude of rain flow counting. As show in Fig. 43.5, the blue curve was the relationship curve between amplitude and frequency in the double logarithmic coordinate for the lateral force of front left tire, the red straight line was the fitting line with the high amplitude region, and the slope of the red line would be the slope of the SN curve. According to formulas (43.1) and (43.2), the slope b was calculated as -0.24951 , and the intercept S_0 was 3000 N which was the maximum amplitude of rain flow counting. So the SN curve to calculate pseudo damage for the lateral force of front left tire was defined. Other SN curves were calculated by this method.

43.3.2 The Method of Program Load Spectrum

After the SN curve for calculating pseudo damage was confirmed, then the rain flow statistics and pseudo damage computing were more important. The process of transforming the time history load data into a series of full or semi cycle was called counting. Rain flow counting method was usually adopted in the calculation of fatigue damage [5]. Based on the lateral force on front left tire, which measured by the wheel force transducer on someone proving ground, through the rain flow counting, got the rain flow matrix as shown in Fig. 43.6, the mean and amplitude of rain flow matrix were equally divided into 100 parts.

From Fig. 43.6, we could see that the random load spectrum could be equivalent to a series of sine spectra by the rain flow counting. And there was a power function

Fig. 43.6 The rain flow matrix for tire lateral force



of SN between the load amplitude and the damage, as shown in the formula (43.3) [6]. Then we can calculate the pseudo damage for the random load spectrum.

$$S = S_0 N_f^b \tag{43.3}$$

- S The load amplitude;
- S_0 SN curve intercept;
- N_f The fatigue life for S ;
- b The slope of the SN curve.

By the formula (43.3) to derive the damage formula (43.4) for a single cycle of the amplitude S_i :

$$D_i = \frac{1}{N_{fi}} = \left(\frac{S_i}{S_0}\right)^{-b} \tag{43.4}$$

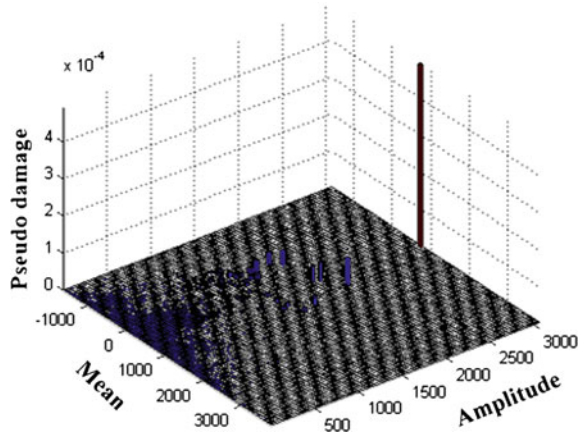
Then based on the theory of Miner, the cumulative damage formula was derived:

$$D_a = n_1 D_1 + n_2 D_2 + \dots + n_i D_i + \dots \tag{43.5}$$

- D_a The cumulative damage of random load;
- n_i The cycle times of rain flow counting under the amplitude S_i ;
- D_i The damage for a single cycle of the amplitude S_i .

The pseudo damage matrix could be calculated for random load form SN curve, rain flow counting matrix and damage power exponent formula. Then based on the Fig. 43.6, got the pseudo damage matrix as shown in Fig. 43.7. It was known that the mean value was not considered in the damage power exponent formula. Therefore, it was necessary to carry out the pseudo damage equivalent analysis under each mean in the late stage.

Fig. 43.7 Damage
 100 × 100 matrix for lateral
 force



Easy to load on a simple uniaxial fatigue test rig, the program load spectrum was generally divided into eight levels. Conover pointed out that the amplitude could be divided into eight levels, according to the eight coefficients 1.000, 0.950, 0.850, 0.725, 0.575, 0.425, 0.275 and 0.125, and the eight program load spectrum could accurately reflect the fatigue effect caused by random load [7]. So the pseudo damage matrix in Fig. 43.7 could be transformed to the matrix with eight levels amplitudes as shown in Fig. 43.8, and the eight level amplitudes were: 3053, 2901, 2595, 2214, 1756, 1298, 840 and 382 N. According to the formula (43.4) calculated the pseudo damage for a single cycle of the each amplitude for the eight levels, then the sum of the pseudo damage under each amplitude in Fig. 43.8 was divided by the pseudo damage for a single cycle under each amplitude, the 8 * 100 rain flow counting matrix which has the same fatigue damage with random load was obtained as show in Fig. 43.9.

According to the formula (43.6), the mean was normalized, and the program load spectrum of the eight levels was obtained [1], then the pseudo damage ratios and the cumulative pseudo damage ratios for the program load spectrum were calculated as show in Table 43.1.

$$M_i = \frac{\sum_j^{100} M_j n_{ij}}{\sum_j^{100} n_{ij}} \tag{43.6}$$

- M_i The mean for the amplitude of i level;
- M_j The mean for the j level;
- n_{ij} The frequency for the amplitude of i level and the mean of j level.

Retained 100% pseudo damage to the equivalent conversion, could remove the eighth level loads, then the total cumulative frequencies were 255 times. On the fatigue bench, the loading frequency of lateral direction was 2 Hz, so the test time

Fig. 43.8 Damage 8×100 matrix for lateral force

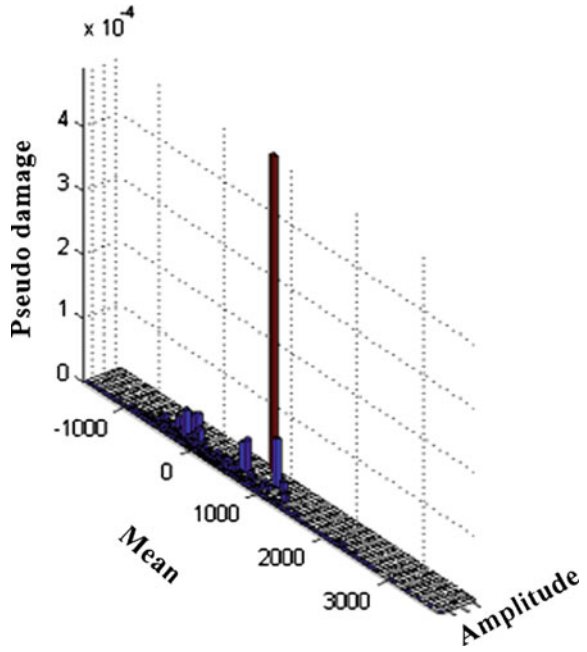


Fig. 43.9 The rain flow 8×100 matrix

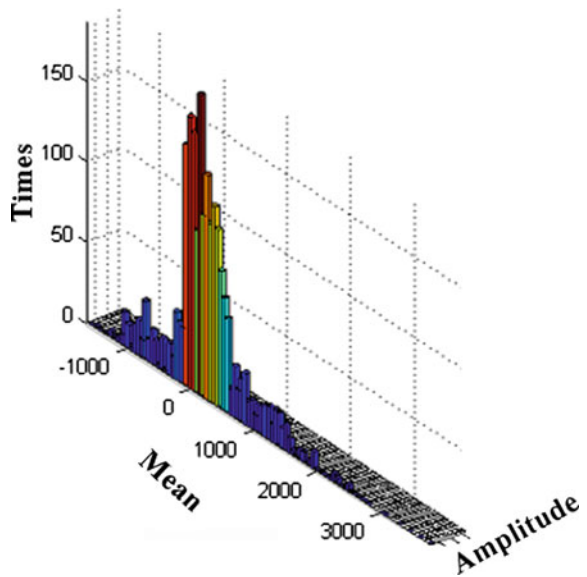


Table 43.1 The program load spectrum of the eight levels

Levels	Mean (N)	Amplitude (N)	Times	Damage ratios (%)	Cumulative damage ratios (%)
1	741	3053	1	39.37	39.37
2	–	2901	0	0	39.37
3	–	2595	0	0	39.37
4	1010	2214	1	7.9	47.27
5	247	1756	8	19.83	67.09
6	42	1298	39	21.33	88.42
7	104	840	206	12.79	101.21
8	247	382	2334	2.82	104.03

on the fatigue bench was 127.5 s, but on proving ground was about 718 s, thus bench test significantly reduced the test time.

43.4 Bench Test and Simulation Result Comparison

There were three forces and three moments on the wheel center, which were along the tire coordinate system. According to the forces and moments loading form, they could be simplified to three forces, the vertical force loaded on the wheel center, the longitudinal force and lateral force loaded on tire ground point, which would include the lateral and longitudinal moment. For the tire turning moment, which was around the vertical direction, it was omitted in the fatigue test bench test because of its low effect in fatigue test.

According to the previous theory, the three directions of random forces could be translated into the program load spectrum of the eight levels, then ordered the program load spectrum based on the mean from small to large, so got the final program load spectrum for single cycle of someone proving ground on the front left wheel center as show in Table 43.2.

According to Miner theory, the final program load spectrums of the three directions were loaded on the bench in turn, would get the same damage with the single cycle of someone proving ground, then carried out the total cycle test based on the road test specification. Because the front suspension was McPherson independent suspension, the left and right loads were simultaneously carried out, and the difference of the left and right phases was not considered. The test benches of three directions were shown in Figs. 43.10, 43.11 and 43.12.

After the end of the uniaxial fatigue bench, the front suspension components were disassembled and check to find that the base metal and weld of the each component done not exist any crack. In the later period, when the reinforced road test for durability was carried out, there were no any crack in the base metal and weld of the each component. It could be seen that the program load spectrum which used this method to be complied could be predicted and controlled the cracking risk for the chassis parts.

Table 43.2 The final program load spectrum for Left front wheel center

Longitudinal load spectrum				Lateral load spectrum				Vertical load spectrum			
Levels	Mean (N)	Amplitude (N)	Times	Levels	Mean (N)	Amplitude (N)	Times	Levels	Mean (N)	Amplitude (N)	Times
1	75	1883	2	1	42	1298	39	1	3614	1916	9
2	153	1982	1	2	104	1092	56	2	3692	2756	43
3	395	1966	25	3	247	1756	8	3	3960	3332	1
4	421	2711	8	4	741	3053	1	4	3999	3165	3
5	451	1871	34	5	1010	2214	1	5	4020	3196	56
6	531	2305	8					6	4058	3359	71
7	619	1437	1					7	4254	3938	24
								8	4413	4401	10
		Total	79			Total	105			Total	217

Fig. 43.10 X direction load



Fig. 43.11 Y direction load



Fig. 43.12 Z direction load



43.5 Conclusion

Based on pseudo damage equivalent principle, the random road load spectrum was transformed into the program load spectrum for uniaxial fatigue test bench, then according to the road test specification, complied the final program load spectrum for suspension system fatigue bench test. Compared the results of bench test with the results of road test, they had similar damage to the suspension component, so the validity of the program load spectrum was verified.

In the indoor Fatigue Bench test, due to the full constraint on the body and there was no powertrain system, the fatigue performance of subframe which would bear the load from powertrain was not comprehensive enough. Therefore, in the future research, the powertrain system will be considered, improving the verification for subframe fatigue performance.

References

1. Yunkai G, Chengmin X, Jianguang F (2014) Study on the programmed load spectrum of the body fatigue bench test. *J Mec Eng* 50(4):92–98
2. Xianzhao S (1992) Loading spectra for the differential axle housing and wheel shaft of a 50t flat truck. *Automotive Eng* 14(3):181–188
3. Wei P, Jin X, Sun S (2004) A Selecting Method of Road Loading Spectra Used in Road Simulation. *J Shanghai Uni Eng Sci* 18(1):6–9
4. Juehui Z, Feng J, Zhuoping Y (2004) A method of selecting load spectra for road simulation test. *Automotive Eng* 1:220–223
5. Power E (1978) Cycle counting methods and the development of block load fatigue programmes. SAE, 780102
6. Han Y, Yuanqin Z, Limin S, Lijia D, Zhanguo L, Shiyong W (2013) Comparison of two rough roads based on vehicle damage distribution of users. *Test Measuring* 1(8):39–44
7. Hao X (1988) Fatigue strength. Higher Education Press, Beijing

Chapter 44

Fatigue Analysis of Car Body Structure Based on Transient Response

Pengbo Wang

Abstract Fatigue simulation is executed for a car body. Loading spectra are collected by real-vehicle test on enhanced road surfaces, and the load history for each interface point is acquired by using multibody dynamics virtual iteration. Based on a finite element model and the mode superposition method, transient response of the car body is simulated. And the stress history is obtained using the modal stress recovery technique. The S-N method is applied to predict fatigue damage distribution of the full car body. In the fatigue analysis, material Haigh diagrams are defined to introduce the mean stress influence and the critical cutting plane method is applied to treat the multi-axial stress. Based on the presented numerical scheme, fatigue analysis and structural improvement for the car body can be carried out at the earlier stage of the vehicle development project.

Keywords Car body · Road loading spectra · Transient response · Mode superposition method · Fatigue analysis

44.1 Introduction

Automotive body is the main load bearing part of the vehicle, which supplies a necessary space for the occupants and packages, and acts as an installation base for the powertrain and the suspension system. Automotive body bears various dynamic loads, thus its fatigue resistance is important [1, 2]. The fatigue life of the automotive body can be measured by durability experiment for a certain number of body samples. But the durability experiment, which consume much money and time, can be executed only after the prototyping bodies are manufactured, and the

P. Wang (✉)

Changan Auto R&D Center, Changan Automobile Co., Ltd, Beijing 102209, China
e-mail: wangpb05@aliyun.com

experimental conclusions may be affected by various accidental factors. While using modern computer simulation technologies, the car body life can be estimated before the durability test to reduce the huge cost of prototyping manufacturing and physical sample experiment.

In automobile travel process, the vehicle body bears multiple loads including the vertical load from road surface roughness, the lateral load from steering or lateral wind and the longitudinal load from acceleration or brake. Those loads are too complex to be calculated with theoretical method and can only be measured by physical or virtual experiments.

In conventional body fatigue simulation, firstly acceleration signal or force signal is collected at wheel center locations, secondly a full vehicle multi-body dynamic model is build to implement virtual iteration, in which the dynamic interface forces of the body are determined by decomposing the wheel center signal, thirdly the finite element method (FEM) is applied to obtain the dynamic stress distribution of the body, and lastly fatigue analysis is executed to get the fatigue life or damage value of the vehicle body [3].

Though virtual road and numerical vehicle provide a method to simulate automobile driving and get the load history [4, 5], the real road experiments with physical prototype are in much better accordance with the actual situation, so real vehicle road test is still the most universal method for present automobile companies to obtain road loading spectra.

The finite element analysis (FEA) on automotive body dynamic stress can adopt quasi-static method or transient method. The former applies a unit static load on the FEM model to replace the actual dynamic load, and executes a static analysis to get the stress field, which is the stress affecting factor for the corresponding load component. Each stress affecting factor multiply the corresponding load history, and the sum of all the products is the stress history of the body structure [6, 7]. Because the quasi-static method ignores the effect of loading frequency and is inadequate when structure resonance occurs due to external excitation at certain frequencies, it is only suitable for the auto parts whose natural frequency is much higher than the loading frequency [8]. Usually a body structure has a lowest natural frequency on the order of tens of Hertz, and therefore its dynamic stress should be calculated by using the transient method.

Research on the body stress in actual driving process proves that the structure stresses are below the material yield limit in most cases. So the body fatigue life can be calculated with high-cycle fatigue assumption [5].

This paper measures the wheel-center acceleration signal of a car with real vehicle road test, obtains the time-domain load data at the body interface points by multibody virtual iteration, calculates the stress history of the car body structure by using transient FEA, and executes fatigue simulation based on the S-N method to estimate the fatigue life and identify the high-risk positions.

44.2 Road Load Data Measurement and Interface Force Generation

44.2.1 Real Vehicle Road Test

The wheel-center acceleration signal of a concept car is measured on 11 enhanced test roads as shown in Fig. 44.1, which includes stone block road, gravel road, cobble stone road et al. The measurement does not require that the test vehicle completely conforms to the new designed model, and it just need to modify a similar reference vehicle to ensure that its rear and front axle loads, wheelbase, track width and chassis hard points are close to the design values. Therefore, the road test can be done at the concept design phase of the automobile developing process.

The whole road test work involves test scheme determination, preparation of parts, measurement on the proving ground, data check and data processing, and finally supply the road load data which will be used in a subsequent virtual iteration to derive interface forces and moments between the body and the chassis parts [3].

Data processing of the original signal from road test is a necessary work before the virtual iteration. Operations such as peak removal, drift compensation, translation and filtering are completed using professional software to correct the measurement errors, then the road load data are appropriately split and combined according to different roads and vehicle durability test requests.

44.2.2 Virtual Iteration

Because the road test can directly measure the wheel-center acceleration rather than the body interface point loads, a multibody model must be built to derive the interface forces and moments from the wheel-center signals. If the wheel-center acceleration signal is directly applied on the multibody model, the dynamic problem will become unsolvable because of unbalanced force system. Before interface force generation, the wheel-center displacement should be calculated by virtual iteration according to the measured wheel-center acceleration by virtual iteration.



Fig. 44.1 Enhanced test roads on the proving ground

The principle of virtual iteration is shown in Fig. 44.2. The multibody model of the whole vehicle acts as a signal input and output system, for which the wheel-center displacement A and acceleration U are respectively the input and output signals. A frequency spectrum analysis of the output signal with applying white noise as input signal provides a transfer function $H(f)$, which means the ratio of output to input under sinusoidal excitation at different frequency. By the transfer function's reciprocal $1/H(f)$, the input can be reversely solved from the output. Because the whole vehicle multibody model is a nonlinear system but the transfer function is based on linearization treatment, the input signal is solved iteratively to make the calculated output signal approach the tested output signal, and finally a relatively accurate solution of input signal is obtained.

The transfer function is defined as

$$H(f) = A(f)/U(f) \tag{44.1}$$

By Fourier transform, the measured time-domain signal of wheel-center acceleration from the road test is converted to frequency-domain signal $A_m(f)$, from which the initial trial solution of wheel-center displacement $U_0(f)$ is derived using the transfer function $H(f)$.

$$U_0(f) = A_m(f)/H(f) \tag{44.2}$$

The trial solution $U_0(f)$ is applied to the multibody model as input signal, and the wheel-center acceleration $A_0(f)$ is obtained as output response signal. The calculated output $A_0(f)$ is compared with $A_m(f)$. If the former agrees well with the latter, $A_0(f)$ is the final solution of the wheel-center displacement, and can be used to derive the body interface loads for the subsequent fatigue analysis. If there is a mismatch between them, the first iteration is executed to obtain an updated wheel-center displacement solution.

$$U_1(f) = U_0(f) + (A_m(f) - A_0(f))/H(f) \tag{44.3}$$

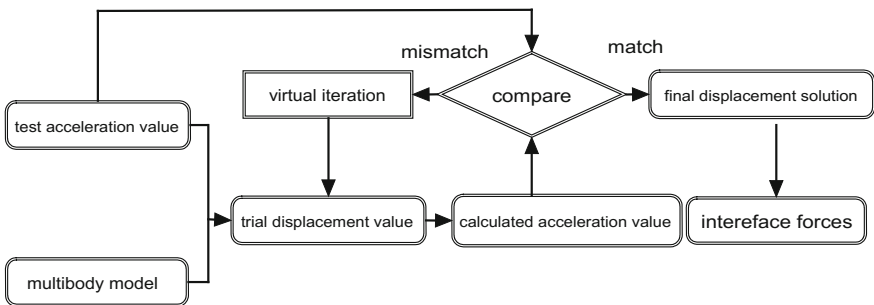


Fig. 44.2 Multibody virtual iteration

The updated trial solution $U_1(f)$ is applied to the multibody model to get a new output response $A_1(f)$, which is also compared with $A_m(f)$. The above procedure is executed iteratively until the calculated output response is in good agreement with the tested signal.

The comparison between the calculated results and the tested data involves time-history signal comparison and power spectral density (PSD) comparison. Usually determining when the iteration can be over depends on subjective evaluation. If the calculated results are acceptable, the virtual iteration process is ended, and the final solution of the wheel-center displacement is input to the multibody model to generate interface loads between the body and the chassis parts. The time history of the interface loads in global coordinate system will be used in the subsequent body FEM analysis and fatigue simulation.

44.3 Transient Dynamic FEA

44.3.1 BIW Finite Element Model

After generating the body interface loads, a finite element model of the body in white (BIW) as shown in Fig. 44.3 is built and a transient dynamic analysis is performed to obtain the stress spatial distribution and time history.

Shell elements is used to simulate the BIW, where 4-node elements occupy a major percentage and 3-node elements account for less than 5%. The whole model contains 1,897,845 nodes and 1,866,466 elements. In driving process, any mass added to the BIW will influence the dynamic response of the whole structure, so

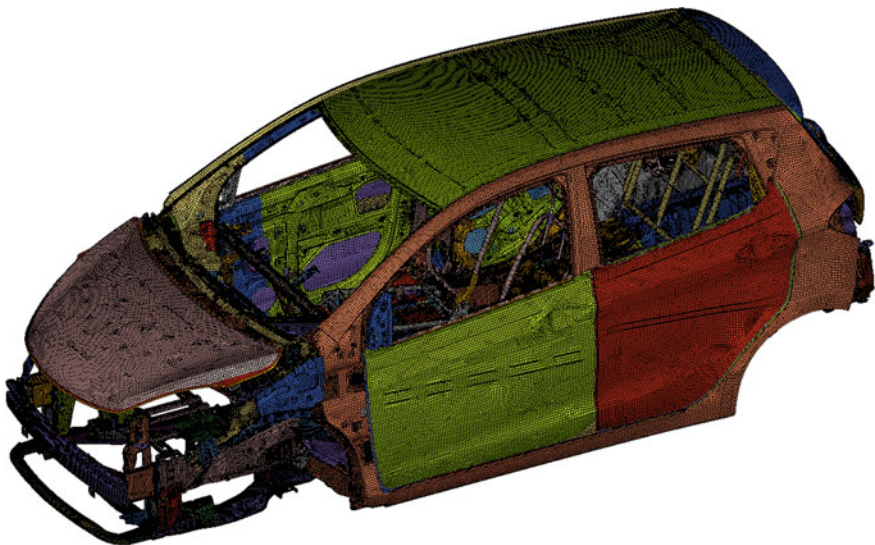


Fig. 44.3 Finite element model of the BIW

distributed masses or concentrated masses are built and connected to the BIW model to simulate the interior and exterior trim parts, luggage and passengers before the dynamic analysis.

44.3.2 Transient Analysis Based on Mode Superposition

Two different numerical schemes can be used in transient dynamic FEA: the direct integration method and the mode superposition method [9]. Since the mode superposition method uses structural mode shapes to reduce the solution space and uncouple the equations of motion, usually it is more efficient than the direct integration method for a problem involving a large-scale model and a large number of time steps. So this paper adopts the mode superposition method in transient analysis.

The transient analysis based on mode superposition is a natural extension of the conventional modal analysis.

As a first step, transform the variables from physical coordinates to modal coordinates by

$$\{\mathbf{u}\} = [\Phi]\{\xi\} \quad (44.4)$$

where $\{\mathbf{u}\}$ is the displacement vector of all the nodes, $[\Phi]$ is a matrix consisting of mode shapes and $\{\xi\}$ is the vector of modal coordinates. Equation (44.4) represents an equality if all modes are used; however, because all modes are rarely used, the equation usually represents an approximation.

To proceed, ignoring the damping and write the equation of motion as

$$[\mathbf{M}]\{\ddot{\mathbf{u}}\} + [\mathbf{K}]\{\mathbf{u}\} = \{\mathbf{p}\} \quad (44.5)$$

where $[\mathbf{M}]$, $[\mathbf{K}]$ and $\{\mathbf{p}\}$ are respectively the mass matrix, stiffness matrix and external load vector.

Substitute Eq. (44.4) into Eq. (44.5) and multiply by $[\Phi^T]$, resulting in

$$[\Phi^T][\mathbf{M}][\Phi]\{\ddot{\xi}\} + [\Phi^T][\mathbf{K}][\Phi]\{\xi\} = [\Phi^T]\{\mathbf{p}\} \quad (44.6)$$

where $[\Phi^T][\mathbf{K}][\Phi]$ and $[\Phi^T]\{\mathbf{p}\}$ are respectively the modal mass matrix, modal stiffness matrix and modal force vector.

Since the generalized mass and stiffness matrices are diagonal matrices, the modal equations of motion are uncoupled and can be written as a set of single degree-of-freedom system equations as

$$m_i \ddot{\xi}_i(t) + k_i \xi_i(t) = p_i(t) \quad (44.7)$$

where m_i , k_i and p_i are respectively the i -th modal mass, modal stiffness and modal force.

Once the single degree-of-freedom equations are solved, individual modal responses are computed by solving the above single degree-of-freedom equations, nodal displacement responses are recovered as the summation of the modal responses by using Eq. (44.4). Then the stress and strain responses are derived from nodal displacements.

If the stress time history of the whole BIW is output to the result file, which means the full-field stress is output at each time step, this will make the result file too large to treat. Under conventional computation conditions, usually the local stress output and fatigue analysis are executed for only the pre-estimated high-risk areas of the BIW [10].

In order to complete a fatigue analysis of the whole BIW structure, this paper does not directly output the stress history in the transient dynamic FEA, but use modal stress recovery to calculate the dynamic stress [11]. The FEA supplies only the modal stresses and modal coordinates, and the stress time history of the whole BIW is calculated as the summation of the modal responses in the following fatigue analysis, as Eq. (44.8).

$$\{\sigma(t)\} = \sum_{i=1} \xi_i(t) \{\sigma_i\} \quad (44.8)$$

where $\{\sigma_i\}$ is the modal stress of the i -th modal shape.

44.4 Fatigue Analysis of the BIW

44.4.1 S-N Curve Method for Low-Cycle Fatigue

The FEA results shows that the dynamic stresses of the BIW are lower than the corresponding material yield limits, which means that it should be consider as a low-cycle problem. Therefore, the S-N curve method, also known as the stress-life method is selected to solve the fatigue problem. An S-N curve for a material defines alternating stress value versus the number of cycle required to cause failure.

The S-N curve method is based on uni-axial fatigue theories. However, because the BIW bears random loads when driving, the amplitude and direction of each principal stress are both changing with the external loads. Therefore, equivalent stress hypotheses are employed to assess the multi-axial stresses with the aid of a uni-axial reference stress.

The conventional equivalent stress hypotheses, such as the maximum shear strain energy criterion and the maximum principal stress hypothesis, whose application is limited in proportional loading, are not applicable for complex random loading. In order to allow a fatigue analysis for non-proportional loading cases, the cutting plane method is applied. It transforms the multi-axial stress to an equivalent stress at the crisis cutting plane with a modified maximum shear strain

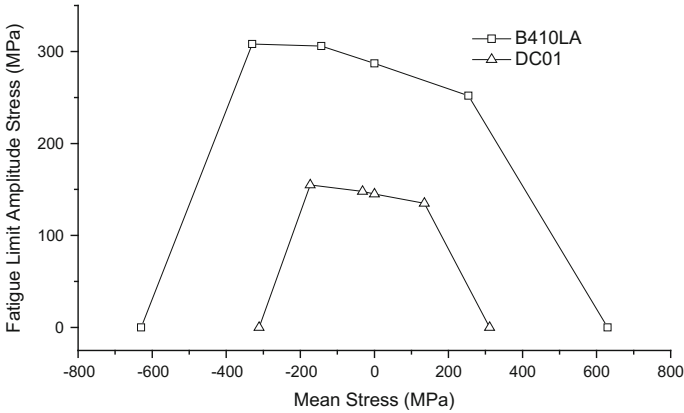


Fig. 44.4 Example of Haigh diagram

energy criterion, and then the uni-axial fatigue theories can be employed to obtain the fatigue damage and life [12].

Usually the S-N curves are defined by means of fully reversible cyclic loading, which means the mean value of the alternating stress is zero. In most actual cases, the mean stress of the BIW is non-zero. For the fatigue life, a mean tension stress is beneficial and a mean compression stress is harmful. The mean stress influence is taken into consideration in this paper with the aid of the Haigh diagram, which defines the relationship between the fatigue strength limit amplitude and the mean stress value, as shown in Fig. 44.4.

In addition, fatigue life of the structure is also affected by stress gradient, surface roughness and technological surface treatment. The influence of these factors can be considered by properly modifying the S-N curve.

An S-N curve is derived with constant-amplitude loading cycles. However, the BIW bearing randomly changing stress histories, for which the division and amplitudes of loading cycles are difficult to determine. In this paper the loading cycles is counted by means of the rain flow counting method, which converts a complex variable amplitude loading history to a series of simple constant-amplitude loads.

44.4.2 Miner Linear Damage Accumulation

The Miner linear damage accumulation rule is widely used in current automobile industry to calculate structural fatigue damage. The Miner rule can be formulated as

$$D = \sum_{i=1}^l D_i = \sum_{i=1}^l \frac{n_i}{N_i} \tag{44.9}$$

where n_i is the actual number of cycles with the stress amplitude S_{ai} and mean stress S_{mi} in the loading history, and N_i is the corresponding number of cycles required to cause failure.

The damage contribution of a single stress cycle is given as the reciprocal of $N_i(1/N_i)$, and the total damage D is the summation of the individual damage contribution induced by each single loading cycle.

When the total damage $D = 1$ is reached, the structure reaches its life limit and failure occurs.

44.4.3 Results of Fatigue Analysis

The fatigue analysis simulates a 7500 km durability test on 11 enhanced roads of the proving ground, the numbers of travel repetition for different roads range from 90 to 270.

On the basis of the modal stresses and modal coordinate responses given by the transient dynamic FEA, the fatigue analysis calculates the stress time history of the whole structure and then obtains the damage value for a single travel on each road. The accumulation of the individual damage values gives the total damage of the complete road test, which is shown in Fig. 44.5.

The result indicates that the maximum damage occurs at the rear floor but its value 0.048 is far less than 1.0, which demonstrates excellent anti-fatigue performance of the new designed car body.

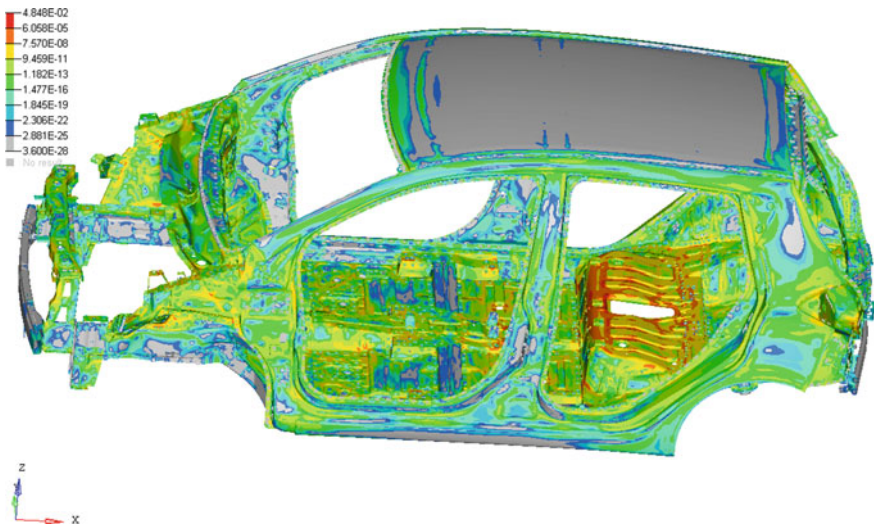


Fig. 44.5 Damage contour of the BIW

44.5 Conclusions

This paper proposed a numerical scheme of vibration fatigue simulation for vehicle bodies, which covers measurement of road load data, interface force generation by virtual iteration, transient dynamic FEA, and fatigue analysis based on stress-life method. Using the presented scheme, fatigue damage analysis, high-risk position identification and structural improvement can be carried out for the designed car body at the earlier stage of the vehicle development project.

The road load data are measured by real vehicle road test that provides more reliable data than virtual road test with numerical vehicle. The stress history of the BIW is calculated by transient dynamic FEA, which can consider the effect of loading frequency and obtain more accurate results than the quasi-static method.

The stress time history is calculated by modal stress recovery method, which avoids outputting a huge result file of BIW stress in the transient FEA, and make it practicable to complete a fatigue analysis for a whole BIW structure under multiple load cases.

References

1. Huang J (2007) Automotive body design. China Machine Press, Beijing, pp 241–244
2. Li M et al (1995) Anti-fatigue design of automotive structures. University of Science and Technology of China Press, Hefei, pp 13–46
3. Mao X, Xiao P, Chen J (2011) Automotive body fatigue analysis based on road spectrum. *Comput Aided Eng* 20(2):78–81
4. Sun H et al (2007) Fatigue analysis for auto parts based on the vehicle virtual road testing. *J Natl Univ Defense Technol* 29(4):121–125
5. Gao Y et al (2010) A simulation analysis on the fatigue life of fuel cell bus body. *Automot Eng* 32(1):7–12
6. Miao B et al (2008) Fatigue life prediction applied to car-body structure with multi-body dynamics and fem. *J Mech Strength* 30(6):1003–2007
7. Miao B et al (2007) Fatigue life simulation of flexible carbody under dynamic loading. *J Southwest Jiaotong Univ* 42(2):217–222
8. Zhang L, Liu Y, Qu Y (2006) FEM-based fatigue analysis method and application in automobile industry. *Comput Aided Eng* 15(S1):195–198
9. Wang X (2003) Finite element method. Tsinghua University Press, Beijing, pp 476–490
10. Xia X et al (2008) CAE simulation on fatigue breach of minibus body. *Comput Aided Eng* 17(4):46–50
11. Sun H et al (2007) Virtual fatigue test method for auto parts based on modal stress recovery. *Automot Eng* 29(4):274–278
12. Wang Y, Yao W (2003) Review on the multiaxial fatigue criteria. *J Mech Strength* 25(3):246–250

Chapter 45

The Study on Fatigue Test of Cab With Suspension Based on 4-Channel Road Simulation Rig

Yunkai Gao, Genhai Wang and Jingpeng Han

Abstract In this chapter, the fatigue test method is studied based on 4-channel road simulation rig, which examine fatigue performance of truck cab with vehicle frame and suspension system. The motion of the cab is analyzed. The inner force of exciter and fixture is reduced through frame design and fixture design, and ADMAS is used to validate the method. Then the acceleration signal is regarded as the target signal, the load spectrum is reproduced in the test rig through physical iteration. Finally, the weakness of the cab obtained is similar to results of proving ground test.

Keywords 4-channel · Cab · Frame design · Test rig design · Road simulation test

45.1 Introduction

Vehicle body endures alternating load, the fracture failure of body frame is mainly caused by fatigue damage [1]. The fatigue resistance of the auto body can be examined accurately through fatigue test. There are three main types: road test, proving ground test and road simulation test. The road simulation test can cut down the testing period greatly, save manpower and the material resources, and be free effect in environment, season and weather comparing with two formers. Gao et al. [2], based on the loading spectrum collected in the road test, designed the bench test. And the design weaknesses were checked out. The remote parameter control technology was applied by Zhou [3] to obtain the loading spectrums for test in the test bench, and the dynamic strength test of car body structures in the test room was

Y. Gao · G. Wang (✉) · J. Han
Shanghai Key Lab of Vehicle Aerodynamics and Vehicle Thermal
Management Systems, Shanghai, China
e-mail: wgenhai@163.com

Y. Gao · G. Wang · J. Han
School of Automotive Studies, Tongji University, Shanghai, China

conducted. The laboratory road simulation test for truck cab was conducted by Gosavi [4], and the development cycle of semi-float truck cab was shortened. The road surface excitation reappearance experiment of a three-axle-heavy-duty truck was carried out with 6-channel road simulator by Jiang [5]. The compression and extrapolation of load spectrum of a heavy off-road vehicle collected from proving ground were conducted by Zhao [6] to obtain the target load spectrum used in bench simulation test.

Based on 4-channel road simulation rig, the cab with suspension is taken the research object in this chapter, the inner force of fixture and the actuator cylinder is decreased through frame processing and test rig design. Taking the acceleration signal as the target signal, the loading spectrum collected in the road test is reproduced in the test rig through physical iteration, and the design weaknesses of the cab are checked out. This paper has great engineering value for evaluating the heavy truck cab through road simulation test.

45.2 Acquisition and Processing of Road Load Spectrum

45.2.1 Acquisition of Road Load Spectrum

In this chapter, the acceleration signal measured at connection point of suspension on the cab is taken as target signal. Meanwhile, the suspension deflections and strain signal of mount point of rear suspension on cab longitudinal beam are measured. The signal acquisition sensors are shown in Table 45.1.

The test roads include beating road, bumpy road, long-wave road, short-wave road, cobblestones road, distortion road, fish-scale pits road, washboard road, Belgium road, sandstone road, pave road, off road and snake road.

45.2.2 Signal Analysis and Processing

To improve the authenticity and reliability of collected data, the signal should be processed. The signal processing usually comprises several parts: data editing and layout, trend component elimination, singular points elimination, stationarity and normality test, etc. The comparison of singular points elimination is shown in the Fig. 45.1.

Table 45.1 Sensors used for acquiring signals

Sensor	Number	Signal	Positional distribution
Accelerometer	12	Frame and cab acceleration	Frame side rail and cab longitudinal beam
Displacement sensor	4	Suspension deflections	Front and rear suspension
Strain gauge	2	Strain signal	Mount point of rear suspension

Fig. 45.1 The comparison of singular points elimination

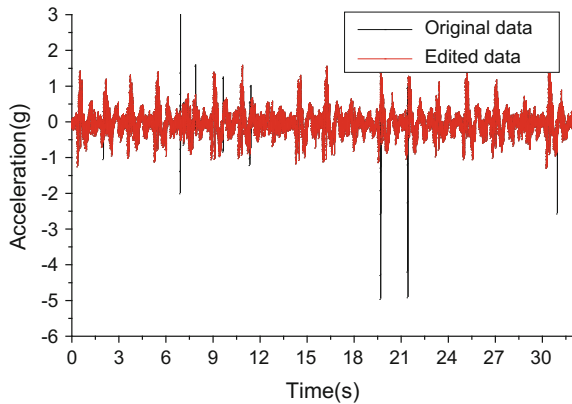


Table 45.2 The amplitude statistic of acceleration signal

Channel	Minimum/g	Maximum/g	RMS/g	Average/g
LF acceleration	-2.25328	1.93766	0.467266	-0.006345
RF acceleration	-2.34484	2.19366	0.520277	0.008221
LR acceleration	-1.56177	1.45071	0.329362	0.05785
RR acceleration	-1.2883	1.50161	0.347018	0.050816

The statistics analysis in amplitude and frequency domain was conducted. The eigenvalue of amplitude includes minimum, maximum, root mean square value and average of the signal. The amplitude statistic of different roads shows that the acceleration in the front part of frame is larger than the rear part. The amplitude statistic of acceleration signal, measured at bumpy road, is shown in Table 45.2. The auto-power spectral density reflects the intensity of different frequency components. According to the auto-power spectral density of acceleration, the energy of acceleration signal concentrates in low frequency, which is lower than 30 Hz.

45.3 The Design of Test Rig

45.3.1 The Motion Analysis of Cab

The frame and cab was mounted on 4 actuator cylinders by 4 spherical hinges which was fixed on the cross beam of the frame. The cab has three degree of freedoms, namely vertical displacement Z , X-rotation Φ and Y-rotation Θ . The left front cylinder, right front cylinder, left rear cylinder and right rear cylinder are given number z_1, z_2, z_3, z_4 respectively. The distance between z_1 and z_2 , or z_3 and z_4 is 750 mm, and between z_1 and z_3 , or z_2 and z_4 is 1630 mm. The freedom synthesis matrix H can be derived from the geometrical relationship,

$$H = \begin{bmatrix} 0.25 & 0.25 & 0.25 & 0.25 \\ 0.667 & -0.667 & 0.667 & -0.667 \\ -0.307 & -0.307 & 0.307 & 0.307 \end{bmatrix}$$

and $DOF = H \cdot L$, $DOF = [Z \ \Phi \ \Theta]^T$, $L = [z_1 \ z_2 \ z_3 \ z_4]^T$. The driving signal of actuator cylinder can be transformed into the motion of cab, and meanwhile the freedom decomposition matrix H^{-1} can be obtained,

$$H^{-1} = \begin{bmatrix} 1 & 0.375 & -0.815 \\ 1 & -0.375 & -0.815 \\ 1 & 0.375 & 0.815 \\ 1 & -0.375 & 0.815 \end{bmatrix}$$

and $L = H^{-1} \cdot DOF$, the motion of cab can be transformed into the driving signal of actuator cylinder by matrix H^{-1} .

45.3.2 Frame Design

The cab is installed on the frame through 4 suspensions. The long frame in actual vehicle can't be installed on the test rig directly, and the kinetics response of suspension system is mainly caused by the front part of frame. So the rear part of frame is cut off. The test rig is a typical redundant actuation mechanism with 4 vertical driving signals. When frame being twisted, the cylinders will be subjected to bending moment, which caused by lateral force. If the frame has large torsion stiffness, the cylinder and fixture would be damaged, and large stiffness will induce inter coupling between response signals. So the two large cross beams are replaced by two small cross beams.

45.3.3 Multi-Body Dynamics Simulation

ADMAS is used to analyze the dynamic response of different frame. In order to reflect the effect of frame stiffness to fixture, the modal neutral file is imported into ADMAS and the rigid frame is converted into flexible. The spherical hinges and fixtures are replaced by spherical pairs in ADMAS. Multi-body dynamic models are shown in Figs. 45.2 and 45.3.

4 sin-wave driving signals, whose amplitude is 15 mm, are applied to 4 actuator cylinders, and induce torsion deformation. And then the lateral forces of 4 spherical pairs are shown in Table 45.3. According to statistical results, the lateral forces of 4 spherical pairs which linked to 4 actuator cylinders, are induced significantly.

The statistic results of collected loading spectrum show that, the acceleration of front part of frame is bigger than rear part. The fixture and spherical hinge installed in front will endure bigger lateral force during the text. 2 spherical hinges are installed at

Fig. 45.2 Initial frame

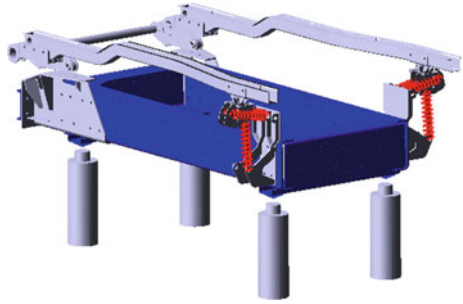


Fig. 45.3 Modified frame

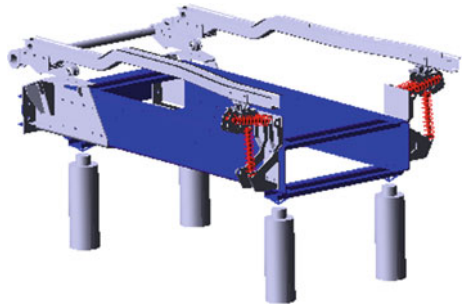


Table 45.3 Lateral forces of 4 spherical pairs

	Initial frame	Modified frame
LF spherical pair/N	97,154	34,767
RF spherical pair/N	97,273	30,652
LR spherical pair/N	91,269	21,780
RR spherical pair/N	96,185	24,621

Fig. 45.4 Lateral force of LF spherical pair

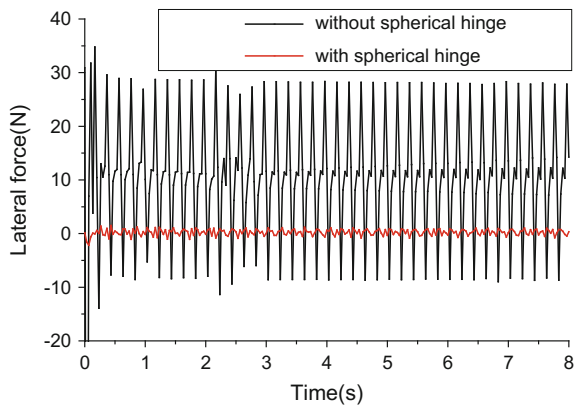
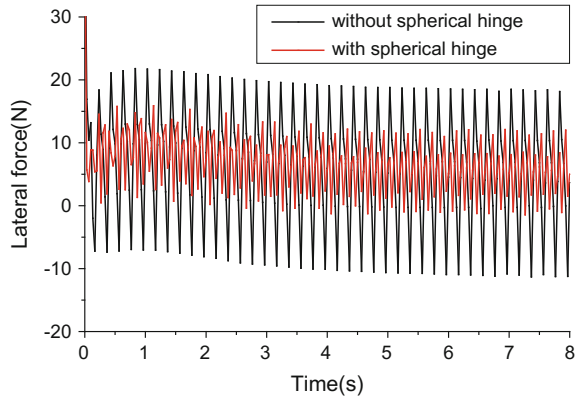


Fig. 45.5 Lateral force of LR spherical pair



the bottom of 2 front cylinders. And simulation is conducted in ADMAS. The comparison of lateral force is shown in Figs. 45.4 and 45.5.

Figures 45.4 and 45.5 show that spherical hinges installed at the bottom of 2 front cylinders can reduce the lateral force of spherical pairs significantly. Simulation results provide theoretical basis and reference for construction of test rig.

45.3.4 Construction of Test Rig

The cab and frame should be installed on test rig before physical iteration and durability test. The test rig can directly influence the accuracy of physical iteration and durability test. Fixtures are designed to link cab and frame to 4 actuator cylinders. 4 spherical hinges are fixed to mount point of leaf spring. The installation method is shown in Fig. 45.6. ADMAS simulation results show that spherical hinges installed at the bottom of 2 front cylinders can reduce the lateral force of spherical pairs significantly, and the installation is shown in Fig. 45.7.

Fig. 45.6 Installation of fixtures

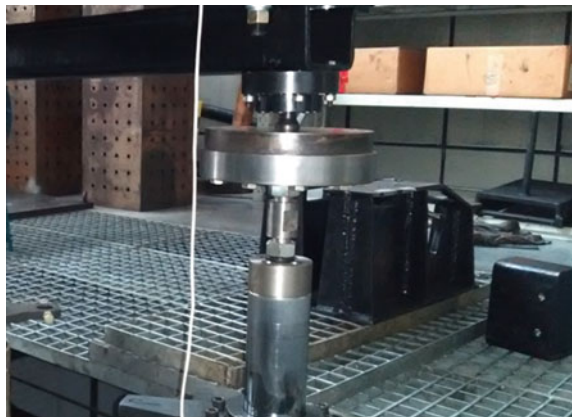


Fig. 45.7 Installation of spherical hinges

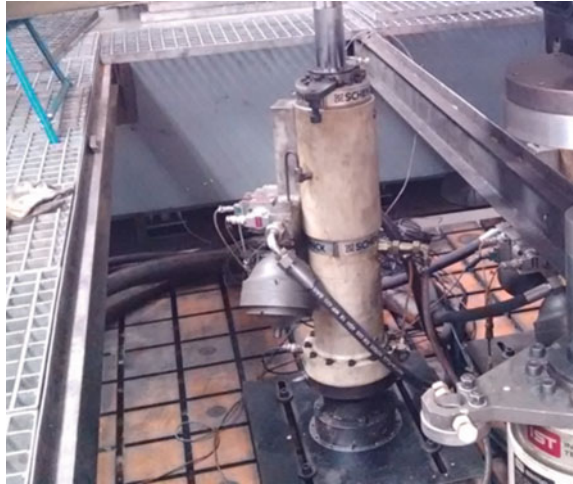


Fig. 45.8 Installation of linear guides



To prevent rear cylinders enduring excessive lateral forces, 2 linear guides are mounted on 2 rear cylinders, and the 2 guides are also fixed to a supporter. Screw connection should have enough pre-tightening force. The installation of linear guides is shown in Fig. 45.8, and the whole test rig is shown in Fig. 45.9.

45.4 Physical Iteration of Load Spectrum

The load spectrum is reproduced through physical iteration. Physical iteration consists of two steps, system identification and target signal iteration.

Fig. 45.9 Test rig

45.4.1 System Identification

The system, which is identified in this chapter, includes controller, electro—hydraulic servo control system, hydraulic cylinder, cab-suspension-frame assembly, acceleration sensors, fixtures, etc. Input signal of the whole system consist of 4 vertical displacements of cylinders. Response signal includes 4 acceleration signals from frame, and the location of acceleration sensors should be consistent with the location, where acceleration sensors located when collecting load spectrum. It is known that the energy of acceleration is concentrated below 30 Hz according to frequency domain analysis. Frequency response function is obtained by white pink noise, whose energy is concentrated below 35 Hz, driving cylinders. The quality of frequency response function is usually evaluated by coherence function. The closer to 1 coherence function is, the better frequency response function is. In engineering practice, the frequency response, whose coherence function is 0.8–0.9, is accurate and reliable.

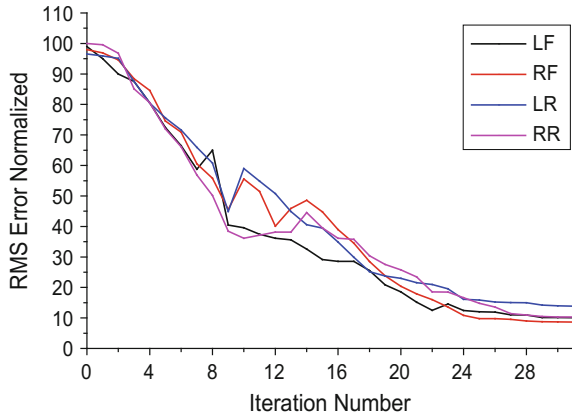
45.4.2 Target Signal Iteration

The driving signals of cylinders can be obtained based on the frequency response function. Errors, caused by nonlinear system, should be eliminated by iteration. The major process is as follows [7].

When obtaining the first driving signal, a weighted coefficient $\alpha(0 < \alpha < 1)$ is introduced to prevent excessive signal and divergence of iteration.

$$U_1(f) = \alpha \cdot H^{-1}(f) \cdot T(f)$$

Fig. 45.10 RMS error plot for iteration



$U_1(f)$ —Fourier transform of Initial driving signal $U_1(t)$; $H^{-1}(f)$ —Inverse matrix of transfer function $H(f)$; $T(f)$ —Fourier transform of target signal $T(t)$; α —weighted coefficient. Response signals of whole system are obtained by playing driving signals. The error $E(t) = T_n(t) - T(t)$ is also obtained ($T_n(t)$ -Response signal of n times iteration), and driving signal of next iteration is revised according to the error.

$$\Delta U(f) = \beta \cdot H^{-1}(f) \cdot E(f)$$

$$U_{n+1}(f) = U_n(f) + \Delta U(f)$$

$\Delta U(f)$ —Increment of driving signal; $E(f)$ —Fourier transform of $E(t)$; β —weighted coefficient ($0 < \beta < 1$); $U_{n+1}(f)$ —Fourier transform of n + 1 times iteration; $U_n(f)$ —Fourier transform of n times iteration. The quality of physical iteration is usually evaluated by relative mean square error between response signal and the target signal for the system whose target signal is acceleration.

Fig. 45.11 Comparison in time domain

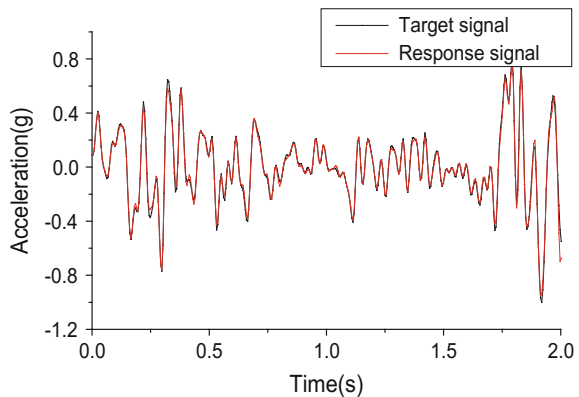


Table 45.4 The results of road simulation test and proving ground test (+: Yes, -: No)

Weak location	Road simulation test	Proving ground test
The lower side of the solder joint of front cab	+	+
The weld between outer panel front wall and engine cabin	+	+
The weld between front wall and engine cabin	+	+
Roundness of front wall	+	-
The weld between front stringer and floor	+	+
The corner floor stringer	+	+
The door cannot be completely closed	+	+
The bolts of the cab tilting mechanism loose	+	+
The weld around the lower part of the front cabin	+	+
The crack of cabin dashboard	+	+

$$\varepsilon = \frac{RMS(E(t))}{RMS(T(t))}$$

ε —Relative mean square error; $RMS(\cdot)$ —Root mean square. Generally speaking, iteration can be stopped as long as $\varepsilon \leq 10\%$. RMS error plot for iteration is shown in Fig. 45.10. The iterative signals and the target signals have a highly consistency in time domain and as shown in Fig. 45.11.

45.5 Test and Result

The driving signal from the last iteration is arranged in accordance with the road load spectrum acquisition sequence. Then the driving signal is played again and again until the test is completed. Finally, the result of road simulation test is consistent with the proving ground test. The test results are shown in Table 45.4 and the weld crack between front wall and engine cabin is shown in Fig. 45.12.

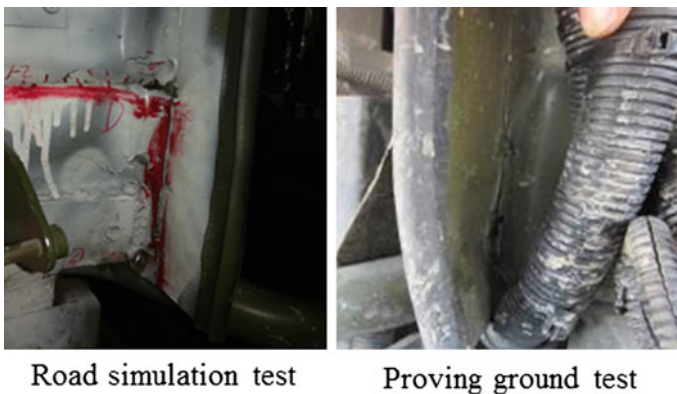


Fig. 45.12 The weld crack between front wall and engine cabin

45.6 Conclusion

Based on the 4-channel road simulator test rig, the fatigue durability performance of the truck cab with vehicle frame and suspension system is checked out. The result of road simulation test is consistent with proving ground test. This test is also a successful further use of 4-channel road simulation rig, and the purpose, small test rig loading a large load, is achieved. This paper has great engineering value for evaluating the heavy truck cab through road simulation test.

References

1. Gao Y (2006) Structural analysis of vehicle body. Beijing Institute of Technology Press, Beijing
2. Gao Y, Fang J, Xie M (2012) Durability analysis and evaluation of a frame-type heavy truck cab. *J Tongji Uni (Natural Sci)* 40(5):723–728
3. Zhou H, Feng Z (2001) The application of remote parameter control technology in dynamic strength test of car body structures. *Automobile Technol* 2:20–22
4. Gosavi SS (2006) In lab truck cab and cab suspension durability validation. SAE Technical Paper
5. Jiang H, Dai Y, Lintao Y (2008) Road surface excitation reappearance experiment on heavy-duty truck based on 6-channel road simulator. *Automobile Technol* 9:46–49
6. Zhao X, Zhang Q, Jiang D (2009) The compression and extrapolation of load spectrum for a heavy off-road vehicle obtained from proving ground testing. *Automotive Eng* 31(9):871–875
7. Yudong H, Zhou H, Gang X (2012) Control algorithm of test rig for vehicle road simulation. *J Tongji Uni (Natural Sci)* 40(8):1244–1248

Chapter 46

Research on the Fluxless Brazing of Aluminum Air Cooled Oil Cooler

Changxing Mei, Hao Liu, Xiaobo Mai, Yongjin Gao
and Renzong Chen

Abstract Controlled atmosphere brazing of aluminum air cooled oil cooler without flux was investigated. The materials of the middle plates and the mounting plates used in the research are fluxless brazing alloy with five layers. The materials of the other parts are conventional 3003 single layer aluminum alloy. After assembling, the oil cooler is put into the CAB brazing furnace, without appended any flux on it. After brazing, the surface of the oil cooler is dark, and the brazing fillets between the middle plates can hardly be seen from the outside of the oil cooler by naked eyes. The metallographic analysis of the sections of the oil cooler shows that the fillets of the brazing seams near the outside of the oil cooler are very small, but the fillets of the brazing seams of the interior are very big. This phenomenon shows that the molten brazing filler flows from the outside of the oil cooler to the inside during brazing. The SEM and EDS analysis results shows that a thin flux layer is covered on the surface of the middle plates of the outside of the oil cooler. The existence of the flux layer effects the oxide removing ability of the fluxless brazing materials. Consequently, the wetting and spreading abilities of the brazing filler on the surface of the aluminum alloy after melting are influenced.

Keywords Air cooled oil cooler · Fluxless CAB brazing · Flux adhesion · Wetting ability · Reaction

46.1 Introduction

There exists an oxide layer on the surface of the aluminum alloy with the thickness of about 10 nm at the room temperature at the atmosphere [1]. When the aluminum alloy is heated to the brazing filler melting point, the thickness of the oxide is

C. Mei (✉) · H. Liu · X. Mai
Zhejiang Yinlun Machinery Co., Ltd, Tiantai, China
e-mail: meichangxing@yinlun.cn

Y. Gao · R. Chen
Huaфон Nikken Aluminum Co., Ltd, Shanghai, China

rapidly increased to several hundred nanometers. The structure of the aluminum oxide is very dense, and the melting point of the oxide is as high as 2050 °C, so it is very hard to broke during brazing. The existence of the oxide layer severely effects the wetting ability of the brazing filler. In a word, the sticking point of aluminum brazing is removing the oxide covered on the surface of the aluminum alloy during brazing.

The state-of-the-art brazing processes of aluminum oil cooler are controlled atmosphere brazing(CAB) and vacuum brazing (VB) [2].

During CAB brazing, Nocolok flux ($KAlF_4 + K_3AlF_6$) is adopted to remove the oxidation film, which covers on the surface of the aluminum parts before brazing. CAB brazing has the advantages of high efficiency and larger-gap adaptability between parts, but the disadvantages are also very clear. The first disadvantage is flux remaining on the inner surface of the product after brazing, which effects the cleanliness of the oil cooler [3, 4]. The second disadvantage is also related to flux remaining. When the brazing gap between parts is very big, the brazing filler is not enough to fill in the gap, so the molten flux fill in the gap. This defect is not able to be detected during manufacture process. When the oil cooler is installed on the car and running on the road, the flux adhered on the brazing seam will broken off under work force and libration, and makes the oil cooler leak and the engine failed.

During vacuum brazing, the atmosphere force is controlled below 5×10^{-3} Pa by vacuumizing. When the aluminum brazing alloy is heated above 400 °C, the Mg element in the brazing filler diffuses to the surface of the aluminum alloy, and reacts with the oxidation film. Vacuum brazing has the edge of high appearance quality [5–7], and high Mg content is allowed in the core layer, which increases the strength of the Al alloy. But vacuum brazing has the disadvantages of high parts cleanness, low efficiency and high cost.

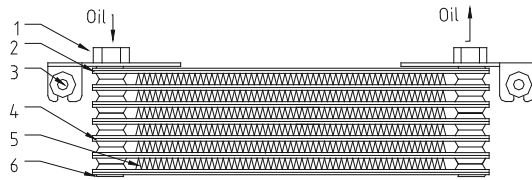
The fluxless CAB brazing means adding no flux after assembling, and putting the products directly into the CAB brazing furnace to braze. The mechanism of the fluxless brazing is nearly the same as vacuum brazing. Both of them use the oxide removing ability of Mg element to remove the oxide covered on the surface of the aluminum alloy during brazing. But the difference is that the structure and chemical content of the fluxless CAB brazing material is optimized, so fewer Mg element is needed, and the request of the atmosphere is not so strict. The fluxless CAB brazing both have the advantages of conventional CAB brazing and vacuum brazing, for instance, cleanliness, high efficiency and no flux remained after brazing.

46.2 The Product Structure and Experimental Materials

46.2.1 The Product Structure

The mechanism of the air cooled oil cooler is using air to cool the engine oil. The main parts of the product are flanges, upper plate, mounting plate, middle plates, fins and lower plate. All of these parts are joined together by brazing. When the oil

Fig. 46.1 Schematic diagram of the structure of the oil cooler 1 flange, 2 upper plate, 3 mounting plate, 4 middle plate, 5 fin, 6 lower plate



cooler is working, the engine oil flows into one of the flange and flows out from the other flange. The engine oil flows between two middle plates when it flows inside of the oil cooler, so the heat of the engine oil is transferred to the atmosphere by fins and plates. There are two sorts of the fins in the oil cooler. One sort of the fins are located at the inside of the oil cooler, and cannot be seen from the outside. They are used as disordering the flowing engine oil and transferring the heat out. The other sort of the fins can be seen from the outside of the oil cooler. They are used to transfer the heat from the middle plates to the atmosphere. The structure of the oil cooler is shown in Fig. 46.1.

46.2.2 Experimental Materials

The materials of the middle plates and the mounting plates are special multi-layers. Both of the surfaces of the middle plates are covered with brazing filler metal, but there is only one surface of the mounting plate covers with brazing filler metal. The materials of the other parts are conventional 3003 aluminum alloy, without brazing filler metal layer.

The materials of the different brazing methods are mainly the difference of the aluminum multi-layers. For instance, if normal CAB brazing (Nocolok brazing) is chosen, the middle plates are usually three-layer aluminum alloy, using 4045 brazing alloy as cover layer with 3003 aluminum alloy as core layer. But if vacuum brazing method is chosen, although the middle plates and mounting plates are also three layers, but the chemical content makes a big difference. The brazing layers contain about 1.0–2.0% Mg, which is strictly controlled in Nocolok brazing.

The five-layer structure is usually adopted in the fluxless brazing alloy. The number of the layers is larger, the easier to add and control alloy element, but the cost is also increased, so the five-layer structure is the best choice. As mentioned before, the mechanism of the fluxless CAB brazing is like vacuum brazing, the Mg element is added in the brazing materials as alloy element to remove the aluminum oxide covered on the surface of the aluminum. The Bi element is also added to increase the wetting ability of the brazing filler metal.

The chemical content of the fluxless CAB brazing material which is called 9181 is shown in Table 46.1. 9181 alloy has five layers, which contains two top layers, two brazing layers and one core layer. Both top layers and brazing layers has high Silicon content, but the content of Si is much higher in the brazing layers.

Table 46.1 The chemical content of 9181

Element	Top layer	Brazing layer	Core layer
Si	4.25–5.2	11.0–13.0	0.60
Fe	0.25	0.25	0.70
Cu	0.25	0.25	0.05–0.20
Mn	0.10	0.10	1.0–1.5
Mg	0.05	0.30	0.05
Cr	0.10	0.05	0.05
Zn	0.05	0.10	0.10
Ti	0.05	0.05	0.05
Zr	–	–	0.05
Bi	–	0.05–0.20	–
Al	Bal.	Bal.	Bal.

During fluxless CAB brazing, when the product is heated to 400 °C, the Mg and Bi elements contained in the brazing filler begin to diffuse to the top layer, the diffusion speed of Mg and Bi is much higher when the temperature raises. When the temperature of the products raises to the brazing filler metal melting point, the brazing filler metal melts and flows to the direction of the top layer. Because the top layer is very thin, the erosion effect of the brazing filler makes the top layer melt. The ideal result is that the Mg and Bi elements diffuse to the surface of the aluminum on time and react with the oxidation film when the brazing layers and top layers are all melting.

The thickness of the top layer and the Mg and Bi content are the key know-how of the fluxless CAB brazing materials. If the top layer is too thin, the Mg and Bi elements diffuse to the surface of the aluminum ahead of time. The Mg element removes the oxide but the brazing filler metal is not melted at the moment, so the surface of the aluminum re-oxidized before all of the brazing filler melting. When the brazing filler melts, the surface of the aluminum is not able to wetting the molten brazing filler.

If the top layer is too thick, the erosion function of the brazing filler is too weak to make all of the top layer melted, the brazing process must be failed either. Moreover, the Mg and Bi content of the brazing filler should be strictly controlled, The Mg content must be controlled less than 0.3%. The Bi content of the top layers should be controlled less than 0.05%.

46.3 Experiment Process

The fluxless CAB brazing materials are stamped into middle plates and mounting plates, and then assemble them with upper plates, fins, lower plates and flanges which are currently used in conventional CAB brazing. All of the parts are assembled together referring to the blueprint. After assembling, put the semi-manufactured products on the press machine to make the gap between parts much smaller.

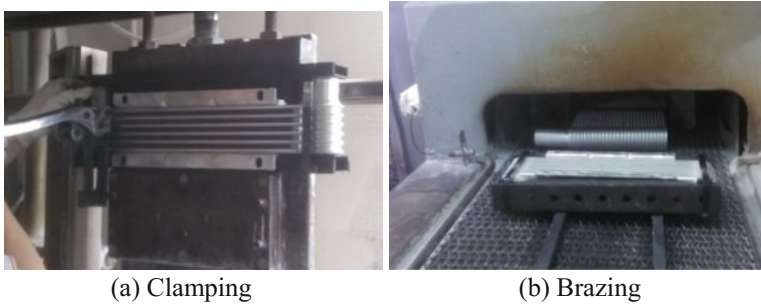


Fig. 46.2 Test process

After assembling and clamping, put the oil coolers directly into the CAB furnace to braze, without dipping or painting flux (Fig. 46.2).

The fluxless brazing oil cooler is put together with Nocolok brazing products in the CAB furnace. The CAB brazing furnace has 6 heating zones, and the brazing temperature of each zone is 250 ± 20 , 530 ± 20 , 580 ± 20 , 610 ± 10 , 625 ± 10 , 625 ± 10 °C. The mesh belt operating speed is 400–520 mm/min.

46.4 Results and Discussions

46.4.1 Analysis of the Appearance of the Oil Cooler

The appearance of the fluxless CAB brazing oil cooler is analyzed after brazing. The appearance of the oil cooler is shown in Fig. 46.3. The surface of the middle plates and the fins of the outside of the oil cooler is dark, even darker than Nocolok brazed products. The quality of the brazing seams is very bad. The brazing seams even cannot be seen from the outside of the oil cooler.

After cutting the product by saw, the appearance of the interior of the oil cooler is shown in Fig. 46.3c. The color of the inside surface of the oil cooler is brighter, and the brazing seam fillets are very full.

46.4.2 Metallographic Analysis

The microstructure of the brazing seam of the middle plate to the middle plate is shown in Fig. 46.4. The brazing seam fillet of the inside of the oil cooler is very big, but the fillet of the outside of the oil cooler is very small. Compared the residual brazing layer of the outside to the inside of the oil cooler, we conclude that the brazing filler flows from the outside of the oil cooler to the interior during brazing, as shown in red arrow in Fig. 46.4.

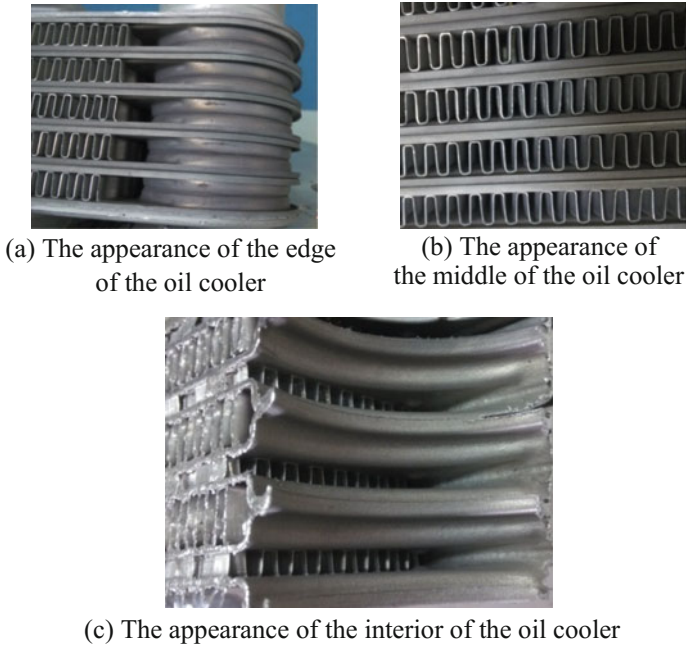
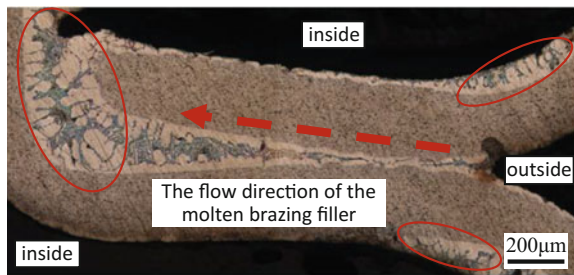


Fig. 46.3 The appearance of the oil cooler after brazing

Fig. 46.4 The brazing seam of the middle plates of the oil cooler



The brazing seam of the middle plate to the inside fin is shown in Fig. 46.5. The fillet of the brazing seam is very big, and the quality of the brazing seam is very excellent, without defects such as porosity and gaps.

The brazing seam of the middle plate to the outside fin is shown in Fig. 46.6. The fillet of the brazing seam is very small. Compared with the brazing seam of the inside of the oil cooler, we know that the quality of the brazing seam of the outside of the oil cooler is very poor, but the brazing seam of the interior is very good. The quality of the brazing seam may be influenced by the furnace atmosphere during brazing. The interior of the oil cooler is isolated relatively to the outside, so the

Fig. 46.5 The brazing seam of the middle plate to the inside fin

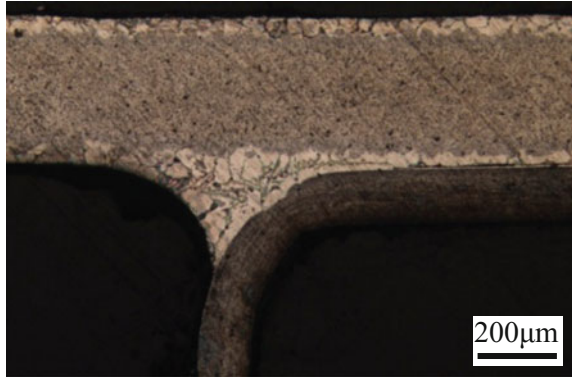
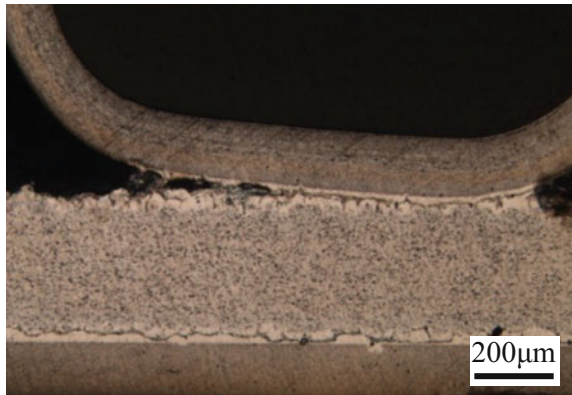


Fig. 46.6 The brazing seam of the middle plate to the outside fin

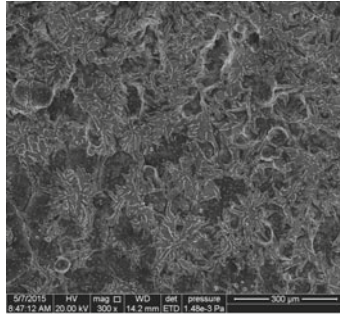


furnace atmosphere hardly effect the brazing process. But the outside of the oil cooler is contacted tightly to the atmosphere, so the brazing process is influenced by the atmosphere.

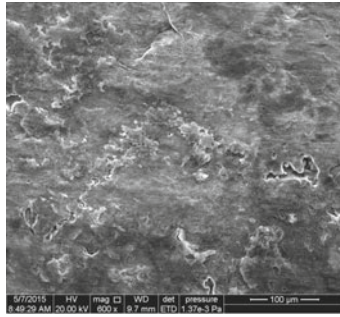
46.4.3 SEM and EDS Analysis

46.4.3.1 Analysis of the Appearance by SEM

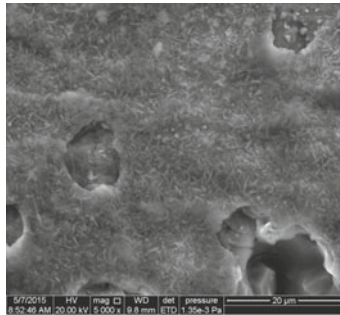
The morphologies the surface of the middle plates of the outside and the inside of the oil cooler by SEM is shown in Fig. 46.7. Figure 46.7a shows the surface morphology of the middle plate of the inside of the oil cooler. The brighter zone of the picture is Al-Si eutectic structure, and the darker zone is α -Al primary phase. These phases are typical after brazing in the aluminum brazing materials. The morphologies of the middle plate of the outside of the oil cooler are shown in



(a) The morphology of the middle plate of the inside of the oil cooler



(b) The morphology of the middle plate of the outside of the oil cooler(600X)

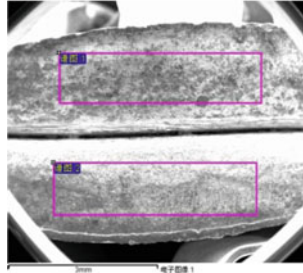


(c) The morphology of the middle plate of the outside of the oil cooler(5000X)

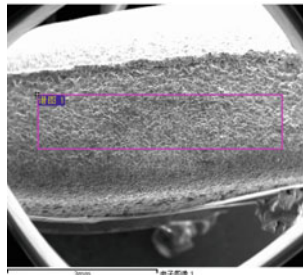
Fig. 46.7 The morphologies of the middle plates of the inside and outside of the oil cooler

Fig. 46.7b, c. When the magnification is 600 \times , the surface of the middle plate is flat and smooth, the Al-Si eutectic structure cannot be seen from the picture. When the magnification is 5000 \times , the morphology of the surface of the middle plate is changed. The surface of the middle plate covers with a layer with many white needle-like substances embedded in it.

Fig. 46.8 EDS analysis areas of the middle plates of the oil cooler



(a) EDS analysis areas of the outside of the oil cooler



(b) EDS analysis area of the inside of the oil cooler

46.4.3.2 EDS Analysis

The EDS analysis areas of the middle plates of the outside of oil cooler are shown in Fig. 46.8a. Two areas of $3\text{ mm} \times 1\text{ mm}$ are chosen to analyze the chemical content of the surface of the middle plates. An area of $3\text{ mm} \times 1\text{ mm}$ of the middle plate of the inside of the oil cooler is chosen to analyze the chemical content, as shown in Fig. 46.8b.

The EDS analysis results of the middle plates of the outside and inside of the oil cooler are shown in Table 46.2. The oxygen content of the middle plate of the inside is higher than outside of the oil cooler, it is concluded that the oxygen content is not the factor which effects the appearance of the oil cooler and reduces the quality of the brazing seam. Compared Table 46.2a, b, we can find that the surface of the middle plate of the outside of the oil cooler contains high K, F, Mg element, but the surface of the middle plate of the inside contains very little F, and contain no K element. We can infer that the dark appearance and poor brazing seams of the outside of the oil cooler are related to the existence of the brazing flux.

As is well-known, during conventional CAB brazing, the Mg element react with KAlF_4 flux at the brazing temperature, and generates MgF_2 , which has higher melting point. and effects the oxide removing ability of the KAlF_4 flux, so the Mg content in the brazing materials is strictly controlled. On the contrary, the existence of the KAlF_4 flux in the brazing furnace effects the oxide removing ability of the

Table 46.2 EDS analysis results of the middle plates of the outside and inside of the oil cooler

Element	Area 1	Area 2
(a) The chemical content of the middle plate of the outside of the oil cooler		
O	9.45	7.56
F	22.15	18.67
Mg	4.23	2.99
Al	44.28	47.98
Si	14.47	18.23
K	3.70	2.85
Mn	–	0.33
Element	Area 1	
(b) The chemical content of the middle plate of the inside of the oil cooler		
O	22.42	
F	0.74	
Mg	0.15	
Al	59.15	
Si	16.47	
K	0.00	
Mn	0.31	

Mg element which contained in the brazing materials when it diffuses to the surface of the aluminum alloy during brazing. The reaction makes the appearance of the oil cooler dark and the quality of the brazing seam poor. The interior of the air cooled oil cooler is relatively isolated from the outside, the $KAlF_4$ flux can hardly contact and effect the brazing process of the interior of the oil cooler. Consequently, the brazing seam of the interior of the oil cooler is very good, with bright color.

46.5 The Conclusions

Fluxless CAB brazing of air cooled oil cooler with fluxless brazing alloy was carried out, the conclusions are as follows:

- (1) The appearance of the oil cooler turns to dark after brazing, and the brazing seam fillets size of the middle plates of the outside of the oil cooler are very small. Hardly can it be seen by naked eyes.
- (2) The microstructure of the brazing seams of the oil cooler are analyzed, The brazing fillets of the interior of the oil cooler are very big, the brazing fillets near the outside of the oil cooler are very small. The molten brazing filler metal flows from the surface of the outside of the oil cooler to the interior during brazing.

- (3) By SEM analyzing, the Al–Si eutectic structure can be seen on the surface of the interior of the product, but it cannot be seen at the outside of the oil cooler. By magnifying 5000×, a layer covered on the surface of the middle plates of the outside of the oil cooler can be found, with white needle-like substance embedded in it.
- (4) The surface of the outside of the oil cooler contains high F, K, Mg content, but the interior contains little F and Mg, with no K element contained. The existence of KAlF₄ flux takes effect on the oxide removing ability of the Mg element contained in the fluxless brazing alloy, and makes the brazing process failed.

References

1. Ren Y (1993) The processes of vacuum brazing. Press of Machinery Industry, Peking
2. Xu S, Xu D (2004) Research status of brazing technology of Al and Al alloy. *Manuf Technol Light Alloy* 32(1):1–4
3. Sekulic DP, Galenko PK, Kivilyov MD, Walker L, Gao F (2005) Dendritic growth in Al–Si alloys during brazing. *Int J Heat Mass Transf* 48(12):2358–2396
4. Pan C, Sekulic DP (2002) The microstructure characteristic of the AA4343/AA3003 aluminum brazing joint. *China J Ferrous Metal* 12(3):481–485
5. Liu H (2010) Research on vacuum brazing of aluminum oil cooler. School of Materials Science and Engineering, Chongqing University, Chongqing
6. Hu G, Kang H (2001) The development of vacuum brazing. *Weld Technol* 30(2):1–3
7. Sun R, Ma Y, Wang G (2009) Analysis on the reason of the leak of the aluminum oil cooler of vacuum brazing. *Process Technol Light Metal* 37(3):47–50

Chapter 47

Analysis of Manufacturing Technology for the Spherical Head Supporting Part

Sanhu Zhao, Laitao Zhai, Baoyang Song,
Kai Cui, Yang Li and Bo Yu

Abstract The spherical head supporting part is an essential part which connects the shell of one kind of front drive axle body, wheel driving and steering, braking structure and other key parts of the body, and to assume the function of load-bearing, steering, driving, braking and so on, it also has an important implications on the load-bearing capacity, steering capability, reliability, service life and safety of the front drive axle. This article mainly introduce the manufacture of the spherical head supporting part which the both ends are thick while the middle part is thin, inside the part is empty, both the inner and outer part are spherical and has special structures. Mainly introduce the technology of dual spherical head forging, hard turning, trundle processing that are used in the manufacture of this spherical head supporting part. Overcome the challenge of dual spherical head forging technology, both ends with reverse fillet shaft induction hardening surface manufacture technology. Smoothly finished debugging and manufacturing the spherical head supporting part. Also finished the test of the front drive axle. The spherical head supporting part's function, strength, stiffness, reliability, fully meet the requirements of bench test, reliable, and fully meet the demand of the vehicle matching.

S. Zhao (✉) · L. Zhai · Y. Li · B. Yu
FAW C., Ltd. R&D CENTER Prototyping Department, Changchun 130011, China
e-mail: zhaosanhu@rdc.faw.com.cn

L. Zhai
e-mail: zhailaitao@rdc.faw.com.cn

Y. Li
e-mail: liyang@rdc.faw.com.cn

B. Yu
e-mail: yubo@rdc.faw.com.cn

B. Song · K. Cui
FAW C., Ltd. R&D CENTER Technology Department, Changchun 130011, China
e-mail: songbaoyang@rdc.faw.com.cn

K. Cui
e-mail: cuikai@rdc.faw.com.cn

Keywords The spherical head supporting part · Dual spherical head forging technology · Hard turning · Trundle processing technology

47.1 Analysis of the Spherical Head Supporting Part

The spherical head supporting part is a key part of the front drive axle. By connecting the shell of the front drive axle body and wheel driving and steering, braking structure etc., to undertake the following functions (see Figs. 47.1 and 47.2):

1. **Load-bearing function;** After welding with the shell of front drive axle body, load-bearing the mass of truck frame and other assembly parts on it;
2. **Steering function;** Through cooperating with the shell of steering knuckle and other steering knuckle part, realize the steering function;

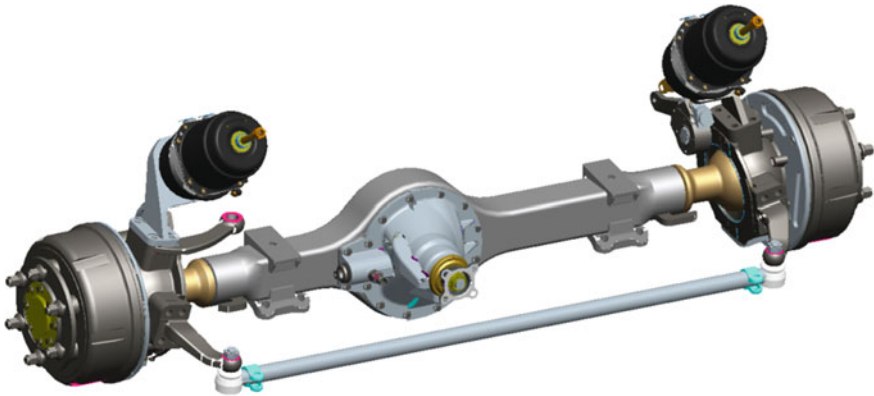


Fig. 47.1 Front drive axle assembly

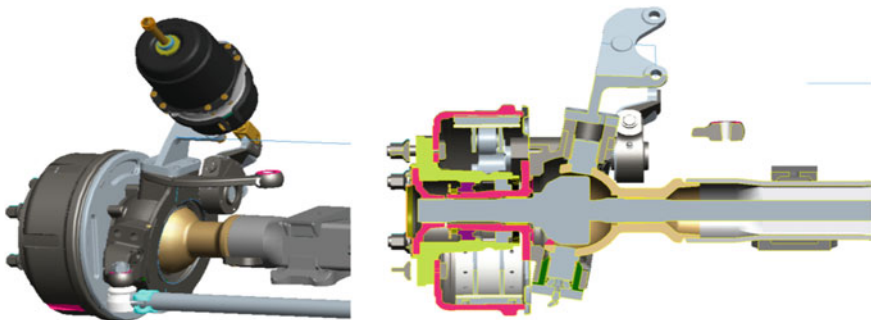


Fig. 47.2 The wheel part structure

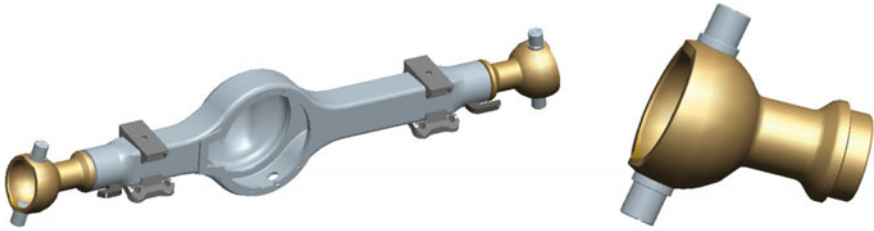


Fig. 47.3 The front drive axle and the spherical head supporting assembly

3. **Force transmitting function;** Through cooperating with the steering knuckle shell, wheel hub, brake drum, and other component of the matching, undertake the transmission of front axle's driving and braking force;

In order to ensure the function, performance and reliability requirements of the front drive axle. The spherical head supporting part has the following characteristics (see Fig. 47.3):

- (1) The spherical head supporting part has hollow structure;
Driving shaft that passes through the inner hole connects half axle gear and the driving wheel, realize the driving function;
- (2) Both ends are thick while the middle part is thin; In order to ensure the front drive axle assembly's welding strength, improve the bending strength, stiffness and reliability of the front drive axle assembly, the diameter of the right guiding and location restricting cylindrical surface and welding part's cylindrical surface is large. In order to avoid turning interference and ensure the front drive axle assembly's steering angle, the diameter in the middle part is small. Because the requirements of steering, braking functional, the diameter in left is large;
- (3) Both the inner and outer surface in the left part are spherical structure.

The ball cage cardan joint is install in the inside spherical, so it can turn freely; The outside spherical surface cooperate with the oil seal of the ball cage cardan joint, to reach the role of dustproof and seal;

The difficulty in manufacturing the spherical head supporting part (see Fig. 47.4):

- (1) **Forging**

The material of the spherical head supporting part is 40Cr, in order to ensure the strength, stiffness and reliability, the workblank must adopt forging forming process, so as to ensure the quality of metal streamline, avoid stress concentration. Both the inner and outer surface in the left part are spherical structure, and the sphere surface is more than half a sphere, it will be very hard to put out of the forging's inside spherical surface if adopt normal forging process.

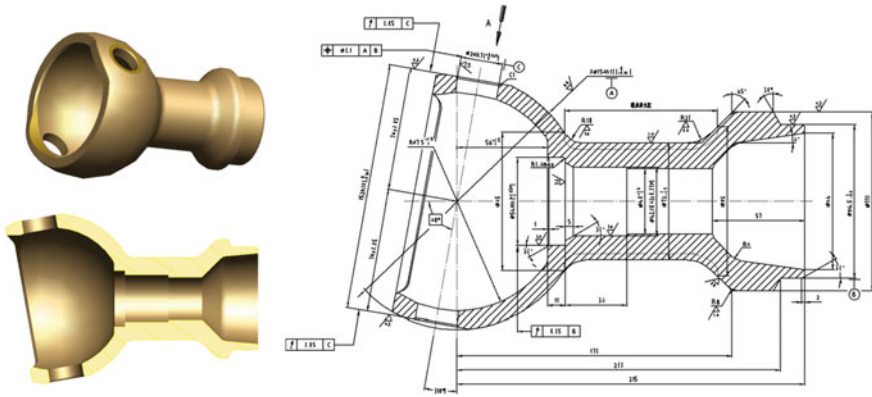


Fig. 47.4 The spherical head supporting part

(2) The manufacture of axis neck

As a part relating to the safety, the strength, stiffness and reliability directly affect the safety of driving personnel. The middle axis neck is the weakest link, excircle diameter is $\Phi 72$ mm, thickness is 16 mm, this part demands induction hardening, the surface hardness is (52–58) HRC, in order to avoid stress concentration, the surface roughness of axis neck surface and the transition fillet between axis neck and both ends must not higher than Ra0.8. Because the hardness of processing site is very high, it can only use grinding processing by normal manufacturing technology, but it's hard to ensure both of the transition fillets transite smoothly by grinding.

47.2 Analysis of Manufacturing Technology for the Spherical Head Supporting Part

47.2.1 Analysis of the Forming of the Spherical Head Supporting Part's Workblank

Because both the inner and outer surface of the part are spherical structure, the difficulty is in the forging of the inside spherical surface. By decomposing the forming of the dual spherical structure in two steps to complete forging the dual spherical structure. (1) To forge the right half sphere, leaving forging allowance for the left half sphere, and forge to annular cylindrical column; (2) To forge the left half sphere by necking down, avoid the problem of putting out of the forging workblank (Fig. 47.5);

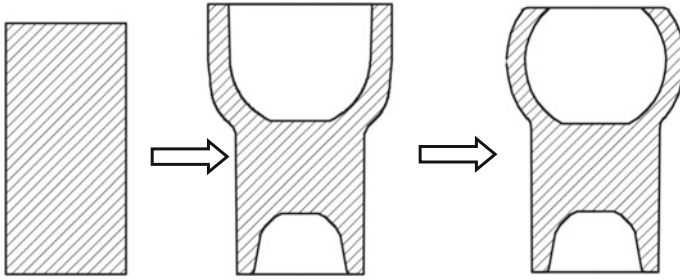
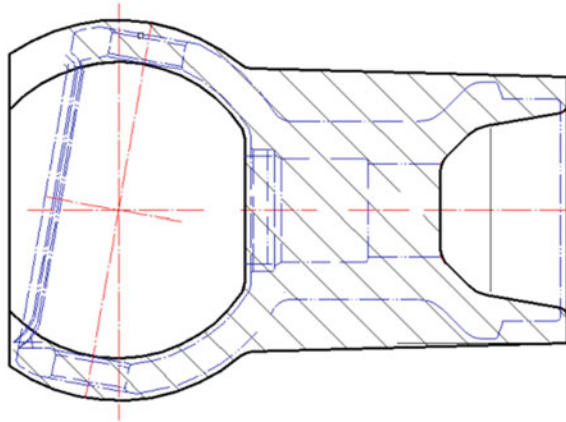


Fig. 47.5 Forging process drawing

Fig. 47.6 The forging workblank drawing



Forging process

Blanking → induction heating → moulding (I forge) → trimming, chamfer → normalizing → cleaning → necking down (II forge) → thermal refining → surface cleaning → examine → rust-proof.

(1) Design the forging workblank drawing

According to the structure of spherical head supporting part and forging process's characteristic, confirm the workblank's machining allowance, forging slope, fillet radius and the tolerance of the workblank (Fig. 47.6).

(2) Choicing of the forging equipment

The forging of the spherical head supporting part has follow characteristics: the part has big forging deformation, need to forge repeatedly; Considering the forging process's characteristic and forging equipment resources, select the electric screw press as forging equipment (Fig. 47.7).

Fig. 47.7 Electric screw press



The characteristics of electric screw press:

- (1) Electric motor directly drive the flywheel, simple construction, strike energy control accurately, high molding precision.
 - (2) Can provide large forging energy.
 - (3) Can adjust stroke height, no bottom dead point, don't need to adjust the mould height, won't jammed; Can forging workpiece according to setting load, to forging and forming through multiple strikes.
- (3) **The choice of equipment nominal pressure**

Electric screw press's nominal pressure is half of its maximum force.

Electric screw press's specification can be selected according to the conversion method:

$$P = (350 \sim 400) \times G$$

In this formula:

- P Electric screw press's nominal pressure (kN);
 G Tonnage of forging hammer calculated based on hammer forging (t)

Tonnage of forging hammer calculated.

Tonnage of forging hammer refers to the quality of forging hammer falling part, with tons of units.

According to the empirical formula:

$$\text{Tonnage of forging hammer } G = (4 \sim 6) \times F / 1000(t)$$

In this Formula:

F projection area of forgings (cm²)

Calculation predicts:

$$\begin{aligned} P &= (350 \sim 400) \cdot (4 \sim 6) \cdot \pi \cdot r^2 / 1000 \\ &= 375 \times 5 \times 3.14 \times 7.9^2 / 1000 \\ &= 1170.2 \text{ KN} \end{aligned}$$

(4) **Workblank calculate**

Common forging can be divided into mushrooming deformation forgings, long pole type forgings, head hammering forgings three types. According to the characteristics of the spherical head supporting part structure, it can be calculated as the type of head hammering forgings.

Head hammering forgings generally select workblank diameter according to indeformable pole diameter, then calculate mushrooming deformation forging head volume V_{head} , trimming volume V_{trim} , indeformable pole volume V_{pole} , the blank volume (see Figs. 47.8 and 47.9):

$$V_p = (V_{\text{head}} + V_{\text{trim}}) \cdot (1 + \delta) + V_{\text{pole}}$$

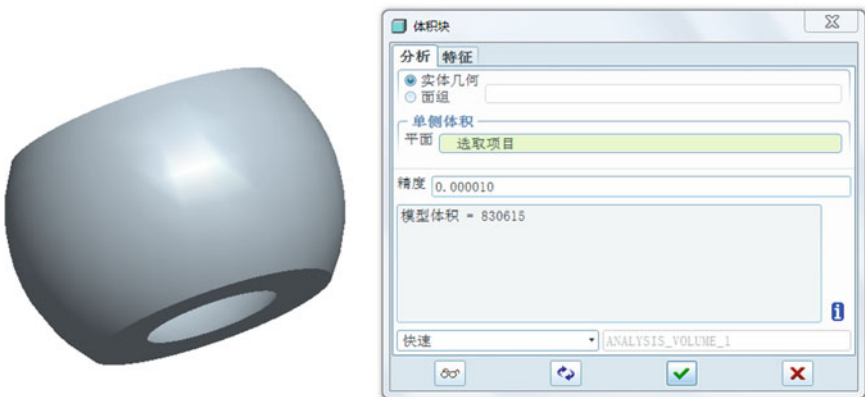


Fig. 47.8 V_{head}

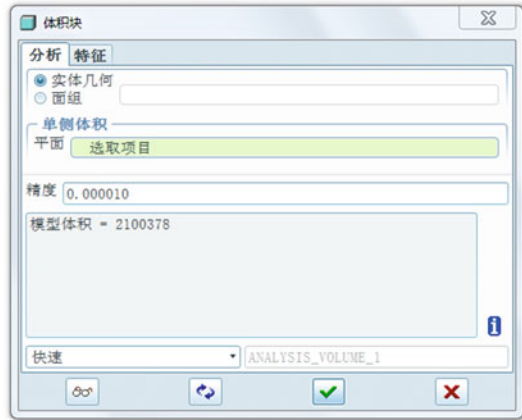


Fig. 47.9 V_{pole}

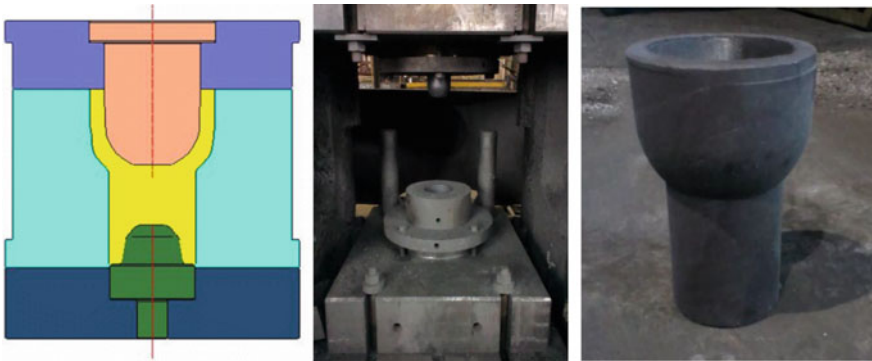


Fig. 47.10 Forming mould

In this formula: δ —loss on heating rate, induction heating select $\delta = 0.5\text{--}1\%$. pole diameter $\Phi 110$ mm;

$$V_{head} = 830615 \times 1.1 + (2100378 - 830615) = 2183439.5 \text{ mm}^2$$

Blanking length:

$$H = V_p / (\pi \cdot r^2) = 2183439.5 \div (3.14 \times 55^2) = 230 \text{ mm}$$

(5) Moulding forming

The spherical head supporting part's forming mould is made up of moulding forming and necking down mould (see Figs. 47.10 and 47.11).

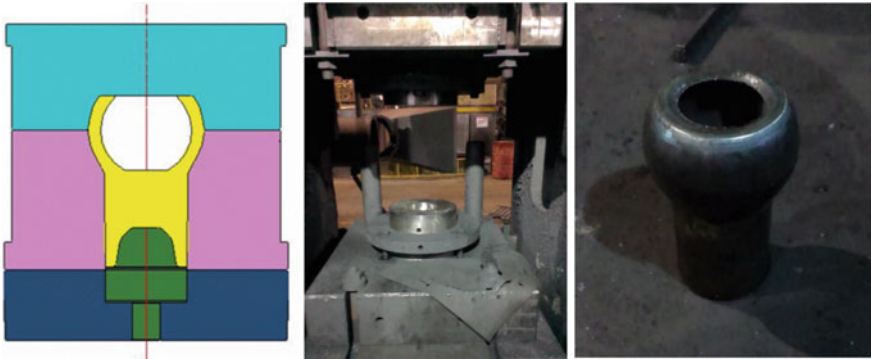


Fig. 47.11 Necking down mould

47.2.2 *The Spherical Head Supporting Part's Middle Axis Neck Machining Process Plans*

When the spherical head supporting part is in the process of practical work time, middle axis neck bear alternating bend torsion load, impact load caused by uneven road, braking, etc. Use under harsh conditions, therefore the middle axis neck's surface roughness, residual stress, hardness and so on are very strict. In the middle of axis neck $\phi 72_{-0.05}^0$ surface roughness is Ra0.8, the transition fillet surface both sides R10, R20 surface roughness is Ra0.8, the middle of axis neck and both sides transition fillet need induction hardening, and it can't have tool marks connection and other tool marks which may cause stress concentration in both of he transition fillet surface.

According to the requirements of parts, adopt the processing technology of hard cutting and trundle processing to trial-manufacture.

(1) **Hard cutting technology**

Hard cutting technology (by turning instead of grinding), means considering the turning of the strain hardening steel as final processing or fashioning, to replace the common grinding technology. it's machining accuracy can get up to IT5, surface roughness $Ra \leq 0.6 \mu\text{m}$, circular degree 0.005 mm.

The general range of hard cutting is 45–65 HRC, hardness of 45 HRC is the start point of hard cutting, but it usually used on the workpiece above 55 HRC. The hardness of axis neck in the middle of spherical head supporting part is (52–58) HRC, so is suitable for hard cutting (see Fig. 47.12).

1. The choice of the blade

CBN blade is most suitable for hard cutting, can provide security blade abrasion rate in the process of continuous cutting. So we choice the CBN blade.

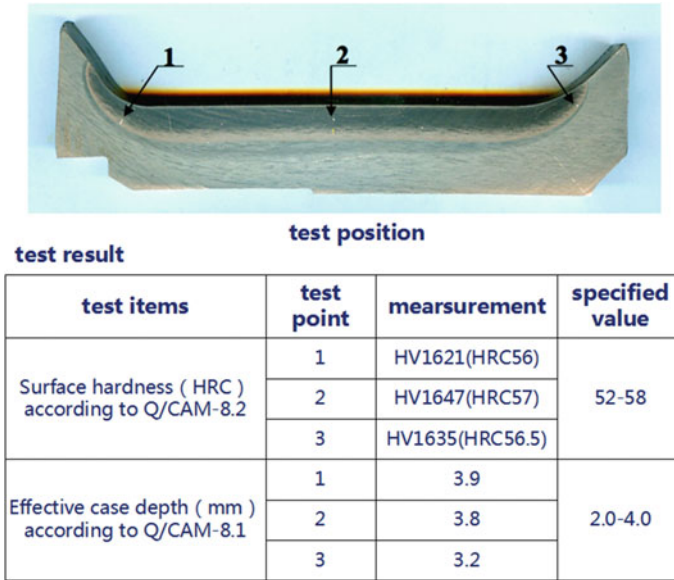


Fig. 47.12 Axis neck hardness

2. Cutting dosage and cutting conditions

The suitable cutting speed's range of hard cutting is 50–200 m/min, commonly used range is 100–150 m/min, the hardness of workpiece material is higher, its cutting speed should be smaller. Normal cutting depth is 0.1–0.3 mm, when require high surface roughness, it should choice small cutting depth. Normally choice feed speed 0.025–0.25 mm/r.

(2) Trundle processing

It is a kind of pressure forming processing for trundle processing. It is the use of plastic deformation characteristics of the metal in the normal temperature. The surface metal of the workpiece produces plastic flow to the original residual dips in the trough, which is pressed by the trundle tool. The purpose is to reduce the workpiece surface roughness value. It happened cold hardening, the density of fiber and residual stress layer of the surface organization. Thereby, it is improve to abrasion resistance, corrosion resistance and coordination of the workpiece surface. The value of the surface roughness will be less than 0.08 um, meanwhile it will be improve the hardness 15–30% and abrasion resistance 30% by pressing the surface of the workpiece.

The process parameters of trundle processing:

1. Roller pressure

Rolling pressure whether it is right choice, is very important to roughness, size and accuracy after rolling the surface. The surface roughness increase with the rolling pressure increases in general. But, as the rolling pressure cross the certain

value, the surface roughness don't increase. If rolling pressure continues to increase, the surface of the part would be to deteriorate, appear crack even.

2. The feed rate is determined by the diameter of the trundle. The smaller the feed, the less the surface roughness. The best feed rate should be determine by test.
3. It is important to the surface roughness and geometry for interference when rolling. The most reasonable interference is 0.027–0.036 mm through experiment, the surface roughness is the minimum now. The most reasonable interference should be determined by many experiments according to the specific conditions.
4. It is not important to the surface roughness for rolling velocity, then we can improve production efficiency by improving the speed of rolling.
5. The times of rolling should not be too much. It is the most significant effect to roller once, which can reduce the roughness 2–3 grade. The more times, the less effect.
6. The trundle processing is to use trundle rolling method, thus the diameter of the workpiece will be changed before and after the processing (inner diameter will expand, outer diameter will reduce). It should consider the change before the last process in order to be processed to dimensional tolerance range diameter variation is related material, hardness of the workpiece and rolling, so it should be determine after trying processing 2–3 times for the initial size (Figs. 47.13 and 47.14).

Fig. 47.13 The trundle tool

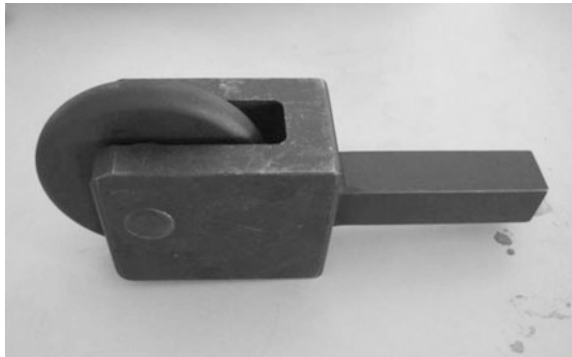


Fig. 47.14 The trundle



47.3 The Manufacturing Process of Spherical Head Supporting Part

Manufacturing process plans: NC rough turning → NC precision turning → surface induction hardening → boring internal hole → hard turning excircle → surface rolling → milling the end face of spherical head → rolling main pin hole, milling end face, chamfer (see Fig. 47.15).

(1) NC rough turning

- (1) Clamping spherical surface and limiting the left end face, rough turning all the excircle surface in the right, turning right end face and taper hole to it's size.
- (2) Clamping right turned excircle surface and limiting the right end face, rough turning left excircle surface, turning inner spherical and inner hole in the middle of axis neck (see Fig. 47.16);

(2) NC precision turning

In order to ensure the shape and position accuracy of the spherical head supporting part. Adopt special turning tooling, use the inner hole $\Phi 42J8$ installing lining and oil seal hole $\Phi 54H8$ limit the workpiece, NC turning the whole excircle surface at one time, so can reduce limiting and clamping, ensure the coaxiality between excircle and inner hole, and ensure the positional accuracy between each cylindrical.

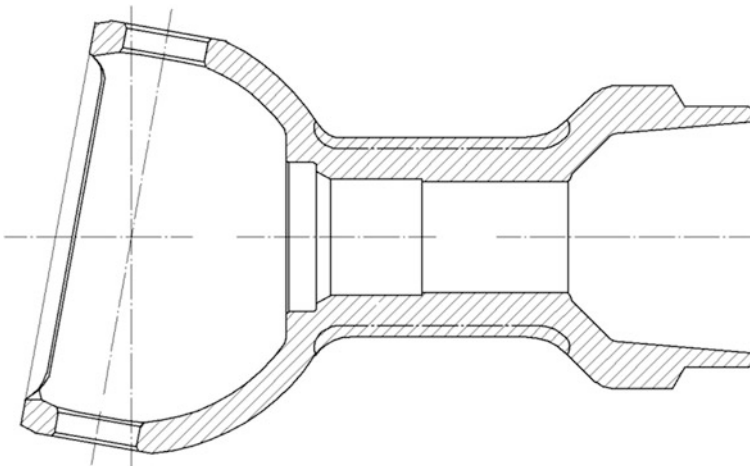
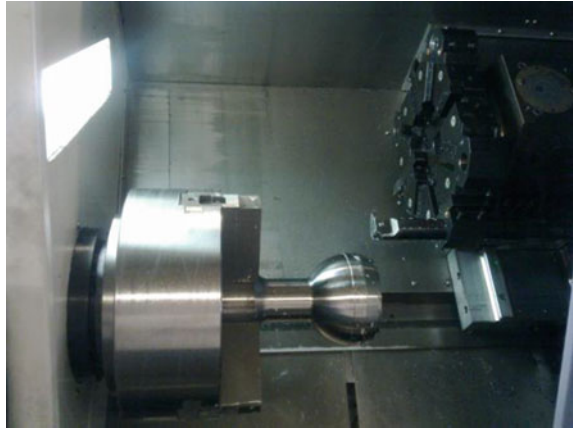


Fig. 47.15 Technology diagram

Fig. 47.16 NC rough turning

(1) Using the mandrel limit, precision turning all the excircle, keep machining allowance for induction heating, each side keep 0.3 mm (see Fig. 47.17);

(3) **Heat treatment-surface induction heating**

To ensure the follow content by design and manufacture special open induction coil to heat the middle of axis neck (see Fig. 47.18).

- (1) Have equal depth of effective hardened layer in the middle.
- (2) The depth of effective hardened layer transit gradually both in the middle of axis neck and two transition fillets beside.

(4) **Boring internal hole**

Use the right excircle and end face to limit the workpiece, boring hole $\Phi 42J8$ installing lining and oil seal hole $\Phi 54H8$.

(5) **NC hard turning excircle**

Use the precision turning mandrel to locate, precision turning all excircle to drawing size, keep 0.004–0.006 mm rolling allowance in middle axis neck.

(6) **Surface rolling**

Rolling the middle axis neck and two transition fillets beside.

(7) **Milling spherical head end face-vertical machining center**

Use the right excircle surface and end face to locate, milling spherical head end face.

(8) **Horizontal machining centre**

Use the right excircle surface and end face to locate, drilling, boring the main pin hole, milling the end face, chamfer (see Fig. 47.19).



Fig. 47.17 NC precision turning mandrel



Fig. 47.18 Induction hardening

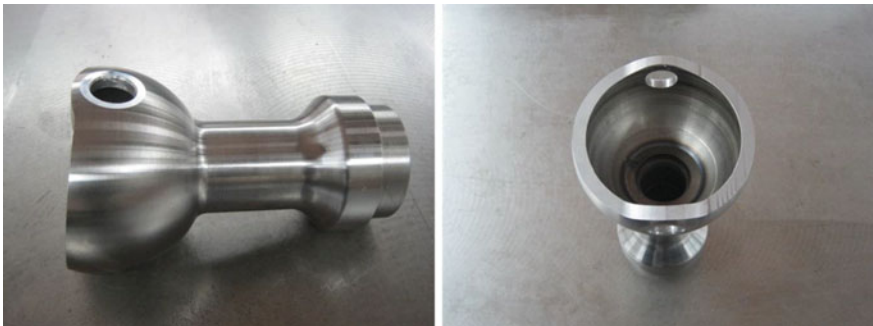


Fig. 47.19 The spherical head supporting finished part

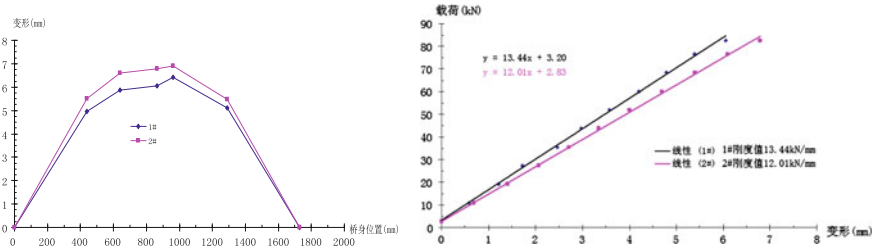


Fig. 47.20 The result of vertical bending and stiffness test of the shell of front drive axle

Sample Number		A1	A2
experiment times (ten thousand)		67.28	>63.50
fatigue life (ten thousand)	experimental result	>16	
	standard request	≥16	
the sample test conditions		annular weld fracture	undamaged

Fig. 47.21 The result of vertical bending fatigue life test of front drive axle

47.4 The Test Results and Conclusions of Spherical Head Supporting Part

- (1) **The vertical bending and stiffness test of the shell of front drive axle** (see Fig. 47.20)

The load and deformation curve at triple load

- (2) **The test of vertical bending fatigue life of front drive axle** (see Figs. 47.21 and 47.22)

Note: A2 sample’s fatigue life reach up to 635,000 times, the sample is still didn’t break and the test was stop.

By installing in the front drive axle and bench testing, the spherical head supporting part’s function, strength, stiffness of supporting structure, reliability, fully meet the requirements of bench test, high safety coefficient, reliable, and fully meet the demand of the vehicle matching.



Fig. 47.22 The broken sample of A1

(3) Conclusion

Through the trial-manufacturing of the spherical head supporting part, verified the machining processability, and provide reference for the quantity production. Increase awareness of special structure part's forging, hard turning and trundle processing. Gather experience for both choicing machining tools and selecting cutting parameters of hard turning and trundle processing.

References

1. Liu J (2011) Car parts forging technology. Beijing Institute of Technology, Beijing, pp 8–23
2. Sun F (2006) MINFRE. In Machining technology, vol 2. China Machine Press, Beijing, 12 (Chapter 1, p. 88, Chapter 10, p. 55)

Chapter 48

Optimization of Design Parameters of Circular Burring

Wenshan Fu, Yinzhi He and Chunyang Lu

Abstract The paper presents an example of an automotive handle bracket. The design parameters of burring include fillet radius R , burring diameter D and burring height H , which are all analyzed in this paper. The objective function is thinning rate of parts. By using quadratic regression, a mathematical model between objective function and design parameters can be established, which can be guidance while selecting design parameters of burring.

Keywords Burring · Quadratic regression · Numerical simulation

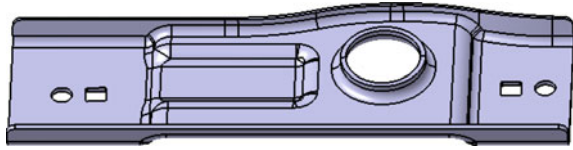
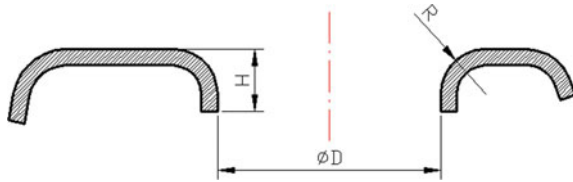
48.1 Introduction

Burring is one of the most commonly used features for stamping parts. It can not only increase the local strength of parts, but also reduce the requirements of the sections' quality, such as assembly holes, threading holes, etc.

Burring, a special kind of flanging, belongs to stretch flanging. The deformation of material is much severer than ordinary flanging. In the stamping process, some defects are very likely to occur, such as crack, thinning, non-perpendicularity [1, 2] etc. There are some methods of eliminating those defects: Adding one or more preforming process to ensure that there is enough material in the process of deformation [3]; using smaller clearance to ensure the burring perpendicularity; adding fine blanking technology to ensure the quality of the burring [4], etc. These methods can reduce the defects of burring, but also lead to rising costs and shorter service life of dies.

Nowadays in the design stage of products, the design of burring is based on experience or optimized to the performance target. The feasibility of manufacturing and cost are controlled by SE engineers [5–7]. This paper uses the automotive handle bracket as an example, establishes the mathematical model between the

W. Fu (✉) · Y. He · C. Lu
School of Automotive Studies, Tongji University, 201804 Shanghai, China
e-mail: madden@163.com

Fig. 48.1 Handle bracket**Fig. 48.2** Burring design parameters (section)

design parameters and manufacturing process, in order to find out the best design parameters that require simpler manufacturing process and lead to lower cost and stabilized products.

48.2 Burring and Design Parameters

Figure 48.1 shows the automotive handle bracket. Burring can not only eliminate the influence of the burr on the assembly precision, but also increase the local strength of surrounding area of the hole.

The main design parameters of burring include fillet radius R , burring diameter D and height H , as Fig. 48.2 shows. In addition, material also plays an important part in the design of burring. In this research, the influence of material is neglected. The handle bracket's material is B250P1, and the yield strength is 250–360 MPa, the tensile strength is not less than 440 MPa and the elongation is approximately 30%.

48.3 Process Analysis and Numerical Simulation

48.3.1 Process Analysis

Manufacturing process analysis was carried out on the handle bracket. Figure 48.3 shows the preliminarily determined manufacturing processes: blanking, forming, piercing and burring.

In the manufacturing process, external flanging is primarily formed, which eliminates the influence of external material flow on the performance of the hole. In this paper, only the influence of three design parameters (burring diameter D , height H and fillet radius R) is considered. The main effect of diameter D and height H lies in their ratio, i.e. H/D [8]. Considering the particularity of the part, this paper makes

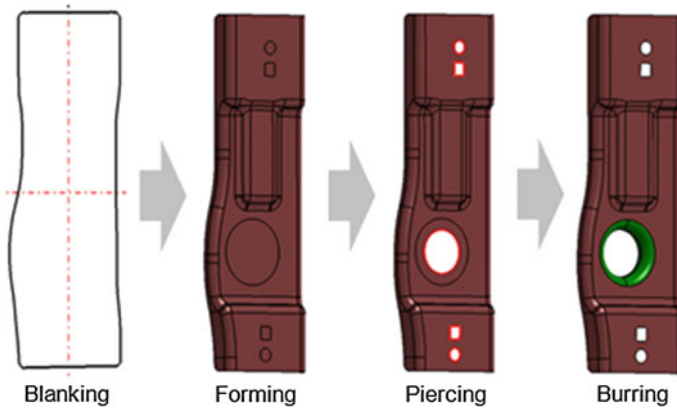


Fig. 48.3 Manufacturing process of handle bracket

an analysis within a scope, namely $H/D \in [0.08, 0.48]$, $R \in [2.5, 7.0]$ and sets the maximum thinning rate as objective function to optimize the parameters.

48.3.2 Numerical Simulation

Process data are imported into numerical simulation software AutoForm and relevant process parameters and tools are set [9, 10], and then begin to analyze the forming performance. The results can be seen in Fig. 48.4.

Figure 48.4 shows the thinning rate of the burring. The maximum thinning rate can be seen in the left figure, and the right one is the Forming Limit Diagram (FLD) [11]. When the thinning rate is not more than the limit value, there will be no crack.

The design parameters fillet radius R and H/D are grouped, and numerical simulation was carried out on the thinning rate of the part. Table 48.1 shows the result.

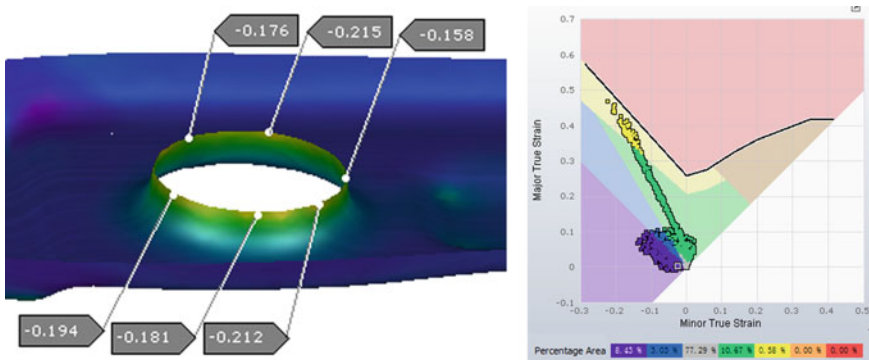
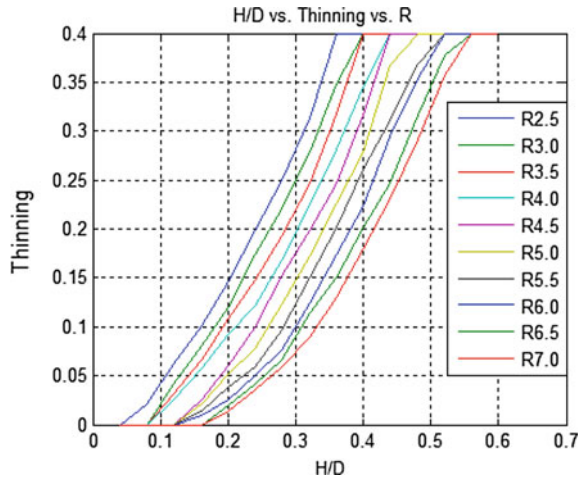


Fig. 48.4 The result of forming thinning rate of the part

Table 48.1 Design parameters and maximum thinning rate

R	H/D										
	0.08	0.12	0.16	0.20	0.24	0.28	0.32	0.36	0.40	0.44	0.48
2.5	0.021	0.062	0.101	0.146	0.199	0.250	0.313	–	–	–	–
3.0	0.010	0.045	0.081	0.125	0.174	0.221	0.278	0.349	–	–	–
3.5	0.006	0.030	0.066	0.108	0.148	0.193	0.246	0.318	–	–	–
4.0	0.003	0.015	0.053	0.086	0.121	0.168	0.225	0.281	0.365	–	–
4.5	0	0.006	0.035	0.065	0.099	0.146	0.199	0.252	0.317	–	–
5.0	0	0.002	0.021	0.045	0.078	0.123	0.173	0.226	0.279	0.368	–
5.5	0	0	0.012	0.035	0.059	0.097	0.148	0.201	0.250	0.330	0.385
6.0	0	0	0.005	0.025	0.050	0.077	0.125	0.174	0.224	0.294	0.354
6.5	0	0	0	0.019	0.041	0.066	0.105	0.150	0.202	0.260	0.316
7.0	0	0	0	0.014	0.035	0.059	0.090	0.130	0.179	0.230	0.292

Fig. 48.5 The relationship among maximum thinning rate, R and R/D



From the result of Table 48.1 can be seen, when the maximum thinning rate is controlled within a certain range, the larger R is, the larger H/D becomes (as shown in Fig. 48.5).

48.4 Regression Analysis

48.4.1 Regression Theory

A collection of data of the function $y = f(x)$ are known, namely $(x_1, y_1), (x_2, y_2), \dots, (x_n, y_n)$. But the expression of the function is unknown. The regression analysis of data is to obtain a function $\varphi(x)$, an approximate model of $f(x)$, from a certain type of function (such as polynomial function, spline function, etc.). There are two

major categories of data modeling methods: one is the interpolation methods, which requires that function $\varphi(x)$ strictly complies with the data $(x_1, y_1), (x_2, y_2), \dots, (x_n, y_n)$. The other is the fitting method, allowing the function $\varphi(x)$ has deviation in the data points, but requires that a certain indexes reaches the minimum value. In general, the interpolation method is suitable for accurate data or smaller amount of data, and the fitting method is more suitable when there are data deviations or a larger amount of data.

Least square method is the most commonly used fitting method, which is described as followed.

Assume that function $y = f(x)$ has m function values,

$$y_i \approx f(x_i); \quad (i = 1, 2, \dots, m)$$

The least square method is to obtain a simple approximation formula $\varphi(x)$, which makes $\varphi(x_i)$ minus y_i

$$e_i = \varphi(x_i) - y_i; \quad (i = 1, 2, \dots, m)$$

has the smallest sum of the square.

$\varphi(x)$ is the least square fitting function of $(x_i, y_i), i = 1, 2, \dots, m$, $f(x)$ is the fitted function.

$y' = \varphi(x)$, namely empirical formula or mathematical model, approximately reflects the function between variable x and variable y , i.e. $y = f(x)$.

48.4.2 Regression Analysis

The maximum thinning rate above is calculated by CAE simulation software, there may be some deviations, and hence the regression is used to modeling. In this study, the least square method is selected.

General regression equation is:

$$f(x, y) = a_1x^2 + a_2y^2 + 2a_3xy + a_4x + a_5y + a_6$$

x stands for the fillet radius R , y stands for height and diameter ratio H/D , $f(x, y)$ stands for the maximum thinning rate, a stands for quadratic regression coefficient. After calculation, the regression coefficients are shown in Table 48.2.

Table 48.2 Quadratic regression coefficient

Coefficient	a_1	a_2	a_3	a_4	a_5	a_6
Value	0.00375	2.24033	-0.09265	-0.02729	0.76012	0.03702

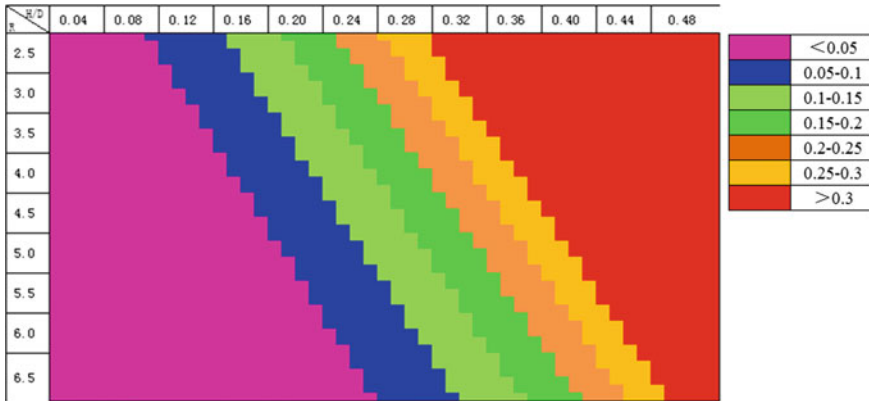


Fig. 48.6 Fillet radius R, H/D and thinning rate

Put the regression coefficient into the general equation, and the thinning rate function is obtained as follows:

$$f(x, y) = 0.00375x^2 + 2.2403y^2 - 0.1853xy - 0.02729x + 0.76012y + 0.03702$$

Burring radius R is on horizon axis, burring height and diameter ratio H/D is on vertical axis, $f(x, y)$ is expressed with different colors in the inner area, as shown in Fig. 48.6. The chart can directly reflect the relationship among H/D, R and rate thinning. In the design stage of burring, the manufacturability of the part can be intuitively estimated based on Fig. 48.6. For example, when the value of R is 4.0, if the thinning rate of burring is smaller than 0.2, the maximum value of H/D can be decided as 0.28.

48.5 Conclusion

In the design process of burring, the manufacturability should be fully considered. It is better to achieve the function of the parts with the lowest cost and the simplest form.

- (1) In the design process of products, the mathematical model between design parameters and manufacture process is established. Forming performances are calculated under the condition of different parameters;
- (2) According to the regression analysis graphics, the design parameters of burring can be intuitively chosen;
- (3) Before the design, a relevant design parameters database of burring can be established.

At the same time, we also can integrate the burring design mathematical model and performance analysis model for a multi-objective optimization, in order to select reasonable design parameters.

References

1. Wei L, Zuo Z, Lan J (2005) Solutions to the problems in adjusting tube fittings stampings dies. *China Metal Form Equip Manufact Technol* 40(6):69–71
2. Guo Y, Luo W, Li Y (2001) Metal flow control method of drawing burring combined forming. *Forg Stamp Technol* 3:22–25
3. Zhou Z (2000) A burring process of thin-wall parts. *Die Mould Ind* 26(1):28–29
4. Yan G, Wang X, Jin J (2014) A study of flanging-upsetting process of flange. *J Netshape Form Eng* 6(2):6–11
5. Fan Z, Qiao X, Yang X (2014) A cost-controlling research of NX program simultaneous engineering stamping. *Equip Manuf Technol* 42(5):190–196
6. Wang J, Huanhuan W, Feng L (2010) Research on parameters of hole flanging based on deform and orthogonal experiment. *Forg Stamp Technol* 53(4):142–145
7. Li J, Wang B, Zhou T (2015) Optimization of progressive die forming based on numerical simulation and response surface method. *J Cent South Univ Sci Technol* 46(1):66–72
8. Liu J, Wang B, Tian J (2005) Numerical simulation of hole flanging of large-size barrel and parameter optimization. *J Plast Eng* 12(4):28–30
9. Zhang C, Lu X, Chu L (2004) Calculation of the diameter of the pre manufactured hole for flange. *Die Mould Ind* 30(1):34–37
10. Zhu H, Wang Z, Wang Z (2013) Simulation and experimental study for drawing-flanging compound forming of axisymmetric holed slab. *J Plast Eng* 20(5):50–55
11. Zhang S, Liu X, Liu C (2016) Obtaining and application of aluminum alloy FLD based on numerical simulation. *China Metal Form Equip Manuf Technol* 51(1):97–100

Chapter 49

Experimental Study on the Application of Hydrogen Detector in Engine Leak Detection

Qi Wang, Wei Zhu, Lei Chen and Sanyan Cao

Abstract The use of hydrogen detector and leak testing equipment is a new technology to leak location. The paper summed up advantages and disadvantages between methods soap-bubble and hydrogen detection to find leaks. Analysis of influences the mixture gas of nitrogen and hydrogen on the leak testing equipment and theoretical analysis. Hope to help others.

Keywords Three leaks · Leak detection · Hydrogen detector · Soap-bubble

Three leaks is a big problem in the production. In order to reduce the rate of leakage of the engine, engine manufacturers layout many leak detection stations in the production line. And it can effectively reduce the leakage and repair cost. In the leak detection process, to find the leak is the key to solve the problem of leakage. But with usual soap-bubble leak detection, part of engines with leakage rate exceeds permissible limit were unable to locate the leak, which increases the cost of repair. Therefore, to find new ways of leak location is still of great significance.

49.1 Introduction and Test Arrangement

The mixed gas of nitrogen and hydrogen is used as a tracer gas in hydrogen detection to locate the leak. The inspection equipment is hydrogen detector, as shown in Fig. 49.1. When looking for the leaks, the workpiece must be filled with mixture gas of nitrogen and hydrogen (Generally 95% nitrogen and 5% hydrogen mixed gas [1], 4% hydrogen in this paper, and the mixed gas is not combustible [2]), and maintain the pressure within a certain range (about 0.2 Bar), then find the possible leak points. If there is a leak, the handheld probe will be able to inspect the leakage of hydrogen and locate the leakage area. If the leak is large enough,

Q. Wang (✉) · W. Zhu · L. Chen · S. Cao
Faw Jiefang Automotive CO. LTD. Wuxi Diesel Engine Works, Wuxi 214026, China
e-mail: wangq@wxdew.com

© Springer Nature Singapore Pte Ltd. 2017
Society of Automotive Engineers of China (SAE-China), *Proceedings of SAE-China Congress 2016: Selected Papers*, Lecture Notes in Electrical Engineering 418,
DOI 10.1007/978-981-10-3527-2_49

Fig. 49.1 Hydrogen detection device



the hydrogen detector alarms. In this paper, the hydrogen detection device model is INFICON ISH2000, as shown in Fig. 49.1.

49.2 Experimental Arrangement

Generally, under the same conditions, nitrogen and hydrogen mixture gas does not cause additional damage to the leak test equipment. In the experiment, filling, keeping and exhaust of the mixed gas are controlled by a leak test device. Adjusted the pressure of the mixture gas to about 5 Bar.

Select engines as follows:

- (a) Oil passage: the leakage rate is greater than $600 \text{ cm}^3/\text{min}$ and cannot find the leak. If there is no engine exceeds $600 \text{ cm}^3/\text{min}$, reduce the requirement.
- (b) Waterway: the leakage rate is greater than $15 \text{ cm}^3/\text{min}$ and cannot find the leak.

49.3 Experimental Study on the Hydrogen Detection Equipment with the Use of the Whole Engine Leakage Test Device

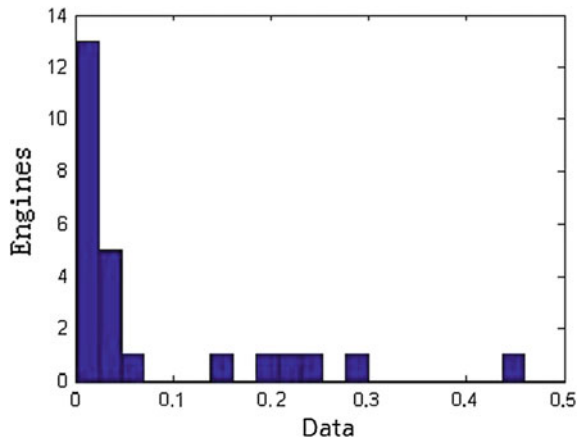
49.3.1 Effectiveness Analysis of the Hydrogen Detection Equipment

A total of 88 engines were tested with mixture gas, from which found 43 waterway leak and 45 oil leak, as listed in Table 49.1.

Table 49.1 Test result of hydrogen detection

	Total number	No leak found	The average leakage rate (cm ³ /min)	Remark
Waterway	43	4	23.5	1 engine retest and qualified
Oil passage	45	3	1036.4	1 engine retest and qualified

Fig. 49.2 Hydrogen detection data distribution of cylinder cover



Through the hydrogen test data and corresponding soap-bubble method data analysis, the advantages and disadvantages of hydrogen detection technology as follows.

The ability to locate leaks: 157 leaks were found by hydrogen detection, involving 35 different leaks, and at the same time 17 different leaks were found by soap-bubble in a total of 21,228 diesel engines. Hydrogen detection can find more locations. And only 3 engines are still unable to locate the leaks in 45 oil leakage engines, 4 in 43 for water leakage engines. So the sensitivity of hydrogen detection is higher.

Analysis of the hydrogen test data: Take the cylinder cover as example, as shown in Fig. 49.2, the hydrogen data is discrete widely. Because of the hydrogen detection data is the leakage data of point, but the actual leak is line or area, it is difficult to get the actual value of the leak. So it is not recommended to set limits for engines rework.

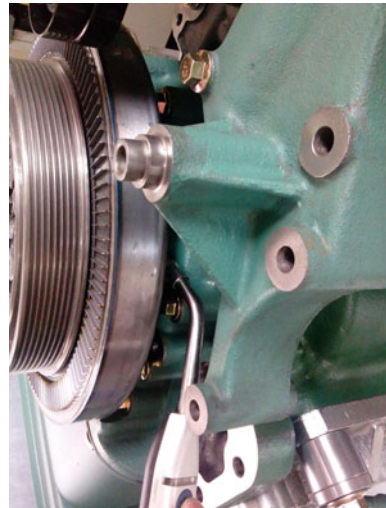
Cost analysis: Hydrogen detection cost less than ¥2.5 per engine and about ¥4 to ¥5 for soap-bubble. Application of hydrogen detection has lower cost.

Production rhythm analysis: Compared with hydrogen detection and soap-bubble, the former takes more time. Hydrogen detection requires a distance and moving speed when working. It is about 15–20 min per engine and too long to production.

Comparison of hydrogen detection and soap-bubble method are shown in Table 49.2.

Table 49.2 Comparison of hydrogen detection and soap-bubble method

	The ability to locate leaks	Location requirements	Operation time	Operating environment	Cost
Hydrogen detection	High	No	Long	Clean	Low
Soap-bubble method	Usual	Liquid must be attached	Short	Liquid residue	High

Fig. 49.3 Front oil seal detection

In addition, the external power supply limits the working space of the device, and inconvenient. Therefore, rechargeable batteries should be equipped in future.

49.3.2 Feasibility Analysis of Online Hydrogen Detection

49.3.2.1 Online Operability Verification

Hydrogen detection not only find all locations that soap-bubble method can, but also find the following 6 kinds of leak that soap-bubble method cannot or difficult to find.

- Oil pan: Since linear and small leak at the oil pan, it is not easy to form a bubble, but hydrogen detection device is able to detect the slight leakage.
- The cylinder cover: The condition to cylinder cover is similar with oil pan, small surface leakage is not easy to be found by soap-bubble method.
- Front oil seal: Due to the block of shock absorber, the soap-bubble method does not work. But hydrogen detector can be placed to locate the leak, as shown in Fig. 49.3.

Fig. 49.4 Rear oil seal detection



Table 49.3 Experimental data of effect of residual mixture gas of hydrogen and nitrogen

Leak point	Non blowing (10^{-3} cm ³ /min)				Blowing (10^{-3} cm ³ /min)			
	02	18	31	28	6	7	7	3
Oil pan gasket	02	18	31	28	6	7	7	3
Cylinder cover bolt	28	32	62	71	150	140	170	130

- (d) Rear oil seal: It is inside of oil pan, and cannot reach and observe. The hydrogen detector can be placed in the hole of the speed sensor to inspect as shown in Fig. 49.4.
- (e) Plug at bottom of pump: It is unable to liquid adhesion, and the operator is difficult to observe.
- (f) Oil level gauge tube: The leakage is mostly caused by welding, the large leak prevents the formation of air bubbles.

In summary, the online hydrogen detection has many advantages. But it cost too many time to production. It should be improve the quality of parts and assembly, optimize the process and so on, then the online hydrogen detection may be feasible.

49.3.2.2 Effect of Residual Mixture Gas on Hydrogen Detection

As online hydrogen detection, the engines stay at a fixed station, gas accumulation may impact on the results of the hydrogen detection. Therefore, the effect on hydrogen detection is verified. In the experiment, a leakage position was tested several times. Plan A: in the case of non blowing, Plan B: air blowing before test.

As shown in Table 49.3, in the case of non blowing, there are some fluctuations to the hydrogen detection data. And there is no readings and no alarm in the vicinity

of the residual gas. In the case of blowing, the data fluctuations too, but the values greater than these of non blowing. Residual mixture gas has little impact on hydrogen detection values. The fluctuations partly due to the changes in direction and position of the handheld sensor and the formation of air bag during inflation. This condition can be improved by increasing inflation time or using vacuum equipment.

49.3.3 Effect of Residual Mixture Gas on the Whole Engine Leakage Test Device

Using mixture gas of nitrogen and hydrogen as a leak testing medium during online test can do leak detection and location at the same time, which helps to reduce the test time. Carried out the test take mixture gas instead of compressed air as an medium gas. In the experiment, 2 diesel engines were selected. The test data are shown in Table 49.4.

As shown in Table 49.4, leakage values with the mixture gas are lower than compressed air. Since the whole engine leakage test device use mass flow sensor to measure the leak, the readings is the volume flow, and the relationship between volume flow and mass flow is $Q = \frac{nRT}{mP} \cdot \hat{m}$, here, Q is volume flow, P is pressure, n is molar mass, R is molar gas constant, T is kelvin temperature, m is mass, \hat{m} is mass flow. P, R, T can be regarded as constants, $\frac{n}{m}$ is the reciprocal of the molar mass. The molar mass of the gas is proportional to the density ρ . So the volume flow rate can be expressed as: $P = \frac{C}{\rho} \cdot \hat{m}$, here C is a constant.

Take mixture gas instead of compressed air, the medium density changes but the coefficients of the instrument does not change. Thus, the relationship between volume flow Q_H measured by mixture gas and volume flow Q_A measured by the

Table 49.4 Mixture gas of nitrogen and hydrogen and compressed air leak detection data

No.	Engine				Medium gas
	A		B		
	Waterway (cm ³ /min)	Oil passage (cm ³ /min)	Waterway (cm ³ /min)	Oil passage (cm ³ /min)	
1	4.03	49.64	4.77	-2.6	Compressed air
2	2.3	51.27	4.64	-10.5	
3	1.78	51.42	3.85	-5.61	
4	0.15	53.22	1.57	-8.62	
5	-3.25	25.85	-0.42	-25.85	Mixture gas
6	-2.39	35.42	-0.37	-26.21	
7	-2.72	39.17	-1.83	-16.63	
8	-4.91	40.37	-0.53	-20.62	

Table 49.5 Conversion leakage rate data

Engine	Compressed air	Mixture gas	Compressed air	Mixture gas
	Waterway	Waterway	Oil passage	Oil passage
A	1.49	0.74	7.65	7.04
B	1.74	1.23	3.69	2.83

compressed air as follow: $\frac{Q_H}{Q_A} = \frac{\rho_H}{\rho_A}$, that is $Q_H = \frac{\rho_H}{\rho_A} \cdot Q_A$, here ρ_H and ρ_A is the density of mixture gas and air.

Calculating the mean leak rate at the flow sensor according to coefficient and offset settings of the test device. And the absolutely leak rate of compressed air multiplied by $Q_H = \frac{\rho_H}{\rho_A} \cdot Q_A$. The test results of the two medium gas are closely and compared in Table 49.5. Thus, the method can be used to calculate an initial coefficient and offset settings of the leakage test device. That is the original coefficients multiplied by $\frac{\rho_A}{\rho_H}$ and offset settings minus $(\frac{\rho_A}{\rho_H} - 1)$. It is conducive to fast the whole engine leakage test device calibration, and the limits are almost constant.

49.4 Summary

Through application study on hydrogen detector, the advantages of hydrogen detection are verified. To the poor performance of soap-bubble method in leak location, the hydrogen detection still has a good performance. It can effectively improve the accuracy of leak location and repair efficiency. Through technology experiments, it demonstrated the online hydrogen detection program and laid the foundation for batch production applications in future. The new method of calculation of coefficients and offsets with mixed gas is useful to the calibration of the test device. And also explained the values change caused by density changes of medium gas. Others can learn from this article or carry out in-depth study.

References

1. Wang F (2004) Application of hydrogen detecting technology into leakage detection of pressure vessel. Refrigeration Air-conditioning 4:78–79
2. ISO10156:2010 Gases and gas mixtures-determination of fire potential and oxidizing ability for the selection of cylinder valve outlets

Chapter 50

Investigation on Induction Hardening Treatment of Cylindrical Drive Gear Shaft

Bo Chen, Da-peng Wang, Hang-yu Li, Kai Cui and Bo Jiang

Abstract The feasibility of applying induction hardening treatment in the production of cylindrical drive gear shaft, which is made of medium carbon low alloy steel and used in heavy duty tandem bridge, is investigated. The approaches, inductor structure, parameters, deformation pattern and torsion strength of the induction hardening treated cylindrical drive gear shaft are analyzed and compared with the carburized parts. The results show that induction hardening can be applied in the strengthening of the cylindrical drive gear shaft and the torsion strength of the parts is higher than those using carburizing treatment, and satisfy loading design specifications. The deformation after quenching is within the required tolerance of the assembly.

Keywords Cylindrical drive gear shaft · Induction hardening · Carburizing · Quenching deformation · Torsion strength

50.1 Introduction

The cylindrical drive gear shaft is the power input of the middle and rear bridge of commercial vehicles with tandem bridges. It drives both the middle and rear bridges, and functions under severe working conditions of high rotational speed and large torque. Because of the critical role of the cylindrical drive gear shaft plays in the drive train, it affects the reliability of the bridge assembly directly. Carburizing treatment has been applied to the strengthening of the cylindrical drive gear shaft over a long time [1]. In recent years, as the designed load of the bridge kept increasing, the torque applied to the cylindrical drive gear shaft also increased significantly. Limited to the dimension chain of the bridge assembly, there is hardly

B. Chen (✉) · D. Wang · H. Li · K. Cui · B. Jiang
Processing Department, China FAW Group Corporation R&D Center, Changchun, China
e-mail: chen634603512@126.com; chenbo2@rdc.faw.com.cn

any possibility of increasing the size of the part, and the maximum load bearing capacity of the carburized part is nearly reached. Many early fractures occurred during service, which resulted in a high customer claim rate. Based on the current situation, with the dimension of the part unchanged, using other strengthening approaches to increase the torsion strength of the cylindrical drive gear shaft is a practical way of solution.

By properly selecting medium carbon low alloy steels and using induction hardening process, the case hardening depth achieved can be several times deeper than carburizing. Thus the torsion strength can be significantly increased [2]. But deep case depth causes large quenching deformation which affects the dimensional precision. Therefore, perfect balance of the case hardening depth, torsion strength and quenching deformation is the key to applying induction hardening process. In recent years, many main companies launched the development of induction hardening of the cylindrical drive gear shaft. Companies such as Mercedes-Bens and Volvo, with a quick head start, have been popularized the process. Companies in China, such as CNHTC and SAG, have also been using induction hardened cylindrical drive gear shaft in high tonnage bridge.

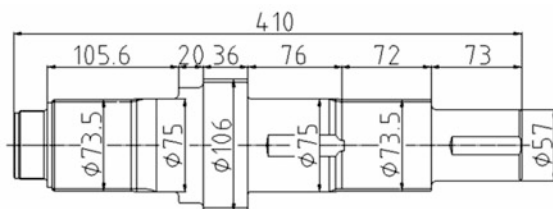
To make a breakthrough, by experimenting on the cylindrical drive gear shaft in heavy duty bridge with the largest rated input torque, the technical key points and parameters are systematically investigated and optimized, building solid ground for generalization of the process.

50.2 Experimental

50.2.1 Structure and Designed Load Capacity of the Part

Figure 50.1 is the schematic of the structure of the cylindrical drive gear shaft. The strength reserve coefficient is ≥ 1.8 . Rated input torque is $\geq 67,700$ N m. And the diameter of the axle is 75 mm.

Fig. 50.1 Structure of the cylindrical drive gear shaft of a heavy duty tandem bridge



50.2.2 Materials of the Part

The materials used in induction hardening experiments are quenching and tempering treated 42CrMoH and 40CrH. The hardness of the matrix and surface hardness are HBW285–321 and HRC52–58, respectively. The case hardening depth is to be determined by experiments.

The material used in carburizing is isothermal normalized 20CrMnTiH with a matrix hardness of $\geq 20\text{HV}30$, surface hardness of HRC58–63 and case hardening depth of CHD550HV1 1.6–2.0.

Table 50.1 shows the main chemical compositions of the three materials used. Table 50.2 is the quality inspection results of the three kinds of materials. Figure 50.2 is the metallographic pictures of the matrix of the parts made of the three different materials. Test parts material and structure comply with standard requirement.

Table 50.1 Chemical compositions of the materials used in experiment (wt%)

Material	C	Si	Mn	P	S	Cr	Mo	Ti
42CrMoH	0.42	0.30	0.65	0.016	0.0021	1.04	0.19	0.015
40CrH	0.41	0.26	0.69	0.015	0.006	1.01	–	–
20CrMnTiH	0.21	0.32	0.99	0.017	0.026	1.15	–	0.064

Table 50.2 Materials quality inspection results

Material	Matrix hardness	Matrix microstructure
42CrMoH	298–306HBW (Q/CAM-7.1)	Tempered sorbite + small amount of ferrite (Q/CAM-7.2)
40CrH	291–303HBW (Q/CAM-7.1)	Tempered sorbite + small amount of ferrite (Q/CAM-7.2)
20CrMnTiH	333–372HV30 (Q/CAM-6.3)	Low carbon martensite + bainite

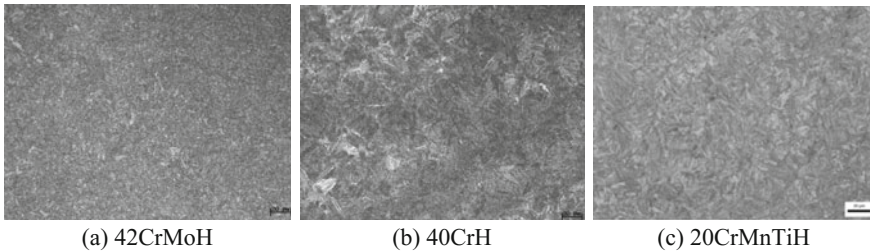


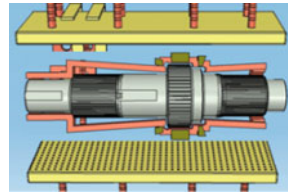
Fig. 50.2 Metallographic pictures of the matrix of the parts used in experiments

Table 50.3 Experiment conditions and parameters of the single-time heating process and the two-time heating process

Experiment conditions	Single-time heating process	Two-time heating process
Induction hardening equipment	SCR power, horizontal equipment	IGBT power, vertical equipment
Rated frequency	4 kHz	10 kHz
Rated power	450 kW	250 kW
Technical specifications	CHD of journal: 5–8 mm; CHD of spline: 4–6 mm below the tooth root; filleted corner: ≥ 3.0 mm	



(a) Single-time heating process



(b) Single-time heating process inductor structure

Fig. 50.3 Schematic of single-time process

50.2.3 Induction Hardening Process

The cylindrical drive gear shaft is a multi-diameter shaft with several filleted corners and steps, and the smallest radius of the fillet is only 2 mm. According to the characteristics of the part, two different induction hardening processes are designed to conduct comparison experiments. One process features a single-time whole-piece induction heating, and the hardness pattern is continuous. While the other process features a separated two-time induction heating with discontinuous hardness patterns that disconnects in the middle of the work piece. Table 50.3 shows the experiment conditions and parameters of the two processes. Figure 50.3 is the schematic of the single-time heating process. Figure 50.4 is the schematic of the two-time heating process.

50.3 Results and Discussions

50.3.1 Comparison of Single-Time and Two-Time Processes

Different heating processes significantly affect the heating effects at the filleted corner and adjacent areas. Experiments showed that for single-time whole-piece heating process, the structure of the longitudinal heating conductor was not suitable

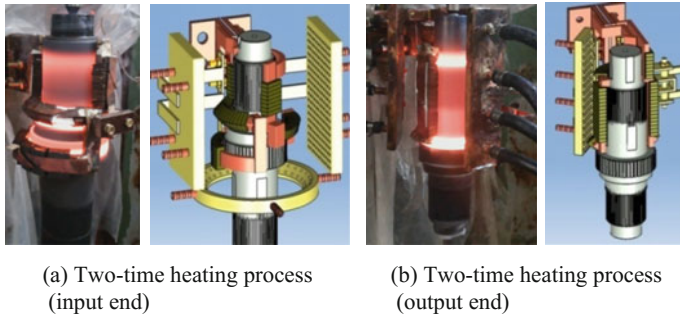


Fig. 50.4 Schematic of two-time heating process

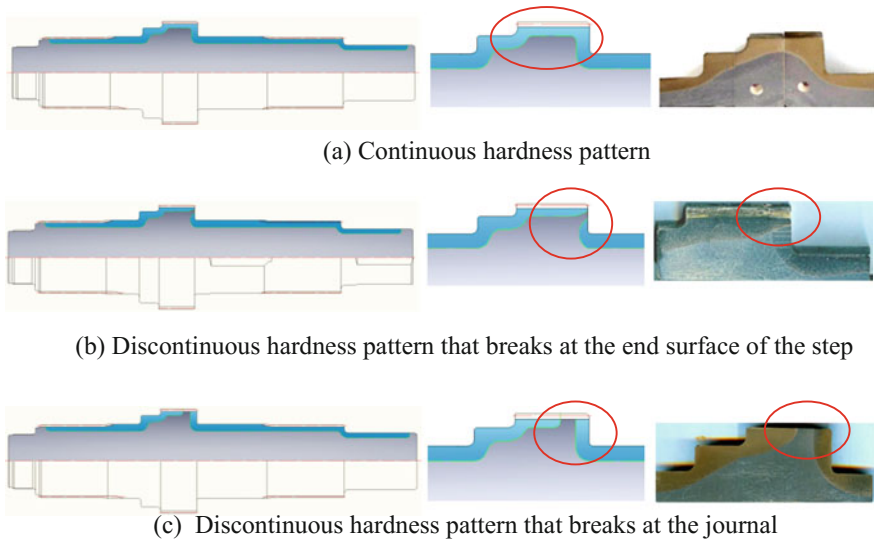


Fig. 50.5 Hardening layer distributions of different heating process

for placing heating conductor specified for the heating of the filleted corners (Fig. 50.3b). The heating were not targeted at the filleted corners and showed a very low heating efficiency, resulting in a shallow hardening layer (Fig. 50.5a). While on the contrary, the heating efficiency at the steps adjacent to the filleted corners was comparably high, resulting in overheating. The balance between the two was hard to achieve. Besides, single-time heating process requires a rigid air gap between the inductor and the work piece, making it unpractical in large scale production.

The hardness pattern disconnects in the middle of the cylindrical drive gear shaft using the two-time heating process, but the integral strength is not affected. One arrangement of the break point of the hardness pattern was at the end surface of the step (Fig. 50.5b). This kind of arrangement could easily cause tempering at the

filleted corner, thus making the optimal range of the process parameters strictly narrow. Another arrangement of the break point was at the journal that is away from the filleted corner (Fig. 50.5c). Such arrangement can fully avoid tempering at the filleted corner and providing sufficient facility for the structure design of the two sets of inductors. A heating conductor specifically designed for the filleted corner improved the heating efficiency, and deeper hardening layer was achieved, which manifested that the two-time separated heating was a more practical process.

50.3.2 Structure of Two-Time Heating Process Inductor and the Heating Uniformity

For multi-diameter shafts, the journal and steps adjacent to the filleted corner shield a large number of flux lines. The smaller the filleted corner and the higher the step are, the stronger the shielding effect will be. Thus the filleted corner is less likely to be heated by self-generated eddy currents. By proper design of the cross-section shape of the heating conductor specified for the filleted corner, fully taking advantage of the flux concentrators to increase the number of flux lines through the filleted corner and assisted heat conducting of the journal and steps, the heating rate of the filleted corner can be largely improved. An ideal heating effect is achieved by balancing heating at the filleted corner and adjacent journal and step.

50.3.2.1 Structure Design of the Inductor for the Input End

As Fig. 50.6 shows, the structure of the input end of the cylindrical drive gear shaft to be hardened has double filleted corners and steps. Two specified heating conductors were assigned to the filleted corners, R1 and R2. When the dimensions of the filleted corners and steps are fixed, the heating balance of the two structures are affected by the following factors, namely: cross-section shape of the filleted corner heating conductor, dimensional relationship between the filleted corner heating conductor and the adjacent journal and the end surface of the step (opening direction of the flux concentrator), air gaps and current frequency. The height of the adjacent steps of R1 and R2 are 9 and 6.5 mm, which is a comparably small dimension that tends to be over heated. According to the experiment results, the heating conductor for R1 adopted asymmetric structure with a 45° angle to the main axis of the part while the heating conductor for R2 adopted an asymmetric structure with a 15° angle to the main axis of the part.

Each part of the valid heating conductor in the inductor was series connected as a whole, forming a series connection in which the current equals everywhere in the conductor. The heating efficiency of different positions of the part related to the length ratio of heating conductor to the gross length of the inductor. Heating conductor length for R1 and R2 was the key point. Figure 50.7a, b show the structures before and after improvement. After the improvement, heating conductor

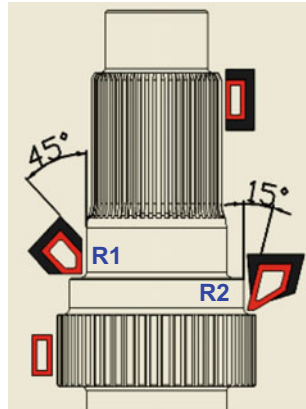


Fig. 50.6 Cross section of input end heating conductor

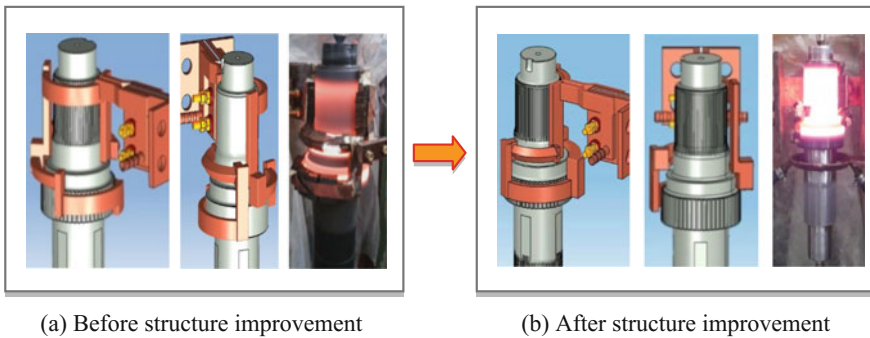


Fig. 50.7 Schematic of the structure of input end heating conductor

distribution was optimized and the whole structure was largely simplified. The improvement reduced the inductor production difficulty and increased its practicality, enabling a more uniform heating through the whole part.

50.3.2.2 Structure Design of the Inductor for the Output End

As Fig. 50.8 shows, the structure of the output end also has double filleted corners and steps. The inductor was series connected with specified heating conductor for R3 and R4. The height of the step adjacent to R3 is 8 mm, having low heat capacity, and obvious edge effect was caused by the longitudinal heating conductor that went over the step, leading to over-heating of the step. As Fig. 50.9 shows, by moving the heating conductor outward, increasing the air gap, the flux density through the edge is effectively reduced. As the heat accumulation rate reduced, the over-heating of the edge was avoided.

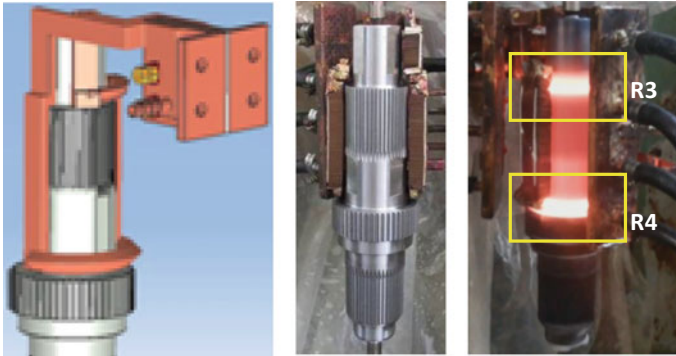
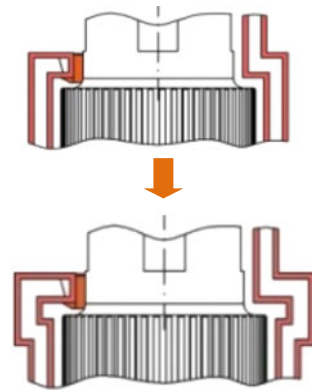


Fig. 50.8 Heating condition of the output end before improvement

Fig. 50.9 Heating conductor over the edge



The radius of the filleted corner R4 is only 2 mm, and the height of the adjacent step is 15.5 mm. Very few flux lines went through the filleted corner because of the high step, so the heating of the filleted corner by self-generated eddy current was extremely limited. Even increasing the effect of assisted conduction heating by adjacent journal and step, it failed to achieve simultaneous heating. As is shown in Fig. 50.10, by changing the cross-section shape of the heating conductor for R4 into parallelogram with a 15° angle to the axis of the part, the problem concerning simultaneous heating was readily solved. Figure 50.11 shows the heating condition after the improvement.

50.3.3 Determination of Optimal Parameter Range

IGBT power was used by the induction heating, as is shown in Table 50.4, three sets of parameters were applied to check the response of 42CrMoH and 40CrH to the corresponding process. Results showed that when frequency was higher than

Fig. 50.10 Heating conductor for R4

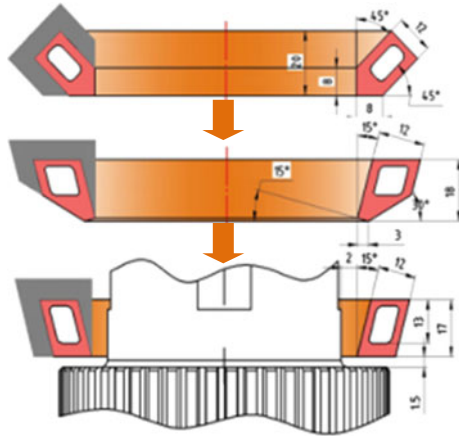


Fig. 50.11 Heating condition after improvement



Table 50.4 Parameters of comparison experiments (IGBT power)

Parameters	Test 1		Test 2		Test 3	
	Input end	Output end	Input end	Output end	Input end	Output end
Power ratio (%)	145	125	133	126	120	107
Output power (kW)	150–180	130–160	140–160	125–150	130–150	120–140
Voltage (V)	430–460	410–440	410–450	390–430	400–440	370–420
Current (A)	420–450	390–430	390–430	370–410	380–420	360–390
Output frequency (kHz)	8.2–9.6	7.6–9.3	7.6–8.6	7.3–8.2	6.6–7.8	6.5–7.9
Heating duration (s)	20	20	22	26	23	31
Quenching time (s)	45	48	47	50	49	52
Medium concentration (%)	6.0		8.0		10.0	
Quenching pressure (Mpa)	0.5					
Rotation speed (r/min)	90					

9.5 kHz, it deteriorated heating uniformity. When heating time was lower than 22 s, filleted corners could not fully austenize, and the case hardening depth could not be over 3.0 mm using 40CrH. When concentration of the quenching medium was lower than 8.0%, the cracking tendency at steps increased using 42CrMoH. The parameter range given by test 3 was proper, acquiring a quenching quality that met all the specifications required by the standard. Table 50.5 is the results of the quality inspection. Figure 50.12 shows the inspection positions.

Table 50.5 Quality inspection results of test 3 (42CrMoH)

Inspection position	1	2	3	4	5	6	7	8	9	10	11	12	13	14	15
Surface hardness (HRC)	56.5	57	57	57.5	57.5	59.5	58.5	59.5	57.5	57.5	57	56.5	58.5	58	58
CHD (mm)	6.2	5.9	6.9	4.4	4.5	6.7	3.6	6.3	7.1	6.8	5.8	6.1	4.6	5.4	5.3
Class of quenching microstructure	6	6	6	5	7	4	6	4	6	6	6	6	6	5	6
Matrix microstructure	Tempering sorbite + small amount of ferrite														
Matrix hardness	296–308 HBW														

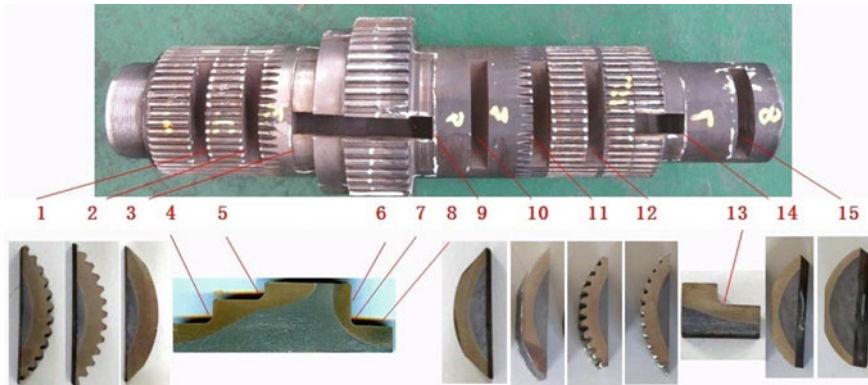
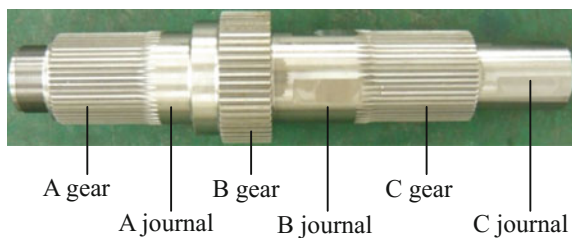


Fig. 50.12 Quality inspection position of test 3

Fig. 50.13 Inspection position of quenching deformation



50.3.4 Analysis of Quenching Deformation

Factors affecting quenching deformation are case hardening depth, process and material. Table 50.6 shows the radial beat, gear lead and tooth thickness data (Fig. 50.13). Table 50.7 shows the data of different case hardening depth affecting quenching deformation. The material was 42CrMoH and case hardening depth was of test 3. Test results showed that while the case hardening depth increased, the radial beat and gear lead variation increased and tooth thickness reduced. When case hardening depth was lower than 5.5 mm, radial beat variation was lower than 0.077 mm and gear lead variation was lower than 0.053. In this case, straightening process can be saved during production. When case hardening depth was between 5.5 and 7.7 mm, 20% of the parts needed straightening. When case hardening depth was deeper than 8.4 mm, the radial beat was lower than 0.100 mm, and 50% of the parts needed straightening.

Table 50.8 shows the effect of three different processes to quenching deformation. The three processes include carburizing, single-time induction hardening and two-time induction hardening. The materials used in two-time induction hardening were 42CrMoH and 40CrH. Case hardening depths were the same of the two materials. Only radial beat was compared in current experiment. Experiment results showed that the radial beat of two-time induction hardening was lower than that of the single-time quenching. Deformation tendency was smaller using 42CrMoH than 40CrH. When case hardening depth was beyond 7.3 mm, radial beat of carburizing was smaller than induction hardening.

50.3.5 Torsion Strength Test Results

Static torsion test was performed to evaluate the torsion strength of the processed parts. The static strengths of carburizing, single-time induction hardening and two-time induction hardening were compared. For two-time induction hardening, the two materials of 42CrMoH and 40CrH were also compared. Results showed that when the case hardening depth of induction hardening was beyond 7.5 mm, the strength was 20% higher than carburizing. The strengths of the parts using single-time quenching and two-time quenching were nearly the same. The strength of the parts using 42CrMoH was higher than those using 40CrH (Table 50.9).

Table 50.6 Radial beat, gear lead and tooth thickness before quenching

No.	Inspection position												
	A gear (pitch circle diameter $\Phi 72$)			B gear (pitch circle diameter $\Phi 104$)			C gear (pitch circle diameter $\Phi 72$)			A journal ($\Phi 75$)		B journal ($\Phi 75$)	C journal ($\Phi 57$)
	Radial beat	Gear lead	Tooth thickness	Radial beat	Gear lead	Tooth thickness	Radial beat	Gear lead	Tooth thickness	Radial beat	Radial beat		
1	0.028	0.041	2.331	0.032	0.033	3.140	0.053	0.034	2.318	0.029	0.051	0.033	
2	0.033	0.035	2.296	0.029	0.022	2.948	0.027	0.031	2.309	0.021	0.022	0.018	
3	0.037	0.024	2.303	0.026	0.020	3.113	0.024	0.030	2.313	0.023	0.025	0.023	
4	0.031	0.036	2.337	0.021	0.018	3.117	0.027	0.022	2.347	0.033	0.023	0.045	
5	0.010	0.038	2.320	0.043	0.030	2.994	0.022	0.019	2.318	0.023	0.027	0.026	
Fluctuation range	0.016–0.037	0.024–0.041	2.296–2.337	0.021–0.043	0.018–0.033	2.948–3.140	0.022–0.053	0.019–0.038	2.309–2.347	0.021–0.033	0.022–0.051	0.018–0.045	

Table 50.7 Quenching deformation relating to different case hardening depths


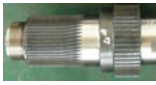

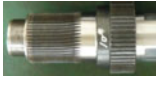
CHD of axle (mm)	No.	Inspection position													
		A gear (pitch circle diameter $\Phi 72$)			B gear (pitch circle diameter $\Phi 104$)			C gear (pitch circle diameter $\Phi 72$)			A journal ($\Phi 75$)		B journal ($\Phi 75$)	C journal ($\Phi 57$)	
		Radial beat	Gear lead	Tooth thickness	Radial beat	Gear lead	Tooth thickness	Radial beat	Gear lead	Tooth thickness	Radial beat	Gear lead	Tooth thickness	Radial beat	
4.9-5.8	1	0.064	0.033	2.321	0.066	0.047	3.110	0.051	0.041	2.307	0.057	0.051	0.053		0.053
	2	0.052	0.041	2.302	0.057	0.053	2.908	0.069	0.039	2.303	0.053	0.62	0.061		0.061
	3	0.060	0.044	2.293	0.046	0.051	3.090	0.070	0.046	2.296	0.077	0.068	0.058		0.058
6.8-7.7	4	0.091	0.068	2.315	0.962	0.046	3.081	0.086	0.059	2.321	0.078	0.086	0.103		0.103
	5	0.086	0.066	2.301	0.107	0.045	2.963	0.093	0.063	2.273	0.106	0.102	0.097		0.097
	6	0.103	0.043	2.986	0.098	0.057	3.091	0.103	0.057	2.285	0.103	0.093	0.089		0.089
8.4-9.1	7	0.123	0.078	2.253	0.125	0.073	3.073	0.133	0.073	2.260	0.115	0.131	0.142		0.142
	8	0.133	0.096	2.291	0.132	0.066	3.053	0.145	0.83	2.281	0.124	0.148	0.133		0.133
	9	0.127	0.073	2.293	0.131	0.064	2.915	0.155	0.079	2.347	0.123	0.137	0.156		0.156

Material: 42CrMoH; frequency: 6.7-7.8 kHz

Table 50.8 Radial beat of different processes

Inspection position	Carburizing	Single-time induction hardening	Two-time induction hardening		Induction hardening parameters and quality standard
	20CrMnTiH	42CrMoH	42CrMoH	40CrH	
A axle	0.065–0.077	0.162–0.177	0.083–0.099	0.139–0.171	Frequency: 6.7–7.8 kHz CHD of axle: 7.3–7.9 mm CHD of spline: 5.9–6.5 mm CHD of filleted corner: 3.2–4.3 mm Quantity: 10 pieces
C axle	0.054–0.081	0.157–0.206	0.098–0.130	0.136–0.189	
D axle	0.083–0.093	0.127–0.213	0.086–0.108	0.160–0.197	
Fluctuation range	0.054–0.093	0.127–0.230	0.083–0.130	0.136–0.197	

Table 50.9 Results of static torsion test

Process	20CrMnTi carburizing	40CrH two-time induction hardening	42CrMoH two-time induction hardening	42CrMoH single-time induction hardening
Surface hardness (HRC)	58.5-61.5	53.5-56.5	53-56.5	53.5-57.0
CHD (mm)	Journal: 2.0-2.2 Spline: 1.8-2.0 Filleted corner: 1.8-1.9	Journal: 7.5-8.3 Spline: 6.8-7.3 Filleted corner: 3.1-4.5	Journal: 7.1-7.6 Spline: 6.2-6.5 Filleted corner: 3.5-4.6	Journal: 7.2-7.6 Spline: 6.1-6.5 Filleted corner: 3.0-4.2
	1 2 3	4 5 6	7 8 9	10 11 12
Max torque (kN m)	59 62 61	79 82 81	91 91 90	91 91 91
Max rotation angle(°)	16.5 15.1 16.7	22.8 17.0 17.2	16.5 15.6 16.4	14.2 16.2 15.5
Fracture position	Spline fracture Journal fracture Spline fracture	Spline deformation Spline deformation Spline deformation	Spline deformation Spline deformation Spline deformation	Spline deformation Spline deformation Spline deformation
Failure mode				

50.4 Conclusions

- (1) Compared with single-time induction hardening process, two-time induction hardening of cylindrical drive gear shaft is superior in the design and production of inductor and reducing quenching deformation.
- (2) For cylindrical drive gear shaft with a typical multi-diameter structure, 42CrMoH is better than 40CrH in induction hardening process, reducing quenching deformation and increasing torsion strength.
- (3) Induction hardening can achieve deep case hardening depth and significantly enhance torsion strength. The strength can be 20% higher than carburized parts. Strength reserve coefficient is more than 2.0, meeting torsion strength requirement.
- (4) When the case hardening depth of the axle is lower than 6 mm, radial beat and gear lead variations are small. Radial beat is lower than 0.08 mm which can ensure the assemble precision, and straightening is not necessary. When case hardening depth is more than 8 mm, radial beat and gear lead variations are high. Radial beat variation of more than 0.12 mm takes up a high percentage of the data and straightening is needed. Case hardening depth of more than 8 mm is not recommended.

References

1. Lin X et al (1998) Induction hardening process and device for automobile parts. Series books of automobile manufacture technologies, p 8
2. Shen Q et al (2008) Modern induction heat treatment technologies. p 1

Chapter 51

Research on Automatic Automobile Air-Conditioning Controller

Bo Yang, Mingming Wang, Ted S. Huang, Fei Peng and Cong Xin

Abstract In order to improve the comfort of riding vehicles, this paper focuses on the automatic air-conditioning controller by introducing the principle of air-conditioner and the design of hardware and software. The controller controls different actuators to achieve the automatic control of head temperature according to automatic control algorithm. Finally, the experiments revealed that the system is stable to achieve the desired requirements.

Keywords Automatic control · Air-conditioner · Controller · Riding comfort · Hardware · Software

51.1 Introduction

With the continuous development of automotive industry, car owners' demand for riding comfort has been increased. Automatic air-conditioner that can keep the driver's head temperature close to the setting temperature on panel plays an important role in a vehicle and has an positive impact on riding comfort. As the core component and the brain of the air-conditioner, air-conditioning controller controls all movements to provide cooling and heating capacity [1].

Figure 51.1 shows an automobile air-conditioner, which mainly consists of blower, compressor, evaporator, heating core, air mix door motor, mode door motor and other components. The blower intakes air from the air inlet and controls winds' blowing speed [2]. When the compressor is connected to engine by the clutch, it will be operating. The liquid refrigerant flows through the evaporator, and changes into gas by absorbing heat of evaporate, which will reduce the temperature of the air blowing through the evaporator [3]. When the engine starts, the temperature of heating core connected with engine coolant pipe and the air through it will rise

B. Yang (✉) · M. Wang · T.S. Huang · F. Peng · C. Xin
GAC Engineering, Guangzhou Automobile Group CO. LTD, Guangzhou, China
e-mail: yangbo@gaei.cn

© Springer Nature Singapore Pte Ltd. 2017
Society of Automotive Engineers of China (SAE-China), *Proceedings of SAE-China Congress 2016: Selected Papers*, Lecture Notes in Electrical Engineering 418,
DOI 10.1007/978-981-10-3527-2_51

605

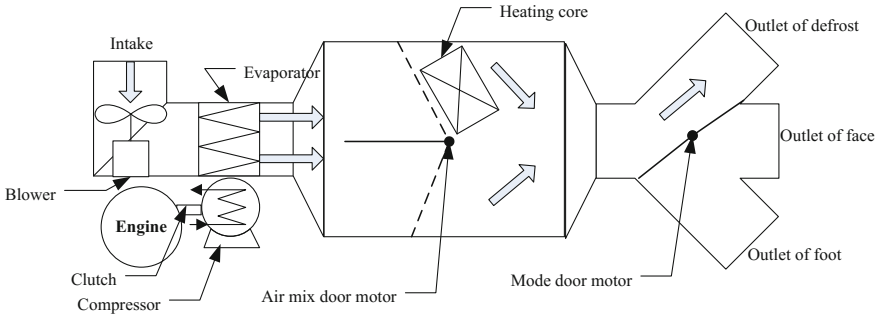


Fig. 51.1 Automobile air-conditioner

rapidly. The air mix door motor controls the ratio of hot air and cold, and the mode door motor controls the direction of the wind blowing out.

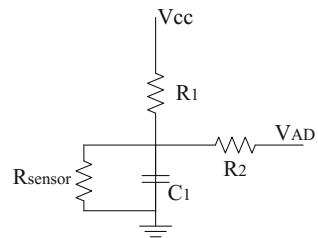
51.2 Hardware Design

Automatic air-conditioner should control all actuators to ensure that the driver’s head temperature is always close to the setting temperature on the vehicle panel according to the change of the ambient temperature, the cabin temperature, the evaporator temperature and sunlight intensity. Therefore, the circuit of automatic air-conditioning controller must include the acquisition circuits to acquire these temperatures and sunlight intensity and the driving circuits to control the blower and door motors [4].

51.2.1 Signal Acquisition Circuit

The resistance of temperature sensor can be changed with different temperature, and the resistance of sunlight intensity sensor can be changed with different sunlight intensity. The signal acquisition circuit is shown in Fig. 51.2, where, R_{sensor} is the

Fig. 51.2 The signal acquisition circuit



sensor’s resistance, V_{cc} is the 5 V voltage in the controller, V_{AD} is the voltage collected by MCU (micro control unit). Finally we will get the temperature or sunlight intensity based on the relationship between temperature and resistance or the relationship between sunlight intensity and resistance.

51.2.2 Circuit for Controlling Blower

The air-conditioning controller controls the speed of blower by providing different driving voltages to the driving module. In Fig. 51.3, a 1 kHz PWM signal sent by the MCU can be switched into a controlling voltage through a high side driver and a two-stage RC filter, which can be changed within a range of 0–5 V by adjusting the duty of the PWM signal.

51.2.3 Circuit for Controlling Motor

Door motor in air-conditioning system is controlled by the servo motor with position feedback, whose position can be calculated by the signal acquisition circuit described in Sect. 51.2.1.

As shown in Fig. 51.4, the MCU controls motors by a half-bridge driver chip, in which MOSI, MISO, SCK, SS are the SPI communication interfaces with MCU. OUT1 to OUT4 are four output ports, which are separately connected with the cold side of the air mix door, the hot side of the air mix door, the face side of the mode door, and the defrost side of the mode door. Take the air mix door motor for example, when OUT1 is high and OUT2 is low, the air mix door motor will rotate to the cold side, when OUT1 is low and OUT2 is high, the air mix door motor will rotate to the hot side, and when OUT1 and OUT2 are both low, the air mix door motor will stop. The MCU could control the motor staying in any position by adjusting the output of OUT1 to OUT4 according to its feedback in real time.

Fig. 51.3 The circuit for controlling blower

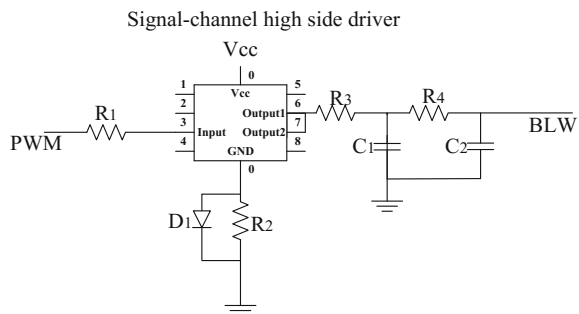
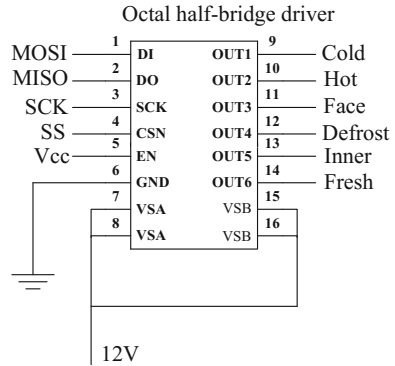


Fig. 51.4 The circuit for controlling motor



51.3 Software Design

51.3.1 Calculation of the Target Outlet Temperature

Target outlet temperature is the key variable of automatic air-conditioning algorithm and directly affects all actuators in the air-conditioning system. It could be calculated by the formula: $TAO = f_1(T_{set}) - f_2(T_R, T_{AM}) - k_1 \times T_S$, where TAO is the target outlet temperature, Tset is the setting temperature, TR is the cabin temperature, TAM is the ambient temperature, TS is the sunlight intensity, and k1 is the sunlight parameter [5].

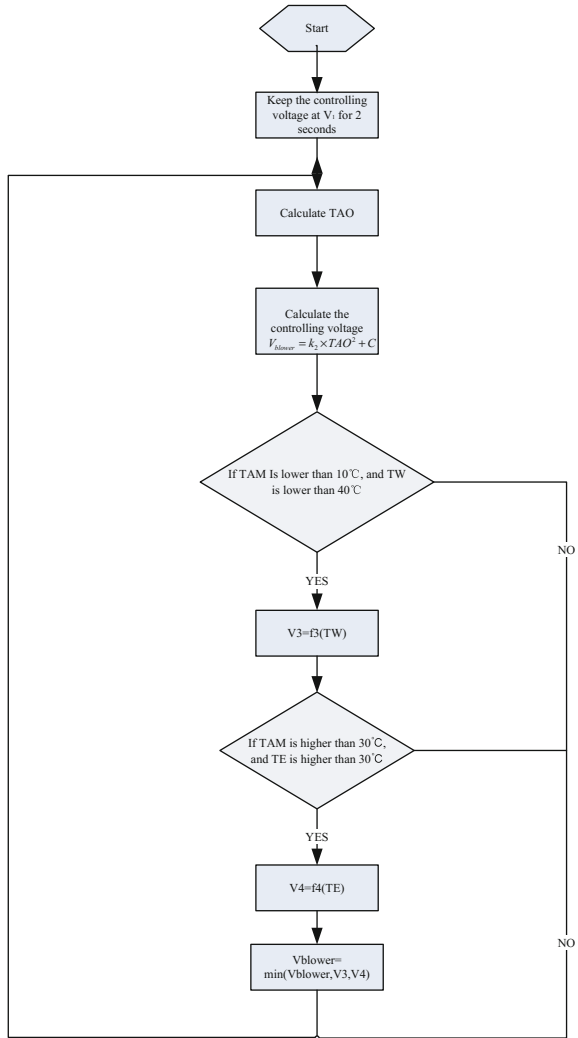
51.3.2 Automatic Control of Blower

Blower is an important actuator of air-conditioning system. Its speed directly determines the wind volume. We should match the starting voltage V_1 depending on the characteristic of different blower types. When the blower is started, the controlling voltage must be kept at V_1 for 2 s to ensure a smooth start and improve the lifetime of the blower.

According to the circuit, the controlling voltage of the blower in automatic air-conditioner is $V_{blower} = K_2 \times TAO^2 + C$, $V_{blower} \in [V_2, 5]$, where k_2 and C are determined by the environment simulation experiment, V_2 is the controlling voltage when blower is 1st wind volume.

In winter, the temperature of engine water (TW) can not rise rapidly to 40 °C slightly higher than the body temperature of human being. In order to avoid blowing out the cold wind, the ECU should do a pre-heating control according to the temperature of engine water. When $TW \leq 40$, $V_3 = f_3(TW)$. In summer, the compressor can not reduce the temperature of evaporator (TE) rapidly. In order to avoid blowing out the hot air, the ECU should do a pre-cooling control according to the temperature of evaporator. When $TE \geq 30$, $V_4 = f_4(TE)$. Finally, the controlling

Fig. 51.5 The automatic control of blower



voltage of blower is determined by $V_{blower} = \min(V_{blower}, V3, V4)$. The flow chart of blower control is shown in Fig. 51.5.

51.3.3 Automatic Control of Compressor

Compressor is the only refrigerating source of automotive air-conditioning system. It compresses low-pressure gaseous refrigerant to high pressure gaseous refrigerant, which will come into the evaporator and take away its heat. When the air sucked by the blower blows through the evaporator surface, it will become cold by heat

exchange. If the compressor has been in operation continuously, it will not only be a waste of engine torque which stands for vehicle energy, but also make evaporator be frozen which may break the air-conditioning system down. If the compressor is stopped, air-conditioner will lose its cooling function. Therefore, in software, when the evaporator temperature is lower than TE_1 , the compressor will be stopped, and when the temperature is higher than TE_2 , the compressor will return to work. $TE_1 = f_5(TAO)$, $TE_1 \in [1, 10]$, $TE_2 = TE_1 + 2$.

51.3.4 Automatic Control of Motor

As shown in Fig. 51.1, air mix door motor allocates the volume of cold air blowing through the heating core, which will come together with other cold air. The position of the air mix door motor that determines the outlet temperature can be calculated by the formula $SWD = f_6(TAO, TW, TE)$, where $SWD \in [0\%, 100\%]$.

According to thermodynamics and related air-conditioning experiences, people do not want the cold air to blow foot and the hot air to blow face. In the software design of automatic air-conditioning controller, the relation between the position of mode door and TAO should be considered. When TAO is higher than T1, the mode door should be at the position of blowing foot. When TAO is lower than T1 but higher than T2, the mode door should be at the position of blowing foot and face. However, when TAO is lower than T2, the mode door should be at the position of blowing foot.

51.4 Experiment Results

In order to verify the effect of the automatic air-conditioning controller, the author conducted an experiment on a vehicle equipped the designed controller in the winter of Heihe and in the summer of Sanya, in which the setting temperature was set at 25°.

In December, the ambient temperature in Heihe is about -20 °C. As shown in Fig. 51.6, after the air-conditioner was started up, the head temperature could reach 25 °C in 20 min, and be at a stable state within 10 min, indicating that the automatic heating control can meet the requirements.

In July, the ambient temperature in Sanya is about 36 °C, the strongest sunlight intensity is about 1 kW. As shown in Fig. 51.7, after the air-conditioner was started up, the head temperature could reach 25 °C in 5 min, and be at a stable state within 10 min, which indicated that the automatic cooling control can meet the requirements.

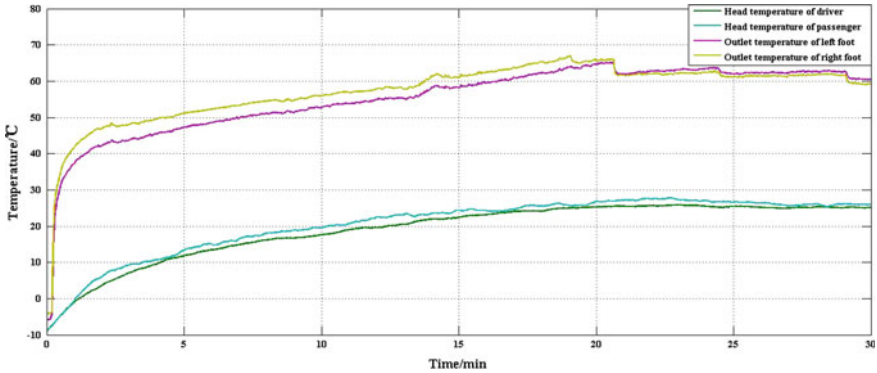


Fig. 51.6 Winter experiment

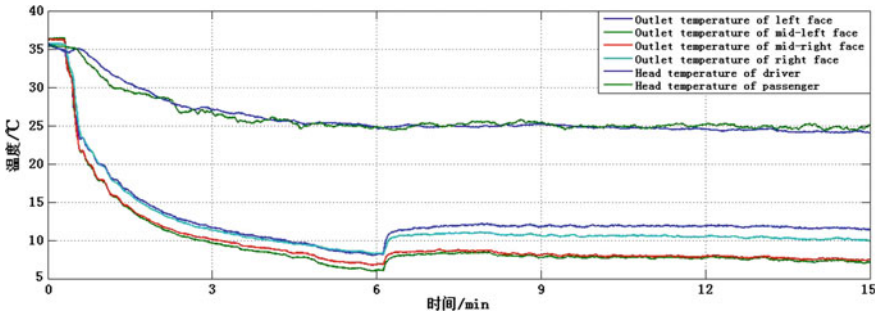


Fig. 51.7 Summer experiment

51.5 Conclusion

This research developed an automatic air-conditioning controller, which controlled the blower, compressor, door motor and achieves automatic control of the head temperature by collecting the ambient temperature, the cabin temperature and sunlight intensity. Experiments on the vehicle equipped with automatic air-conditioning controller revealed that the designed controller is high-precision and helpful for improving riding comfort.

References

1. Bedbak SS, Gopal MR (2005) Performance analysis of a compressor driven metal hydride cooling system. *Hydrogen Energy* 30(10):1127–1137
2. Fan Y-q, Hayashi T, Ito K (2012) Coupled simulation of BES-CFD and performance assessment of energy recovery ventilation system for office model. *J Cent South Univ* 19 (3):633–638

3. Kim KJ, Montoya B, Razani A (2001) Metal hydride compacts of improved thermal conductivity. *Hydrogen Energy* 26(6):609–613
4. Ahmed SS, Murthy SS (2004) Analysis of a novel metal hydride cycle for simultaneous heating and cooling. *Renew Energy* 29(4):615–631
5. Sanchez AR, Klein HP, Groll M (1999) Expand graphite as heat transfer matrix in metal hydride beds. *Hydrogen Energy* 28(5):515–527

Chapter 52

Research on the Control Algorithm of EPS for Vehicle Handling Stability

ChenXi Fang and Shang Liu

Abstract Based on the problem of the Control Algorithm in the electric power steering (EPS) system, a current controller of EPS for vehicle handling stability is designed. The dynamic models of EPS and the vehicle were constructed, simplifying the evaluation system of vehicle handling stability, putting forward an EPS designed controller that has H_∞ mixed sensibility based on the evaluation index of vehicle handling stability. The test results indicate that the designed controller for EPS shows a favorable handling performance, it also could effectively restrain the noises and disturbances caused by sensors and road conditions. The designed controller has robust stability and performance, and can effectively in prove the handling stability and safety of vehicles.

Keywords Vehicle handling performance · Control algorithm · Road feeling · H_∞ mixed sensibility

52.1 Introduction

With the development of automotive technology, as one of the important indexes of vehicle safety performance, vehicle handling stability requirement is increasing day by day. Vehicle handling stability refers to the vehicle in the process of driving, can run follow the direction given by the driver and maintain a stable running ability under external interference. Electric power steering system (EPS) is based on the traditional mechanical system to add power motor, to achieve the power steering function, compared with the original system; the dynamic performance of the vehicle steering will have a great change. In the comparison of steering road feeling, steering sensitivity and lateral acceleration of steering by EPS and traditional mechanical power steering, Yoshihiro ONIWA et al. found that the steering stability of the vehicle with EPS becomes worse and tends to be unstable [1].

C. Fang (✉) · S. Liu
Hirain Technologies, Beijing, China
e-mail: chenxi.fang@hirain.com

Currently the EPS algorithm design pattern mainly includes basic power control and compensation current control and active return control three modules. The basic power can be classified as linear basic power, broken line basic power and curve line basic power. Current compensation control can be divided into three parts, which including motor inertia compensation control, motor damping compensation control and motor friction compensation control. Return control also includes low speed control and high-speed control. The control parameters selection is mainly based on the late vehicle calibration.

On the EPS power algorithm design, a lot of research has been done at home and abroad. Manu Parma et al. proposed an electric power steering optimal control method, designed the power algorithm without torque sensor and carried on the relevant experimental demonstration [2]. Tsung-Hsien Hu et al. studied in EPS system integration control based on multi-sensor signal, including basic power control, return control and compensation control, and studied each control mode switching mechanism and achieved good control effect [3]. Chen Hui, Yu Zhuoping from Tongji University researched the effect of EPS on the vehicle steering stability, on the basis of the basic power control, the motor inertia compensation control, motor damping compensation control and torque differential control are introduced in order to improve the dynamic performance of EPS system [4]. These studies enhance the control and stability of the EPS itself. It is assumed that the vehicle dynamics on the EPS system can be ignored.

With the continuous improvement of vehicle performance and automatic driving trends, the EPS robustness requirement is higher and higher. Kohn et al. studied the robustness of the EPS, established the mathematical model of the rack power EPS system, and designed the robust controller, and analyzed the impact on power performance by the tyre elasticity coefficient changes [5]. Ji Xuewu and Chen Kuiyuan from Tsinghua University studied the current tracking performance and anti-interference performance of EPS, and designed the optimal controller based on linear matrix inequality [6]. Tsung-Hsien et al. Studied the motor control of the electric power steering system by using the mixed sensitivity method, and the simulation experiment was carried out to verify the effectiveness of the mixed sensitivity method [3]. Sugitani et al. [7] studied the EPS road feeling, abstracted the evaluation function of the road feeling and used H^∞ control theory to design controller. These methods in the design of EPS algorithm achieved good effect, the robustness of these methods is only for the EPS system, the research and demonstration on robust performance from the perspective of vehicle control has not been done.

Through the above analysis, we can get the following problems in the design of the existing EPS algorithm:

Vehicle handling stability is considered only on the late parameters calibration debugging. Therefore, the vehicle handling stability problems cannot be exposed early in the whole process of EPS design, high design risk, high rework cost, and the existing calibration method is time-consuming and power-consuming, higher requirements for calibration engineer.

The existing EPS power algorithm research take the torque sensor as the single input of the control system, and the popularity of vehicle network and whole vehicle sensors make this traditional model has been unable to meet the design requirements of EPS power algorithm.

With the complexity of driving cycle and the trend of automatic driving, requirements on vehicle handling stability and robustness of the EPS are increasingly high, the existing EPS algorithm design cannot meet the needs of functional safety.

Therefore, this paper proposes the EPS algorithm design method for vehicle steering stability, namely the vehicle handling stability evaluation function as EPS power input, and puts forward a mixed sensitivity EPS controller design method, simulation and experimental results show that this method improves the robustness of the EPS system, the vehicle handling stability and anti-interference ability are enhanced.

52.2 Model Formulation

52.2.1 Vehicle Lateral Dynamic

The single-track model is used as shown in Fig. 52.1. The differential equations describing the vehicle dynamics are

$$\begin{aligned} -2k_1 \cdot \left(\beta + \frac{a_f \omega_r}{u} - \delta \right) - 2k_2 \cdot \left(\beta - \frac{b_r \omega_r}{u} \right) &= m(\dot{v} + u\omega_r) \\ -2a_f k_1 \cdot \left(\beta + \frac{a_f \omega_r}{u} - \delta \right) + 2b_r k_2 \cdot \left(\beta - \frac{b_r \omega_r}{u} \right) &= I_z \dot{\omega}_r \end{aligned} \quad (52.2.1)$$

where m is vehicle mass, a_f is distance C.G. to front axle, b_r is rear cornering coefficient, I_z is vehicle moment of inertia, β is sideslip angle, δ is steering angle, ω_r is yaw rate, k_1 is front cornering coefficient, k_2 is rear cornering coefficient and u is vehicle velocity.

The equations after Laplace transforms are

$$\begin{bmatrix} w_r \\ \beta \end{bmatrix} = \begin{bmatrix} s + \frac{2a_f^2 k_1 + 2b_r^2 k_2}{I_z u} & \frac{2a_f k_1 - 2b_r k_2}{I_z} \\ 1 + \frac{2a_f k_1 - 2b_r k_2}{mu^2} & s + \frac{2(k_1 + k_2)}{mu} \end{bmatrix}^{-1} \begin{bmatrix} \frac{2a_f k_1}{I_z} \\ \frac{2k_1}{mu} \end{bmatrix} \delta = \begin{bmatrix} A_1 \\ A_2 \end{bmatrix} \delta \quad (52.2.2)$$

When normal running of the vehicle, the lateral acceleration is not more than 0.4 g, and tyre sideslip angle is less than 5° . Tyre lateral force F_Y and sideslip angle α is linear relationship. Therefore, the linear tyre model is adopted.

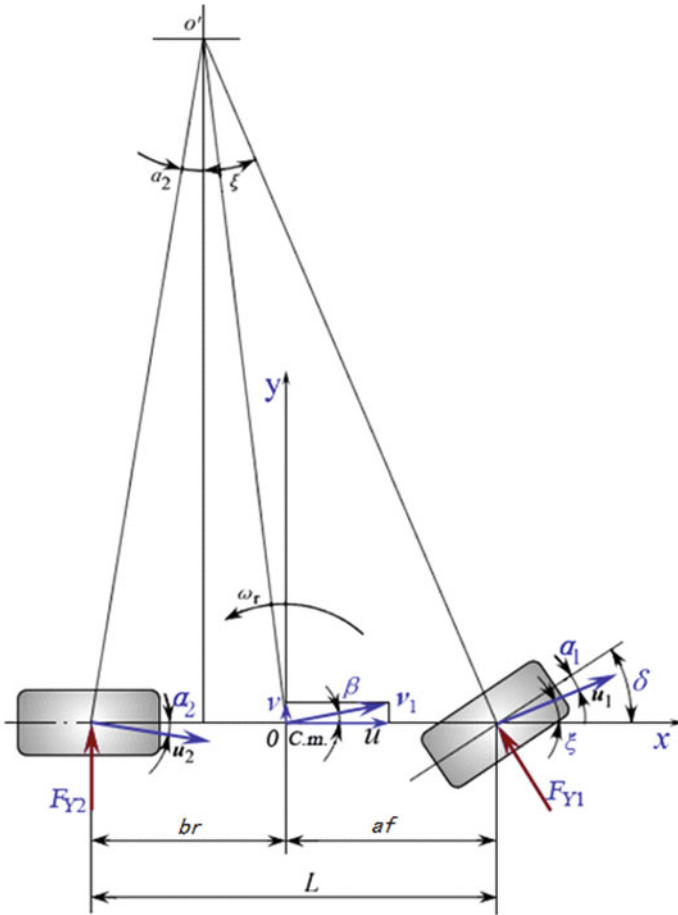


Fig. 52.1 Vehicle 2-DOF model

$$T_r = -2k_1 \cdot \left(\beta + \frac{a_f \omega_r}{u} - \delta \right) \cdot d = K_T \cdot \delta \tag{52.2.3}$$

$$K_T = 2k_1 - 2k_1 \cdot A_1 \cdot a_f / u - 2k_1 \cdot A_2 \tag{52.2.4}$$

where T_r is Reaction torque from road wheels.

52.2.2 Steering System Dynamic

The EPS system consists of steering wheel, torque sensor, ECU, power assisted motor and steering gear, as shown in Fig. 52.2. The inertia, damping are considered in model, and Ignoring the effect of nonlinearity.

The differential equations of the EPS system are:

$$T_s = J_s \ddot{\theta}_s + B_s \dot{\theta}_s + T_{det} \tag{52.2.5}$$

$$T_a = T_m - J_m \ddot{\theta}_p k_m - B_m \dot{\theta}_p k_m \tag{52.2.6}$$

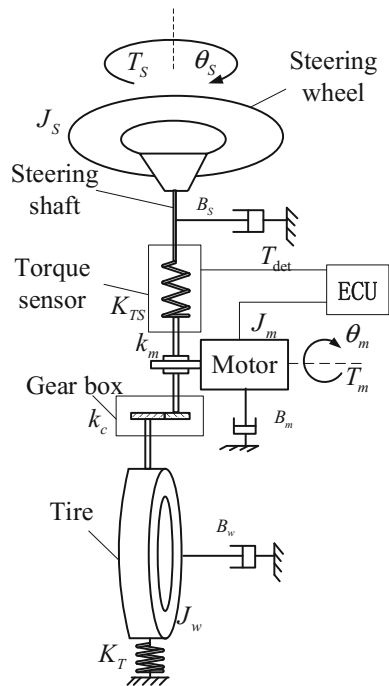
$$T_m = K_t \cdot i_m \tag{52.2.7}$$

$$k_m T_a + T_{det} = J_w \ddot{\theta}_p / k_c^2 + B_w \dot{\theta}_p / k_c^2 + T_r / k_c \tag{52.2.8}$$

$$T_{det} = K_{TS} \cdot (\theta_s - \theta_p) \tag{52.2.9}$$

where θ_s is steering wheel angle, θ_p is output pinion angle, J_s is steering wheel moment of inertia, B_m is steering wheel damping coefficient, k_m is motor reduction ratio, k_c is steering gear ratio, J_w is tyre moment of inertia, B_w is tyre damping coefficient, K_{TS} is stiffness of torque sensor.

Fig. 52.2 EPS system model



52.2.3 State Space Equation

State Space Equation of the whole system can be established, by Integrated the vehicle and EPS dynamics above. Suppose $X = [\dot{\theta}_s \ \theta_s \ \dot{\theta}_p \ \theta_p \ \omega_r \ \beta]^T$ is state vector of the system, $u = [T_s \ i]^T$ is input vector, $Y = [T_{\text{det}} \ \omega_r]^T$ is output vector. The state equations are:

$$G : \begin{cases} \dot{X} = AX + Bu \\ Y = CX + Du \end{cases} \quad (52.2.10)$$

$$\begin{aligned} \ddot{\theta}_s &= -B_1\dot{\theta}_s/J_1 - K_{TS}\theta_s/J_1 + K_{TS}\theta_p/J_1 + T_s/J_1 \\ \ddot{\theta}_p &= 1/(\frac{J_2}{k_c^2} + J_mk_m^2) \cdot (-\frac{B_2}{k_c^2} + B_mk_m^2)\dot{\theta}_p - (\frac{2k_1d}{k_c^2} \\ &\quad + K_{TS})\theta_p + K_{TS}\theta_s + \frac{2k_1da_f}{uk_c}\omega_r + \frac{2k_1d}{k_c}\beta + k_mK_t i \\ \dot{\omega}_r &= \frac{2a_fk_1}{I_zk_c}\theta_p - \frac{2a_f^2k_1 + 2b_r^2k_2}{I_zu}\omega_r - \frac{2a_fk_1 - 2b_rk_2}{I_z}\beta \\ \dot{\beta} &= \frac{2k_1}{muk_c}\theta_p - (1 + \frac{2a_fk_1 - 2b_rk_2}{mu^2})\omega_r - \frac{2(k_1 + k_2)}{mu}\beta \end{aligned} \quad (52.2.11)$$

set:

$$\begin{aligned} J_G &= \frac{J_2}{k_c^2} + J_mk_m^2 \\ B_G &= \frac{B_2}{k_c^2} + B_mk_m^2 \\ K_G &= \frac{2k_1d}{k_c^2} + K_{TS} \end{aligned} \quad (52.2.12)$$

Hence, we can obtain:

$$\begin{aligned} A &= \begin{bmatrix} -\frac{B_s}{J_s} & -\frac{K_{TS}}{J_s} & 0 & \frac{K_{TS}}{J_s} & 0 & 0 \\ 1 & 0 & 0 & 0 & 0 & 0 \\ 0 & \frac{K_{TS}}{J_G} & -\frac{B_G}{J_G} & -\frac{K_G}{J_G} & \frac{2k_1da_f}{J_Guk_c} & \frac{2k_1d}{J_Gk_c} \\ 0 & 0 & 1 & 0 & 0 & 0 \\ 0 & \frac{2a_fk_1}{I_zk_c} & 0 & 0 & -\frac{2a_f^2k_1 + 2b_r^2k_2}{I_zu} & -\frac{2a_fk_1 - 2b_rk_2}{I_z} \\ 0 & \frac{2k_1}{muk_c} & 0 & 0 & -(1 + \frac{2a_fk_1 - 2b_rk_2}{mu^2}) & -\frac{2(k_1 + k_2)}{mu} \end{bmatrix} \\ B &= \begin{bmatrix} 1/J_s & 0 & 0 & 0 & 0 & 0 \\ 0 & 0 & k_mK_t/J_G & 0 & 0 & 0 \end{bmatrix}^T \\ C &= \begin{bmatrix} 0 & K_{TS} & 0 & -K_{TS} & 0 & 0 \\ 0 & 0 & 0 & 0 & 1 & 0 \end{bmatrix} \\ D &= 0 \end{aligned}$$

52.3 EPS Algorithm Design

First, we need to determine the control objectives considering the criteria of vehicle handling stability, the two indexes are adopted in this paper: steering sensitivity and road feeling. We can model it as below.

$$E_1 = \frac{\omega_r}{\theta_s} \quad (52.3.1)$$

$$E_2 = \frac{T_s}{T_r} \quad (52.3.2)$$

The vehicle steering sensitivity (Eq. 52.3.1) represents response bandwidth of the system. When turning a certain angle of the steering wheel, the larger the wheel angle is, the higher the sensitivity is. Steering sensitivity is an important indicator of vehicle handling stability, which reflects the transient response characteristics of the vehicle to the steering input.

Road feeling (Eq. 52.3.2) is relationship between driver hand torque and vehicle lateral force. It's very important for driving comfortable and safe. Road feeling is impacted by road conditions, vehicle design and EPS algorithm.

The both indexes are related to EPS very closely. The impact of the EPS on the two evaluation indexes are analyzed below.

From Eqs. (52.2.5)–(52.2.9), we can obtain:

$$E_{1_Manual} = \omega_r/\theta_s = H \cdot K_{TS}/(K_{TS}k_c + K_T/k_c + J_w s^2/k_c + B_w s/k_c) \quad (52.3.3)$$

$$E_{1_EPS} = (1 + k_m k_{eps})K_{TS} \cdot H/(K_T/k_c + J_w s^2/k_c + B_w s/k_c + k_c \cdot (J_m s^2 k_m^2 + B_m s k_m^2) + (1 + k_m k_{eps})k_c K_{TS}) \quad (52.3.4)$$

$$E_{2_Manual} = T_s/T_r = 1/((J_w s^2/k_c + B_w s^2/k_c)/K_{TS} + k_c) \quad (52.3.5)$$

$$E_{2_EPS} = T_s/T_r = 1/(k_c k_m k_{eps} + k_c + k_c((\frac{J_2}{k_c^2} + J_m k_m^2)s^2 + (\frac{B_2}{k_c} + B_m k_m^2)s)/K_{TS}) \quad (52.3.6)$$

Equation (52.3.3) represents steering sensitivity of mechanical steering system without power assistant. Equation (52.3.4) represents steering sensitivity of EPS system. Equation (52.3.5) represents Road feeling of mechanical steering system without power assistant. Equation (52.3.6) represents Road feeling of EPS system.

As shown in Figs. 52.3 and 52.4, for EPS system, the bandwidth of the steering sensitivity is reduced, and the phase delay is increased. Also for EPS system, the frequency domain energy of the Road feeling decreases and overshoot appears. Overall, steering stability becomes worse.

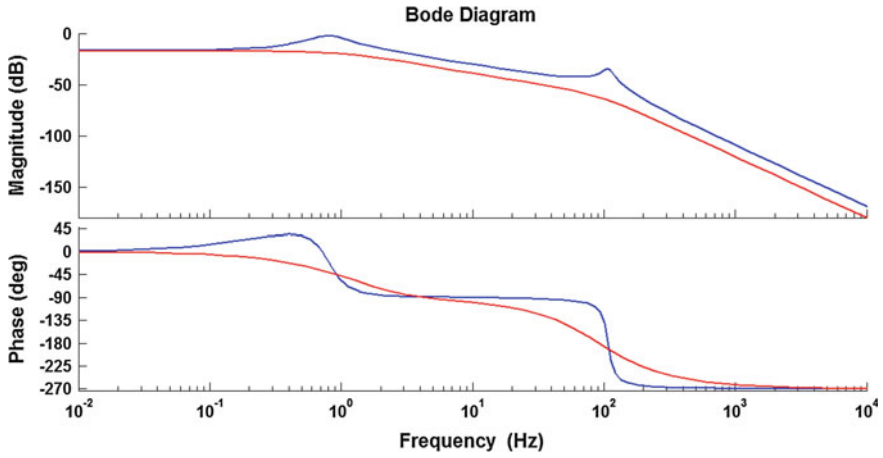


Fig. 52.3 Steering sensitivity BODE diagram

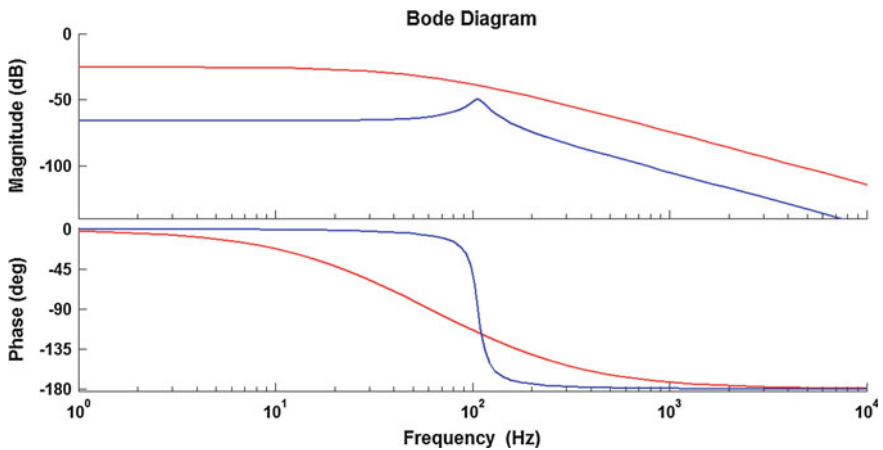


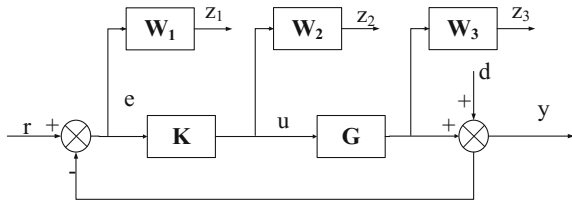
Fig. 52.4 Road feeling BODE diagram

Therefore, the design of EPS system should not only consider the steering effort, but also consider the vehicle handling stability and robustness. Based on this, the mixed sensitivity design method is adopted in this paper for algorithm design.

Figure 52.5 shows mixed sensitivity model. Weighted function W_1 , W_2 and W_3 respectively reflects the system performance requirements constraints, additive uncertainty constraints, and Multiplicative uncertainty constraints. z_1, z_2, z_3 is evaluation signal. r is input signal. e is tracking error. u is control signal. d is disturbing signal. y is output signal. K is H_∞ controller; G is controlled plant [8].

So, closed loop transfer function between r, e, u, y are

Fig. 52.5 Mixed sensitivity model



$$\begin{cases} S = (I + GK)^{-1} \\ R = K(I + GK)^{-1} = KS \\ T = GK(I + GK)^{-1} = I - S \end{cases} \quad (52.3.7)$$

$$P = \begin{bmatrix} W_1 S \\ W_2 R \\ W_3 T \end{bmatrix} \quad (52.3.8)$$

$W_1 S$, $W_2 R$ and $W_3 T$ represent requirements for performance and robustness of the system. the goal of the system design is to Achieve optimal performance Under the robust stability constraints. The mixed sensitivity problem is to find a real rational controller K , which makes the closed-loop system stable and satisfied $\|P\|_\infty < 1$.

The standard framework of Weighted mixed sensitivity problem is

$$\begin{bmatrix} z_1 \\ z_2 \\ z_3 \\ e \end{bmatrix} = \begin{bmatrix} W_1 & -W_1 G \\ 0 & W_2 \\ 0 & W_3 G \\ I & -G \end{bmatrix} \begin{bmatrix} r \\ u \end{bmatrix} = P_0 \begin{bmatrix} r \\ u \end{bmatrix} \quad (52.3.9)$$

where I is identity matrix; $P_0 = \begin{bmatrix} A_P & B_P \\ C_P & D_P \end{bmatrix}$ is Generalized controlled state matrix.

$$\begin{cases} W_1 = \begin{bmatrix} A_{W1} & B_{W1} \\ C_{W1} & D_{W1} \end{bmatrix} \\ W_2 = \begin{bmatrix} A_{W2} & B_{W2} \\ C_{W2} & D_{W2} \end{bmatrix} \\ W_3 = \begin{bmatrix} A_{W3} & B_{W3} \\ C_{W3} & D_{W3} \end{bmatrix} \end{cases} \quad (52.3.10)$$

then, A_P, B_P, C_P, D_P can be obtained:

$$\begin{aligned}
 A_P &= \begin{bmatrix} A_g & 0 & 0 & 0 \\ -B_{W1}C_g & A_{W1} & 0 & 0 \\ 0 & 0 & A_{W2} & 0 \\ B_{W3} & 0 & 0 & A_{W3} \end{bmatrix} \\
 B_P &= \begin{bmatrix} 0 & B_g \\ B_{W1} & -B_{W1}D_g \\ 0 & B_{W2} \\ 0 & B_{W3}D_g \end{bmatrix} \\
 C_P &= \begin{bmatrix} -D_{W1}C_g & C_{W1} & 0 & 0 \\ 0 & 0 & C_{W2} & 0 \\ B_{W3}C_g & 0 & 0 & C_{W3} \\ -C_g & 0 & 0 & 0 \end{bmatrix} \\
 D_P &= \begin{bmatrix} D_{W1} & -D_{W1}D_g \\ 0 & D_{W2} \\ 0 & D_{W3}D_g \\ I & D_g \end{bmatrix}
 \end{aligned}$$

According to the design goal above, two evaluation outputs are introduced.

(1) Ensure vehicle handling stability

The steering sensitivity function indicates the stability of vehicle dynamics. reducing the error of the actual yaw rate ω_r and the ideal yaw rate ω_{aimr} can make the response faster and the tracking more Accurate of the vehicle to the driver steering command, so $\|W_{\omega_r}e_{\omega_r}\|_2 = \|W_{\omega_r}(\omega_r - \omega_{aimr})\|_2$, where W_{ω_r} is weight function.

(2) Linear road feeling

To ensure the driver feel the road conditions in a certain frequency range, while avoiding the steering wheel Vibration, the road feeling is set the difference between the measurement of Torque sensor T_{det} and the resistance torque of tyre T_r , so $\|W_{e_s}e_{e_s}\|_2 = \|W_{e_s}(T_{det} - \varphi T_r)\|_2$, where φ is road feeling coefficient, W_{ω_r} is road feeling weight function.

52.4 Design Example

52.4.1 EPS Controller Design

According to the analysis above, the robust controller of the EPS system can be designed based on established mathematical model and relevant parameters. From the formula, generalized controlled plant $G_P(s)$ is obtained:

$$G'_p(s) : \begin{cases} \dot{X} = A_1 X + B_1 w + B_2 u \\ Z = C_1 X + D_{11} w + D_{12} u \\ Y = C_2 X + D_{21} w + D_{22} u \\ u = K \cdot Y \end{cases} \quad (52.4.1)$$

where $w = [T_s \quad d_{\det} \quad d_r]^T$ is reference input and disturbing signal, $Y = [e_s \quad e_{\omega_r}]^T$ is measurement output, $u = [i]$ is controlled input, $Z = [e_s \quad e_{\omega_r} \quad T_{\det} \quad \omega_r]^T$ is evaluation output, W is weighted diagonal matrix composed by W_1, W_2, W_3 .

$$A_1 = \begin{bmatrix} -\frac{B_s}{J_s} & -\frac{K_{TS}}{J_s} & 0 & \frac{K_{TS}}{J_s} & 0 & 0 \\ 1 & 0 & 0 & 0 & 0 & 0 \\ 0 & \frac{K_{TS}}{J_G} & -\frac{B_G}{J_G} & -\frac{K_G}{J_G} & \frac{2k_1 d a_f}{J_G u k_c} & \frac{2k_1 d}{J_G k_c} \\ 0 & 0 & 1 & 0 & 0 & 0 \\ 0 & \frac{2a_f k_1}{I_z k_c} & 0 & 0 & -\frac{2a_f^2 k_1 + 2b_r^2 k_2}{I_z u} & -\frac{2a_f k_1 - 2b_r k_2}{I_z} \\ 0 & \frac{2k_1}{m u k_c} & 0 & 0 & -(1 + \frac{2a_f k_1 - 2b_r k_2}{m u^2}) & -\frac{2(k_1 + k_2)}{m u} \end{bmatrix}$$

$$B_1 = \begin{bmatrix} 1/J_s & 0 & 0 & 0 & 0 & 0 \\ 1/J_s & 0 & 0 & 0 & 0 & 0 \\ 0 & 0 & -1/J_G & 0 & 0 & 0 \end{bmatrix}^T \quad B_2 = [0 \quad 0 \quad k_m K_t / J_G \quad 0 \quad 0 \quad 0]^T$$

$$C_1 = \begin{bmatrix} 0 & K_{TS} & 0 & 2\phi k_1 d / k_c - K_{TS} & 2\phi k_1 d a_f / u & 2\phi k_1 d \\ 0 & -K_{\omega_r} & 0 & 0 & 1 & 0 \\ 0 & K_{TS} & 0 & -K_{TS} & 0 & 0 \\ 0 & 0 & 0 & 0 & 0 & 1 \end{bmatrix}$$

$$C_2 = \begin{bmatrix} 0 & K_{TS} & 0 & 2\phi k_1 d / k_c - K_{TS} & 2\phi k_1 d a_f / u & 2\phi k_1 d \\ 0 & -K_{\omega_r} & 0 & 0 & 1 & 0 \end{bmatrix}$$

$$D_{11} = D_{12} = D_{21} = D_{22} = 0$$

According to the characteristics of EPS system and vehicle handling stability requirements, the weight function matrix is set:

$$W_1 = \begin{bmatrix} \frac{10}{s+0.01} & 0 \\ 0 & \frac{10}{s+0.01} \end{bmatrix}$$

$$W_2 = 0.1$$

$$W_3 = \begin{bmatrix} \frac{s+1000}{s+0.01} & 0 \\ 0 & \frac{s+1000}{s+0.01} \end{bmatrix}$$

Using MATLAB software, the EPS system controller K is solved by command $[gopt \ K] = h \text{ inf limi}(G, [m \ n])$. After reducing order of the system, the result is:

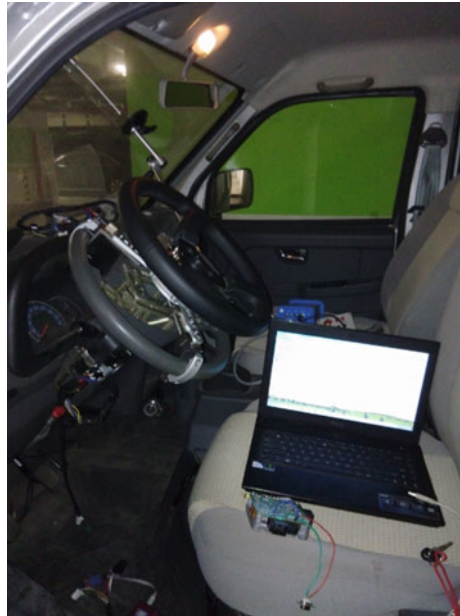
$$K(s) = \frac{238s^2 + 1843s + 9876}{s^3 + 121s^2 + 12151s + 8763}, \quad \gamma = 0.8993$$

52.4.2 Experimental Verification

In order to verify the proposed design method, vehicle handling stability test is done on a domestic minivan equipped with EPS. As shown in Fig. 52.6, the test system is including EPS controller, data acquisition system and steering torque-measuring wheel. Controller is based on Freescale MC9S12DG128, and data acquisition system is based on Vector CANoe. The step angle input experiment of steering wheel is carried out first. Keeping the vehicle speed of 30 km/h, then suddenly input positive 90 angle on the steering wheel. The output value of torque sensor is recorded and analyzed by CANoe. Then the tyre excitation experiment is carried out, keeping the vehicle speed of 30 and 0 km/h respectively, applied pseudo random excitation to the tyre and record the torque sensor output values.

Figures 52.7 and 52.8 show the response of steering wheel angle step input between legacy control strategy contrasts to the mixed sensitivity control strategy.

Fig. 52.6 Test system



The result illustrates that mixed sensitivity control strategy can decrease the overshoot, shorten the response time, and reduce the fluctuation. It means the better tracking performance, the more comfortable for driver, and effectively improvement for vehicle handling maneuverability.

Figures 52.9 and 52.10 show that after adding noise to the sensor, the result in the same test conditions. It illustrates that mixed sensitivity control strategy can effectively suppress the influence of measurement noise; ensure the driver's perception of road information accurately.

Figures 52.11 and 52.12 show responses to tyre continuous excitation input when car stops. Figures 52.13 and 52.14 show responses when car to 30 km/h through deceleration zone. It illustrates that mixed sensitivity control strategy can reduce the impact torque on the steering wheel effectively, but not to full

Fig. 52.7 Step response under legacy control

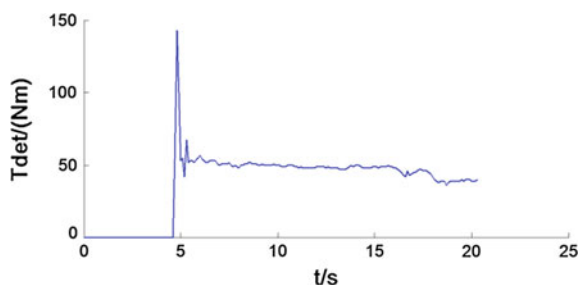


Fig. 52.8 Step response under mixed sensitivity control

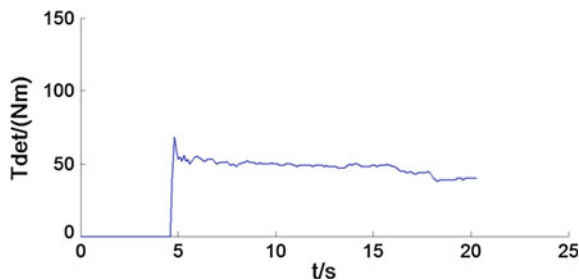


Fig. 52.9 Step response after adding noise to the sensor under legacy control

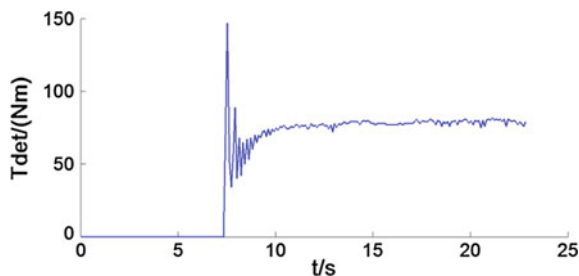


Fig. 52.10 Step response after adding noise to the sensor under mixed sensitivity control

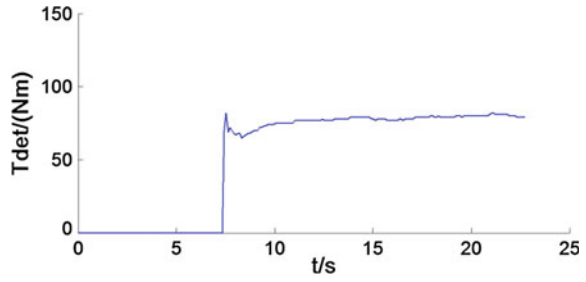


Fig. 52.11 Tyre continuous excitation response under legacy control

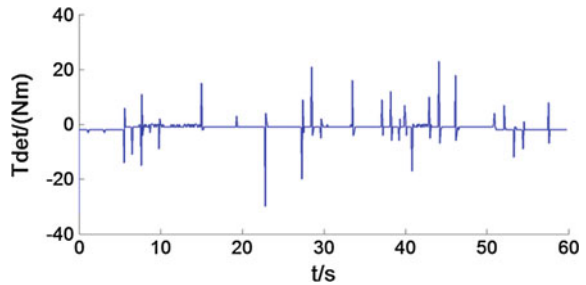


Fig. 52.12 Tyre continuous excitation response under mixed sensitivity control

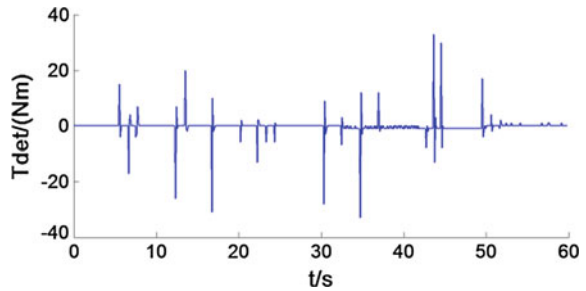


Fig. 52.13 Deceleration zone response under legacy control

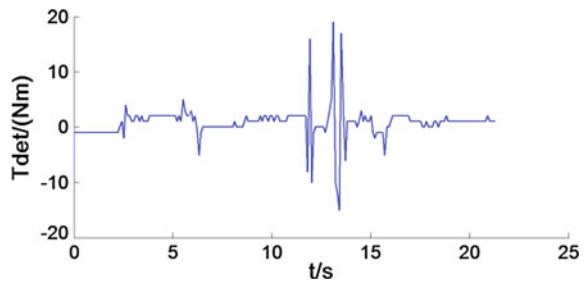
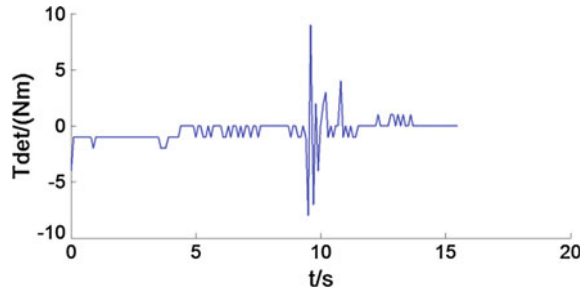


Fig. 52.14 Deceleration zone response under mixed sensitivity control



attenuation, which means the driver can feel the feedback of the road condition and not lose road feeling.

52.5 Conclusions

Aim at the problem of vehicle handling stability in EPS assistance algorithm design, the H_∞ mixed sensitivity algorithm design was put forward which could decrease the instability of control system, enhance the robust stability of EPS, improve the steering portability and handling stability sharply, keep the road sense. The evaluation index of vehicle handling stability is proposed, such as steering sensitivity and road feeling. Therefore, an abstract design objective was gained; the controller was designed based on H_∞ mixture sensitivity algorithm design. The test results indicated that:

1. It's possible to evaluate vehicle handling stability from these aspects of steering sensitivity and steering road feeling, the two aspects could reflect the vehicles' maneuverability accurately.
2. Compared with traditional current compensation controller, the controller was designed on the basis of H_∞ mixture sensitivity algorithm design, which could improve EPS and the stability of full vehicle model obviously, restrain the high frequency pumping on road and the measurement noise of sensor. It provided an effective solution for the performance of anti-jamming of EPS. To some extent, it not only improved vehicles' handling stability, but also ensured vehicles' driving safety.

References

1. Oniwa Y, Shimizu Y (2008) Evaluation method for steer assist feeling around steering center and control design on EPS. *J Mech Syst Transp Logistics* 10(1299):2063–2064
2. Parmar M, Hung JY (2004) A sensorless optimal control system for an automotive electric power assist steering system. *IEEE Trans Industr Electron* 51(2):290–298

3. Hu T-H, Yeh C-J, Ho S-R, et al (2008) Design of control logic and compensation strategy for electric power steering systems. In: IEEE vehicle power and propulsion conference, Harbin, pp 1–6
4. Tao M, Hui C, Zhuoping Y et al (2007) Study on the control strategy to improve dynamic characteristics of electric power steering and vehicle test. *Chin J Mech Eng* 18(2):235–237
5. Kohno T, Takeuchi S, Moniyama M, Nimura H (2000) Development of electric power steering system with H_∞ control. SAE Paper. No. 2000-1-0813
6. Wu W, Du Y, Ji X, et al (2004) Study on stability and disturbance resistance of electric power steering control system. *J Vib Eng* 17(2):196–200
7. Sugitani N, Fujuwara Y, Uchida K (1997) Electric power steering with H-infinity control designed to obtain road information. In: American control conference, vol 5. IEEE, pp 2935–2939
8. Li P, Yu X, Zhao B (2016) H_∞ Robust voltage control of AC-DC interface based on mixed sensitivity in AC-DC hybrid microgrid. In: Proceedings of the CSEE, vol 36, no 1, pp 0258–8013

Chapter 53

Research on Flux Weakening Speed Control Strategy for PMSM

Lei Qian, Haizhen Liu, Rui He and Weiwen Deng

Abstract Electronic assisted brake systems require permanent magnet synchronous motor (PMSM) to work in a larger speed range, and to maintain a certain ability to resist load disturbance. In this paper, the mathematical model of PMSM and the flux weakening control theory are analyzed at first. Then a control strategy is proposed based on maximum torque per ampere (MTPA) control combined with flux weakening control principle, which also takes the current compensation decoupling into account. In the MATLAB/Simulink environment, a double closed-loop model of flux weakening speed control of PMSM is presented. Finally simulation experiments prove that the control strategy can improve both the speed range of PMSM and the ability to resist load disturbance.

Keywords Electronic assisted brake · PMSM · MTPA · Flux weakening control

53.1 Introduction

With the development of new energy vehicles, many manufactures are devoting themselves to electronic assisted brake systems, which not only provide more excellent braking performance than traditional braking system, but also recycle braking energy efficiently to improve the fuel economy of vehicles. In case of an emergency, it can also realize the function of the automatic emergency braking to ensure the safety of the vehicle. However, the automatic emergency braking requires that motor speed is as high as possible, while the system nonlinear friction needs that the motor has certain ability to resist load disturbance.

Many scholars bend themselves to flux weakening speed control of PMSM to improve the speed of the motor constant power operation scope and the ability to resist load disturbance of the machine. The literature [1] proposes a sliding mode current decoupling control strategy based on an internal model, which improves the

L. Qian (✉) · H. Liu · R. He · W. Deng
State Key Laboratory of Automotive Simulation and Control, Jilin, China
e-mail: 787270986@qq.com

system dynamic performance and has good robustness. The literature [2] uses the gradient descending method to make motor running along the weak magnetic curve by real-time adjustment of weak magnetic direction, but it is difficult to achieve because of the large amount of calculation. The literature [3] adopts the negative d axis current compensation method, which adjusts d axis degaussing current size according to deviation between the d axis, q axis voltage reference value and its maximum limit. The literature [4] builds a model based on voltage feedback weak magnetic algorithm of the control system, and the simulation results verify the feasibility and effectiveness of the weak magnetic control method based on voltage feedback.

In this paper, a new control strategy is put forward based on maximum torque per ampere (MTPA) control combined with flux weakening control principle, which also takes the current compensation decoupling into account. And in the MATLAB/Simulink environment, the simulation results improve the effectiveness of the strategy.

53.2 PMSM Model and Flux Weakening Control Principle

In the d/q coordinate system, the following assumptions is proposed for the simplified model for deduction.

1. Ignoring iron core saturation.
2. Regardless of the eddy current and hysteresis losses.
3. Rotor without damping windings and permanent magnet without damping effect.
4. The three-phase winding is completely symmetrical, and the stator current and rotor magnetic field distribution is symmetrical.

Based on the above assumptions, in the d/q coordinate system, the voltage equation of PMSM is:

$$\begin{cases} u_q = R_s i_q + L_q \frac{di_q}{dt} + \omega L_d i_d + \omega \psi_f \\ u_d = R_s i_d + L_d \frac{di_d}{dt} - \omega L_q i_q \end{cases} \quad (53.1)$$

Electromagnetic torque equation is:

$$T_e = 1.5P_n [\psi_f i_q - (L_d - L_q) i_d i_q] \quad (53.2)$$

Motion equation is:

$$T_e = J \frac{d\omega_r}{dt} + B\omega_r + T_l \quad (53.3)$$

In Eqs. (53.1), (53.2), and (53.3), u_q, u_d is the q, d axis voltage of the motor. i_q, i_d is the q, d axis stator current. L_q, L_d is the q, d axis inductance. ω, ω_r is the rotor electrical angular velocity and mechanical angular velocity. R_s is the stator resistance. ψ_f is the rotor flux linkage. P_n is the magnetic poles logarithmic. T_e is the electromagnetic torque. J is the moment of inertia of the motor. B is the motor damping coefficient. T_l is the motor load torque.

For surface-mounted PMSM, Eq. (53.2) can be simplified as follows:

$$T_e = 1.5P_n\psi_f i_q \tag{53.4}$$

By DC side voltage and output current largest capacity constraints of PMSM, motor stator voltage and current have a limit value, which will affect the range of maximum speed and output torque of the motor. The flux weakening control is to reduce the induction electromotive force by weakening the air-gap flux, and make it less than the input voltage in order to expand the scope of the motor speed.

When the current maximum value is I_{max} , the current limit equation is:

$$i_d^2 + i_q^2 \leq I_{max}^2 \tag{53.5}$$

When the voltage maximum value is U_{max} , the voltage limit equation is:

$$(L_d i_d + \psi_f)^2 + (L_q i_q)^2 \leq \left(\frac{U_{max}}{\omega}\right)^2 \tag{53.6}$$

On the basis of Eqs. (53.5) and (53.6), current limit circle and voltage limit ellipse are drawn under the d/q axis coordinates as shown in Fig. 53.1.

Figure 53.1 shows that when the motor is running, stator current vector must be in the intersection of the current limit circle and voltage limit ellipse (the shadow

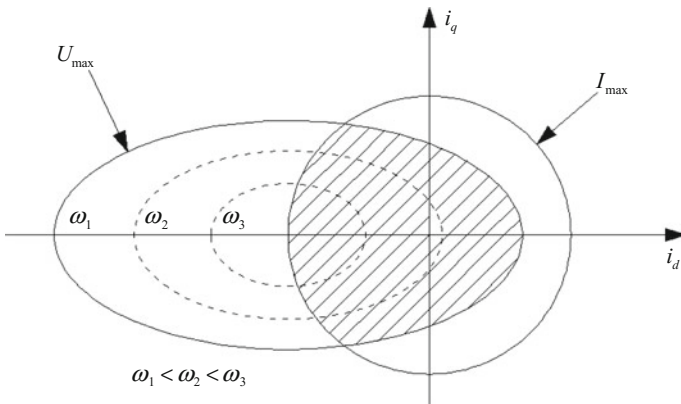


Fig. 53.1 The current limit circle and voltage limit ellipse

part of the figure). At the same time, with the increase of rotor electrical angular velocity, the voltage limit ellipse and the motor working range will decrease. Decreasing i_q or negatively increasing i_d can make the working point to keep within the shadow of the machine.

53.3 Strategy of Flux Weakening Speed Control

Taking surface-mounted PMSM as an example, a control strategy is put forward based on the current compensation decoupling and the combination of the maximum torque current ratio control and weak magnetic control. The constant torque area adopts the maximum torque current ratio control, while the constant power area carries out the flux-weakening control strategy.

When motor mechanical angular velocity is less than the base velocity, it is in the constant torque area, and the maximum torque current ratio control strategy works. In order to make the electromagnetic torque as bigger as possible under the condition of certain stator current, there will be:

$$\begin{cases} i_d = 0 \\ i_q = i_s \end{cases} \quad (53.7)$$

Equation (53.7) is the basis of maximum torque current ratio control strategy (i_s is stator current vector).

When the motor mechanical angular velocity is greater than the base velocity, it is in the constant power area, and the weak magnetic control works. Due to the constant power, there are:

$$i_q = \frac{\omega_{rt}}{\omega_r} i_s \quad (53.8)$$

$$i_d = -i_s \sqrt{1 - \left(\frac{\omega_{rt}}{\omega_r}\right)^2} \quad (53.9)$$

The flux weakening speed control strategy can be executed according to Eqs. (53.8) and (53.9).

By the voltage Eq. (53.1), it can be seen that d axis and q axis exist coupling voltage, which will increase with the rise of rotor electrical angular velocity. It will seriously affect the current loop regulation performance during the high speed range. In this paper, the current feedback is adopted to compensate current loop, which weakens the effect of rotating electromotive force and the disturbance.

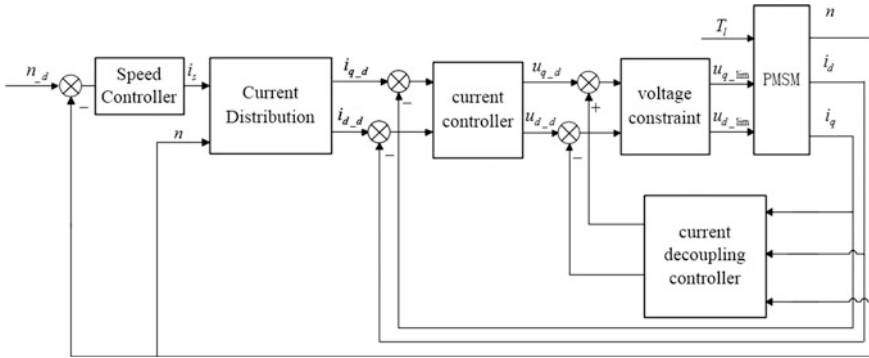


Fig. 53.2 Frame of the strategy of flux weakening speed control

$$\begin{cases} \bar{u}_q = u_q + \omega L_d i_d + \omega \psi \\ \bar{u}_d = u_d - \omega L_q i_q \end{cases} \quad (53.10)$$

Equation (53.10) can be used to current compensation decoupling.

Based on current compensation decoupling, a new control strategy is proposed which is shown in Fig. 53.2. With double closed loop control scheme, outer ring is speed loop that makes actual speed consistent with the target speed, while inner ring is current loop that plays a role on the distribution of current. Then through current decoupling controller the rotating electromotive force and the disturbance are eliminated. Finally d axis and q axis voltage are input to PMSM model by the voltage constraints module.

53.4 Simulation Experiment and Results

Based on the control frame in Fig. 53.2, the whole weak magnetic speed control is divided into the following several modules: speed controller module, current distribution module, current controller module, voltage constraints module, current decoupling controller module, PMSM module, etc. And each module is modeled in the MATLAB/Simulink environment. Below two groups of simulation experiments are done to validate that the flux weakening speed control strategy is effective.

The parameters of PMSM in the simulation experiment are shown in Fig. 53.3.

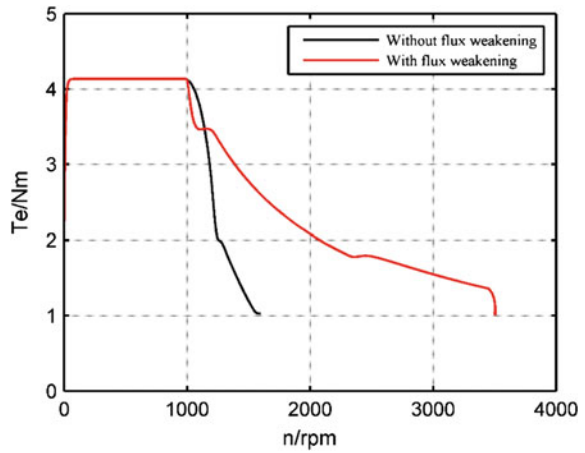
1. Simulation Experiment One

The motor starts with 1 Nm load from zero speed. The target speed is 3500 rpm. And the simulation time is set to 0.2 s. Conduct simulation experiments without flux weakening speed control strategy and with flux weakening speed control strategy in turn. The result is shown in Fig. 53.4.

Fig. 53.3 The parameters of PMSM in the simulation experiment

Motor Parameter	value
Stator Resistance (Ω)	0.0085
q/d Axis Inductance (mH)	0.00017
Magnetic Poles logarithmic	4
Rotor Flux Linkage (Wb)	0.00875
Rated Torque(Nm)	4.2
Rated Speed (rpm)	1000
Rated Current (A)	80
DC Bus Voltage (V)	12
Moment of Inertia ($\text{kg}\cdot\text{m}^2$)	1×10^{-4}

Fig. 53.4 Torque and speed characteristic curve of PMSM



In Fig. 53.4, the black curve is the torque and speed characteristic curve without flux weakening speed control strategy, while the red curve is with flux weakening speed control strategy. Comparing the two curves, it can be found that the working speed range is extended after adding flux weakening speed control strategy.

2. Simulation Experiment Two

The motor speed starts with no-load from zero speed. A given motor target speed is 2000 rpm. A 1 NM load is applied on the motor suddenly at 0.1 s. And the simulation time is set to 0.2 s. Conduct simulation experiments with flux weakening speed control strategy. The result is shown in Figs. 53.5, 53.6 and 53.7.

In Fig. 53.5, the time that motor starts to achieve speed 2000 rpm is about 10 ms. And in the high speed with no load, it is running smoothly and less volatile. When a 1 NM load is applied on the motor suddenly at 0.1 s, motor speed

Fig. 53.5 Speed curve of PMSM with flux weakening speed control strategy

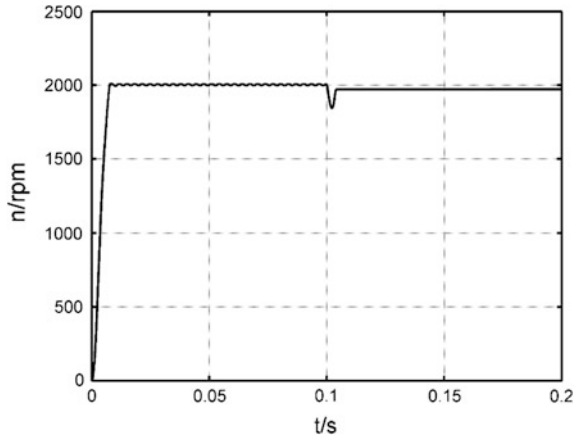
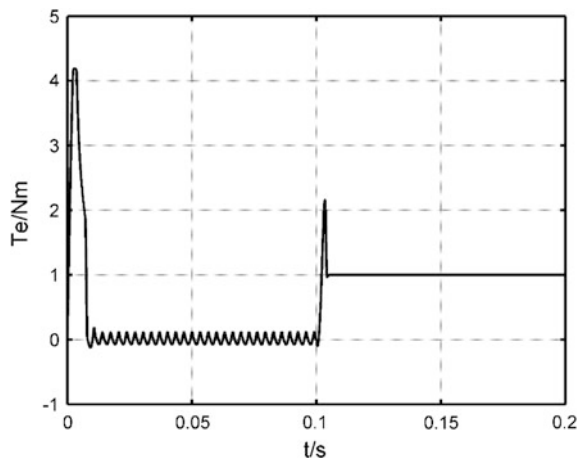


Fig. 53.6 Torque curve of PMSM with flux weakening speed control strategy

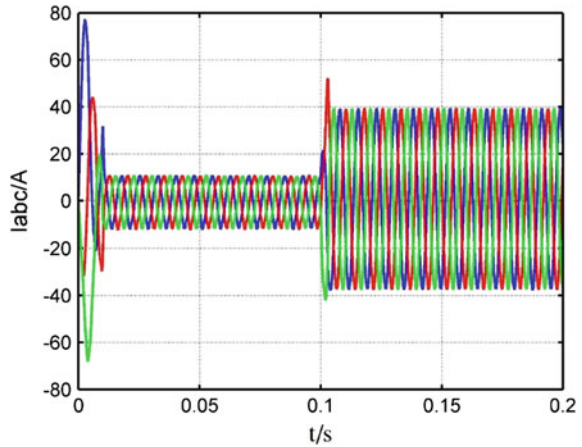


decreases slightly. But within 5 ms it is back to about 2000 rpm and motor keeps steady state. It proves that the motor has a good ability to resist the torque disturbance in high speed range.

As shown in Fig. 53.6, electromagnetic torque increases to a maximum first for making motor to approach the target speed faster, and then keep stable around 0. When a 1 NM load is applied at 0.1 s, the motor rapidly promotes electromagnetic torque to 1 NM or so.

In Fig. 53.7, three phase stator current can be separated clearly in the three different stages: motor start, weak magnetic with no load, weak magnetic with load. And the waveform of each stage is good.

Fig. 53.7 Three phase stator current curve of PMSM with flux weakening speed control strategy



53.5 Conclusions

In this paper, a control strategy is proposed based on maximum torque per ampere control combined with flux weakening control principle, which also takes the current compensation decoupling into account. Then in the MATLAB/Simulink environment, a PMSM model with flux weakening speed control strategy is established. Simulation experiments show that the control strategy is simple, reliable and good robustness, which can improve the speed range of permanent magnet synchronous motor and the ability to resist load disturbance.

References

1. Zhou H, Zhou X, Zhao F, Zhang J (2012) Decoupled current control of permanent magnet synchronous motors drives with sliding mode control strategy based on internal model. Proc CSEE 15:91–99+10
2. Sheng Y, Yu S, Gui W, Hong Z (2010) Field weakening operation control strategies of permanent magnet synchronous motor for railway vehicles. Proc CSEE 09:74–79
3. Wang A, Jia X, Dong S (2012) Flux-weakening control for interior permanent magnet synchronous motor considering voltage saturation. J North China Electric Power Univ 05:17–21
4. Ma C (2014) Research on field-weakening control methods of permanent magnet synchronous motor. Chang'an University

Chapter 54

A Study of Three-Way Catalyst Deterioration Monitoring

Song Yan, Tonghao Song and Tingwei Liu

Abstract To meet the demand for Euro 6 regulations, a three-way catalyst (TWC) oxygen storage model and diagnosis algorithm are designed to detect the TWC deterioration. Oscillations are produced based on oxygen storage measurement, and then catalyst performance is evaluated based on catalyst oxygen storage states which are obtained by analyzing rear lambda signal. The algorithm is verified on the bench and the vehicle, and can meet the catalyst monitoring requirements of the EU 6 regulations.

Keywords Three-way catalyst (TWC) · Deterioration · Monitoring · Oxygen storage capability (OSC)

54.1 Introduction

As environment pollution has aggravated due to the development of industry, the emission standards are becoming stricter worldwide. Table 54.1 shows a comparison of the emission limits for vehicles of categories M between the Euro emission standards and the EOBD regulations.

The most common aftertreatment device for gasoline engines nowadays is the three-way catalytic converter (TWC). It is able to reduce the HC, CO, and NO_x emissions significantly. However, the efficiency of these reactions significantly decreases with the ageing of the TWC. Under Euro V and Euro VI standards, a TWC fault must be reported when the emission limit of NO_x or HC is exceeded due to the deterioration of TWC.

There are many factors that influence the conversion efficiency of TWC, such as λ , catalyst temperature, and exhaust gas velocity [2]. Figure 54.1 shows the conversion efficiencies of NO_x, HC, and CO as a function of λ . As can be seen, only when λ within a very narrow range around the stoichiometric ratio, all the

S. Yan (✉) · T. Song · T. Liu
China FAW Corporation Limited R&D Center, Changchun, China
e-mail: yansong@rdc.faw.com.cn

Table 54.1 Limits according to the European emission standards and EOBD regulations [1]

	CO (mg/km)	THC (mg/km)	NMHC (mg/km)	NO _x (mg/km)	PM (mg/km)	PN (Nb/km)
Euro 5b	1000	100	68	60	4.5	–
EU5 + EOBD	1900	–	250	300	50	–
Euro 6	1000	100	68	60	4.5	6.0 * E11
EU6 EOBD	1800	–	170	90	12	–

three components can be reduced by more than 90%. Figure 54.2 shows the effect of catalyst temperature on the conversion efficiencies. To keep high conversion efficiencies, the temperature of TWC should be located in the range between about 500 °C and thermal deterioration temperature. The exhaust gas velocity also affects the conversion efficiency of TWC, because the gas flow speed determines the duration of the gas stay in TWC. The lower exhaust gas velocity, the longer time exhaust gas stay in TWC, and the higher conversion efficiency of NO_x, HC, and CO.

The main causes of the conversion efficiency decrease are thermal deterioration, substrate meltdown, physical damage and poisoning. It is difficult to distinguish among all those failures causes. Fortunately, some researches have shown that the OSC (Oxygen Storage Capacity) of TWC has a close relationship with the emission conversion efficiency [3, 4]. Engineers usually use indirect method, such as a method based on catalyst temperature and a method based on catalyst OSC, to detect the failure of TWC [5, 6]. For cost reason, the second mentioned method is

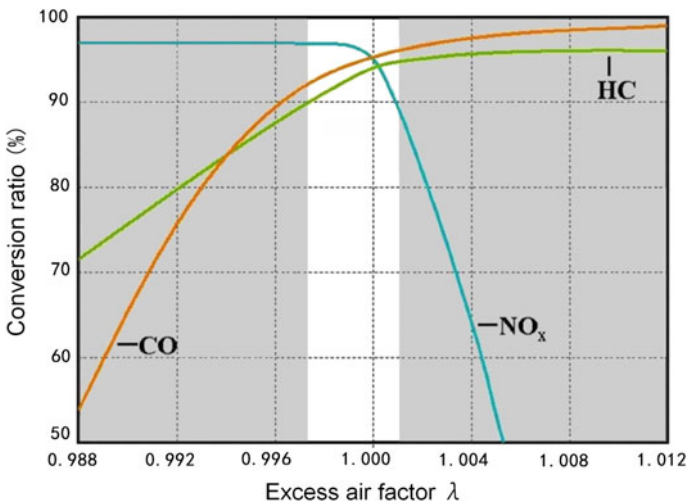
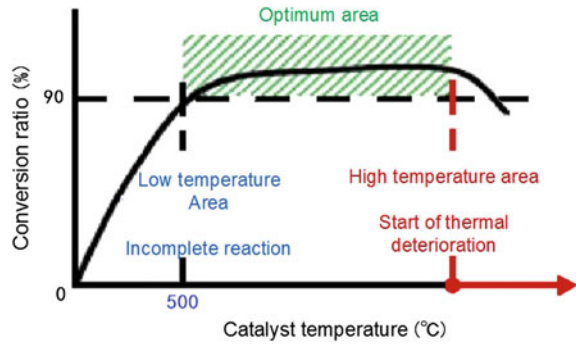


Fig. 54.1 The relationship between catalyst conversion efficiency and oxygen storage capacity

Fig. 54.2 The relationship between catalyst conversion efficiency and catalyst temperature



used most commonly, which can be categorized into passive way and active way according to whether λ is interfered. The passive approach contains step counting method, amplitude ratio method and signal modeling method etc. The active approach contains sensor-/controller switch method and circuit-entering of rich-/lean-steps method etc.

In this paper, an active method including four steps is developed. At first, the OSC of boardline catalyst is measured; Secondly, the amplitude of post-catalyst oxygen sensor signal is measured under certain oxygen load with boardline catalyst installed, which is regarded as a reference signal; In the third step, also the amplitude of rear oxygen signal is measured, but under certain oxygen load with an in-use catalyst installed which need to be monitored; Finally, those two amplitude values are compared each other to determine whether to report a final catalyst failure. This active method is different from other OSC based methods mentioned above.

54.2 Project Target and Scheme

In order to meet the OBD limitations of the Euro VI regulation, the eigenvalues of fault diagnosis, which is used to distinguish between aged catalysts and boardline catalysts, should meet the following requirements: $\varphi_{\mu+6\sigma} < \theta_{\mu-6\sigma}$, where $\theta_{\mu-6\sigma}$ represents the lower bound of the boardline catalyst deterioration factor statistics, and $\varphi_{\mu+6\sigma}$ represents the upper bound of the aged catalyst deterioration factor statistics, μ is the average of statistics, and σ is the standard deviation of statistics.

54.3 Oxygen Storage Model of TWC

54.3.1 Boundary Conditions

Since the limited effect on OSC measurement, the time that the exhaust gas spend to passes through TWC and the reaction time of the pre-catalyst and post- catalyst oxygen sensors are ignored.

54.3.2 Formula of TWC Oxygen Storage Capacity

The amount of oxygen that flow into TWC can be deduced according to the following steps:

$$\lambda_f = \frac{\dot{m}_{\text{air}}}{\dot{m}_{\text{airref}}} = \frac{\dot{m}_{\text{air}} \times 23\%}{\dot{m}_{\text{airref}} \times 23\%} = \frac{\dot{m}_{\text{O}_2}}{\dot{m}_{\text{O}_2\text{ref}}} \quad (54.1)$$

where λ_f is the air/fuel ratio from the oxygen sensor upstream of TWC; \dot{m}_{air} is the actual intake air mass flow; \dot{m}_{airref} is the intake air mass flow that is needed to get perfect combustion; \dot{m}_{O_2} is the actual intake oxygen mass flow; and $\dot{m}_{\text{O}_2\text{ref}}$ is the oxygen mass flow desired.

Such that:

$$\dot{m}_{\text{O}_2\text{ref}} = \frac{\dot{m}_{\text{O}_2}}{\lambda_f} \quad (54.2)$$

Then the difference between the actual oxygen mass flow and the desired oxygen mass flow can be denoted as:

$$\dot{m}_{\text{O}_2} - \dot{m}_{\text{O}_2\text{ref}} = \left(1 - \frac{1}{\lambda_f}\right) \dot{m}_{\text{O}_2} = \left(1 - \frac{1}{\lambda_f}\right) \dot{m}_{\text{air}} \times 23\% \quad (54.3)$$

The oxygen mass flow is a value not smaller than 0, so the formula (54.3) should be rewritten as:

$$\dot{m}_{\text{O}_2} - \dot{m}_{\text{O}_2\text{ref}} = \left(1 - \frac{1}{\text{fun}(\lambda_f)}\right) \dot{m}_{\text{air}} \times 23\% \quad (54.4)$$

$$\text{and fun}(x) = \begin{cases} 1 & x < 1 \\ x & x \geq 1 \end{cases}$$

The oxygen mass that flow into TWC can be denoted as:

$$m_{O_2f} = 0.23 \int_0^t \left(1 - \frac{1}{\text{fun}(\lambda_f)} \right) \dot{m}_{\text{air}} dt \tag{54.5}$$

Similarly, the oxygen mass that flow out TWC can be denoted as:

$$m_{O_2r} = 0.23 \int_0^t \left(1 - \frac{1}{\text{fun}(\lambda_r)} \right) \dot{m}_{\text{air}} dt \tag{54.6}$$

where λ_r is the air/fuel ratio from the oxygen sensor downstream of TWC.

The oxygen mass that is stored in TWC can be denoted as:

$$m_{O_2s} = m_{O_2f} - m_{O_2r} = 0.23 \int_0^t \left(\frac{1}{\text{fun}(\lambda_r)} - \frac{1}{\text{fun}(\lambda_f)} \right) \dot{m}_{\text{air}} dt \tag{54.7}$$

There are several restrictions for formula (54.7) to be applied, the reasons are:

1. The delay caused by gas flow is not considered.
2. The delay caused by oxygen sensor response is not considered.
3. Every signal from sensor contains signal error, and it causes accumulative error.
4. For physical reason, the upper limit of m_{O_2s} is the OSC of the TWC, and the lower limit of m_{O_2s} is zero.

In addition, linear oxygen sensor is located upstream of TWC, but usually two-point oxygen sensor is located downstream of TWC. Based on the two oxygen sensors, an OSC measurement process is designed as shown in Fig. 54.3, the steps are:

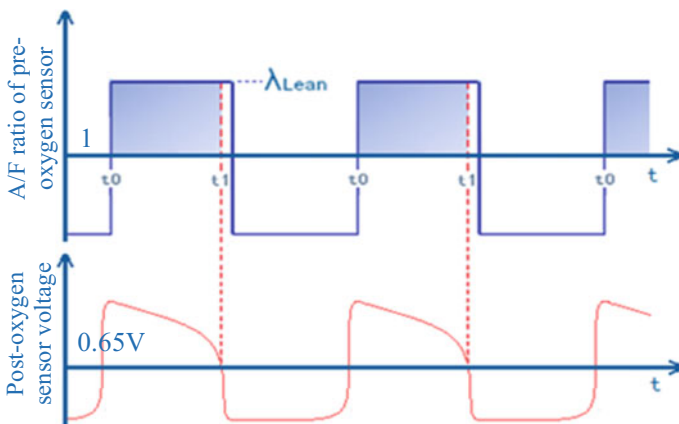


Fig. 54.3 Test process of OSC

1. Setting the lambda setpoint to rich side to clean the oxygen stored in the TWC.
2. The voltage from the downstream oxygen sensor go to high state at time t_0 means the oxygen in the TWC is cleared.
3. Setting the lambda setpoint to lean side at time t_0 to get oxygen to flow into the TWC.
4. The voltage from the downstream oxygen sensor converts to low state at time t_1 means the TWC is saturated and cannot store more oxygen.
5. According to formula (54.7), the OSC can be calculated with the following formula:

$$OSC = 0.23 \int_{t_0}^{t_1} \left(1 - \frac{1}{\lambda_f} \right) \dot{m}_{air} dt.$$

54.4 Verification and Improvement

The test has been performed on a three-cylinder gasoline engine. This engine is equipped with a linear oxygen sensor upstream of the TWC and a two-point oxygen sensor downstream of the TWC. The CANape and Matlab software tools are used to acquire and analyze the ECU data.

54.4.1 The OSC Measurement Result

OSC of substrate, boardline catalyst, aged catalyst and fresh catalyst are measured. The OSC distribution of each catalyst is shown in Fig. 54.4, and the x-axis is the internal temperature of catalyst during OSC measurement.

When catalyst temperature above 450 °C, the OSC of each catalyst meet the following inequality which indicates TWC deterioration level.

$$OSC_{\text{substrate}} < OSC_{\text{boardline}} < OSC_{\text{aged}} < OSC_{\text{fresh}}$$

The lower catalyst temperature, the smaller the difference between boardline catalyst OSC and substrate OSC, when catalyst temperature blows 450 °C. It implies that the TWC light-off temperature is about 450 °C.

But the standard deviation of each catalyst OSC sampling data is too high to distinguish a failure catalyst from other catalysts with the “6σ” confidence interval.

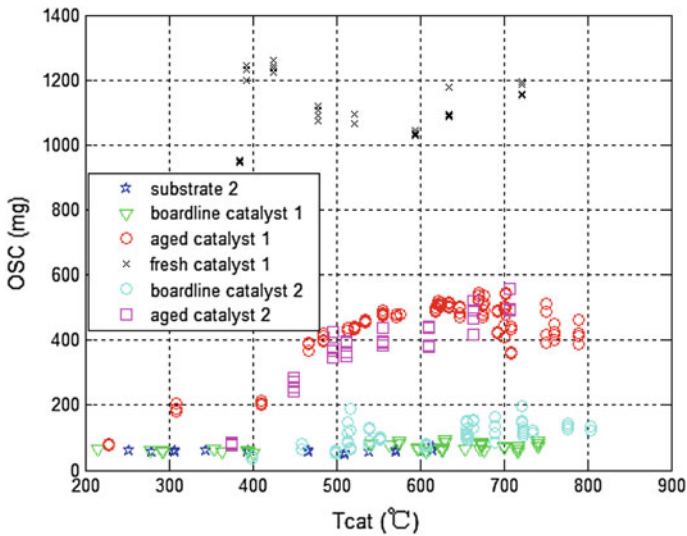
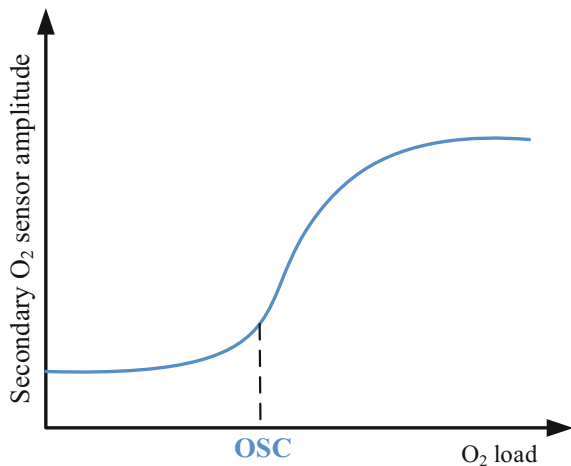


Fig. 54.4 Relationship between OSC and temperature

54.4.2 Diagnosis Algorithm Improvement

In order to distinguish between the boardline and aged catalyst more accurately, the nonlinearity, as shown in Fig. 54.5, between the amplitude of the downstream oxygen sensor voltage and the oxygen load, is taken into account in the proposed diagnosis algorithm. The oxygen load of a catalyst equals the oxygen mass flowing into the catalyst during an air/fuel ratio oscillation period in the engine working process.

Fig. 54.5 The nonlinearity between the amplitude of the secondary oxygen sensor and the O₂ load



When oxygen load is less than OSC, the oxygen that flows into catalyst can be stored completely. The amplitude of downstream oxygen sensor voltage grows slowly with the increase of oxygen load.

When oxygen load is larger than OSC, the oxygen that cannot be stored will flow out of catalyst. The amplitude of downstream oxygen sensor voltage grows quickly with the increase of the oxygen load.

Based on the OSC measurement and the nonlinearity mentioned above, a TWC can be monitored as following:

1. Install a boardline catalyst on a vehicle, and use the steps mentioned in Sect. 54.3.2 to measure the boardline catalyst OSC at several defined operation points.
2. Find the maximum value of the OSC sampling data measured in step 1, and label it as $O_2 \text{ Load}_{\text{set}}$.
3. At the same defined operation points, set the oxygen load to $O_2 \text{ Load}_{\text{set}}$, and save the amplitude of downstream oxygen sensor signal at each operation point as reference value map.
4. Install an in-use catalyst on a vehicle. Set the oxygen load to $O_2 \text{ Load}_{\text{set}}$ when monitoring, and get the amplitude of downstream oxygen sensor signal.
5. Divide the amplitude by reference value from the reference value map to get the deterioration factor sampling data of the in-use catalyst.

The reference value mentioned above is to reduce the effect of engine operation points on deterioration factor sampling data.

54.4.3 Diagnosis Algorithm Verification

On a vehicle equipped with a 1.0L turbo charged gasoline engine, set the oxygen load equal to 100 mg, and set the reference value equal to a constant of 0.0035, then the deterioration factor sampling data of an Euro VI standard boardline catalyst and an Euro VI standard aged catalyst at several engine operation points are obtained, which is shown in Fig. 54.6 and Table 54.2.

For the aged catalyst: $\varphi_{\mu+6\sigma} = 1.3603 + 6 \times 0.6827 = 5.4565$;

For the boardline catalyst: $\theta_{\mu-6\sigma} = 13.6013 - 6 \times 0.6584 = 9.6509$;

$\varphi_{\mu+6\sigma} < \theta_{\mu-6\sigma}$ means that the new diagnostic strategy can distinguish fault catalyst from aged catalyst, and the gap between $\varphi_{\mu+6\sigma}$ and $\theta_{\mu-6\sigma}$ provides the necessary security space for the practical application of the strategy.

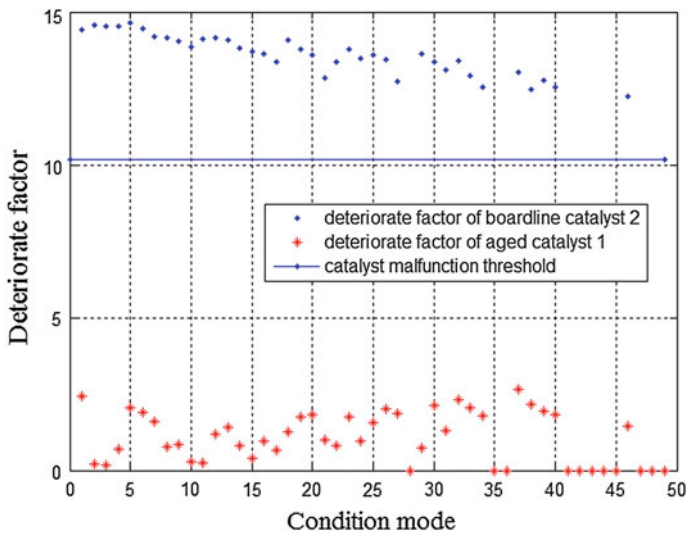


Fig. 54.6 The catalyst deterioration factor statistics of boardline and aged catalytic

Table 54.2 The statistics of the aged and boardline catalyst deterioration factors

		Engine speed (RPM)						
		1200	1600	2000	2400	2800	3200	4000
Aged catalyst: average $\mu = 1.3603$ variance $\sigma = 0.6827$								
Mass flow (mg/cyl)	100	2.44	0.21	0.17	0.7	2.06	1.88	1.6
	150	0.78	0.85	0.3	0.25	1.19	1.4	0.79
	200	0.41	0.96	0.64	1.26	1.74	1.83	1.01
	250	0.82	1.75	0.94	1.55	2.01	1.85	
	300	0.74	2.13	1.28	2.33	2.06	1.77	
	350		2.64	2.15	1.92	1.82		
	400				1.46			
Boardline catalyst: average $\mu = 13.6013$ variance $\sigma = 0.6584$								
Mass flow (mg/cyl)	100	14.41	14.55	14.54	14.52	14.65	14.47	14.2
	150	14.17	14.04	13.84	14.13	14.14	14.08	13.81
	200	13.72	13.61	13.38	14.09	13.78	13.6	12.82
	250	13.37	13.76	13.46	13.6	13.44	12.72	
	300	13.61	13.35	13.11	13.4	12.91	12.55	
	350		13.04	12.47	12.76	12.53		
	400				12.22			

54.5 Conclusion

1. Using the approach designed in this paper, the OSC values of several TWCs are measured. The OSC values of each TWC meet the following inequality:

$$\text{OSC substrate} < \text{OSC boardline} < \text{OSC aged} < \text{OSC fresh}$$

This means that the OSC value of a catalyst has relevance to its deterioration.

2. The 6σ probability distribution of boardline catalyst OSC and aged catalyst OSC are overlapped. This means that it is not precise to separate fault catalysts from good catalysts according to OSC value.
3. A new diagnostic strategy, determining a TWC fault according to the amplitude of downstream oxygen sensor signal when the TWC work under certain oxygen load, is proposed. The experiment result shows that the new diagnostic strategy can distinguish boardline catalysts from aged catalysts and can be taken into application to meet requirements of the EU 6 regulations.

References

1. European Commission (2008) Commission regulation (EC) No 692/2008 of 18 July 2008 implementing and amending regulation (EC) No 715/2007 of the European Parliament and of the council on type-approval of motor vehicles with respect to emissions from light passenger and commercial vehicles (Euro 5 and Euro 6) and on access to vehicle repair and maintenance information. *Off J Eur Commun* 1–136
2. Wang A (2006) A study of the TWC conversion efficiency temperature monitoring model based on the chemical kinetics. Chang'an University, Xi'an
3. Hepburn JS, Gandhi HS (1992) The relationship between catalyst hydrocarbon conversion efficiency and oxygen storage capacity (No. 920831). SAE Technical Paper
4. Theis JR (2011) An engine test to measure the oxygen storage capacity of a catalyst. *Spinal Cord* 49(4):493–501
5. Muske KR, Jones JCP (2004) Estimating the oxygen storage level of a three-way automotive catalyst, vol 5, pp 4060–4065
6. Auckenthaler TS, Onder CH, Geering HP (2004) Online estimation of the oxygen storage level of a three-way catalyst. SAE SP-1822: Electronic Engine Controls 2004, 167–176

Chapter 55

Functional Safety System Design on EPS

Zhihong Wu, Xiezu Su, Yuan Zhu and Luke

Abstract This paper aims to present the safety design and analysis method complied with ISO 26262 based on EPS (Electric Power Steering) application. There are six sections included in this paper. At the first section, it introduces the functional safety basic idea for risk reduction and the work principle of pinion-EPS. Then the hazard analysis and risk assessment of EPS system is carried out which is significant for the concept stage of functional safety. With HARA (Hazard Analysis and Risk Assessment) result, safety goal and safety requirement are derived, and also the safety mechanism is designed. To verify the plausibility of safety mechanism design, a failure analysis is conducted to perform as evidence for safety case report. The failure analysis is finished by means of FMEDA and PMHF. And as innovative part of this paper, a Markov model for safety path is created and the qualitative analysis is applied. Last but not the least, a conclusion of the paper is finished on the sixth section.

Keywords Functional safety · Safety concept · Safety analysis · Markov method · EPS

Z. Wu · X. Su (✉)
School of Automotive Engineering, Tongji University, Shanghai, China
e-mail: suxiezu@126.com

Z. Wu
e-mail: zhihong.wu@tongji.edu.cn

Z. Wu · Y. Zhu · Luke
Sino-German School for Postgraduate Studies, Tongji University, Shanghai, China
e-mail: yuan.zhu@tongji.edu.cn

Luke
e-mail: luke@tongji.edu.cn

55.1 Introduction for EPS System & Functional Safety

Functional safety related with ISO 26262 in automotive is a hot topic for researchers these days. Some papers focus on ASIL decomposition algorithm investigation [1–3]. These three papers translate ASIL allocation and decomposition task to different mathematical models which make the components ASIL allocation automatically. Paper [4] presents the hazard analysis techniques which is very important for concept stage. Paper [5] covers the safety case report from customer points of view. Paper [6] writes about safety mechanism which is critical for functional safety. However, all these papers either describe functional safety in a theoretical way or just offer partial solution for functional safety. This paper tries to present the complete methodology for functional safety based on electrical power steering application which makes the reader understand the standard much easier.

Electric power steering is a typical critical safety item for vehicle. The functional safety requirement for EPS is originally from car maker. To initialize the lifecycle of functional safety development, the system function should be known. For EPS system, the driver firstly input the steering command from the steering wheel and this input is captured by the torque sensor which will feed the signal into MCU (Micro Control Unit). Besides, other system related signals such as wheel steering angle, vehicle speed, environmental temperature and battery voltage are also feed into MCU. The software’s main functional tasks are calculating the motor output torque and motor control regulation. The torque is calculated based on kinds of sensor signals as stated before, road condition and related steering strategies. This calculated motor torque is the reference input of motor vector control regulation with FOC algorithm. And finally the torque output by the motor will force the steering system to work correctly. Figure 55.1a shows the hardware architecture of two pinions EPS system.

The target for functional safety is about to reducing the risk of harm by kinds of failure to a safe level. As Fig. 55.1b shows, there are residual risk, tolerable risk and inherent process risk. The safe level of risk is to reducing the harm risk to tolerable level. The so called residual risk is the risk that no safety mechanism covers. The

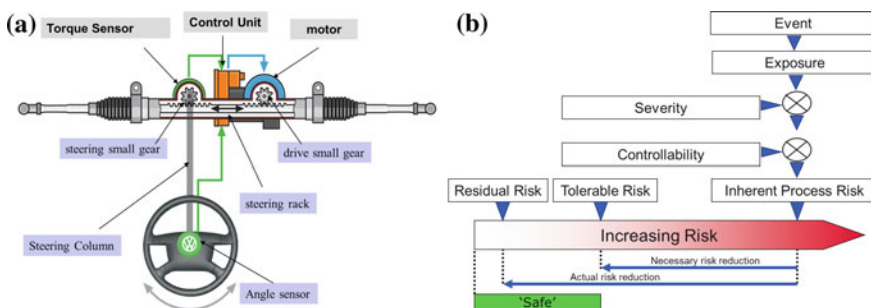


Fig. 55.1 a P-EPS hardware architecture b Risk reduction for ISO 26262

inherent process risk is brought by events that happen in specific scenario and it is necessary to be reduced by safety mechanism. According to safety requirement, the risk reduction by safety measures (actual risk reduction) should be more than the risk that the hazard brought in (necessary risk reduction). The risk level is evaluated in the HARA phase which will be detailed in the next section.

Since ISO 26262 only deals with electric and electronic system, the EPS E/E system is presented as Fig. 55.2. This item contains elements like sensors, safety power supply, safety MCU, safety driver, MOSFET B6, load switch and anti-polarity circuit, phase separation unit and also CAN bus network. Since the malfunctions of the item will be allocated into the elements failure modes in the FMEDA report, then each element’s failure modes should be carefully checked and classified.

Functional safety is not only about product design but also goes through all the production procedures. The lifecycle of functional safety is involved in the implementation of safety-related systems and it starts at the concept phase of a project and finishes when all of the E/E/PE safety-related systems and other risk reduction measures are no longer available for use [8–10].

Noted from the functional safety life cycle block diagram as showed in Fig. 55.3a [1], the concept phase is the starting stage of the lifecycle which contains item definition, initialization of safety lifecycle, HARA and functional safety concept. Among the four parts of the concept phase, HARA is the most important one. One work product for HARA is deriving safety goals which are important inputs for functional safety concept.

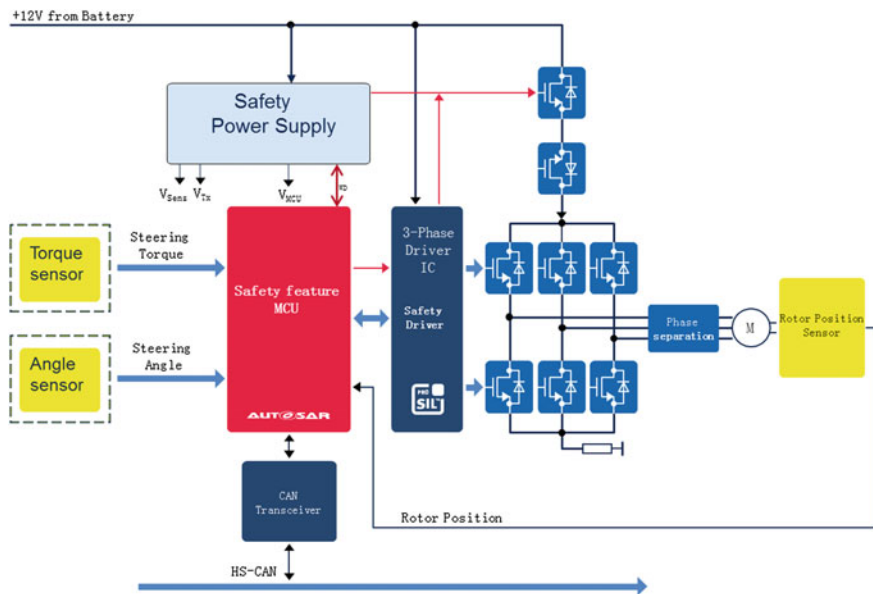


Fig. 55.2 PMSM EPS topology

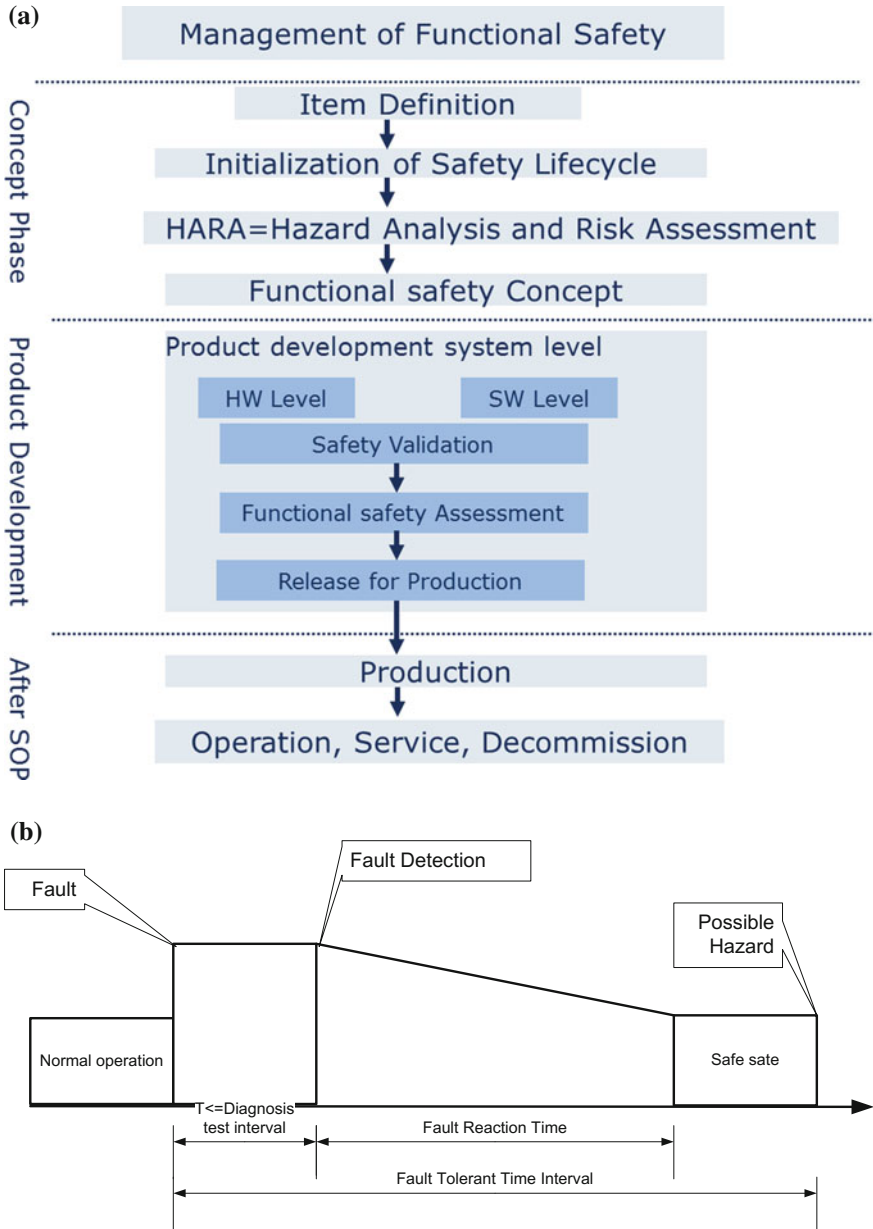


Fig. 55.3 a Functional safety life cycle b FTI block diagram

55.2 Hazard Analysis and Risk Assessment

The main task of HARA is classifying hazard which caused by malfunction of the item into different risk levels based on the severity of hazard (S), the exposure probability (E) and the controllability to avoid the harm (C). The combination of ‘SEC’ will result in five different hazard levels as QM, ASIL A, ASIL B, ASIL C and ASIL D. Each hazard will be assigned a SG (Safety Goal) and the SG shares the same ASIL rating as hazard. The safety goal is the top safety requirement of the system, and is realized by the combination of correct function and properly safety mechanism. The ASIL rating is directly related with the developing complexity and developing resources. Generally speaking, the ASIL C and ASIL D level demands considerable more resources than ASIL B and ASIL A. Thus, over rating of the ASIL level is not recommended for cost and technique reasons.

As for EPS application, the HARA result is briefly introduced as Table 55.1. The complete HARA contains more content than this table. Here the ASIL allocation part is kept and presented. Take the malfunction of ‘blocked steering’ for instance, if it happened the steering would not available. And this hazard may cause the vehicle be collided which will cause serious injure even death, so ‘S3’ is assigned. This hazard could happen at all driving situation, thus the probability of the hazard is high which means ‘E4’. Last but not least, the vehicle could not be controlled if the hazard happened. Thus, ‘C3’ is allocated to this hazard. According to ISO 26262, the combination of S3, E4 and C3 makes the item ASIL level to be D. Other malfunction can be analyzed similarly. As Table 55.1 shows, the final item ASIL rating follows up the highest one, which is ASIL D.

Table 55.1 Hazard analysis and risk assessment for EPS application

Malfunction	Hazard	S	E	C	‘SEC’ comment	ASIL
Erratic EPS	Turning not accurate	S2	E4	C2	Steering possible but need high skill; it can happen at all driving situation; drivers have to react fast to adapt to new steering performance.	B
Sudden EPS loss	Turning mechanically	S0	E4	C1	Vehicle can be controlled	QM
Sudden EPS reactivation	Turning assist normally	S0	E4	C1	Vehicle can be controlled	QM
Self steering	Turning automatically	S3	E4	C3	Steering impossible will cause serious injure; it can happen at all driving situation; impossible to control the vehicle	D
Blocked steering	Turning impossible	S3	E4	C3	Steering impossible will cause serious injure; it can happen at all driving situation; impossible to control the vehicle	D

Table 55.2 Safety goal on EPS application level

ID	Safety goals	ASIL	Safety state
APP-SG-01	Self-steering less than 20 ms	ASIL D	Switch and keep off min. 5 FETs
APP-SG-02	Blocked steering less than 100 ms	ASIL D	Switch and keep off min. 5 FETs
APP-SG-03	Erratic support of steering assist less than 100 ms	ASIL B	Switch and keep off min. 5 FETs
APP-SG-04	Sudden loss of steering assist	QM	Switch and keep off min. 5 FETs
APP-SG-05	Sudden reactivation of steering assist	QM	Switch and keep off min. 5 FETs

Table 55.3 Safety requirement on MOSFET driver [7]

ID	Functional safety requirement	ASIL	Corresponding SG
DR-SR-01	Two or more FETs unintended 'on' less than 100 ms	ASIL D	APP-SG-02
DR-SR-02	Protect μC against destruction when driver IC damaged	ASIL D	Not derived from SG
DR-SR-03	Undetected wrong current measurement (>20%)	ASIL B	APP-SG-03
DR-SR-04	Protect driver against destruction when μC damaged	ASIL D	Not derived from SG
DR-SR-05	Unwanted activation of phase separation	QM	APP-SG-04

55.3 Safety Goal and Safety Requirement

As stated above, safety goals are derived from hazard analysis and risk assessment. Corresponding to the hazard analysis and risk assessment, the safety goal is listed as Table 55.2. One of the important parameters that matters a lot in the product development is the FTTI (fault tolerant time interval) as Fig. 55.2b shows. FTTI means that a time slot starts at fault happens and ends at possible hazard starts. For functional safety, the system should have entered into safety state within FTTI. FTTI is usually acquired by theory calculation on vehicle model and practical vehicle test, especially road test. Normally, it is offered by OEM. This system parameter can be independently pointed out or be integrated into safety goals. In this paper, the latter method is chosen. Different OEMs or Tiers may describe their safety goals differently, but the meaning behind the word should be the same.

Safety requirements are derived from safety goals. Different elements may have different safety requirements for certain safety goals. In other words, some elements' failure may not result in the violation of certain safety goals while some ones may result in safety goals violation. Take EPS MOSFET driver for example, the functional safety requirements are list as Table 55.3. Most safety requirements are allocated to related elements by FTA (fault tree analysis) method. Safety goal is

the reverse of the top event of fault tree, while safety requirements for each element are reverses of bottom events of fault tree. The fault tree number is as the same as safety goals number. Each safety goal has its fault tree respectively.

55.4 Safety Concept

Safety concept is the theory, method and technology that make the system enter into safety state or avoid the hazard happen. Safety state means that no hazard will happen. The hazard if happened would violate the safety goals, thus the system should enter into safety state for functional safety purpose. For EPS application, the safety state for all safety goals is switching off the motor current which means shutting down the inverter or enabling the phase cutting off unit. Safety mechanism is part of safety concept which implements the safety requirement. By safety mechanism, the risk of hazard will be reduced to acceptably low.

There are three key elements in EPS E&E system as power supply, micro-controller and MOSFET driver (also called pre-driver). The safety requirements for these three elements are derived from safety goals. As stated above, the EPS E&E system is rated as ASIL D level. Thus, the safety requirements for power supply, micro controller and pre-driver are also ASIL D level. However, that does not mean every part of the elements should be ASIL D but only safety related.

The purpose of the safety mechanism can be made into three parts: 'safe acquisition', 'safe calculation' and 'safe actuation'. 'Safe acquisition' means the sensor information is correct. Sensor is relative simple compared with micro controller and MOSFET driver. The usual way to make safe acquisition is redundancy which means two sensors are used for one signal sense.

'Safe calculation' means the micro controller works correctly, see as Fig. 55.4a. There are three things need to be considered for 'safe calculation': operational condition; random hardware fault; software fault. Operational condition is mainly about power supply, temperature etc. The random hardware fault for micro controller is about soft fault and hard fault. Soft fault is related with memory data transient transition, like '0' change to '1'. Hard fault is permanent fault, e.g. GPIO stuck at '1'. The software fault is systematic fault. It can be avoided by correct developing procedure. The random hardware is not avoidable but only reduced. It is protected by internal safety mechanism (e.g. lockstep CPU) and the internal safety mechanism is monitored by self-test unit. However, the internal safety mechanism and self-test may be malfunction during worst work condition, e.g. over voltage, under voltage, over temperature. Thus, external safety mechanism is applied on micro controller.

'Safe actuation' means the MOSFET driver can output correctly according to the input and can be shut down at failure situation, shown as Fig. 55.4b. The MOSFET driver contains functional units such as charge pump and sub power supply. Their failure modes such as over temperature, over-voltage and under-voltage should be monitored by safety mechanism. And the MOSFET failure modes should also be

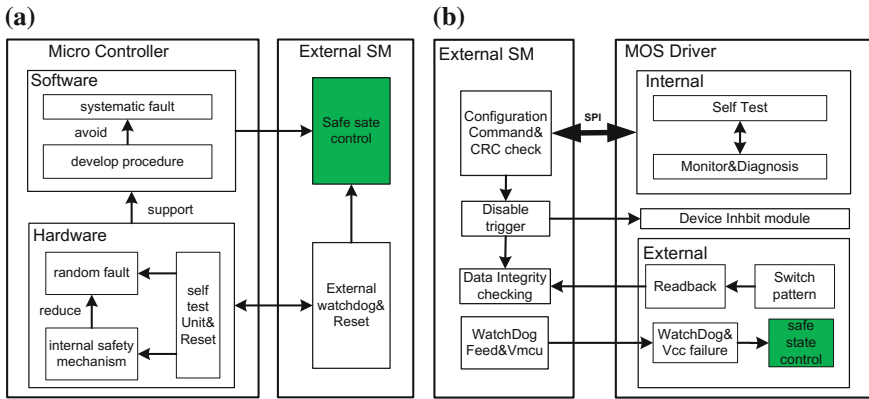


Fig. 55.4 a Safe calculation concept diagram b Safe actuation concept diagram

diagnosed such as short to GND or short to battery by safety mechanism. All these safety mechanism is also monitored by self-test unit. These safety mechanisms are referred as internal safety mechanism. And they can be configured by a safe SPI interface (CRC check applied). What’s more, the switch pattern need to be checked to guarantee the MOSFETs is switched as the software commands. Thus an independent read back loop from MOSFETs are integrated. Then the read back result can be compared with the original switching command. If not the same, the micro controller can inhibit the MOSFET driver which makes the system into safe state. A watchdog is also integrated for monitoring the MCU. The watchdog feed failure or MCU supply Vcc failure will trigger the safe state control active which will output a signal to cut off the motor phase current.

As functional safety focuses on E/E system, all parts need power supply. Then, ‘safe supply’ should be included in the safety concept. The basic safety function for the supply IC is detecting under voltage and overvoltage failure events in supplying the attached elements (MCU, sensors, and transceiver), and generates the reset or interrupt signals as configured. It shall also read the hardware status of MCU, which indicates on ERR pin of MCU. What’s more, the supply IC shall monitor the microcontroller software operation by means of watchdog and it shall provide a Safe State Control (SSC) capability in case the watchdog feed failure. The whole safety mechanism is presented as Fig. 55.5 considering safe supply, safe calculation, safe actuation and safe acquisition.

55.5 Safety Analysis

The main task of safety analysis is to examine the consequences of faults and failures on the functions, behavior and design of items and elements and check target safe state is achieved or not. Safety analysis is not only able to verify the

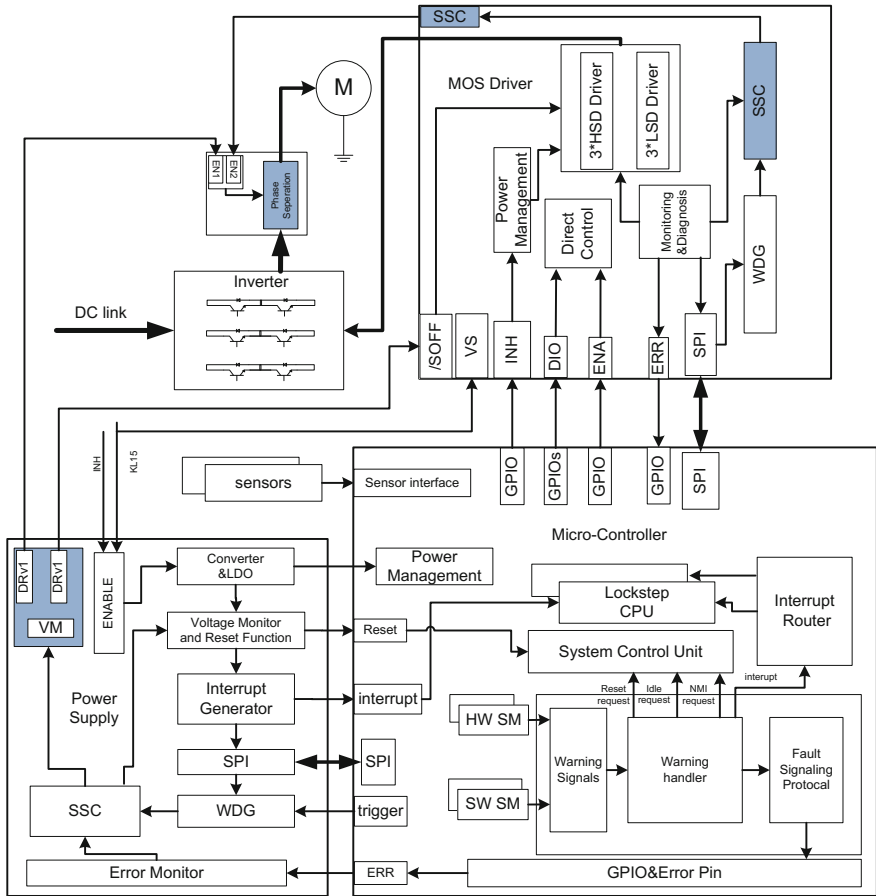


Fig. 55.5 Safety mechanism block diagram

Table 55.4 Single point fault metric for ASIL ratings

	ASIL B	ASIL C	ASIL D
SPFM	≥ 90%	≥ 97%	≥ 99%

Table 55.5 Latent fault metric for ASIL ratings

	ASIL B	ASIL C	ASIL D
LFM	≥ 60%	≥ 80%	≥ 90%

safety concept but also can correct the defect part of the preliminary safety design. Safety analysis is a dynamic process. It should be done from the concept phase to the development phase; thus it will be updated frequently. Safety analysis can be performed on different level of abstraction such as item level or element level (system, hardware, software) (Tables 55.4 and 55.5).

FMEDA is the typical quantitative method for safety analysis, which means failure mode effect and diagnostic analysis. FMEDA is a powerful tool that it can be used for different levels analysis such as system, sub system, component, component part etc. The key point for FMEDA is making a worksheet according to ISO 26262 requirement. Normally, the FMEDA format is changeable, but the FMEDA need to cover failure rate related with dedicated failure mode (also failure distribution and classification, for example microcontroller has permanent and transient failures), the safety mechanism that mitigates the hazard and the required hardware metrics as residual or single point fault metric and latent fault metric for the failure mode. FMEDA is the IP of the designer for functional safety and usually it is confidential. Table 55.6 is an example of the FMEDA. For real application, the FMEDA need consider each part of the hardware design. It performs as an important rational to support the functional safety argument. Sometimes, the FMEDA is made up with two parts as FMEA (failure mode and effect analysis) and DC (diagnosis coverage) worksheets.

Different ASIL rating level item requires different quantitative specifications. According to ISO 26262, there are two kinds of hardware evaluation parameters which are hardware architectural fault metrics and random hardware failure rate. The hardware architectural fault metrics contains single point fault and latent fault metrics which are integrated into FMEDA. The definition of SPFM and LFM are list as Eq. 55.1 and Eq. 55.2.

$$SPFM = 1 - \frac{\sum_{SR,HW} (\lambda_{SPF} + \lambda_{RF})}{\sum_{SR,HW} \lambda} = \frac{\sum_{SR,HW} (\lambda_{MPF} + \lambda_S)}{\sum_{SR,HW} \lambda} \quad (55.1)$$

$$LFM = 1 - \frac{\sum_{SR,HW} (\lambda_{MPF,L})}{\sum_{SR,HW} (\lambda_{MPF} + \lambda_S)} = \frac{\sum_{SR,HW} (\lambda_{MPF,DP} + \lambda_S)}{\sum_{SR,HW} (\lambda_{MPF} + \lambda_S)} \quad (55.2)$$

Notes:

SPF	single point fault;
RF	residual fault;
MPF	multi-point fault;
S	safe fault;
SR	safety related;
MPF, L	latent multi-point fault;
MPF, DP	detected or perceived multi-point fault.

The fault metrics requirements for different ASIL levels are contained in Table 55.6.

The other parameter that needs to be calculated is the system random hardware failure rate. ISO 26262 suggests the method of using a probabilistic metric called “Probabilistic Metric for random Hardware Failures” (PMHF) to evaluate the violation of the considered safety goal. As stated in ISO 26262, if the fault point number is more than three, then the fault is considered to be safe multipoint fault

Table 55.6 FMEDA example

Component	Sub-part	Safety related?	Failure mode	Failure rate	SM preventing SG violation	Failure mode coverage wit. SG violation	Residual or singles point fault failure rate	SM preventing latent fault	Failure mode coverage wit. Latent failures	Latent fault failure rate
Pre-driver	Power supply	SR	S2G	20	SM1	70%	6	SM1	90%	$(20-6) * 10\% = 1.2$
							
Safety mechanism	SM1	SR								
	...									
							Total single point failure rate: xxx			Total latent failure rate: xxx
							SPFM: XXX			LFM: XXX
							Total failure rate: xxx			
							Total Safety Related: xxx			
							Total Not Safety Related: xxx			

Table 55.7 PMHF for ASIL ratings

	ASIL B	ASIL C	ASIL D
PMHF	$<10^{-7}h^{-1}$ or $< 100FIT$	$<10^{-7}h^{-1}$ or $< 100FIT$	$<10^{-8}h^{-1}$ or $< 10FIT$

Table 55.8 Failure rates for ‘blocked steering’

Name	Parameters	Failures for ‘blocked steering’
Total failure rate	λ	51.3 FIT
Safe faults	λ_s	21.9 FIT
Single point and residual faults	$\lambda_{SPF} + \lambda_{RF}$	0.3 FIT
Detected multiple point faults	$\lambda_{MPF,D}$	26.3 FIT
Latent multiple point faults	$\lambda_{MPF,L}$	2.8 FIT
Not safety related faults	λ_{NSR}	35.9 FIT
Single point fault metric	SPMF	99.5%
Latent fault metric	LFM	94.5%
Probabilistic metric for random hardware failures	PMHF	0.3 FIT

unless other evidence is provided. Thus, PMHF only consider the single point fault and the dual point fault. Usually, a mission block is monitored by safety mechanism. The failure of safety mechanism should be considered when evaluating the failure of the mission. And the calculation method is carried on as Eq. 55.3 stated. The target of different ASIL level hardware failure rate is as Table 55.7. The total failure result is shown as Table 55.8, taking ‘blocked steering’ as an example. The SPMF, LFM and PMHF of ‘blocked steering’ are all located in ASIL D range

$$M_{PMHF} = \lambda_{m,RF} + \frac{1}{2} \lambda_{m,DPF} (\lambda_{sm,RF} + \lambda_{sm,DPF,latent}) T_{lifetime} \tag{55.3}$$

Notes:

- m, RF residual fault of mission block;
- m, DPF dual point fault of mission block;
- sm, RF residual fault of safety mechanism;
- sm, DPF, latent latent fault of safety mechanism.

55.6 Markov Analysis for Safety Path

Safety path (short as SP) means a signal loop that makes the item enter into safety state. As for EPS application, the signal will trigger the phase separation module or shutting down the power supply. The safety path is very significant for system safety. If safety path is failed, the safety state cannot be reached when there is item

malfunction. For functional safety purpose, one safety path is not safe enough. The common way is to offer at least two safety paths to achieve ASIL D functional safety rating. These two safety paths should be independent with each other. Hereafter, the safety paths for EPS system are presented. There are three main parts in the EPS control unit which are power supply, micro-controller and MOSFET driver. Each device is possible to trigger the safety path. There are three implementation topologies for safety path as Fig. 55.6 shows. The basic idea of the safety path is to activate the phase separation unit or cut off the power supply of the power stage which makes the motor stop running. Then power steering is lost when enter into safe state and only manual steering is possible.

- Safety path by supply and driver, as showed in Fig. 55.6a. SP1 is triggered by safety power supply safety mechanism such as watchdog feeding failure by MCU, over voltage, under voltage, short circuit and over temperature. If these hazards happen, the safety mechanism of power supply will activate the safety path signal. The signal form can be low, high, PWM or PFM etc. SP2 is triggered by safety driver. The trigger command is issued from MCU or the internal mechanism of safety driver. For instance, if the MCU fails to feed the watchdog of safety driver and the MCU supply is under voltage, the safety sate control unit of the driver will be activated. Also there will be short circuit on the MOSFET,

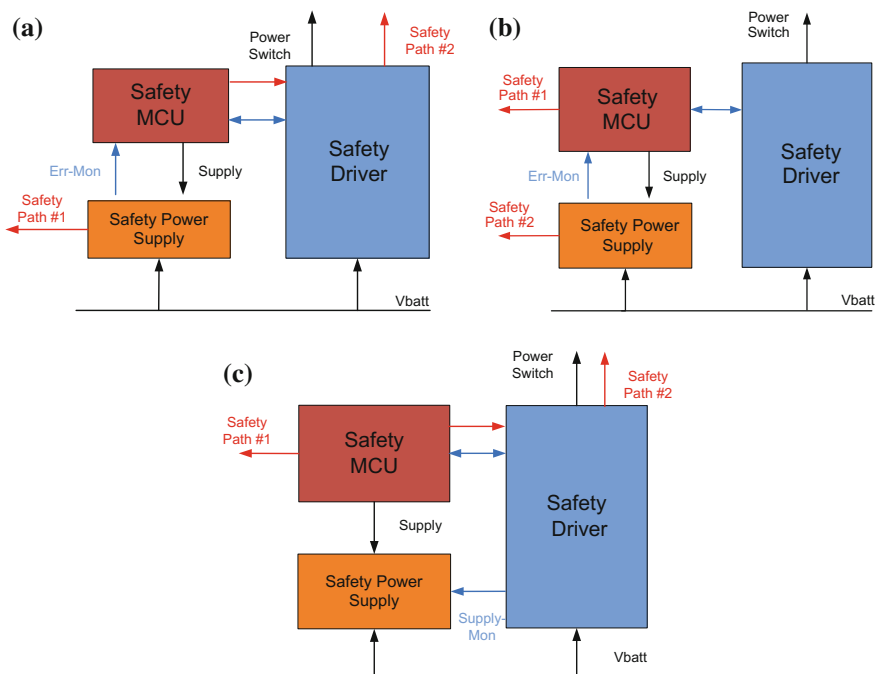


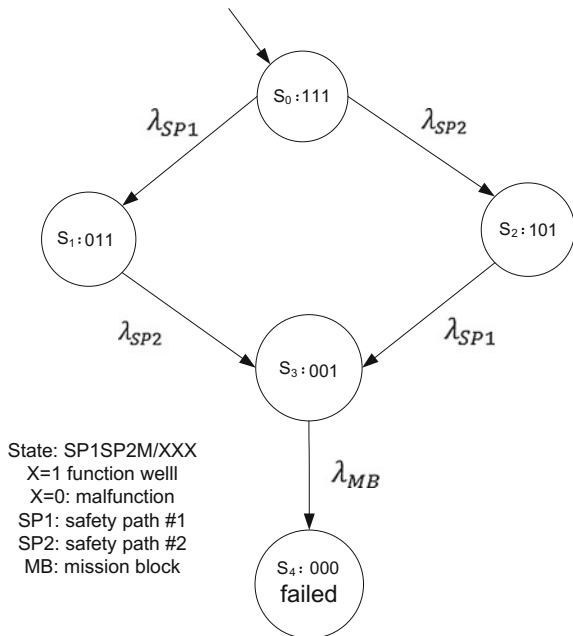
Fig. 55.6 a SP by supply and driver b SP by MCU and supply c SP by MCU and driver

wrong switching pattern, communication fault alike, all these faults will be sensed by MCU and MCU will trigger the SP2 according to the software strategy.

- Safety path by MCU and supply, as showed in Fig. 55.6b. This scenario is a little different from Fig. 55.6a. The safety driver does not contain safe state control unit to generate the safety path signal for entering into safety state, however other general safety mechanism still exist. Instead, the safety MCU is able to issue a safety path signal directly which will trigger the external module (for EPS, it is phase separation module or power supply load switch) which will make the EPS system into safe state.
- Safety path by MCU and driver, as showed in Fig. 55.6c. For this scenario, the safety power supply does not generate the safety path signal as previous stated. The two safety paths are implemented by the safety MCU and the safety driver. In this case, the MCU performs significant role for safety path. It not only can trigger the safety path related with safety driver, but also it can independently issue a safety path. However, the SP2 is independent with MCU since the driver has internal mechanism to trigger the SP2 without the involvement of MCU.

As stated before, the safety path concept is critical for the item functional safety. The three safety path topologies for EPS can be modeled by Markov model as Fig. 55.7 shows. Markov model is suitable for system level failure analysis. Three elements need to be considered which are mission block, the first safety path and the second safety path. There is no priority difference between these two safety paths. The system is sentenced to be failed only the three elements are all failed,

Fig. 55.7 Markov chain modeling for safety path



assuming the safety paths is more robust than the mission block. The failure rate of the mission block and safety path can be found in FMEDA and PMHF results.

In order to implement Markov method, you have to define the operating states of the item and figure out the state transfer diagram; then write down the equations according to the state transfer diagram and solve the differential equation. The state failure probability changing rate is decided by the input failure probability changing rate and the output failure probability changing rate. The failure probability changing rate is the product of failure rate and failure probability. And the input flow of the state in state transfer diagram is referred to as positive. And output is negative.

Here we define the EPS system state. We consider SP1, SP2, MB (mission block) and define element function variable X_i and item state variable S_i as bellow:

$$X_i = \begin{cases} 1 & \text{if } SP1, SP2 \text{ or } MB \text{ function well} \\ 0 & \text{if } SP1, SP2 \text{ or } MB \text{ malfunction} \end{cases}, i = SP1, SP2, MB$$

$$S_i = X_{SP1}X_{SP2}X_{MB}, i = 0, 1, 2, 3, 4$$

As stated above, SP1 and SP2 are independent with each other. Their failures are also independent with each other. Thus, there are two failure paths as showed in Fig. 55.7. The item's initial state is S_0 , in which safety paths and mission block all works well. Then the item can either run into S_1 or S_2 , with one safety path fails, but the whole system still works. Then the system will run into S_3 , where both safety paths fails, but the mission block still works. Last but not the least, the item will run into failure state, which is S_4 , mission block does not works anymore. The failure rate of safety path #1, safety path #2 and mission block are written as λ_{SP1} , λ_{SP2} , λ_{MB} . The Markov chain of the item is illustrated as Fig. 55.7.

The differential equation of the Markov chain is list as bellow. The state S_4 is the system failure state and the calculation of the probability of P_{S4} is significant for item performance evaluation.

$$\begin{cases} \frac{dP_{S0}}{dt} = -(\lambda_{SP1} + \lambda_{SP2})P_{S0} \\ \frac{dP_{S1}}{dt} = \lambda_{SP1}P_{S0} - \lambda_{SP2}P_{S1} \\ \frac{dP_{S2}}{dt} = \lambda_{SP2}P_{S0} - \lambda_{SP1}P_{S2} \\ \frac{dP_{S3}}{dt} = \lambda_{SP1}P_{S2} + \lambda_{SP2}P_{S1} - \lambda_{MB}P_{S3} \\ \frac{dP_{S4}}{dt} = \lambda_{MB}P_{S3} \end{cases} \quad (55.4)$$

Assume the following:

$$\begin{cases} \lambda_{MB} \neq \lambda_{SP1} \\ \lambda_{MB} \neq \lambda_{SP2} \\ \lambda_{MB} \neq \lambda_{SP1} + \lambda_{SP2} \end{cases}$$

The initial state $P(0) = [1, 0, 0, 0, 0]$, then the solutions of P_{S4} can be found:

$$P_{S4} = 1 - \left[\frac{\lambda_{SP1} + \lambda_{SP2}}{\lambda_{MB} - \lambda_{SP1} - \lambda_{SP2}} - \frac{\lambda_{SP1}}{\lambda_{MB} - \lambda_{SP1}} - \frac{\lambda_{SP2}}{\lambda_{MB} - \lambda_{SP2}} \right] e^{-\lambda_{MB}T} - \frac{\lambda_{MB}}{\lambda_{MB} - \lambda_{SP1}} e^{-\lambda_{SP1}T} - \frac{\lambda_{MB}}{\lambda_{MB} - \lambda_{SP2}} e^{-\lambda_{SP2}T} + \frac{\lambda_{MB}}{\lambda_{MB} - \lambda_{SP1} - \lambda_{SP2}} e^{-(\lambda_{SP1} + \lambda_{SP2})T}$$
(55.5)

Here T is the lifecycle of item; λ_{MB} is the mission block failure rate; λ_{SP1} is the first safety path failure rate; λ_{SP2} is the second safety path failure rate. Normally, the inequations as bellow are correct for real application since safety mechanism should be more reliable than mission block.

$$\begin{cases} \lambda_{MB} > \lambda_{SP1} \\ \lambda_{MB} > \lambda_{SP2} \end{cases}$$

Considering different failure rate of safety path, two scenarios are considered as Table 55.9 shows. A Matlab program is made to simulate the Markov model. To verify the plausibility of the safety path, a raw failure rate set is chosen $[\lambda_m, \lambda_{SP1}, \lambda_{SP2}]$ as $[1E-03/h, 1E-04/h, 1E-04/h]$ on purpose. For reality, the failure rate is much smaller. The reason for choosing this set is to show that although the block mission and the safety path have considerable high failure rate, but the combination of these two ones make the failure rate decrease a lot. Figure 55.8a shows that the safety path makes the safety performance improved a lot for the item lifecycle. The ‘safety improvement’ curve shows that the greatest improvement point happens at the middle range time of the vehicle life cycle. Figure 55.8b indicates that the lower of the safety path failure rate, the more reliable of the system. Scenario #1’s failure probability of the item is greatly decreased compared with scenario #2. It also indicates that scenario #1 is one of failure rate allocation to safety elements to fulfill ASIL D item.

Table 55.9 Typical values of parameters for Fig. 55.8b

Senario1: $\lambda_m > \lambda_{SP1} + \lambda_{SP2}$		Senario2: $\lambda_m < \lambda_{SP1} + \lambda_{SP2}$	
λ_m	1E-06/h	λ_m	1E-06/h
λ_{SP1}	1E-07/h	λ_{SP1}	6E-07/h
λ_{SP2}	1E-07/h	λ_{SP2}	5E-07/h
T	10 000 h	T	10 00 h

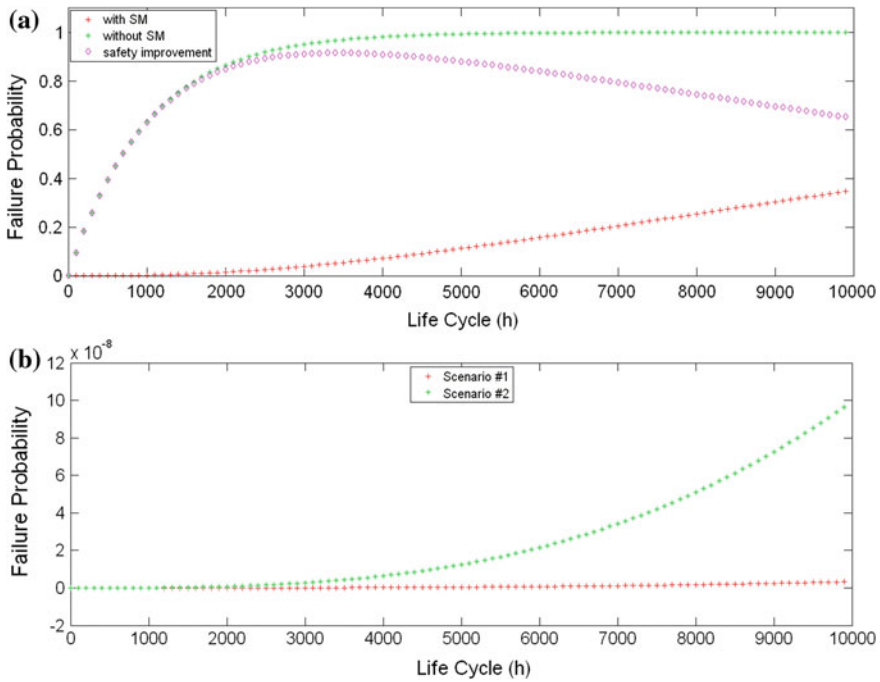


Fig. 55.8 a Safety path performance evaluation ($[\lambda_m, \lambda_{SP1}, \lambda_{SP2}] = [1E-03/h, 1E-04/h, 1E-04/h]$)
 b Two failure rate scenarios of SP (parameters see Table 55.9)

55.7 Conclusion

Functional safety requirement is becoming more and more compulsory these days. What makes safety related item development different is that the item is driven by safety goal. And safety goals of the item are generated from hazard analysis and risk assessment. By achieving the safety goals via V model design method, the risk of harm from item malfunction thus can be decreased to an acceptable low level. To make this argument persuasive enough, safety analysis need to be conducted. This paper proposed safety path concept and fulfilled the safety concept design. And also the item safety performance is investigated by Markov model. The simulation result shows that the safety path improved the item safety a lot even the raw failure rate of the item is somehow large. This paper mainly covers the concept design and hardware evaluation, the principle of system safety software design is the further work direction.

References

1. Dhoubi MS, Perquis JM, Saintis L, Barreau M (2014) Automatic decomposition and allocation of safety integrity level using system of linear equations. In: The fourth international conference on performance, Safety and robustness in complex systems and applications
2. Mader R, Armengaud E, Leitner A, Steger C (2012) Automatic and optimal allocation of safety integrity levels. In: Proceedings—annual reliability and maintainability symposium (RAMS)
3. Parker D, Walker M etc(2013) Automatic decomposition and allocation of safety integrity levels using a penalty-based genetic algorithm. In: Ali M et al. (eds.): IEA/AIE 2013, LNAI 7906, pp 449–459
4. Baumgart S (2012) Investigations on hazard analysis techniques for safety critical product lines. In: IRSCE'12, Västerås, Sweden, Nov. 11
5. Birch J, Rivett R, Habli I (2013) Safety cases and their role in ISO 26262. In: Functional safety assessment, safety, reliability, and security lecture notes in computer science Vol 8153 pp. 154–165
6. Cherfi A (2014) Modeling automotive safety mechanisms: a markov chain approach reliability engineering and system safety 130 pp. 42–49
7. Infineon internal training notes, 2014
8. ISO: ISO 26262-3 Road Vehicles—Functional Safety. ISO Standard (2011)
9. ISO: ISO 26262-4 Road Vehicles—Functional Safety. ISO Standard (2011)
10. ISO: ISO 26262-5 Road Vehicles—Functional Safety. ISO Standard (2011)